Hospital data chaos threatens COVID-19 response p. 1148

New books to inspire young scientists p. 1156

Probing beetle flight to improve robot stability pp. 1165 & 1214

Science

$15
4 DECEMBER 2020
sciencemag.org

AAAS

SUBTERRANEAN COMPETITION

Plant root growth adjusts to optimize nutrient foraging pp. 1167 & 1197

CONTENTS

4 DECEMBER 2020 • VOLUME 370 • ISSUE 6521

NEWS

IN BRIEF

1142 News at a glance

IN DEPTH

1144 'The game has changed.' AI triumphs at protein folding
In milestone, software predictions finally match structures calculated from experimental data *By R. F. Service*

1145 Why were salmon dying? The answer washed off the road
Common tire chemical implicated in coho salmon kills *By E. Stokstad*
REPORT BY Z. TIAN *ET AL.* 10.1126/SCIENCE.ABD6951

1146 Scientists fear no-deal Brexit as deadline looms
U.K. researchers in limbo, weeks from crashing out of EU trade and travel rules *By C. O'Grady*

1147 How cats get their stripes and spots
Newly uncovered mechanism may pattern the coats of other mammals, too *By E. Pennisi*

1148 Federal hospital data system falters at tracking pandemic
HHS Protect data, which influence how pandemic supplies and support are allocated, conflict with other data sources *By C. Piller*

1150 New challenges emerge for planned human challenge trials
Scientists debate risks and benefits of intentionally exposing volunteers to dangerous virus *By W. Cornwall*

1151 Amid the cheering, some vaccines face questions
A candidate from AstraZeneca and the University of Oxford has puzzling efficacy data *By J. Cohen*

FEATURES

1152 Saving sanctuaries
Critics charge that sanctuaries for retired research chimpanzees are failing their animals. Can a new tool help? *By D. Grimm*

INSIGHTS

BOOKS *ET AL.*

1156 Fodder for future scientists

PERSPECTIVES

1162 Quantum-limited sound attenuation
Resonantly interacting atoms confined by lasers have implications for neutron stars *By T. Schaefer*
REPORT p. 1222

Celebrity chimpanzee Hercules is making new friends at Project Chimps.

1163 Enzyme formation by immune receptors
Upon pathogen recognition, some plant immune receptors assemble into active enzyme complexes *By L. Tian and X. Li*
RESEARCH ARTICLES pp. 1184 & 1185

1165 Miniaturization of robots that fly on beetles' wings
The shock-absorbing wings of the rhinoceros beetle battle in-flight collisions *By J. Sun*
REPORT p. 1214

1166 Probing the dark side of the exciton
Photoemitted electrons reveal large-momentum ("dark") excitons in monolayer WSe_2 *By M. X. Na and Z. Ye*
REPORT p. 1199

1167 Constraints on selfish behavior in plants
Plants overproduce roots to secure resources nearby but avoid costly trips to neighbors' patches *By M. Semchenko*
REPORT p. 1197

1168 Stimulating the brain to restore vision
High-definition brain prostheses are developed for treating blindness *By M. S. Beauchamp and D. Yoshor*
RESEARCH ARTICLE p. 1191

1170 Mario J. Molina (1943–2020)
Visionary environmental chemist *By K. A. Prather*

POLICY FORUM

1171 Fossil electricity retirement deadlines for a just transition
A 2035 deadline for decarbonizing U.S. electricity would strand only about 15% of fossil capacity-years *By E. Grubert*

ILLUSTRATION: HANNAH AGOSTA; PHOTO: ALYSSA NEWBERRY

Published by AAAS

LETTERS

1174 Evidence-based hunting policy needed in Slovakia
By M. Kutal and M. Dula

1174 Computational social science: On measurement
By A. X. Wu et al.

1175 Chinese sturgeon needs urgent rescue
By X. Zhou et al.

1175 Errata

RESEARCH

IN BRIEF

1177 From *Science* and other journals

REVIEW

1180 Microbiota
The role of the microbiota in human genetic adaptation
T. A. Suzuki and R. E. Ley
REVIEW SUMMARY; FOR FULL TEXT: DX.DOI.ORG/10.1126/SCIENCE.AAZ6827

RESEARCH ARTICLES

1181 Coronavirus
Comparative host-coronavirus protein interaction networks reveal pan-viral disease mechanisms *D. E. Gordon* et al.
RESEARCH ARTICLE SUMMARY; FOR FULL TEXT: DX.DOI.ORG/10.1126/SCIENCE.ABE9403

1182 Innate immunity
Enteroviral 3C protease activates the human NLRP1 inflammasome in airway epithelia
K. S. Robinson et al.
RESEARCH ARTICLE SUMMARY; FOR FULL TEXT: DX.DOI.ORG/10.1126/SCIENCE.AAY2002

1183 Evolution
Selection enhances protein evolvability by increasing mutational robustness and foldability *J. Zheng* et al.
RESEARCH ARTICLE SUMMARY; FOR FULL TEXT: DX.DOI.ORG/10.1126/SCIENCE.ABB5962

Plant science

1184 Direct pathogen-induced assembly of an NLR immune receptor complex to form a holoenzyme *S. Ma* et al.
RESEARCH ARTICLE SUMMARY; FOR FULL TEXT: DX.DOI.ORG/10.1126/SCIENCE.ABE3069

1185 Structure of the activated ROQ1 resistosome directly recognizing the pathogen effector XopQ *R. Martin* et al.
RESEARCH ARTICLE SUMMARY; FOR FULL TEXT: DX.DOI.ORG/10.1126/SCIENCE.ABD9993
PERSPECTIVE p. 1163

1186 Developmental biology
The N-glycome regulates the endothelial-to-hematopoietic transition *D. M. Kasper* et al.

1191 Neuroscience
Shape perception via a high-channel-count neuroprosthesis in monkey visual cortex
X. Chen et al.
PERSPECTIVE p. 1168; PODCAST

REPORTS

1197 Plant science
The exploitative segregation of plant roots
C. Cabal et al.
PERSPECTIVE p. 1167

1199 Physics
Directly visualizing the momentum-forbidden dark excitons and their dynamics in atomically thin semiconductors
J. Madéo et al.
PERSPECTIVE p. 1166

1204 Spectroscopy
Super-resolution lightwave tomography of electronic bands in quantum materials
M. Borsch et al.

1208 Coronavirus
De novo design of potent and resilient hACE2 decoys to neutralize SARS-CoV-2
T. W. Linsky et al.

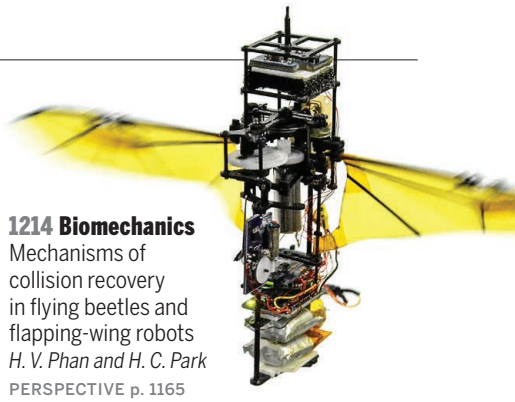

1214 Biomechanics
Mechanisms of collision recovery in flying beetles and flapping-wing robots
H. V. Phan and H. C. Park
PERSPECTIVE p. 1165

1219 Tropical forest
Long-term collapse in fruit availability threatens Central African forest megafauna
E. R. Bush et al.

1222 Quantum gases
Universal sound diffusion in a strongly interacting Fermi gas
P. B. Patel et al.
PERSPECTIVE p. 1162

1227 Coronavirus
Robust neutralizing antibodies to SARS-CoV-2 infection persist for months
A. Wajnberg et al.

1230 Deep biosphere
Temperature limits to deep subseafloor life in the Nankai Trough subduction zone
V. B. Heuer et al.

DEPARTMENTS

1141 Editorial
Low-income students lose ground
By Christopher Avery et al.

1242 Working Life
Coming out *By Bec Roldan*

ON THE COVER

Root systems of two different plants, stained with red and blue dye for fresh cut flowers. Root dyeing provided experimental validation of theoretical predictions regarding plants' response to competition. Neighbor plants segregate their root systems in the soil space but develop more roots locally when a competitor is close than when growing alone. See pages 1167 and 1197.
Photo: Mikel Ponce

New Products.....1235
Science Careers.....1236

PHOTO: H. V. PHAN AND H. C. PARK

SCIENCE (ISSN 0036-8075) is published weekly on Friday, except last week in December, by the American Association for the Advancement of Science, 1200 New York Avenue, NW, Washington, DC 20005. Periodicals mail postage (publication No. 484460) paid at Washington, DC, and additional mailing offices.

Copyright © 2020 by the American Association for the Advancement of Science. The title SCIENCE is a registered trademark of the AAAS.

Domestic individual membership, including subscription (12 months): $165 ($74 allocated to subscription). Domestic institutional subscription (51 issues): $2148; Foreign postage extra: Air assist delivery: $98. First class, airmail, student, and emeritus rates on request. Canadian rates with GST available upon request, GST #125488122. Publications Mail Agreement Number 1069624. **Printed in the U.S.A.**
Change of address: Allow 4 weeks, giving old and new addresses and 8-digit account number. **Postmaster:** Send change of address to AAAS, P.O. Box 96178, Washington, DC 20090–6178. **Single-copy sales:** $15 each plus shipping and handling available from backissues.sciencemag.org; bulk rate on request. **Authorization to reproduce** material for internal or personal use under circumstances not falling within the fair use provisions of the Copyright Act can be obtained through the Copyright Clearance Center (CCC), www.copyright.com. The identification code for *Science* is 0036-8075. *Science* is indexed in the *Reader's Guide to Periodical Literature* and in several specialized indexes.

Published by AAAS

EDITORIAL

Low-income students lose ground

Income inequality in college attendance and graduation in the United States was troublingly large before the pandemic. Without an aggressive infusion of federal support for schools and students, these already sizable gaps will likely widen into chasms.

Historically, a poor child in the United States has had a 10% chance of eventually earning a college degree; for children from well-off families, it's over 50%. The pandemic is widening these differences, thereby increasing poverty, reducing social mobility, and stunting economic growth. Data from the National Student Clearinghouse show that first-time enrollment at colleges and universities in the United States decreased by 13% from fall 2019 to fall 2020. At community colleges, the traditional gateway for disadvantaged students, freshman enrollment plunged 19%. Drops were largest among Black (18.7%), Hispanic (19.9%), and Native American (23.2%) students.

Low-income college students have historically been half as likely to graduate as their wealthier classmates. The pandemic is likely to worsen those odds. Effective remote learning requires a broadband connection, laptop, and a quiet, private space. Low-income students are the least likely to have this critical set of resources.

The hit to college enrollment may be even greater in fall 2021. Freshmen who entered college this past fall had only the tail end of their admissions cycle disrupted; the entire process has been turned upside down for next year's freshmen. Low-income and first-generation students depend on teachers, counselors, and coaches to get them through the bureaucratic and academic hurdles of college applications. Upper-income students typically have a family member who is a college graduate to play this role.

All schools are challenged by remote instruction, but those serving low-income students are also struggling with connecting their students to the internet and delivering school meals. There is now little time to spare for the formal and informal college counseling that schools traditionally provide. A leading indicator of the weakening support is a national drop in financial aid applications: FAFSA (Free Application for Federal Student Aid) filings are down by 16% among high school seniors, with the largest decreases among poor students.

The pandemic is not just hampering the process of applying for college, but also profoundly affecting student learning. Remote learning is difficult for most students, but financially secure families can afford to hire tutors, buy broadband connections, and provide computers for their children. In poorer families, there may not even be an adult at home to supervise children's schooling: Low-paid service jobs can rarely be completed remotely. A high school or college student from a low-income family may be watching over siblings, with all of them sharing a single electronic device to connect to the internet and coursework.

Public schools and colleges need more resources to provide high-quality remote learning, as well as to prepare schools for safe, in-person learning. Yet states are slashing education budgets. Public colleges (which serve the majority of American college students) are still reeling from funding cuts of the Great Recession of 2007–2009, and if state support continues to plummet, they will be forced to raise tuition and cut critical services. Rising tuition and shrinking supports will further reduce college attendance and intensify education inequality.

> "Rising tuition and shrinking supports will further... intensify education inequality."

Public schools, from preschool through college, need a financial rescue. But the states that traditionally fund these schools are facing enormous drops in tax revenue and cannot answer the call. The good news is that there are several sensible proposals to boost school spending with federal funds. The dollars need to flow, and quickly.

We cannot ask college students to borrow their way out of this pandemic, nor to work more, given the collapse of the labor market. Financial aid for college students must adjust to the economic devastation caused by the pandemic. The standard response of the aid system to a sharp downturn in a family's income is to demand supplementary paperwork. This protocol is designed for unusual cases, but right now the modal family is worse off than a year ago. The aid process should be streamlined and simplified to quickly get money out the door. For example, students who have already qualified for public assistance (such as food stamps through the Supplemental Nutrition Assistance Program or school meals) could automatically get grant aid.

Spending on education is an investment in the nation's future. An aggressive federal response is critical for getting students and schools through this perilous time.

–Christopher Avery, Susan Dynarski, Sarah Turner

Christopher Avery is the Roy E. Larsen Professor of Public Policy at the Harvard Kennedy School, Harvard University, Cambridge, MA, USA. chris_avery@harvard.edu

Susan Dynarski is a University Professor of Diversity and Social Transformation at the Ford School of Public Policy, School of Education and Department of Economics, University of Michigan, Ann Arbor, MI, USA. dynarski@umich.edu

Sarah Turner is a University Professor in the Department of Economics and Education and the Souder Family Chair at the University of Virginia, Charlottesville, VA, USA. sturner@virginia.edu

10.1126/science.abf9375

Published by AAAS

NEWS

> "I feel sick in my stomach. ... It's a really hard morning."
>
> **Ramon Lugo**, director of the Florida Space Institute at the University of Central Florida, which manages the 57-year-old Arecibo Observatory, after learning on 1 December that the already crippled radio telescope was destroyed when its 900-ton instrument platform collapsed.

Mohsen Fakhrizadeh's body was carried through the streets of Tehran, Iran.

PHOTO: IRANIAN DEFENSE MINISTRY VIA AP

IN BRIEF

Edited by **Lucy Hicks**

NONPROLIFERATION

Killing of Iran nuclear scientist dims diplomatic hopes

Last week's assassination of a prominent scientist who led Iran's clandestine nuclear weapons R&D program could chill prospects for reinvigorating a 2015 agreement impeding Iran's path to an atomic bomb in exchange for economic concessions. Physicist Mohsen Fakhrizadeh—often referred to as Iran's J. Robert Oppenheimer, who led the Manhattan Project in the United States during World War II—was slain in an attack on a highway outside of Tehran. His death follows a July explosion at an advanced centrifuge facility at Iran's Natanz nuclear site, which Iran labeled an act of sabotage. Neither of the blows, which Iran blamed on Israel, is likely to deal more than a tactical setback to Iran's nuclear ambitions, analysts say. Ali Akbar Salehi, president of the Atomic Energy Organization of Iran, says the country intends to carry on Fakhrizadeh's work. But Iran's actions in response to the assassination may determine the fate of the Iran nuclear deal, a multilateral pact that has gradually unraveled since President Donald Trump withdrew in May 2018. U.S. President-elect Joe Biden has said he hopes to revive it.

Nature sets open-access fee

PUBLISHING | The elite Nature family of 33 research journals, including the flagship *Nature*, announced on 24 November it will begin to charge authors €9500 to publish an article immediately free to read. The fee is thought to be the highest for any journal for open access. The Nature Research publishing group says the amount is necessary to cover the costs of the full-time editors and others who produce its primary research journals. The new policy is meant to satisfy open-access mandates by European funders seeking to eliminate subscription paywalls in order to speed the flow of scientific information. Nature Research intends to eventually convert its research journals to solely open access. The group also unveiled a pilot under which it will charge lower fees to determine whether a manuscript is worth consideration for one of six journals other than *Nature*, then peer review it, with an additional charge if the paper is ultimately accepted.

Integrity survey stumbles

RESEARCH INTEGRITY | The world's largest multidisciplinary survey on research integrity is falling short of its goals after two-thirds of invited institutions declined to collaborate. That left researchers leading the Dutch National Survey on Research Integrity to scrape many email addresses and solicit responses on their own. The survey will close next week, but the team has gathered responses from less than 15% of 40,000

Published by AAAS

targeted participants: all academics working in the Netherlands. Ten out of the nation's 15 universities declined to participate, with some university presidents saying the survey was too focused on bad behaviors, such as data falsification. Survey leaders had assured universities that the study would not generate an institutional ranking of misbehavior.

Ocean conservation gets boost

MARINE PLANNING | In a show of unity, 14 countries this week pledged to begin to manage all their national waters sustainably by 2025. The countries—including Australia, Indonesia, and Chile—control nearly 40 million square kilometers of ocean. The pledges lack specific targets, but instead offer a vision of ocean economies that protect marine resources and share benefits equitably. Led by Norway and Palau, the High Level Panel for a Sustainable Ocean Economy in 2018 commissioned some 250 scientists from 45 countries to analyze potential solutions, such as improving fisheries management and cutting ship pollution. The nations also pledged to support a global goal of protecting 30% of the ocean by 2030.

Permit denied for Pebble Mine

CONSERVATION | The U.S. Army Corps of Engineers on 25 November delivered a potentially fatal blow to plans for a controversial gold and copper mine in the Alaskan headwaters of the world's largest sockeye salmon runs. Corps officials determined the Pebble Mine was "contrary to the public interest" and denied a federal permit needed to build it. It was a surprise victory for mine opponents, including environmentalists and Alaska Native groups. In July, the corps had issued an environmental study concluding the mine posed little threat to the salmon. But in recent months, some conservatives spoke against the project, including President Donald Trump's son, Donald Trump Jr., who has fished for salmon there. Mine company officials said they would appeal the decision.

ESA nominates next director

SPACE | Space scientist Josef Aschbacher of Austria has been nominated as the next director general of the European Space Agency. An ESA insider, Aschbacher has since 2016 led the agency's highly successful Earth observation program, its largest directorate. If the nomination is approved by ESA's 22 member states on 17 December, Aschbacher will take the reins of the €6.7 billion agency from the current director general, Jan Wörner, in mid-2021.

Progeria treatment approved

DRUG DEVELOPMENT | Progeria, an ultrarare and fatal genetic disease that causes features of premature aging, now has its first approved treatment in the United States: a drug called lonafarnib. Fewer than 200 people worldwide are diagnosed with the condition, caused by a mutation in a gene for a protein that acts as a scaffold for cell nuclei. Defective forms of the protein accumulate in cells, causing young children to show signs of aging, including plaque buildup in the arteries. Most patients die from stroke, heart attack, or heart failure by their teens. Lonafarnib, developed by academic researchers and licensed by Eiger Biopharmaceuticals, curbs the abnormal protein buildup. It's far from a cure, but after 11 years of follow-up on 62 treated progeria patients in two small clinical trials, the drug extended expected life span by an average of 2.5 years. The Food and Drug Administration approved the drug on 20 November for both progeria and a set of related conditions known as progeroid laminopathies.

Japan primatologist fired

ANIMAL WELFARE | International researchers are defending renowned Kyoto University primatologist Tetsuro Matsuzawa, after his dismissal on 24 November for the improper handling of funds for construction work at two chimpanzee facilities. The dismissal stems from a university investigation citing Matsuzawa and others for the unauthorized use of funds and inappropriate handling of contract procedures involving 500 million yen ($4.8 million) to build large, interconnected cages at two primate research institutes. A separate investigation by the Board of Audit of Japan identified an additional 600 million yen also mishandled, though no funds were diverted for private use or to other projects. Matsuzawa says these conclusions reflect misunderstandings of the contracts with the two companies hired for the project. Other researchers say the firing seems harsh, given that all funds were spent building outstanding habitats.

This koala is recovering from burns from a wildfire.

PHOTO: NATHAN EDWARDS/GETTY IMAGES

CONSERVATION

Australia to count koalas

After massive bushfires last year killed thousands of koalas and incinerated up to 85% of their habitat in some regions, the Australian government has announced a $13 million effort to help these iconic animals bounce back. The spending includes $1.5 million for a population survey. Koalas are tricky to count, as they tend to hide in the treetops and spread out across a landscape, so this survey will involve heat-sensing drones, sound recordings, dogs that detect scat, and data collected by nonscientist observers. The program also allots $1.5 million to boost koala health research, because chlamydia and other diseases are the second largest recorded source of their mortality.

Published by AAAS

Structures of a protein that were predicted by artificial intelligence (blue) and experimentally determined (green) match almost perfectly.

IN DEPTH

STRUCTURAL BIOLOGY

'The game has changed.' AI triumphs at protein folding

In milestone, software predictions finally match structures calculated from experimental data

By **Robert F. Service**

Artificial intelligence (AI) has solved one of biology's grand challenges: predicting how proteins fold from a chain of amino acids into 3D shapes that carry out life's tasks. This week, organizers of a protein-folding competition announced the achievement by researchers at DeepMind, a U.K.-based AI company. They say the DeepMind method will have far-reaching effects, among them dramatically speeding the creation of new medications.

"What the DeepMind team has managed to achieve is fantastic and will change the future of structural biology and protein research," says Janet Thornton, director emeritus of the European Bioinformatics Institute. "This is a 50-year-old problem," adds John Moult, a structural biologist at the University of Maryland, Shady Grove, and co-founder of the competition, Critical Assessment of Protein Structure Prediction (CASP). "I never thought I'd see this in my lifetime."

The body uses tens of thousands of different proteins, each a string of dozens to hundreds of amino acids. The order of the amino acids dictates how the myriad pushes and pulls between them give rise to proteins' complex 3D shapes, which, in turn, determine how they function. Knowing those shapes helps researchers devise drugs that can lodge in proteins' crevices. And being able to synthesize proteins with a desired structure could speed development of enzymes to make biofuels and degrade waste plastic.

For decades, researchers deciphered proteins' structures using experimental techniques such as x-ray crystallography or cryo–electron microscopy (cryo-EM). But such methods can take years and don't always work. Structures have been solved for only about 170,000 of the more than 200 million proteins discovered across life forms.

In the 1960s, researchers realized if they could work out all interactions within a protein's sequence, they could predict its shape. But the amino acids in any given sequence could interact in so many different ways that the number of possible structures was astronomical. Computational scientists jumped on the problem, but progress was slow.

In 1994, Moult and colleagues launched CASP, which takes place every 2 years. Entrants get amino acid sequences for about 100 proteins whose structures are not known. Some groups compute a structure for each sequence, while others determine it experimentally. The organizers then compare the computational predictions with the lab results and give the predictions a global distance test (GDT) score. Scores above 90 on the 100-point scale are considered on par with experimental methods, Moult says.

Even in 1994, predicted structures for small, simple proteins could match experimental results. But for larger, challenging proteins, computations' GDT scores were about 20, "a complete catastrophe," says Andrei Lupas, a CASP judge and evolutionary biologist at the Max Planck Institute for Developmental Biology. By 2016, competing groups had reached scores of about 40 for the hardest proteins, mostly by drawing insights from known structures of proteins that were closely related to the CASP targets.

When DeepMind first competed, in 2018, its algorithm, called AlphaFold, relied on this comparative strategy. But AlphaFold also incorporated a computational approach called deep learning, in which the software is trained on vast data troves—in this case, the sequences and structures of known proteins—and learns to spot patterns. DeepMind won handily, beating the competition by an average of 15% on each structure, and winning GDT scores of up to about 60 for the hardest targets.

But the predictions were still too coarse, says John Jumper, who heads AlphaFold's development at DeepMind. "We knew how far we were from biological relevance." So

Getting real

At the Critical Assessment of Protein Structure Prediction (CASP) competition, AlphaFold matched experimental findings on a measure of accuracy.

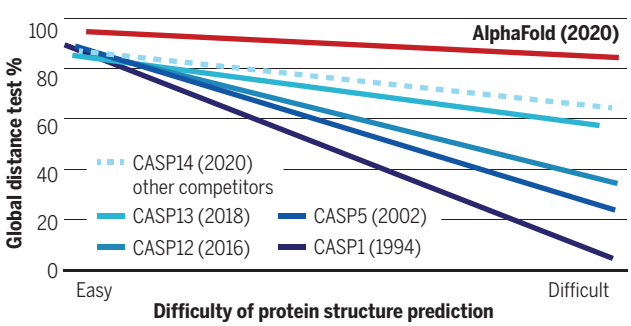

CREDITS: (IMAGE) DEEPMIND; (GRAPH) C. BICKEL/*SCIENCE*; (DATA) CASP

Published by AAAS

the team combined deep learning with an "attention algorithm" that mimics the way a person might assemble a jigsaw puzzle: connecting pieces in clumps—in this case clusters of amino acids—and then searching for ways to join the clumps in a larger whole. Working with a computer network built around 128 machine learning processors, they trained the algorithm on all 170,000 or so known protein structures.

And it worked. In this year's CASP, AlphaFold achieved a median GDT score of 92.4. For the most challenging proteins, AlphaFold scored a median of 87, 25 points above the next best predictions. It even excelled at solving structures of proteins that sit wedged in cell membranes, which are central to many human diseases but notoriously difficult to solve with x-ray crystallography. Venki Ramakrishnan, a structural biologist at the Medical Research Council Laboratory of Molecular Biology, calls the result "a stunning advance on the protein folding problem."

All groups in this year's competition improved, Moult says. But with AlphaFold, Lupas says, "The game has changed." The organizers even worried DeepMind may have cheated somehow. So Lupas set a special challenge: a membrane protein from a species of archaea, an ancient group of microbes. For 10 years, his team had tried to get its x-ray crystal structure. "We couldn't solve it."

But AlphaFold had no trouble. It returned a detailed image of a three-part protein with two helical arms in the middle. The model enabled Lupas and his team to make sense of their x-ray data; within half an hour, they had fit their experimental results to AlphaFold's predicted structure. "It's almost perfect," Lupas says. "They could not possibly have cheated on this. I don't know how they do it."

As a condition of entering CASP, DeepMind—like all groups—agreed to reveal sufficient details about its method for other groups to re-create it. That will be a boon for experimentalists, who will be able to use structure predictions to make sense of opaque x-ray and cryo-EM data. It could also enable drug designers to work out the structure of every protein in new and dangerous pathogens like SARS-CoV-2, a key step in the hunt for molecules to block them, Moult says.

Still, AlphaFold doesn't do everything well. In CASP, it faltered on one protein, an amalgam of 52 small repeating segments, which distort each others' positions as they assemble. Jumper says the team now wants to train AlphaFold to solve such structures, as well as those of complexes of proteins that work together to carry out key functions in the cell.

Even though one grand challenge has fallen, others will undoubtedly emerge. "This isn't the end of something," Thornton says. "It's the beginning of many new things." ■

PHOTO: KEVIN SCHAFER/GETTY IMAGES

WATER POLLUTION

Why were salmon dying? The answer washed off the road

Common tire chemical implicated in coho salmon kills

By **Erik Stokstad**

For decades, something in urban streams has been killing coho salmon in the U.S. Pacific Northwest. Even after Seattle began to restore salmon habitat in the 1990s, up to 90% of the adults migrating up certain streams to spawn would suddenly die after rainstorms. Researchers suspected the killer was washing off nearby roads, but couldn't identify it. "This was a serious mystery," says Edward Kolodziej, an environmental engineer at the University of Washington's (UW's) Tacoma and Seattle campuses.

Online this week in *Science*, researchers led by Kolodziej report the primary culprit comes from a chemical widely used to protect tires from ozone, a reactive atmospheric gas. The toxicant, called 6PPD-quinone, leaches out of the particles that tires shed onto pavement. Even small doses killed coho salmon in the lab. "It's a brilliant piece of work," says Miriam Diamond, an environmental chemist at the University of Toronto. "They've done a tremendous job at sleuthing out a very challenging problem."

Particles that erode from tires wash into streams used by coho salmon.

Manufacturers annually produce some 3.1 billion tires worldwide. Tire rubber is a complex mixture of chemicals, and companies closely guard their formulations. Because tire particles are a common component of water pollution, researchers have been examining how they affect aquatic life.

After Kolodziej arrived at UW's Center for Urban Waters in 2014, he joined the effort to solve the coho salmon mystery. The group created a mixture of particles from nine tires—some bought new, others provided by two undergraduates who moonlight as mechanics—to mimic what might wash off typical highways. They found several thousand unidentified chemicals in the mixture. Postdoc Zhenyu Tian spent more than 2 years narrowing down the list, separating the molecules based on their electrical charge and other properties. By May 2019, he had narrowed the focus to about 50 unknown chemicals, and then further work revealed the chemical formula of a prime suspect. "If you're looking for an unexplained toxicant that's killing fish, we had the perfect instruments and expertise," Kolodziej recalls.

But what was it? A 2019 report from the Environmental Protection Agency on chemicals in recycled tires mentioned 6PPD, which has a similar formula. The final clue was buried in an industry report from 1983, which contained the exact formula of 6PPD-quinone, the molecule created when 6PPD reacts with ozone. The team synthesized 6PPD-quinone and found it was highly lethal to coho salmon.

Now, the team is working to understand how the chemical kills fish. Kolodziej and colleagues say other species of fish should also be evaluated for sensitivity. Because you can't buy the molecule, Kolodziej's team is making it. "My lab might even be the only place that actually has this," he says.

The researchers suspect the compound is present on busy roads everywhere. They've found it washes off pavement and into streams in Los Angeles and San Francisco, for example. The simplest solution might be for tire manufacturers to switch to an environmentally benign alternative. But Sarah Amick, vice president of environment, health, safety, and sustainability at the U.S. Tire Manufacturers Association, says it's too early to discuss alternatives. "It's important that additional research be done to validate and verify these results."

Another way to protect salmon is to filter stormwater through soil, but installing enough infiltration basins to treat road runoff before it reaches spawning streams would be very expensive, says co-author Jenifer McIntyre, an ecotoxicologist at Washington State University's Puyallup Research and Extension Center. In the meantime, Kolodziej says he "can't walk along a street without staring at all the skid marks," thinking about tire chemicals, and "wondering what's there." ■

Published by AAAS

EUROPE

Scientists fear no-deal Brexit as deadline looms

U.K. researchers in limbo, weeks from crashing out of EU trade and travel rules

By **Cathleen O'Grady**

Brexit is set to become a reality, but its likely consequences for researchers are still emerging. The United Kingdom left the European Union on 31 January, but has remained part of EU trade and travel agreements while the final Brexit deal is negotiated. On 1 January 2021, those ties will be severed—and a Brexit deal has yet to materialize.

The future of research funding, international collaboration, and wrinkle-free supply chains of lab stocks hinge on the details of the final deal, but those issues are "some way back in the queue" behind the sticking points of a trade agreement, says James Wilsdon, a science policy expert at the University of Sheffield.

For U.K. scientists, the biggest question is whether they can be a part of the €85 billion 2021–27 Horizon Europe research funding program. Non-EU members can participate, but the United Kingdom is wavering over a potentially hefty price tag. The EU offer would see the United Kingdom pay in about £15 billion, plus a top-up payment if U.K. applicants win more than that in research grants. But because U.K. success rates in winning Horizon grants have fallen by almost one-third since the vote to leave Europe in 2016, it is likely to pay in much more than it gets out. Vivienne Stern, director of Universities UK International, estimates the 7-year premium at about £3 billion. Although Stern supports joining Horizon Europe, she told a parliamentary committee on 22 October the price is too high.

The benefits of international collaboration and access to diverse funding schemes could justify paying extra, but not such an "eye-watering" sum, says Kieron Flanagan, a science policy expert at the University of Manchester. U.K. research advocates have proposed a cap on any premium paid into Horizon Europe by non-EU countries, but the European Union has shown no sign of budging since its initial offer in March, says Martin Smith, a policy manager at the Wellcome Trust, a U.K. philanthropic research funder. "I'm currently optimistic that a way forward on costs can be found," he says, "but all this is moot if the wider negotiations collapse." Wilsdon is more pessimistic and suggests Horizon participation could stall even if a trade deal squeaks through.

Another issue that could disrupt research collaborations is data privacy. EU negotiators may deem U.K. data protection laws inadequate because of its broad use of surveillance, says Rosie Richards, head of digital policy at the NHS Confederation, which represents U.K. health providers. That could disrupt studies including those from the COVID-19 Genomics UK Consortium, which is working with the European Bioinformatics Institute to track clinical data and changes in the coronavirus genome to establish whether they link to easier transmission of the virus or more severe disease.

Less data sharing will also make it harder for the U.K. Medicines and Healthcare products Regulatory Agency (MHRA) to approve drugs. The agency was a major player in the European Medicines Agency, which relocated from London to Amsterdam in 2019. In January 2021, MHRA will go its own way, and it is likely to have a heftier workload looking at coronavirus drugs and vaccines, says Olivier Wouters, a health policy researcher at the London School of Economics. Brexit, he says, "couldn't come at a more inopportune time."

New customs regulations could disrupt the flow of critical university lab supplies, says Helen Dodd-Williams, head of strategic procurement at the North Western Universities Purchasing Consortium (NWUPC). A supply gap in some stocks—such as the liquid helium used to chill MRI machines—would cause severe disruption, she says, while products like antibodies have a short shelf life and can't be stored long in advance. Suppliers are developing contingency plans, such as routing lab supplies through other ports to avoid expected logjams in southeastern England.

No matter what deal emerges, Brexit is sure to change the flow of researchers themselves. EU citizens wishing to work in the United Kingdom will now need a visa, with requirements for a job offer, a salary above a certain threshold, and English language testing. The U.K. government is offering a new "global talent visa" that eliminates some bureaucratic hoops for researchers and technicians named on grants—including ones from Horizon Europe. But the cost of a 5-year visa for a family of four is nearly £15,000. "It's really quite prohibitively expensive," and might persuade researchers to land elsewhere in Europe, says James Tooze, a policy officer at the U.K. Campaign for Science and Engineering.

The visa requirements will also affect essential university workers, like building cleaners. NWUPC's suppliers are helping European employees with the paperwork that allows pre-Brexit residents to remain, but in the future they might not be able to recruit that labor so easily, Dodd-Williams says.

Brexit talks are still ongoing, with stubborn disagreements over rules that would prevent businesses on either side having an unfair advantage because of labor and environmental standards, or state subsidies. But even if a deal is struck and ratified by both sides before the end of the year, many details will linger. If the United Kingdom does not join Horizon Europe now, it could still choose to join months or years down the line. And the fallout from the new immigration restrictions and customs bureaucracy will take time to unfold.

Flanagan says Brexit means a permanently different relationship between the United Kingdom and Europe that will demand constant shifts and negotiations. "This is what people don't really understand," he says. "It will never be over." ■

ILLUSTRATION: DAVIDE BONAZZI/SALZMANART

Published by AAAS

DEVELOPMENTAL GENETICS

How cats get their stripes and spots

Newly uncovered mechanism may pattern the coats of other mammals, too

A mutated gene gives this tabby blotchy spots instead of the typical stripes.

PHOTO: JEAN-MICHEL LABAT/SCIENCE SOURCE

By **Elizabeth Pennisi**

When Rudyard Kipling told how the leopard got his spots, he missed the mark. Leopards have "rosettes"; spots are for cheetahs, says Gregory Barsh, a geneticist at the HudsonAlpha Institute for Biotechnology. But whatever you call the markings, how wild cats and their domestic counterparts acquire them has long been a mystery. Now, Barsh and his colleagues have found an answer. In so doing, they have shown that a 70-year-old theory explaining patterns in nature holds true for fur color in cats, and likely other mammals as well.

"This is an important paper unveiling part of the genetic basis [of] coat color markings so prominent in many mammals," says Denis Headon, a developmental biologist at the Roslin Institute. It also offers a glimpse of how those genes operate during development, forming what he calls a "highly adaptable mechanism" that responds to genetic tweaks to produce diverse coat patterns, from stripes to spots.

Biologists have identified hair follicle cells as the source of the black, brown, yellow, and red pigments that color hair or fur. "But we didn't know when and where the process of the establishment of the color pattern took place," Barsh says.

In 1952, computing pioneer Alan Turing suggested molecules that inhibit and activate each other could create periodic patterns in nature if they diffused through tissue at different rates. Thirty years later, other scientists applied his theory to develop a hypothesis about how spots, stripes, and other color patterns form during development. In this scheme, activator molecules color a cell but also trigger the production of inhibitors, which diffuse faster than the activators and can shut off pigment production. Last year, that idea was proved correct in plants called monkeyflowers: Researchers showed that dark, activated speckles on the petals become ringed with unpigmented tissue as inhibitors spread (*Science*, 30 August 2019, p. 854). And researchers had shown molecules following the Turing pattern help trigger the development of hair follicles in mice. But how coat color develops in mammals remained largely mysterious because mice and other easy-to-study lab animals lack spots or stripes.

So Barsh's team turned to domestic cats to track the identity of molecular activators and inhibitors of coat color. A decade ago, they tracked down a gene, *Tabby*, that, when mutated, gives tabby cats black blotches instead of their usual dark stripes. HudsonAlpha geneticist Christopher Kaelin found that same mutation in king cheetahs whose spots were unusually big and blotchy, suggesting the same genes color both wild and domestic cats.

To see what other genes and their mutations operate during development, Kaelin and HudsonAlpha colleague Kelly McGowan spent several years collecting discarded tissue from clinics that spay feral cats, which are often pregnant. They first noticed temporary thickenings of the skin of 28- to 30-day-old embryos, where black stripes would later appear in the fur. "There's a change [in the skin] that precedes and mimics what you observe in adult [fur]," McGowan explains.

The researchers then isolated and sequenced the active genes in individual skin cells of early embryos. At about 20 days old, embryos showed a sharp increase in the activity of several genes involved in a key developmental pathway, known as Wnt signaling, in skin areas destined to briefly thicken before the area becomes permanently dark. One of the most active genes was *Dkk4*, as they reported on 16 November in a preprint on bioRxiv. The team also found that mutations that inactivated *Dkk4* accounted for the loss of distinct markings in Abyssinian and Singpura breeds, making their spots too small to distinguish. *Tabby* and *Dkk4* "are in the same pathway," and likely work in both domestic and wild cats, Barsh explains, though he doesn't yet know how they are connected.

Dkk4 is a known inhibitor of Wnt signaling, which helps determine cell fates and spurs cell growth during development in many animals. The team found that in domestic cats, Wnt and Dkk4, respectively, are the activator and inhibitor. In dark skin, they exist in about equal amounts. But in paler areas, the faster moving Dkk4 protein most likely turns off Wnt, shutting down pigment production and thereby generating stripes, just as Turing's theory had predicted. "It is remarkable, although not altogether surprising, that we see Wnt-Dkk4 signaling again playing a critical early role," says Larissa Patterson, a developmental biologist at Rhode Island College.

"This paper provides thought-provoking insights into potential mechanisms of pattern diversity in wild cats," Patterson adds. It "greatly adds to the evidence" that this process is at work in cats and, most likely, other mammals, agrees Roland Baddeley, a computational neuroscientist at the University of Bristol.

Researchers had already shown the Turing mechanism involving Wnt and Dkk4 sets up the formation of hair follicles—but not coat color—later in mouse development. Barsh's team, however, found that the color pattern in cats and possibly other mammals is established well before hair follicles appear, suggesting early color patterns may guide hair follicle pigmentation.

That simple interactions among well-known molecules can explain the variety of coat color patterns in mammals is an example of nature's thriftiness, Headon says. "It suggests that the same molecules and pathways are likely to be reused for patterning of very different structures and at very different scales to form the intricate elements of the vertebrate anatomy." ■

Published by AAAS

COVID-19 wards like this one at University of Wisconsin Health in Madison are filling up fast, but federal data may not show that.

PHOTO: JOHN HART/*WISCONSIN STATE JOURNAL*/AP IMAGES

COVID-19

Federal hospital data system falters at tracking pandemic

HHS Protect data, which influence how pandemic supplies and support are allocated, conflict with other data sources

By **Charles Piller**

In mid-November, as the United States set records for newly diagnosed COVID-19 cases day after day, the hospital situation in one hard-hit state, Wisconsin, looked concerning but not yet urgent by one crucial measure. The main pandemic data tracking system run by the Department of Health and Human Services (HHS), dubbed HHS Protect, reported that on 16 November, 71% of the state's hospital beds were filled. Wisconsin officials who rely on the data to support and advise their increasingly strained hospitals might have concluded they had some margin left.

Yet a different federal COVID-19 data system painted a much more dire picture for the same day, reporting 91% of Wisconsin's hospital beds were filled. That day was no outlier. A *Science* examination of HHS Protect and confidential federal documents found the HHS data for three important values in Wisconsin hospitals—beds filled, intensive care unit (ICU) beds filled, and inpatients with COVID-19—often diverge dramatically from those collected by the other federal source, from state-supplied data, and from the apparent reality on the ground.

"Our hospitals are struggling," says Jeffrey Pothof, a physician and chief quality officer for the health system of the University of Wisconsin (UW), Madison. During recent weeks, patients filled the system's COVID-19 ward and ICU. The university's main hospital converted other ICUs to treat the pandemic disease and may soon have to turn away patients referred to the hospital for specialized care. Inpatient beds—including those in ICUs—are nearly full across the state. "That's the reality staring us down," Pothof says, adding: The HHS Protect numbers "are not real."

HHS Protect's problems are a national issue, an internal analysis completed this month by the Centers for Disease Control and Prevention (CDC) shows. (The report is available at https://scim.ag/36saba3.) That analysis, other federal reports, and emails obtained by *Science* suggest HHS Protect's data do not correspond with alternative hospital data sources in many states. "The HHS Protect data are poor quality, inconsistent with state reports, and the analysis is slipshod," says one CDC source who had read the agency's analysis and requested anonymity because of fear of retaliation from the Trump administration. "And the pressure on hospitals [from COVID-19] is through the roof."

Both federal and state officials use HHS Protect's data to assess the burden of disease across the country and allocate scarce resources, from limited stocks of COVID-19 medicines to personal protective equipment (PPE). Untrustworthy numbers could lead to supply and support problems in the months ahead, as U.S. cases continue to rise during an expected winter surge, according to current and former CDC officials. HHS Protect leaders vigorously defend the system and blame some disparities on inconsistent state and federal definitions of COVID-19 hospitalization. "We have made drastic improvements in the consistency of our data … even from September to now," says one senior HHS official. (Three officials from the department spoke with *Science* on the condition that they not be named.)

CDC had a long-running, if imperfect, hospital data tracking system in place when the pandemic started, but the Trump administration and White House Coronavirus Task Force Coordinator Deborah Birx angered many in the agency when they shifted much of the responsibility for COVID-19 hospital data in July to private contractors. TeleTracking Technologies Inc., a small Pittsburgh-based company, now collects most of the data, while Palantir, based in Denver, helps manage the database. At the time, hundreds of public health organizations and experts warned the change could gravely disrupt the ability to understand the U.S. pandemic and mount a response (*Science*, 23 October, p. 394).

The feared data chaos now seems a reality, evident when recent HHS Protect figures are compared with public information from states or data documented by another hospital tracking system run by the HHS Office of the Assistant Secretary for Preparedness and Response. ASPR manages the Strategic National Stockpile of medicines, PPE—in perilously short supply in many areas—and other pandemic necessities. ASPR collects data nationwide to help states and hospitals respond to the pandemic, although it is less comprehensive than HHS Protect.

In Alabama, HHS Protect figures differ by 15% to 30% from daily state COVID-19 inpatient totals. Karen Landers, assistant state health officer, said nearly all of the state's hospitals report data to HHS via the Alabama Department of Public Health. Although

Published by AAAS

reporting delays sometimes prevent the systems from syncing precisely, Landers says, she cannot account for the sharp differences.

Many state health officials contacted by *Science* were reluctant to directly criticize HHS Protect or attribute supply or support problems to its data. Landers notes that Alabama relies on its own collected data, rather than HHS Protect's, for its COVID-19 response. "We are very confident in our data," she says, because the state reporting system was developed over several years and required little adjustment to add COVID-19. HHS, she adds, has generally been responsive to state requests for medicines and supplies, although Alabama has not always gotten all the PPE it has requested.

Other states, however, say they do rely on HHS Protect. A spokesperson for the Wisconsin Department of Health Services wrote in a response to questions, "When making decisions at the state level we use the HHS Protect data," but declined to comment about its accuracy. HHS informed Wisconsin officials that it distributes scarce supplies based on need indicated by HHS Protect data, the spokesperson wrote.

Pothof says UW's hospital system has its own sophisticated data dashboard that draws on state, local, and internal sources to plan and cooperate on pandemic response with other hospitals. But small hospitals in Wisconsin—now experiencing shortages of some medicines, PPE, and other supplies—are more dependent on federal support largely based on HHS Protect data. Help might not arrive, Pothof says, if the data show "things look better than they are."

If the HHS Protect data are suspect, "that's a very large problem," says Nancy Cox, former director of CDC's influenza division and now an affiliated retiree of the agency. If HHS officials use bad data, they will not distribute medicines and supplies equitably, Cox notes, adding: "Undercounting in the hardest hit states means a lower level of care and will result in more severe infections and ultimately in more deaths."

Birx and the other managers of HHS Protect "really had no idea what they were doing," says Tom Frieden, CDC director under former President Barack Obama. (Birx declined to comment for this article.) Frieden cautions that ASPR data might also be erroneous—pointing to the need for an authoritative and clear federal source of hospital data. The original CDC system, called the National Healthcare Safety Network (NHSN), should be improved, he said, but it handles nursing home COVID-19 data skillfully and could do the same with hospitals. NHSN is "not just a computer program. It's a public health program" built over 15 years and based on relationships with individual health facilities, Frieden says. (CDC insiders say HHS officials recently interfered with publication of an analysis showing that NHSN performed well early in the pandemic. See https://scim.ag/MMWRQuestions.)

An HHS official says HHS Protect's data are complex and the department can't verify any findings in the reports reviewed by *Science* without conducting its own analysis, which it did not do. But the official says HHS Protect has improved dramatically in the past 2 months and provides consistent and reliable results.

Conflicting bed counts

Two Department of Health and Human Services (HHS) sections collect hospital patient data to battle the COVID-19 pandemic—HHS Protect and the Office of the Assistant Secretary for Preparedness and Response (ASPR). Their data sometimes conflict sharply, as shown in this 16 November summary of intensive care unit (ICU) beds occupied in six hard-hit Midwestern states. The difference noted parenthetically is ASPR's bed total minus HHS Protect's.

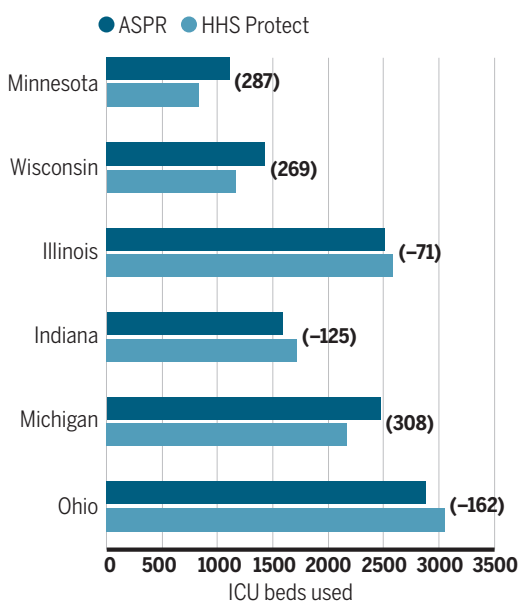

As for the difference between state and HHS Protect data, an HHS official contends state numbers "are always going to be lower" by up to 20%. That's because hospitals could lose Medicare funding if they do not report to HHS, the official says, but face no penalty for failing to report to the state. So rather than expect identical numbers, HHS looks for state and federal data to reflect the same trajectory—which they do in all cases for the number of COVID-19 inpatients, according to another confidential CDC analysis of HHS Protect, covering all 50 states.

Yet the same analysis found 27 states recently alternated between showing more or fewer COVID-19 inpatients than HHS Protect—not always just fewer, as HHS says should be the case. Thirty states also showed differences between state and HHS Protect figures that were frequently well above the 20% threshold cited by HHS, and HHS Protect data fluctuated erratically in 21 states.

"Hospital capacity metrics can and should be a national bellwether," the CDC data expert says. "One important question raised by the discordant data reported by HHS Protect and the states is whether HHS Protect is systematically checking data validity." HHS has not provided the methodology behind HHS Protect data estimates for review by independent experts. But an HHS official says a team of data troubleshooters, including CDC and ASPR field staff, work to resolve anomalies and respond to spikes in cases in a state or hospital.

Along with improving trust in its data, HHS Protect needs to make it more accessible, CDC data scientists say. The publicly accessible HHS Protect data are far less complete than the figures in its password-protected database. This effectively hides from public view key pandemic information, such as local supplies of protective equipment.

The site also does not provide graphics highlighting patterns and trends. This might explain, in part, why most media organizations—as well as President-elect Joe Biden's transition team—instead have relied on state or county websites that vary widely in completeness and quality, or on aggregations such as *The Atlantic* magazine's COVID Tracking Project, which collects, organizes, and standardizes state data. (In comparing state and federal data, CDC also used the COVID Tracking Project.)

Frieden and other public health specialists call reliable, clear federal data essential for an effective pandemic response. "The big picture is that we're coming up to 100,000 hospitalizations within the next few weeks. Hospital systems all over the country are going to be stressed," Frieden says. "There's not going to be any cavalry coming over the hill from somewhere else in the country, because most of the country is going to be overwhelmed. We're heading into a very hard time with not very accurate information systems. And the government basically undermined the existing system." ■

This story was supported by the *Science* Fund for Investigative Reporting.

CREDITS: (GRAPHIC) V. ALTOUNIAN/*SCIENCE*; (DATA) HHS PROTECT; ASPR

Published by AAAS

Earlier challenge trials deliberately infected volunteers with flu virus and other pathogens.

PHOTO: AP PHOTO/CHARLES DHARAPAK

COVID-19

New challenges emerge for planned human challenge trials

Scientists debate risks and benefits of intentionally exposing volunteers to dangerous virus

By **Warren Cornwall**

In the early days of the COVID-19 pandemic, tens of thousands of young volunteers offered to risk their health by letting scientists intentionally infect them with the pandemic coronavirus, hoping to speed the hunt for a vaccine or treatment. Several research groups announced plans to run these so-called human challenge trials, even as some scientists questioned whether they could be conducted ethically.

Now, with recent news that conventional human trials have produced several promising vaccines, scientists are debating whether planned challenge trials are still needed. In the United States, one nascent effort is on hold. In the United Kingdom, however, researchers say they are moving ahead. "There are still many strong arguments for pursuing" challenge trials, says immunologist Christopher Chiu of Imperial College London, leader of the proposed U.K. trial.

In traditional human trials, researchers give volunteers either a vaccine or a placebo, then wait months or longer for enough cases to emerge to gather statistically rigorous results. Challenge trials can move faster by first vaccinating volunteers and then intentionally exposing them to SARS-CoV-2 in a controlled setting. Researchers would then closely monitor the volunteers for days or weeks.

But challenge trials are also rife with ethical concerns. For example, because there are no reliable treatments for severe COVID-19, people who volunteer to test a vaccine could die if they get sick. So, medical authorities around the world have adopted a cautious approach. Even 1 year after the outbreak began, no such trial is underway. Meanwhile, 11 vaccines have entered the final phase of conventional human testing, with promising results already emerging: Four vaccines have shown up to 95% efficacy (see p. 1151).

Science's COVID-19 reporting is supported by the Pulitzer Center and the Heising-Simons Foundation.

Proponents say challenge experiments could still advance science and save lives. They could be used to compare the effectiveness of different vaccines, for instance, and help quickly screen the most promising second-generation candidates from the dozens now in the works. Challenge studies could also help answer unknowns, such as whether vaccines block infection entirely or simply prevent people from getting sick.

It's hard to use large trials to determine whether a vaccinated person still sheds the virus, says epidemiologist Marc Lipsitch of Harvard University. "It's almost prohibitively expensive because in a 30,000-person trial you have to test 30,000 people a week," he says.

The initiative Chiu heads, the Human Challenge Consortium, is backed by £33 million from the U.K. government. If regulators approve, scientists could infect the first volunteers in January 2021. The first studies, involving up to 100 volunteers ages 18 to 30, would identify the lowest viral dose needed to cause an infection. Then they could move forward with head-to-head comparisons of different vaccine candidates. Although the experiment won't replace traditional efficacy trials, it could highlight which vaccines warrant further investment, Chiu says.

Chiu is comfortable with intentionally infecting people with SARS-CoV-2 because there is growing evidence that young adults have a low risk of serious illness. He consulted with researchers at King's College London who help manage an app tracking COVID-19 symptoms for more than 4 million people. Among 650 young adults with confirmed cases, 90% had no symptoms after 3 weeks, and the symptoms of a few "outliers" resolved after a few months, Chiu says.

In the United States, however, the encouraging recent vaccine results have put a damper on human challenge trials. A month ago, virologist Matthew Memoli put the final touches on plans for a challenge trial at the National Institute of Allergy and Infectious Diseases (NIAID). But Anthony Fauci, head of NIAID, and Francis Collins, head of the National Institutes of Health, recently suggested the experiment is no longer necessary.

That's welcome news to some, who fear that challenge trials present serious risks to volunteers. Others, however, say the apparent success of some vaccines could strengthen the case for challenge trials. Once viable vaccines are available, it's harder to justify continuing with traditional trials, in which thousands of people are given a placebo while others are vaccinated, says bioethicist Nir Eyal of Rutgers University, New Brunswick. "Are you going to hope that tens of thousands of people will altruistically be willing to forgo access to a proven vaccine?" he asks.

Seema Shah, a bioethicist at Northwestern University, thinks human challenge trials could still be useful, but there is less urgency now. And she would like to see more ways to ensure participants' safety, such as finding biological markers for people at greater risk of getting sick. "I think I would feel more comfortable waiting a bit to see how those things developed and whether the risk could be minimized further," she says.

Lipsitch agrees that "the immediate need is not great" for human challenge trials. But, he adds, researchers "need to keep preparing in case we have reason to start doing them." ■

Published by AAAS

COVID-19

Amid the cheering, some vaccines face questions

A candidate from AstraZeneca and the University of Oxford has puzzling efficacy data

By **Jon Cohen**

The drumbeat of good news about COVID-19 vaccines has continued, albeit with some dissonant notes. By now four makers have reported results ranging from encouraging to stunningly positive from phase III clinical trials. The announcements, delivered by press release, have left scientists hungering for more data, but have persuaded many that having a safe and effective vaccine against SARS-CoV-2, the pandemic coronavirus, has moved from a question of if to when and how. "It's very good to have positive results from different platforms," says Ana Maria Henao Restrepo, who leads an effort at the World Health Organization to stage COVID-19 vaccine comparisons.

At the same time, two of the four COVID-19 vaccines face more questions than the other pair. AstraZeneca and the University of Oxford promoted their candidate, which uses an adenovirus to deliver the gene for the spike protein of SARS-CoV-2, as being nearly as protective as vaccines from Moderna and Pfizer and BioNTech. Those vaccines, which rely on messenger RNA (mRNA) to deliver the genetic code for spike, prevented symptomatic disease with 95% efficacy and appeared to block serious COVID-19 almost entirely.

But the AstraZeneca/Oxford announcement last week came from an interim analysis blending two trials of the vaccine in which people received different doses—apparently by accident. Efficacy ranged from 62% to 90%, depending on the dosing strategy. Meanwhile, Russia's Gamaleya Research Institute of Epidemiology and Microbiology, which also uses adenoviruses as vectors to deliver spike's gene, claimed 91.4% efficacy based on a second interim analysis of its candidate, Sputnik V. But that rested on far fewer COVID-19 cases than Moderna or Pfizer and BioNTech reported and the Gamaleya trial is still ongoing.

The AstraZeneca/Oxford effort conducted initial efficacy trials in the United Kingdom and Brazil. *Science* has learned from a scientist working with the partnership who asked not to be named that a calculation error early in the U.K. study led to vaccine vials being filled with half the intended dose. Rather than drop people who had already received that shot, the team modified the trial protocol to compare people who received a half dose followed by a full dose with those given two full doses.

An AstraZeneca official acknowledged the half dosing was a mistake, but Oxford researchers challenged this, and neither side would respond to requests to further discuss the issue. "It's a head scratcher on a number of levels, and this is the worst aspect of science by press release," says immunologist John Moore of Weill Cornell Medicine.

AstraZeneca says it can produce at least 3 billion doses of its COVID-19 vaccine next year.

PHOTO: VINCENZO PINTO/AFP/GETTY IMAGES

The collaboration reported people who received the half-dose priming shot were best protected from symptomatic COVID-19. But Moncef Slaoui, chief scientist of the U.S. government's Operation Warp Speed, which has invested heavily in the vaccine, notes that this substudy excluded elderly people.

The leading hypothesis for why various groups responded differently to the AstraZeneca/Oxford vaccine depending on dosing is an immune response against the adenovirus vector. With both that vaccine and the Russian one, volunteers received a "prime" first dose and a booster shot at least 1 month later. But the Gamaleya scientists used different adenoviruses for the prime and boost, so that an immune response to the first adenovirus would not thwart the booster shot. AstraZeneca and Oxford used the same adenovirus vector for both shots, which could explain why the larger boost dose produced the weaker result in its trial. "I would bet on that being a contributor, but not the whole story," says Adrian Hill, director of Oxford's Jenner Institute, which designed the vaccine.

Moore says the vaccines' versions of the spike protein may also matter. In nature, viral surface proteins can "wobble." His group in 2002 added stabilizing mutations to HIV's surface protein, which other groups later showed led to more robust antibody responses when it was injected into animals. Moderna, Pfizer and BioNTech, and other COVID-19 vaccinemakers have added similar mutations to spike. Hill's team did not. "Oxford is out on a limb," Moore says.

In the United States, Warp Speed has enrolled about 11,000 of a planned 40,000 participants in a third efficacy trial of the AstraZeneca/Oxford vaccine that uses the full-dose prime. The study may obtain an efficacy signal before being fully enrolled or it could switch to a half-dose prime, Slaoui adds, if researchers tease out the factors that led to 90% protection.

Henao Restrepo says it's important to factor in that the AstraZeneca/Oxford vaccine is relatively cheap, about $3 per dose, and only needs refrigeration temperatures for storage. The mRNA vaccines will cost at least $20 per dose and must be kept at subzero temperatures. AstraZeneca also says it can produce at least 3 billion doses next year, far more than projections from any other manufacturer.

A U.S. Food and Drug Administration vaccine advisory group plans to publicly review applications for emergency use authorization from Pfizer and BioNTech on 10 December and from Moderna 1 week later. The candidate from Pfizer and BioNTech appears poised to receive similar U.K. authorization as soon as this week.

But Hill says the COVID-19 vaccine race isn't over. "If we provide more vaccine next year, particularly in places where there's a lot of disease like Brazil and India, and save more lives, that's winning to us—not having done the press release first," he says. ■

Published by AAAS

SAVING SANCTUARIES

Critics charge that sanctuaries for retired research chimpanzees are failing their animals. Can a new tool help?

By **David Grimm**, *in Morganton, Georgia*

On a chilly morning in early October, primatologist Steve Ross drives up to a chain-link gate blocking a narrow dirt road in northern Georgia. He steps out of his car into a swath of the Blue Ridge Mountains and watches the cresting Sun illuminate low fog on the wooded hills. "When I went to Tanzania," he says, thinking back on the first time he saw wild chimpanzees, "it was just like this."

A green sign on the gate reveals why Ross is here: "Project Chimps," it reads. "Providing Lifelong Sanctuary to Chimpanzees Retired from Research."

The refuge is one of about a half-dozen chimp sanctuaries in North America, all designed to give the primates a more natural life than they had in labs, homes, or the entertainment industry. Founded just 6 years ago, Project Chimps made a name for itself by promising to retire more than 200 chimpanzees—about one-third of all ex–research chimps at the time—from a major biomedical facility.

Yet, since April, about a dozen former workers have alleged that the sanctuary is jeopardizing the welfare of its apes with inadequate veterinary care, insufficient outdoor access, and failing infrastructure. Similar charges have been leveled against two other major chimp sanctuaries, rais-

PHOTO: D. GRIMM/*SCIENCE*

Corrected 3 December 2020. See full text.

Published by AAAS

Primatologist Steve Ross begins his assessment at Project Chimps.

ing concerns about nearly half of the North American system.

"I think sanctuaries are going to be questioned very seriously going forward," says Cindy Buckmaster, chair of the board of directors of Americans for Medical Progress. When the U.S. government decided to retire its chimpanzees in 2015, she and others in the biomedical community predicted these problems, saying animals would actually fare worse in sanctuaries. The facilities have taken on too many chimps too quickly, Buckmaster argues, and lack the resources and experience to properly care for them.

Ross is here to see whether that's true. The director of ape study and conservation at Chicago's Lincoln Park Zoo, he's a proponent of sanctuaries and the board chair of the world's largest, Louisiana's Chimp Haven. He's also one of the country's most respected chimp experts and has published dozens of studies on how to best care for the animals in captivity. By his own account, he has visited every chimp facility in North America, from tiny roadside zoos to giant biomedical operations. "As long as it wasn't born in the past 5 years," he says, "I've met that chimp."

Today, Ross has arranged to arrive unannounced at Project Chimps to try out a new tool he's developing to assess chimpanzee welfare. Based on what the latest science says these animals need, the approach considers everything from the size of chimp social groups to the thickness of their bedding. The result: a comprehensive report of what a sanctuary is doing right and wrong, as well as an overall score that the public can see.

Ross hopes his tool, a pilot project funded by the Arcus Foundation, will give sanctuaries more scientific guidance and help the system keep its trust with the outside world, including the donors critical to its survival. If widely adopted, he thinks his approach could lead to better lives for chimps in facilities throughout the world. But all of that depends on how the tool performs today at Project Chimps.

A STAFFER DRIVES UP and opens the gate. Ross, 50, with salt-and-pepper stubble, continues down the narrow road until it ends at a tan, three-story building known as the Chateau. At 650 square meters, this is the largest structure on campus and home to two groups of 14 chimpanzees, more than one-third of the 78 animals that live at Project Chimps. The Chateau and four other chimp "villas" punctuate a tall concrete wall topped with electric wire that encircles a forested, 2.5-hectare habitat.

Soon after we arrive, employees open the Chateau's outer gates. One group of chimps, hooting and banging the walls in anticipation, makes its way into the habitat. The gang includes celebrity pair Hercules and Leo, the oldest males in the group. For several years, they were the subject of an animal rights campaign to have them declared legal persons and released from their university lab. Today, the two have made new friends and "appear to enjoy life," says Project Chimps Executive Director Ali Crumpacker, who has joined us for the visit.

Chimps on the move

After invasive research on chimpanzees in the United States ended in 2015, sanctuaries began to take large numbers of retired chimps from biomedical facilities.

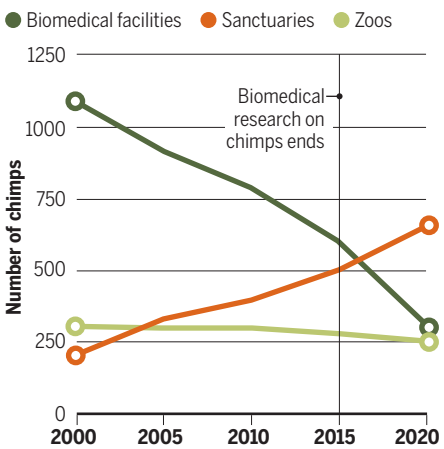

Ross, his pen perennially pressed to a stack of papers in his left hand, eyes the chimps from the roof as they expand into the hilly thicket of sourwood, pine, and walnut trees. Some scour for coconut shavings and pistachios the staff has scattered on the ground. Others sprawl on Sun-soaked climbing platforms. And others poke sticks into an artificial termite mound, pulling up peanut butter, applesauce, or whatever employees have loaded it with today. "Subjectively speaking," Ross says, "this is the best chimp yard in North America."

But it's also the subject of controversy. The habitat has been Project Chimps's main selling point, helping it secure millions of dollars in donations as well as the confidence of the New Iberia Research Center, which in 2016 pledged to send all 220 of its chimpanzees here. Yet a website run by former sanctuary employees claims the animals spend "90% of their retirement in concrete rooms," not much different from their housing at New Iberia.

Former workers also allege that Project Chimps brought in more animals than it could handle, leading to vicious fights and an uptick in stress behaviors like rocking and hair pulling. And they claim the sanctuary's only veterinarian had no primate experience and that buildings are in disrepair. "There doesn't seem to be much reason to continue to uproot these chimps, only to offer care that's worse than they had at the research facility," says Crystal Alba, who worked at Project Chimps for 3 years before she says she was fired for speaking up.

The accusations, detailed in local news coverage and in *National Geographic*, have attracted the attention of animal rights groups. Many have criticized the sanctuary online. One group, in a campaign reminiscent of those animal advocates typically stage against research labs, protested outside the home of a board member of the Humane Society of the United States, the sanctuary's biggest funder. Signs called him an "animal abuser" and featured photos of a chimp with a deeply split lip.

Former employees have also leveled charges against Florida's Save the Chimps, where 228 chimpanzees reside. A 3-month probe by a local news outlet detailed allegations including employee fights over how to care for the animals, which may have led to the death of one chimpanzee, and a short-staffed medical department that was slow to euthanize a dying chimp. The U.S. Department of Agriculture (USDA) has cited the sanctuary for 12 breaches of the Animal Welfare Act over the past 5 years, three for significant violations of medical care.

One former caregiver at Chimp Haven, who spoke to *Science* on condition of anonymity because of a nondisclosure agreement, raises complaints against that facility as well. She contends that the sanctuary—the only one funded by the U.S. government, and the home of more than 300 chimpanzees—didn't treat serious wounds and didn't fix heating issues in older buildings. She also alleges that staff was spread so thin it lost track of a male chimp that drowned in the sanctuary's moat.

Sanctuaries have pushed back against the accusations. Crumpacker says stress behaviors like hair pulling can predate an animal's time at Project Chimps. She says the sanctuary's veterinarian routinely consulted with primate experts and that a newly hired vet has some chimp experience. And although Crumpacker admits the animals here don't go outside as much as she would like—she estimates 12 to 24 hours per week—she points out that the New Iberia chimps have no outdoor habitat at all.

To increase outside access, she'd have to further divide the sanctuary's habitat, already split in two, so more groups could go outdoors at the same time. But that would deplete funds for bringing more chimpan-

CREDITS: (GRAPHIC) N. DESAI/*SCIENCE*; (DATA) PROJECT CHIMPCARE

Corrected 3 December 2020. See full text.

Published by AAAS

zees to the sanctuary, she says. "We not only have to do the right thing for the animals that are here, but also for those that are not here yet."

A spokesperson for Save the Chimps says, "Chimpanzee care is an extremely complicated undertaking," but "we have both the expertise and the best interests of chimps in mind." Chimp Haven President Rana Smith adds that her sanctuary has enough staff to closely monitor every chimpanzee, and that it's constantly improving its infrastructure. "We pride ourselves on exceptional welfare."

Inspections over the past few years by USDA and the Global Federation of Animal Sanctuaries (GFAS) have found no major problems at either Project Chimps or Chimp Haven. And although USDA cited Save the Chimps, it has not levied fines. But many experts across the sanctuary world say such evaluations are often superficial, inconsistent, and not tailored to chimpanzees. That's something Ross hopes to change today.

Chimpanzees browse an outdoor habitat at Florida's Save the Chimps (top). Leo, pictured at Project Chimps (bottom), was the subject of an animal rights campaign to have him declared a legal person.

WHILE THE CHATEAU chimps enjoy their outside time, Ross enters their enclosure. There are 11 rooms, including two large playrooms and two porches with views of the habitat. "It's like a house," Crumpacker says. "You can decide which room you want to be in, and whether you want to hang out with other people."

Ross measures the size of each room; the floor space covered in hay, blankets, and other substrates; and the number of perches and ropes the animals can climb. He also looks for steel panels that partially block the view of other rooms, allowing the primates to hide from their comrades if they're feeling stressed. "All of these are things we know from the literature are important for chimp well-being," he says.

Word comes over a walkie-talkie that another group of chimpanzees is about to be let out on the other side of the habitat. So we hop in a golf cart and head over to the Chimps Ahoy Villa, home to a special group of apes.

Project Chimps, like most zoos and sanctuaries, is always trying to increase the size of its chimpanzee groups to better replicate wild troops of more than 100 individuals of mixed genders and ages. It's a tricky business, as you never know who's going to get along with whom. Just last week, staff merged nine males with 10 females at Chimps Ahoy, making the group one of the biggest in the sanctuary system.

Ross says biomedical facilities sometimes separate chimpanzees by sex to avoid babies. "It's so unnatural for chimps," he says. "When you have single-sex groups, you miss out on all the things chimps do, including mating." (Males here get vasectomies, and the females are on birth control.)

We watch the chimps through a window in the giant concrete wall. Soon, a 32-year-old chimp with a graying muzzle named Justin ambles by. He has a deep gash in his back, looking a bit like a velociraptor took a swipe at him. It's the kind of untreated wound that might show up in a whistleblower complaint.

Ross is unfazed, however. He says Justin is a low-ranking chimp, which means he gets beat up to make sure he knows his place—the same sort of hierarchical conflict that happens in the wild. "If the sanctuary took him out of his group and gave him vet care," Ross says, "they might beat him up worse."

Still, Ross doesn't take wounds lightly. As he travels from villa to villa throughout the day, he spot checks every chimp, looking for injuries and stress behaviors that could be a sign of poor welfare or unstable groups.

Everything Ross records feeds into his new tool, which produces three scores: "social," assessing all chimps and the size, composition, and stability of their groups; "spaces," based on the size and complexity of the animals' environments; and "programs," gauging vet care, staff experience, and diets. The sanctuary gets a full report, and the public sees a summary and final grade.

Ross's inspection is much more chimp-specific than that of USDA, whose 336-page guidelines mention the word "chimpanzee" only three times. The agency's assessments also tend to be brief to the point of obscurity. A recent review of Project Chimps contained a single sentence: "No noncompliant items identified during this inspection."

In addition, Ross says, "USDA standards haven't changed much over my lifetime," whereas his review is based on the latest research. For example, Crumpacker says according to the agency's metrics, Project Chimps's smaller villas could house up to 45 chimpanzees. "Steve says 15. It's not just about how many chimps can occupy a space—it's about how well they live there."

GFAS inspections are more thorough than those of USDA, but they're not made public and not chimp-specific. Ross's approach is also more scientific, Crumpacker says. "Steve was asking about all of the [bedding] materials we use, and how much each chimp got, in inches," she says. "GFAS might just say a group of chimps should get 12 blankets a day. And USDA just cares that we wash them."

GFAS Executive Director Valerie Taylor agrees Ross's tool adds value. "We would absolutely welcome something like that," she says. "There's power in pooling resources."

Andrew Halloran, director of chimpanzee care at Save the Chimps, also embraces the tool. "Taking care of chimpanzees is a complicated science, and Steve's approach treats it like one," he says. His facility has recently adopted new guidelines with a more scientific approach to chimp welfare. Sanctuaries,

PHOTOS: (TOP TO BOTTOM) MEGHAN MCCARTHY/*THE PALM BEACH POST*/ALAMY; FRED RUBIO

Corrected 3 December 2020. See full text.

Published by AAAS

Project Chimps's large, lush outdoor habitat has been one of its main selling points—and one of its biggest sources of controversy.

Halloran says, are evolving from rescue organizations into more sophisticated operations that realize that an "evidence-based way of doing things is critical to providing good care."

Experienced biomedical facilities, meanwhile, would likely have no use for Ross's tool, says Steven Schapiro, who oversees primate welfare at the MD Anderson Cancer Center. He says operations like his, which cared for hundreds of chimps for decades, already have the knowledge they need.

Still, Schapiro says he thinks Ross's tool could help sanctuaries, which he believes "are 100% committed to the welfare of their chimpanzees." The problem, he says, is that they lack access to the same knowledge and funding as the biomedical community.

There's no easy fix for those deficiencies, Buckmaster argues. If Ross recommends sanctuaries hire more experienced staff, for example, she says, "I don't know where they're going to find them." That's why she and others in the biomedical community have argued that ex–research chimps should "retire in place" at research labs. That debate continues to play out as the National Institutes of Health considers which of its remaining 135 or so chimpanzees will move to sanctuaries as planned. Last year, the agency announced that nearly four dozen chimps would stay at the Alamogordo Primate Facility in New Mexico because they were too old or sick for transport. It reiterated that position last month despite congressional pressure.

Ross's approach also raises an existential issue for sanctuaries: Is it even possible to give chimpanzees what they need in captivity? That's the concern of primatologist John Mitani, professor emeritus at the University of Michigan, Ann Arbor, who has studied chimpanzees in the wild for more than 30 years. He notes that chimp groups in Africa regularly split apart and come back together, which they can't do in captivity—and that even a large habitat like the one at Project Chimps can't match the more than 30-square-kilometer range of wild chimps. "Chimps like to come and go, just like people," Mitani says. Without that, he says, they can become anxious and violent—something even the best sanctuaries can't prevent.

AT THE END OF THE DAY, Ross returns to Project Chimps's main office to talk about next steps with Crumpacker. Photos of more than 200 chimpanzees hang on the wall, with black-and-white pictures denoting animals still at New Iberia. The research center still plans to transfer most of its 123 remaining apes here. "They have been quite diligent in their approach to the care of the chimps," says Director Francois Villinger.

Ross's review, announced earlier this week, turns out to be mostly good news for Project Chimps. The sanctuary earns a total score of 81 out of 100, with high marks for its large group sizes and exceptional outdoor space. But the report also dings the sanctuary for the apes' limited access to that space and for its relatively inexperienced veterinary and care staff.

"Based on the allegations, I went in pretty skeptical," Ross says. "But overall I think the chimps are well cared for."

Crumpacker says Project Chimps will "try and make strides" toward addressing the recommendations—although she isn't conceding every point. Ross recommends more scattering of food to better replicate natural foraging, for example, but she says hand feeding ensures that chimps get the right portions.

For his part, Ross says he will continue to refine his tool as he visits more North American chimpanzee sanctuaries, all of which have signed on. He hopes to expand the approach to other types of chimp facilities, and to eventually help create similar tools for monkeys, horses, and other animals.

Although Mitani doesn't think it's possible to give chimpanzees an ideal life in captivity, he welcomes Ross's attempt to improve conditions. "He's trying to make the best of a bad situation, so more power to him," he says. "Even if this tool just makes things a bit better, we owe these animals more than they have right now." ■

PHOTO: STEVE MANGO

Corrected 3 December 2020. See full text.

Published by AAAS

INSIGHTS

BOOKS *et al.*

AAAS/SUBARU SB&F PRIZES FOR EXCELLENCE IN SCIENCE BOOKS

Fodder for future scientists

From a monarch mystery unlocked with the help of Indigenous people to an environmental disaster averted by a chemist who was not afraid of a fight, this year's finalists for the Science Books and Films (SB&F) Prizes for Excellence in Science Books highlight how diverse perspectives, grit, and a healthy dose of hope are essential to the effective practice of science. Read on for reviews of the finalists written by the staff of the *Science* family of journals, with help from a few friends. **—Valerie Thompson**

HANDS-ON SCIENCE BOOK

Chemistry for Kids

Reviewed by **Pamela J. Hines**[1]

If you were to choose 25 discoveries to document the progress of chemistry through millennia, what would you pick? In *Chemistry for Kids*, Liz Lee Heinecke takes us on such a journey, using familiar objects and simple scientific instruments to create straightforward chemistry experiments that chart the field's evolution over time.

Each chapter is centered on a different experiment and begins with a vivid illustration that highlights a scientist and his or her work. A few paragraphs of engagingly written introduction are followed by colorful photographs of youngsters demonstrating the steps of the experiment. A brief explanation of the chemistry that underlies each experiment wraps up each chapter.

The author's decision to include many women, even those not officially known as "scientists," is most welcome. Marie Curie's process of elemental precipitation, by which she extracted radium, is modeled (much more safely) with food coloring and rosemary leaves. Meanwhile, the environmental spread of the insecticide DDT that Rachel Carson brought attention to is visualized by the diffusion of food coloring through gelatin. Agnes Pockels, a pioneer of surface science, found inspiration in the bubbles that formed as she washed dishes. Using dish soap, milk, and food coloring, we can see for ourselves how surface tension drives the formation of colorfully abstract patterns.

The topics covered range broadly. Some chapters detail things we think of as part of everyday life (for example, soap or carbonated drinks). Other chapters touch on frontiers, including medicinal plant chemistry and crystallography. Older children could do many of these experiments on their own; younger children might need supervision.

Chemistry for Kids: Homemade Science Experiments and Activities Inspired by Awesome Chemists, Past and Present, Liz Lee Heinecke, Quarry Books, 2020, 128 pp.

This Is a Book to Read with a Worm

Reviewed by **Caroline Ash**[2]

Charles Darwin's final book was dedicated to the gradual way in which earthworms change the world by turning over soil (*1*). He was not the only early naturalist to appreciate this diminutive invertebrate. In the 18th century, Gilbert White acknowledged the "lamentable chasm" that would be left without the "small and despicable" worm to help make soil (*2*).

This Is a Book to Read with a Worm is a colorful delight and an important little book that follows in White and Darwin's footsteps, promising to help nurture a new generation of naturalists. It offers a mix of activities and facts about earthworms that a curious child could do independently (or, to be more precise, with an earthworm). The book starts

ILLUSTRATION: HANNAH AGOSTA

Published by AAAS

with guidance for how to catch a worm and how to care for it in a simple homemade terrarium. Several suggested experiments reveal information about worms' sensory responses and anatomy. For instance, by crafting a listening tube made from paper, you can hear them crawling thanks to the scratching of their barely visible setae.

Readers learn that in the United States, imported worm species are eating all the leaves that make up native earthworms' diet, to the detriment of native species. This could have profound consequences, not only for life underground but also for the viability of the forests that rely on the leaf consumption and soil churning capacity of native worms.

This Is a Book to Read with a Worm, Jodi Wheeler-Toppen, Illustrated by Margaret McCartney, Charlesbridge, 2020, 32 pp.

REFERENCES AND NOTES

1. C. Darwin, *The Formation of Vegetable Mould Through the Action of Worms, with Observations on Their Habits* (John Murray, 1881).
2. G. White, *The Natural History and Antiquities of Selborne* (Benjamin White, 1789).

You're Invited to a Moth Ball

Reviewed by **Seth Scanlon**[3]

Of all the insects that flitter and flutter into our homes, among the least welcome is the common clothes moth (*Tineola bisselliella*), which has a penchant for ruining shirts, sweaters, and sundry other garments. However, this perfidious pest is just one of more than 150,000 different moth species. In *You're Invited to a Moth Ball*, Loree Griffin Burns invites budding entomologists to embrace the "moth ball," a nocturnal occasion to encounter the myriad moth species that live just outside our homes.

The text, written in a warm and casual register, first describes how to employ a combination of fruit smeared on trees and specialized ultraviolet lights to attract moths to viewing stations made using light-colored sheets hung on clothes lines. The book then details what to expect of your lepidopteran guests and offers some advice for maximally enjoying your nighttime rendezvous (although it fails to offer advice about how to handle other wildlife that might seek to gate-crash the ball). Along the way, Burns provides some useful, if basic, information about moth biology.

The book's vibrant and inviting photographs, captured by Ellen Harasimowicz, are a true highlight. Indeed, the great variety and beauty of moths shown made me seriously consider gathering up the necessary supplies and having my own backyard moth party. However, the decision to omit captions, which might have explained the moths depicted in the photos, was a missed opportunity for further edification. I would have also liked to have seen more options for families who do not have access to backyards with trees. Still, this is a fun and engaging book that encourages children to explore the wonders of the world around them and that should hopefully spur them to seek out more in-depth sources of information, helpfully signposted in the book's "Resources" section.

You're Invited to a Moth Ball: A Nighttime Insect Celebration, Loree Griffin Burns, Photography by Ellen Harasimowicz, Charlesbridge, 2020, 40 pp.

Creek Critters

Reviewed by **Trista Wagoner**[4]

Small streams are often overlooked and underappreciated, but they provide ample opportunities for curious kids to learn what it is like to be a scientist. In *Creek Critters*, a girl whose name we never learn invites her younger brother Lucas to explore a stream one might find in the mid-Atlantic region of the United States. The pair turn over rocks and scoop up rotting leaves in search of aquatic macroinvertebrates that ecologists use as indicators of a healthy ecosystem. Most of this short book focuses on insects, especially in larval forms, describing their sizes and shapes along with appealing, detailed illustrations and photographs. The children's goal is to find species, such as the mayfly and the caddis fly, that are sensitive to pollutants. "If we find them," the girl explains, "we'll know our creek is healthy."

The book ends with a few pages of activi-

Published by AAAS

A girl and her brother seek signs of stream health in *Creek Critters*.

ties, including a scavenger hunt and a template for recording observations about the environment. The last page lists noninsect biological indicators of stream health, such as snails, crayfish, and planaria. The publisher's website includes Spanish-language versions of the story (audio and text), and the Audubon Naturalist Society offers a "Creek Critters" companion app and additional activities.

I found myself wanting more from the book—more information about the importance of healthy streams, more explanation of how pollutants affect flora and fauna, and more illustrations—but most of all, it left me with the feeling that I want more time to explore my own nearby creeks. It may likewise provide inspiration and direction for children who enjoy getting their hands wet and their boots muddy.

Creek Critters, Jennifer Keats Curtis with Stroud Water Research Center, Illustrated by Phyllis Saroff, Arbordale Publishing, 2020, 32 pp.

CHILDREN'S SCIENCE PICTURE BOOK

Mario and the Hole in the Sky

Reviewed by **Sacha Vignieri**[5]

During the 1970s, a time when many embraced the motto "better living through chemistry," Mexican chemist Mario Molina questioned the safety of chlorofluorocarbons (CFCs) that had begun appearing in an increasing number of products, from refrigerants to medical aerosols. He wondered about the persistence of these compounds and their effects on the environment. When he realized that they were degrading the ozone layer, a key component of our atmosphere, he fought tirelessly against their use. In the end, he won the fight; laws were put in place around the world to limit the use of CFCs, but the path was not easy, and Molina and his colleagues faced vitriolic criticism.

With gentle and engaging imagery, *Mario and the Hole in the Sky* conveys Molina's story, rendering him first as a curious child obsessed with his microscope and later as a worried scientist determined to convince a skeptical public of the dangers of CFCs. The book urges readers to follow their curiosity and to be prepared to fight hard for the health of the planet. "We saved our planet once. We can do it again," Molina concludes at the end of the story, evoking an optimistic view of the world that is comforting and full of potential.

Molina, who passed away in October of this year (see Retrospective, p. 1170), worked tirelessly to educate the world about CFCs and overcame naysayers and critics to ensure that they were phased out of use. Today, the threats we face are even more complex, the resistance to change stronger, and the global political environment even less conducive to collaboration. Nonetheless, the impact of solid science, collaboration, and inspiration is still powerful. Molina's story, as presented in this lovely book, may help young readers see hope in similar efforts, and such hope will carry us forward in these challenging times.

Mario and the Hole in the Sky: How a Chemist Saved Our Planet, Elizabeth Rusch, Illustrated by Teresa Martínez, Charlesbridge, 2019, 40 pp.

The Boy Who Dreamed of Infinity

Reviewed by **Kelly Servick**[6]

This coming-of-age tale is so vibrant and imaginative that a reader might forget that it is also the true story of Indian mathematician Srinivasa Ramanujan, who made substantial contributions to number theory and the study of infinite series. Author Amy Alznauer, a math professor at Northwestern University, takes readers to Ramanujan's birthplace in South India at the turn of the 20th century.

We meet Ramanujan first as a cherished infant prophesied to become a great thinker. But for most of this story, we see a more relatable character: a bored student, irritating teachers with his precociousness and sneaking off to be alone with his thoughts. When Ramanujan contemplates a mango—mentally cutting it into smaller and smaller pieces—he stares into infinity. In clouds, temple statues, and his mother's folktales, Ramanujan sees numbers and mysteries. Despite his mathematical brilliance, he fails out of college and is left destitute, despairing that his ideas will never reach the wider world. Alznauer's story ends as Ramanujan accepts an invitation from mathematician G. H. Hardy to work and study in England—a decision that will propel Ramanujan to greatness.

By focusing mainly on his youth, *The Boy Who Dreamed of Infinity* offers only vague glimpses of Ramanujan's ultimate contributions to mathematics. But the book's message transcends the world of academic research. This vivid story, which tumbles across the book's pages in Daniel Miyares's kinetic

ILLUSTRATION: PHYLLIS SAROFF FOR *CREEK CRITTERS*

Published by AAAS

illustrations, celebrates the power of a self-assured and independent child. It could encourage young readers to identify their own passions and acknowledge their own brilliance before the adult world gets wise.

The Boy Who Dreamed of Infinity: A Tale of the Genius Ramanujan, Amy Alznauer, Illustrated by Daniel Miyares, Candlewick, 2020, 48 pp.

Winged Wonders

Reviewed by **Jeffrey Mervis**[7]

It should not be hard to interest children in a story about monarch butterflies. But Meeg Pincus, the author of *Winged Wonders*, has a more ambitious goal: to teach them how scientists go about their work.

Her story starts by introducing readers to Canadian zoologists Fred and Norah Urquhart, who began studying monarch migration patterns in the 1940s. Pincus then presents a cast of supporting characters, including citizens who answered ads asking people to tag the monarchs living in their neighborhoods, a couple who followed the monarchs throughout Mexico, and the villagers who celebrated the fall arrival of the monarchs, which roost in the oyamel tree groves high in the Sierra Madre. Large, lush drawings by illustrator Yas Imamura invite children to insert themselves into the story.

Pincus does not stop at retelling the Urquharts' story. Instead, she encourages readers to contribute to the ongoing research on monarchs and to work to protect their habitats.

The book's bare narrative is supplemented by a final page filled with details about the Urquharts and those who have followed in their footsteps. However, those with additional questions—for example, why do monarchs migrate, and do they all travel such great distances?—will need to consult other sources. But that is a minor quibble if this mystery story kindles your child's interest in this iconic species and environmental stewardship.

Winged Wonders: Solving the Monarch Migration Mystery, Meeg Pincus, Illustrated by Yas Imamura, Sleeping Bear Press, 2020, 40 pp.

Honeybee

Reviewed by **Jennifer Sills**[8]

In *Honeybee: The Busy Life of Apis Mellifera*, Candace Fleming uses rhythmic, meditative prose to describe the short life of a honey bee. The story begins as Apis "squirms, pushes, chews" through her wax cell into the "teeming, trembling flurry" of the hive. She feeds larvae, tends to the queen, builds honeycomb cells, handles food, and guards the hive. Finally, in a climactic four-page spread, Apis takes flight. But her work is not done; before she stills, Apis will fly 500 miles and visit 30,000 flowers. On her 35th day, as Apis's story comes to an end, another honey bee emerges from her "solitary cell."

Vivid oil paintings illustrate Apis in meticulous detail, along with her fellow bees and the world she travels. The story gives readers an appreciation of the many hidden tasks that take place inside a beehive, as well as the cooperative structure of a bee colony, where each individual contributes to the group in a variety of ways.

At the end of the book, an appendix provides information about honey bees' crucial role in human food production, the threat of colony collapse disorder, and what readers can do to help. A final section adds information about the other occupants of the hive—the queen and drones—and more details about the intriguing dance performances that honey bees use to communicate the location of flowers to one another.

Honeybee: The Busy Life of *Apis Mellifera*, Candace Fleming, Illustrated by Eric Rohmann, Neal Porter Books, 2020, 40 pp.

MIDDLE GRADES SCIENCE BOOK

Can You Hear the Trees Talking?

Reviewed by **Marc S. Lavine**[9]

We often think of trees when the leaves change color in the fall or when devastating forest fires, disease, or invasive species lead to widescale loss. Few of us take the time to consider, however, the many parallels that exist between trees and more mobile creatures. Trees can form communities, in which elders nurture and educate the young. Collectively, they can moderate the local temperature and humidity, store water, and protect each other. Isolated trees may mature faster than trees surrounded by others of the same species, but this accelerated growth can harm the lone tree's longevity. In *Can You Hear the Trees Talking?*, Peter Wohlleben provides a fascinating and detailed guide to these less appreciated aspects of tree life.

Trees use senses akin to taste and smell to detect and deter predators and alert neighboring trees. However, much of the communication in a forest occurs belowground. Neighboring tree roots of the same species share nutrients and pass along messages about local threats. Fungi that live off dead trees or leaves send out a network of fine threads that act like a highway for chemical messages. But this relay service comes at a cost: Fungi can demand up to a third of the sugar that a tree produces, and they will sometimes share that sugar with trees of other species to aid their own preservation.

Wohlleben wrote this book as a young reader's edition of *The Hidden Life of Trees* and has done a remarkable job ensuring that each page tells a complete story, answering questions ranging from how trees know when it is spring to why trees are important in the city. Activities and quizzes appear throughout the book to engage readers of all ages.

Can You Hear the Trees Talking? Discovering the Hidden Life of the Forest, Peter Wohlleben, Translated by Shelley Tanaka, Greystone Kids, 2019, 84 pp.

Eclipse Chaser

Reviewed by **Adrian Cho**[10]

On 21 August 2017, the Moon glided between Earth and the Sun, creating an eclipse visible across the United States. Millions of people flocked to the path through 13 states along which the Moon would completely cover the disk of the Sun and create a total eclipse—among them were Shadia Habbal, a solar physicist, and her team. In *Eclipse Chaser*, science reporter Ilima Loomis recounts their exciting yet sometimes anxious expedition to study the solar corona, the Sun's atmosphere, which is visible only during a total eclipse.

Whereas many solar physicists rely on huge purpose-built telescopes on the ground and in space to study our at times capricious little star, Habbal relies instead on eclipses and portable telescopes to probe the still poorly understood corona, trekking to remote peaks and deserts, where bad weather or a sudden sandstorm can spoil months of preparation.

Loomis deftly explains the mechanics of

ILLUSTRATION: © BY ERIC ROHMANN

Published by AAAS

Physicist Shadia Habbal and her team study the solar corona in *Eclipse Chaser*.

an eclipse and the questions Habbal is trying to answer. She conveys the homey feel of the expedition, on which Habbal's sister treats the team to a homemade chicken dinner. In a gratifying nuance, Loomis notes that, for years, Habbal seldom looked at the corona herself, as she was always too busy tending to her instruments and cameras. Only now that the systems run automatically can she turn her eyes skyward.

Eclipse Chaser teems with intriguing photos snapped by Amanda Cowan. Visually, the Sun is the real star of the show. The eerie photos of its gossamer corona stretching out across the darkened sky may make the reader long to see it in person. If he or she is so inclined, the book includes a handy map that shows the paths of total eclipses through 2060.

Eclipse Chaser: Science in the Moon's Shadow, Ilima Loomis, Photography by Amanda Cowan, HMH Books for Young Readers, 2019, 80 pp.

Growing Up Gorilla

Reviewed by **Cathleen O'Grady**[11]

Baby gorilla Yola faces a singular challenge: Her mom, Nadiri, was raised by humans and does not know how to parent. *Growing Up Gorilla* tells the story of the pair's blossoming bond as the keepers at Seattle's Woodland Park Zoo care for the newborn gorilla and gently encourage Nadiri's maternal instincts.

Clare Hodgson Meeker's deft storytelling weaves together Yola's first few months of life and Nadiri's experience of being raised by humans. The zookeepers explain that they are eager to develop the bond between mother and baby because Yola will best learn life skills that way. The result is a gentle but surprisingly gripping narrative with finely drawn central characters.

Animal-mad children will love both the story and the abundant photography. Close-up shots of Yola and her family offer insight into the emotional bond and life of the gorillas. Sidebars that explain gorilla biology, society, and behavior serve as either useful breathers or mildly jarring distractions, depending on the reader's attention span.

This is a book that packs a hefty educational punch in a delightful package. Readers will finish with an understanding of the close evolutionary relationship between humans and other primates and the precarious conservation status of gorillas. Most importantly, as they watch Yola flourish by "growing up gorilla," they will learn that the best way to love and respect nonhuman animals is by keeping a little bit of distance.

Growing Up Gorilla: How a Zoo Baby Brought Her Family Together, Clare Hodgson Meeker, Millbrook Press, 2019, 48 pp.

Condor Comeback

Reviewed by **Laura M. Zahn**[12]

In 1987, the last California condor in the wild was taken into captivity. Along with 21 others of its kind—together representing the last of the species—the bird was used to launch a captive breeding program. The eventual goal of the program was to return condors to the wilds of the western United States. Part of the Scientists in the Field series, this book tells the condor's comeback story through the work of conservation scientist Estelle Sandhaus, director of conservation and science at the Santa Barbara Zoo, and her collaborators. The book details Sandhaus's efforts to identify how human intervention can ensure that individual birds thrive outside of captivity, thereby ensuring that the wild population will grow.

Condors still face multiple threats, including potentially serious health risks associated with eating "microtrash" (for example, small pieces of metal, shards of glass, or plastic packaging) and carcasses containing lead shot. The book takes readers along on a health assessment of wild birds and highlights the many ways in which they are monitored, providing insight into the job of a conservation scientist. Monitoring, together with captive breeding and reintroduction programs, community outreach, and policies banning lead shot, has resulted in successful reproduction and reintroduction into the wild.

Today, there are more than 450 California condors, about half of which are living in the wild. However, more conservation scientists are needed to ensure the species' continued success. Hopefully this book will encourage children to consider entering this field.

Condor Comeback, Sy Montgomery, Photography by Tianne Strombeck, HMH Books for Young Readers, 2020, 96 pp.

YOUNG ADULT SCIENCE BOOK

The Last Stargazers

Reviewed by **Keith T. Smith**[13]

When a young person imagines an astronomer, they likely picture a white-coated individual who spends each night peering at the sky through a small refracting telescope on a roof. But, as Emily Levesque recounts in *The Last Stargazers*, the reality of being a professional astronomer is very different.

Observational astronomers must apply months in advance for competitive time on a limited number of giant telescopes in remote locations, perhaps securing just a few nights per year. After traveling to the observatory, they must work through the night from a control room, trying to collect enough photons to produce a result. The weather is a constant threat—if it is unfavorable, weeks of work and travel could result in no data at all. Levesque successfully captures the strange mix of excitement, impatience, camaraderie, and sleep deprivation that I recognized from my own observing trips and relates numerous anecdotes about uncooperative wildlife, malfunctioning equipment, natural disasters, and idiosyncratic observatory staff.

The book is partly autobiographical—Levesque is a professional astronomer who studies massive stars—weaving the author's experiences with highlights from interviews. Historical tales of famous observers, such as Edwin Hubble and Vera Rubin, include a discussion of how many female astronomers

PHOTO: MILOSLAV DRUCKMÜLLER, SHADIA HABBAL, PAVEL ŠTARHA, JUDD JOHNSON, JANA HODEROVÁ; IMAGE PROCESSING BY MILOSLAV DRUCKMÜLLER

Published by AAAS

had to overcome gender bias. Levesque's emphasis is on optical astronomy, although she does mention radio telescopes and the new methods of gravitational wave astronomy, with a disappointingly heavy focus on American astronomers and U.S. facilities.

The book's final chapters cover recent shifts toward remote-controlled, queue-scheduled, or fully automated observing. While such methods are cheaper, more efficient, and more environmentally friendly, they do diminish the drama and wonder of professional astronomical observing. *The Last Stargazers* may ultimately become a historical record of a dying way of doing science.

The Last Stargazers: The Enduring Story of Astronomy's Vanishing Explorers, Emily Levesque, Sourcebooks, 2020, 336 pp.

Borrowing Life

Reviewed by **Yevgeniya Nusinovich**[14]

Borrowing Life by Shelley Fraser Mickle tells the story of the pioneering 20th-century surgeons, scientists, and patients who made organ transplantation a reality. Although the book's primary focus is on kidney transplantation, Charles Woods—a young pilot who, in 1944, was severely burned in an airplane accident and unexpectedly survived with the aid of donor skin grafts—takes center stage in the first half of the story.

Joe Murray, the surgeon who treated Charles, and one of the central figures in Mickle's book, would go on to join a team of talented physicians under the supervision of surgeon Francis Moore, where he drew on immunologist Peter Medawar's animal studies to successfully execute the first human kidney transplant in identical twins in 1954. Mickle recounts how the subsequent application of the team's technique using unrelated donors gradually became feasible with careful calibration of immunosuppression.

Although Mickle met both Murray and Moore decades before writing this book, *Borrowing Life* draws primarily from archival documents, including memoirs written by the participants and contemporaneous news coverage. It is written in an informal style, as a series of disparate anecdotes that gradually converge on a single story.

Mickle makes an unusual narrative decision, framing the medical tale with the love stories of the key participants (Woods, Murray, Moore, and Medawar) and their wives. Her attempt to recognize the efforts and personal costs incurred by women with history-making husbands is appreciated, as many biographies take such sacrifices for granted. Unfortunately, the execution of this strategy often falls flat because Mickle offers few details about the wives' actual contributions. Nevertheless, the book presents a set of compelling stories that may be eye-opening for readers who have grown up in a time when organ transplantation is taken for granted.

Borrowing Life: How Scientists, Surgeons, and a War Hero Made the First Successful Organ Transplant a Reality, Shelley Fraser Mickle, Imagine, 2020, 288 pp.

Wading Right In

Reviewed by **Andrew Sugden**[15]

Too often, wetland ecosystems are viewed as an unproductive obstacle to useful human projects, and they have accordingly suffered—like so many other natural ecosystems—the depredations of development. Recognizing that the general public may "lag in their appreciation" of wetlands, Catherine Koning and Sharon Ashworth have set out on a mission to generate a wider interest in these fascinating and beautiful ecosystems, with a blend of science, natural history, and the personal stories of ecologists, wetland managers, conservationists, and more.

Their focus is mainly the wetlands of the northeast United States—the plants and creatures that inhabit them and the people whose lives are enhanced by them. The book's chapters are organized by wetland type—saltmarsh, forest wetlands, swamps, vernal pools, etc.—with final chapters on wetland restoration and on the connections between people and wetlands, both at the personal and community level. The book has a bibliography and plenty of further reading for readers wanting to dive in more deeply.

The importance of wetlands cannot be overstated. They play a vital carbon sequestration role in a changing climate. Coastal wetlands are also a protective bulwark between ocean and dry land and provide a haven for a huge range of resident and migratory wildlife. The authors' efforts to highlight these benefits and to inspire a love of—or at least a tolerance for—mud, wind, and damp, flat horizons make this book an excellent and engaging introduction to these ever-changing ecosystems.

Wading Right In: Discovering the Nature of Wetlands, Catherine Owen Koning and Sharon M. Ashworth, Illustrated by Catherine Owen Koning, University of Chicago Press, 2019, 264 pp.

The Alchemy of Us

Reviewed by **Mark Miodownik**[16]

The questions of how much of our humanity is due to material wealth and how our cultural values are baked into the materials we create are the subject of Ainissa Ramirez's fascinating new treatise, *The Alchemy of Us*.

Ramirez's meditation on the materials that have facilitated community is particularly illuminating. Here, she writes about the phonograph's impact on how music was enjoyed. The ability to record music meant that the experience of listening to it no longer had to be a communal one and spelled the end of much homemade folk music defined by materials such as brass, wind, or strings, but it also opened up uncharted horizons. The recordings allowed a cross-fertilization of musical culture between jazz, blues, and rock and roll, even as the musicians themselves remained segregated by race politics.

On the subject of race, Ramirez argues that a society that is racist will reflect racism in the substances that it makes. Because dark skin absorbs more light than white skin, for example, early photographs of black people were often barely recognizable. And although the cultural bias embedded in color film was corrected through chemical reformulations, it reemerged decades later in digital photography's automatic facial recognition, which frequently fails to detect darker skin tones.

The culture of innovation, Ramirez maintains, does not belong only to privileged elites; it can be found in all those who care enough to reinvent the material world and, as a result, themselves. ■

The Alchemy of Us: How Humans and Matter Transformed One Another, Ainissa Ramirez, MIT Press, 2020, 328 pp.

For a full-length review of *The Alchemy of Us,* see *Science* **368**, 41 (2020).

10.1126/science.abf5636

[1]The reviewer is a senior editor at *Science*. Email: phines@aaas.org [2]The reviewer is a senior editor at *Science*. Email: cash@science-int.co.uk [3]The reviewer is an associate editor at *Science*. Email: sscanlon@science-int.co.uk [4]The reviewer is a managing editor at the *Science* journals. Email: twagoner@aaas.org [5]The reviewer is a deputy editor at *Science*. Email: svignier@aaas.org [6]The reviewer is a news writer at *Science*. Email: kservick@aaas.org [7]The reviewer is a senior correspondent at *Science*. Email: jmervis@aaas.org [8]The reviewer is the Letters editor at *Science*. Email: jsills@aaas.org [9]The reviewer is a senior editor at *Science*. Email: mlavine@aaas.org [10]The reviewer is a news writer at *Science*. Email: acho@aaas.org [11]The reviewer is a news intern at *Science*. Email: cogrady@science-int.co.uk [12]The reviewer is a senior editor at *Science*. Email: lzahn@aaas.org [13]The reviewer is a senior editor at *Science*. Email: ksmith@science-int.co.uk [14]The reviewer is a senior editor at *Science*. Email: ynusinov@aaas.org [15]The reviewer is a senior editorial fellow at *Science*. Email: asugden@science-int.co.uk [16]The reviewer is at the Department of Mechanical Engineering, University College London, London WC1E 7JE, UK. Email: m.miodownik@ucl.ac.uk

Published by AAAS

PERSPECTIVES

QUANTUM GASES

Quantum-limited sound attenuation

Resonantly interacting atoms confined by lasers have implications for neutron stars

By **Thomas Schaefer**

Ordinary sound is a harmonic oscillation in the density, temperature, and velocity of air. Sound intensity decreases because of the spreading of the sound wave, but ultimately, sound attenuation is due to the diffusion of momentum and energy from the crest to the trough of the wave. This effect can be characterized in terms of the diffusivity D of sound. In air, there is a very large separation of scales between the shortest scale, the distance between molecules; an intermediate scale, the mean free path of air molecules, which controls the diffusivity; and the longest scale, the wavelength of the sound mode. On page 1222 of this issue, Patel *et al.* (*1*) study a very different and deeply quantum version of sound attenuation. The authors' result illuminates the transport properties of strongly correlated quantum fluids (*2*), with direct implications for the stability of spinning neutron stars (*3*).

Patel *et al.* confined 2 million lithium atoms in a cylindrical box created using beams of laser light (see the figure). The box is about 100 μm long and 60 μm in radius. A typical standing wave in the experiment has a wavelength that is only about 10 times larger than the mean distance between atoms. To observe sharp collective modes in this regime, the gas must be very strongly correlated. Making the gas very cold and tuning the interaction between atoms to a resonance achieves this correlation. The temperature of the gas is between 50 and 500 nK, which implies that the de Broglie wavelength of the atoms is equal to or larger than the mean atomic distance. The de Broglie wavelength is the wavelength of the quantum mechanical wave function of the atoms. The interaction between the atoms is tuned by means of a so-called Feshbach resonance (*4*). At resonance, we can think of the interaction as having zero range but infinite scattering length. This means that the wave function of two low-energy atoms is modified by interactions even if the atoms are arbitrarily far apart.

The resonant limit is referred to as the unitary Fermi gas, because the isotropic part of the scattering cross section is as large as the conservation of probability (unitarity) in quantum mechanics allows it to be. The unitary Fermi gas is also scale invariant. This means that physical observables are fixed by dimensional analysis and universal functions of dimensionless ratios. We can apply this type of argument to the sound diffusivity. On dimensional grounds, D is proportional to $\hbar/m$, where $\hbar$ is the reduced Planck's constant and m is the mass of the atoms.

The constant of proportionality is determined by the detailed mechanism for energy and momentum transfer. If momentum transfer is governed by the diffusion of atoms, then $D \sim \bar{p} l_{mfp}/m$, where $\bar{p}$ is the mean momentum of an atom and l_{mfp} is the mean free path. In a classical gas, $\bar{p} l_{mfp} >> \hbar$, but in a strongly correlated gas, we expect the product of $\bar{p}$ and l_{mfp} to be limited by quantum uncertainty, so that D is of order $\hbar/m$.

The results of Patel *et al.* demonstrate this limiting behavior. In the experiment, sound modes are excited by shaking the endcaps of the cylindrical box. The position of resonances determines the speed of sound, and the width of the resonance determines the diffusivity. Patel *et al.* find that the diffusivity drops as the temperature is lowered, settling around $D \sim 1.5\hbar/m$ near the transition to a superfluid. This value is consistent with attempts to measure the shear viscosity and thermal conductivity of the unitary Fermi gas individually (*5*, *6*), as well as with theoretical calculations (*7*). Below the critical temperature, the unitary gas forms a superfluid that is roughly analogous to Bardeen-Cooper-Schrieffer superconductivity, but with a parametrically large pairing gap and critical temperature. Notably, no sharp features are found in the diffusivity at the phase-transition temperature.

The results of Patel *et al.* have direct implications for the structure of spinning neutron stars. The matter in the outer layer, below the crust but outside the core, of a neutron star is a dilute liquid of neutrons. The neutron-neutron scattering length is much larger than the distance between neutrons, making observations of the unitary Fermi gas directly applicable, even though the temperatures and densities are many orders of magnitude larger in the star. The dimensionless ratios, such as the mean particle distance in units of the thermal de Broglie wavelength, being similar is what matters for modeling the stellar interior.

Neutron stars have many possible modes of oscillations. A special class that arises owing to the Coriolis force in rotating stars is

Observing quantum sound waves

A cylindrical box made of laser beams, 100 μm long and 60 μm in radius, contains about 2 million ultracold lithium atoms. Changing the light intensity of the cylinder's endcaps excites sound waves. The decay of the sound waves (diffusivity) is measured by tracking the frequency width of the standing waves.

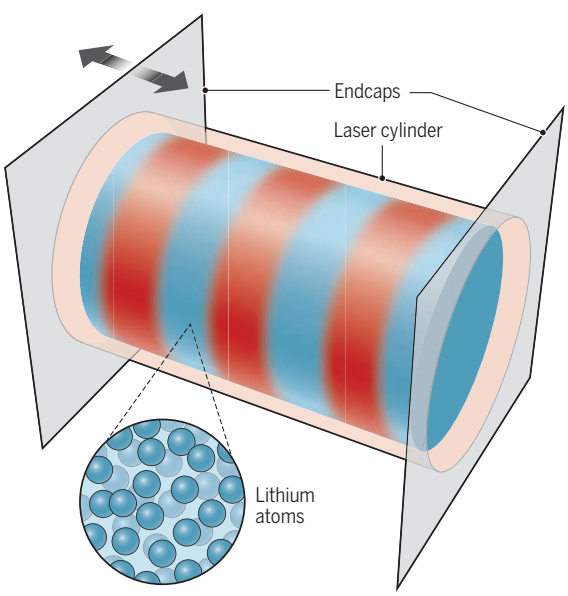

GRAPHIC: KELLIE HOLOSKI/*SCIENCE*

Department of Physics, North Carolina State University, Raleigh, NC 27695, USA. Email: tmschaef@ncsu.edu

Published by AAAS

known as Rossby modes, also called r-modes. These r-modes are unstable, and they would lead to strong gravitational wave emission and a rapid spin-down of the star if not damped by momentum or energy diffusion. Understanding the diffusivity of neutron star matter is crucial to predicting the range of allowed spin frequencies and possible r-mode signals in gravitational wave detectors.

More generally, Patel *et al.* illuminate the mechanism of transport in other strongly correlated quantum gases, such as the quark-gluon plasma investigated in heavy-ion collisions at the Relativistic Heavy Ion Collider and the Large Hadron Collider. The quark-gluon plasma is a state of matter that existed microseconds after the Big Bang, at a temperature $T \sim 2 \times 10^{12}$ K. Measurements indicate that the momentum diffusivity of the quark-gluon plasma is quite low. In a relativistic setting, the mass of the particles is very small, and the natural scale for D is $\hbar c^2/(k_B T)$,

"...observations of the unitary Fermi gas [are] directly applicable [to the physics of neutron stars], even though the temperatures and densities are many orders of magnitude larger in the star."

where c is the speed of sound and k_B is the Boltzmann constant. Experiments based on the hydrodynamic expansion of the plasma give values as small as $D \sim 0.1\ \hbar c^2/(k_B T)$. This number has been interpreted in terms of holographic models inspired by advances in string theory (*8*). However, in relativistic heavy-ion collisions, the precise mechanism of momentum transport is difficult to determine. This problem can potentially be tackled in future experiments with cold gases, for example, by carefully mapping the frequency dependence of the response of the gas to external perturbations. ■

REFERENCES AND NOTES

1. P. B. Patel *et al.*, *Science* **370**, 1222 (2020).
2. T. Schäfer, D. Teaney, *Rep. Prog. Phys.* **72**, 126001 (2009).
3. M. Alford, S. Mahmoodifar, K. Schwenzer, *Phys. Rev. D Part. Fields Gravit. Cosmol.* **85**, 024007 (2012).
4. I. Bloch, J. Dalibard, W. Zwerger, *Rev. Mod. Phys.* **80**, 885 (2008).
5. M. Bluhm, J. Hou, T. Schäfer, *Phys. Rev. Lett.* **119**, 065302 (2017).
6. L. Baird, X. Wang, S. Roof, J. E. Thomas, *Phys. Rev. Lett.* **123**, 160402 (2019).
7. T. Enss, R. Haussmann, W. Zwerger, *Ann. Phys.* **326**, 770 (2011).
8. P. K. Kovtun, D. T. Son, A. O. Starinets, *Phys. Rev. Lett.* **94**, 111601 (2005).

10.1126/science.abb6155

PLANT IMMUNOLOGY

Enzyme formation by immune receptors

Upon pathogen recognition, some plant immune receptors assemble into active enzyme complexes

By **Lei Tian** *and* **Xin Li**

Higher plants have evolved complex immune systems. Intracellular immune receptors known as nucleotide-binding leucine-rich repeat (NLR) proteins are present in both plants and animals; they are essential for immune responses (*1*). Upon infection, NLRs can recognize specific pathogen molecules and activate defense. In contrast to animals, which have a limited NLR repertoire, higher plants usually harbor hundreds of diverse *NLR* genes. However, little is known about their activation and signaling mechanisms. On pages 1184 and 1185 of this issue, Ma *et al.* (*2*) and Martin *et al.* (*3*), respectively, reveal the structure and activation mechanism of two NLRs: *Arabidopsis thaliana* RECOGNITION OF PERONOSPORA PARASITICA 1 (RPP1) and *Nicotiana benthamiana* RECOGNITION OF XOPQ 1 (ROQ1). Both NLRs self-assemble in a similar manner into tetrameric holoenzymes to activate defense responses upon direct effector recognition.

There are two classes of typical plant NLRs for sensing pathogen effectors: Toll–interleukin-1 receptor (TIR)–type NLRs (TNLs) and coiled-coil (CC)–type NLRs (CNLs), which are defined by their different amino-terminal domains. As with mammalian NLRs, plant NLRs also contain a central nucleotide-binding domain (NBD) involved in oligomerization, as well as carboxyl-terminal leucine-rich repeats (LRRs) that often participate in auto-inhibition and ligand recognition (*1*). TNLs and CNLs are activated with dissimilar mechanisms and signal through different downstream components.

Cryo–electron microscopy (cryo-EM) structural analysis of the *A. thaliana* CNL HOPZ-ACTIVATED RESISTANCE 1 (ZAR1) revealed that it assembles into a pentameric "resistosome" upon effector recognition, reminiscent of animal inflammasome rings that mediate innate immune responses (*4*). ZAR1 and an adaptor protein recognize the pathogen effector indirectly through monitoring the status of a host protein (called a decoy) that is directly targeted by the effector. The pentameric ring assembles upon binding of the effector-modified decoy, leading to the formation of a funnel-shaped structure composed of the amino-terminal CC domains of ZAR1. It has been hypothesized that this funnel associates with the cell membrane and triggers immune-related cell death (*5*). Until now, the resistosome structures of full-length TNLs have not been elucidated.

TIR-containing proteins are widely present in bacteria, archaea, mammals, and higher plants (*6*). In mammals, TIR is a signature scaffold domain of immune receptors, including Toll-like receptors (TLRs) and interleukin-1 receptors (IL-1Rs), and of some downstream adaptor proteins. Interactions of TIR domains between receptor and adaptor proteins are required for immune and inflammatory signal transduction. For example, TLR4 recruits the signaling adaptors MYD88 (myeloid differentiation primary response 88) and MAL (MYD88 adaptor-like) through TIR-TIR interactions, thereby activating downstream transcription factors such as nuclear factor κB (NF-κB) to induce inflammation (*7*). By contrast, a large number of TIR domains found in bacteria, archaea, and higher plants seem to serve as oxidized nicotinamide adenine dinucleotide (NAD^+) hydrolases (NADases) upon self-association (*6*, *8*, *9*). TIR NADase activity was discovered in mammalian SARM1 (sterile alpha and TIR motif–containing protein 1), a major executor of neuronal axon degeneration (*10*). Like SARM1, TIR domains in a number of plant TNLs also exhibit NADase activity (*8*, *9*).

Cryo-EM analysis of full-length SARM1 revealed that in its resting state, it assembles into an octamer. The carboxyl-terminal Armadillo/HEAT motif (ARM) domains block the contact between adjacent TIRs through binding to NAD^+ (*11*). With nicotinamide mononucleotide activator elicitation, the SARM1 octamer undergoes a conformational change, disrupting NAD^+ binding sites of the ARM domains to enable TIR-TIR dimerization (*11*, *12*). Interactions be-

Michael Smith Laboratories, University of British Columbia, Vancouver, BC V6T 1Z4, Canada, and Botany Department, University of British Columbia, Vancouver, BC V6T 1Z4, Canada. Email: xinli@msl.ubc.ca

Published by AAAS

tween the TIR domains then activate their NADase function. The depletion of NAD^+ and the generation of products including nicotinamide, adenosine diphosphate ribose (ADPR), and cyclic ADPR (cADPR) together seem to serve as signals to trigger cell death. Because plant TNLs lack ARM domains, it was unclear whether plant TNLs form similar octamers or adopt a parallel self-inhibition mechanism.

The *A. thaliana* TNL RPP1 recognizes its cognate effector protein ARABIDOPSIS THALIANA RECOGNIZED 1 (ATR1) from the oomycete pathogen *Hyaloperonospora arabidopsidis*. In nature, both *RPP1* and *ATR1* genes are highly polymorphic; different ATR1s are perceived by specific RPP1 variants (*13*). By contrast, the *N. benthamiana* TNL ROQ1 monitors *Xanthomonas* bacterial infections through direct recognition of the conserved effector XANTHOMONAS OUTER PROTEIN Q (XopQ) (*14*). RPP1 and ROQ1 both recognize their respective effectors ATR1 and XopQ through direct NLR-effector protein-protein interactions, which trigger strong immune responses to restrict pathogen colonization, including host cell death.

Ma *et al.* and Martin *et al.* used cryo-EM to determine the structures of the purified TNL-effector resistosome complexes. Despite the differences of the pairs, RPP1-ATR1 and ROQ1-XopQ form highly similar tetrameric clover-like structures (see the figure), which suggests that there may be a common activation mechanism for TNLs. These resistosome structures provide key insight about how RPP1 and ROQ1 can directly recognize their cognate effectors and tetramerize to promote NADase activity, thereby activating downstream immune responses. A structurally distinct domain was uncovered at the carboxyl termini of RPP1 and ROQ1, which is referred to as the C-terminal jelly-roll and Ig-like domain (C-JID). The C-JID and LRRs mediate effector binding specificity. Mutations of residues in these domains can disrupt their interaction interfaces with the effectors, resulting in reduced host cell death responses.

For both RPP1 and ROQ1, direct binding of the effectors to the LRRs and C-JID likely releases the NBDs, which can then undergo conformational change and oligomerize into a tetramer. The tetrameric ring brings the TIR domains into close contact, allowing them to form the final active TNL resistosome with NADase holoenzyme activity. Intriguingly, unlike in ZAR1 and ROQ1 resistosomes, where deoxyadenosine triphosphate (dATP) and ATP are bound to the activated NLRs, RPP1 is bound by adenosine diphosphate (ADP) in the tetrameric ring, challenging the paradigm that NLRs are activated through exchanging ADP with ATP. Future analysis of additional TNL resistosomes may help to resolve the biological role of this observation.

In both the RPP1 and ROQ1 resistosomes, tetramerization of the NBDs brings the four TIR domains close together. They form a two-fold dimer of dimers instead of a four-fold symmetric tetramer. The asymmetric TIR dimer forms one predicted NAD^+ binding site while the symmetric TIR dimers stabilize the complex. Upon activation, two dimers arise in a head-to-tail manner mediated by the BB-loop (see the figure). Subsequent TIR NADase activity induces host cell death. Mutations of amino acids within the BB-loop that only affected the head-to-tail interactions were found to alter RPP1 and ROQ1 NADase activity and their function in immunity. Therefore, tetramerization of TIR domains of TNLs to form a holoenzyme likely represents a common activation mechanism for this large class of plant NLRs. Instead of homotetramerization as observed for ROQ1 and RPP1 resistosomes, hetero-NLR pairs with atypical domains or carboxyl-terminally truncated NLRs with only the TIR or TIR-NBD domains may serve to diversify the activation possibilities of these immune receptors in higher plants through heterotetramerization (*1*).

The RPP1 and ROQ1 structures reveal a new type of TNL resistosome distinct from that of the CNL ZAR1. These findings represent a major step forward in understanding the activation mechanisms of plant TNLs. However, it remains unclear how the TIR NADase activity activates downstream immunity. In the two activated TNL resistosome structures reported by Ma *et al.* and Martin *et al.*, no NAD^+ substrate was detected. One explanation could be that activated TIR domains quickly cleave NAD^+. Alternatively, NAD^+ may not be the preferred or only in planta substrate, because the detected in vitro NADase activities of plant TNLs are often weaker than those of bacterial TIRs and mammalian SARM1 (*8*, *9*). Consequently, the complete spectrum of TNL TIR products should be investigated. Furthermore, the NADase activity of TNLs signals through key downstream components and helper NLRs (including the CNLs ADR1 and NRG1) for immune signaling in a manner that is still enigmatic (*15*). Finally, both RPP1 and ROQ1 resistosomes comprise TNLs that recognize their effectors directly. In many other cases, such as with ZAR1, other host proteins are required for effector recognition and likely for resistosome assembly. Therefore, additional structures of resistosomes of different natures will provide better understanding of the diverse activation mechanisms of higher plant NLRs. ■

Formation of a major type of plant resistosome

Direct effector binding drives the tetramerization of a plant TNL receptor, such as RPP1 and ROQ1. Formation of the holoenzyme complex through their BB-loop enables NADase activity, activating downstream immune responses.

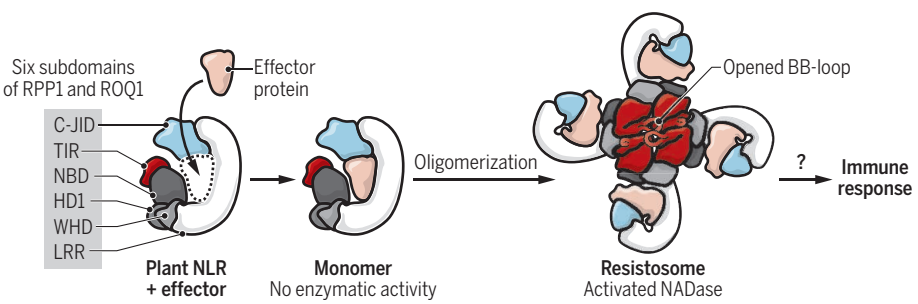

C-JID, C-terminal jelly-roll and Ig-like domain; HD1, helical domain 1; LRR, leucine-rich repeats; NADase, nicotinamide adenine dinucleotide hydrolase; NBD, nucleotide-binding domain; NLR, nucleotide-binding leucine-rich repeat; RPP1, RECOGNITION OF PERONOSPORA PARASITICA 1; ROQ1, RECOGNITION OF XOPQ 1; TNL, TIR-type NLR; TIR, Toll–interleukin-1 receptor; WHD, winged helix domain.

REFERENCES AND NOTES

1. J. D. Jones *et al.*, *Science* **354**, aaf6395 (2016).
2. S. Ma *et al.*, *Science* **370**, eabe3069 (2020).
3. R. Martin *et al.*, *Science* **370**, eabd9993 (2020).
4. J. Wang *et al.*, *Science* **364**, 44 (2019).
5. J. M. Zhou, Y. Zhang, *Cell* **181**, 978 (2020).
6. K. Essuman *et al.*, *Curr. Biol.* **28**, 421 (2018).
7. T. Ve *et al.*, *Nat. Struct. Mol. Biol.* **24**, 743 (2017).
8. S. Horsefield *et al.*, *Science* **365**, 793 (2019).
9. L. Wan *et al.*, *Science* **365**, 799 (2019).
10. K. Essuman *et al.*, *Neuron* **93**, 1334 (2017).
11. Y. Jiang *et al.*, *Nature* 10.1038/s41586-020-2862-z (2020).
12. M. Bratkowski *et al.*, *Cell Rep.* **32**, 107999 (2020).
13. K. V. Krasileva *et al.*, *Plant Cell* **22**, 2444 (2010).
14. A. Schultink *et al.*, *Plant J.* **92**, 787 (2017).
15. L. M. Jubic *et al.*, *Curr. Opin. Plant Biol.* **50**, 82 (2019).

ACKNOWLEDGMENTS

We apologize for original literature not cited because of space limitations. We thank J. Chai and K. Ao for discussions and careful reading of the manuscript. Supported by Natural Sciences and Engineering Research Council of Canada (NSERC)–Discovery and NSERC-CREATE-PRoTECT programs and by a scholarship from China Scholarship Council (L.T.).

10.1126/science.abf2833

GRAPHIC: A. KITTERMAN/*SCIENCE*

Published by AAAS

ENGINEERING

Miniaturization of robots that fly on beetles' wings

The shock-absorbing wings of the rhinoceros beetle battle in-flight collisions

By **Jiyu Sun**

For centuries, humans have been fascinated by flight. Leonardo da Vinci (1452–1519) meshed his skills as an artist, biologist, and engineer to sketch designs for flying machines modeled after bird and bat anatomy. Today, multidisciplinary scientists work systematically from investigating biological prototypes to conducting flight performance tests on new bionic robots. On page 1214 of this issue, Phan and Park (*1*) describe how they used biology, robotics, and a little bit of art to design a new miniaturized micro air vehicle (MAV) that is bioinspired by the rhinoceros beetle (*Allomyrina dichotoma*). Their MAV mimics the beetle's hindwings, which have origami-like folds that allow the insect to recover from flight collision.

Insects and birds can both fly, but they have different mechanisms and anatomy. Birds use muscles in their wings to control flight movements. Insects control flight with muscles in their wing base or thoracic region and also with the wing's compliant structures, which include folding patterns, small hairs, veins, and the elastic protein resilin. Because miniaturization of MAVs drives the research, scientists increasingly have turned to insects such as beetles for bioinspired MAV blueprints. These robotic devices must be small, lightweight, and robust. They should also exhibit excellent wind resistance, a sustained energy supply, and rapid folding of wings.

The anatomy of various organisms can inform MAV-deployable wing design. For example, four-dimensional–printed elastic wings mimic the wing of the earwig (*2*). Four-degrees-of-freedom deformable folding wings (*3*) and passive unfolding wings (*4*) were bioinspired by bats. However, the sizes of these wings are larger than those of beetle-bioinspired wings. Beetles differ from other insects in that their forewings (elytra) are hardened and encased, whereas their hindwings—which they use to fly—are deployable, a feature that directly enables a reduction in body size. Despite their small size, beetles exhibit an impressive flight ability. For *Anoplophora glabripennis* beetles, the maximum distances traveled in a season are reported to be 2644 m for females and 2394 m for males (*5*). The largest flight distance recorded over the life span of an adult Asian long-horned beetle was more than 14 km (*6*), and their maximum observed flight speed was 5.3 m/s (*7*).

Previous beetle-based miniature flying robots have made use of compliant origami structures inspired by the wing vein in ladybird beetles to achieve gliding and jumping functions (*8*). A mini drone has also been built with deployable wings whose design was based on the origami-like mechanism of insect wings (*9*).

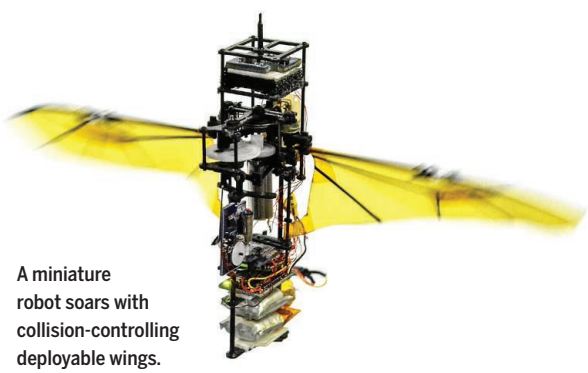

A miniature robot soars with collision-controlling deployable wings.

PHOTO: PHAN AND PARK (*1*)

Phan and Park report that, in the rhinoceros beetle, the origami-like folds in their hindwings provided a shock-absorbing function during in-flight collisions without completely folding. The authors used this mechanism to build a beetle-inspired, flapping robot that collides without folding its wings, thereby enabling stable flight recovery after collision.

Using a high-speed multicamera system, Phan and Park observed that beetle wings unfold by aerodynamic forces produced by flapping and then locked in place to sustain flight. Through experiments with beetles flying between narrow poles at different angles and positions, the authors defined two means by which the insects withstand in-flight collisions. One response involves perching on an obstacle with its legs when it hits the inner, rigid segment of the hindwing. The other response is to continue flight if the obstacle hits the outer, folding segment of the wing, which passively folds and springs back into place when the obstacle is passed.

Phan and Park validated the beetle design principle by fabricating a miniature folding wing and integrating it in a previously described, small, flapping-wing robot (*10*). The new miniature MAV displayed both wing unfolding and resilience to an obstacle hitting the outer, folding segment of the wing. This robustness should spur interest in this wing mechanism for aerial robots.

Challenges remain for the development of deployable MAVs. Deployment inevitably depends on the fatigue resistance of the MAV wings, which is directly related to the design and use of the MAV. In nature, beetles have resilin in their hindwings at positions that require repeated folding (*11*) or joints that can soften and fold during a collision to avoid damage (*12*). These features can inspire future designs of deployable MAV wings. For flapping MAVs, vibration generated by the drivers, airborne components, and flapping actions can create uncontrolled takeoffs and unstable free flight. Beetles can resolve these problems with flexible elastic biomaterials in their hindwings and joints to absorb the energy caused by vibration. Thus, researchers might consider incorporating these features into MAVs with deployable flapping wings to increase the overall wing strength and flight stability.

Future research should also focus on resolving the unsteady aerodynamics problem for MAVs with low Reynolds numbers (the ratio of inertial forces to viscous forces). Scientists could then tackle the manufacturing technology for miniaturization of MAV components (such as airfoil and fuselage) and for flight control under unsteady aerodynamics conditions (*13*). ■

Key Laboratory of Bionic Engineering (Ministry of Education, China), Jilin University, Changchun, The People's Republic of China. Email: sjy@jlu.edu.cn

REFERENCES AND NOTES

1. H. V. Phan, H. C. Park, *Science* **370**, 1214 (2020).
2. J. Deiters, W. Kowalczyk, T. Seidl, *Biol. Open* **5**, 638 (2016).
3. A. Ramezani *et al.*, *Sci. Robot.* **2**, eaal2505 (2017.)
4. A. K. Stowers, D. Lentink, *Bioinspir. Biomim.* **10**, 025001 (2015).
5. M. T. Smith *et al.*, *Environ. Entomol.* **33**, 435 (2004).
6. M. Javal *et al.*, *J. Appl. Entomol.* **142**, 282 (2017).
7. D. W. Williams *et al.*, *Environ. Entomol.* **33**, 644 (2004).
8. S. M. Baek *et al.*, *Sci. Robot.* **5**, eaaz6262 (2020).
9. L. Dufour, K. Owen, S. Mintchev, D. Floreano, 2016 IEEE/RSJ International Conference on Intelligent Robots and Systems (IEEE, 2016), pp. 1576–1581.
10. H. V. Phan *et al.*, *IEEE Robot. Autom. Lett.* **5**, 5059 (2020).
11. F. Haas *et al.*, *Proc. R. Soc. London Ser. B* **267**, 1375 (2000).
12. S. Mintchev *et al.*, *IEEE Robot. Autom. Lett.* **2**, 1248 (2017).
13. J. Sun *et al.*, *J. Mech. Behav. Biomed. Mater.* **94**, 63 (2019).

10.1126/science.abf1925

Published by AAAS

SEMICONDUCTOR PHYSICS

Probing the dark side of the exciton

Photoemitted electrons reveal large-momentum ("dark") excitons in monolayer WSe_2

By **Meng Xing Na**[1,2] *and* **Ziliang Ye**[1,2]

Two-dimensional (2D) semiconductors, such as transition-metal dichalcogenides, may enable new optoelectronic technologies (*1*). The optical excitation in these atomically thin materials creates tightly bound excitons composed of an excited electron and a valence-state hole (*2*), as well as a plethora of exciton complexes due to the reduced screening in Coulomb attraction (*3*–*5*). So far, excitons with large momenta have not been directly probed because photons only carry very small momenta and cannot directly interact with large-momentum excitons, but these dark excitons are predicted to exist in certain 2D semiconductors (*6*, *7*). On page 1199 of this issue, Madéo *et al.* (*8*) used time- and angle-resolved photoemission spectroscopy (TR-ARPES) to directly probe dark excitons in monolayer tungsten diselenide (WSe_2). By tracking the dynamics of electrons that constitute both bright and dark excitons, the authors reveal how both are formed and show that the latter outnumber the former at steady state.

[1]Department of Physics and Astronomy, University of British Columbia, Vancouver, BC V6T 1Z1, Canada. [2]Quantum Matter Institute, University of British Columbia, Vancouver, BC V6T 1Z4, Canada. Email: zlye@phas.ubc.ca

There are two families of excitons in 2D semiconductors, with electrons at different valley-like local minima of the conduction band. Each valley is named after its location in the Brillouin zone (momentum-space). Bright excitons consist of electrons and holes both located in K valleys that form through the direct transition of the electron to an excited state with the same momentum (see the first figure). As the momentum of the exciton is defined by the momentum difference between its constituting electron and hole, these so-called K-K excitons have zero momentum and can directly interact with light. Dark Q-K excitons are composed of an electron excited indirectly into a Q valley with a different momentum than that of the hole left in a K valley. Valleys with opposite momenta are equally populated in this study.

"These results...constitute a direct probe of dark-exciton formation and its binding energy and dynamics..."

Madéo *et al.* performed their TR-ARPES experiment by combining a photoemission electron microscope (PEEM) with an extreme ultraviolet (XUV) light source (see the second figure). They first shine an ultrafast visible-light pulse at the WSe_2 monolayer. By tuning the wavelength of this pulse, they can excite either excitons or free carriers. After a variable delay time, an ultrafast XUV pulse is shone onto the sample. The high photon energy of the XUV light then ejects electrons from the monolayer.

With no surface state present, the authors directly accessed the electrons' energy and momentum inside the material by analyzing the kinetic energy and emission angle of the ejected electron (measured here by an angle-resolved time-of-flight analyzer). Both the visible and XUV light are ultrafast pulses. The first visible pulse excites the system, and the second XUV pulse acts effectively as a camera shutter. By fine-tuning the delay between the excitation and the shutter, the authors obtain a "movie" of electrons in momentum space in which free carriers, bright excitons, and dark excitons all have distinct signatures.

The authors find that both bright and dark excitons exist in the monolayer WSe_2. Notably, the bright K-K excitons preferentially convert into dark Q-K excitons through phonon scattering and lead to a density of dark excitons double that of the

Bright and dark excitons

Bright excitons have electrons in the K valley conduction bands and have zero momentum. Dark excitons have electrons in the Q valley conduction bands and carry momentum.

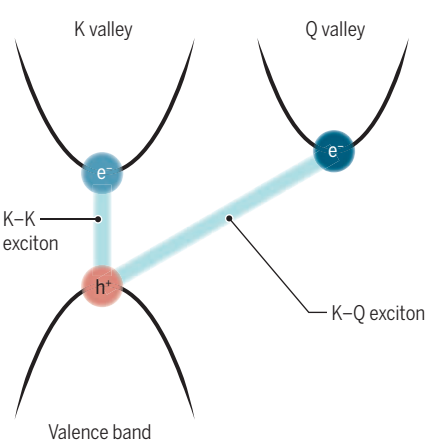

Movies of dark-exciton formation

Dark excitons cannot be probed directly with photons. Madéo *et al*. used photoemission microscopy to reveal them in monolayer tungsten diselenide (WSe_2).

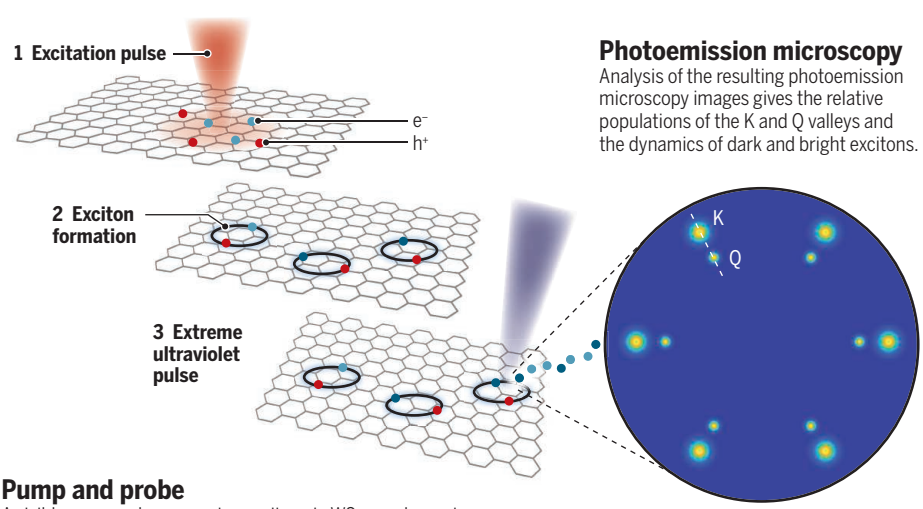

Photoemission microscopy
Analysis of the resulting photoemission microscopy images gives the relative populations of the K and Q valleys and the dynamics of dark and bright excitons.

Pump and probe
A visible pump pulse generates excitons in WSe_2, and an extreme ultraviolet probe pulse ejects electrons.

GRAPHIC: C. BICKEL/*SCIENCE*

Published by AAAS

bright excitons. The dark excitons also have a longer lifetime, so they become a reservoir for the bright excitons at steady state. Tuning the excitation light off the exciton resonance excites free electrons and holes, and after about 500 fs, a quasi-equilibrium exciton ensemble forms.

By comparing the photoemission signal from excitons with the free-electron energy at the band edge, Madéo *et al.* deduce the exciton binding energy for both bright and dark excitons. These results, which constitute a direct probe of dark-exciton formation and its binding energy and dynamics, were made possible by a convergence of improvements in the spatial resolution of the ARPES instrument as well as the high photon energy of the ultrafast high-harmonic XUV source that could probe the entire Brillouin zone of WSe_2 (*9*).

Although dark excitons do not interact directly with light, the electrons that constitute such dark excitons are accessible by photoemission (*10*, *11*). Besides the Q-K exciton, other dark excitons in 2D semiconductors that are accessible by the technique of Madéo *et al.* include intervalley excitons, spin-triplet excitons, Rydberg states with finite angular momentum, and higher-order exciton complexes (*12*–*14*). Another equally rewarding direction would be to study the wave function of a single exciton that was obscured in the current study by phonon scattering and other scattering channels (*10*, *11*). The rapid progress in van der Waals heterostructures also calls for more direct techniques to resolve their emerging electronic structures (*15*). It is expected that there will be many exciting opportunities to apply these powerful electronic probes in studying the excited states of quantum materials. ■

REFERENCES AND NOTES

1. K. F. Mak, J. Shan, *Nat. Photonics* **10**, 216 (2016).
2. G. Wang *et al.*, *Rev. Mod. Phys.* **90**, 021001 (2018).
3. S.-Y. Chen, T. Goldstein, T. Taniguchi, K. Watanabe, J. Yan, *Nat. Commun.* **9**, 3717 (2018).
4. Z. Ye *et al.*, *Nat. Commun.* **9**, 3718 (2018).
5. Z. Li *et al.*, *Nat. Commun.* **9**, 3719 (2018).
6. A. Steinhoff *et al.*, *Nano Lett.* **15**, 6841 (2015).
7. M. Selig *et al.*, *Nat. Commun.* **7**, 13279 (2016).
8. J. Madéo *et al.*, *Science* **370**, 1199 (2020).
9. M. X. Na *et al.*, *Science* **366**, 1231 (2019).
10. A. Rustagi, A. F. Kemper, *Phys. Rev. B* **97**, 235310 (2018).
11. D. Christiansen, M. Selig, E. Malic, R. Ernstorfer, A. Knorr, *Phys. Rev. B* **100**, 205401 (2019).
12. Z. Li *et al.*, Nat. Commun. 10, 2469 (2019).
13. X.-X. Zhang, Y. You, S. Y. F. Zhao, T. F. Heinz, *Phys. Rev. Lett.* **115**, 257403 (2015).
14. Z. Ye *et al.*, *Nature* **513**, 214 (2014).
15. C. Jin *et al.*, *Nat. Nanotechnol.* **13**, 994 (2018).

ACKNOWLEDGMENTS

We are supported by the Max Planck–UBC–UTokyo Centre for Quantum Materials, the Canada First Research Excellence Fund, the Natural Sciences and Engineering Research Council of Canada, and the Canada Research Chairs Program (Z.Y.).

10.1126/science.abf0371

PLANT SCIENCE

Constraints on selfish behavior in plants

Plants overproduce roots to secure resources nearby but avoid costly trips to neighbors' patches

By **Marina Semchenko**[1,2]

We are used to human behavior, and the actions of other animals, being described as selfish, aggressive, or cooperative. Such words come up less often when contemplating plants. Yet plants too have evolved a fascinating array of behavioral strategies in their struggle for resources, although these are hard to demonstrate and quantify. Whether and when it pays for plants to selfishly overproduce roots and preempt resource capture by competitors, or cooperate by restraining root growth, has been the subject of extended debate (*1*, *2*). On page 1197 of this issue, Cabal *et al.* (*3*) tackle this question with a new theoretical model and an empirical test that highlight spatial costs of nutrient foraging as key to resolving apparent discrepancies between previous studies.

Besides establishing which behaviors occur in the plant kingdom, determining the extent of root overproduction in the scramble for limited soil nutrients is vital for understanding global carbon cycling and finding solutions to major challenges that face humanity. Plants capture atmospheric carbon during photosynthesis, and a large fraction is channeled into root production, representing a vast capacity for carbon storage and a potential focus for approaches to mitigate climate change (*4*). Global models of primary productivity and carbon storage—and ecosystem responses to climate change—could be substantially modified by accounting for overinvestment into capture of shared resources (*5*). Moreover, understanding the factors that enhance or suppress competitive root proliferation could open new avenues in crop breeding and agricultural practice (*6*).

Rather than focusing on the total mass of roots produced by competing plants, Cabal *et al.* bring a spatial dimension to root foraging by modeling the increasing cost of nutrient transport from locations further away from the plant stem. This cost constrains the extent of root foraging, leading to partial segregation of root systems between neighboring plants. However, the situation is different in areas close to the plant stem: Low nutrient-transportation costs make excessive root production cheap and give a competitive advantage against neighbors' roots that have traveled from afar; the model predicts that plant roots should avoid costly trips to neighboring territories but invest in securing resources closer to home. Empirical observations appear to support the predictions of the model. Cabal *et al.* corroborated the model using pepper plants, and an independent study that mapped the spatial distribution of roots in several grassland species showed that some plants shrank their foraging ranges when experiencing stronger competition but aggregated roots in the remaining core areas (*7*). Therefore, it seems that a successful strategy involves excessive root production in areas with low costs, but reduced overlap with neighboring root systems (see the figure). The latter has previously been interpreted as cooperative behavior or territorial defense (*8*) but seems to emerge as part of a selfish strategy restrained by nutrient transportation costs.

By manipulating relevant model parameters, Cabal *et al.* provide further insights: Excessive root production should be strongest in dense vegetation, where short distances between competing plants preclude exclusive access to resources, and in productive ecosystems or species with low root-construction costs. This suggests that agricultural practices that involve high fertilization rates and high planting densities are particularly conducive to competitive root proliferation at the expense of economically essential yield. Hence, optimal fertilizer use efficiency and improved yield might be achieved by adjusting crop spacing and fertilization practices in light of root spatial behavior and by breeding varieties that are less responsive to neighbor presence and show more restrained growth of competitive organs (*9*). Such advances have already been achieved, sometimes unintentionally, aboveground by breeding crop

[1]School of Natural Sciences, University of Manchester, Manchester, UK. [2]Department of Botany, University of Tartu, Tartu, Estonia. Email: marina.semchenko@manchester.ac.uk

Published by AAAS

Mapping plant roots

Roots (white dots) explore soil widely in the absence of neighbors (left-hand cirles; root density increases from blue to yellow). In the presence of neighbor roots (black dots in the right-hand circles), the plant in the top row keeps roots close to its stem, whereas the plant in the bottom row places them toward neighbors' roots (*7*). Root mapping enables testing of plant behavioral theory.

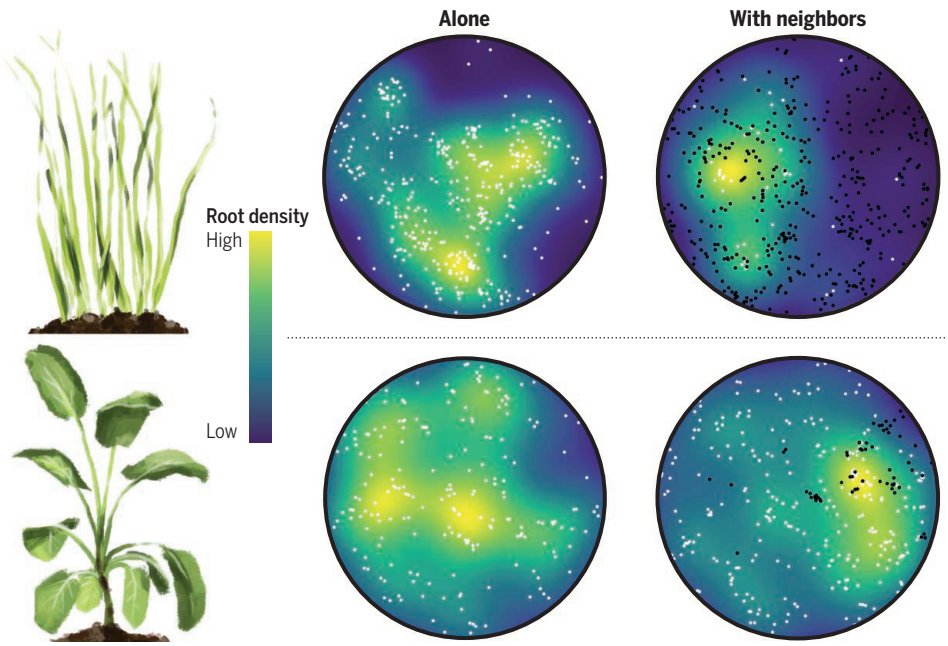

varieties with low stature (*6*) and reduced responsiveness to shading by neighbors (*10*). Conversely, overproliferation of roots could be enhanced in cover crops to maximize the positive effects on soil organic matter and associated benefits for soil fertility and disease resistance (*11*).

The dependence of root production on the spatial locations of interacting roots highlights the importance of fine-scale spatial measurements in resolving ongoing debate about plant behavior. By measuring only total root production or root production over large spatial scales, we may miss local over- and underproliferation and risk gathering data that reflect experimental artifacts of soil volume and nutrients (*2*, *12*). However, it should also be recalled that many plant species have evolved in conditions of perpetual competition, seldom growing in the absence of neighbors. Some plants may therefore always overproduce roots close to their stems, independent of neighbor presence. Verifying the existence of selfish overinvestment in root growth would be extremely challenging in such instances. Just as we do not expect trees to stop producing trunks in the absence of surrounding trees, we should not necessarily expect root overproduction to be curtailed in the absence of competition (*13*).

Current evolutionary models of plant root production do not require that plants are able to detect competitors but are purely driven by resource dynamics, which nonetheless require the existence of complex signaling mechanisms. However, we know that some plant species are capable of detecting the proximity and even genetic identity of neighbors, which may trigger measures to secure resources before direct competition takes place (see the figure) (*14*). Plants may also assess the relative competitive rank of their neighbors and choose to avoid costly battles with opponents that they have no chance of winning (*7*, *14*). This raises the prospect of greater diversity in plant foraging strategies and points to further avenues for exploration. ■

REFERENCES AND NOTES

1. C. E. Farrior, *Proc. Biol. Sci.* **286**, 20191129 (2019).
2. G. G. McNickle, *Funct. Ecol.* **34**, 2199 (2020).
3. C. Cabal, R. Martínez-García, A. de Castro Aguilar, F. Valladares, S. W. Pacala, *Science* **370**, 1197 (2020).
4. R. Lal, *Science* **304**, 1623 (2004).
5. G. G. McNickle, M. A. Gonzalez-Meler, D. J. Lynch, J. L. Baltzer, J. S. Brown, *Proc. Biol. Sci.* **283**, 20161993 (2016).
6. R. F. Denison, E. T. Kiers, S. A. West, *Q. Rev. Biol.* **78**, 145 (2003).
7. A. Lepik, M. Abakumova, J. Davison, K. Zobel, M. Semchenko, *J. Ecol.* 10.1111/1365-2745.13535 (2020).
8. H. J. Schenk, R. M. Callaway, B. E. Mahall, *Adv. Ecol. Res.* **28**, 145 (1999).
9. Y. H. Zhu, J. Weiner, M. X. Yu, F. M. Li, *Evol. Appl.* **12**, 733 (2018).
10. M. Semchenko, K. Zobel, *Field Crops Res.* **93**, 151 (2005).
11. R. P. Larkin, *Annu. Rev. Phytopathol.* **53**, 199 (2015).
12. L. Hess, H. de Kroon, *J. Ecol.* **95**, 241 (2007).
13. A. Hodge, D. Robinson, B. S. Griffiths, A. H. Fitter, *Plant Cell Environ.* **22**, 811 (1999).
14. A. Novoplansky, *Plant Cell Environ.* **32**, 726 (2009).

10.1126/science.abf2785

NEUROSCIENCE

Stimulating the brain to restore vision

High-definition brain prostheses are developed for treating blindness

By **Michael S. Beauchamp** *and* **Daniel Yoshor**

More than 70 years ago, electrical stimulation of the human visual cortex was shown to elicit the perception of a brief flash of light, or phosphene (*1*). Subsequently, there were numerous attempts to develop cortical visual prostheses (CVPs) that electrically stimulate the visual cortex to restore vision to people with acquired blindness (*2*–*4*). The basic design of a CVP is simple: A head-mounted camera captures the visual scene, and a computer translates it into patterned brain stimulation. However, CVP implementation foundered on technological limitations, especially the size and complexity of the stimulation hardware. Advances in miniaturization and the efficiency of digital circuits suggest that it is time to try again (*5*, *6*). On page 1191 of this issue, Chen *et al.* (*7*) describe the implantation of more than 1000 electrodes in the visual cortex of nonhuman primates (NHPs) to create artificial vision.

This technical tour de force relied on features of early visual cortex shared by humans and NHPs. The visual cortex takes up a substantial fraction of the cerebral tissue, ~20% in humans. This creates a surface area of many square centimeters that can accommodate the implantation of electrodes. The visual cortex is retinotopic, meaning that there is an orderly mapping between each location in the visual scene and each location in the brain. A CVP with an array of electrodes can provide an array of phosphenes, similar to individual lights comprising a stadium scoreboard, that can be activated to produce visual sensations (percepts).

In natural vision, information from the visual scene moves through a hierarchical network of processing stages, from the retina to the thalamus to primary visual

Department of Neurosurgery, Perelman School of Medicine at the University of Pennsylvania, Philadelphia, PA, USA. Email: michael.beauchamp@pennmedicine.upenn.edu; daniel.yoshor@pennmedicine.upenn.edu

GRAPHIC: V. ALTOUNIAN/*SCIENCE* FROM M. SEMCHENKO

Published by AAAS

cortex (V1) and higher visual areas, such as the fourth visual area (V4). Chen *et al.* implanted electrode arrays in both V1 and V4 of NHPs. For CVPs to function effectively, the current level for each electrode must be individually adjusted so that the current is sufficient to produce a detectable phosphene but not so high that the phosphene expands to cover an extended region of space. This requires time-consuming calibration in which the participant reports their percept at multiple different current levels for every electrode. Chen *et al.* address this problem by stimulating electrodes in V1 while recording from electrodes in V4. They show that it is possible to estimate the appropriate V1 stimulation current from the recorded neuronal responses in V4, a process that could be conducted automatically and rapidly for multiple electrodes.

For millions of patients with damaged or diseased eyes leading to blindness, there are few or no treatment options. Recently, six patients were implanted with a CVP in a U.S. Food and Drug Administration (FDA)–approved clinical trial. However, the device has only 60 electrodes, limiting patients to simple tasks such as detecting the light or dark areas in a visual scene. By contrast, the device developed by Chen *et al.* comprises 16 arrays of 64 electrodes each, for a total of 1024 electrodes. The high electrode count meant that Chen *et al.* could arrange phosphenes in the shape of different letters, which the NHPs were trained to discriminate (see the figure). In addition, the NHPs were able to accurately perform simpler tasks, such as making eye movements to the location of a phosphene, determining whether two phosphenes were in a horizontal or vertical configuration, and deciding whether two phosphenes were stimulated in one order or another, creating the impression of apparent motion.

The electrodes used by Chen *et al.* penetrated into the cortex. Because intracortical electrodes are near the stimulated neurons, the stimulation currents are 10- to 100-fold less than that required for electrodes that sit further away atop the cortex, as in the FDA-approved CVP. When hundreds of electrodes are stimulated at once, low currents are essential to minimize both the power consumption of the device and the amount of current injected into the brain.

A number of technological and biological issues remain. On the technological front, the electrode arrays used by Chen *et al.* require a wired connection between the brain and the rest of the CVP. A wireless device will be necessary for long-term implantation of a clinical device in humans. Fortunately, considerable advances in neural stimulation with biocompatible wireless devices mean that solutions are close at hand (*8*).

Phosphenes are experienced as bright flashes, not the rich colors and forms that characterize natural vision. The reason for this difference is likely that neurons in V1 respond to simple visual features, such as oriented lines. Stimulating these neurons produces a correspondingly simple percept (*9*, *10*). Neurons in higher-level visual areas respond to more complex features, and electrical stimulation of these areas can produce the experience of seeing colors (*11*) or faces (*12*). It is intriguing to speculate whether the NHPs in the Chen *et al.* study could be induced to see more naturalistic patterns if V4 and V1 were stimulated at the same time.

Even with 1024 electrodes, the letter shapes that can be generated are crude (see the figure). New array technologies with orders-of-magnitude more electrodes will facilitate the generation of more refined shapes. Advanced stimulation algorithms, akin to software that accompanies the CVP hardware, can also be applied. With current steering, electricity is delivered to adjacent electrodes to stimulate tissue between the implanted electrodes, creating more phosphene locations that fill in the retinotopic map (*13*). Another technique, called dynamic stimulation, uses the sequence of stimulated electrodes to convey information. For instance, the letter T could be conveyed as a horizontal stroke followed by a vertical stroke. Human patients implanted with small numbers of visual cortex electrodes were able to identify letter shapes delivered using a combination of current steering and dynamic stimulation (*14*).

Future studies should also investigate the full realm of possible transformations between the visual scene and patterned brain stimulation. Advanced machine vision can extract relevant information from the visual scene, which could change based on circumstance. For example, in a navigation task, arrow shapes could by delivered to signal the correct heading direction (*15*). After decades of false starts, there is a bright future for CVPs. Chen *et al.* set a new benchmark for the next generation of CVPs by demonstrating that 1000 electrodes are sufficient to create percepts of letters, orientation, and motion. Advances in wireless stimulation, high-density electrode fabrication, and stimulation algorithms offer hope that new devices will provide useful visual function for people living with blindness. ■

Brain stimulation to create artificial vision

Electrical stimulation of the visual cortex is used to create the perception of letters. Letter shapes were decomposed into dot patterns and shown on a computer display to train nonhuman primates (NHPs). The NHPs learned 16 different letters. (An example training pattern for the letter "A" is shown.) Then, between 8 and 15 visual cortex electrodes were stimulated to create artificial percepts. Simulated percepts for the letters "A" (left) and "L" (right) are shown.

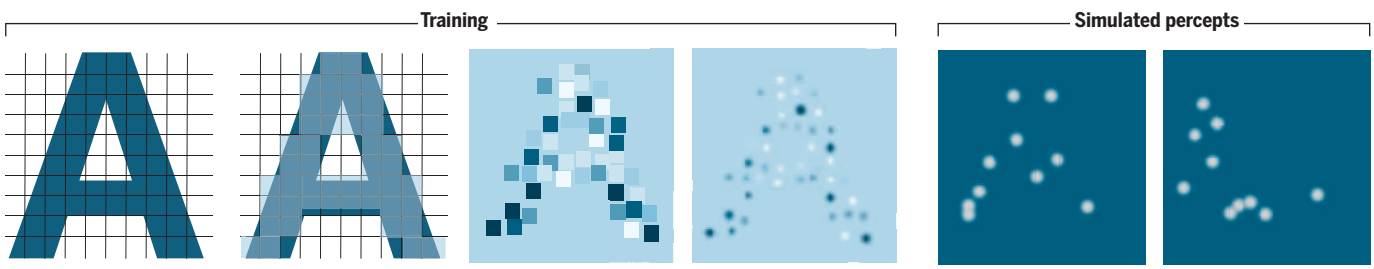

GRAPHIC: N. CARY/*SCIENCE* FROM CHEN *ET AL.* (*7*)

REFERENCES AND NOTES

1. W. Penfield, T. Rasmussen, *The Cerebral Cortex of Man* (The Macmillan Company, 1950).
2. G. S. Brindley, W. S. Lewin, *J. Physiol.* **196**, 479 (1968).
3. W. H. Dobelle *et al.*, *Nature* **259**, 111 (1976).
4. E. M. Schmidt *et al.*, *Brain* **119**, 507 (1996).
5. P. R. Troyk, in *Artificial Vision: A Clinical Guide*, V. P. Gabel, Ed. (Springer, 2017).
6. W. H. Bosking *et al.*, *Annu. Rev. Vis. Sci.* **3**, 141 (2017).
7. X. Chen *et al.*, *Science* **370**, 1191 (2020).
8. A. Singer *et al.*, *Neuron* **107**, 631 (2020).
9. J. Winawer, J. Parvizi, *Neuron* **92**, 1213 (2016).
10. D. K. Murphey *et al.*, *Proc. Natl. Acad. Sci. U.S.A.* **106**, 5389 (2009).
11. D. K. Murphey *et al.*, *Curr. Biol.* **18**, 216 (2008).
12. V. Rangarajan *et al.*, *J. Neurosci.* **34**, 12828 (2014).
13. J. B. Firszt *et al.*, *Otol. Neurotol.* **28**, 629 (2007).
14. M. S. Beauchamp *et al.*, *Cell* **181**, 774 (2020).
15. Y. Liu *et al.*, *eLife* **7**, e37841 (2018).

ACKNOWLEDGMENTS

D.Y. is a principal investigator for a clinical trial of the Second Sight Orion CVP.

10.1126/science.abf3684

Published by AAAS

RETROSPECTIVE

Mario J. Molina (1943–2020)

Visionary environmental chemist

By **Kimberly A. Prather**

Mario J. Molina, an environmental chemist who dedicated his life to explaining and solving key societal challenges, died on 7 October. He was 77 years old. Molina showed how chlorofluorocarbons (CFCs) were destroying Earth's protective ozone layer over Antarctica and worked to ban them. He also spearheaded efforts to improve air quality in Mexico, the United States, and Asia. He was one of the first to sound the alarm that continuing business as usual would likely lead to a climate catastrophe. With his passing, the world has lost a tireless advocate for our environment.

Born in Mexico City on 19 March 1943, Molina loved science at an early age, converting a bathroom in his family home into his own personal chemistry laboratory. He received his bachelor's degree in chemical engineering at the National Autonomous University of Mexico in 1965, his master's degree from the Albert Ludwig University of Freiburg, Germany, in 1967, and his Ph.D. in physical chemistry from the University of California, Berkeley, in 1972. In 1973, Molina became a postdoctoral fellow at the University of California, Irvine (UCI), in the lab of chemist F. Sherwood Rowland, who would become his lifelong friend and collaborator. Molina spent the next 30 years teaching and researching at UCI, the Jet Propulsion Laboratory, the Massachusetts Institute of Technology, and the University of California, San Diego (UCSD). In 2005, he established the Molina Center for Strategic Studies in Energy and the Environment in Mexico City.

As part of their Nobel Prize–winning efforts on the environmental fate of the widely used refrigerants and propellants known as CFCs, Molina and Rowland were the first to propose that once CFCs made their way into the stratosphere, they could be broken down by solar radiation into chlorine atoms that could destroy the ozone layer. They published their predictions in 1974, but their calls to stop all production of CFCs fell on deaf ears because there was no evidence yet of ozone degradation. By 1985, evidence of a hole in the ozone was building. Molina published his laboratory findings in 1987, showing that stable chlorine-containing gases could catalytically break down and lead to ozone loss, bolstering a key connection between lab studies and global observations of the ozone hole.

Throughout his career, Molina advocated for scientists to apply scientific research directly to solve societal problems. With Rowland, he helped implement the Montreal Protocol, which is considered the most successful and effective environmental global treaty ever negotiated and implemented. It provides an inspirational success story of how fundamental chemistry can be used to address global environmental problems. In 1995, Molina became the first Mexican-born scientist to receive a Nobel Prize in Chemistry, which he shared with F. Sherwood Rowland and Paul J. Crutzen for "contributing to our salvation from a potential global environmental catastrophe."

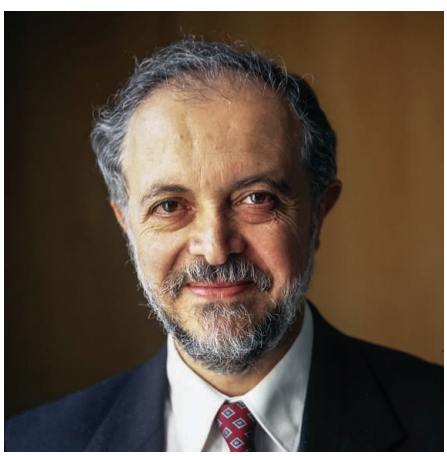

PHOTO: LOUIS MONIER/GAMMA-RAPHO VIA GETTY IMAGES

I met Molina in the late 1990s at a conference. He was gracious, soft-spoken, and generous from the moment I nervously introduced myself. Over the years, Molina became my mentor, scientific collaborator, colleague, and close friend. While working on climate and air quality policy issues at his center in Mexico City, he joined forces with scientists at UCSD on fundamental chemistry issues related to atmospheric chemistry and climate and helped establish the National Science Foundation Center for Aerosol Impacts on Chemistry of the Environment (CAICE), headquartered at UCSD. As director of CAICE, I was honored to have Molina as my science adviser, providing guidance and support as our team strove to reproduce realistic tropospheric aerosol surfaces representative of the marine atmosphere. Molina often marveled at how his lab studies on chemistry occurring on stratospheric surfaces were far easier than our efforts to reproduce more chemically complex tropospheric marine aerosol surfaces. This represents Molina's character perfectly—always downplaying his own (Nobel Prize–winning) accomplishments.

Molina dedicated substantial time to communicating the urgent need to enact policies grounded in science. He encouraged scientists to avoid getting caught up in figuring out every final detail before working to implement fixes. He applied this philosophy to the ozone hole, air quality, climate change, and ultimately COVID-19. This year, he spent extensive time communicating how to protect against airborne transmission of severe acute respiratory syndrome coronavirus 2 (SARS-CoV-2). His efforts, and those of many of the scientists he trained and mentored, myself included, are now leading to greater public awareness of the critical need for wearing masks to save lives.

Molina was an elected member of the National Academy of Sciences, the National Academy of Medicine, the Vatican's Pontifical Academy of Sciences, El Colegio Nacional de México, the Mexican Academy of Sciences, and the Mexican Academy of Engineering. He also served on the U.S. President's Council of Advisors on Science and Technology under former presidents Bill Clinton and Barack Obama. He has been recognized with 29 honorary degrees and many awards, including the Presidential Medal of Freedom in 2013.

I first realized that I was not alone in considering Molina a hero when we worked together in Mexico City (where he introduced me to the very best of our shared favorite food, molé). Throngs of people surrounded him wherever we went. I had never seen a scientist treated like a rock star before, and I will always remember how gracious he was—smiling, answering questions, and taking pictures with his "fan club."

Molina's inspirational combination of outstanding science and global impact has shaped my own career and the lives of many others. By setting an example, he showed the importance of communicating science to implement positive change. He loved teaching and interacting with students and served as a role model for generations of scientists. The world has lost an exceptional scientist and an even better human being in Mario Molina. I am sure that, like so many of us, Mother Earth has shed tears of her own over the loss of one of her greatest champions. ■

CAICE, University of California, San Diego, San Diego, CA 92093, USA. Email: kprather@ucsd.edu

10.1126/science.abf4521

Published by AAAS

POLICY FORUM

PHOTO: ROBERT NICKELSBERG/GETTY IMAGES

Advance planning can help communities adjust to fossil fuel–fired power plant closures, as with the 2019 shutdown of the Bruce Mansfield Power Plant in Shippingport, Pennsylvania.

ENERGY AND CLIMATE

Fossil electricity retirement deadlines for a just transition

A 2035 deadline for decarbonizing U.S. electricity would strand only about 15% of fossil capacity-years

By **Emily Grubert**

Decarbonizing the electricity sector is critical for addressing climate change, particularly given the expected role of an expanded clean electricity system for home heating, transportation, and industry (*1*). This will require vast investment in new infrastructure such as renewable-energy power plants and batteries. Absent major investment in carbon-capture equipment or fuel switching, it will also require the retirement of carbon-based power plants. Both motivate explicit attention to a "just transition" (*2*) that ensures material well-being and distributional justice for individuals and communities affected by a transition from fossil to nonfossil electricity systems (*3*). Determining which assets are "stranded," or required to close earlier than expected absent policy, is vital for managing compensation for remaining debt and/or lost revenue (*4*, *5*). Here, I introduce a generator-level model to show that in the United States, a 2035 electricity decarbonization deadline, as proposed by President-elect Biden and the 2020 Democratic party platform (*6*, *7*), would strand only about 15% of fossil capacity-years and 20% of job-years, which is unusually low from a global perspective [see supplementary materials (SM)] (*4*). Such insights into the location and timing of potential plant closures are critical for informing specific, coordinated, and locally grounded planning, which can substantially improve transition outcomes but is neither widespread nor supported by a national framework (*8*).

In 2018, 10,435 fossil fuel–fired generators produced 63% of U.S. electricity with 841 GW of capacity. They also emitted 1.9 billion tonnes (Gt) of carbon dioxide ($GtCO_2$), 1.3 Mt of nitrogen oxides ($MtNO_x$), and 1.4 Mt of sulfur dioxide ($MtSO_2$), while consuming 3.2 billion m^3 of water for plant operations and fuel extraction. These facilities operated in 1248 of 3141 counties, directly employed about 157,000 people at generators and fuel-extraction facilities, and paid sometimes locally meaningful taxes (see SM) (*8*).

Retirements are already under way: 126 GW of fossil generator capacity was retired between 2009 and 2018, including 33 GW in 2017 and 2018 alone (see data S1). But simply understanding that a closure is coming in some indeterminate future does not prevent economic shock when closures are announced with layoffs (*9*). We have seen before what happens without adequate planning and preparation, such as with the collapse of the U.S. steel industry in the 1970s and 1980s. Policy interventions for a just transition might include planning, training, and funding to stabilize local conditions (*8*) or political efforts to address broad social costs of transition (*3*). Effective just transition planning is participatory and government supported, with emphasis on stabilizing revenue, context-specific consideration of existing strengths and needs, fostering a willingness to change, and ensuring environmental remediation (*8*). All of these are much easier to achieve if the location and timing of step changes such as plant closures are known, which is a key focus of the work described below.

By establishing a deadline, a 2035 electricity decarbonization target represents a major opportunity to facilitate a just transition. Relevant locations are already known: The facilities that need to close exist. Policy can ensure that timing is also known—for example, through closure deadlines that are consistent with overall decarbonization targets. This new model supports such steps and extends committed climate emissions work (*10*, *11*) to inform just transition–oriented industrial policy by evaluating spatially and temporally explicit implications of explicit plant closure deadlines for climate pollution, air pollution, water use, and plant and fuel extraction labor.

THE 2035 CHALLENGE

Understanding which generators would have completed their reasonably anticipated life span before decarbonization deadlines can clarify where policy is stranding an asset (recognizing that financial liability depends on conditions such as ownership, regulatory setting, and depreciation status). To contextualize the impact of a 2035 electricity decarbonization target in the United States, this work assumes that all fossil fuel–fired electricity generators that were operational as of 2018 maintain their 2018 outputs until retiring at the capacity-weighted mean age on retirement observed for generators with the same pri-

School of Civil and Environmental Engineering, Georgia Institute of Technology, Atlanta, GA USA. Email: gruberte@gatech.edu.

Published by AAAS

Most capacity reaches the end of its life span by 2035

U.S. fossil fuel–fired power plant capacity by fuel and date generator reaches fuel- and technology-specific life span (left axis), and system characteristics (generation, water consumption, employment, CO_2 emissions, SO_2 emissions, and NO_x emissions) as percentage of 2018 value (right axis), 2018–2070. Most capacity reaches the end of its life span by 2035, and all by 2066. Leftmost stacked bar shows capacity that has already reached the end of its life span as of 2018.

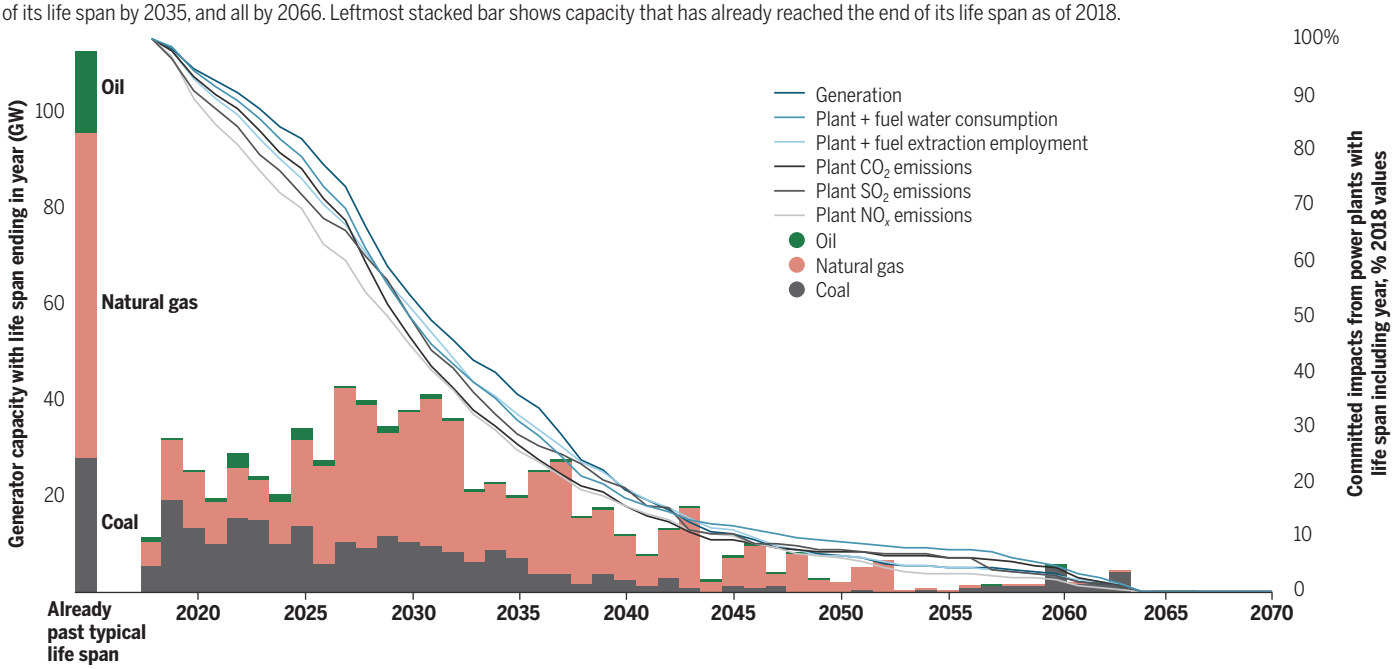

mary fuel and technology (prime mover) between 2002 and 2018 (see table S2). Observed mean age on retirement is an aggregate outcome variable that depends on a combination of physical, economic, policy, and other factors. This age is consistent across regions and time, at about 50 years for steam turbine–based generators and about 30 years for other generators (*11*).

This work assumes that generators achieve a typical life span if they (i) retire at the end of their fuel- and prime mover–specific typical life spans and (ii) maintain constant 2018 outputs through retirement (see SM). The goal is to illustrate conditions that are consistent with what interested parties might reasonably expect at the asset level. For example, investor compensation would not generally be considered necessary if a generator maintains historical outputs and retires at a typical age, and a host community or employee would not be unusually burdened by closure under such conditions.

Given these assumptions, this work shows a plausible, generator-level future for fossil fuel–fired electricity generation in the United States, with details on how requiring each generator to close at the end of its fuel- and prime mover–specific life span (see table S2) would affect generation, CO_2 emissions, NO_x emissions, SO_2 emissions, water consumption, and labor associated with both the plant and its fuel extraction (see the first figure, data S1, and SM).

Under these conditions, committed combustion CO_2 emissions from existing U.S. fossil electricity generators account for an estimated 25 Gt of CO_2 (see SM). Of operable U.S. fossil fuel–fired generation capacity (630 out of 840 GW), 73% reaches the end of its typical life span by 2035 (810 GW, or 96%, by 2050; 100% by 2066). About 13% of U.S. fossil fuel–fired generation capacity (110 GW) operating in 2018 had already exceeded its typical life span. The remaining 27% would need to close or convert earlier than a typical life span to meet a 2035 decarbonization deadline (see the second figure, data S1, figures S3 to S15, and movie S1).

Because typical life spans are averages, some generators run longer. Simply allowing facilities to run until they retire is thus likely insufficient for a 2035 decarbonization deadline. Closure deadlines that strand assets relative to reasonable life span expectations, however, could create financial liability for debts and other costs that can no longer be paid because of policy action. A key finding of this research is that a 2035 deadline for completely retiring fossil-based electricity generators would strand only about 15% (1700 GW-years) of fossil fuel–fired capacity life, alongside about 20% (380,000 job-years) of direct power plant and fuel extraction jobs remaining as of 2018. This is unusually low from a global perspective (largely because U.S. infrastructure is older than average) (*4*), limiting the scope of potential financial liabilities while enabling important, no-cost local benefits of closure deadlines, such as certainty regarding timelines.

POLICY ACTION FOR A JUST TRANSITION

U.S. policy to decarbonize the electricity sector by 2035 can facilitate a just transition by establishing explicit retirement deadlines for fossil fuel–fired electricity generators. In the large majority of cases (73%), such deadlines could be at or later than the reasonably expected end of life for a given generator and still comply with the 2035 target, allowing for years of advance planning grounded in the specific assets and needs of a community, enabling development of concrete and shared visions of the future (*12*). Facilities that would be partly stranded by a 2035 deadline would have more than a decade for transition planning if policy were enacted in the early- to mid-2020s. Advance planning is particularly important because utility-owned facilities that would be stranded by a 2035 deadline, leaving rate payers responsible for debts, are disproportionately in states with higher poverty rates (see figure S16), possibly indicating a role for federal support.

Even when financial aid is not expected, knowing when and where a facility closure will happen can enable targeted deployment of training resources for people who need them, long-term budgeting that accounts for tax revenue losses, and advance planning for transitioning individuals to local jobs in environmental remediation of fossil facilities. Clear expectations about when and where generator retirements will occur can also facilitate synergistic behavior in support industries, such as by allowing

GRAPHIC: N. DESAI/*SCIENCE* FROM E. GRUBERT

Published by AAAS

coal mines to operate at efficient scales to stockpile fuel to close out existing contracts.

Closure deadlines could be implemented in multiple ways. One option is to require generators to close by fuel- and prime mover–based typical end of life (see table S2) or 2035, whichever is first. Under the assumptions described here, this approach results in cumulative emissions of 20 Gt of CO_2, 12 Mt of NO_x, and 13 Mt of SO_2, supporting 1.7 million fossil job-years. Extending the retirement deadline to 5 years past typical life span or 2035, whichever is first, supports 26% more fossil job-years but also commits 30% more CO_2, 32% more NO_x, and 29% more SO_2. Using U.S. Bureau of Labor Statistics wage data and federal guidelines for emissions costs, these differences are worth an estimated additional $55 billion in direct wages (in high-paying industries that support, on average, about three indirect jobs/direct jobs, for people who could potentially seek alternative employment), at the cost of an estimated $250 billion in air pollution costs and $400 billion in CO_2 costs (excluding methane emissions) (2018 dollars) (see SM).

Decarbonizing the electricity system cannot occur through plant closures alone. Large amounts of infrastructure will need to be built, with associated issues related to community identity and the just transition (*13*). However, large amounts of infrastructure will need to not be built. A commitment to a just transition away from fossil fuels also demands that we minimize new liabilities in the form of new-build power plants that will require transition before the end of their useful lives (*14*). The federal Energy Information Administration's 2020 "Reference Case" for electricity through 2050, which assumes static policy conditions, includes more than 50 Gt of CO_2 of potential committed emissions from not-yet-built fossil fuel–fired electricity capacity. Proscribing construction of new fossil fuel–fired generators is likely the simplest available action toward a just transition, particularly because proposed new utility fossil assets (which would be paid for by rate payers) are also disproportionately in states with higher poverty rates (see SM and figure S17).

Transition policy is political (*3*), and success relies on political support. Transition policy that includes not only implementation details such as retirement deadlines but also universal social and economic programs that address transition impacts both in and beyond fossil fuel host communities—such as affordable housing, a $15 minimum wage, and job guarantees—can advance normative ideals of a just transition while also increasing political support (*1*, *3*, *15*). Emphasizing universal programs recognizes that a transition focused solely on fossil fuel workers and communities is not just and that support is also badly needed for the many people who lose jobs or more as a result of climate change, as well as those likely to be affected by zero-carbon industrialization.

Mapping plants whose life spans extend beyond 2035

Shown are U.S. fossil fuel–fired generators with estimated fuel- and technology-specific life span extending past 2035, operable as of 2018, with capacity aggregated to plant level and labels based on largest fuel share burned at combined generators in 2018. Larger circle size indicates larger capacity. Direct employment (at plants, coal mines, and natural gas extraction facilities) associated with plants with life span extending past 2035 are shown by county. County locations for plant employment match plant locations; county locations for coal mining employment match the location of the known or assumed mine responsible for the largest share of coal supply for a given plant; and county locations for natural gas extraction employment are approximated based on spatial distribution of natural gas extraction employment in the U.S. overall.

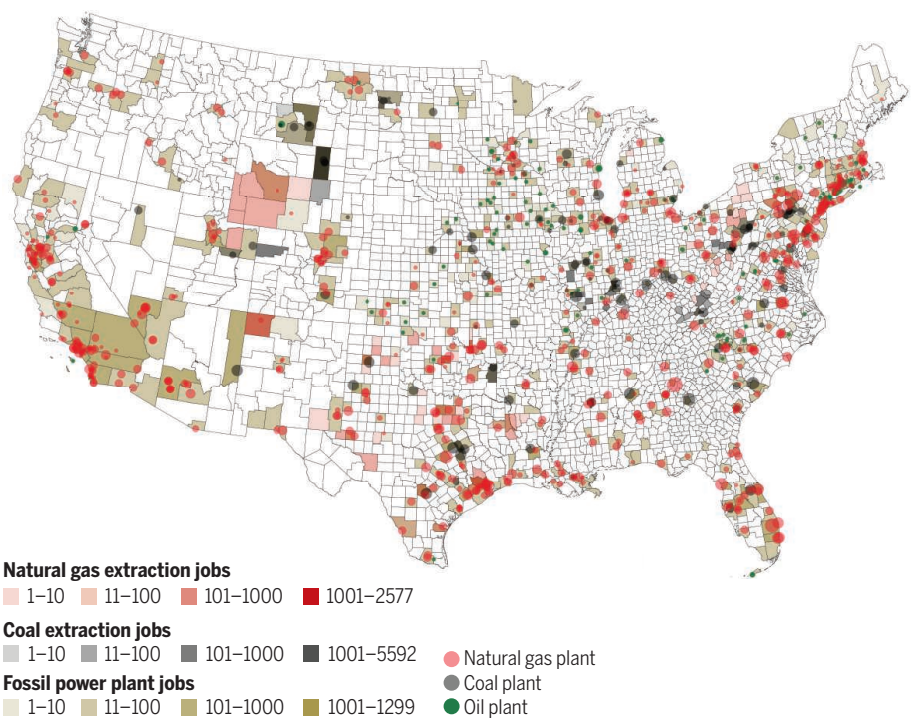

GRAPHIC: N. DESAI/*SCIENCE* FROM E. GRUBERT

CONCLUSIONS

Policy proposals to decarbonize the U.S. electricity sector require not only the addition of zero-carbon electricity generation but also the subtraction of carbon-intensive generation. Requiring fossil generators to close by 2035 would result in limited, although sometimes locally impactful, asset stranding relative to typical life spans. Actions such as Clean Energy Standards to set explicit retirement deadlines or New Source Performance Standards to restrict new fossil fuel–fired generation capacity, combined with universal social programs, can support a just transition. ■

REFERENCES AND NOTES

1. J. Rissman *et al.*, *Appl. Energy* **266**, 114848 (2020).
2. A. Ocasio-Cortez, "H.Res.109 - Recognizing the duty of the Federal Government to create a Green New Deal" [116th Congress (2019–2020), 2019]; www.congress.gov/bill/116th-congress/house-resolution/109/text.
3. N. Healy, *J. Barry, Energy Pol.* **108**, 451 (2017).
4. B. M. Kefford, B. Ballinger, D. R. Schmeda-Lopez, C. Greig, S. Smart, *Energy Pol.* **119**, 294 (2018).
5. K. Bos, J. Gupta, *Energy Res. Soc. Sci.* **56**, 101215 (2019).
6. Joe Biden for President: Official Campaign Website, "The Biden plan to build a modern, sustainable infrastructure and an equitable clean energy future" (2020); https://joebiden.com/clean-energy.
7. Democratic National Committee, "2020 Democratic Party Platform" (2020), p. 92.
8. J. H. Haggerty, M. N. Haggerty, K. Roemer, J. Rose, *Resour. Policy* **57**, 69 (2018).
9. S. Carley, T. P. Evans, D. M. Konisky, *Energy Res. Soc. Sci.* **37**, 133 (2018).
10. D. Tong *et al.*, *Nature* **572**, 373 (2019).
11. S. J. Davis, R. H. Socolow, *Environ. Res. Lett.* **9**, 084018 (2014).
12. E. Grubert, W. Skinner, *Energy Res. Soc. Sci.* **30**, 43 (2017).
13. G. Bridge, S. Bouzarovski, M. Bradshaw, N. Eyre, *Energy Pol.* **53**, 331 (2013).
14. A. Pfeiffer, R. Millar, C. Hepburn, E. Beinhocker, *Appl. Energy* **179**, 1395 (2016).
15. P. Bergquist, M. Mildenberger, L. Stokes, *Environ. Res. Lett.* (2020). 10.1088/1748-9326/ab81c1

SUPPLEMENTARY MATERIALS

science.sciencemag.org/content/370/6521/1171/suppl/DC1

10.1126/science.abe0375

Published by AAAS

Hunting wolves is legal in Slovakia unless it threatens populations, but available data are insufficient to determine its effects.

PHOTO: IMAGEBROKER/ALAMY STOCK PHOTO

Edited by **Jennifer Sills**

Evidence-based hunting policy needed in Slovakia

The Swiss people recently rejected a law that would have allowed protected animals to be hunted (*1*), but hunting of vulnerable species such as wolves still occurs in Slovakia and elsewhere in Europe. The European Union's Habitats Directive allows deliberate killing of wolves in nine countries (*2*) unless hunting would threaten the sustainability of the population, but population data are inadequate in some countries. Slovakia must implement evidence-based policies to protect wolf populations.

In 2016, Slovakia made changes to increase wolf hunting regulation and improve population monitoring (*3*). However, the changes have not been implemented nationally. Recently, the Slovak Ministry of Agriculture and Rural Development approved a quota of 50 wolves for the upcoming winter season (*4*). Such policies should be based on a scientific assessment of the viability of wolf populations (*5*). Instead, the Ministry justified the number by citing misleading arguments about sheep farming and food security (*4*).

In contrast to the government's claims, wolves kill less than 0.1% of Slovakia's sheep and goats (*3*). The recent policy also fails to acknowledge that sheep breeding in Slovakia declined between 2009 and 2019, when 28 to 158 wolves were killed per year, suggesting that hunting did not mitigate the problem (*6*). The food security justification is also specious: Sheep and goat products are only a small part of Slovak diet and accounted for less than 0.4% of gross agricultural production in the past 10 years (*7*). Instead of relying on misleading justifications for hunting, Slovakia should find alternative methods to minimize the risk of damages from large carnivores. However, the country has so far opted not to use EU funds available for this purpose (*8*).

Policies in Slovakia target wolves as the only source of problems in the agricultural sector and ignore the market-based causes of the sheep decline that have been shown elsewhere in Europe (*9*, *10*). Although wolf numbers are trending positively in Europe (*11*), Slovak hunting affects wolf recovery in neighboring Czechia, where the wolf population is protected (*12*). Without reliable evaluation of hunting impact, Slovakia cannot make informed policy decisions, despite the country's nominal adherence to EU regulations. Slovakia's failure to collect adequate data and base policy on science is a dangerous precedent that undermines biodiversity conservation efforts in Europe and worldwide.

Miroslav Kutal[1,2]* and Martin Duľa[1,2]
[1]Department of Forest Ecology, Faculty of Forestry and Wood Technology, Mendel University Brno, 613 00, Brno, Czech Republic. [2]Olomouc Friends of the Earth Czech Republic, 77900 Olomouc, Czech Republic.
*Corresponding author.
Email: miroslav.kutal@mendelu.cz

REFERENCES AND NOTES

1. S. Misicka, "Voters decide not to water down wolf protection," swissinfo.ch (2020).
2. A. Trouwborst, *Rev. Eur. Compar. Int. Environ. Law* **27**, 306 (2018).
3. V. Antal *et al.*, "Program starostlivosti o vlka dravého (*Canis lupus*) na Slovensku" (2016); www.minzp.sk/files/sekcia-ochranyprirodyakrajiny/druhova-ochrana-prirody/programy-starostlivosti/ps-vlka-draveho-slovensku.pdf [in Slovak].
4. Ministry of Agriculture and Rural Development of the Slovak Republic, "Slovensku sa bude aj naďalej loviť vlk (2020); www.mpsr.sk/na-slovensku-sa-bude-aj-nadalej-lovit-vlk/52---15984/ [in Slovak].
5. J. D. C. Linnell, V. Salvatori, L. Boitani, "Guidelines for population level management plans for large carnivores: A Large Carnivore Initiative for Europe report prepared for the European Commission" (2008).
6. Forest protection movement WOLF, Wolf hunting (2020); https://vlci.wolf.sk/sk/sumar/ [in Slovak].
7. Statistical Office of the Slovak Republic, "Gross animal production by commodities" (2020); http://datacube.statistics.sk/#!/view/en/VBD_SLOVSTAT/pl2019rs/v_pl2019rs_00_00_00_en.
8. K. Marsden, *CDP News* **18**, 8 (2019).
9. P. Kovařík, M. Kutal, I. Machar, *J. Nat. Conserv.* **22**, 479 (2014).
10. G. Chapron, J. V. López-Bao, *Science* **343**, 1199 (2014).
11. G. Chapron *et al.*, *Science* **346**, 1517 (2014).
12. M. Kutal, M. Váňa, J. Suchomel, G. Chapron, J. Lopez-Bao, *PLOS ONE* **11**, e0168292 (2016).

COMPETING INTERESTS

M. K. is a member of the International Union for Conservation of Nature Large Carnivore Initiative for Europe and Olomouc Friends of the Earth Czech Republic.

10.1126/science.abf5155

Computational social science: On measurement

In their Policy Forum "Computational social science: Obstacles and opportunities" (28 August, p. 1060), D. M. J. Lazer *et al.* propose ethical data infrastructures for computational social science research. Concentrating on access to platform trace data, they dismiss third-party market data from such companies as Nielsen and comScore because of "opaque" methods and

Published by AAAS

high cost. We believe both have virtues, but their proper use requires a keener appreciation of each measurement regime.

All data result from measurement processes designed and executed to serve a given institutional context (*1*, *2*). Platforms profit from shaping usage and they measure toward that end. Using their trace data to understand human conduct remains problematic as long as platforms are themselves opaque about their methods for managing user behavior (*3*). Social Science One and Twitter's COVID-19 application programming interface may be productive precedents of platform data provision, but computational social science should reckon with the effects of platform measurement.

Unlike platforms, third-party measurement firms are not invested in how users behave. As with public-sector data (such as the U.S. Census), third-party measurement is periodically audited (*4*). Its procedures and consequences are constantly appraised by actors with competing interests (*5*). Serving industries, policy-makers, and academics, third-party market research has invested for decades in refining what Lazer *et al.* aspire to: "an administrative infrastructure… enforcing compliance with privacy and ethics rules," which aligns "with critical research norms" including "transparency, reproducibility, replication, and consent" (*3*, *6*, *7*).

Third-party measurement firms such as Nielsen and comScore supply data to a broad subscriber base of advertising agencies and content publishers, which lowers data costs. Academic institutions worldwide may access numerous such third-party datasets via Wharton Research Data Services and Chicago Booth, brokers that partner with third-party firms for this purpose. Meanwhile, public data can be cost prohibitive (such as CDC's National Death Index).

What ensures data's "public accountability" is not a public-sector origin but how the measurement regime is institutionally arranged (*3*). In addition to expanding data collaborations and data infrastructures, attention to the measurement regimes of "found data" and reflexive triangulation across data sources are indispensable to development of computational social science.

Angela Xiao Wu[1]*, Harsh Taneja[2], danah boyd[3], Paul Donato[4], Matthew Hindman[5], Philip Napoli[6], James Webster[7]
[1]New York University, New York, NY 10003, USA. [2]University of Illinois Urbana-Champaign, Urbana, IL 61801, USA. [3]Microsoft Research/Data & Society Research Institute, New York, NY 10011, USA. [4]Advertising Research Foundation, New York, NY 10011, USA. [5]George Washington University, Washington, DC 20052, USA. [6]Duke University, Durham, NC 27708, USA. [7]Northwestern University, Evanston, IL 60208, USA.
*Corresponding author. Email: angelaxwu@nyu.edu

REFERENCES AND NOTES
1. T. M. Porter, *Trust in Numbers: The Pursuit of Objectivity in Science and Public Life* (Princeton University Press, Princeton, NJ, 1995).
2. W. N. Espeland, M. L. Stevens, *Arch. Eur. Sociol.* **49**, 401 (2008).
3. A. X. Wu, H. Taneja, *New Media Society* 10.1177/1461444820933547 (2020).
4. P. M. Napoli, A. B. Napoli, *First Monday* **24**, 10.5210/fm.v24i12.10124 (2019).
5. N. Anand, R. A. Peterson, *Org. Sci.* **11**, 270 (2000).
6. Advertising Research Foundation, Member Code of Conduct (2019); https://thearf.org/code-of-conduct/.
7. ESOMAR, The ICC/ESOMAR Code (2020); www.esomar.org/what-we-do/code-guidelines.

10.1126/science.abe8308

Chinese sturgeon needs urgent rescue

China's construction of large hydropower stations on the Yangtze and Jinsha rivers has had a devastating impact on the resources, spawning and reproduction behavior, and migration habits of the Chinese sturgeon (*Acipenser sinensis*), a "living fossil" (*1*) with immeasurable scientific, ecological, social, and economic value. In the 1970s, there were more than 10,000 Chinese sturgeon breeding populations in the Yangtze River, but the number dropped to 2176 in the 1980s when the Yangtze's first dam and hydropower station opened, then to 363 in 2000, and to 57 in 2010 (*2*). The International Union for Conservation of Nature (IUCN) now lists the Chinese sturgeon as Critically Endangered (*3*), and the Convention on International Trade in Endangered Species of Wild Fauna and Flora (CITES) lists the species under Appendix II (*4*). China must take action to save this vulnerable species.

The Jinsha River, located in the upper reaches of the Yangtze River, is the traditional spawning ground and natural breeding habitat of the Chinese sturgeon (*5*), as well as the largest hydropower base in China (*6*). The construction of the cascade dams on the Jinsha River hinders the Chinese sturgeon's ability to swim upstream to spawn and migrate and damages their habitat (*7*). Moreover, a series of dams on the upper reaches of the Yangtze River and the Three Gorges Reservoir have affected Chinese sturgeon spawning activities by leading to warmer water temperatures (*8*). Since the Three Gorges, Xiangjiaba, and Xiluodu projects began operation in 2008, 2012, and 2013, respectively, the effective reproduction of the Chinese sturgeon has mostly been lost, and the wild population is facing extinction.

China has established three Chinese sturgeon nature reserves (*9*) and implemented a 10-year fishing ban in the Yangtze River (*10*), which began in January 2020. These efforts are not enough. Although China artificially breeds and releases Chinese sturgeon, this strategy is not effectively restoring population numbers (*11*). To save the wild Chinese sturgeon population, targeted measures must be taken to decrease the impact of the Yangtze River dams and restore natural reproduction. The government should immediately reassess the ecological impact of the Jinsha River hydropower project, especially with regard to Chinese sturgeon and other migratory fish habitats. A Chinese sturgeon channel should be built in the hydropower stations along the Jinsha River to ensure the smooth flow of migratory fish in the Yangtze River. China should also prioritize the protection of aquatic organisms in the Yangtze River, increase protection of the habitats of the Chinese sturgeon in the Yangtze River and its coastal areas, strictly control fishing, and increase the number of artificial releases.

Xinfa Zhou[1]*, Lu Chen[2], Jing Yang[3], Haiqing Wu[1]
[1]School of Economics, Peking University, Beijing, China. [2]Law School, Hunan University, Changsha, China. [3]School of Public Administration, Hunan University, Changsha, China.
*Corresponding author.
Email: zhouxinfa@pku.edu.cn

REFERENCES AND NOTES
1. G. Z. Zhou *et al.*, *J. Fish Biol.* **73**, 8 (2008).
2. UFO Talk, "Those creatures who never come back, now we can only look at pictures and talk" (2017); www.sohu.com/a/135759216_158217 [in Chinese].
3. W. Qiwei, *Acipenser sinensis* (IUCN Red List of Threatened Species, 2010).
4. Shanghai Yangtze River Estuary Chinese Sturgeon Nature Reserve Management Office, *China Fish.* **12**, 21 (2016) [in Chinese].
5. P. Xie, *J. Lake Sci.* **32**, 4 (2020).
6. Y. X. Cheng, *Sci. Technol. Innovation Appl.* **10**, 238 (2017).
7. P. Xie, *Science* **302**, 1149 (2003).
8. M. Fang *et al.*, *Chin. J. Ecol.* **33**, 4 (2014) [in Chinese].
9. S. Q. Zeng. *Agricult. Prod. Market* **16**, 9 (2020).
10. X. Wang. *et al.*, *J. Central Chin. Normal Univ. Nat. Sci.* **54**, 4 (2020).
11. L. H. Wang, Z. L. Huang, *J. Lake Sci.* **4**, 924 (2020).

10.1126/science.abf4946

ERRATA

Erratum for the Report "Large contribution from anthropogenic warming to an emerging North American megadrought" by A. P. Williams *et al.*, *Science* **370**, eabf3676 (2020). Published online 30 October 2020; 10.1126/science.abf3676

Erratum for the Report "Meta-analysis reveals declines in terrestrial but increases in freshwater insect abundances" by R. Van Klink *et al.*, *Science* 370, eabf1915 (2020). Published online 23 October 2020; 10.1126/science.abf1915

Erratum for the Report "Generation of influenza A viruses as live but replication-incompetent virus vaccines" by L. Si *et al.*, *Science* 369, eabe5323 (2020). Published online 4 September 2020; 10.1126/science.abe5323

Published by AAAS

RESEARCH

IN *SCIENCE* JOURNALS

Edited by **Michael Funk**

PHOTO: GREENSHOOTS COMMUNICATIONS/ALAMY STOCK PHOTO

TROPICAL FOREST

Fruit decline threatens forest elephants

Large mammal herbivores in African tropical forests are major consumers of fruit, and many tree species rely on these consumers for dispersal of their seeds. Bush *et al*. monitored fruit production over three decades in a protected national park in Gabon, showing an 80% decline across the 73 plant species monitored. At the same time, photographic records of forest elephants over the past decade indicate a substantial decline in body condition in these major herbivores. These results suggest that the capacity of the ecosystem to support the elephant population is decreasing, a worrying prospect in an environment that is still protected from other threats such as hunting and deforestation. —AMS *Science*, this issue p. 1219

African elephants in tropical forests depend on fruit, a food source that has greatly declined in the past ~30 years.

DEVELOPMENTAL BIOLOGY

Sugar code regulates blood stem cells

During embryonic development, blood stem cells are derived from vascular endothelial cells that line the walls of developing arteries. The transition from endothelial cells to blood stem cells is highly regulated and restricted to a small portion of endothelial cells during a brief period of time. The mechanisms regulating this transition are also poorly understood. Kasper *et al*. found that microRNA-223 intrinsically restrains the vascular hematopoietic transition by regulating N-glycan biosynthesis to restrict hematopoietic stem and progenitor cell production and differentiation. Genetics or chemicals could be used to alter the sugar code and change the efficiency of blood production in embryos. Thus, genetically or pharmacologically altering N-glycan biosynthesis in endothelial cells could improve the efficiency of the production of blood stem cells, which could then be used to treat blood diseases such as leukemia. —BAP

Science, this issue p. 1186

SPECTROSCOPY

Probing quantum materials

Unraveling the functionalities of quantum materials such as spin-valley-electronic, topological, and many-body effects provides a route to exploiting these materials for applications. Borsch *et al*. introduce a spectroscopic technique based on the concept of crystal-momentum combs. By extending the ideas of frequency combs of metrology and superresolution imaging, they demonstrate the ability to directly map out the properties of quantum electronic structures under ambient conditions. Using this technique combined with accurate many-body computations, they were able to reveal tomographic images of two-dimensional quantum materials. —ISO

Science, this issue p. 1204

CORONAVIRUS

SARS-CoV-2 antibodies persist

As the number of daily COVID-19 cases continues to mount worldwide, the nature of the humoral immune response to severe acute respiratory syndrome coronavirus 2 (SARS-CoV-2) remains uncertain. Wajnberg *et al*. used a cohort of more than 30,000 infected individuals with mild to moderate COVID-19 symptoms to determine the robustness and longevity of the anti–SARS-CoV-2 antibody response. They found that neutralizing antibody titers

Published by AAAS

against the SARS-CoV-2 spike protein persisted for at least 5 months after infection. Although continued monitoring of this cohort will be needed to confirm the longevity and potency of this response, these preliminary results suggest that the chance of reinfection may be lower than is currently feared. —STS

Science, this issue p. 1227

CELL DEATH

Paring down pyroptosis

Shiga toxin is a phage-encoded exotoxin that interrupts protein translation and functions as a virulence factor for enterohemorrhagic *Escherichia coli* (EHEC), a human pathogen causing hemorrhagic colitis and acute renal failure. Havira *et al*. screened a panel of EHEC mutants lacking various virulence factors to find those that interfered with inflammasome-mediated cell death. EHEC strains lacking Shiga toxin were more potent inducers of macrophage pyroptosis and interleukin-1β secretion than wild-type EHEC. Shiga toxin from wild-type EHEC interfered with pyroptosis by blocking the ability of the activated form of caspase-11, a cytoplasmic lipopolysaccharide sensor, to cleave gasdermin D and initiate the formation of gasdermin pores in the plasma membrane. This unanticipated activity of Shiga toxin provides EHEC with an additional means of evading the innate immune system. —IW

Sci. Immunol. **5**, eabc0217 (2020).

Colored transmission electron microscope image of a pathogenic strain of *Escherichia coli* that produces Shiga toxin

DEEP BIOSPHERE

Deep, hot, and more alive than we thought

Marine sediments represent a massive microbial ecosystem, but we still do not fully understand what factors shape and limit life underneath the seafloor. Analyzing samples from a subduction zone off the coast of Japan, Heuer *et al*. found that microbial life, in particular bacterial vegetative cells, decreases as depth and temperature increases down to ~600 meters below the seafloor, corresponding to temperatures of ~70°C. Below this limit, endospores are common—a remnant, and a potential reservoir, of bacterial life. Deeper still is a sterile zone, and below 1000 meters is a scalding realm populated by vegetative cells. At such great depths, high concentrations of acetate and sulfate coexist, and there are also signs of hyperthermophilic methanogenesis. These data provide a fascinating window into an extreme and inhospitable environment that nonetheless supports microbial life. —MAF

Science, this issue p. 1230

METABOLISM

A regulatory switch in obesity

The liver not only produces glucose but also consumes a large amount of glucose, making this organ critical for glucose homeostasis. Kokaji *et al*. performed multiomics analyses on the liver and blood of normal mice and in a genetic mouse model for obesity (*ob/ob*). Whereas normal hepatic metabolic responses to glucose were rapid and relied on regulation by metabolites, those in *ob/ob* mice were slow and depended on changes in gene expression. Thus, obesity in this model not only slows hepatic metabolic responses to glucose but also makes these responses more energy consuming and less precise. —WW

Sci. Signal. **13**, eaaz1236 (2020).

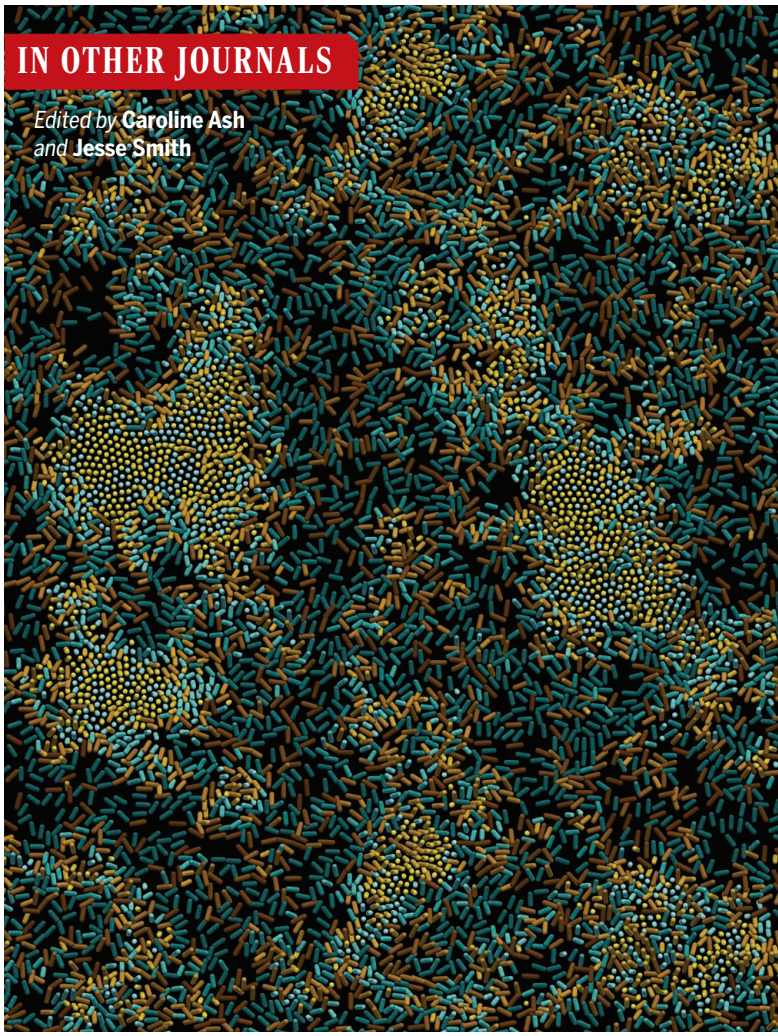

IN OTHER JOURNALS

Edited by **Caroline Ash** *and* **Jesse Smith**

NEUROIMMUNOLOGY

Neuroprotective neutrophils?

The infiltration of activated immune cells into the central nervous system can contribute to the pathophysiology of conditions such as multiple sclerosis and traumatic brain injury. The roles that immune cells play in the resolution of inflammation and the regeneration of damaged tissue are less well understood. Sas *et al*. report the existence of a distinct population of Ly6G^{lo} cells resembling immature neutrophils that were elicited in a mouse model of optic nerve injury. Intraocular injection of a fungal cell wall extract induced the migration of these cells into the eye, where they promoted retinal ganglion cell survival and axonal regeneration, in part through a range of secreted nerve growth factors. These Ly6G^{lo} cells also spurred axonal regeneration in a mouse model of spinal cord injury. Similar regenerative capacity by an immature human neutrophil cell line suggests that immature granulocytes may be an attractive potential target for future neuroregenerative therapies. —STS

Nat. Immunol. **21**, 1496 (2020).

ALLERGY

Sensing an allergen

Dendritic cells (DCs) can initiate allergic immune responses, but how allergens influence DCs is unclear. Using a mouse model in which the allergen papain was injected into the skin, Perner *et al*. report that TRPV1^{+} sensory neurons are required for an immune response to allergens.

CREDITS (FROM LEFT): CENTRE FOR INFECTIONS/PUBLIC HEALTH ENGLAND/SCIENCE SOURCE; OLIVER J. MEACOCK

Published by AAAS

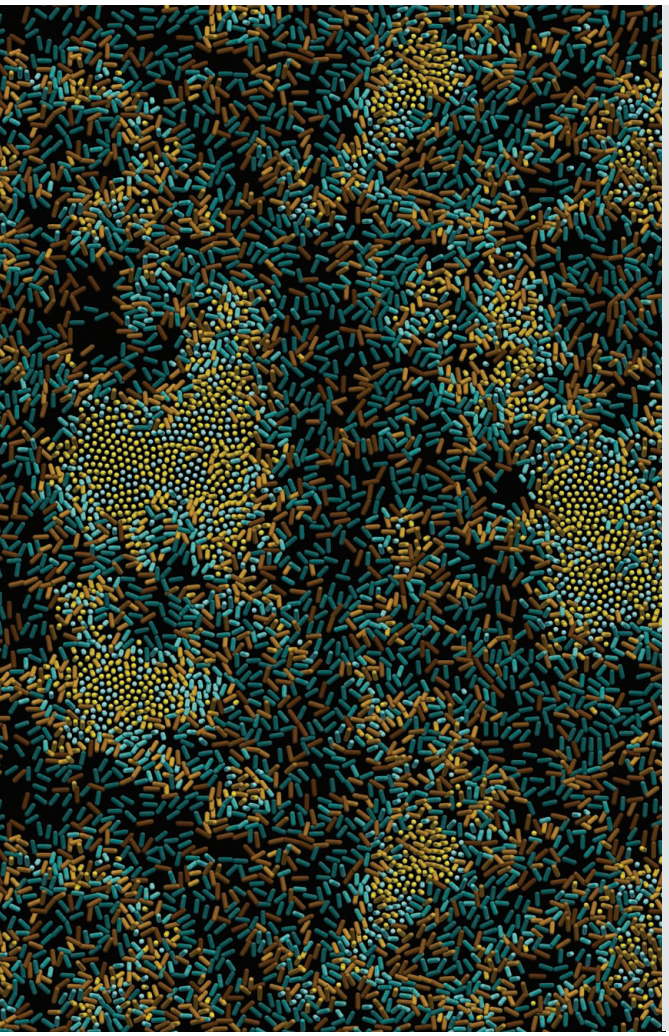

MICROBIOLOGY

Slow pokes avoid gridlock

Bacterial colonies contain millions of cells yet show coordinated movement toward more favorable conditions at a colony's margins. Species such as *Pseudomonas aeruginosa* contain external appendages called pili that grab the substrate and pull cells along. Meacock *et al*. found that mutants that had more pili and that could move faster were disadvantaged under crowded conditions. Theory developed from liquid crystal research shows that, when densely packed, particles tend to align. In a densely packed colony, slow bacterial cells overtake fast cells. This happens because when cells with differing orientations collide, the fast cells tend to spin vertically and become trapped in "rosettes." This means that the trapped cells are left behind in the nutrient-poor and oxygen-depleted center of the colony. —CA

Nat. Phys. 10.1038/s41567-020-01070-6 (2020).

A bacterial colony resembling liquid crystal, in which fast-moving *Pseudomonas aeruginosa* cells are forced to align into "rosettes" and are overtaken by slow cells

PHOTOCHEMISTRY

Dynamic control of boron esters

Visible light at different frequencies can photoswitch azobenzenes between their *E* and *Z* isomers. Accardo *et al*. used the isomerization of ortho-substituted azobenzene boronic acids to tune the affinity for diols to bind and form esters. Methoxy groups ortho to the azo group on the ring opposite the boronic acid group destabilized diol binding to the *E* isomer. The *E* isomer also formed favorable hydrogen bonds to water that inhibited displacement by the diol. Both effects helped to boost the relative binding affinity for ethylene glycol binding to the *Z* versus *E* isomer to more than 20. They exploited this effect to create photoswitchable gels formed between four-arm amine-terminated poly(ethylene glycol)s that had end groups of either azobenzene boronic acids or extended diols. —PDS

J. Am. Chem. Soc. 10.1021/jacs 0c08551 (2020).

Allergen-driven activation of TRPV-expressing neurons caused the release of the neuropeptide substance P, which resulted in the migration of CD301b$^+$ DCs to the draining lymph nodes. The induction of adaptive T helper 2 immunity, including itching and pain responses, was observed. —PNK

Immunity **53**, 1063 (2020).

BIOSYNTHESIS

Escherichia coli as the king's dye maker

Clothing colored with Tyrian purple, a dye extracted from mollusks in a laborious and expensive process, has been used over the ages as a marker of wealth and royal status. The main pigment, 6,6-dibromoindigo, is simple but remains a challenge to synthesize in pure form. Lee *et al*. engineered two strains of *Escherichia coli* with enzymes that first convert tryptophan to 6-bromotryptophan and then oxidize and dimerize two molecules to form 6,6-dibromoindigo. Switching out different tryptophan halogenase enzymes, the authors created a spectrum of halogenated dye variants. The resulting dyes can be used directly to stain fabrics without purification. —MAF

Nat. Chem. Biol. 10.1038/s41589-020-00684-4 (2020).

NEURODEGENERATION

Seeding the problem

A key pathological event in Alzheimer's disease (AD) is the aggregation and deposition of amyloid-β (Aβ). However, the formation of Aβ deposits is a relatively late readout of the Aβ aggregation process. Treatments that affect such deposits may fail to interrupt the critical early seeding stage of Aβ deposition. It remains unclear when pathogenic Aβ seeds begin to form, propagate, and spread through the brain. Furthermore, the precise nature of the initial Aβ seeds remains unknown. Working in mouse models of AD, Uhlmann *et al*. tested a variety of known antibodies for their ability to neutralize Aβ seeds before amyloid deposition was detectable. Early administration of one such antibody, aducanumab, significantly reduced Aβ deposition and the resulting pathology. This work points to targeting and removal of early Aβ seeds as promising future therapies for patients developing AD. —SMH

Nat. Neurosci. 10.1038/s41593-020-00737-w (2020).

MACHINE LEARNING

Protein IR spectra from machine learning

Infrared (IR) absorption spectroscopy is among the most powerful tools used to understand the atomic-level structure and the function of proteins. Theoretical interpretation of IR spectra generally depends on the ability to perform first-principles simulations, which may be very costly. Machine learning (ML) has recently emerged as an alternative way to overcome the need for such calculations. Ye *et al*. propose a ML method based on a few key structural descriptors and ab initio data to predict amide I region IR spectra, which is rich in fingerprints of protein structure and dynamics. Their trained model was able to provide fast and accurate characterization of IR spectra for different proteins under varying conditions. —YS

J. Am. Chem. Soc. **142**, 19071 (2020).

Published by AAAS

ALSO IN *SCIENCE* JOURNALS

Edited by **Michael Funk**

MICROBIOTA

Getting to the guts of local evolution

The microbiota of mammals is a product of coevolution. However, humans exhibit a range of adaptive peculiarities that can be quite geographically specific. The human microbiota also displays a variety of community compositions and a range of overlapping and redundant metabolic characteristics that can alter host physiology. For example, lactase persistence is a genetic characteristic of European populations, but in populations lacking the lactase gene, milk sugar digestion is endowed by the microbiota instead. Suzuki and Ley review the evidence for the role that the microbiota plays in local adaptation to new and changing human circumstances. —CA

Science, this issue p. 1180

CORONAVIRUS

How lethal coronaviruses engage hosts

Severe acute respiratory syndrome coronavirus 2 (SARS-CoV-2) is closely related to the deadly coronaviruses SARS-CoV-1 and Middle East respiratory syndrome coronavirus (MERS-CoV). Considerable efforts are focused on developing treatments, and therapies that work across coronaviruses would be particularly valuable. Shedding light on the host factors hijacked by the viruses, Gordon *et al*. mapped the interactions between viral and human proteins for SARS-CoV-2, SARS-CoV-1, and MERS-CoV; analyzed the localization of viral proteins in human cells; and used genetic screening to identify host factors that either enhance or inhibit viral infection. For a subset of the interactions essential for the virus life cycle, the authors determined the cryo–electron microscopy structures and mined patient data to understand how targeting host factors may be relevant to clinical outcomes. —VV

Science, this issue p. 1181

INNATE IMMUNITY

A ligand is located, at long last!

Members of the Nod-like receptor (NLR) family act as intracellular sensors of infection. Once they recognize pathogen-associated molecular patterns, they assemble into signaling complexes called inflammasomes, which induce proinflammatory cytokines and pyroptotic cell death. Although rodent NLR family pyrin domain containing 1 (NLRP1) can recognize bacterial toxins and protozoan pathogens, the ligands for human NLRP1 have remained elusive. Robinson *et al*. found that human NLRP1 senses and is activated by enteroviruses. During human rhinovirus (HRV) infection, the HRV 3C protease cleaves an autoinhibitory N-terminal fragment from NLRP1, which is subsequently degraded. The NLRP1 C-terminal fragment that is released then initiates inflammasome formation. This work offers insights into immune sensing of respiratory viral infections and provides an example of the N-terminal glycine degron pathway in human innate immunity. —STS

Science, this issue p. 1182

EVOLUTION

Selection enhances mutation toleration

Mutations generate variability that is either neutral or subject to natural selection. Robustness is a measure of the ability to withstand deleterious mutational effects. Zheng *et al*. exposed *Escherichia coli* populations expressing a yellow fluorescent protein to strong, weak, or no selection for yellow fluorescence for four generations. They then selected these populations to a related function, green fluorescence, for four more generations. The strong selection first for yellow and then green fluorescence resulted in the most green fluorescence and the accumulation of the most mutations. This outcome likely was due to the increased foldability of the protein. Selection thus provides a threshold for mutation accumulation, but robustness maintains a buffer necessary for protein evolution. —LMZ

Science, this issue p. 1183

BIOMECHANICS

Protection in the wings

Beetles have hardened forewings for the protection of their bodies and hindwings, and their use during crawling or burrowing is well understood. However, the behavior of the larger hindwings during collisions in flight has not been clear because they do not readily flex. Phan and Park present a detailed study of the folding and unfolding mechanisms of the hindwings in free-flying rhinoceros beetles in which the wings were impacted during flight to simulate a cluttered environment (see the Perspective by Sun). They found that origami-like folds in the wing could rapidly collapse on impact and then spring back, thus acting as shock absorbers and stabilizers. The authors replicated this behavior in a flapping-wing robot, enabling it to fly safely after collisions. —MSL

Science, this issue p. 1214; see also p. 1165

PLANT SCIENCE

Competitive roots

Much of the world's plant biomass exists out of sight underground in the form of roots. Cabal *et al*. developed a theoretical model and tested it empirically to explain the rules that govern root growth (see the Perspective by Semchenko). Plants adjust how and where their roots grow according to how close neighboring—and competing—plants might be. The model extracts some of the rules about how root balls differ when grown close to neighboring plants compared with being grown in the absence of competition. —PJH

Science, this issue p. 1197; see also p. 1167

QUANTUM GASES

Watching sound die out

A gas of strongly interacting fermionic atoms can serve as a model for systems with densities and energies spanning many orders of magnitude. This universality of physics comes about thanks to a property known as scale invariance. Patel *et al*. exploited this concept to draw universal conclusions about the attenuation of sound in such systems by studying a homogeneous gas of lithium-6 atoms at very low temperatures (see the Perspective by Schaefer). They found that below the superfluid transition, the sound diffusivity behaved not unlike what has been observed in helium-4, a fluid of strongly interacting bosons. —JS

Science, this issue p. 1222; see also p. 1162

NEUROSCIENCE

Restoring vision by stimulating the brain

Electrical stimulation of the visual cortex has long been proposed as an approach to restoring vision in blind people. Previous studies positioned electrodes on the surface of the brain and thus required delivery of relatively high currents. However, this approach limits the number of electrodes that can be safely stimulated simultaneously, and such surface electrodes activate several millimeters of cortex, which results in a low spatial resolution.

Published by AAAS

Chen *et al*. demonstrated that the simultaneous stimulation of multiple intracortical electrodes in the monkey primary visual cortex gives rise to the perception of shape and successive stimulation to the perception of motion (see the Perspective by Beauchamp and Yoshor). This major improvement provides proof of concept for the use of electrical microstimulation to create a form of artificial vision in the blind. —PRS

Science, this issue p. 1191; see also p. 1165

PHYSICS

Probing the dark state

Excitons, electron-hole pairs held together by Coulomb attraction, can be generated in semiconductors under excitation and greatly influence the material's optoelectronic properties. Although bright excitons are optically active, their dark-state cousins have been more difficult to detect. They do, however, affect the optoelectronic properties through their interaction with light and bright excitons. Madéo *et al*. developed a pump-probe photoemission technique that is used reveal the spatial, temporal, and spectral dynamics of excitons (see the Perspective by Na and Ye). Demonstrated in two-dimensional monolayer films of tungsten diselenide, the technique could also be applicable to other semiconductor systems hosting excitonic excitations. —ISO

Science, this issue p. 1199; see also p. 1166

PLANT SCIENCE

Tetrameric immune receptors

Nucleotide-binding/leucine-rich repeat (NLR) immune receptors detect pathogen effectors and trigger a plant's immune response. Two groups have now defined the structures of two NLRs that carry Toll-like interleukin-1 receptor (TIR) domains (TIR-NLRs) (see the Perspective by Tian and Li). Ma *et al*. studied the *Arabidopsis thaliana* TIR-NLR RPP1 (recognition of *Peronospora parasitica* 1) and its response to effectors from an oomycete pathogen. Martin *et al*. studied the *Nicotiana benthamiana* TIR-NLR ROQ1 (recognition of XopQ 1) and its response to the *Xanthomonas* effector. Both groups found that these TIR-NLRs formed tetramers that, when activated by binding to the pathogen effector, exposed the active site of a nicotinamide adenine dinucleoside (NAD) hydrolase. Thus, recognition of the pathogen effector initiates NAD hydrolysis and begins the immune response. —PJH

Science, this issue p. 1184, p. 1185; see also p. 1163

GENE THERAPY

Gene therapy for CLN2 disease

Late infantile Batten disease (CLN2 disease), a pediatric progressive brain disorder, is currently treated by infusion of human recombinant tripeptidyl peptidase 1 (TPP1) into the cerebrospinal fluid every other week, which slows but does not halt progression of the disease. Sondhi *et al*. sought an alternative treatment using gene therapy. They injected an adeno-associated virus vector enabling expression of the normal human coding sequence for the *CLN2* gene directly into the brain parenchyma of children with the disease. Progression of CLN2 was slowed in treated children but not to the same degree as in those treated with recombinant TPP1. Further improvements in gene therapy are needed before the progression of CLN2 disease can be halted. —MN

Sci. Transl. Med. **12**, eabb5413 (2020).

HUMAN GENETICS

Histone H3.3 mutations alter development

Dominant de novo germline mutations in the human *H3F3A* or *H3F3B* genes that encode the H3.3 histone variant cause developmental delays, neurodegeneration, and structural abnormalities. Bryant *et al*. describe 37 different missense mutations in 46 patients with overlapping phenotypes of variable severity. H3.3 marks active genes and influences gene expression and DNA damage repair. The mutations likely affect only 25% of the total H3.3, indicating exquisite sensitivity of development to H3.3 function. Prior studies report somatic mutations affecting H3.3 tails in cancer, but the germline mutations are located throughout the protein and differentially alter interaction with DNA, other histones, or other proteins. RNA sequencing with patient cell lines suggest that the common effects of the mutations stem from increased cell proliferation. —DD

Sci. Adv. 10.1126/sciadv.abc9207 (2020).

CORONAVIRUS

A decoy to neutralize SARS-CoV-2

Many efforts to develop therapies against severe acute respiratory syndrome coronavirus 2 (SARS-CoV-2) are focused on the interaction between the spike protein, which decorates the surface of the virus, and its host receptor, human angiotensin-converting enzyme 2 (hACE2). Linsky *et al*. describe a de novo design strategy that allowed them to engineer decoy proteins that bind to the spike protein by replicating the hACE2 interface. The best decoy, CTC-445, bound with low nanomolar affinity, and selection of viral mutants that decrease binding is unlikely because this would also affect binding to hACE2. A bivalent version of CTC-445 bound even more tightly, neutralized SARS-CoV-2 infection of cells, and protected hamsters from a SARS-CoV-2 challenge. The stable decoy has the potential for respiratory therapeutic delivery. —VV

Science, this issue p. 1208

Published by AAAS

REVIEW SUMMARY

MICROBIOTA

The role of the microbiota in human genetic adaptation

Taichi A. Suzuki and Ruth E. Ley*

BACKGROUND: When human populations expanded across the globe, they adapted genetically to local environments in response to novel selection pressures. Drivers of selection include exposure to new diets, climates, or pathogens. Humans harbor microbiotas that also respond to changes in local conditions and changes in their hosts. As a result, microbiotas may alter the adaptive landscape of the host through modification of the environment. Examples include changes to a food's nutritional value, the host's tolerance to cold or low amounts of oxygen, or susceptibility to invading pathogens. By buffering or altering drivers of selection, the microbiota may change host phenotypes without coevolution between host and microbiota. Functions of the microbiota that are beneficial to the host may arise randomly or be acquired from the environment. These beneficial functions can be selected without the host exerting genetic control over them. Hosts may evolve the means to maintain beneficial microbes or to pass them to offspring, which will affect the heritability and transmission modes of these microbes. Examples in humans include the digestion of lactose via lactase activity (encoded by the *LCT* gene region) in adults and the digestion of starch by salivary amylase (encoded by the *AMY1* gene)—both are adaptations resulting from shifts in diet. The allelic variation of these genes also predicts compositional and functional variation of the gut microbiota. Such feedback between host alleles and microbiota function has the potential to influence variation in the same adaptive trait in the host. How the microbiota modifies host genetic adaptation remains to be fully explored.

ADVANCES: In this paper, we review examples of human adaptations to new environments that indicate an interplay between host genes and the microbiota, and we examine in detail the *LCT*–*Bifidobacterium* and the *AMY1*–*Ruminococcus* interactions. In these examples, the adaptive host allele and adaptive microbial functions are linked. We propose host mechanisms that can replace or recruit beneficial microbiota functions during local adaptation. Finally, we search for additional examples where microbiotas are implicated in human genetic adaptations, in which the genetic basis of adaptation is well described. These range from dietary adaptations, where host and microbial enzymes can metabolize the same dietary components (e.g., fatty acid and alcohol metabolism), through climate-related adaptations, where host and microbes can induce the same physiological pathway (e.g., cold-induced thermogenesis, skin pigmentation, and blood pressure regulation), to adaptations where hosts and microbes defend against the same local pathogens (e.g., resistance to malaria, cholera, and others). These examples suggest that microbiota has the potential to affect host evolution by modifying the adaptive landscape without requiring coevolution.

OUTLOOK: Well-studied examples of local adaptation across diverse host species can be revisited to elucidate previously unappreciated roles for the microbiota in host-adaptive evolution. In the context of human adaptation, knowledge of microbial functions and host gene–microbe associations is heavily biased toward observations made in Western populations, as these have been the most intensively studied to date. Testing many of the interactions proposed in this Review between host genes under selection and the microbiota will require a wider geographic scope of populations in their local contexts. Because genes under strong selection in humans are often involved in metabolic and other disorders and can vary between populations, future investigations of host gene–microbe interactions that relate to human adaptation may contribute to a deeper understanding of microbiota-related diseases in specific populations. Investigating host gene–microbe interactions in a wider variety of human populations will also help researchers go beyond collections of anecdotes to form the basis of a theory that takes microbial contributions to host adaptation into account in a formal framework. A better understanding of reciprocal interactions between the host genome and microbiota in the context of adaptive evolution will add another dimension to our understanding of human evolution as we moved with our microbes through time and space. ■

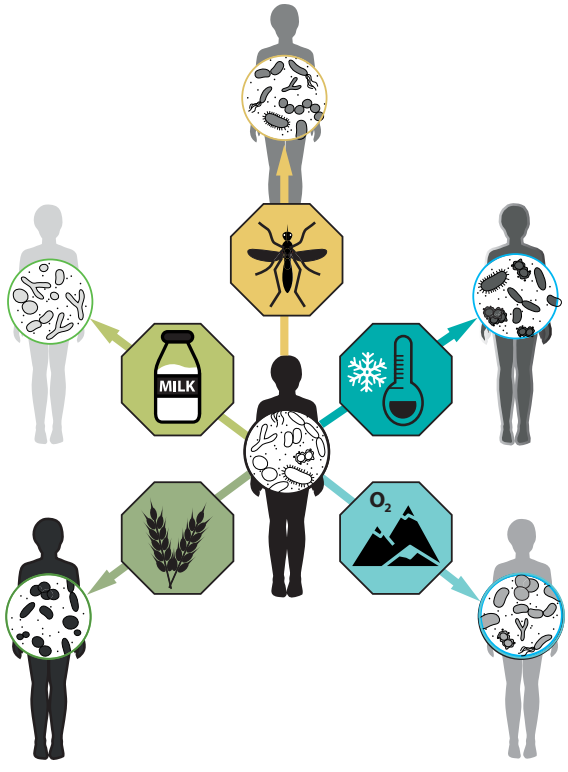

Local adaptation by humans and their microbiotas. When human populations adapt genetically to new environments, their microbiotas may also participate in the process. Microbes can evolve faster than their host, which allows them to respond quickly to environmental change. They also filter the host's environment, thereby altering selective pressures on the host. Illustrated here are examples of interactions between adaptive host alleles and adaptive microbiota functions where the microbiota likely modified the adaptive landscape in response to changes in diet (e.g., changes in levels of starch and milk consumption), exposure to local pathogens (e.g., malaria parasites and *Plasmodium* spp.), and changes in local climate (e.g., cold stress and hypoxia). In this paper, we discuss the resulting relationships between host-adaptive alleles and microbiota functions.

Department of Microbiome Science, Max Planck Institute for Developmental Biology, Tübingen, Germany.
*Corresponding author. Email: rley@tuebingen.mpg.de
Cite this article as T. A. Suzuki, R. E. Ley, *Science* **370**, eaaz6827 (2020). DOI: 10.1126/science.aaz6827

READ THE FULL ARTICLE AT
https://doi.org/10.1126/science.aaz6827

GRAPHIC: DAPHNE WELTER

REVIEW

MICROBIOTA

The role of the microbiota in human genetic adaptation

Taichi A. Suzuki and Ruth E. Ley*

As human populations spread across the world, they adapted genetically to local conditions. So too did the resident microorganism communities that everyone carries with them. However, the collective influence of the diverse and dynamic community of resident microbes on host evolution is poorly understood. The taxonomic composition of the microbiota varies among individuals and displays a range of sometimes redundant functions that modify the physicochemical environment of the host and may alter selection pressures. Here we review known human traits and genes for which the microbiota may have contributed or responded to changes in host diet, climate, or pathogen exposure. Integrating host–microbiota interactions in human adaptation could offer new approaches to improve our understanding of human health and evolution.

How organisms adapt to new environments is a central question in evolutionary biology that is gaining importance in the face of rapid environmental change. A vast diversity of eukaryotic species harbor microbial communities, or microbiotas, which influence their health and fitness (*1*). Host-associated microbiotas can provide novel ecological capabilities, evolve quickly, and exchange microbes or genes with other microbiotas, their hosts, and the environment (*2*–*5*). The list of microbes known to be beneficial to animals and plants is expanding, as is knowledge of their associated mechanisms. How host populations adapt to changing environments through natural selection involving genetic change across generations is well explored (*2*–*5*), but the role of microbiotas in mediating adaptation, particularly at the population level, is less well understood (Box 1).

Drivers of local adaptation include changes in host diet, local climate, and novel pathogen encounters. During the process of local adaptation, natural selection can act on the host, the microbiota, or their interactions (*6*). In host–microbiota partnerships where microbes are strictly transmitted from parent to offspring, selection can act on the host and its symbionts as a unit to favor microbial functions that enhance host fitness. This is known as the hologenome theory of evolution (*2*, *3*), in which reciprocal selection between partners (i.e., host–microbial coevolution) is invoked. Coevolution is exemplified by the formation of organelles in eukaryotes and of endosymbionts in insects (*7*). The two partners become irreversibly dependent on each other and enhance each other's fitness. The microbe, as an endosymbiont, must be transmitted vertically because of genetic interdependence with the host. Several models have been developed that present the necessary conditions for host–microbial coevolution (*2*–*5*, *8*, *9*).

For host–microbiota systems that are diverse, complex, and dynamic—such as the gut microbiotas of animals or the leaf microbiotas of plants—many members of the community do not fit the criteria for coevolution (*5*, *6*, *8*). Members of complex microbiotas may have mixed transmission routes, and selection pressures on the host and microbes may be decoupled. Under these conditions, environmental acquisition and ecological filtering are the dominant processes that shape microbial community composition (*10*). As a result, members of microbiotas are rarely selected to improve host fitness (*11*, *12*). Rather, by maximizing their own fitness (Box 1), microbes can impose a fitness cost to the host—for instance, when they act as opportunistic pathogens or pathobionts (*11*, *12*). Indeed, many human gut microbes, such as *Bacteroides* species, are considered both beneficial and opportunistic pathogens, owing to their occasional participation in infection by mucosal invasion, causing pathology (*11*). Just as most new mutations are deleterious to a genome, most new random changes to a microbiota will likely not improve host fitness, and those that are beneficial to the host will be rare.

Rare and random acquisitions of a beneficial microbe or function are required for the microbiota to make a positive impact on host fitness and influence adaptation. There are two main ways the beneficial functions of a microbiota may be favored by natural selection without coevolution. First, selection on microbial community processes alone can favor a beneficial microbiota (*6*). For example, Kikuchi *et al.* showed that stinkbugs can acquire soil microbes that have been preselected for the detoxification of insecticide in soil, thereby rendering the host resistant to insecticide (*13*). Kohl *et al.* showed that toxin-naive woodrats can acquire gut microbes that detoxify plant toxins in their diet (*14*). In both cases, the selective agent driving the detoxification ability of the microbes is likely the toxic compounds themselves, rather than selection on host fitness. A notable example in humans was

Department of Microbiome Science, Max Planck Institute for Developmental Biology, Tübingen, Germany.
*Corresponding author. Email: rley@tuebingen.mpg.de

Box 1. Terminology

Adaptation: We use the term "adaptation" to mean evolution through natural selection that involves genetic changes in a population across generations, as opposed to acclimation that occurs within an individual's lifetime. Local adaptation is when a subpopulation of a species genetically adapts to its local condition.

Microbiota: The assemblages of bacterial, archaeal, and eukaryotic microorganisms and their viruses that make up a microbial community.

Narrow-sense heritability (h^2): The ratio of additive genetic variance to phenotypic variance within a population (*96*, *97*). Note that h^2 of microbiota measurements can be confounded by vertical transmission of microbes in some studies including chip heritability (the proportion of phenotypic variation that can be explained by the distribution of genetic markers or single-nucleotide polymorphisms) (*98*). However, h^2 estimates in twin studies are independent of transmission modes because monozygotic and dizygotic twins are not expected to have different amounts of vertically transmitted microbes (*98*). Relative abundances of both vertically and horizontally transmitted microbes can have significant h^2 estimates if there are significant additive genetic variants in the host genomes that affect the relative abundances of the microbes. Heritability in Box 2 is h^2.

Vertical transmission: A process of passing on a microbe(s) from parents to their offspring (*99*). Transfer of microbes from the mother's birth canal or skin to the offspring is an example of vertical transmission (*100*, *101*).

Horizontal transmission: A process of passing a microbe(s) between hosts that are not in a parent–offspring relationship (i.e., interhost transmission) (*99*). Transfer of microbes among social partners is an example of horizontal transmission (*102*, *103*). The term may also include environmental transmissions (e.g., environmental acquisition of microbes from food and soil) (*104*).

uncovered by Hehemann *et al.*, who showed that in Japanese populations the gut bacterium *Bacteroides plebeius* has acquired a porphyranase gene from the seaweed-dwelling bacterium *Zobellia galactanivorans*, and people harboring this microbe have thereby acquired the ability to break down algal carbohydrates (*15*). More recent evidence shows that the enzymatic capacity to break down glycans from seaweed is generally enriched in the gut microbiomes of several Asian populations compared with those of other groups and is prevalent in different species of *Bacteroides* (*16*). Although the fitness consequences of the seaweed-derived energy to the host are unclear, these examples show that selection acting on microbiota-encoded processes alone may benefit the host without requiring the host to evolve adaptive mutations.

Selection based on differences in host traits has been shown experimentally to also drive differences in the microbiota that promote those host traits. For instance, Panke-Buisse *et al.* performed an experimental evolution study in which transfer of soil microbiota from batch to batch of *Arabidopsis thaliana* seeds, while keeping the plant genetic stock constant, drove divergence in flowering time (*17*). Similarly, others have selected for soil microbiotas that alter the biomass of *A. thaliana* (*18*) and *Medicago sativa* (*19*). In these examples, selection for soil microbiotas alone was sufficient to drive changes in host phenotype, without coevolution. Beyond affecting host phenotype, the microbiota can shape the patterns of host genetic adaptation. Rudman *et al.* showed that selection based on differences in the *Drosophila melanogaster* microbiota caused divergence in host populations. These authors identified divergent loci that were previously associated with adaptation in natural populations (*20*). Together, these empirical studies establish the potential for the microbiota to drive host adaptation by altering the host's environment.

A few evolutionary models predict how the microbiota affects the rate of host-adaptive evolution by extending host phenotypic plasticity through the microbiota (*4*) and incorporating the microbiota into models of quantitative genetics (*21*). Formal models that assess the evolutionary dynamics between host-adaptive alleles and the microbiota are lacking, but first we need evidence for such interactions.

Here we propose examples that suggest an interplay between host genes and the microbiota during the process of adaptation. We highlight two examples of interactions across multiple generations between human alleles and associated microbes and discuss how the host can replace or recruit beneficial microbes without requiring specifically coevolved organisms. We also discuss other adaptive traits in humans, where microbes may have interacted with host alleles during local adaptation.

Host gene–microbe associations in human adaptation

Adaptation of modern human populations to local environments and the genetic bases of these adaptations are well characterized (*22*). Differences in selection pressures, including diet, climate, and pathogen exposure, have resulted in differences among human populations in traits related to digestion (*23*, *24*), physiology (*25*, *26*), and immunity (*27*, *28*). These differences result from local genetic adaptations occurring across multiple generations and are distinguishable from adaptations by the immune system or physiological acclimations within the lifetime of a host (Box 1). In many cases, the primary genetic variants responsible for these adaptive traits have been identified: These include mutation and truncation of lactase (encoded by the gene region *LCT*) required in lactose digestion (*29*), the role of hypoxia-inducible factor 2-alpha (encoded by *EPAS1*) in high-altitude adaptation (*26*), and beta-globin gene haplotypes or sickle cell traits (encoded by *HBB*) in engendering malaria resistance (*27*), all of which represent classic examples of local adaptation (*22*). Moreover, compositional and functional variation of the human microbiota has been described extensively (*30*). Amato *et al.* recently reviewed beneficial functions of the microbiota that have likely affected local adaptation in humans, such as the microbiota's enhancement of nutrition and protection from infectious disease (*31*). However, specific interactions between host-adaptive alleles and adaptive microbiota functions during local adaptation in humans remain to be explored.

Host genes replace beneficial microbiota functions

Mammals are characterized by the behavior of feeding their offspring maternal milk—the main energy supply to infants coming from milk sugar lactose. In the upper gastrointestinal tract (GIT), the host enzyme lactase cleaves the milk sugar lactose into glucose and galactose, which are then absorbed. After weaning, when milk is no longer part of the diet, the production of lactase ceases [lactase nonpersistence (LNP) is the ancestral condition]. Animal domestication on different continents (2500 to 10,000 years ago) and the consumption of nonhuman milk repeatedly led to strong selective pressure for lactase production to persist into adulthood [lactase persistence (LP)] (*29*). In the present, allelic variation at the *LCT* locus predicts the LP phenotype in multiple human populations, and the independent development of LP has resulted in a variety of LP alleles (*29*).

Many microbes that are common constituents of the gut microbiota can use β-galactosidases to cleave lactose and then ferment the products, and lactose may be sequestered by lactic acid bacteria. Regardless of how it is processed, the by-products of microbial lactose usage yield less energy to the host (*32*). This implies that the host and the microbes are in competition for lactose and that the host has an energetic incentive to outcompete the microbes (Fig. 1, A and B). LP hosts outcompete microbes for lactose, because lactase is active in the upper GIT where microbial biomass is low. LNP hosts, by contrast, mainly access the less–energy-dense products of microbial lactose metabolism in the lower GIT. Undigested lactose passing to the colon can thus be considered a form of fiber that requires microbial enzymes to process. As with fiber degradation in the colon, the microbiotas able to degrade lactose derive energy from fermentation, and their fermentation products [short-chain fatty acids (SCFAs)] constitute an energy source for the host. Thus, although the microbiota takes a share of the energy content of lactose, the alternative in a LNP host is to lose the energy source entirely.

Recent studies performed in Western populations have associated the same variant at the *LCT* locus with the relative abundance of *Bifidobacterium* in the gut microbiota. This association is the most consistent signal of microbiota genome-wide association studies (GWASs) to date (*33*) (Box 2), and the link depends on milk consumption (*34*). The inverse relationship between LP genotype and relative abundances of *Bifidobacterium* supports the notion that the mammalian lactase enzyme and bacterial β-galactosidase enzyme are in direct competition for lactose. *Bifidobacteria* are important lactose degraders (*35*, *36*) and may have helped adult hosts extract energy from milk after domestication of dairy-producing animals and before selection on the LP alleles. After the rise of pastoralism, lactose-metabolizing bacteria likely had a positive effect on the fitness of hosts in the absence of LP alleles (*29*). Later, the beneficial host allele arose and replaced the microbiota function, becoming nearly fixed in some populations (*23*, *35*). The production of β-galactosidase by *Bifidobacterium* (or functionally redundant microbes) may also have relaxed the selection pressure on the LP allele by reducing the fitness differences between *LCT* genotypes. Additionally, if microbial consumption of lactose minimizes the disease outcome related to lactose maldigestion and promotes milk consumption that carries additional benefits (*36*), the microbiota may be mitigating energetic tradeoffs and maintaining *LCT* polymorphisms in human populations.

Host genes recruit beneficial microbiota functions

The lactose example suggests that activities encoded by both the microbiome and the host genome may be particularly susceptible to competition between host and microbiota.

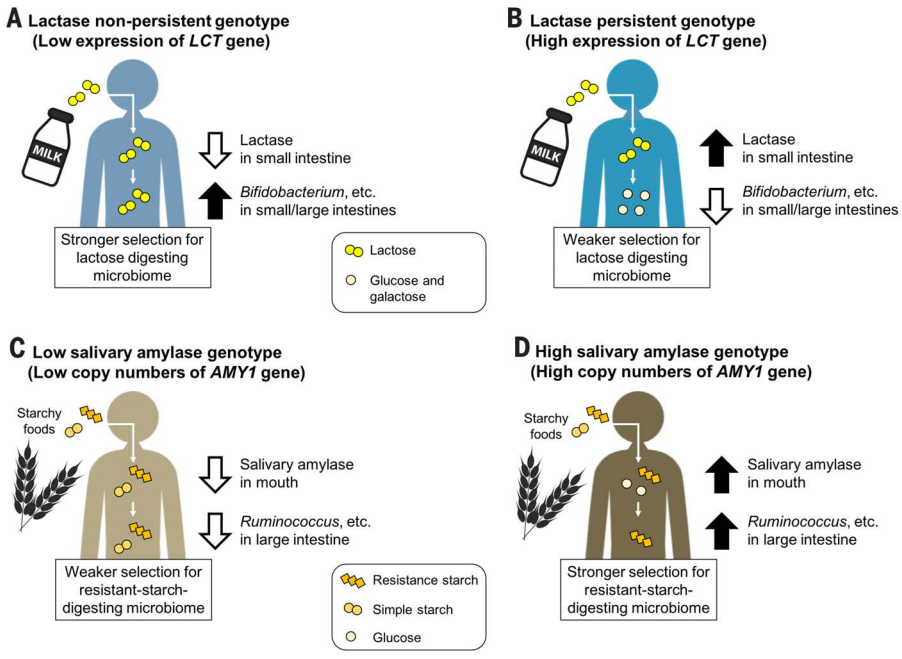

Fig. 1. Examples of associations between host genotype and the microbiota. The inverse associations between *LCT* genotypes and the relative abundance of *Bifidobacterium* are described for (**A**) LNP hosts and (**B**) LP hosts. The positive associations between *AMY1* gene copy number (CN) and relative abundance of *Ruminococcus* are described for (**C**) low–*AMY1* CN hosts and (**D**) high–*AMY1* CN hosts. Different types of sugars are shown in different shapes and colors.

In contrast to lactose, which is a single sugar, the variety of starches in the human diet provides an opportunity for the host to access one form of starch with amylase in the upper GIT, leaving resistant starches for the microbiota to digest in the lower GIT. Indeed, starches take many different forms, including structures recalcitrant to degradation by the host enzyme amylase, which cleaves starch into glucose subunits. The degree to which host and microbiota partition the starch substrates likely depends on host genotype.

Salivary amylase, encoded by the *AMY1* gene, begins the process of starch breakdown to glucose in the mouth. Individual differences in salivary amylase activity are positively correlated with the copy number (CN) of the *AMY1* gene, which typically ranges from 2 to 15 (*24*, *37*). Compared with individuals that have low *AMY1* CNs, those with high *AMY1* CNs more thoroughly deplete a given diet of amylase-susceptible starches before these foods reach the lower GIT and its microbiota (Fig. 1, C and D). A low *AMY1* CN of 2 is the ancestral condition: The expansion of *AMY1* CN in humans was likely driven by a dietary shift from a low-starch diet to a high-starch diet (*24*, *38*, *39*). Indeed, the flanking regions of the *AMY1* genes show evidence of a selective sweep in human populations, which supports the origin of *AMY1* duplications after the split from Neanderthals but before the origin of agriculture (*38*, *39*). Higher levels of salivary amylase likely promoted fitness of individuals in populations with a high-starch diet as agriculture developed. Similar to the evolution of LP, host amylase conferred a fitness advantage by its greater energy yield compared with that of microbial fermentation products. Hosts with high *AMY1* CNs additionally benefit from enhanced degradation of resistant starch by colonic microbes.

Compared with the gut microbiotas of individuals with low *AMY1* CNs, those of high–*AMY1* CN hosts are enriched in *Ruminococcus* (*37*), a genus important in resistant-starch fermentation (*40*, *41*). In low–*AMY1* CN hosts, gut bacteria preferentially ferment amylase-susceptible starch that hosts cannot use because they have low levels of salivary amylase. *Ruminococcus*, or functionally redundant microbes, may have strengthened the selection pressure on the expansion of *AMY1* CN by amplifying the relative fitness difference between individuals with high and low *AMY1* CNs and may have reinforced the host gene–microbe association (Fig. 1, C and D). This dynamic could thus lead to the recruitment of microbes on the basis of host genotype.

Human adaptations that may involve gene–microbe interactions

There is emerging evidence of microbial involvement in several other human genetic adaptations (Fig. 2) in which the role of microbes was previously underappreciated.

Adaptation to dietary shifts

Lactose and starch consumption (*33*, *37*) are probably the first known examples of gene–microbe interactions related to diet that could be investigated further for a role in human adaptation, but others are likely to emerge. For instance, long-chain polyunsaturated fatty acids (LC-PUFAs) are key nutrients that can be acquired directly from animal-based diets or synthesized from plant-derived precursors using host-derived enzymes (*42*–*45*). Evidence of positive selection on genes related to fatty-acid metabolism—including fatty-acid desaturase (*FADS*) (*42*–*45*), carnitine palmitoyltransferase 1A (*CPT1A*) (*46*), and pancreatic lipase related protein 2 (*PLRP2*) (*47*)—has been associated with dietary adaptations in multiple human populations. The ancestral allele of the *FADS* gene region is associated with populations that consume a plant-based diet (*44*, *45*), and the derived allele is associated with current and historical populations that favor a high-fat diet (*42*). Bacteria belonging to at least 10 phyla appear to biosynthesize LC-PUFAs (*48*). Among human gut microbes, *Lactobacillus plantarum* and others have been shown to metabolize the plant-derived precursors and affect the bioavailability of PUFA-derived metabolites in vitro and in vivo (*49*–*51*). Human gut microbes that are enriched by a plant-based diet (*52*–*54*) or a high-fat diet (*55*), respectively, have been described (Fig. 2). Similarly, the alcohol dehydrogenase 1B (*ADH1B*) locus shows evidence of positive selection in humans (*56*, *57*) and has been associated with increased ethanol intake, which is thought to have accompanied the development of agriculture (*57*). Human and bacterial enzymes can convert ethanol to acetaldehyde; variation in the gut microbiota has been associated with alcohol consumption and related diseases (*58*, *59*) (Fig. 2). These observations suggest that during shifts from a predominantly plant-based to a largely animal-based diet, and toward increased alcohol consumption, members of the microbiota may have played an adaptive role.

Adaptation to climate-related factors

Humans have adapted to local climates (*60*). Populations living at high latitudes face cold stress, and genes related to temperature sensing (*TRPM8*) and energy harvest (e.g., *FADS* and *CPT1A*) have been associated with climate-related adaptations (*42*, *60*, *61*). The human microbiota also varies by latitude and may contribute to climate-related adaptation by increasing the efficiency of energy extraction from the diet and subsequent fat storage (*62*). Some of this variation in the microbiota is associated with ambient temperature (*63*–*66*) and host body size (*67*, *68*) (Fig. 2). Experimental studies in mice have shown that changes in ambient temperature alone can induce changes in the gut microbiota (*63*–*66*). The microbiotas

Box 2. Microbial heritability in relation to host adaptation.

As used here, the term "heritability" differs from the terms related to transmission modes of microbiota, such as "inheritance." Heritability is a statistical measurement used to estimate the proportion of phenotypic variation in a population that is explained by genetic variation (*96*) (see Box 1 for definitions). Heritability has been estimated for the relative abundances of taxa or genes (*33*, *72*). For the human gut microbiota, ~10% of gut taxa have been shown to be heritable (*105*), and similar proportions of heritable microbes have been reported in maize root microbiotas (*106*). Note that microbial heritability estimated in twin studies is independent of microbial transmission mode (see Box 1).

In general, heritability estimates of relative abundances of microbial taxa in the human gut microbiota tend to be low compared with estimates for traits such as height (*33*). Low heritability estimates for microbiota traits can be attributed to environmental noise and/or nonadditive genetic variance (*107*, *108*). For example, temporary changes in the gut microbiota caused by dietary shifts (*40*, *41*) or pathogen overgrowth (*11*, *12*, *31*) may lower heritability estimates. Alternatively, strong purifying selection acting on host genetic mechanisms that affect the microbiota could lead to fixation of genetic variants and also reduce heritability estimates. Indeed, population genetic theories (*109*) and empirical studies (*108*, *110*, *111*) demonstrate that the traits most tightly associated with fitness tend to show lower heritability (e.g., fecundity) than traits that are less associated with fitness (e.g., morphology). Thus, heritability does not provide the relative contributions of genetics and environment to a trait. Despite its limitations, heritability does provide information on how well genetics can predict a trait, which then motivates GWASs to identify the genetic basis of heritable microbial traits (*98*). Furthermore, heritability and related measurements (*112*) have been used to predict responses to selection in evolutionary, agricultural, and medical studies (*97*). Many of the same microbes are heritable across several human populations (*33*) and mammalian species (*113*). These findings support the value of characterizing heritable components of the microbiota for use in studies that investigate the underlying genetic and nongenetic mechanisms.

Heritable components of the microbiota are more likely than nonheritable components to be involved in genetic adaptations. In the early stages of adaptation, locally beneficial microbes can be acquired by the host population and may not necessitate a change in the host genome to facilitate their maintenance (*13*–*15*). During host acclimation to the new environment, beneficial microbes would therefore remain nonheritable. In the long term, however, the host population may evolve genetic variants to replace or recruit these beneficial microbes (Fig. 1), such that nonheritable microbes will become heritable. In principle, when the allele that maintains the beneficial microbiota function reaches complete fixation, the heritable component of the microbiota will revert to being nonheritable, because every individual in the population will carry the allele. However, complete fixation of a locally beneficial allele is unlikely in the face of migration from nonadapted populations (*114*). Thus, heritable microbial measurements provide a starting point to identify components of a microbiota that may be involved in ongoing host genetic adaptations to local environments.

Relationship between heritability and transmission modes

Transmission modes will likely play a role in the stability of microbial heritability over time. For the relative abundances of microbial taxa or genes to be stably heritable over time, they must be present every generation and associated with host genetic variation. If acquisition of microbes from the environment or other individuals is less reliable than acquisition from parents, the heritability of horizontally acquired microbes should be less stable over time than the heritability of vertically acquired microbes. For many microbes within the human microbiota, the degree of vertical transmission remains to be characterized, but more and more microbial taxa show evidence of parent-to-offspring transmission (*100*, *101*) and population-level transmission across many generations (*115*–*117*).

of cold-exposed hosts exhibit higher absorptive capacity and energy harvest (*63*), as well as elevated heat production by brown adipose tissue (*63*–*66*). However, whether microbiota-mediated thermogenesis and *TRPM8* polymorphisms are linked in humans remains to be determined.

Climate is known to be an important selective pressure for genes involved in common metabolic disorders (*47*, *60*, *69*). The most consistent and highly heritable (Box 1) taxon in the human gut, the bacterial family *Christensenellaceae*, is associated with lower body mass index (BMI) (*67*) and metabolic disorders (*70*). *Methanobacteriaceae*, *Dehalobacteriaceae*, and members of *Tenericutes* also show heritability in multiple human populations (*33*) and co-occur with the *Christensenellaceae* (*67*). Recent evidence points to metabolic interactions between these partners that may affect metabolite availability to the host (*71*). Despite the significant heritability estimates for these taxa, no significant host genetic variants have been identified by GWASs. This suggests that some clearly heritable taxa may have polygenic nature with many genes with small effects (*72*). *Akkermansia*, a mucin degrader, has also been associated with BMI (*73*) and shown as a heritable taxon across multiple studies (*33*). The relative abundance of *Akkermansia* has been associated with a host genetic variant in *PLD1* (*74*), a gene previously associated with BMI (*75*). *PLD1* shows evidence of positive selection in African populations, but the selective agent is unclear (*76*).

Populations living at low latitudes face high levels of solar radiation, and genes related to skin pigmentation are classic examples of local adaptations in humans (*25*, *60*) (Fig. 2). Melanin in skin protects from ultraviolet (UV) radiation, and its antimicrobial properties have been suggested as an alternative hypothesis for the latitudinal gradient of skin pigmentation (*77*). Accordingly, an increase in skin pigmentation in human melanocytes can be induced by exposure to microbial products such as lipopolysaccharide (*77*). Guéniche *et al.* reported a protective effect of *Lactobacillus* spp. against skin and systemic immune responses after UV exposure (*78*). Given the emerging role for the gut microbiota in the regulation of skin homeostasis (*79*), further research may help to identify the potential interactions between pigmentation genes and microbes of the skin and gut.

High-altitude environments also impose many physiological challenges, including hypoxic stress (*26*), which may also be altered by the microbiota. A variety of adaptive traits and genes related to oxygen respiration and blood circulation that often involve the regulation of blood pressure have been identified in high-altitude environments (*26*) (Fig. 2). Recently, the gut microbiota has been shown to regulate blood pressure via production of SCFAs (*80*), and it is possible that SCFAs help regulate blood pressure in high-altitude environments (*81*–*83*). The production of SCFAs, including butyrate, influences the activity of hypoxia-inducible factors in mice (*84*), which is also a key pathway involved in high-altitude adaptation in multiple human populations (*26*). Production of bacterial angiotensin-converting enzymes (ACEs) that act on the renin-angiotensin system may also alter blood pressure in high-altitude environments (*83*). Bacterial ACEs have been shown to convert mammalian angiotensins in vitro (*85*).

Adaptation to local pathogens

Pathogens are considered one of the main drivers of adaptive evolution in humans (*86*) (Fig. 2), and the interface between the microbiota with pathogen defense and immunity has been extensively studied (*11*, *30*). A textbook example of local adaptation in humans is the genetic basis for resistance to malaria, caused by several species of parasitic protozoans in the genus *Plasmodium* (*27*). Skin and gut microbiotas may influence different stages of malaria (*87*). Genetic variations in the same cytokine-related genes, including *IL10*, *IL12*, *TNF*, and *IFNAR1*, have been associated with variations in malaria severity (*27*) and microbiota composition (*33*, *88*). Ippolito *et al.* summarized several hypotheses for multiple roles the microbiota may play in malaria resistance: (i) production of volatile compounds

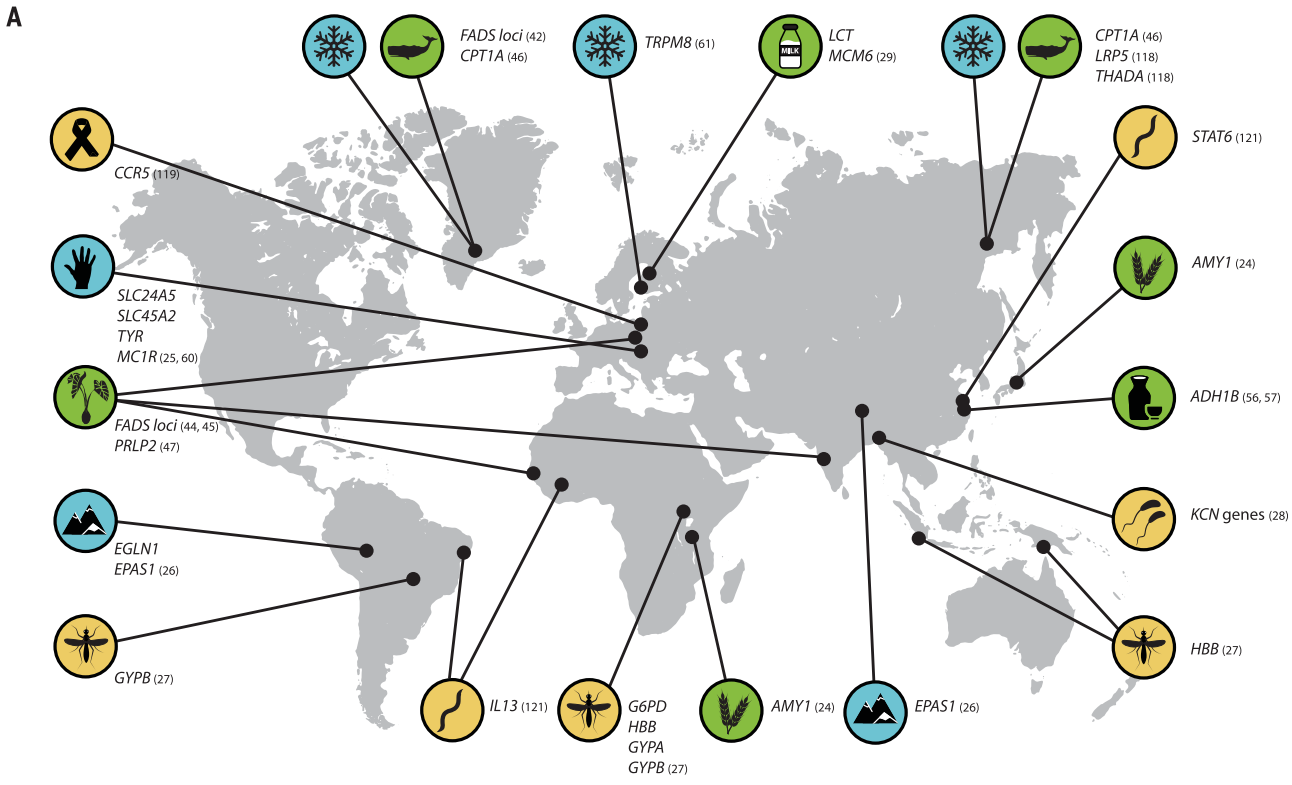

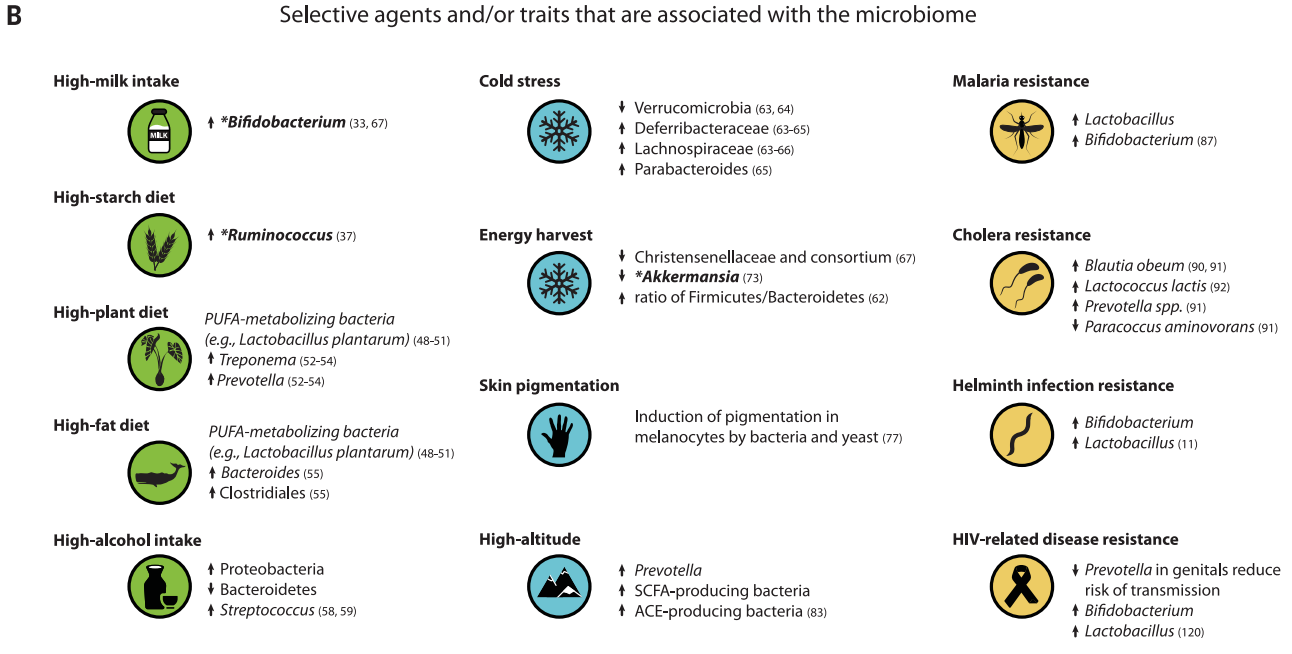

Fig. 2. Local adaptations in humans where the involvement of microbiota has also been suggested. (**A**) Global distribution of human genetic loci associated with adaptive traits. The symbols correspond to selective agents and/or traits in (B). (**B**) Features of microbiota that are associated with the selective agents and/or traits. Tendencies of positive or negative associations with relative abundances of microbial taxa are indicated by upward- and downward-pointing arrows, respectively. Note that the study populations of the microbiota do not match the study populations of host genetic loci. Asterisks and boldface type indicate microbial taxa that are associated with host genetic loci under positive selection: *LCT* and *Bifidobacterium*, *AMY1* and *Ruminococcus*, and *PLD1* and *Akkermansia* (see main text for details). Figure adapted from (*22*, *95*). See also (*11*, *24*–*29*, *33*, *37*, *42*, *44*–*67*, *73*, *77*, *83*, *87*, *90*–*92*, *118*–*121*), as indicated in the figure.

by skin bacteria that alter the attraction of mosquito vectors, (ii) antigen expression by gut microbes that induce antibodies conferring protection against *Plasmodium* transmission, and (iii) differences in the microbiota affecting the severity of blood-stage *Plasmodium* infections (*87*).

Other infections that may be influenced by the combination of microbiota and host genetic variation include cholera, HIV, and helminth infection. Cholera toxin targets several ion channels with genes that show signatures of selection (*28*, *89*). Gut microbial taxa associated with susceptibility to, and recovery from, cholera have been identified in human populations (*90*, *91*). Experimental studies have identified bacterial taxa that provide colonization resistance (*90*, *92*) and suppression of *Vibrio cholerae* virulence (*90*). Given that expression and function of ion channels are often altered in gastrointestinal disorders (*93*), there may be value in exploring links between microbiota and ion channel genes for treatment or prevention of diarrheal diseases. The vaginal microbiota has been suggested to play a role in acquisition and transmission of HIV (*94*), and the gut microbiota has been suggested to interact with helminths and alter disease outcome (*11*). Further investigation of interactions between well-studied host-adaptive alleles (*22*, *95*) and emerging beneficial microbiota functions may uncover previously unknown mechanisms of disease resistance.

All of the host gene–microbe examples mentioned here (Fig. 2) are still at the early stages of investigation. But in each of these cases, the microbiota has the potential to affect host evolution by modifying the adaptive landscape. These microbes likely modified the host's environment, resulting in altered selection pressures on host phenotypes. In future research on the relationship between adaptive host genotypes and adaptive microbiota functions, GWASs, candidate gene approaches, or transplant experiments using gene knockout models could help to identify host genetic mechanisms that maintain beneficial microbiota function and to test whether replacement and recruitment of microbiotas are general features of adaptation.

Conclusions

Host-associated microbiotas have affected the ecology and evolution of a variety of organisms, including humans, yet studying the interaction between adaptive host alleles and the microbiota remains a challenge. There are many opportunities, however, to revisit well-established examples of local adaptation in humans to search for previously unappreciated roles for the microbiota. This will require research into human populations and microbiomes across the globe and in their local contexts. Genetic studies have taken more and more populations into consideration, as have studies that characterize microbiomes. But so far, studies that include both host genetics and the microbiota have, with few exceptions, been performed predominantly in Western populations. We need to expand the reach of human genetic studies that include a microbiome component to a wider range of populations and locations. Findings from these types of studies will test the ubiquity of current findings and characterize more cases of microbiota-mediated adaptations, including perhaps some of the examples suggested here. The heritability of specific taxa could also be investigated further to better characterize underlying genetic polymorphisms. Many, but not all, heritable taxa are heritable across several human populations and even across species. These types of patterns could be further explored to understand the local contexts and selective forces. Heritability can apply to microbial functions as well as taxa, so extending the traits associated with human genetic variation from taxa to functions through metagenomics should further help to clarify the role of microbiomes in human adaptation. We have here focused on the evolution of the host (and mostly on humans), but microbes also rapidly evolve in response to their host environments. A better understanding of reciprocal interactions between the host genome and microbiota in the context of adaptive evolution will elucidate how humans and other animals, together with their microbiotas, have adapted to a changing world.

REFERENCES AND NOTES

1. M. McFall-Ngai *et al*., Animals in a bacterial world, a new imperative for the life sciences. *Proc. Natl. Acad. Sci. U.S.A.* **110**, 3229–3236 (2013). doi: 10.1073/pnas.1218525110; pmid: 23391737
2. I. Zilber-Rosenberg, E. Rosenberg, Role of microorganisms in the evolution of animals and plants: The hologenome theory of evolution. *FEMS Microbiol. Rev.* **32**, 723–735 (2008). doi: 10.1111/j.1574-6976.2008.00123.x; pmid: 18549407
3. S. R. Bordenstein, K. R. Theis, Host biology in light of the microbiome: Ten principles of holobionts and hologenomes. *PLOS Biol.* **13**, e1002226 (2015). doi: 10.1371/journal.pbio.1002226; pmid: 26284777
4. A. Alberdi, O. Aizpurua, K. Bohmann, M. L. Zepeda-Mendoza, M. T. P. Gilbert, Do vertebrate gut metagenomes confer rapid ecological adaptation? *Trends Ecol. Evol.* **31**, 689–699 (2016). doi: 10.1016/j.tree.2016.06.008; pmid: 27453351
5. N. A. Moran, H. Ochman, T. J. Hammer, Evolutionary and ecological consequences of gut microbial communities. *Annu. Rev. Ecol. Evol. Syst.* **50**, 451–475 (2019). doi: 10.1146/annurev-ecolsys-110617-062453; pmid: 32733173
6. R. E. Ley, D. A. Peterson, J. I. Gordon, Ecological and evolutionary forces shaping microbial diversity in the human intestine. *Cell* **124**, 837–848 (2006). doi: 10.1016/j.cell.2006.02.017; pmid: 16497592
7. N. A. Moran, J. P. McCutcheon, A. Nakabachi, Genomics and evolution of heritable bacterial symbionts. *Annu. Rev. Genet.* **42**, 165–190 (2008). doi: 10.1146/annurev.genet.41.110306.130119; pmid: 18983256
8. N. A. Moran, D. B. Sloan, The hologenome concept: Helpful or hollow? *PLOS Biol.* **13**, e1002311 (2015). doi: 10.1371/journal.pbio.1002311; pmid: 26636661
9. S. van Vliet, M. Doebeli, The role of multilevel selection in host microbiome evolution. *Proc. Natl. Acad. Sci. U.S.A.* **116**, 20591–20597 (2019). doi: 10.1073/pnas.1909790116; pmid: 31548380
10. F. Mazel *et al*., Is Host Filtering the Main Driver of Phylosymbiosis across the Tree of Life? *mSystems* **3**, e00097-18 (2018). doi: 10.1128/mSystems.00097-18; pmid: 30417109
11. J. M. Leung, A. L. Graham, S. C. L. Knowles, Parasite-microbiota interactions with the vertebrate gut: Synthesis through an ecological lens. *Front. Microbiol.* **9**, 843 (2018). doi: 10.3389/fmicb.2018.00843; pmid: 29867790
12. K. R. Foster, J. Schluter, K. Z. Coyte, S. Rakoff-Nahoum, The evolution of the host microbiome as an ecosystem on a leash. *Nature* **548**, 43–51 (2017). doi: 10.1038/nature23292; pmid: 28770836
13. Y. Kikuchi *et al*., Symbiont-mediated insecticide resistance. *Proc. Natl. Acad. Sci. U.S.A.* **109**, 8618–8622 (2012). doi: 10.1073/pnas.1200231109; pmid: 22529384
14. K. D. Kohl, R. B. Weiss, J. Cox, C. Dale, M. D. Dearing, Gut microbes of mammalian herbivores facilitate intake of plant toxins. *Ecol. Lett.* **17**, 1238–1246 (2014). doi: 10.1111/ele.12329; pmid: 25040855
15. J.-H. Hehemann *et al*., Transfer of carbohydrate-active enzymes from marine bacteria to Japanese gut microbiota. *Nature* **464**, 908–912 (2010). doi: 10.1038/nature08937; pmid: 20376150
16. N. A. Pudlo *et al*., Extensive transfer of genes for edible seaweed digestion from marine to human gut bacteria. bioRxiv 2020.06.09.142968 [Preprint]. 10 June 2020. https://doi.org/10.1101/2020.06.09.142968.
17. K. Panke-Buisse, A. C. Poole, J. K. Goodrich, R. E. Ley, J. Kao-Kniffin, Selection on soil microbiomes reveals reproducible impacts on plant function. *ISME J.* **9**, 980–989 (2015). doi: 10.1038/ismej.2014.196; pmid: 25350154
18. W. Swenson, D. S. Wilson, R. Elias, Artificial ecosystem selection. *Proc. Natl. Acad. Sci. U.S.A.* **97**, 9110–9114 (2000). doi: 10.1073/pnas.150237597; pmid: 10890915
19. L. M. Kaminsky, G. L. Thompson, R. V. Trexler, T. H. Bell, J. Kao-Kniffin, Medicago sativa has Reduced Biomass and Nodulation When Grown with Soil Microbiomes Conditioned to High Phosphorus Inputs. *Phytobiomes J.* **2**, 237–248 (2018). doi: 10.1094/PBIOMES-06-18-0025-R
20. S. M. Rudman *et al*., Microbiome composition shapes rapid genomic adaptation of *Drosophila melanogaster*. *Proc. Natl. Acad. Sci. U.S.A.* **116**, 20025–20032 (2019). doi: 10.1073/pnas.1907787116; pmid: 31527278
21. L. P. Henry, M. Bruijning, S. K. G. Forsberg, J. F. Ayroles, Can the microbiome influence host evolutionary trajectories? bioRxiv 700237 [Preprint]. 14 July 2019. https://doi.org/10.1101/700237.
22. S. Fan, M. E. B. Hansen, Y. Lo, S. A. Tishkoff, Going global by adapting local: A review of recent human adaptation. *Science* **354**, 54–59 (2016). doi: 10.1126/science.aaf5098; pmid: 27846491
23. Y. Itan, B. L. Jones, C. J. E. Ingram, D. M. Swallow, M. G. Thomas, A worldwide correlation of lactase persistence phenotype and genotypes. *BMC Evol. Biol.* **10**, 36 (2010). doi: 10.1186/1471-2148-10-36; pmid: 20144208
24. G. H. Perry *et al*., Diet and the evolution of human amylase gene copy number variation. *Nat. Genet.* **39**, 1256–1260 (2007). doi: 10.1038/ng2123; pmid: 17828263
25. R. A. Sturm, D. L. Duffy, Human pigmentation genes under environmental selection. *Genome Biol.* **13**, 248 (2012). doi: 10.1186/gb-2012-13-9-248; pmid: 23110848
26. T. S. Simonson, Altitude adaptation: A glimpse through various lenses. *High Alt. Med. Biol.* **16**, 125–137 (2015). doi: 10.1089/ham.2015.0033; pmid: 26070057
27. D. P. Kwiatkowski, How malaria has affected the human genome and what human genetics can teach us about malaria. *Am. J. Hum. Genet.* **77**, 171–192 (2005). doi: 10.1086/432519; pmid: 16001361
28. E. K. Karlsson *et al*., Natural selection in a bangladeshi population from the cholera-endemic ganges river delta. *Sci. Transl. Med.* **5**, 192ra86 (2013). doi: 10.1126/scitranslmed.3006338; pmid: 23825302
29. L. Ségurel, C. Bon, On the evolution of lactase persistence in humans. *Annu. Rev. Genomics Hum. Genet.* **18**, 297–319 (2017). doi: 10.1146/annurev-genom-091416-035340; pmid: 28426286
30. R. Knight *et al*., The microbiome and human biology. *Annu. Rev. Genomics Hum. Genet.* **18**, 65–86 (2017). doi: 10.1146/annurev-genom-083115-022438; pmid: 28375652
31. K. R. Amato, T. Jeyakumar, H. Poinar, P. Gros, Shifting climates, foods, and diseases: The human microbiome through evolution. *BioEssays* **41**, e1900034 (2019). doi: 10.1002/bies.201900034; pmid: 31524305

32. M. B. Roberfroid, Caloric value of inulin and oligofructose. *J. Nutr.* **129** (Suppl.), 1436S–1437S (1999). doi: 10.1093/jn/129.7.1436S; pmid: 10395615
33. J. K. Goodrich, E. R. Davenport, A. G. Clark, R. E. Ley, The relationship between the human genome and microbiome comes into view. *Annu. Rev. Genet.* **51**, 413–433 (2017). doi: 10.1146/annurev-genet-110711-155532; pmid: 28934590
34. M. J. Bonder *et al.*, The effect of host genetics on the gut microbiome. *Nat. Genet.* **48**, 1407–1412 (2016). doi: 10.1038/ng.3663; pmid: 27694959
35. H. Hove, H. Nørgaard, P. Brøbech Mortensen, Lactic acid bacteria and the human gastrointestinal tract. *Eur. J. Clin. Nutr.* **53**, 339–350 (1999). doi: 10.1038/sj.ejcn.1600773; pmid: 10369488
36. A. Szilagyi, Adaptation to lactose in lactase non persistent people: Effects on intolerance and the relationship between dairy food consumption and evaluation of diseases. *Nutrients* **7**, 6751–6779 (2015). doi: 10.3390/nu7085309; pmid: 26287234
37. A. C. Poole *et al.*, Human salivary amylase gene copy number impacts oral and gut microbiomes. *Cell Host Microbe* **25**, 553–564.e7 (2019). doi: 10.1016/j.chom.2019.03.001; pmid: 30974084
38. G. H. Perry, L. Kistler, M. A. Kelaita, A. J. Sams, Insights into hominin phenotypic and dietary evolution from ancient DNA sequence data. *J. Hum. Evol.* **79**, 55–63 (2015). doi: 10.1016/j.jhevol.2014.10.018; pmid: 25563409
39. C. E. Inchley *et al.*, Selective sweep on human amylase genes postdates the split with Neanderthals. *Sci. Rep.* **6**, 37198 (2016). doi: 10.1038/srep37198; pmid: 27853181
40. A. W. Walker *et al.*, Dominant and diet-responsive groups of bacteria within the human colonic microbiota. *ISME J.* **5**, 220–230 (2011). doi: 10.1038/ismej.2010.118; pmid: 20686513
41. X. Ze, S. H. Duncan, P. Louis, H. J. Flint, Ruminococcus bromii is a keystone species for the degradation of resistant starch in the human colon. *ISME J.* **6**, 1535–1543 (2012). doi: 10.1038/ismej.2012.4; pmid: 22343308
42. M. Fumagalli *et al.*, Greenlandic Inuit show genetic signatures of diet and climate adaptation. *Science* **349**, 1343–1347 (2015). doi: 10.1126/science.aab2319; pmid: 26383953
43. C. E. Amorim *et al.*, Genetic signature of natural selection in first Americans. *Proc. Natl. Acad. Sci. U.S.A.* **114**, 2195–2199 (2017). doi: 10.1073/pnas.1620541114; pmid: 28193867
44. K. S. D. Kothapalli *et al.*, Positive selection on a regulatory insertion-deletion polymorphism in FADS2 influences apparent endogenous synthesis of arachidonic acid. *Mol. Biol. Evol.* **33**, 1726–1739 (2016). doi: 10.1093/molbev/msw049; pmid: 27188529
45. K. Ye, F. Gao, D. Wang, O. Bar-Yosef, A. Keinan, Dietary adaptation of FADS genes in Europe varied across time and geography. *Nat. Ecol. Evol.* **1**, 0167 (2017). doi: 10.1038/s41559-017-0167; pmid: 29094686
46. F. J. Clemente *et al.*, A selective sweep on a deleterious mutation in CPT1A in arctic populations. *Am. J. Hum. Genet.* **95**, 584–589 (2014). doi: 10.1016/j.ajhg.2014.09.016; pmid: 25449608
47. A. M. Hancock *et al.*, Colloquium paper: Human adaptations to diet, subsistence, and ecoregion are due to subtle shifts in allele frequency. *Proc. Natl. Acad. Sci. U.S.A.* **107** (Suppl. 2), 8924–8930 (2010). doi: 10.1073/pnas.0914625107; pmid: 20445095
48. C. N. Shulse, E. E. Allen, Widespread occurrence of secondary lipid biosynthesis potential in microbial lineages. *PLOS ONE* **6**, e20146 (2011). doi: 10.1371/journal.pone.0020146; pmid: 21629834
49. S. Kishino *et al.*, Polyunsaturated fatty acid saturation by gut lactic acid bacteria affecting host lipid composition. *Proc. Natl. Acad. Sci. U.S.A.* **110**, 17808–17813 (2013). doi: 10.1073/pnas.1312937110; pmid: 24127592
50. C. Druart *et al.*, Role of the lower and upper intestine in the production and absorption of gut microbiota-derived PUFA metabolites. *PLOS ONE* **9**, e87560 (2014). doi: 10.1371/journal.pone.0087560; pmid: 24475308
51. C. Druart *et al.*, Ability of the gut microbiota to produce PUFA-derived bacterial metabolites: Proof of concept in germ-free versus conventionalized mice. *Mol. Nutr. Food Res.* **59**, 1603–1613 (2015). doi: 10.1002/mnfr.201500014; pmid: 25820326
52. C. De Filippo *et al.*, Impact of diet in shaping gut microbiota revealed by a comparative study in children from Europe and rural Africa. *Proc. Natl. Acad. Sci. U.S.A.* **107**, 14691–14696 (2010). doi: 10.1073/pnas.1005963107; pmid: 20679230
53. S. L. Schnorr *et al.*, Gut microbiome of the Hadza hunter-gatherers. *Nat. Commun.* **5**, 3654 (2014). doi: 10.1038/ncomms4654; pmid: 24736369
54. C. De Filippo *et al.*, Diet, environments, and gut microbiota. A preliminary investigation in children living in rural and urban Burkina Faso and Italy. *Front. Microbiol.* **8**, 1979 (2017). doi: 10.3389/fmicb.2017.01979; pmid: 29081768
55. R. K. Singh *et al.*, Influence of diet on the gut microbiome and implications for human health. *J. Transl. Med.* **15**, 73 (2017). doi: 10.1186/s12967-017-1175-y; pmid: 28388917
56. Y. Han *et al.*, Evidence of positive selection on a class I ADH locus. *Am. J. Hum. Genet.* **80**, 441–456 (2007). doi: 10.1086/512485; pmid: 17273965
57. Y. Peng *et al.*, The ADH1B Arg47His polymorphism in east Asian populations and expansion of rice domestication in history. *BMC Evol. Biol.* **10**, 15 (2010). doi: 10.1186/1471-2148-10-15; pmid: 20089146
58. A. Tsuruya *et al.*, Ecophysiological consequences of alcoholism on human gut microbiota: Implications for ethanol-related pathogenesis of colon cancer. *Sci. Rep.* **6**, 27923 (2016). doi: 10.1038/srep27923; pmid: 27295340
59. M. Meroni, M. Longo, P. Dongiovanni, Alcohol or gut microbiota: Who is the guilty? *Int. J. Mol. Sci.* **20**, 4568 (2019). doi: 10.3390/ijms20184568; pmid: 31540133
60. A. M. Hancock *et al.*, Adaptations to climate-mediated selective pressures in humans. *PLOS Genet.* **7**, e1001375 (2011). doi: 10.1371/journal.pgen.1001375; pmid: 21533023
61. F. M. Key *et al.*, Human local adaptation of the TRPM8 cold receptor along a latitudinal cline. *PLOS Genet.* **14**, e1007298 (2018). doi: 10.1371/journal.pgen.1007298; pmid: 29723195
62. T. A. Suzuki, M. Worobey, Geographical variation of human gut microbial composition. *Biol. Lett.* **10**, 20131037 (2014). doi: 10.1098/rsbl.2013.1037; pmid: 24522631
63. C. Chevalier *et al.*, Gut microbiota orchestrates energy homeostasis during cold. *Cell* **163**, 1360–1374 (2015). doi: 10.1016/j.cell.2015.11.004; pmid: 26638070
64. M. Ziętak *et al.*, Altered microbiota contributes to reduced diet-induced obesity upon cold exposure. *Cell Metab.* **23**, 1216–1223 (2016). doi: 10.1016/j.cmet.2016.05.001; pmid: 27304513
65. A. Worthmann *et al.*, Cold-induced conversion of cholesterol to bile acids in mice shapes the gut microbiome and promotes adaptive thermogenesis. *Nat. Med.* **23**, 839–849 (2017). doi: 10.1038/nm.4357; pmid: 28604703
66. B. Li *et al.*, Microbiota depletion impairs thermogenesis of brown adipose tissue and browning of white adipose tissue. *Cell Rep.* **26**, 2720–2737.e5 (2019). doi: 10.1016/j.celrep.2019.02.015; pmid: 30840893
67. J. K. Goodrich *et al.*, Human genetics shape the gut microbiome. *Cell* **159**, 789–799 (2014). doi: 10.1016/j.cell.2014.09.053; pmid: 25417156
68. T. A. Suzuki, F. M. Martins, M. Phifer-Rixey, M. W. Nachman, The gut microbiota and Bergmann's rule in wild house mice. *Mol. Ecol.* **29**, 2300–2311 (2020). doi: 10.1111/mec.15476; pmid: 32419280
69. A. M. Hancock *et al.*, Adaptations to climate in candidate genes for common metabolic disorders. *PLOS Genet.* **4**, e32 (2008). doi: 10.1371/journal.pgen.0040032; pmid: 18282109
70. J. L. Waters, R. E. Ley, The human gut bacteria Christensenellaceae are widespread, heritable, and associated with health. *BMC Biol.* **17**, 83 (2019). doi: 10.1186/s12915-019-0699-4; pmid: 31660948
71. A. Ruaud *et al.*, Syntrophy via interspecies H2 transfer between Christensenella and Methanobrevibacter underlies their global cooccurrence in the human gut. *mBio* **11**, e03235-19 (2020). doi: 10.1128/mBio.03235-19; pmid: 32019803
72. S. Sandoval-Motta, M. Aldana, E. Martínez-Romero, A. Frank, The Human Microbiome and the Missing Heritability Problem. *Front. Genet.* **8**, 80 (2017). doi: 10.3389/fgene.2017.00080; pmid: 28659968
73. A. Everard *et al.*, Cross-talk between *Akkermansia muciniphila* and intestinal epithelium controls diet-induced obesity. *Proc. Natl. Acad. Sci. U.S.A.* **110**, 9066–9071 (2013). doi: 10.1073/pnas.1219451110; pmid: 23671105
74. E. R. Davenport *et al.*, Genome-Wide Association Studies of the Human Gut Microbiota. *PLOS ONE* **10**, e0140301 (2015). doi: 10.1371/journal.pone.0140301; pmid: 26528553
75. M. C. Y. Ng *et al.*, Genome-wide association of BMI in African Americans. *Obesity* **20**, 622–627 (2012). doi: 10.1038/oby.2011.154; pmid: 21701570
76. J. M. Granka *et al.*, Limited evidence for classic selective sweeps in African populations. *Genetics* **192**, 1049–1064 (2012). doi: 10.1534/genetics.112.144071; pmid: 22960214
77. J. A. Mackintosh, The antimicrobial properties of melanocytes, melanosomes and melanin and the evolution of black skin. *J. Theor. Biol.* **211**, 101–113 (2001). doi: 10.1006/jtbi.2001.2331; pmid: 11419954
78. A. Guéniche, J. Benyacoub, T. M. Buetler, H. Smola, S. Blum, Supplementation with oral probiotic bacteria maintains cutaneous immune homeostasis after UV exposure. *Eur. J. Dermatol.* **16**, 511–517 (2006). pmid: 17101471
79. I. Salem, A. Ramser, N. Isham, M. A. Ghannoum, The gut microbiome as a major regulator of the gut-skin axis. *Front. Microbiol.* **9**, 1459 (2018). doi: 10.3389/fmicb.2018.01459; pmid: 30042740
80. J. Pluznick, A novel SCFA receptor, the microbiota, and blood pressure regulation. *Gut Microbes* **5**, 202–207 (2014). doi: 10.4161/gmic.27492; pmid: 24429443
81. L. Li, X. Zhao, Comparative analyses of fecal microbiota in Tibetan and Chinese Han living at low or high altitude by barcoded 454 pyrosequencing. *Sci. Rep.* **5**, 14682 (2015). doi: 10.1038/srep14682; pmid: 26443005
82. D. Lan *et al.*, Correlations between gut microbiota community structures of Tibetans and geography. *Sci. Rep.* **7**, 16982 (2017). doi: 10.1038/s41598-017-17194-4; pmid: 29209019
83. T. A. Suzuki, F. M. Martins, M. W. Nachman, Altitudinal variation of the gut microbiota in wild house mice. *Mol. Ecol.* **28**, 2378–2390 (2019). doi: 10.1111/mec.14905; pmid: 30346069
84. C. J. Kelly *et al.*, Crosstalk between microbiota-derived short-chain fatty acids and intestinal epithelial HIF augments tissue barrier function. *Cell Host Microbe* **17**, 662–671 (2015). doi: 10.1016/j.chom.2015.03.005; pmid: 25865369
85. G. Rivière *et al.*, Characterization of the first angiotensin-converting like enzyme in bacteria: Ancestor ACE is already active. *Gene* **399**, 81–90 (2007). doi: 10.1016/j.gene.2007.05.010; pmid: 17597310
86. M. Fumagalli *et al.*, Signatures of environmental genetic adaptation pinpoint pathogens as the main selective pressure through human evolution. *PLOS Genet.* **7**, e1002355 (2011). doi: 10.1371/journal.pgen.1002355; pmid: 22072984
87. M. M. Ippolito, J. E. Denny, C. Langelier, C. L. Sears, N. W. Schmidt, Malaria and the microbiome: A systematic review. *Clin. Infect. Dis.* **67**, 1831–1839 (2018). doi: 10.1093/cid/ciy374; pmid: 29701835
88. J. Wang *et al.*, Of genes and microbes: Solving the intricacies in host genomes. *Protein Cell* **9**, 446–461 (2018). doi: 10.1007/s13238-018-0532-9; pmid: 29611114
89. S. E. Gabriel, K. N. Brigman, B. H. Koller, R. C. Boucher, M. J. Stutts, Cystic fibrosis heterozygote resistance to cholera toxin in the cystic fibrosis mouse model. *Science* **266**, 107–109 (1994). doi: 10.1126/science.7524148; pmid: 7524148
90. A. Hsiao *et al.*, Members of the human gut microbiota involved in recovery from Vibrio cholerae infection. *Nature* **515**, 423–426 (2014). doi: 10.1038/nature13738; pmid: 25231861
91. F. S. Midani *et al.*, Human gut microbiota predicts susceptibility to Vibrio cholerae infection. *J. Infect. Dis.* **218**, 645–653 (2018). doi: 10.1093/infdis/jiy192; pmid: 29659916
92. N. Mao, A. Cubillos-Ruiz, D. E. Cameron, J. J. Collins, Probiotic strains detect and suppress cholera in mice. *Sci. Transl. Med.* **10**, eaao2586 (2018). doi: 10.1126/scitranslmed.aao2586; pmid: 29899022
93. I. M. Fuentes, J. A. Christianson, Ion channels, ion channel receptors, and visceral hypersensitivity in irritable bowel syndrome. *Neurogastroenterol. Motil.* **28**, 1613–1618 (2016). doi: 10.1111/nmo.12979; pmid: 27781369
94. B. Williams, A. Landay, R. M. Presti, Microbiome alterations in HIV infection a review. *Cell. Microbiol.* **18**, 645–651 (2016). doi: 10.1111/cmi.12588; pmid: 26945815
95. S. Tishkoff, Strength in small numbers. *Science* **349**, 1282–1283 (2015). doi: 10.1126/science.aad0584; pmid: 26383935
96. D. S. Falconer, T. F. C. Mackay, *Introduction to Quantitative Genetics* (Pearson, ed. 4, 1996).
97. P. M. Visscher, W. G. Hill, N. R. Wray, Heritability in the genomics era—Concepts and misconceptions. *Nat. Rev. Genet.* **9**, 255–266 (2008). doi: 10.1038/nrg2322; pmid: 18319743
98. E. R. Davenport, Elucidating the role of the host genome in shaping microbiome composition. *Gut Microbes* **7**, 178–184 (2016). doi: 10.1080/19490976.2016.1155022; pmid: 26939746

99. P. E. Fine, Vectors and vertical transmission: An epidemiologic perspective. *Ann. N. Y. Acad. Sci.* **266**, 173–194 (1975). doi: 10.1111/j.1749-6632.1975.tb35099.x; pmid: 829470
100. M. G. Dominguez-Bello *et al.*, Delivery mode shapes the acquisition and structure of the initial microbiota across multiple body habitats in newborns. *Proc. Natl. Acad. Sci. U.S.A.* **107**, 11971–11975 (2010). doi: 10.1073/pnas.1002601107; pmid: 20566857
101. C. Milani *et al.*, Exploring Vertical Transmission of Bifidobacteria from Mother to Child. *Appl. Environ. Microbiol.* **81**, 7078–7087 (2015). doi: 10.1128/AEM.02037-15; pmid: 26231653
102. J. Tung *et al.*, Social networks predict gut microbiome composition in wild baboons. *eLife* **4**, e05224 (2015). doi: 10.7554/eLife.05224; pmid: 25774601
103. A. H. A. H. Moeller *et al.*, Social behavior shapes the chimpanzee pan-microbiome. *Sci. Adv.* **2**, e1500997 (2016). doi: 10.1126/sciadv.1500997; pmid: 26824072
104. D. Ebert, The epidemiology and evolution of symbionts with mixed-mode transmission. *Annu. Rev. Ecol. Evol. Syst.* **44**, 623–643 (2013). doi: 10.1146/annurev-ecolsys-032513-100555
105. J. K. Goodrich *et al.*, Genetic determinants of the gut microbiome in UK twins. *Cell Host Microbe* **19**, 731–743 (2016). doi: 10.1016/j.chom.2016.04.017; pmid: 27173935
106. W. A. Walters *et al.*, Large-scale replicated field study of maize rhizosphere identifies heritable microbes. *Proc. Natl. Acad. Sci. U.S.A.* **115**, 7368–7373 (2018). doi: 10.1073/pnas.1800918115; pmid: 29941552
107. N. H. Barton, M. Turelli, Evolutionary quantitative genetics: How little do we know? *Annu. Rev. Genet.* **23**, 337–370 (1989). doi: 10.1146/annurev.ge.23.120189.002005; pmid: 2694935
108. A. A. Hoffmann, J. Merilä, T. N. Kristensen, Heritability and evolvability of fitness and nonfitness traits: Lessons from livestock. *Evolution* **70**, 1770–1779 (2016). doi: 10.1111/evo.12992; pmid: 27346243
109. R. A. Fisher, *The Genetical Theory of Natural Selection* (Clarendon Press, 1930).
110. L. Gustafsson, Lifetime reproductive success and heritability: Empirical support for Fisher's fundamental theorem. *Am. Nat.* **128**, 761–764 (1986). doi: 10.1086/284601
111. T. A. Mousseau, D. A. Roff, Natural selection and the heritability of fitness components. *Heredity* **59**, 181–197 (1987). doi: 10.1038/hdy.1987.113; pmid: 3316130
112. D. Houle, Comparing evolvability and variability of quantitative traits. *Genetics* **130**, 195–204 (1992). pmid: 1732160
113. T. A. Suzuki *et al.*, Host genetic determinants of the gut microbiota of wild mice. *Mol. Ecol.* **28**, 3197–3207 (2019). doi: 10.1111/mec.14905; pmid: 31141224
114. A. W. Bigham, Genetics of human origin and evolution: High-altitude adaptations. *Curr. Opin. Genet. Dev.* **41**, 8–13 (2016). doi: 10.1016/j.gde.2016.06.018; pmid: 27501156
115. J. C. Atherton, M. J. Blaser, Coadaptation of Helicobacter pylori and humans: Ancient history, modern implications. *J. Clin. Invest.* **119**, 2475–2487 (2009). doi: 10.1172/JCI38605; pmid: 19729845
116. A. H. Moeller *et al.*, Cospeciation of gut microbiota with hominids. *Science* **353**, 380–382 (2016). doi: 10.1126/science.aaf3951; pmid: 27463672
117. D. T. Truong, A. Tett, E. Pasolli, C. Huttenhower, N. Segata, Microbial strain-level population structure and genetic diversity from metagenomes. *Genome Res.* **27**, 626–638 (2017). doi: 10.1101/gr.216242.116; pmid: 28167665
118. A. Cardona *et al.*, Genome-wide analysis of cold adaptation in indigenous Siberian populations. *PLOS ONE* **9**, e98076 (2014). doi: 10.1371/journal.pone.0098076; pmid: 24847810
119. J. Novembre, A. P. Galvani, M. Slatkin, The geographic spread of the CCR5 Delta32 HIV-resistance allele. *PLOS Biol.* **3**, e339 (2005). doi: 10.1371/journal.pbio.0030339; pmid: 16216086
120. G. Zilberman-Schapira *et al.*, The gut microbiome in human immunodeficiency virus infection. *BMC Med.* **14**, 83 (2016). doi: 10.1186/s12916-016-0625-3; pmid: 27256449
121. V. D. Mangano, D. Modiano, Host genetics and parasitic infections. *Clin. Microbiol. Infect.* **20**, 1265–1275 (2014). doi: 10.1111/1469-0691.12793; pmid: 25273270

ACKNOWLEDGMENTS

We thank the reviewers, the members of the Department of Microbiome Science, M. Nachman, M. Ballinger, and A. Moeller for comments. D. Welter created the print page summary figure.
Funding: This work was funded by the Max Planck Society.
Competing interests: The authors declare no conflicts of interest.

10.1126/science.aaz6827

RESEARCH ARTICLE SUMMARY

CORONAVIRUS

Comparative host-coronavirus protein interaction networks reveal pan-viral disease mechanisms

David E. Gordon*, Joseph Hiatt*, Mehdi Bouhaddou*, Veronica V. Rezelj*, Svenja Ulferts*, Hannes Braberg*, Alexander S. Jureka*, Kirsten Obernier*, Jeffrey Z. Guo*, Jyoti Batra*, Robyn M. Kaake*, Andrew R. Weckstein*, Tristan W. Owens*, Meghna Gupta*, Sergei Pourmal*, Erron W. Titus*, Merve Cakir* *et al.*

INTRODUCTION: The emergence of three lethal coronaviruses in <20 years and the urgency of the COVID-19 pandemic have prompted efforts to develop new therapeutic strategies, including by repurposing existing agents. After performing a comparative analysis of the three pathogenic human coronaviruses severe acute respiratory syndrome coronavirus 1 (SARS-CoV-1), SARS-CoV-2, and Middle East respiratory syndrome coronavirus (MERS-CoV), we identified shared biology and host-directed drug targets to prioritize therapeutics with potential for rapid deployment against current and future coronavirus outbreaks.

RATIONALE: Expanding on our recent SARS-CoV-2 interactome, we mapped the virus-host protein-protein interactions for SARS-CoV-1 and MERS-CoV and assessed the cellular localization of each viral protein across the three strains. We conducted two genetic screens of SARS-CoV-2 interactors to prioritize functionally-relevant host factors and structurally characterized one virus-host interaction. We then tested the clinical relevance of three more host factors by assessing risk in genetic cohorts or observing effectiveness of host factor–targeting drugs in real-world evidence.

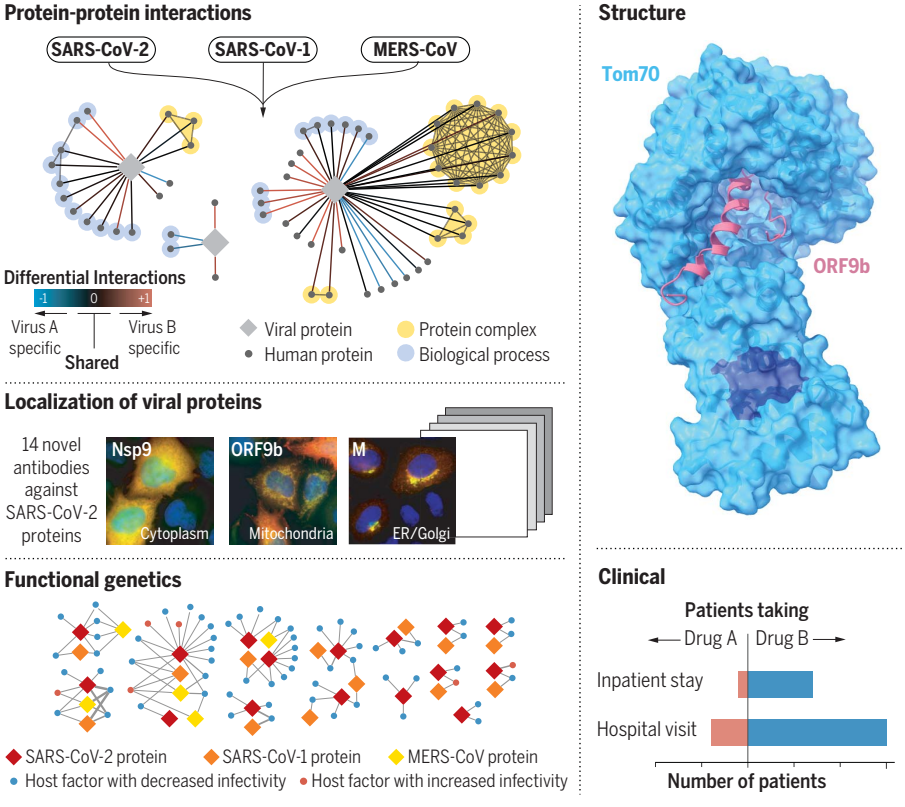

Overview of the approaches taken for systemic and functional comparison of pathogenic human coronaviruses. (Left) Viral-human protein-protein interaction network mapping, viral protein localization studies, and functional genetic screens provide key insights into the shared and individual characteristics of each virus. (Right) Structural studies and hypothesis testing in clinical datasets demonstrate the utility of this approach for prioritizing therapeutic strategies. Nsp, nonstructural protein; ORF, open reading frame; ER, endoplasmic reticulum.

RESULTS: Quantitative comparison of the 389 interactors of SARS-CoV-2, 366 of SARS-CoV-1, and 296 of MERS-CoV highlighted interactions with host processes that are conserved across all three viruses, including where nonorthologous proteins from different virus strains seem to fill similar roles. We also localized each individually-expressed viral protein by microscopy and then raised and validated antisera against 14 SARS-CoV-2 proteins to determine their localization during infection.

On the basis of two independent genetic perturbation screens, we identified 73 host factors that, when depleted, caused significant changes in SARS-CoV-2 replication. From this list of potential drug targets, we validated the biological and clinical relevance of Tom70, IL17RA, PGES-2, and SigmaR1.

A 3-Å cryo–electron microscopy structure of Tom70, a mitochondrial import receptor, in complex with SARS-CoV-2 ORF9b, provides insight into how ORF9b may modulate the host immune response. Using curated genome-wide association study data, we found that individuals with genotypes corresponding to higher soluble IL17RA levels in plasma are at decreased risk of COVID-19 hospitalization.

To demonstrate the value of our data for drug repurposing, we identified SARS-CoV-2 patients who were prescribed drugs against prioritized targets and asked how they fared compared with carefully matched patients treated with clinically similar drugs that do not inhibit SARS-CoV-2. Both indomethacin, an inhibitor of host factor PGES-2, and typical antipsychotics, selected for their interaction with sigma receptors, showed effectiveness against COVID-19 compared with celecoxib and atypical antipsychotics, respectively.

CONCLUSION: By employing an integrative and collaborative approach, we identified conserved mechanisms across three pathogenic coronavirus strains and further investigated potential drug targets. This versatile approach is broadly applicable to other infectious agents and disease areas. ■

The list of author affiliations is available in the full article online.
*These authors contributed equally to this work.
Corresponding authors: Nevan J. Krogan (nevan.krogan@ucsf.edu); Pedro Beltrao (pbeltrao@ebi.ac.uk); Marco Vignuzzi (marco.vignuzzi@pasteur.fr); Christopher F. Basler (cbasler@gsu.edu); Kliment A. Verba (verba@msg.ucsf.edu); Oren S. Rosenberg (oren.rosenberg@ucsf.edu); Andrew A. Peden (a.peden@sheffield.ac.uk); Robert Grosse (robert.grosse@pharmakol.uni-freiburg.de); Jeremy A. Rassen (jeremy.rassen@aetion.com); Adolfo García-Sastre (adolfo.garcia-sastre@mssm.edu)
This is an open-access article distributed under the terms of the Creative Commons Attribution license (https://creativecommons.org/licenses/by/4.0/), which permits unrestricted use, distribution, and reproduction in any medium, provided the original work is properly cited.
Cite this article as D. E. Gordon *et al.*, *Science* **370**, eabe9403 (2020). DOI: 10.1126/science.abe9403

READ THE FULL ARTICLE AT
https://doi.org/10.1126/science.abe9403

RESEARCH ARTICLE

CORONAVIRUS

Comparative host-coronavirus protein interaction networks reveal pan-viral disease mechanisms

David E. Gordon[1,2,3,4]*, Joseph Hiatt[1,4,5,6,7]*, Mehdi Bouhaddou[1,2,3,4]*, Veronica V. Rezelj[8]*, Svenja Ulferts[9]*, Hannes Braberg[1,2,3,4]*, Alexander S. Jureka[10]*, Kirsten Obernier[1,2,3,4]*, Jeffrey Z. Guo[1,2,3,4]*, Jyoti Batra[1,2,3,4]*, Robyn M. Kaake[1,2,3,4]*, Andrew R. Weckstein[11]*, Tristan W. Owens[12]*, Meghna Gupta[12]*, Sergei Pourmal[12]*, Erron W. Titus[12]*, Merve Cakir[1,2,3,4]*, Margaret Soucheray[1,2,3,4], Michael McGregor[1,2,3,4], Zeynep Cakir[1,2,3,4], Gwendolyn Jang[1,2,3,4], Matthew J. O'Meara[13], Tia A. Tummino[1,2,14], Ziyang Zhang[1,2,3,15], Helene Foussard[1,2,3,4], Ajda Rojc[1,2,3,4], Yuan Zhou[1,2,3,4], Dmitry Kuchenov[1,2,3,4], Ruth Hüttenhain[1,2,3,4], Jiewei Xu[1,2,3,4], Manon Eckhardt[1,2,3,4], Danielle L. Swaney[1,2,3,4], Jacqueline M. Fabius[1,2], Manisha Ummadi[1,2,3,4], Beril Tutuncuoglu[1,2,3,4], Ujjwal Rathore[1,2,3,4], Maya Modak[1,2,3,4], Paige Haas[1,2,3,4], Kelsey M. Haas[1,2,3,4], Zun Zar Chi Naing[1,2,3,4], Ernst H. Pulido[1,2,3,4], Ying Shi[1,2,3,15], Inigo Barrio-Hernandez[16], Danish Memon[16], Eirini Petsalaki[16], Alistair Dunham[16], Miguel Correa Marrero[16], David Burke[16], Cassandra Koh[8], Thomas Vallet[8], Jesus A. Silvas[10], Caleigh M. Azumaya[12], Christian Billesbølle[12], Axel F. Brilot[12], Melody G. Campbell[12,17], Amy Diallo[12], Miles Sasha Dickinson[12], Devan Diwanji[12], Nadia Herrera[12], Nick Hoppe[12], Huong T. Kratochvil[12], Yanxin Liu[12], Gregory E. Merz[12], Michelle Moritz[12], Henry C. Nguyen[12], Carlos Nowotny[12], Cristina Puchades[12], Alexandrea N. Rizo[12], Ursula Schulze-Gahmen[12], Amber M. Smith[12], Ming Sun[12,18], Iris D. Young[12], Jianhua Zhao[12], Daniel Asarnow[12], Justin Biel[12], Alisa Bowen[12], Julian R. Braxton[12], Jen Chen[12], Cynthia M. Chio[12], Un Seng Chio[12], Ishan Deshpande[12], Loan Doan[12], Bryan Faust[12], Sebastian Flores[12], Mingliang Jin[12], Kate Kim[12], Victor L. Lam[12], Fei Li[12], Junrui Li[12], Yen-Li Li[12], Yang Li[12], Xi Liu[12], Megan Lo[12], Kyle E. Lopez[12], Arthur A. Melo[12], Frank R. Moss III[12], Phuong Nguyen[12], Joana Paulino[12], Komal Ishwar Pawar[12], Jessica K. Peters[12], Thomas H. Pospiech Jr.[12], Maliheh Safari[12], Smriti Sangwan[12], Kaitlin Schaefer[12], Paul V. Thomas[12], Aye C. Thwin[12], Raphael Trenker[12], Eric Tse[12], Tsz Kin Martin Tsui[12], Feng Wang[12], Natalie Whitis[12], Zanlin Yu[12], Kaihua Zhang[12], Yang Zhang[12], Fengbo Zhou[12], Daniel Saltzberg[1,2,19], QCRG Structural Biology Consortium[12]†, Anthony J. Hodder[20], Amber S. Shun-Shion[20], Daniel M. Williams[20], Kris M. White[21,22], Romel Rosales[21,22], Thomas Kehrer[21,22], Lisa Miorin[21,22], Elena Moreno[21,22], Arvind H. Patel[23], Suzannah Rihn[23], Mir M. Khalid[4], Albert Vallejo-Gracia[4], Parinaz Fozouni[4,5,7], Camille R. Simoneau[4,7], Theodore L. Roth[5,6,7], David Wu[5,7], Mohd Anisul Karim[24,25], Maya Ghoussaini[24,25], Ian Dunham[16,25], Francesco Berardi[26], Sebastian Weigang[27], Maxime Chazal[28], Jisoo Park[29], James Logue[30], Marisa McGrath[30], Stuart Weston[30], Robert Haupt[30], C. James Hastie[31], Matthew Elliott[31], Fiona Brown[31], Kerry A. Burness[31], Elaine Reid[31], Mark Dorward[31], Clare Johnson[31], Stuart G. Wilkinson[31], Anna Geyer[31], Daniel M. Giesel[31], Carla Baillie[31], Samantha Raggett[31], Hannah Leech[31], Rachel Toth[31], Nicola Goodman[31], Kathleen C. Keough[4], Abigail L. Lind[4], Zoonomia Consortium‡, Reyna J. Klesh[32], Kafi R. Hemphill[33], Jared Carlson-Stevermer[34], Jennifer Oki[34], Kevin Holden[34], Travis Maures[34], Katherine S. Pollard[4,35,36], Andrej Sali[1,2,14,19], David A. Agard[1,2,12,37], Yifan Cheng[1,2,12,15,37], James S. Fraser[1,2,12,19], Adam Frost[1,2,12,37], Natalia Jura[1,2,3,12,38], Tanja Kortemme[1,2,12,19,39], Aashish Manglik[1,2,12,14], Daniel R. Southworth[1,12,37], Robert M. Stroud[1,2,12,37], Dario R. Alessi[31], Paul Davies[31], Matthew B. Frieman[30], Trey Ideker[29,40], Carmen Abate[26], Nolwenn Jouvenet[27,28], Georg Kochs[27], Brian Shoichet[1,2,14], Melanie Ott[4,41], Massimo Palmarini[23], Kevan M. Shokat[1,2,3,15], Adolfo García-Sastre[21,22,42,43]§, Jeremy A. Rassen[11]§, Robert Grosse[9,44]§, Oren S. Rosenberg[1,2,12,36,37,41]§, Kliment A. Verba[1,2,12,14]§, Christopher F. Basler[10]§, Marco Vignuzzi[8]§, Andrew A. Peden[20]§, Pedro Beltrao[16]§, Nevan J. Krogan[1,2,3,4,21]§

The COVID-19 pandemic, caused by severe acute respiratory syndrome coronavirus 2 (SARS-CoV-2), is a grave threat to public health and the global economy. SARS-CoV-2 is closely related to the more lethal but less transmissible coronaviruses SARS-CoV-1 and Middle East respiratory syndrome coronavirus (MERS-CoV). Here, we have carried out comparative viral-human protein-protein interaction and viral protein localization analyses for all three viruses. Subsequent functional genetic screening identified host factors that functionally impinge on coronavirus proliferation, including Tom70, a mitochondrial chaperone protein that interacts with both SARS-CoV-1 and SARS-CoV-2 ORF9b, an interaction we structurally characterized using cryo–electron microscopy. Combining genetically validated host factors with both COVID-19 patient genetic data and medical billing records identified molecular mechanisms and potential drug treatments that merit further molecular and clinical study.

[1]Quantitative Biosciences Institute (QBI) COVID-19 Research Group (QCRG), San Francisco, CA 94158, USA. [2]QBI, University of California, San Francisco, CA 94158, USA. [3]Department of Cellular and Molecular Pharmacology, University of California, San Francisco, CA 94158, USA. [4]J. David Gladstone Institutes, San Francisco, CA 94158, USA. [5]Medical Scientist Training Program, University of California, San Francisco, CA 94143, USA. [6]Department of Microbiology and Immunology, University of California, San Francisco, CA 94143, USA. [7]Biomedical Sciences Graduate Program, University of California, San Francisco, CA 94143, USA. [8]Viral Populations and Pathogenesis Unit, CNRS UMR 3569, Institut Pasteur, 75724, Paris, cedex 15, France. [9]Institute for Clinical and Experimental Pharmacology and Toxicology I, University of Freiburg, 79104 Freiburg, Germany. [10]Center for Microbial Pathogenesis, Institute for Biomedical Sciences, Georgia State University, Atlanta, GA 30303, USA. [11]Aetion, Inc., New York, NY 10001, USA. [12]QBI Coronavirus Research Group Structural Biology Consortium, University of California, San Francisco, CA 94158, USA. [13]Department of Computational Medicine and Bioinformatics, University of Michigan, Ann Arbor, MI 48109, USA. [14]Department of Pharmaceutical Chemistry, University of California, San Francisco, CA 94158, USA. [15]Howard Hughes Medical Institute, San Francisco, CA 94158, USA. [16]European Molecular Biology Laboratory, European Bioinformatics Institute (EMBL-EBI), Wellcome Genome Campus, Hinxton, Cambridgeshire CB10 1SD, UK. [17]Division of Basic Sciences, Fred Hutchinson Cancer Research Center, Seattle, WA 98109, USA. [18]Beam Therapeutics, Cambridge, MA 02139, USA. [19]Department of Bioengineering and Therapeutic Sciences, University of California, San Francisco, CA 94158, USA. [20]Department of Biomedical Science, Centre for Membrane Interactions and Dynamics, University of Sheffield, Firth Court, Sheffield S10 2TN, UK. [21]Department of Microbiology, Icahn School of Medicine at Mount Sinai, New York, NY 10029, USA. [22]Global Health and Emerging Pathogens Institute, Icahn School of Medicine at Mount Sinai, New York, NY 10029, USA. [23]MRC–University of Glasgow Centre for Virus Research, Glasgow G61 1QH, Scotland, UK. [24]Wellcome Trust Sanger Institute, Wellcome Genome Campus, Hinxton, Cambridgeshire CB10 1SA, UK. [25]Open Targets, Wellcome Genome Campus, Hinxton, Cambridgeshire CB10 1SD, UK. [26]Dipartimento di Farmacia-Scienze del Farmaco, Università degli Studi di Bari 'ALDO MORO', Via Orabona, 4 70125, Bari, Italy. [27]Institute of Virology, Medical Center–University of Freiburg, 79104 Freiburg, Germany. [28]Département de Virologie, CNRS UMR 3569, Institut Pasteur, Paris 75015, France. [29]Department of Medicine, University of California, San Diego, CA 92093, USA. [30]Department of Microbiology and Immunology, University of Maryland School of Medicine, Baltimore, MD 21201, USA. [31]MRC Protein Phosphorylation and Ubiquitylation Unit, College of Life Sciences, University of Dundee, Dundee DD1 5EH, UK. [32]HealthVerity, Philadelphia, PA 19103, USA. [33]Department of Neurology, University of California, San Francisco, CA 94143, USA. [34]Synthego Corporation, Redwood City, CA 94063, USA. [35]Department of Epidemiology & Biostatistics, University of California, San Francisco, CA 94158, USA. [36]Chan-Zuckerberg Biohub, San Francisco, CA 94158, USA. [37]Department of Biochemistry and Biophysics, University of California, San Francisco, CA 94158, USA. [38]Cardiovascular Research Institute, University of California, San Francisco, CA 94158, USA. [39]The University of California, Berkeley–University of California, San Francisco Graduate Program in Bioengineering, University of California, San Francisco, CA 94158, USA. [40]Department to Bioengineering, University of California, San Diego, CA 92093, USA. [41]Department of Medicine, University of California, San Francisco, CA 94143, USA. [42]Department of Medicine, Division of Infectious Diseases, Icahn School of Medicine at Mount Sinai, New York, NY 10029, USA. [43]The Tisch Cancer Institute, Icahn School of Medicine at Mount Sinai, New York, NY 10029, USA. [44]Centre for Integrative Biological Signaling Studies (CIBSS), University of Freiburg, 79104 Freiburg, Germany.

*These authors contributed equally to this work.

†The QCRG Structural Biology Consortium collaborators and their affiliations are listed in the supplementary materials.

‡The Zoonomia Consortium collaborators and their affiliations are listed in the supplementary materials.

§Corresponding author. Email: nevan.krogan@ucsf.edu (N.J.K.); pbeltrao@ebi.ac.uk (P.B.); marco.vignuzzi@pasteur.fr (M.V.); cbasler@gsu.edu (C.F.B.); verba@msg.ucsf.edu (K.A.V.); oren.rosenberg@ucsf.edu (O.S.R.); a.peden@sheffield.ac.uk (A.A.P.); robert.grosse@pharmakol.uni-freiburg.de (R.G.); jeremy.rassen@aetion.com (J.A.R.); Adolfo.Garcia-Sastre@mssm.edu (A.G.-S.)

In the past two decades, three deadly human respiratory syndromes associated with coronavirus (CoV) infections have emerged: severe acute respiratory syndrome (SARS) in 2002, Middle East respiratory syndrome (MERS) in 2012, and COVID-19 in 2019. These three diseases are caused by the zoonotic coronaviruses severe acute respiratory syndrome coronavirus 1 (SARS-CoV-1), Middle East respiratory syndrome coronavirus (MERS-CoV), and SARS-CoV-2 (*1*), respectively. Before their emergence, human coronaviruses were associated with usually mild respiratory illness. To date, SARS-CoV-2 has sickened millions and killed more than 1 million people worldwide. This unprecedented challenge has prompted widespread efforts to develop vaccine and antiviral strategies, including repurposed therapeutics, which offer the potential for treatments with known safety profiles and short development timelines. The successful repurposing of the antiviral nucleoside analog Remdesivir (*2*) as well as the host-directed anti-inflammatory steroid dexamethasone (*3*) provide clear proof that existing compounds can be crucial tools in the fight against COVID-19. Despite these promising examples, there is still no curative treatment for COVID-19. Additionally, as with any virus, the search for effective antiviral strategies could be complicated over time by the continued evolution of SARS-CoV-2 and possible resulting drug resistance (*4*).

Current endeavors are appropriately focused on SARS-CoV-2 because of the severity and urgency of the ongoing pandemic. However, the frequency with which highly virulent coronavirus strains have emerged highlights an additional need to identify promising targets for broad coronavirus inhibitors with high barriers to resistance mutations and the potential for rapid deployment against future emerging strains. Although traditional antivirals target viral enzymes that are often subject to mutation and thus the development of drug resistance, targeting the host proteins required for viral replication is a strategy that can avoid resistance and lead to therapeutics with the potential for broad-spectrum activity because families of viruses often exploit common cellular pathways and processes.

Here, we identified shared biology and potential drug targets among the three highly pathogenic human coronavirus strains. We expanded on our recently published map of virus-host protein interactions for SARS-CoV-2 (*5*) and mapped the full interactomes of SARS-CoV-1 and MERS-CoV. We investigated the localization of viral proteins across strains and quantitatively compared the virus-human interactions for each virus. Using functional genetics and structural analysis of selected host-dependency factors, we identified drug targets and performed real-world analysis on clinical data from COVID-19 patients.

A cross-coronavirus study of protein function

A central goal of this study is to understand, from a systems level, the conservation of target proteins and cellular processes between SARS-CoV-2, SARS-CoV-1, and MERS-CoV, thereby identifying shared vulnerabilities that can be targeted with antiviral therapeutics. All three strains encode four homologous structural proteins (E, M, N, and S) and 16 nonstructural proteins (Nsps). The latter are proteolytically cleaved from a polyprotein precursor that is expressed from one large open reading frame (ORF), ORF1ab (Fig. 1A). Additionally, coronaviruses contain a variable number of accessory factors encoded by ORFs. Although the genome organization and sequence of ORF1ab is mainly conserved between the three viruses under study, it diverges markedly in the region encoding the accessory factors, especially between MERS-CoV and the two SARS coronaviruses (Fig. 1, A to D, and table S1). These differences in conservation of genes and genome organization are linked to differences in host-targeting systems that we have studied through large-scale protein localization and interaction profiling (Fig. 1E). Building on our earlier work on the interactome of SARS-CoV-2 (*5*), we identified the host factors physically interacting with each SARS-CoV-1 and MERS-CoV viral protein. To this end, structural proteins, mature Nsps, and predicted ORF proteins were codon optimized, 2xStrep tagged, and cloned into a mammalian expression vector (figs. S1 and S2; see below and Materials and methods section). Each protein construct was transfected into HEK293T cells and affinity purified, and high-confidence interactors were identified by mass spectrometry (MS) and scored using SAINTexpress (significance analysis of interactome) and MiST (mass spectrometry interaction statistics) scoring algorithms (*6*, *7*) (table S2 and figs. S3 to S6). Additionally, we performed MS analysis on SARS-CoV-2 Nsp16, which was not analyzed in our earlier work (*5*) (table S2 and fig. S7). In all, we now report 389 high-confidence interactors for SARS-CoV-2, 366 interactors for SARS-CoV-1, and 296 interactors for MERS-CoV (table S2).

Conserved coronavirus proteins often retain the same cellular localization

As protein localization can provide important information regarding function, we assessed the cellular localization of individually expressed coronavirus proteins in addition to mapping their interactions (Fig. 2A and Materials and methods). Immunofluorescence localization analysis of all 2xStrep-tagged SARS-CoV-2, SARS-CoV-1, and MERS-CoV proteins highlights similar patterns of localization for most shared protein homologs in HeLaM cells (Fig. 2B), which supports the hypothesis that conserved proteins share functional similarities. A notable exception is Nsp13, which appears to localize to the cytoplasm for SARS-CoV-2 and SARS-CoV-1, but to the mitochondria for MERS-CoV (Fig. 2B, figs. S8 to S13, and table S3). To assess the localization of SARS-CoV-2 proteins in the context of infected cells, we raised antibodies against 20 SARS-CoV-2 proteins and validated them with the individually expressed 2xStrep-tagged proteins (fig. S14). Using the 14 antibodies with confirmed specificity, we observed that localization of viral proteins in infected Caco-2 cells sometimes differed from their localization when expressed individually (Fig. 2B, fig. S15, and table S3). This likely results from recruitment of viral proteins and complexes into replication compartments, as well as from remodeling of the secretory pathway during viral infection. Such differences could also result from mislocalization caused by protein tagging. For example, the localization of expressed ORF7B does not match the known SARS-CoV-1 Golgi localization seen in the infection state. For proteins such as Nsp1 and ORF3a, which are not known to be involved in viral replication, their localization is consistent both when expressed individually and in the context of viral infection (Fig. 2, C and D). We have compared the localization of the expressed viral proteins with the localization of their interaction partners using a cellular compartment gene ontology (GO) enrichment analysis (fig. S16). Several examples exist where the localization of the viral protein is in agreement with the localization of the interaction partners, including enrichment of the nuclear pore for Nsp9 interactors and endoplasmic reticulum (ER) enrichment for interactions with ORF8.

Our localization studies suggest that most orthologous proteins have the same localization across the viruses (Fig. 2B). Moreover, small changes in localization, as observed for some viral proteins across strains, do not coincide with strong changes in virus-host protein interactions (Fig. 2E). Overall, these results suggest that changes in protein localization, as measured by expressed, tagged proteins, are not common and therefore are unlikely to be a major source of differences in host-targeting mechanisms.

Comparison of host-targeted processes identifies conserved mechanisms with divergent implementations

To study the conservation of targeted host factors and processes, we first used a clustering approach (Materials and methods) to compare the overlap in protein interactions for the three viruses (Fig. 3A). We defined seven clusters of virus-host interactions corresponding to those that are specific to each virus or are shared among sets of viruses. The largest pairwise overlap was observed between SARS-CoV-1

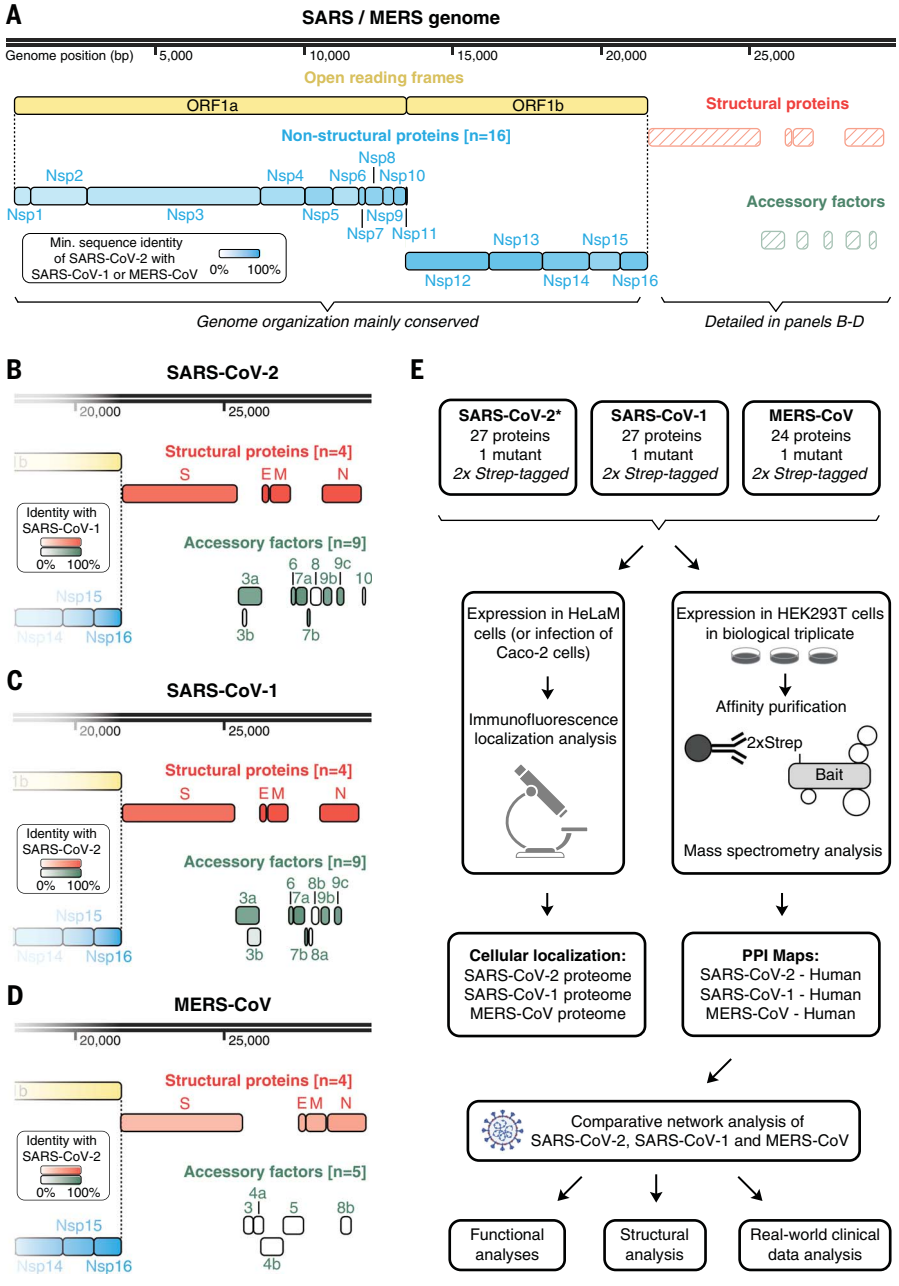

Fig. 1. Coronavirus genome annotations and integrative analysis overview. (**A**) Genome annotation of SARS-CoV-2, SARS-CoV-1, and MERS-CoV with putative protein coding genes highlighted. Intensity of filled color indicates the lowest sequence identity between SARS-CoV-2 and SARS-CoV-1 or between SARS-CoV-2 and MERS. (**B** to **D**) Genome annotation of structural protein genes for SARS-CoV-2 (B), SARS-CoV-1 (C), and MERS-CoV (D). Color intensity indicates sequence identity to specified virus. (**E**) Overview of comparative coronavirus analysis. Proteins from SARS-CoV-2, SARS-CoV-1, and MERS-CoV were analyzed for their protein interactions and subcellular localization, and these data were integrated for comparative host interaction network analysis, followed by functional, structural, and clinical data analyses for exemplary virus-specific and pan-viral interactions. The asterisk indicates that the SARS-CoV-2 interactome was previously published in a separate study (5). SARS, both SARS-CoV-1 and SARS-CoV-2; MERS, MERS-CoV; Nsp, nonstructural protein; ORF, open reading frame.

and SARS-CoV-2 (Fig. 3A), as is expected from their closer evolutionary relationship. A functional enrichment analysis (Fig. 3B and table S4) highlighted host processes that are targeted through interactions conserved across all three viruses, including ribosome biogenesis and regulation of RNA metabolism. Conserved interactions between SARS-CoV-1 and SARS-CoV-2—but not MERS-CoV—were enriched in endosomal and Golgi vesicle transport (Fig. 3B). Despite the small fraction (7.1%) of interactions conserved between SARS-CoV-1 and MERS-CoV—but not SARS-CoV-2—these were strongly enriched in translation initiation and myosin complex proteins (Fig. 3B).

We next asked whether the conserved interactions were specific for certain viral proteins (Fig. 3C) and found that some proteins (M, N, Nsp7, Nsp8, and Nsp13) showed a disproportionately high fraction of shared interactions conserved across the three viruses. This suggests that the processes targeted by these proteins may be more essential and more likely to be required for other emerging coronaviruses. Such differences in conservation of interactions should be encoded, to some extent, in the degree of sequence differences. Comparing pairs of homologous proteins shared between SARS-CoV-2 and SARS-CoV-1 or MERS-CoV, we observed a significant correlation between sequence conservation and protein-protein interaction (PPI) similarity (calculated as Jaccard index) [Fig. 3D; correlation coefficient (r) = 0.58, P = 0.0001]. This shows that the evolution of protein sequences strongly determines the divergence in virus-host interactions.

While studying the function of host proteins interacting with each virus, we noted that some shared cellular processes were targeted by different interactions across the viruses. To study this in more detail, we identified the cellular processes significantly enriched in the interactomes of all three viruses (fig. S17A and table S4) and ranked them by the degree of overlapping proteins (Fig. 3E). This identified proteins related to the nuclear envelope, proteasomal catabolism, cellular response to heat, and regulation of intracellular protein transport as biological functions that are hijacked by these viruses through different human proteins. Additionally, we found that up to 51% of protein interactions with a conserved human target occurred via a different (nonorthologous) viral protein (Fig. 3F), and, in some cases, the overlap of interactions for two nonorthologous virus baits was greater than that for the orthologous pair (Fig. 3G and fig. S17, B and C). For example, several interacting proteins of SARS-CoV-2 Nsp8 are also targeted by MERS-CoV ORF4a, and interactions of MERS-CoV ORF5 share interactors with SARS-CoV-2 ORF3a (Fig. 3G). In the case of Nsp8, we found some degree of structural homology between its C-terminal region and a predicted structural model of ORF4a (Materials and methods and fig. S17D), which is indicative of a possible common interaction mechanism.

We find that sequence differences determine the degree of changes in virus-host interactions and that often the same cellular process can be targeted by different viral or host proteins. These results suggest a degree of plasticity in

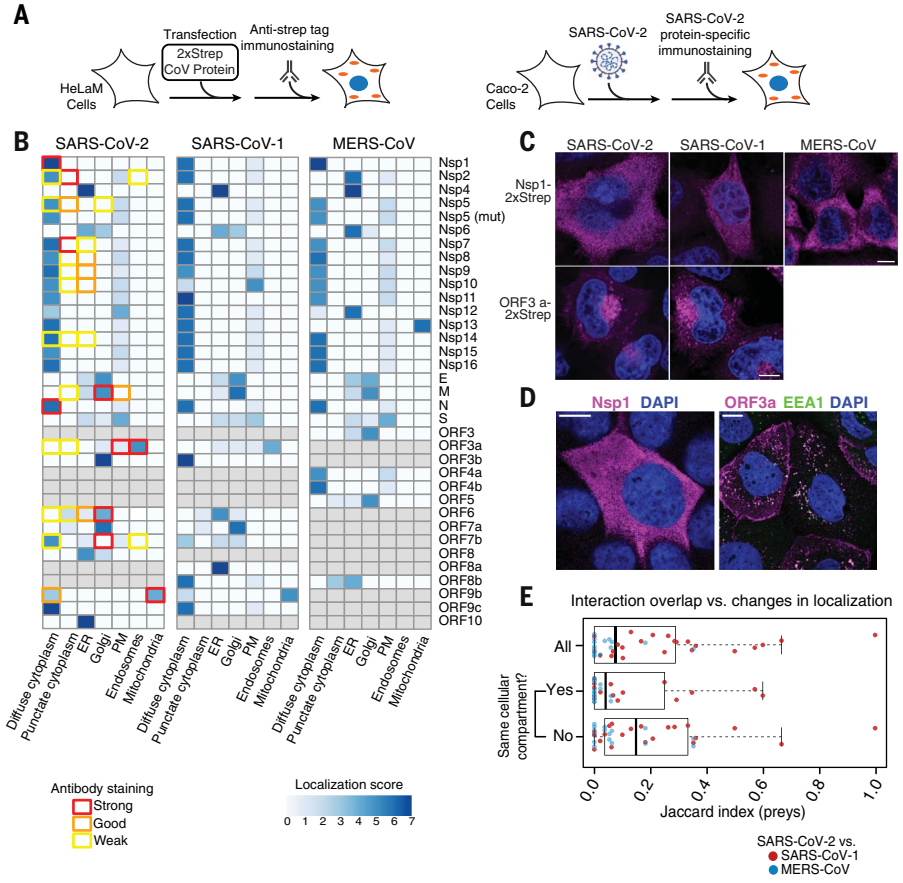

Fig. 2. Coronavirus protein localization analysis. (**A**) Overview of experimental design to determine localization of Strep-tagged SARS-CoV-2, SARS-CoV-1, and MERS-CoV proteins in HeLaM cells (left) or of viral proteins upon SARS-CoV-2 infection in Caco-2 cells (right). (**B**) Relative localization for all coronavirus proteins across viruses expressed individually (blue color bar) or in SARS-CoV-2–infected cells (colored box outlines). (**C** and **D**) Localization of Nsp1 and ORF3a expressed individually (C) or during infection (D); for representative images of all tagged constructs and viral proteins imaged during infection, see figs. S8 to S14 and fig. S15, respectively. Scale bars, 10 μm. (**E**) Prey overlap per bait measured as Jaccard index comparing SARS-CoV-2 versus SARS-CoV-1 (red dots) and SARS-CoV-2 versus MERS-CoV (blue dots) for all viral baits (all), viral baits found in the same cellular compartment (yes), and viral baits found in different compartments (no).

the way that these viruses can control a given biological process in the host cell.

Quantitative differential interaction scoring identifies interactions conserved between coronaviruses

The identification of virus-host interactions conserved across pathogenic coronaviruses provides the opportunity to reveal host targets that may remain essential for these and other emerging coronaviruses. For a quantitative comparison of each virus-human interaction from viral baits shared by all three viruses, we developed a differential interaction score (DIS). A DIS is calculated between any pair of viruses and is defined as the difference between the interaction scores (K) from each virus (Fig. 4A, table S5, and Materials and methods). This kind of comparative analysis is beneficial as it permits the recovery of conserved interactions that may fall just below strict cutoffs. For each comparison, a DIS was calculated for interactions residing in certain clusters as defined in the previous analysis (see Fig. 3A). For example, for the SARS-CoV-2 to MERS-CoV comparison, a DIS was computed for interactions residing in all clusters except cluster 3, where interactions are either not found or scores were very low for both SARS-CoV-2 and MERS-CoV. A DIS of 0 indicates that the interaction is confidently shared between the two viruses being compared, whereas a DIS of +1 or −1 indicates that the host-protein interaction is specific for the virus listed first or second, respectively.

In agreement with our previous results (Fig. 3A), DIS values for the comparison between SARS-CoV-2 and SARS-CoV-1 are enriched near zero, which indicates a high number of shared interactions (Fig. 4B, yellow). By contrast, comparing interactions from either SARS-CoV-1 or SARS-CoV-2 with MERS-CoV resulted in DIS values closer to ±1, which indicates a higher divergence (Fig. 4B, blue and green). The breakdown of DISs by homologous viral proteins reveals a high similarity of interactions for proteins N, Nsp8, Nsp7, and Nsp13 (Fig. 4C), reinforcing the observations made by overlapping thresholded interactions (Fig. 3, C and D). As the greatest dissimilarity was observed between the SARS coronaviruses and MERS-CoV, we computed a fourth DIS (SARS-MERS) by averaging K from SARS-CoV-1 and SARS-CoV-2 before calculating the difference with MERS-CoV (Fig. 4, B and C, purple). We next created a network visualization of the SARS-MERS comparison (Fig. 4D), permitting an appreciation of SARS-specific (red; DIS near +1) versus MERS-specific (blue; DIS near −1) interactions as well as those conserved between all three coronavirus species (black; DIS near 0). SARS-specific interactions include DNA polymerase α interacting with Nsp1, stress granule regulators interacting with N protein, TLE transcription factors interacting with Nsp13, and AP2 clathrin interacting with Nsp10. Notable MERS-CoV–specific interactions include mammalian target of rapamycin (mTOR) and Stat3 interacting with Nsp1; DNA damage response components p53 (*TP53*), MRE11, RAD50, and UBR5 interacting with Nsp14; and the activating signal cointegrator 1 (ASC-1) complex interacting with Nsp2. Interactions shared between all three coronaviruses include casein kinase II and RNA processing regulators interacting with N protein; inosine 5′-monophosphate (IMP) dehydrogenase 2 (*IMPDH2*) interacting with Nsp14; centrosome, protein kinase A, and TBK1 interacting with Nsp13; and the signal recognition particle, 7SK small nuclear ribonucleoprotein (snRNP), exosome, and ribosome biogenesis components interacting with Nsp8 (Fig. 4D).

Cell-based genetic screens identify SARS-CoV-2 host-dependency factors

To identify host factors that are critical for infection and therefore potential targets for host-directed therapies, we performed genetic perturbations of 332 human proteins—331 previously identified to interact with SARS-CoV-2 proteins (*5*) plus ACE2—and observed their effect on infectivity. To ensure a broad coverage of potential hits, we carried out two screens in different cell lines, investigating the effects on infection: small interfering RNA (siRNA) knockdowns in A549 cells stably expressing ACE2 (A549-ACE2) (Fig. 5A) and CRISPR-based knockouts in Caco-2 cells (Fig. 5B). ACE2 was included as positive control in both screens as were nontargeting siRNAs or nontargeted Caco-2 cells as negative controls. After SARS-CoV-2 infection, effects on virus infectivity were quantified by real-time quantitative

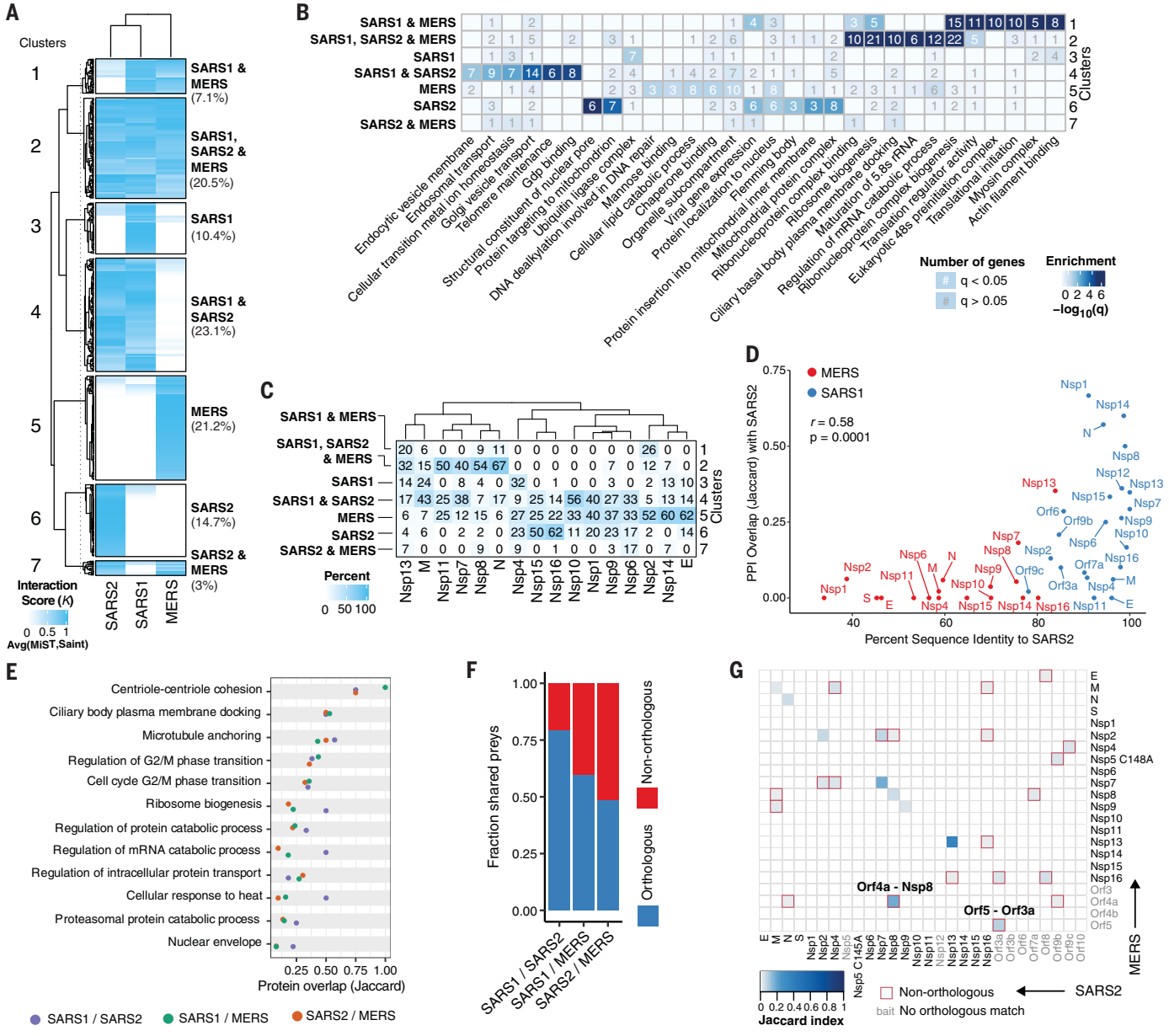

Fig. 3. Comparative analysis of coronavirus-host interactomes. (**A**) Clustering analysis (*K*-means) of interactors from SARS-CoV-2, SARS-CoV-1, and MERS-CoV, weighted according to the average between their MiST and SAINT scores (interaction score *K*). Included are only viral protein baits represented amongst all three viruses and interactions that pass the high-confidence scoring threshold for at least one virus. Seven clusters highlight all possible scenarios of shared versus individual interactions, and percentages of total interactions are noted. (**B**) GO enrichment analysis of each cluster from (A), with the top six most-significant terms per cluster. Color indicates $-\log_{10}(q)$, and the number of genes with significant ($q < 0.05$; white) or nonsignificant enrichment ($q > 0.05$; gray) is shown. (**C**) Percentage of interactions for each viral protein belonging to each cluster identified in (A). (**D**) Correlation between protein sequence identity and PPI overlap (Jaccard index) comparing SARS-CoV-2 and SARS-CoV-1 (blue) or MERS-CoV (red). Interactions for PPI overlap are derived from the final thresholded list of interactions per virus. (**E**) GO biological process terms significantly enriched ($q < 0.05$) for all three virus PPIs with Jaccard index indicating overlap of genes from each term for pairwise comparisons between SARS-CoV-1 and SARS-CoV-2 (purple), SARS-CoV-1 and MERS-CoV (green), and SARS-CoV-2 and MERS-CoV (orange). (**F**) Fraction of shared preys between orthologous (blue) and nonorthologous (red) viral protein baits. (**G**) Heatmap depicting overlap in PPIs (Jaccard index) between each bait from SARS-CoV-2 and MERS-CoV. Baits in gray were not assessed, do not exist, or do not have high-confidence interactors in the compared virus. Nonorthologous bait interactions are highlighted with a red square. GO, gene ontology; PPI, protein-protein interaction; SARS2, SARS-CoV-2; SARS1, SARS-CoV-1; MERS, MERS-CoV.

polymerase chain reaction (RT-qPCR) on cell supernatants (siRNA) or by titrating virus-containing supernatants on Vero E6 cells (CRISPR) (see Materials and methods for details). Cells were monitored for viability, and knockdown or editing efficiency was determined as described (Materials and methods and fig. S18). This revealed that 93% of the genes were knocked down at least 50% in the A549-ACE2 screen, and 95% of the knockdowns exhibited a <20% decrease in viability. In the Caco-2 assay, we observed an editing efficiency of at least 80% for 89% of the genes tested (Materials and methods and fig. S18). Of the 332 human SARS-CoV-2 interactors, the

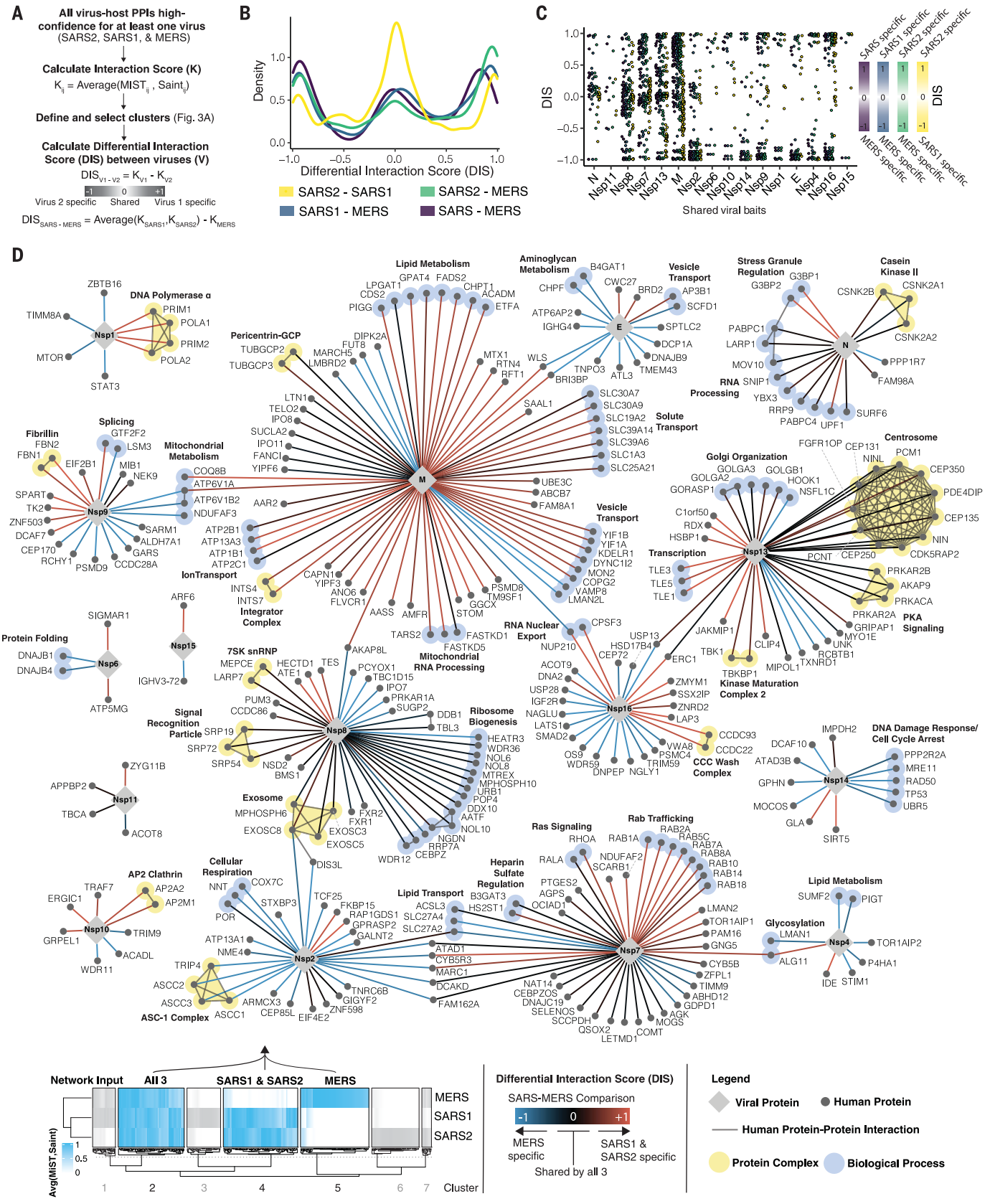
A
All virus-host PPIs high-confidence for at least one virus (SARS2, SARS1, & MERS)
Calculate Interaction Score (K)
K_{ij} = Average($MIST_{ij}$, $Saint_{ij}$)
Define and select clusters (Fig. 3A)
Calculate Differential Interaction Score (DIS) between viruses (V)
$DIS_{V1 - V2} = K_{V1} - K_{V2}$
-1 0 +1
Virus 2 specific Shared Virus 1 specific
$DIS_{SARS - MERS}$ = Average(K_{SARS1},K_{SARS2}) - K_{MERS}
B
Density
Differential Interaction Score (DIS)
SARS2 - SARS1
SARS2 - MERS
SARS1 - MERS
SARS - MERS
C
DIS
Shared viral baits
N Nsp11 Nsp8 Nsp7 Nsp13 M Nsp2 Nsp6 Nsp10 Nsp14 Nsp9 Nsp1 E Nsp4 Nsp16 Nsp15
SARS specific
SARS1 specific
SARS2 specific
SARS2 specific
MERS specific
MERS specific
MERS specific
SARS1 specific
DIS
D
Nsp1
ZBTB16
DNA Polymerase α
PRIM1
POLA1
PRIM2
POLA2
TIMM8A
MTOR
STAT3
Nsp9
Fibrillin
FBN2
FBN1
Splicing
GTF2F2
LSM3
EIF2B1
MIB1
NEK9
Mitochondrial Metabolism
COQ8B
ATP6V1A
ATP6V1B2
NDUFAF3
SPART
TK2
ZNF503
DCAF7
CEP170
RCHY1
PSMD9
CCDC28A
GARS
ALDH7A1
SARM1
Nsp6
Protein Folding
SIGMAR1
DNAJB1
DNAJB4
ATP5MG
Nsp15
ARF6
IGHV3-72
Nsp11
ZYG11B
APPBP2
TBCA
ACOT8
Nsp10
AP2 Clathrin
TRAF7
AP2A2
AP2M1
ERGIC1
GRPEL1
TRIM9
ACADL
WDR11
Nsp2
Cellular Respiration
NNT
COX7C
POR
STXBP3
ATP13A1
NME4
TRIP4
ASCC2
ASCC3
ASCC1
ASC-1 Complex
ARMCX3
CEP85L
EIF4E2
ZNF598
GIGYF2
TNRC6B
TCF25
FKBP15
RAP1GDS1
GPRASP2
GALNT2
DIS3L
Nsp8
Pericentrin-GCP
TUBGCP2
TUBGCP3
Lipid Metabolism
GPAT4
FADS2
LPGAT1
CDS2
CHPT1
ACADM
PIGG
ETFA
DIPK2A
FUT8
MARCH5
LMBRD2
MTX1
RTN4
RFT1
WLS
LTN1
TELO2
IPO8
SUCLA2
IPO11
FANCI
YIPF6
SAAL1
M
UBE3C
ABCB7
FAM8A1
AAR2
IonTransport
ATP2B1
ATP13A3
ATP1B1
ATP2C1
INTS4
INTS7
Integrator Complex
CAPN1
YIPF3
ANO6
FLVCR1
AASS
AMFR
STOM
GGCX
PSMD8
TM9SF1
Vesicle Transport
YIF1B
YIF1A
KDELR1
DYNC1I2
MON2
COPG2
VAMP8
LMAN2L
Aminoglycan Metabolism
B4GAT1
CHPF
CWC27
BRD2
ATP6AP2
IGHG4
E
TNPO3
ATL3
BRI3BP
TMEM43
DNAJB9
DCP1A
SPTLC2
Vesicle Transport
AP3B1
SCFD1
Solute Transport
SLC30A7
SLC30A9
SLC19A2
SLC39A14
SLC39A6
SLC1A3
SLC25A21
Stress Granule Regulation
G3BP1
G3BP2
Casein Kinase II
CSNK2B
CSNK2A1
CSNK2A2
PABPC1
LARP1
N
MOV10
SNIP1
PPP1R7
FAM98A
RNA Processing
YBX3
RRP9
PABPC4
UPF1
SURF6
Centrosome
FGFR1OP
CEP131
NINL
PCM1
CEP350
PDE4DIP
CEP135
NIN
CDK5RAP2
Golgi Organization
GOLGA3
GOLGB1
GOLGA2
HOOK1
GORASP1
NSFL1C
Nsp13
C1orf50
RDX
HSBP1
Transcription
TLE3
TLE5
TLE1
PCNT
CEP250
PRKAR2B
AKAP9
PRKACA
PRKAR2A
GRIPAP1
MYO1E
PKA Signaling
UNK
RCBTB1
TXNRD1
MIPOL1
TBKBP1
CLIP4
TBK1
JAKMIP1
Kinase Maturation Complex 2
RNA Nuclear Export
CPSF3
NUP210
USP13
HSD17B4
CEP72
ERC1
Nsp16
ACOT9
DNA2
USP28
IGF2R
NAGLU
LATS1
SMAD2
OS9
WDR59
DNPEP
NGLY1
ZMYM1
SSX2IP
ZNRD2
LAP3
CCDC93
CCDC22
VWA8
PSMC4
TRIM59
CCC Wash Complex
7SK snRNP
MEPCE
LARP7
HECTD1
ATE1
TES
AKAP8L
PCYOX1
TBC1D15
IPO7
PRKAR1A
SUGP2
DDB1
TBL3
Mitochondrial RNA Processing
TARS2
FASTKD1
FASTKD5
Signal Recognition Particle
SRP19
SRP72
SRP54
NSD2
BMS1
CCDC86
PUM3
Ribosome Biogenesis
HEATR3
WDR36
NOL6
NOL8
MTREX
MPHOSPH10
URB1
POP4
DDX10
AATF
NOL10
NGDN
RRP7A
CEBPZ
WDR12
Exosome
MPHOSPH6
EXOSC8
FXR2
FXR1
EXOSC3
EXOSC5
Nsp14
DNA Damage Response/ Cell Cycle Arrest
IMPDH2
DCAF10
ATAD3B
GPHN
MOCOS
GLA
SIRT5
PPP2R2A
MRE11
RAD50
TP53
UBR5
Nsp7
Ras Signaling
RHOA
RALA
Rab Trafficking
RAB2A
RAB1A
RAB5C
RAB7A
RAB8A
RAB10
RAB14
RAB18
NDUFAF2
SCARB1
Heparin Sulfate Regulation
PTGES2
AGPS
OCIAD1
B3GAT3
HS2ST1
Lipid Transport
ACSL3
SLC27A4
SLC27A2
ATAD1
CYB5R3
MARC1
DCAKD
FAM162A
LMAN2
TOR1AIP1
PAM16
GNG5
CYB5B
ZFPL1
TIMM9
ABHD12
GDPD1
AGK
MOGS
COMT
LETMD1
NAT14
CEBPZOS
DNAJC19
SELENOS
SCCPDH
QSOX2
Nsp4
Lipid Metabolism
SUMF2
PIGT
Glycosylation
LMAN1
ALG11
TOR1AIP2
P4HA1
IDE
STIM1
Network Input
All 3
SARS1 & SARS2
MERS
MERS
SARS1
SARS2
Avg(MIST,Saint)
1
0.5
0
1 2 3 4 5 6 7 Cluster
Differential Interaction Score (DIS)
SARS-MERS Comparison
-1 0 +1
MERS specific
SARS1 & SARS2 specific
Shared by all 3
Legend
Viral Protein
Human Protein
Human Protein-Protein Interaction
Protein Complex
Biological Process

Fig. 4. Comparative differential interaction analysis reveals shared virus-host interactions. (**A**) Flowchart depicting calculation of DIS values using the average between the SAINT and MiST scores between every bait (*i*) and prey (*j*) to derive interaction score (*K*). The DIS is the difference between the interaction scores from each virus. The modified DIS (SARS-MERS) compares the average *K* from SARS-CoV-1 and SARS-CoV-2 to that of MERS-CoV (see Materials and methods). Only viral bait proteins shared between all three viruses are included. (**B**) Density histogram of the DISs for all comparisons. (**C**) Dot plot depicting the DISs of interactions from viral bait proteins shared between all three viruses, ordered left to right by the mean DIS per viral bait. (**D**) Virus-human PPI map depicting the SARS-MERS comparison [purple in (B) and (C)]. The network depicts interactions derived from cluster 2 (all three viruses), cluster 4 (SARS-CoV-1 and SARS-CoV-2), and cluster 5 (MERS-CoV only). Edge color denotes DIS: red indicates interactions specific to SARS-CoV-1 and SARS-CoV-2 but absent in MERS-CoV; blue indicates interactions specific to MERS-CoV but absent from both SARS-CoV-1 and SARS-CoV-2; and black indicates interactions shared between all three viruses. Human-human interactions (thin dark gray line) and proteins sharing the same protein complexes or biological processes (light yellow or light blue highlighting, respectively) are shown. Host-host physical interactions, protein complex definitions, and biological process groupings are derived from CORUM (*46*), GO (biological process), and manually curated from literature sources. Thin dashed gray lines are used to indicate the placement of node labels when adjacent node labels would have otherwise been obscured. DIS, differential interaction score; SARS2, SARS-CoV-2; SARS1, SARS-CoV-1; MERS, MERS-CoV; SARS, both SARS-CoV-1 and SARS-CoV-2.

final A549-ACE2 dataset includes 331 gene knockdowns, and the Caco-2 dataset includes 286 gene knockouts, with the difference mainly owing to the removal of essential genes (Materials and methods). The readouts from both assays were then separately normalized using robust *z*-scores (Materials and methods), with negative and positive *z*-scores indicating proviral-dependency factors (perturbation leads to decreased infectivity) and antiviral host factors with restrictive activity (perturbation leads to increased infectivity), respectively. As expected, negative controls resulted in neutral *z*-scores (Fig. 5, C and D, and tables S6 and S7). Similarly, perturbations of the positive control ACE2 resulted in strongly negative *z*-scores in both assays (Fig. 5, C and D). Overall, the *z*-scores did not exhibit any trends related to viability, knockdown efficiency, or editing efficiency (fig. S18). With a cutoff of $|z| > 2$ to highlight genes that notably affect SARS-CoV-2 infectivity when perturbed, 31 and 40 dependency factors ($z < -2$) and 3 and 4 factors with restrictive activity ($z > 2$) were identified in A549-ACE2 and Caco-2 cells, respectively (Fig. 5E). Of particular interest are the host-dependency factors for SARS-CoV-2 infection, which represent potential targets for drug development and repurposing. For example, non-opioid receptor sigma 1 (sigma-1, encoded by *SIGMAR1*) was identified as a functional host-dependency factor in both cell systems, in agreement with our previous report of antiviral activity for sigma receptor ligands (*5*). To provide a contextual view of the genetics results, we generated a network that integrates the hits from both cell lines and the PPIs of their encoded proteins with SARS-CoV-2, SARS-CoV-1, and MERS-CoV proteins (Fig. 5F). Notably, we observed an enrichment of genetic hits that encode proteins interacting with viral Nsp7, which has a high degree of interactions shared across all three viruses (Fig. 3C). Prostaglandin E synthase 2 (PGES2, encoded by *PTGES2*), for example, is a functional interactor of Nsp7 from SARS-CoV-1, SARS-CoV-2, and MERS-CoV. Other dependency factors were specific to SARS-CoV-2, including interleukin-17 (IL-17) receptor A (*IL17RA*), which interacts with SARS-CoV-2 ORF8. We also identify dependency factors that are shared interactors between SARS-CoV-1 and SARS-CoV-2 such as the aforementioned sigma receptor 1 (*SIGMAR1*), which interacts with Nsp6, and the mitochondrial import receptor subunit Tom70 (*TOMM70*), which interacts with ORF9b. We will use these interactions to validate virus-host interactions (ORF8-IL17RA and ORF9b-Tom70), connect our systems biology data to evidence for the clinical impact of the host factors we identified (IL17RA), and analyze outcomes of COVID-19 patients treated with putative host-directed drugs against PGES-2 and sigma receptor 1.

SARS ORF9b interacts with Tom70

ORF9b of SARS-CoV-1 and SARS-CoV-2 were found to be localized to mitochondria upon overexpression as well as in SARS-CoV-2–infected cells. In line with this, the mitochondrial outer membrane protein Tom70 (encoded by *TOMM70*) is a high-confidence interactor of ORF9b in both SARS-CoV-1 and SARS-CoV-2 interaction maps (Fig. 6A), and it acts as a host-dependency factor for SARS-CoV-2 (Fig. 6B). Tom70 falls below the scoring threshold as a putative interactor of MERS-CoV Nsp2, a viral protein not associated with mitochondria (table S2). Tom70 is one of the major import receptors in the translocase of the outer membrane (TOM) complex that recognizes and mediates the translocation of mitochondrial preproteins from the cytosol into the mitochondria in a chaperone-dependent manner (*8*). Additionally, Tom70 is involved in the activation of the mitochondrial antiviral signaling (MAVS) protein, which leads to apoptosis upon viral infection (*9*, *10*).

To validate the interaction between viral proteins and Tom70, we performed a coimmunoprecipitation experiment in the presence or absence of Strep-tagged ORF9b from SARS-CoV-1 and SARS-CoV-2 as well as Strep-tagged Nsp2 from all three coronaviruses. Endogenous Tom70—but not other translocase proteins of the outer membrane including Tom20, Tom22, and Tom40—coprecipitated only in the presence of ORF9b but not Nsp2 in both HEK293T and A549 cells, which confirms our affinity purification–mass spectrometry (AP-MS) data and suggests that ORF9b specifically interacts with Tom70 (Fig. 6C and fig. S19A). Further, upon coexpression in bacterial cells, we were able to copurify the ORF9b-Tom70 protein complex, which indicates a stable complex (Fig. 6D). We found that SARS-CoV-1 and SARS-CoV-2 ORF9b expressed in HeLaM cells colocalized with Tom70 (Fig. 6E) and observed that SARS-CoV-1 or SARS-CoV-2 ORF9b overexpression led to decreases in Tom70 expression (Fig. 6, E and F). Similarly, ORF9b was found to colocalize with Tom70 on SARS-CoV-2 infection (Fig. 6G). This is in agreement with the known outer mitochondrial membrane localization of Tom70 (*11*) and ORF9b localization to mitochondria upon overexpression and during SARS-CoV-2 infection (Fig. 2B). We also saw decreases in Tom70 expression during SARS-CoV-2 infection (Fig. 6G) but did not see pronounced changes in expression levels of the mitochondrial protein Tom20 after individual Strep-ORF9b expression or upon SARS-CoV-2 infection (fig. S19, B and C).

Cryo–electron microscopy structure of ORF9b-Tom70 complex reveals ORF9b interacting at the substrate binding site of Tom70

Tom70, as part of the TOM complex, is involved in the recognition of mitochondrial preproteins from the cytosol (*12*). To further understand the molecular details of ORF9b-Tom70 interactions, we obtained a 3-Å cryo–electron microscopy (cryo-EM) structure of the ORF9b-Tom70 complex (Fig. 7A and fig. S20). Notably, although purified proteins failed to interact upon attempted in vitro complex reconstitution, they yielded a stable and pure complex when coexpressed in *Escherichia coli* (Fig. 6D). This may be because of the fact that ORF9b alone purifies as a dimer (as inferred by the apparent molecular weight on size-exclusion chromatography) and would need to dissociate to interact with Tom70 on the basis of our structure. Tom70 preferentially binds preproteins with internal hydrophobic targeting sequences (*13*). It contains an N-terminal transmembrane domain and tetratricopeptide

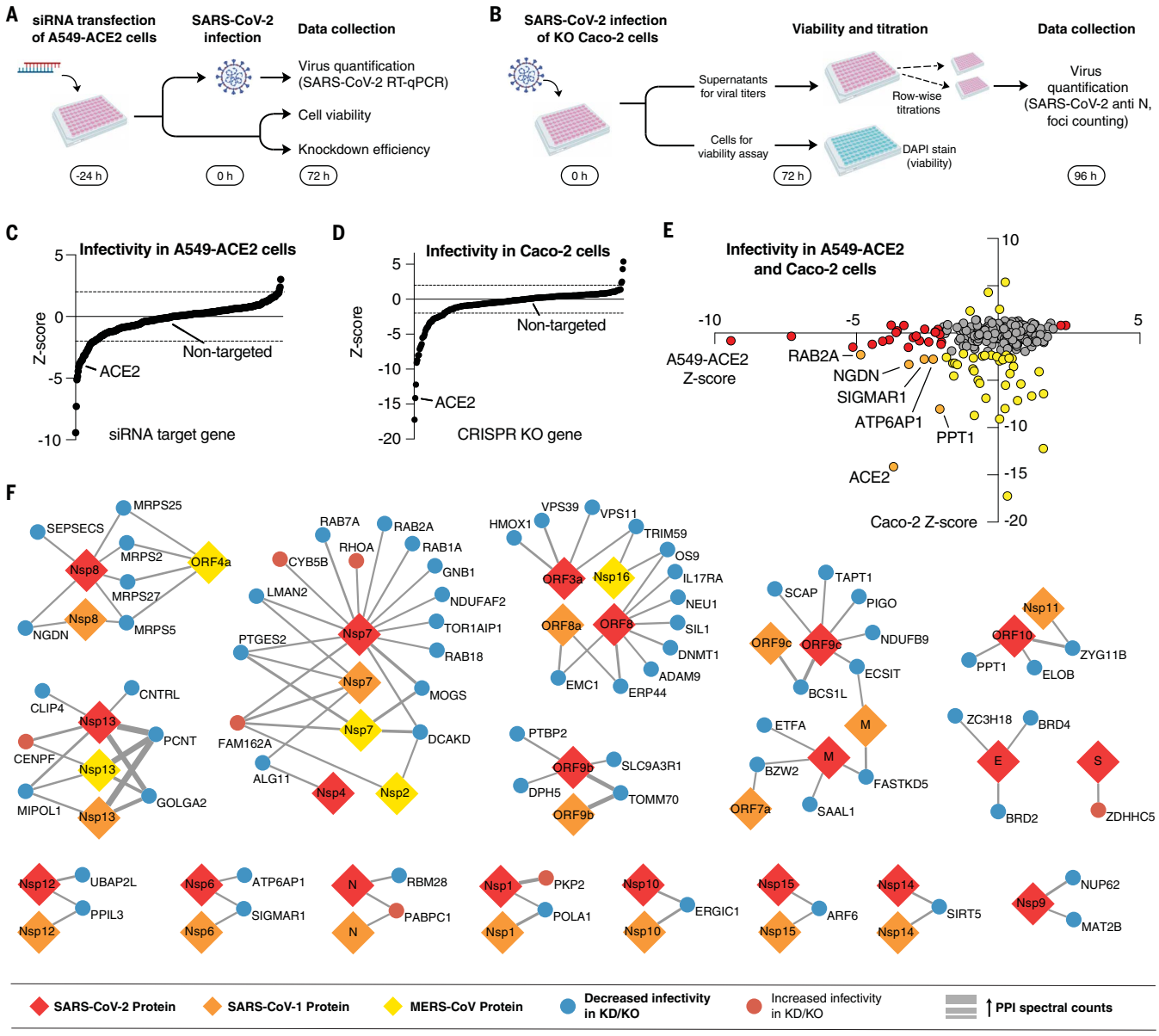

Fig. 5. Functional interrogation of SARS-CoV-2 interactors using genetic perturbations. (**A**) A549-ACE2 cells were transfected with siRNA pools targeting each of the human genes from the SARS-CoV-2 interactome, followed by infection with SARS-CoV-2 and virus quantification using RT-qPCR. Cell viability and knockdown efficiency in uninfected cells was determined in parallel. (**B**) Caco-2 cells with CRISPR knockouts (KO) of each human gene from the SARS-CoV-2 interactome were infected with SARS-CoV-2, and supernatants were serially diluted and plated onto Vero E6 cells for quantification. Viabilities of the uninfected CRISPR knockout cells after infection were determined in parallel by DAPI staining. (**C** and **D**) Plot of results from the infectivity screens in A549-ACE2 knockdown cells (C) and Caco-2 knockout cells (D) sorted by *z*-score ($z < 0$, decreased infectivity; $z > 0$ increased infectivity). Negative controls (nontargeting control for siRNA, nontargeted cells for CRISPR) and positive controls (ACE2 knockdown or knockout) are highlighted. (**E**) Results from both assays with potential hits ($|z| > 2$) highlighted in red (A549-ACE2), yellow (Caco-2), and orange (both). (**F**) Pan-coronavirus interactome reduced to human preys with significant increase (red nodes) or decrease (blue nodes) in SARS-CoV2 replication upon knockdown or knockout. Viral proteins baits from SARS-CoV-2 (red), SARS-CoV-1 (orange), and MERS-CoV (yellow) are represented as diamonds. The thickness of the edge indicates the strength of the PPI in spectral counts. KD, knockdown; KO, knockout; PPI, protein-protein interaction.

repeat (TPR) motifs in its cytosolic segment. The C-terminal TPR motifs recognize the internal mitochondrial targeting signals (MTSs) of preproteins, and the N-terminal TPR clamp domain serves as a docking site for multichaperone complexes that contain preprotein (*14*, *15*). Obtained cryo-EM density allowed us to build atomic models for residues 109 to 600 of human Tom70 and residues 39 to 76 of SARS-CoV-2 ORF9b (Fig. 7A and table S8). ORF9b makes extensive hydrophobic interactions at the pocket on Tom70 that have been implicated in its binding to MTS, with the total buried surface area at the interface being quite extensive—~2000 Å^2 (Fig. 7B). In addition to the mostly hydrophobic interface, four salt bridges further stabilize the interaction (Fig. 7C). On interaction with ORF9b, the interacting helices on Tom70 move inward to tightly wrap around ORF9b as compared with previously crystallized yeast Tom70 homologs (movie S1).

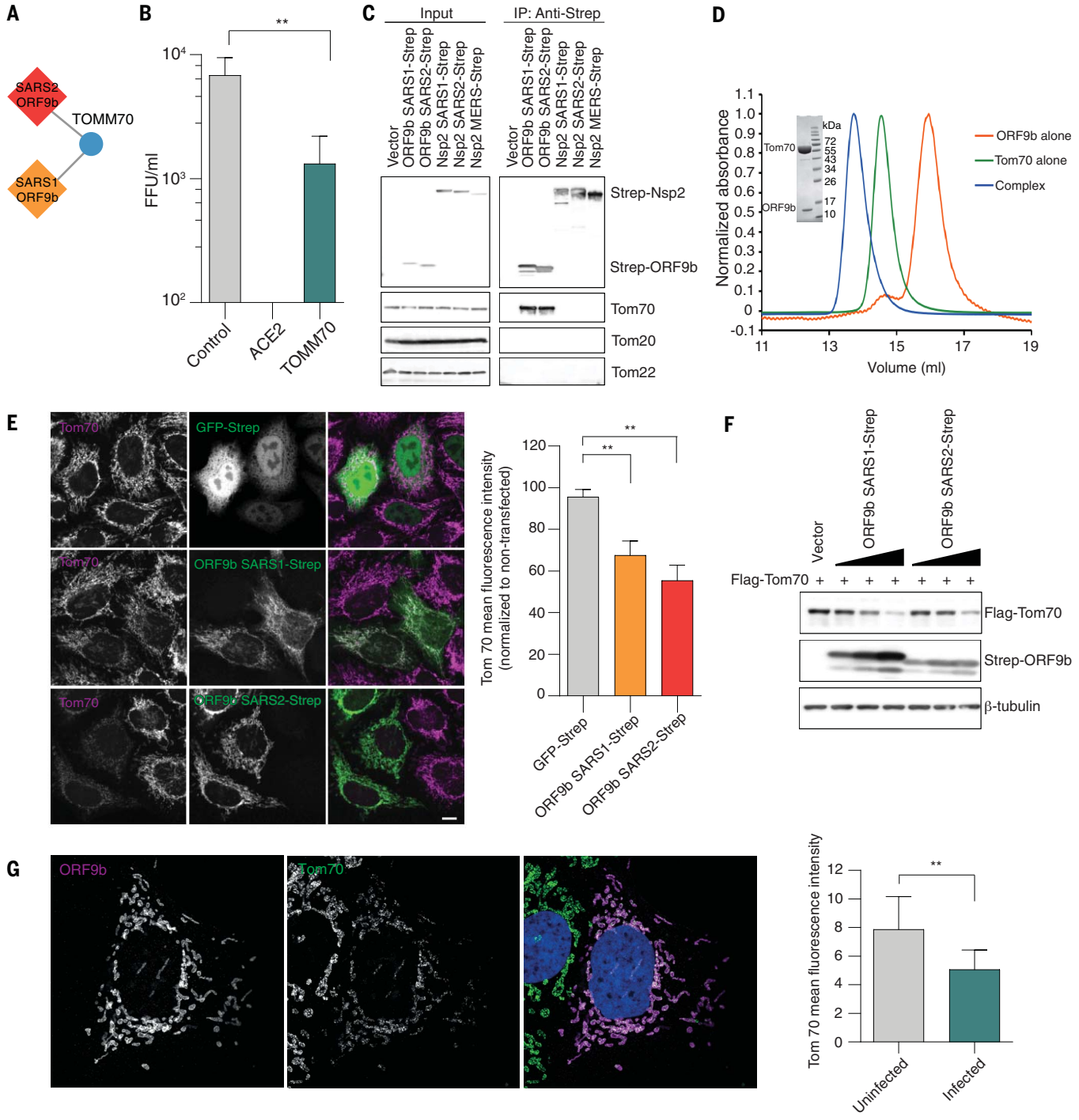

Fig. 6. Interaction between ORF9b and human Tom70. (**A**) ORF9b-Tom70 interaction is conserved between SARS-CoV-1 and SARS-CoV-2. (**B**) Viral titers in Caco-2 cells after CRISPR knockout of *TOMM70* or controls. (**C**) Coimmunoprecipitation of endogenous Tom70 with Strep-tagged ORF9b from SARS-CoV-1 and SARS-CoV-2; Nsp2 from SARS-CoV-1, SARS-CoV-2, and MERS-CoV; or vector control in HEK293T cells. Representative blots of whole-cell lysates and eluates after IP are shown. (**D**) Size exclusion chromatography traces (10/300 S200 increase) of ORF9b alone, Tom70 alone, and coexpressed ORF9b-Tom70 complex purified from recombinant expression in *E. coli*. Insert shows SDS-PAGE of the complex peak indicating presence of both proteins. (**E**) Immunostainings for Tom70 in HeLaM cells transfected with GFP-Strep and ORF9b from SARS-CoV-1 and SARS-CoV-2 (left) and mean fluorescence intensity ± SD values of Tom70 in GFP-Strep and ORF9b expressing cells (normalized to nontransfected cells) (right). Scale bar, 10 μm. (**F**) Flag-Tom70 expression levels in total cell lysates of HEK293T cells upon titration of cotransfected Strep-ORF9b from SARS-CoV-1 and SARS-CoV-2. (**G**) Immunostaining for ORF9b and Tom70 in Caco-2 cells infected with SARS-CoV-2 (left) and mean fluorescence intensity ± SD values of Tom70 in uninfected and SARS-CoV-2–infected cells (right). SARS2, SARS-CoV-2; SARS1, SARS-CoV-1; MERS, MERS-CoV; IP, immunoprecipitation. $^{**}P < 0.05$, Student's *t* test.

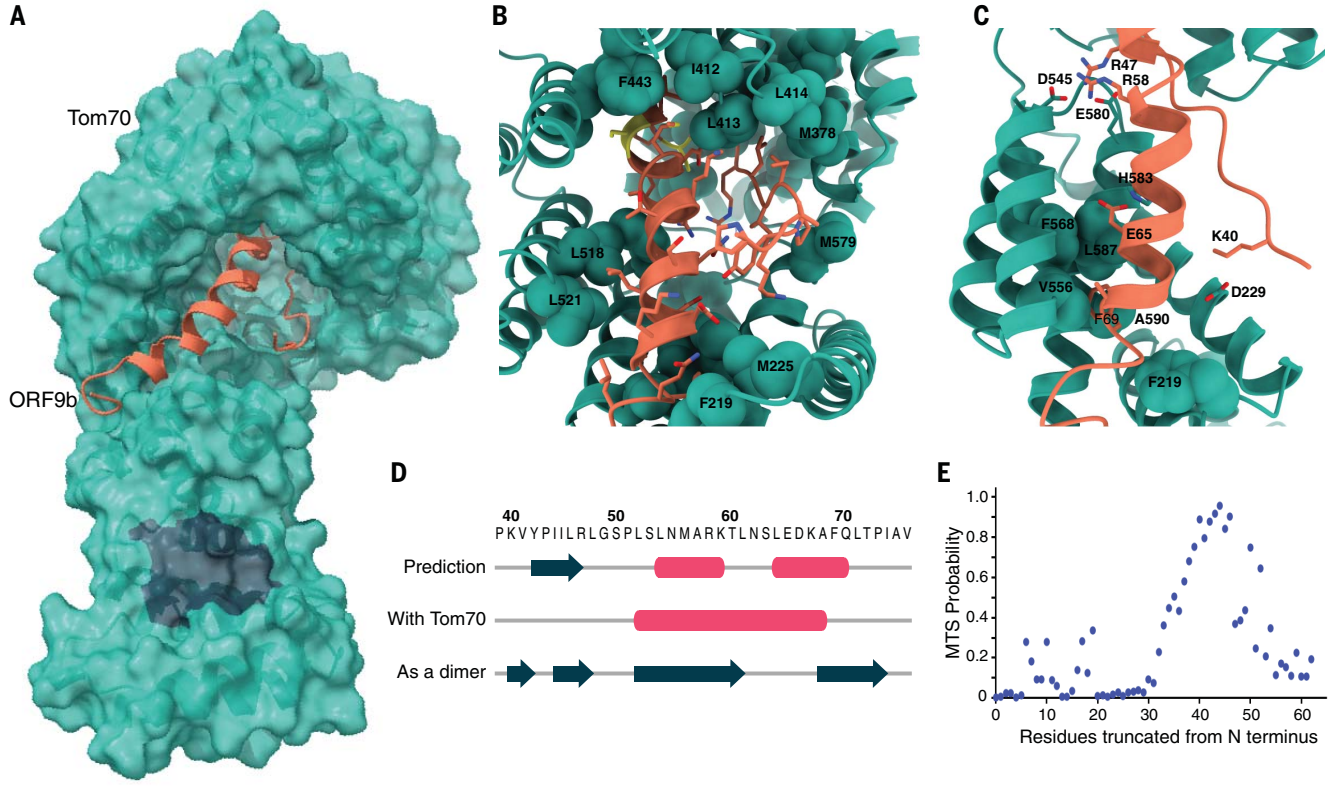

Fig. 7. Cryo-EM structure of ORF9b-Tom70 complex reveals ORF9b adopting a helical fold and binding at the substrate recognition site of Tom70. (**A**) Surface representation of the ORF9b-Tom70 structure. Tom70 is depicted as molecular surface in green, ORF9b is depicted as ribbon in orange. Region in charcoal indicates Hsp70 or Hsp90 binding site on Tom70. (**B**) Magnified view of ORF9b-Tom70 interactions with interacting hydrophobic residues on Tom70 indicated and shown in spheres. The two phosphorylation sites on ORF9b, S50 and S53, are shown in yellow. (**C**) Ionic interactions between Tom70 and ORF9b are depicted as sticks. Highly conserved residues on Tom70 making hydrophobic interactions with ORF9b are depicted as spheres. (**D**) Diagram depicting secondary structure comparison of ORF9b as predicted by JPred server—as visualized in our structure—or as visualized in the previously crystallized dimer structure (PDB ID: 6Z4U) (*16*). Pink tubes indicate helices, charcoal arrows indicate beta strands, and the amino acid sequence for the region visualized in the cryo-EM structure is shown on top. (**E**) Predicted probability of having an internal MTS as output by TargetP server by serially running N-terminally truncated regions of SARS-CoV-2 ORF9b. Region visualized in the cryo-EM structure (amino acids 39 to 76) overlaps with the highest internal MTS probability region (amino acids 40 to 50). MTS, mitochondrial targeting signal. Single-letter abbreviations for the amino acid residues are as follows: A, Ala; C, Cys; D, Asp; E, Glu; F, Phe; G, Gly; H, His; I, Ile; K, Lys; L, Leu; M, Met; N, Asn; P, Pro; Q, Gln; R, Arg; S, Ser; T, Thr; V, Val; W, Trp; and Y, Tyr.

No structure for human Tom70 without a substrate has been reported to date, and therefore we cannot rule out the idea that the conformational differences are because of differences between homologs. However, it is possible that this conformational change upon substrate binding is conserved across homologs, as many of the Tom70 residues interacting with ORF9b are highly conserved, which likely indicates residues essential for endogenous MTS substrate recognition.

Although a previously published crystal structure of SARS-CoV-2 ORF9b revealed that it entirely consists of beta sheets [Protein Data Bank (PDB) ID: 6Z4U] (*16*), we observed that, upon binding Tom70 residues 52 to 68, ORF9b forms a helix (Fig. 7D). This is consistent with the fact that MTS sequences recognized by Tom70 are usually helical, and analysis with the TargetP MTS prediction server revealed a high probability for this region of ORF9b to have an MTS (Fig. 7E). This shows structural plasticity in this viral protein where, depending on the binding partner, ORF9b changes between helical and beta strand folds. Furthermore, we had previously identified two infection-driven phosphorylation sites on ORF9b, S50 and S53 (*17*), which map to the region on ORF9b buried deep in the Tom70 binding pocket (Fig. 7B, yellow). S53 contributes two hydrogen bonds to the interaction with Tom70 in this overall hydrophobic region. Therefore, once phosphorylated, it is likely that the ORF9b-Tom70 interaction is weakened. These residues are surface exposed in the dimeric structure of ORF9b, which could potentially allow phosphorylation to partition ORF9b between Tom70-bound and dimeric populations.

The two binding sites on Tom70—the substrate binding site and the TPR domain that recognizes Hsp70 and Hsp90—are known to be conformationally coupled (*18*). Tom70's interaction with a C-terminal EEVD motif of Hsp90 via the TPR domain is key for its function in the interferon pathway and induction of apoptosis on viral infection (*10*, *19*). Whether ORF9b, by binding to the substrate recognition site of Tom70, allosterically inhibits Tom70's interaction with Hsp90 at the TPR domain remains to be investigated; but notably we observe in our structure that R192, a key residue in the interaction with Hsp70 and Hsp90, is moved out of position to interact with the EEVD sequence, which suggests that ORF9b may modulate interferon and apoptosis signaling via Tom70 (fig. S21). Alternatively, Tom70 has been described as an essential import receptor for PTEN induced kinase 1 (PINK1), and therefore the loss of mitochondrial import efficiency as a result of ORF9b binding to the Tom70 substrate binding pocket may induce mitophagy.

Implications of the ORF8-IL17RA interaction for COVID-19

As described above, we found that IL-17 receptor A (IL17RA) physically interacts with ORF8 from SARS-CoV-2, but not SARS-CoV-1 or MERS-CoV (Fig. 5D, table S2, and Fig. 8A). Several recent studies have identified high IL-17 levels or aberrant IL-17 signaling as a correlate of severe COVID-19 (*20*–*23*). We demonstrated that the physical interaction of SARS-CoV-2 ORF8 with IL17RA occurs with or without IL-17A treatment, which suggests that signaling through the receptor does not disrupt the interaction with ORF8 (Fig. 8B). Furthermore, knockdown of IL17RA led to a significant decrease in SARS-CoV-2 viral replication in A549-ACE2 cells (Fig. 8C). These data suggest that the ORF8-IL17RA interaction modulates systemic IL-17 signaling.

One manner in which this signaling is regulated is through the release of the extracellular domain of the receptor as soluble IL17RA (sIL17RA), which acts as a decoy in circulation by soaking up IL-17A and inhibiting IL-17 signaling (*24*). Production of sIL17RA has been demonstrated by alternative splicing in cultured cells (*25*), but the mechanism by which IL17RA is shed in vivo remains unclear (*26*). ADAM family metalloproteases are known to mediate the release of other interleukin receptors into their soluble form (*27*). We found that SARS-CoV-2 ORF8 physically interacted with both ADAM9 and ADAMTS1 in our previous study (*5*). We find that knockdown of ADAM9, like that of IL17RA, leads to significant decreases in SARS-CoV-2 replication in A549-ACE2 cells (Fig. 5D and table S2).

To test the in vivo relevance of sIL17RA in modulating SARS-CoV-2 infection, we leveraged a genome-wide association study (GWAS) which identified 14 single-nucleotide polymorphisms (SNPs) near the *IL17RA* gene that causally regulate sIL17RA plasma levels (*28*). We then used generalized summary-based Mendelian randomization (GSMR) (*28*, *29*) on the curated GWAS datasets of the COVID-19 Host Genetics Initiative (COVID-HGI) (*30*) and observed that genotypes that predicted higher sIL17RA plasma levels were associated with lower risk of COVID-19 when compared with the population (Fig. 8D and table S9), which is seemingly consistent with our molecular data. Similar results were obtained when comparing only hospitalized COVID-19 patients to the population. However, there was no evidence of association in hospitalized versus non-hospitalized COVID-19 patients. Though the COVID-HGI dataset is underpowered and this observation needs to be replicated in other cohorts, the clinical observations, functional genetics, and clinical genetics all suggest that SARS-CoV-2 benefits from modulating IL-17 signaling. One potentially contradictory caveat is that we find high-level IL-17A treatment diminishes SARS-CoV-2 replication in A549-ACE2 cells (fig. S22); however, IL-17 is a pleiotropic cytokine and it is likely to play multiple roles during SARS-CoV-2 infection in the context of a competent immune system.

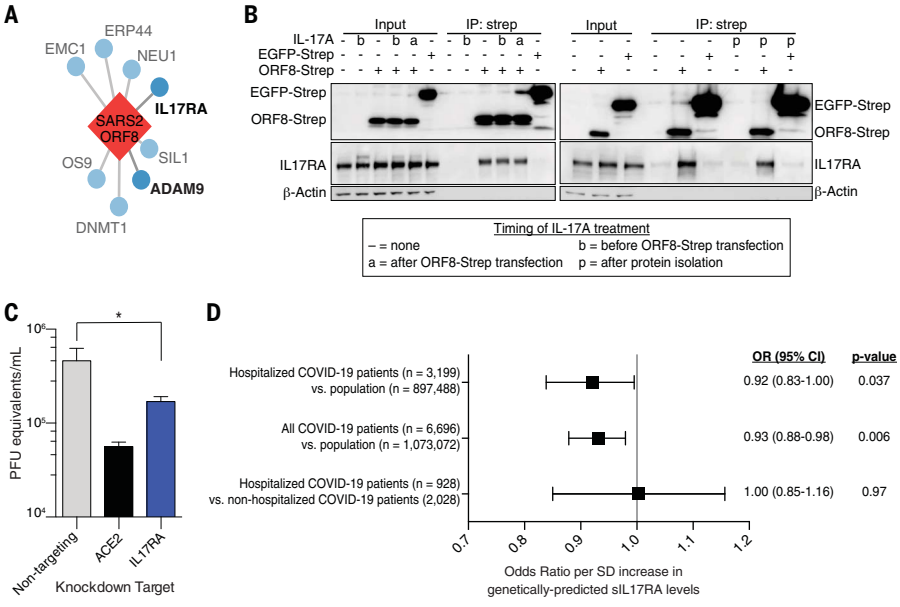

Fig. 8. SARS-CoV-2 ORF8 and functional interactor IL17RA are linked to viral outcomes. (**A**) IL17RA and ADAM9 are functional interactors of SARS-CoV-2 ORF8. Only interactors identified in the genetic screening are shown. (**B**) Coimmunoprecipitation of endogenous IL17RA with Strep-tagged ORF8 or EGFP with or without IL-17A treatment at different times. Overexpression was done in HEK293T cells. (**C**) Viral titer after *IL17RA* or control knockdown in A549-ACE2 cells. (**D**) OR of membership in indicated cohorts by genetically predicted sIL17RA levels. SARS2, SARS-CoV-2; IP, immunoprecipitation; SD, standard deviation; OR, odds ratio; CI, confidence interval; sIL17RA, soluble IL17RA. *$P < 0.05$, unpaired *t* test. Error bars in (C) indicate SDs; in (D), they indicate 95% CIs.

Infectious and transmissible SARS-CoV-2 viruses with large deletions of ORF8 have arisen during the pandemic and have been associated with milder disease and lower concentrations of proinflammatory cytokines (*31*). Notably, compared with healthy controls, patients infected with wildtype, but not ORF8-deleted virus, had threefold elevated plasma levels of IL-17A (*31*). More work will be needed to understand if and how ORF8 manipulates the IL-17 signaling pathway during the course of SARS-CoV-2 infection.

Investigation of druggable targets identified as interactors of multiple coronaviruses

The identification of druggable host factors provides a rationale for drug repurposing efforts. Given the extent of the current pandemic, real-world data can now be used to study the outcome of COVID-19 patients coincidentally treated with host factor–directed, U.S. Food and Drug Administration (FDA)–approved therapeutics. Using medical billing data, we identified 738,933 patients in the United States with documented SARS-CoV-2 infection (Materials and methods). In this cohort, we probed the use of drugs against targets identified here that were shared across coronavirus strains and found to be functionally relevant in the genetic perturbation screens. In particular, we analyzed outcomes for an inhibitor of prostaglandin E synthase type 2 (PGES-2, encoded by *PTGES2*) and for potential ligands of sigma nonopioid receptor 1 (sigma-1, encoded by *SIGMAR1*), and investigated whether these patients fared better than carefully matched patients treated with clinically similar drugs without predicted anti-coronavirus activity.

PGES-2, an interactor of Nsp7 from all three viruses (Fig. 4D), is a dependency factor for SARS-CoV-2 (Fig. 5F). It is inhibited by the FDA-approved prescription nonsteroidal anti-inflammatory drug (NSAID) indomethacin. Computational docking of Nsp7 and PGES-2 to predict binding configuration showed that the dominant cluster of models localizes Nsp7 adjacent to the PGES-2–indomethacin binding site (fig. S23). However, indomethacin did not inhibit SARS-CoV-2 in vitro at reasonable antiviral concentrations (fig. S24 and table S10). A previous study also found that similarly high levels of the drug were needed for inhibition of SARS-CoV-1 in vitro, but this study still showed efficacy for indomethacin against canine coronavirus in vivo (*32*). This motivated

us to observe outcomes in a cohort of outpatients with confirmed SARS-CoV-2 infection who by happenstance initiated a course of indomethacin compared with those who initiated the prescription NSAID celecoxib, which lacks anti–PGES-2 activity. We compared the odds of hospitalization by risk-set sampling (RSS) patients treated at the same time and at similar levels of disease severity and then by further matching on propensity score (PS) (*33*) (Fig. 9A and table S11). RSS and PS—combined with a new user, active comparator design that mimics the interventional component of parallel group randomized studies—are established design and analytic

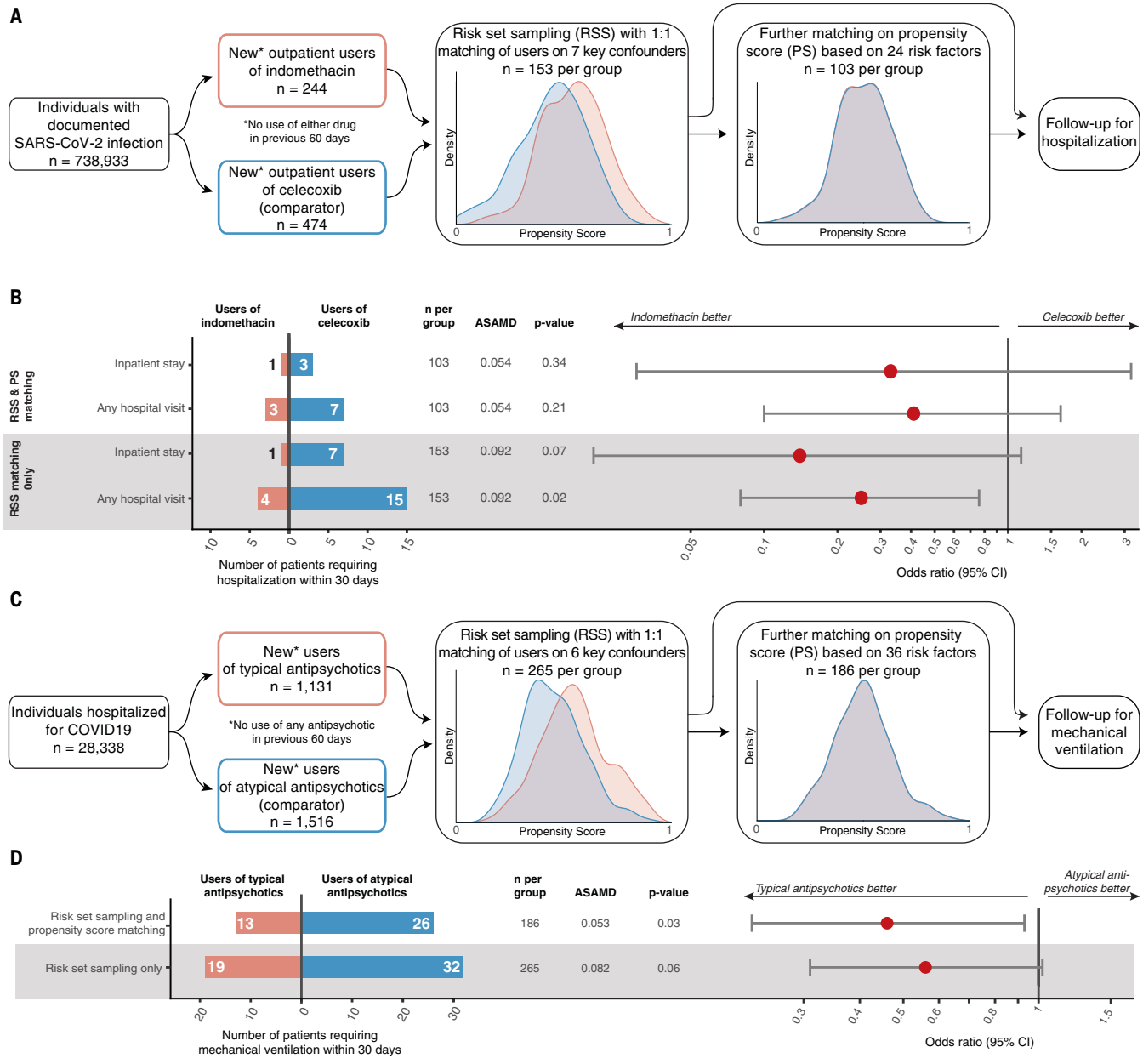

Fig. 9. Real-world data analysis of drugs identified through molecular investigation support their antiviral activity. (**A**) Schematic of retrospective real-world clinical data analysis of indomethacin use for outpatients with SARS-CoV-2. Plots show distribution of propensity scores (PSs) for all included patients (red, indomethacin users; blue, celecoxib users). For a full list of inclusion, exclusion, and matching criteria, see Materials and methods and table S11. (**B**) Effectiveness of indomethacin versus celecoxib in patients with confirmed SARS-CoV-2 infection treated in an outpatient setting. Average standardized absolute mean difference (ASAMD) is a measure of balance between indomethacin and celecoxib groups calculated as the mean of the absolute standardized difference for each PS factor (table S11); *P* value and ORs with 95% CIs are estimated using the Aetion Evidence Platform r4.6. No ASAMD was >0.1. (**C**) Schematic of retrospective real-world clinical data analysis of typical antipsychotic use for inpatients with SARS-CoV-2. Plots show distribution of PSs for all included patients (red, typical users; blue, atypical users). For a full list of inclusion, exclusion, and matching criteria see Materials and methods and table S11. (**D**) Effectiveness of typical versus atypical antipsychotics among hospitalized patients with confirmed SARS-CoV-2 infection treated in hospital. ASAMD is a measure of balance between typical and atypical groups calculated as the mean of the absolute standardized difference for each PS factor (table S11); *P* value and ORs with 95% CIs are estimated using the Aetion Evidence Platform r4.6. No ASAMD was >0.1.

techniques that mitigate biases that can arise in observational studies. A complete list of risk factors used for matching, which include demographic data, baseline health care utilization, comorbidities, and measures of disease severity, are found in table S11.

Among SARS-CoV-2–positive patients, new users of indomethacin in the outpatient setting were less likely than matched new users of celecoxib to require hospitalization or inpatient services [Fig. 9B; odds ratio (OR) = 0.33; 95% confidence interval (CI): 0.03 to 3.19]. The CI of our primary analysis included the null value. In sensitivity analyses, neither using the larger, risk-set–sampled cohort nor relaxing our outcome definition to include any hospital visit appreciably changed the interpretation of our findings, but it did narrow the CIs, particularly when both approaches were combined (OR = 0.25; 95% CI: 0.08 to 0.76). Although we acknowledge that this is a small, noninterventional study, it is nonetheless an example of how molecular insight can rapidly generate testable clinical hypotheses and help prioritize candidates for prospective clinical trials or future drug development.

To create larger patient cohorts, we next grouped drugs that shared activity against the same target—sigma receptors. We previously identified sigma-1 and sigma-2 as drug targets in our SARS-CoV-2–human PPI map, and multiple potent, nonselective sigma ligands were among the most promising inhibitors of SARS-CoV-2 replication in Vero E6 cells (*5*). As shown above, knockout and knockdown of *SIGMAR1*, but not of *SIGMAR2* (also known as *TMEM97*), led to robust decreases in SARS-CoV-2 replication (fig. S24 and Fig. 5F), which suggests that sigma-1 may be a key therapeutic target. We analyzed *SIGMAR1* sequences across 359 mammals and observed positive selection of several residues within beaked whale, mouse, and ruminant lineages, which may indicate a role in host-pathogen competition (fig. S25). Additionally, the sigma ligand drug amiodarone inhibited replication of SARS-CoV-1 as well as SARS-CoV-2, consistent with the conservation of the Nsp6–sigma-1 interaction across the SARS viruses (fig. S24 and Fig. 4D). We then looked for other FDA-approved drugs with reported nanomolar affinity for sigma receptors or those that fit the sigma ligand chemotype (*5*, *34*–*41*), and we selected 13 such therapeutics. We find that all are potent inhibitors of SARS-CoV-2 with half-maximal inhibitory concentration (IC_{50}) values <10 μM, though there is a wide range in reported sigma receptor affinity with no clear correlation between sigma receptor binding affinity and antiviral activity (fig. S24D). Several clinical drug classes were represented by more than one candidate, including typical antipsychotics and antihistamines. Over-the-counter antihistamines are not well represented in medical billing data and are therefore poor candidates for real-world analysis, but users of typical antipsychotics can be easily identified in our patient cohort. By grouping these individual drug candidates by clinical indication, we were able to build a better-powered comparison.

We constructed a cohort for retrospective analysis on new, inpatient users of antipsychotics. In inpatient settings, typical and atypical antipsychotics are used similarly, most commonly for delirium. We compared the effectiveness of typical antipsychotics, which have sigma activity and antiviral effects (fig. S24E), versus atypical antipsychotics, which do not have antiviral activity (fig. S24F), for treatment of COVID-19 (Fig. 9C). Observing mechanical ventilation outcomes in inpatient cohorts is a proxy for the worsening of severe illness rather than the progression from mild disease signified by the hospitalization of indomethacin-exposed outpatients above. We again used RSS plus PS to build a robust, directly comparable cohort of inpatients (table S11). In our primary analysis, half as many of the new users of typical antipsychotics compared with the new users of atypical antipsychotics progressed to the point of requiring mechanical ventilation, demonstrating significantly lower use with an OR of 0.46 (95% CI: 0.23 to 0.93; $P = 0.03$; Fig. 9D). As above, we conducted a sensitivity analysis in the RSS-only cohort and observed the same trend (OR = 0.56; 95% CI: 0.31 to 1.02; $P = 0.06$), which emphasizes the primary result of a beneficial effect for typical versus atypical antipsychotics observed in the RSS-plus-PS–matched cohort. Although a careful analysis of the relative benefits and risks of typical antipsychotics should be undertaken before considering prospective studies or interventions, these data and analyses demonstrate how molecular information can be translated into real-world implications for the treatment of COVID-19—an approach that can ultimately be applied to other diseases in the future.

Discussion

In this study, we generated and compared three different coronavirus-human PPI maps in an attempt to identify and understand pan-coronavirus molecular mechanisms. The use of a quantitative DIS allowed for the identification of virus-specific as well as shared interactions among distinct coronaviruses. We also systematically carried out subcellular localization analysis using tagged viral proteins and antibodies targeting specific SARS-CoV-2 proteins. Our results suggest that protein localization can often differ when comparing individually expressed viral proteins with the localization of the same protein in the context of infection. This can be because of factors such as mislocation driven by tagging, changes in localization due to interaction partners, or cellular compartments that are specific to the infection state. These differences are notable caveats of virus-host interaction studies performed with tagged, expressed proteins. However, previous studies and the work performed here show how these data can be powerful for the identification of host-targeted processes and relevant drug targets.

These data were integrated with genetic data where the interactions uncovered with SARS-CoV-2 were perturbed using RNA interference (RNAi) and CRISPR in different cellular systems and viral assays—an effort that functionally connected many host factors to infection. One of these, Tom70, which we have shown binds to ORF9b from both SARS-CoV-1 and SARS-CoV-2, is a mitochondrial outer membrane translocase that has been previously shown to be important for mounting an interferon response (*42*). Our functional data, however, show that Tom70 has at least some role in promoting infection rather than inhibiting it. Using cryo-EM, we obtained a 3-Å structure of a region of ORF9b binding to the active site of Tom70. Notably, we found that ORF9b is in a markedly different conformation than previously visualized. This suggests the possibility that ORF9b may partition between two distinct structural states, with each having a different function and possibly explaining its apparent pleiotropy. The exact details of functional significance and regulation of the ORF9b-Tom70 interaction will require further experimental elucidation. This interaction, however, which is conserved between SARS-CoV-1 and SARS-CoV-2, could have value as a pan-coronavirus therapeutic target.

Finally, we attempted to connect our in vitro molecular data to clinical information available for COVID-19 patients to understand the pathophysiology of COVID-19 and explore therapeutic avenues. To this end, using GWAS datasets of the COVID-HGI (*30*), we observed that increased predicted sIL17RA plasma levels were associated with lower risk of COVID-19. Notably, we find that IL17RA physically binds to SARS-CoV-2 ORF8, and genetic disruption results in decreased infection. These collective data suggest that future studies should be focused on this pathway as both an indicator and therapeutic target for COVID-19. Furthermore, using medical billing data, we also observed trends in COVID-19 patients on specific drugs indicated by our molecular studies. For example, inpatients prescribed sigma-ligand typical antipsychotics appear to have better COVID-19 outcomes compared with users of atypical antipsychotics, which do not have anti–SARS-CoV-2 activity in vitro. However, we cannot be certain that the sigma receptor interaction is the mechanism underpinning this effect, as typical antipsychotics are known to bind to a multitude of cellular targets, and some atypical antipsychotics,

which lack anti–SARS-CoV-2 activity, nonetheless have reported affinity for rodent sigma receptors (table S10). Replication in other patient cohorts and further work will be needed to see whether there is therapeutic value in these connections, but we have at least demonstrated a strategy wherein protein network analyses can be used to make testable predictions from real-world clinical information.

We have described an integrative and collaborative approach to study and understand pathogenic coronavirus infection, identifying conserved targeted mechanisms that are likely to be of high relevance for other viruses of this family, some of which have yet to infect humans. We used proteomics, cell biology, virology, genetics, structural biology, biochemistry, and clinical and genomic information in an attempt to provide a holistic view of SARS-CoV-2 and other coronaviruses' interactions with infected host cells. We propose that such an integrative and collaborative approach could and should be used to study other infectious agents as well as other disease areas.

Materials and methods

Cells

HEK293T/17 (HEK293T) cells were procured from the University of California, San Francisco (UCSF) Cell Culture Facility, and are available through UCSF's Cell and Genome Engineering Core (https://cgec.ucsf.edu/cell-culture-and-banking-services). HEK293T cells were cultured in Dulbecco's modified Eagle's medium (DMEM) (Corning) supplemented with 10% fetal bovine serum (FBS) (Gibco, Life Technologies) and 1% penicillin-streptomycin (Corning) and maintained at 37°C in a humidified atmosphere of 5% CO_2. Short tandem repeat (STR) analysis by the Berkeley Cell Culture Facility on 8 August 2017 authenticates these as HEK293T cells with 94% probability.

HeLaM cells (RRID: CVCL_R965) were originally obtained from the laboratory of M. S. Robinson (CIMR, University of Cambridge, UK) and have been routinely tested for mycoplasma contamination. HeLaM cells were grown in DMEM supplemented with 10% FBS, 100 U/ml penicillin, 100 μg/ml streptomycin, and 2 mM glutamine at 37°C in a 5% CO_2 humidified incubator.

A549 cells stably expressing ACE2 (A549-ACE2) were a gift from O. Schwartz. A549-ACE2 cells were cultured in DMEM supplemented with 10% FBS, blasticidin (20 μg/ml) (Sigma) and maintained at 37°C with 5% CO_2. STR analysis by the Berkeley Cell Culture Facility on 17 July 2020 authenticates these as A549 cells with 100% probability.

Caco-2 cells (ATTC, HTB-37, RRID:CVCL_0025) were cultured in DMEM with GlutaMAX and pyruvate (Gibco, 10569010) and supplemented with 20% FBS (Gibco, 26140079). For Caco-2 cells utilized in Cas9-RNP knockouts, STR analysis by the Berkeley Cell Culture Facility on 23 April 2020 authenticates these as Caco-2 cells with 100% probability.

Vero E6 cells were purchased from the American Type Culture Collection (ATCC) and thus authenticated [VERO C1008 (Vero 76, clone E6, Vero E6)] (ATCC, CRL-1586). Vero E6 cells tested negative for mycoplasma contamination. Vero E6 cells were cultured in DMEM (Corning) supplemented with 10% FBS (Gibco, Life Technologies) and 1% penicillin-streptomycin (Corning) and maintained at 37°C in a humidified atmosphere of 5% CO_2.

Microbes

LOBSTER *E. coli* Expression Strain: LOBSTR-[BL21(DE3)] Kerafast no. EC1002.

Antibodies

Commercially available primary antibodies used in this study

Rabbit anti-beta-actin (Cell Signaling Technology #4967, RRID:AB_330288); mouse anti-beta tubulin (Sigma-Aldrich #T8328, RRID:AB_1844090); rabbit anti-BiP (Cell Signaling Technology #3177S, RRID:AB_2119845); mouse anti-EEA1 (BD Biosciences #610457, RRID:AB_397830, used at 1:200); mouse anti-ERGIC53 (Enzo Life Sciences #ALX-804-602-C100, RRID:AB_2051363, used at 1:200); anti-GM130; rabbit anti-GRP78 BiP (Abcam #Ab21685, RRID:AB_2119834); rabbit anti–SARS-CoV–nucleocapsid protein (NP) (Rockland #200-401-A50, RRID:AB_828403); rabbit anti-PDI (protein disulfide isomerase) (Cell Signaling Technology #3501, RRID:AB_2156433); mouse anti-Strep tag (QIAGEN #34850, RRID:AB_2810987, used at 1:5000); mouse anti-strepMAB (IBA Lifesciences #2-1507-001, used at 1:1000); rabbit anti–Strep-tag II (Abcam #ab232586); rabbit anti-Tom20 (Proteintech #11802-1-AP, RRID:AB_2207530, used at 1:1000); rabbit anti-Tom20 (Cell Signaling Technology #42406, RRID:AB_2687663); mouse anti-Tom22 (Santa Cruz Biotechnology #sc-101286, RRID:AB_1130526); rabbit anti-Tom40 (Santa Cruz Biotechnology #sc-11414, RRID:AB_793274); mouse anti-Tom70 (Santa Cruz #sc-390545, RRID:AB_2714192, used at 1:500); Rabbit anti-STX5 (Synaptic Systems 110 053, used at 1:500); and ActinStaining Kit 647-Phalloidin (Hypernol #8817-01, used at 1:400).

Commercially available secondary antibodies used in this study

Alexa Fluor 488 chicken anti-mouse immunoglobulin G (IgG) (Invitrogen #A21200, RRID_AB_2535786, used at 1:400); Alexa Fluor 488 chicken anti-rabbit IgG (Invitrogen #A21441, RRID_AB_10563745, used at 1:400); Alexa Fluor 568 donkey anti-sheep IgG (Invitrogen #A21099, RRID_AB_10055702, used at 1:400); Alexa Fluor Plus 488 goat anti-rabbit (ThermoFisher A32731, used at 1:500); Alexa Fluor Plus 594 goat anti-mouse (ThermoFisher A32742, used at 1:500); and goat anti-mouse IgG-HRP (horseradish peroxidase) (BioRad #170-6516, RRID:AB_11125547, used at 1:20000).

Noncommercial antisera

Rabbit anti–SARS-CoV-2–NP antiserum was produced by the Garcia-Sastre laboratory and used at 1:10000. For information on polyclonal sheep antibodies targeting SARS-CoV-2 proteins, see below, table S3, and https://mrcppu-covid.bio/.

Coronavirus annotation and plasmid cloning

SARS-CoV-1 isolate Tor2 (NC_004718) and MERS-CoV (NC_019843) were downloaded from GenBank and utilized to design 2xStrep-tagged expression constructs of ORFs and proteolytically mature Nsps derived from ORF1ab (with N-terminal methionines and stop codons added as necessary). Protein termini were analyzed for predicted acylation motifs, signal peptides, and transmembrane regions, and either the N or C terminus was chosen for tagging as appropriate. Finally, reading frames were codon optimized and cloned into pLVX-EF1alpha-IRES-Puro (Takara/Clontech) including a 5′ Kozak motif.

Immunofluorescence microscopy of viral protein constructs

Approximately 60,000 HeLaM cells were seeded onto glass coverslips in a 12-well dish and grown overnight. The cells were transfected using 0.5 μg of plasmid DNA and either polyethylenimine (Polysciences) or Fugene HD (Promega; 1 part DNA to 3 parts transfection reagent) and grown for a further 16 hours.

Transfected cells were fixed with 4% paraformaldehyde (Polysciences) in phosphate-buffered saline (PBS) at room temperature for 15 min. The fixative was removed and quenched using 0.1 M glycine in PBS. The cells were permeabilized using 0.1% saponin in PBS containing 10% FBS. The cells were stained with the indicated primary and secondary antibodies for 1 hour at room temperature. The coverslips were mounted onto microscope slides using ProLong Gold antifade reagent (ThermoFisher) and imaged using a UplanApo 60x oil (NA 1.4) immersion objective on a Olympus BX61 motorized wide-field epifluorescence microscope. Images were captured using a Hamamatsu Orca monochrome camera and processed using ImageJ.

To gain insight into the intracellular distribution of each Strep-tagged construct, ~100 cells per transfection were manually scored. Each construct was assigned an intracellular distribution in relation to the plasma membrane, ER, Golgi, cytoplasm, and mitochondria (scored out of 7). Many of the constructs

had several localizations so this was also reflected in the scoring. The scoring also took into account the impact of expression level on the localization of the constructs.

Meta-analysis of immunofluorescence data

We first sorted the data concerning viral protein location for all Strep-tagged viral proteins expressed individually in three heatmaps (one per virus) using a custom R script ("pheatmap" package). The information concerning protein localization during SARS-CoV-2 infection was added as a square border color code in the first heatmap, to compare the two different localization patterns. To compare the predicted versus the experimentally determined locations, for each protein we took the top scoring sequence-based localization prediction from DeepLoc (*43*) if the score was >1. When more than one localization can be assigned to the same protein, we took as many top scoring ones as experimentally assigned localizations we had for the same protein. Finally, for each cell compartment, we count the number of experimentally assigned viral proteins and the subset of them predicted to that same compartment as correct predictions. To compare changes in protein interactions with changes in protein localization (Strep-tagged experiment versus sequence-based prediction), we calculated the Jaccard index of prey overlap for each viral protein (SARS-CoV-2 versus SARS-CoV-1 and SARS-CoV-2 versus MERS-CoV) and plotted them together, for proteins with the same localization and for proteins with different localization.

Generation of polyclonal sheep antibodies targeting SARS-CoV-2 proteins

Sheep were immunized with individual N-terminal glutathione *S*-transferase (GST)–tagged SARS-CoV-2 recombinant proteins or N-terminal maltose binding protein (MBP)–tagged proteins (for SARS-CoV-2 S, S-RBD, and ORF7a), followed by up to five booster injections 4 weeks apart from each other. Sheep were subsequently bled and IgGs were affinity purified using the specific recombinant N-terminal MBP-tagged viral proteins. Each antiserum specifically recognized the appropriate native viral protein. Characterization of each antibody can be found at https://mrcppu-covid.bio/. All antibodies generated can be requested at https://mrcppu-covid.bio/. Also see table S3.

Immunofluorescence microscopy of infected Caco-2 cells

For infection experiments in human colon epithelial Caco-2 cells (ATCC, HTB-37), SARS-CoV-2 isolate Muc-IMB-1 (provided by the Bundeswehr Institute of Microbiology, Munich, Germany) was used. SARS-CoV-2 was propagated in Vero E6 cells in DMEM supplemented with 2% FBS. All work involving live SARS-CoV-2 was performed in the BSL3 facility of the Institute of Virology, University Hospital Freiburg, and was approved according to the German Act of Genetic Engineering by the local authority (Regierungspraesidium Tuebingen, permit UNI.FRK.05.16/05).

Caco-2 human colon epithelial cells seeded on glass coverslips were infected with SARS-CoV-2 {Strain Muc-IMB-1/2020, second passage on Vero E6 cells [2×10^6 plaque-forming units (PFU)/ml]} at a multiplicity of infection (MOI) of 0.1. At 24 hours postinfection, cells were washed with PBS and fixed in 4% paraformaldehyde in PBS for 20 min at room temperature, followed by 5 min of quenching in 0.1 M glycine in PBS at room temperature. Cells were permeabilized and blocked in 0.1% saponin in PBS supplemented with 10% FBS for 45 min at room temperature and incubated with primary antibodies for 1 hour at room temperature. After washing 15 min with blocking solution, AF568-labeled donkey–anti-sheep (Invitrogen, #A21099; 1:400) secondary antibody as well as AF4647-labeled Phalloidin (Hypermol, #8817-01; 1:400) were applied for 1 hour at room temperature. Subsequent washing was followed by embedding in Diamond Antifade Mountant with 4′,6-diamidino-2-phenylindole (DAPI) (ThermoFisher, #P36971). Fluorescence images were generated using a LSM800 confocal laser-scanning microscope (Zeiss) equipped with a 63X, 1.4 NA oil objective and Airyscan detector and the Zen blue software (Zeiss) and processed with Zen blue software and ImageJ/Fiji.

Transfection and cell harvest for immunoprecipitation experiments

For each affinity purification [SARS-CoV-1 baits, MERS-CoV baits, green fluorescent protein (GFP)–2xStrep, or empty vector controls], 10 million HEK293T cells were transfected with up to 15 μg of individual expression constructs using PolyJet transfection reagent (SignaGen Laboratories) at a 1:3 μg:μl ratio of plasmid to transfection reagent on the basis of the manufacturer's protocol. After >38 hours, cells were dissociated at room temperature using 10 ml PBS without calcium and magnesium (D-PBS) with 10 mM ethylenediaminetetraacetic acid (EDTA) for at least 5 min, pelleted by centrifugation at 200 × *g*, at 4°C for 5 min, washed with 10 ml D-PBS, pelleted once more, and frozen on dry ice before storage at −80°C for later immunoprecipitation analysis. For each bait, three independent biological replicates were prepared.

Whole-cell lysates were resolved on 4 to 20% Criterion SDS–polyacrylamide gel electrophoresis (SDS-PAGE) gels (Bio-Rad Laboratories) to assess Strep-tagged protein expression by immunoblotting using mouse anti-Strep tag antibody 34850 (QIAGEN) and anti-mouse HRP secondary antibody (BioRad).

Anti–Strep tag affinity purification

Frozen cell pellets were thawed on ice for 15 to 20 min and suspended in 1 ml lysis buffer [immunoprecipitation (IP) buffer (50 mM tris-HCl, pH 7.4 at 4°C; 150 mM NaCl, 1 mM EDTA) supplemented with 0.5% Nonidet P 40 Substitute (NP-40; Fluka Analytical) and cOmplete mini EDTA-free protease and PhosSTOP phosphatase inhibitor cocktails (Roche)]. Samples were then freeze-fractured by refreezing on dry ice for 10 to 20 min, then rethawed and incubated on a tube rotator for 30 min at 4°C. Debris was pelleted by centrifugation at 13,000 × *g*, at 4°C for 15 min. Up to 56 samples were arrayed into a 96-well Deepwell plate for affinity purification on the KingFisher Flex Purification System (Thermo Scientific) as follows: MagStrep "type3" beads (30 μl; IBA Lifesciences) were equilibrated twice with 1 ml wash buffer (IP buffer supplemented with 0.05% NP-40) and incubated with 0.95 ml lysate for 2 hours. Beads were washed three times with 1 ml wash buffer and then once with 1 ml IP buffer. Beads were released into 75 μl denaturation-reduction buffer [2 M urea, 50 mM Tris-HCl pH 8.0, 1 mM dithiothreitol (DTT)] in advance of on-bead digestion. All automated protocol steps were performed at 4°C using the slow mix speed and the following mix times: 30 s for equilibration and wash steps, 2 hours for binding, and 1 min for final bead release. Three 10-s bead collection times were used between all steps.

On-bead digestion for affinity purification

Bead-bound proteins were denatured and reduced at 37°C for 30 min, alkylated in the dark with 3 mM iodoacetamide for 45 min at room temperature, and quenched with 3 mM DTT for 10 min. To offset evaporation, 22.5 μl 50 mM Tris-HCl, pH 8.0 were added before trypsin digestion. Proteins were then incubated at 37°C, initially for 4 hours with 1.5 μl trypsin (0.5 μg/μl; Promega) and then another 1 to 2 hours with 0.5 μl additional trypsin. All steps were performed with constant shaking at 1100 rpm on a ThermoMixer C incubator. Resulting peptides were combined with 50 μl 50 mM Tris-HCl, pH 8.0 used to rinse beads and acidified with trifluoroacetic acid (0.5% final, pH < 2.0). Acidified peptides were desalted for MS analysis using a BioPureSPE Mini 96-Well Plate (20 mg PROTO 300 C18; The Nest Group, Inc.) according to standard protocols.

MS operation and peptide search

Samples were resuspended in 4% formic acid, 2% acetonitrile solution, and separated by a reversed-phase gradient over a nanoflow C18 column (Dr. Maisch). HPLC buffer A was composed of 0.1% formic acid, and HPLC buffer B was composed of 80% acetonitrile in 0.1% formic acid. Peptides were eluted by

a linear gradient from 7 to 36% B over the course of 52 min, after which the column was washed with 95% B and re-equilibrated at 2% B. Each sample was directly injected by means of an Easy-nLC 1200 (Thermo Fisher Scientific) into a Q-Exactive Plus mass spectrometer (Thermo Fisher Scientific) and analyzed with a 75-min acquisition, with all MS1 and MS2 spectra collected in the orbitrap; data were acquired using the Thermo software Xcalibur (4.2.47) and Tune (2.11 QF1 Build 3006). For all acquisitions, QCloud was used to control instrument longitudinal performance during the project (*44*). All proteomic data were searched against the human proteome (uniprot reviewed sequences downloaded 28 February 2020), enhanced green fluorescent protein (EGFP) sequence, and the SARS-CoV or MERS protein sequences using the default settings for MaxQuant (version 1.6.12.0) (*45*). Detected peptides and proteins were filtered to 1% false discovery rate in MaxQuant. All MS raw data and search results files have been deposited to the ProteomeXchange Consortium via the PRIDE partner repository with the dataset (PXD identifier PXD021588).

High-confidence protein interaction scoring

Identified proteins were then subjected to PPI scoring with both SAINTexpress (version 3.6.3) and MiST (https://github.com/kroganlab/mist) (*6*, *7*). We applied a two-step filtering strategy to determine the final list of reported interactors, which relied on two different scoring stringency cut-offs. In the first step, we chose all protein interactions that had a MiST score ≥0.7, a SAINTexpress Bayesian false-discovery rate (BFDR) ≤0.05, and an average spectral count ≥2. For all proteins that fulfilled these criteria, we extracted information about the stable protein complexes that they participated in from the CORUM (*46*) database of known protein complexes. In the second step, we then relaxed the stringency and recovered additional interactors that (i) formed complexes with interactors determined in filtering step 1 and (ii) fulfilled the following criteria: MiST score ≥0.6, SAINTexpress BFDR ≤0.05, and average spectral counts ≥2. Proteins that fulfilled filtering criteria in either step 1 or step 2 were considered to be high-confidence protein-protein interactions (HC-PPIs).

Using this filtering criteria, nearly all of our baits recovered a number of HC-PPIs in close alignment with previous datasets reporting an average of around six PPIs per bait (*47*). However, for a subset of baits, we observed a much higher number of PPIs that passed these filtering criteria. For these baits, the MiST scoring was instead performed using a larger in-house database of 87 baits that were prepared and processed in an analogous manner to this SARS-CoV-2 dataset. This was done to provide a more comprehensive collection of baits for comparison, to minimize the classification of nonspecifically binding background proteins as HC-PPIs. This was performed for SARS-CoV-1 baits (M, Nsp12, Nsp13, Nsp8, and ORF7b), MERS-CoV baits (Nsp13, Nsp2, and ORF4a), and SARS-CoV-2 Nsp16. SARS-CoV-2 Nsp16 MiST was scored using the in-house database as well as all previous SARS-CoV-2 data (*5*).

Hierarchical clustering of virus-human protein interactions

Hierarchical clustering was performed on interactions for (i) viral bait proteins shared across all three viruses and (ii) passed the high-confidence scoring criteria (MiST score ≥0.6, SAINTexpress BFDR ≤0.05, and average spectral counts ≥2) in at least one virus. We clustered using a new interaction score (*K*), which we defined as the average between the MiST and SAINT score for each virus-human interaction. This was done to provide a single score that captured the benefits from each scoring method. Clustering was performed using the ComplexHeatmap package in R, using the "average" clustering method and "euclidean" distance metric. *K*-means clustering (k = 7) was applied to capture all possible combinations of interaction patterns between viruses.

GO enrichment analysis on clusters

Sets of genes found in seven clusters were tested for enrichment of GO terms, which was performed using the enricher function of clusterProfiler package in R (*48*). The GO terms were obtained from the C5 collection of Molecular Signature Database (MSigDBv7.1) and include biological process, cellular component, and molecular function ontologies. Significant GO terms were identified (adjusted $P < 0.05$) and further refined to select nonredundant terms. To select nonredundant gene sets, we first constructed a GO term tree based on distances (1 – Jaccard similarity coefficients of shared genes) between the significant terms. The GO term tree was cut at a specific level (h = 0.99) to identify clusters of nonredundant gene sets. For results with multiple significant terms belonging to the same cluster, we selected the term with the lowest adjusted *P* value.

Sequence similarity analysis

Protein sequence similarity was assessed by comparing the protein sequences from SARS-CoV-1 and MERS-CoV to SARS-CoV-2 for orthologous viral bait proteins. The corresponding PPI similarity was represented by a Jaccard index, using the high-confidence interactomes for each virus.

GO enrichment and PPI similarity analysis

The high-confidence interactors of the three viruses were tested for enrichment of GO terms as described above. We then identified GO terms that are significantly enriched (adjusted *P* value < 0.05) in all three viruses. For each enriched term, we generated the list of its associated genes and computed the Jaccard index of pairwise comparisons of the three viruses.

Orthologous versus nonorthologous interactions analysis

For a given pair of viruses, we identified all pairs of baits that share interactors and categorized these into orthologous and nonorthologous groups on the basis of whether the two baits were orthologs or not. We then summed up the total number of shared interactors in each group to calculate the corresponding fractions. This was performed for all pairwise combinations of the three viruses.

Structural modeling and comparison of MERS-CoV ORF4a and SARS-CoV-2 Nsp8

To obtain a sensitive sequence comparison between MERS-CoV ORF4a and SARS-CoV-2 Nsp8, we took into consideration their homologs. We first searched for homologs of these proteins in the UniRef30 database using hhblits (1 iteration, E-value cutoff 1×10^{-3}) (*49*). Subsequently, the resulting alignments were filtered to include only sequences with at least 80% coverage to the corresponding query sequence, and hidden Markov models (HMMs) were created using hhmake. Finally, the HMMs of ORF4a and Nsp8 homologs were locally aligned using hhalign. The structure of ORF4a was predicted de novo using trRosetta (*50*). To provide greater coverage than that provided by experimental structures, SARS-CoV-2 Nsp8 was modeled using the structure of its SARS-CoV homolog as template (PDB ID: 2AHM) (*51*) using SWISS-MODEL (*52*). To search for local structural similarities between ORF4a and Nsp8, we used Geometricus, a structure embedding tool based on three-dimensional (3D) rotation invariant moments (*53*). This generates so-called shape-mers, analogous to sequence k-mers. The structures were fragmented into overlapping k-mers on the basis of the sequence (k = 20) and into overlapping spheres surrounding each residue (radius = 15 Å). To ensure that the similarities found between these distinct structures were significant, we used a high resolution of 7 to define the shape-mers. This resulted in the identification of four different shape-mers common to ORF4a and Nsp8. We aligned the entire ORF4a structure with residues 96 to 191 of the Nsp8 structure (i.e., after removal of the long N-terminal helix) using the Caretta structural alignment algorithm (*54*), using 3D rotation invariant moments (*53*) for initial superposition. We optimized parameters to maximize the Caretta score. The resulting alignment used k = 30, radius = 16 Å, gap open penalty = 0.05, gap extend penalty = 0.005,

and had a root mean square deviation (RMSD) of 7.6 Å across 66 aligning residues.

DIS analysis

We computed a DIS for interactions that (i) originated from viral bait proteins shared across all three viruses and (ii) passed the high-confidence scoring criteria (see above) in at least one virus. We defined the DIS to be the difference between the interaction scores (K) from each virus. A DIS near 0 indicates that the interaction is confidently shared between the two viruses being compared, whereas a DIS near −1 or +1 indicates that the host-protein interaction is specific for one virus or the other. We computed a fourth DIS (SARS-MERS) by averaging K from SARS-CoV-1 and SARS-CoV-2 before calculating the difference with MERS-CoV. Here, a DIS near +1 indicates SARS-specific interactions (shared between SARS-CoV-1 and SARS-CoV-2 but absent in MERS-CoV), a DIS near −1 indicates MERS-specific interactions (present in MERS-CoV and absent or lowly confident in both SARS-CoVs), and a DIS near 0 indicates interactions shared between all three viruses.

For each pairwise virus comparison, as well as the SARS-MERS comparison, the DIS was defined on the basis of cluster membership of interactions (Fig. 3A). For the SARS2-SARS1 comparison, interactions from every cluster except 5 were used, as those interactions are considered absent from both SARS-CoV-2 and SARS-CoV-1. For the SARS2-MERS comparison, interactions from all clusters except 3 were used. For the SARS1-MERS comparison, interactions from all clusters except 6 were used. For the SARS-MERS comparison, only interactions from clusters 2, 4, and 5 were used.

Network generation and visualization

PPI networks were generated in Cytoscape (*55*) and subsequently annotated using Adobe Illustrator. Host-host physical interactions, protein complex definitions, and biological process groupings were derived from CORUM (*46*), GO (biological process), and manually curated from literature sources. All networks were deposited in NDEx (*56*).

siRNA library and transfection in A549-ACE2 cells

An OnTargetPlus siRNA SMARTpool library (Horizon Discovery) was purchased targeting 331 of the 332 human proteins previously identified to bind SARS-CoV-2 (*5*) (PDE4DIP was not available for purchase and was excluded from the assay). This library was arrayed in a 96-well format, with each plate also including two nontargeting siRNAs and one siRNA pool targeting ACE2 (table S12). The siRNA library was transfected into A549 cells stably expressing ACE2 (A549-ACE2, provided by O. Schwartz), using Lipofectamine RNAiMAX reagent (Thermo Fisher). Briefly, 6 pmol of each siRNA pool were mixed with 0.25 μl RNAiMAX transfection reagent and OptiMEM (Thermo Fisher) in a total volume of 20 μl. After a 5 min incubation period, the transfection mix was added to cells seeded in a 96-well format. Twenty-four hours after transfection, the cells were subjected to SARS-CoV-2 infection, as described in the section Viral infection and quantification assay in A549-ACE2 cells, or incubated for 72 hours to assess cell viability using the CellTiter-Glo luminescent viability assay according to the manufacturer's protocol (Promega). Luminescence was measured in a Tecan Infinity 2000 plate reader, and percentage viability calculated relative to untreated cells (100% viability) and cells lysed with 20% ethanol or 4% formalin (0% viability), included in each experiment.

Viral infection and quantification assay in A549-ACE2 cells

Cells seeded in a 96-well format were inoculated with a SARS-CoV-2 stock (BetaCoV/France/IDF0372/2020 strain, generated and propagated once in Vero E6 cells and a gift from the National Reference Centre for Respiratory Viruses at Institut Pasteur, Paris, originally supplied through the European Virus Archive goes Global platform) at a MOI of 0.1 PFU per cell. After a 1-hour incubation period at 37°C, the virus inoculum was removed, and replaced by DMEM containing 2% FBS (Gibco, Thermo Fisher). Seventy-two hours postinfection, the cell culture supernatant was collected, heat inactivated at 95°C for 5 min, and used for RT-qPCR analysis to quantify viral genomes present in the supernatant. Briefly, SARS-CoV-2–specific primers targeting the N gene region: 5′-TAATCAGACAAGGAACTGATTA-3′ (forward) and 5′-CGAAGGTGTGACTTCCATG-3′ (reverse) (*57*) were used with the Luna Universal One-Step RT-qPCR Kit (New England Biolabs) in an Applied Biosystems QuantStudio 6 thermocycler, with the following cycling conditions: 55°C for 10 min, 95°C for 1 min, and 40 cycles of 95°C for 10 s, followed by 60°C for 1 min. The number of viral genomes is expressed as PFU equivalents per milliliter, and was calculated by performing a standard curve with RNA derived from a viral stock with a known viral titer.

Knockdown validation with RT-qPCR in A549-ACE2 cells

Gene-specific qPCR primers targeting all genes represented in the OnTargetPlus library were purchased and arrayed in a 96-well format identical to that of the siRNA library (IDT; table S13). A549-ACE2 cells treated with siRNA were lysed using the Luna Cell Ready Lysis Module (New England Biolabs) following the manufacturer's protocol. The lysate was used directly for gene quantification by RT-qPCR with the Luna Universal One-Step RT-qPCR Kit (New England Biolabs), using the gene-specific PCR primers and glyceraldehyde-3-phosphate dehydrogenase (GAPDH) as a housekeeping gene. The following cycling conditions were used in an Applied Biosystems QuantStudio 6 thermocycler: 55°C for 10 min, 95°C for 1 min, and 40 cycles of 95°C for 10 s, followed by 60°C for 1 min. The fold change in gene expression for each gene was derived using the $2^{-\Delta\Delta CT}$, 2 (Delta Delta CT) method (*58*), normalized to the constitutively expressed housekeeping gene *GAPDH*. Relative changes were generated comparing the control siRNA knockdown transfected cells to the cells transfected with each siRNA.

Single guide RNA selection for Cas9 knockout screen

Single guide RNAs (sgRNAs) were designed according to Synthego's multiguide gene knockout (*59*). Briefly, two or three sgRNAs are bioinformatically designed to work in a cooperative manner to generate small, knockout-causing, fragment deletions in early exons (fig. S18). These fragment deletions are larger than standard indels generated from single guides. The genomic repair patterns from a multiguide approach are highly predictable on the basis of the guide spacing and design constraints to limit off-targets, resulting in a higher probability protein knockout phenotype (table S14).

sgRNA synthesis for Cas9 knockout screen

RNA oligonucleotides were chemically synthesized on Synthego solid-phase synthesis platform, using CPG solid support containing a universal linker. 5-benzylthio-1H-tetrazole (BTT, 0.25 M solution in acetonitrile) was used for coupling, [3-((dimethylamino-methylidene)amino)-3H-1,2,4-dithiazole-3-thione (DDTT, 0.1 M solution in pyridine)] was used for thiolation, dichloroacetic acid (DCA, 3% solution in toluene) was used for detritylation. Modified sgRNA were chemically synthesized to contain 2′-O-methyl analogs and 3′ phosphorothioate nucleotide interlinkages in the terminal three nucleotides at both 5′ and 3′ ends of the RNA molecule. After synthesis, oligonucleotides were subject to a series of deprotection steps, followed by purification by solid-phase extraction (SPE). Purified oligonucleotides were analyzed by electrospray ionization mass spectrometry (ESI-MS).

Arrayed knockout generation with Cas9-RNPs

For Caco-2 transfection, 10 pmol Streptococcus Pyogenes NLS-Sp.Cas9-NLS (SpCas9) nuclease (Aldevron; 9212) was combined with 30 pmol total synthetic sgRNA (10 pmol each sgRNA, Synthego) to form ribonucleoproteins (RNPs) in 20 μl total volume with SF Buffer (Lonza V5SC-2002) and allowed to complex at room temperature for 10 min.

All cells were dissociated into single cells using TrypLE Express (Gibco), resuspended in

culture media and counted. 100,000 cells per nucleofection reaction were pelleted by centrifugation at 200 × *g* for 5 min. After centrifugation, cells were resuspended in transfection buffer according to cell type and diluted to 2 × 10^4 cells/μl. Five μl of cell solution was added to preformed RNP solution and gently mixed. Nucleofections were performed on a Lonza HT 384-well nucleofector system (Lonza, #AAU-1001) using program CM-150 for Caco-2. Immediately after nucleofection, each reaction was transferred to a tissue-culture treated 96-well plate containing 100 μl of normal culture media and seeded at a density of 50,000 cells per well. Transfected cells were incubated following standard protocols.

Quantification of arrayed knockout efficiency

Two days after nucleofection, genomic DNA was extracted from cells using DNA QuickExtract (Lucigen, #QE09050). Briefly, cells were lysed by removal of the spent media followed by addition of 40 μl of QuickExtract solution to each well. Once the QuickExtract DNA Extraction Solution was added, the cells were scraped off the plate into the buffer. After transfer to compatible plates, DNA extract was then incubated at 68°C for 15 min followed by 95°C for 10 min in a thermocycler before being stored for downstream analysis.

Amplicons for indel analysis were generated by PCR amplification with NEBNext polymerase (NEB, #M0541) or AmpliTaq Gold 360 polymerase (Thermo Fisher Scientific, #4398881) according to the manufacturer's protocol. The primers were designed to create amplicons between 400 and 800 base pairs (bp), with both primers at least 100 bp from any of the sgRNA target sites (table S15). PCR products were cleaned-up and analyzed by Sanger sequencing (Genewiz). Sanger data files and sgRNA target sequences were input into Inference of CRISPR Edits (ICE) analysis (ice.synthego.com) to determine editing efficiency and to quantify generated indels (*60*). Percentage of alleles edited is expressed as an ice-d score. This score is a measure of how discordant the sanger trace is before versus after the edit. It is a simple and robust estimate of editing efficiency in a pool, especially suited to highly disruptive editing techniques like multiguide.

Identification of essential genes for siRNA and Cas9 knockout screen

We used longitudinal imaging in A549 cells to assess cell viability (fig. S18). For benchmarking, relative cell viability was measured by CellTiter-Glo Luminescent Cell Viability Assay (Promega; G7571) as per manufacturer's instructions. Briefly, two passages postnucleofection A549 siRNA pools cultured in 96-well tissue-culture treated plates (Corning, #3595) were lysed in the CellTIter-Glo reagent, by removing spent media and adding 100 μl of the CellTiter-Glo reagent containing the CellTiter-Glo buffer and CellTiter-Glo Substrate. Cells were placed on an orbital shaker for 2 min on a SpectraMax iD5 (Molecular Devices) and then incubated in the dark at room temperature for 10 min. Completely lysed cells were pipette mixed and 25 μl were transferred to a 384-well assay plate (Corning, #3542). The luminescence was recorded on a SpectraMax iD5 (Molecular Devices) with an integration time of 0.25 s per well. Luminescence readings were all normalized to the without-sgRNA control condition.

To determine cell viability in Caco-2 knockouts we used longitudinal imaging (fig. S18). All gene knockout pools were maintained for a minimum of six passages to determine the effect of loss of protein function on cell fitness before viral infection. Viability was determined through longitudinal imaging and automated image analysis using a Celigo Imaging Cytometer (Celigo). Each gene knockout pool was split in triplicate wells on separate plates. Every day, except the day of seeding, each well was scanned and analyzed using built-in Confluence imaging parameters using autoexposure and autofocus with an offset of −45 μm. Analysis was performed with standard settings except for an intensity threshold setting of 8. Confluency was averaged across three wells and plotted over time. Viability genes were determined as pools that, after six passages, remained <20% confluent 5 days after seeding. Genes deemed essential were excluded from the knockout screen.

Cells, virus, and infections for Caco-2 Cas9 knockout screen

Wild-type and CRISPR-edited Caco-2 cells were grown at 37°C, 5% CO_2 in DMEM, 10% FBS. SARS-CoV-2 stocks were grown and titered on Vero E6 cells as described previously (*61*). Wild-type and CRISPR-edited Caco-2 cell lines were infected with SARS-CoV-2 at a MOI of 0.01 in DMEM supplemented with 2% FBS. Seventy-two hours postinfection, supernatants were harvested and stored at −80°C and the Caco-2 wild-type (WT) and CRISPR knockout (KO) cells were fixed with 10% neutral buffered formalin (NBF) for 1 hour at room temperature to enable further analysis.

Focus-forming assay for Caco-2 Cas9 knockout screen

Vero E6 cells were plated into 96-well plates at confluence (50,000 cells per well) in DMEM supplemented with 10% heat-inactivated FBS (Gibco). Before infection, supernatants from infected Caco-2 WT and CRISPR KO cells were thawed and serially diluted from 10^{-1} to 10^{-8}. Growth media was removed from the Vero E6 cells and 40 μl of each virus dilution was plated. After 1 hour of adsorption at 37°C, 5% CO_2, 40 μl of 2.4% microcrystalline cellulose (MCC) overlay supplemented with DMEM powdered media (Gibco) to a concentration of 1x was added to each well of the 96-well plate to achieve a final MCC overlay concentration of 1.2%. Plates were then incubated at 37°C, 5% CO_2 for 24 hours. The MCC overlay was gently removed and cells were fixed with 10% NBF for 1 hour at room temperature. After removal of NBF, monolayers were washed with ultrapure water and ice-cold 100% methanol/0.3% H_2O_2 was added for 30 min to permeabilize the cells and quench endogenous peroxidase activity. Monolayers were then blocked for 1 hour in PBS with 5% nonfat dry milk (NFDM). After blocking, monolayers were incubated with SARS-CoV N primary antibody (Novus Biologicals; NB100-56576; 1:2000) for 1 hour at room temperature in PBS, 5% NFDM. Monolayers were washed with PBS and incubated with an HRP-conjugated secondary antibody for 1 hour at room temperature in PBS with 5% NFDM. Secondary antibody was removed, monolayers were washed with PBS, and then developed using TrueBlue substrate (KPL) for 30 min. Plates were imaged on a Bio-Rad Chemidoc utilizing a phosphorscreen and foci were counted by eye to calculate focus-forming units per ml (FFU/ml) for each knockout. The original formalin-fixed Caco-2 WT and CRISPR KO cells were stained with DAPI (Thermo Scientific) and imaged on a Cytation 5-plate reader to determine cell viability. Wells containing no cells were excluded from further analyses.

Quantitative analysis and scoring of knockdown and knockout library screens

Virus readout by qPCR (A549-ACE2, expressed as plaque-forming units per milliliter) and focus-forming assay readouts (Caco-2, focus-forming units per milliliter) were processed using the RNAither package (www.bioconductor.org/packages/release/bioc/html/RNAither.html) in the statistical computing environment R. The two datasets were normalized separately, using the following method. The readouts were first log transformed (natural logarithm), and robust *z*-scores [using median and MAD (median absolute deviation) instead of mean and standard deviation] were then calculated for each 96-well plate separately. *z*-scores of multiple replicates of the same perturbation were averaged into a final *z*-score for presentation in Fig. 5. No filtering was done on the basis of differences in replicate *z*-scores, but all replicate scores are individually listed in tables S6 and S7. We suggest consulting the replicate *z*-scores for all genes and perturbations of interest. The A549-ACE2 siRNA screen includes three replicates (or more) of each perturbation, and the Caco-2 CRISPR screen includes two replicates (or more) of each perturbation. The results from the A549-ACE2 screen cover all 332 screened genes (331 SARS-CoV-2 interactors plus ACE2). The results from the

Caco-2 screen cover 286 of the screened genes plus ACE2. The remaining Caco-2 genes were either deemed essential, failed editing, or failed in the focus-forming assay.

Antiviral drug and cytotoxicity assays (A549-ACE2 cells)

In total, 2500 A549-ACE2 cells were seeded into 96- or 384-well plates in DMEM (10% FBS) and incubated for 24 hours at 37°C, 5% CO_2. Two hours before infection, the media was replaced with 120 μl (96-well format) or 50 μl (384-well format) of DMEM (2% FBS) containing the compound of interest at the indicated concentration. At the time of infection, the media was replaced with virus inoculum (MOI 0.1 PFU per cell) and incubated for 1 hour at 37°C, 5% CO_2. After the adsorption period, the inoculum was removed, replaced with 120 μl (96-well format) or 50 μl (384-well format) of drug-containing media, and cells were incubated for an additional 72 hours at 37°C, 5% CO_2. At this point, the cell culture supernatant was harvested, and viral load was assessed by RT-qPCR (as described in the section Viral infection and quantification assay in A549-ACE2 cells). Viability was assayed using the CellTiter-Glo assay following the manufacturer's protocol (Promega). Luminescence was measured in a Tecan Infinity 2000 plate reader, and percentage viability calculated relative to untreated cells (100% viability) and cells lysed with 20% ethanol or 4% formalin (0% viability), included in each experiment.

Antiviral drug and cytotoxicity assays (Vero E6 cells)

Viral growth and cytotoxicity assays in the presence of inhibitors were performed as previously described (*5*). In total, 2000 Vero E6 cells were seeded into 96-well plates in DMEM (10% FBS) and incubated for 24 hours at 37°C, 5% CO_2. Two hours before infection, the medium was replaced with 100 μl of DMEM (2% FBS) containing the compound of interest at concentrations 50% greater than those indicated, including a DMSO control. SARS-CoV-2 virus (100 PFU; MOI 0.025) was added in 50 μl of DMEM (2% FBS), bringing the final compound concentration to those indicated. Plates were then incubated for 48 hours at 37°C. After infection, supernatants were removed, and cells were fixed with 4% formaldehyde for 24 hours before being removed from the BSL3 facility. The cells were then immunostained for the viral NP protein (rabbit antisera produced in the Garcia-Sastre laboratory; 1:10,000) with a DAPI counterstain. Infected cells (488 nm) and total cells (DAPI) were quantified using a Celigo (Nexcelcom) imaging cytometer. Infectivity is measured by the accumulation of viral NP protein in the nucleus of the cells (fluorescence accumulation). Percent infection was quantified as {[(number of infected cells / total cells) − background] × 100}, and the DMSO control was then set to 100% infection for analysis. The IC_{50} and IC_{90} for each experiment was determined using the Prism (GraphPad Software) software. Cytotoxicity measurements were performed using the MTT assay (Roche), according to the manufacturer's instructions. Cytotoxicity was performed in uninfected Vero E6 cells with same compound dilutions and concurrent with viral replication assay. All assays were performed in biologically independent triplicates. Sourcing information for all drugs tested may be found in table S10.

Coimmunoprecipitation assays for ORF9b and Tom70

HEK293T and A549 cells were transfected with the indicated mammalian expression plasmids using Lipofectamine 2000 (Invitrogen) and TransIT-X2 (Mirus Bio), respectively. Twenty-four hours after transfection, cells were harvested and lysed in NP-40 lysis buffer [0.5% Nonidet P 40 Substitute (NP-40; Fluka Analytical), 50 mM Tris-HCl, pH 7.4 at 4°C, 150 mM NaCl, 1 mM EDTA] supplemented with cOmplete mini EDTA-free protease and PhosSTOP phosphatase inhibitor cocktails (Roche). Clarified cell lysates were incubated with Streptactin Sepharose beads (IBA) for 2 hours at 4°C, followed by five washes with NP-40 lysis buffer. Protein complexes were eluted in the SDS loading buffer and were analyzed by Western blotting with the indicated antibodies.

Quantification of Tom70 down-regulation in HeLaM cells overexpressing ORF9b

HeLaM cells were transiently transfected with plasmids encoding GFP-Strep, SARS-CoV-1 ORF9b-Strep, or SARS-CoV-2 ORF9b-Strep. The next day, the cells were fixed using 4% paraformaldehyde and immunostained with antibodies against Strep tag, and Tom20 or Tom70. Representative images for each construct were captured by acquiring a single optical section using a Nikon A1 confocal fitted with a CFI Plan Apochromat VC 60x oil objective (NA 1.4). For image quantification multiple fields of view were captured for each construct using a CFI Super Plan Fluor ELWD 40x objective (NA 0.6). The mean fluorescent intensity for Tom20 and Tom70 was measured by manually drawing a region of interest around each cell using ImageJ. Between 30 and 60 cells were quantified for each construct.

Quantification of Tom70 down-regulation in infected Caco-2 cells

Caco-2 cells were seeded on glass coverslips in triplicate and infected with SARS-CoV-2 at a MOI of 0.1 as described above. At 24 hours postinfection, cells were fixed with 4% paraformaldehyde and immunostained with antibodies against Tom70, Tom20, and ORF9b. For signal quantification images of noninfected and neighboring infected cells were acquired using a LSM800 confocal laser-scanning microscope (Zeiss) equipped with a 63X, 1.4 NA oil objective and the Zen blue software (Zeiss). The mean fluorescence intensity of each cell was measured by ImageJ software. Forty-three cells were quantified for each condition—infected or noninfected—from three independent experiments.

Coexpression and purification of ORF9b-Tom70 (residues 109 to end) complexes

SARS-CoV-2 ORF9b and Tom70 (residues 109 to end) were coexpressed using a pET29-b(+) vector backbone where ORF9b was tag-less and Tom70 had an N-terminal 10XHis-tag and SUMO-tag. LOBSTR *E. coli* cells transformed with the above construct were grown at 37°C until they reached an optical density at 600 nm (OD_{600}) of 0.8, then expression was induced at 37°C with 1 mM IPTG for 4 hours. Frozen cell pellets were resuspended in 25 ml of lysis buffer (200 mM NaCl, 50 mM Tris-HCl pH 8.0, 10% v/v glycerol, 2 mM $MgCl_2$) per liter of cell culture, supplemented with cOmplete protease inhibitor tablets (Roche), 1 mM phenylmethylsulfonyl fluoride (PMSF) (Sigma), 100 μg/ml lysozyme (Sigma), 5 μg/ml DNaseI (Sigma), and then homogenized with an immersion blender (Cuisinart). Cells were lysed by 3x passage through an Emulsiflex C3 cell disruptor (Avestin) at ~103,000 kPa, and the lysate clarified by ultracentrifugation at 100,000 × *g* for 30 min at 4°C. The supernatant was collected, supplemented with 20 mM imidazole, loaded into a gravity flow column containing Ni-NTA superflow resin (Qiagen), and rocked with the resin at 4°C for 1 hour. After allowing the column to drain, resin was rinsed twice with 5 column volumes (cv) of wash buffer [150 mM KCl, 30 mM Tris-HCl pH 8.0, 10% v/v glycerol, 20 mM imidazole, 0.5 mM tris(hydroxypropyl)phosphine (THP, VWR)] supplemented with 2 mM ATP (Sigma) and 4 mM $MgCl_2$, then washed with 5 cv wash buffer with 40 mM imidazole. Resin was then rinsed with 5 cv Buffer A (50 mM KCl, 30 mM Tris-HCl pH 8.0, 5% glycerol, 0.5 mM THP) and protein was eluted with 2 × 2.5 cv Buffer A plus 300 mM imidazole. Elution fractions were combined, supplemented with Ulp1 protease, and rocked at 4°C for 2 hours. Ulp1-digested Ni-NTA eluate was diluted 1:1 with additional Buffer A, loaded into a 50 ml Superloop, and applied to a MonoQ 10/100 column on an Äkta pure system (GE Healthcare) using 100% Buffer A, 0% Buffer B (1000 mM KCl, 30 mM Tris-HCl pH 8.0, 5% glycerol, 0.5 mM THP). The MonoQ column was washed with 0 to 40% Buffer B gradient over 15 cv, peak fractions

were analyzed by SDS-PAGE and the identity of tagless Tom70 (109 to end) and ORF9b proteins confirmed by intact protein MS (Xevo G2-XS Mass Spectrometer, Waters). Peak fractions eluting at ~15% B contained relatively pure Tom70 (109 to end) and ORF9b, and these were concentrated using 10 kDa Amicon centrifugal filter (Millipore) and further purified by size exclusion chromatography using a Superdex 200 increase 10/300 GL column (GE Healthcare) in buffer containing 150 mM KCl, 20 mM HEPES-NaOH pH 7.5, 0.5 mM THP. The sole size-exclusion peak contained both Tom70 (109 to end) and ORF9b, and the center fraction was used directly for cryo-EM grid preparation.

Expression and purification of SARS-CoV-2 ORF9b

ORF9b with N-terminal 10XHis-tag and SUMO-tag was expressed using a pET-29b(+) vector backbone. LOBSTR *E. coli* cells transformed with the above construct were grown at 37°C until they reached an optical density at 600 nm (OD_{600}) of 0.8, then expression was induced at 37°C with 1 mM IPTG for 6 hours. Frozen cell pellets were lysed, homogenized, clarified, and subject to Ni affinity purification as described above for ORF9b-Tom70 complexes, with several small changes. Lysis buffers and Ni-NTA wash buffers contained 500 mM NaCl, and an additional wash step using 10 cv wash buffer plus 0.2% TWEEN20 plus 500 mM NaCl was carried out before the ATP wash. ORF9b was eluted from Ni-NTA resin in Buffer A (50 mM NaCl, 25 mM Tris pH 8.5, 5% glycerol, 0.5 mM THP) supplemented with 300 mM imidazole. This eluate was diluted 1:1 with additional Buffer A, loaded into a 50 ml Superloop, and applied to a MonoQ 10/100 column on an Äkta pure system (GE Healthcare) using 100% Buffer A, 0% Buffer B (1000 mM NaCl, 25mM Tris-HCl pH 8.5, 5% glycerol, 0.5 mM THP). The MonoQ column was washed with 0 to 40% Buffer B gradient over 15 cv, and relatively pure ORF9b eluted at 20 to 25% Buffer B, whereas ORF9b and contaminating proteins eluted at 30 to 35% buffer B. Fractions from these two peaks were combined and incubated with Ulp1 and HRV3C proteases at 4°C for 2 hours, supplemented with 10 mM imidazole, then thrice flowed back through 1 ml of Ni-NTA resin equilibrated with size-exclusion buffer (as above) plus10 mM imidazole. The reverse-Ni purified sample was concentrated using 10 kDa Amicon centrifugal filter and then further purified by size exclusion chromatography using a Superdex 200 increase 10/300 GL column.

Expression and purification of Tom70 (109-end)

Tom70 (109 to end) with N-terminal 10XHis-tag and SUMO-tag and C terminus Spy-tag, HRV-3C protease cleavage site, and eGFP-tag was expressed using a pET-21(+) vector backbone. LOBSTR *E. coli* cells transformed with the above construct were grown at 37°C until they reached an optical density at 600 nm (OD_{600}) of 0.8, then expression was induced at 16°C with 0.5 mM IPTG overnight. The soluble domain of Tom70 [Tom70 (109-end)] was purified as described in (*62*) with some modifications. Frozen cell pellets of LOBSTR *E. coli* transformed with the above construct were resuspended in 50 ml lysis buffer (500 mM NaCl, 20 mM KH_2PO_4 pH 7.5) per liter cell culture, supplemented with 1 mM PMSF (Sigma) and 100 μg/ml, and homogenized. Cells were lysed by 3x passage through an Emulsiflex C3 cell disruptor (Avestin) at ~103,000 kPa, and the lysate clarified by ultracentrifugation at 100,000 × *g* for 30 min at 4°C. The supernatant was collected, supplemented with 20 mM imidazole, loaded into a gravity flow column containing Ni-NTA superflow resin (Qiagen), and rocked with the resin at 4°C for 1 hour. After allowing the column to drain, resin was rinsed twice with 5 column volumes (cv) of wash buffer (500 mM KCl, 20 mM KH_2PO_4 pH 8.0, 20 mM imidazole, 0.5 mM THP) supplemented with 2 mM ATP (Sigma) and 4 mM $MgCl_2$, then washed with 5 cv wash buffer with 40 mM imidazole. Bound Tom70 (109 to end) was then cleaved from the resin by 2-hour incubation with Ulp1 protease in 4 cv elution buffer (150 mM KCl, 20 mM KH_2PO_4 pH 8.0, 5 mM imidazole, 0.5 mM THP). After cleavage with Ulp1, the flow through was collected along with a 2-cv rinse of the resin with additional elution buffer. These fractions were combined and HRV3C protease was added to remove the C-terminal EGFP tag (1:20 HRV3C to Tom70). After 2-hour HRV3C digestion at 4°C, the double-digested Tom70 (109 to end) was concentrated using a 30 kDa Amicon centrifugal filter (Millipore) and further purified by size exclusion chromatography using a Superdex 200 increase 10/300 GL column (GE Healthcare) in buffer containing 150 mM KCl, 20 mM HEPES-NaOH pH 7.5, 0.5 mM THP.

Prediction of SARS-CoV-2 ORF9b internal mitochondrial targeting sequence

ORF9b was analyzed for the presence of an internal mitochondrial targeting sequence (i-MTS) as described in (*63*) using the TargetP-2.0 server (*64*). Sequences corresponding to ORF9b N-terminal truncations of 0 to 62 residues were submitted to the TargetP-2.0 server, and the probability of the peptides containing an MTS plotted against the numbers of residues truncated. A similar analysis using the MitoFates server (*65*) predicted that ORF9b residues 54 to 63 were the most likely to make up a presequence MTS on the basis of their propensity to form a positively charged amphipathic helix. Notably this analysis was consistent with the secondary structure prediction from JPRED (*66*).

Cryo-EM sample preparation and data collection

Three μl of ORF9b-Tom70 complex (12.5 μM) was added to a 400 mesh 1.2/1.3R Au Quantifoil grid previously glow discharged at 15 mA for 30 s. Blotting was performed with a blot force of 0 for 5 s at 4°C and 100% humidity in a FEI Vitrobot Mark IV (ThermoFisher) before plunge freezing into liquid ethane. A total of 1534 118-frame super-resolution movies were collected with a 3 by 3 image-shift collection strategy at a nominal magnification of 105,000x (physical pixel size: 0.834 Å per pixel) on a Titan Krios (ThermoFisher) equipped with a K3 camera and a Bioquantum energy filter (Gatan) set to a slit width of 20 eV. Collection dose rate was 8 electrons per pixel per second for a total dose of 66 electrons per square angstrom. Defocus range was −0.7 to −2.4 μm. Each collection was performed with semiautomated scripts in SerialEM (*67*).

Cryo-EM image processing and model building

We motion corrected 1534 movies using Motioncor2 (*68*), and we imported dose-weighted summed micrographs in cryosparc (version 2.15.0). Then, 1427 micrographs were curated on the basis of contrast transfer function (CTF) fit (better than 5 Å) from a patch CTF job. Template-based particle picking resulted in 2,805,121 particles, and 1,616,691 particles were selected after 2D classification. Five rounds of 3D classification using multiclass ab initio reconstruction and heterogeneous refinement yielded 178,373 particles. Homogeneous refinement of these final particles led to a 3.1-Å electron density map which was used for model building. The reconstruction was filtered by the masked Fourier shell correlation (FSC) and sharpened with a b-factor of −145.

To build the model of Tom70 (109 to end), the crystal structure of *Saccharomyces cerevisiae* Tom71 (PDB ID: 3fp3; sequence identity 25.7%) was first fit into the cryo-EM density as a rigid body in UCSF ChimeraX and then relaxed into the final density using Rosetta FastRelax mover in torsion space. This model, along with a BLAST alignment of the two sequences (*69*), was used as a starting point for manual building using COOT (*70*). After initial building by hand, the regions with poor density fit or geometry were iteratively rebuilt using Rosetta (*71*). ORF9b was built de novo into the final density using COOT, informed and facilitated by the predictions of the TargetP-2.0, MitoFates, and JPRED servers. The ORF9b-Tom70 complex model was submitted to the Namdinator web server (*72*) and further refined in ISOLDE 1.0 (*73*) using the plugin for UCSF ChimeraX (*74*). Final model b-factors were estimated using Rosetta. The model was validated using phenix.validation_cryoem (*75*). The final model contains residues 109 to 272 and 298 to 600 of human Tom70 and 39

to 76 of SARS-CoV-2 ORF9b. Molecular interface between ORF9b and Tom70 was analyzed using the PISA web server (*76*). Figures were prepared using UCSF ChimeraX.

Computational human genetics analysis

To look for genetic variants associated with our list of proteins that had a meaningful impact on SARS-CoV-2 replication, we used the largest proteomic GWAS study to date (*28*). We identified IL17RA as one of the proteins assayed in Sun *et al.*'s proteomic GWAS and observed that it had multiple cis-acting protein quantitative trait loci (pQTLs) at a corrected P value of 1×10^{-5}, where cis-acting is defined as within 1 Mb of the transcription start site of *IL17RA*.

We used the GSMR method (*29*) to perform Mendelian randomization (MR) using near-independent [linkage disequilibrium (LD) R^2 = 0.05, where R^2 is the coefficient of determination] cis-pQTLs for *IL17RA*. The advantage of the GSMR method over conventional MR methods is twofold. First, GSMR performs MR adjusting for any residual correlation between selected genetic variants by default. Second, GSMR has a built-in method called HEIDI (heterogeneity in dependent instruments)–outlier that performs heterogeneity tests in the near-independent genetic instruments and removes potentially pleiotropic instruments (i.e., where there is evidence of heterogeneity at $P < 0.01$). Details of the GSMR and HEIDI method have been published previously (*29*).

Summary statistics generated by COVID-HGI (round 3; www.covid19hg.org/results/) for COVID-19 versus population, hospitalized COVID-19 versus population and hospitalized COVID-19 versus nonhospitalized COVID-19 were used for *IL17RA* MR analysis. We used the 1000 genomes phase 3 European population genotype data to derive the LD correlation matrix for this analysis. The phenotype definitions as provided by COVID-HGI are as follows. COVID-19 versus population: Case, individuals with laboratory confirmation of SARS-CoV-2 infection, EHR/ICD coding/Physician-confirmed COVID-19, or self-reported COVID-19 positive; control, everybody that is not a case. Hospitalized COVID-19 versus population: case, hospitalized, laboratory confirmed SARS-CoV-2 infection or hospitalization due to COVID-19-related symptoms; control, everybody that is not a case, e.g., population. Hospitalized COVID-19 versus nonhospitalized COVID-19: case, hospitalized, laboratory confirmed SARS-CoV-2 infection or hospitalization due to COVID-19-related symptoms; control, laboratory confirmed SARS-CoV-2 infection and not hospitalized 21 days after the test.

Infections and treatments for IL-17A treatment studies

The WA-1 strain (BEI resources) of SARS-CoV-2 was used for all experiments. All live virus experiments were performed in a BSL3 laboratory. SARS-CoV-2 stocks were passaged in Vero E6 cells (ATCC) and titer was determined via plaque assay on Vero E6 cells as previously described (*77*). Briefly, virus was diluted 1:10^2 to 1:10^6 and incubated for 1 hour on Vero E6 cells before an overlay of Avicel and complete DMEM (Sigma Aldrich, SLM-241) was added. After incubation at 37°C for 72 hours, the overlay was removed and cells were fixed with 10% formalin, stained with crystal violet, and counted for plaque formation. SARS-CoV-2 infections of A549-ACE2 cells were done at a MOI of 0.05 for 24 hours. Inhibitors and cytokines were added concurrently with virus. All infections were done in technical triplicate. Cells were treated with the following compounds: Remdesivir (SELLECK CHEMICALS LLC, S8932) and IL-17A (Millipore-Sigma, SRP0675).

RNA extraction, RT, and RT-qPCR for IL-17A treatment studies

Total RNA from samples was extracted using the Direct-zol RNA kit (Zymogen, R2060) and quantified using the NanoDrop 2000c (ThermoFisher). cDNA was generated using 500 ng of RNA from infected A549-ACE2 cells with Superscript III reverse transcription (ThermoFisher, 18080-044) and oligo(dT)$_{12\text{-}18}$ (ThermoFisher, 18418-012) and random hexamer primers (ThermoFisher, S0142). RT-qPCR reactions were performed on a CFX384 (BioRad) and delta cycle threshold (ΔCt) was determined relative to RPL13A levels. Viral detection levels and target host genes in treated samples were normalized to water-treated controls. The SYBR green qPCR reactions contained 5 μl of 2x Maxima SYBR green/Rox qPCR Master Mix (ThermoFisher; K0221), 2 μl of diluted cDNA, and 1 nmol of both forward and reverse primers, in a total volume of 10 μl. The reactions were run as follows: 50°C for 2 min and 95°C for 10 min, followed by 40 cycles of 95°C for 5 s and 62°C for 30 s. Primer efficiencies were ~100%. Dissociation curve analysis after the end of the PCR confirmed the presence of a single and specific product. RT-qPCR primers were used against the SARS-CoV-2 E gene (PF_042_nCoV_E_F: ACAGGTACGTTAATAGTTAATAGCGT; PF_042_nCoV_E_R: ATATTGCAGCAGTACGCACACA), the CXCL8 gene (CXCL8 For: ACTGAGAGTGATTGAGAGTGGAC; CXCL8 Rev: AACCCTCTGCACCCAGTTTTC), and the RPL13A gene (RPL13A For: CCTGGAGGAGAAGAGGAAAGAGA; RPL13A Rev: TTGAGGACCTCTGTGTATTTGTCAA).

Transfections for IL-17A treatment studies

HEK293T cells were seeded 5×10^5cells per well (in 6-well plate) or 3×10^6 cells per 10-cm^2 plates. The next day, 2 or 10 μg of plasmids was transfected using X-tremeGENE 9 DNA Transfection Reagent (Roche) in 6-well plate or 10-cm^2 plates, respectively. For IL-17A (Millipore-Sigma, SRP0675) incubation in cells, 0.5 μg of IL-17A was treated either before or after transfection and incubated at 37°C. After 48 hours, cells were collected by trypsinization. For IL-17A incubation with cell lysates, transfected cell lysates were incubated in the presence of 0.5 or 5 μg/ml IL-17A at 4°C on a rotator overnight. Plasmids pLVX-EF1alpha–SARS-CoV-2–orf8-2xStrep-IRES-Puro (ORF8) and pLVX-EF1alpha-eGFP-2xStrep-IRES-Puro (EGFP-Strep) were a gift from N. J. Krogan. (Addgene plasmid #141390, 141395) (*5*). pLVX-EF1alpha- IRES-Puro (Vector) was obtained from Takara/Clontech.

SARS-CoV-2 ORF8 and IL17RA coimmunoprecipitation

Transfected and treated HEK293T cells were pelleted and washed in cold D-PBS and later resuspended in Flag-IP Buffer (50 mM Tris HCl, pH 7.4, with 150 mM NaCl, 1 mM EDTA, and 1% NP-40) with 1x HALT (ThermoFisher Scientific, 78429), incubated with buffer for 15 min on ice then centrifuged at 13,000 rpm for 5 min. The supernatant was collected and 1 mg of protein was used for immunoprecipitation (IP) with 100 μl of Streptactin Sepharose (IBA, 2-1201-010) on a rotor overnight at 4°C. Immunoprecipitates were washed five times with Flag-IP buffer and eluted with 1x Buffer E (100 mM Tris-Cl, 150 mM NaCl, 1 mM EDTA, 2.5 mM Desthiobiotin). Eluate was diluted with 1x-NuPAGE (ThermoFisher Scientific, #NP0008) LDS Sample Buffer with 2.5% β-Mercaptoethanol and blotted for targeted antibodies. Antibodies used were Strep tag II (Qiagen, #34850), B-Actin (Sigma, #A5316), and IL17RA (Cell Signaling, #12661S).

Computational docking of PGES-2 and Nsp7

A model for human PGES-2 dimer was constructed by homology using MODELER (*78*) from the crystal structure of *Macaca fascularis* mPGES-2 [PDB ID: 1Z9H (*79*); 98% sequence identity] bound to indomethacin. Indomethacin was removed from the structure utilized for docking. The structure of SARS-CoV-2 Nsp7 was extracted from PDB ID 7BV2 (*80*). Docking models were produced using ClusPro (*81*), ZDock (*82*), HDock (*83*), Gramm-X (*84*), SwarmDock (*85*), and PatchDock (*86*) with SOAP-PP score (*87*). For each protocol, up to 100 top scoring models were extracted (fewer for those that do not report >100 models); for PatchDock, models with SOAP-PP z-scores >3.0 were used (fig. S23A). The 420 models were clustered at 4.0-Å RMSD, resulting in 127 clusters. The two largest clusters, composed of 192 models, are related by dimer symmetry. All other clusters contain <15 models.

Assessment of positive selection signatures in SIGMAR1

SIGMAR1 protein alignments were generated from whole-genome sequences of 359 mammals

curated by the Zoonomia consortium. Protein alignments were generated with TOGA (https://github.com/hillerlab/TOGA), and missing sequence gaps were refined with CACTUS (*88*, *89*). Branches undergoing positive selection were detected with the branch-site test aBSREL (*90*) implemented in the HyPhy package (*90*, *91*). PhyloP was used to detect codons undergoing accelerated evolution along branches detected as undergoing positive selection by aBSREL relative to the neutral evolution rate in mammals, determined using phyloFit on third nucleotide positions of codons which are assumed to evolve neutrally. *P* values from phyloP were corrected for multiple tests using the Benjamini-Hochberg method (*92*). PhyloFit and phyloP are both part of the PHAST package version 1.4 (*93*, *94*).

Comparative SARS-CoV-1 inhibition by amiodarone

SARS-CoV-1 (Urbani) drug screens were performed with Vero E6 cells (ATCC #1568, Manassas, VA) cultured in DMEM (Quality Biological), supplemented with 10% (v/v) heat-inactivated FBS (Sigma), 1% (v/v) penicillin-streptomycin (Gemini Bio-products), and 1% (v/v) L-glutamine (2 mM final concentration, Gibco). Cells were plated in opaque 96-well plates 1 day before infection. Drugs were diluted from stock to 50 μM and an 8-point 1:2 dilution series prepared in duplicate in Vero Media. Every compound dilution and control were normalized to contain the same concentration of drug vehicle (e.g., DMSO). Cells were pretreated with drug for 2 hours at 37°C (5% CO2) before infection with SARS-CoV-1 at MOI 0.01. In addition to plates that were infected, parallel plates were left uninfected to monitor cytotoxicity of drug alone. All plates were incubated at 37°C (5% CO2) for 3 days before performing CellTiter-Glo (CTG) assays as per the manufacturer's instruction (Promega, Madison, WI). Luminescence was read on a BioTek Synergy HTX plate reader (BioTek Instruments Inc., Winooski, VT) using the Gen5 software (version 7.07, Biotek Instruments Inc., Winooski, VT).

Real-world data source and analysis

This study used deidentified patient-level records from HealthVerity's Marketplace dataset, a nationally representative dataset covering >300 million patients with medical and pharmacy records from >60 health care data sources in the United States. The current study used data from 738,933 patients with documented COVID-19 infection between 1 March 2020 and 17 August 2020, defined as a positive or presumptive positive viral laboratory test result or an International Classification of Diseases, 10th Revision, Clinical Modification (ICD-10-CM) diagnosis code of U07.1 (COVID-19).

For this population, we analyzed medical claims, pharmacy claims, laboratory data, and hospital chargemaster data containing diagnoses, procedures, medications, and COVID-19 laboratory results from both inpatient and outpatient settings. Claims data included open (unadjudicated) claims sourced in near-real time from practice management and billing systems, claims clearinghouses, and laboratory chains, as well as closed (adjudicated) claims encompassing all major U.S. payer types (commercial, Medicare, and Medicaid). For inpatient treatment evaluations, we used linked hospital chargemaster data containing records of all billable procedures, medical services, and treatments administered in hospital settings. Linkage of patient-level records across these data types provides a longitudinal view of baseline health status, medication use, and COVID-19 progression for each patient under study. Data for this study covered the period of 1 December 2018 through 17 August 2020. All analyses were conducted with the Aetion Evidence Platform version r4.6.

This study was approved by the New England institutional review board (IRB) (no. 1-9757-1). Medical records constitute protected health information and can be made available to qualified individuals on reasonable request.

Observation of hospitalization outcomes in outpatient new users of indomethacin (treatment arm) versus celecoxib (active comparator) using real-world data

We used an incident (new) user, active comparator design (*95*, *96*) to assess the risk of hospitalization among newly diagnosed COVID-19 patients who were subsequently treated with indomethacin or the comparator agent, celecoxib. Patients were required to have COVID-19 infection recorded in an outpatient setting during the study period of 1 March 2020 to 17 August 2020 and occurring in the 21 days before (and including) the date of indomethacin or celecoxib treatment initiation. Prevalent users of prescription-only NSAIDs (any prescription fill for indomethacin, celecoxib, ketoprofen, meloxicam, sulindac, or piroxicam 60 days prior) and patients hospitalized in the 21 days before and including the date of treatment initiation were excluded from this analysis.

Using RSS, patients treated with indomethacin were matched at a 1:1 ratio to controls randomly selected among patients treated with celecoxib, with direct matching on calendar date of treatment (±7 days), age (±5 years), sex, Charlson comorbidity index (exact) (*97*), time since confirmed COVID-19 (±5 days), and disease severity based on the highest-intensity COVID-19–related health service in the 7 days before and including the date of treatment initiation (laboratory service only versus outpatient medical visit versus emergency department visit) and symptom profile in the 21 days before and including the date of treatment initiation (recorded symptoms versus none). This risk-set–sampled population was further matched on a PS (*33*) estimated using logistic regression with 24 demographic and clinical risk factors, including covariates related to baseline medical history and COVID-19 severity in the 21 days before treatment (table S11). Balance between indomethacin and celecoxib treatment groups was evaluated by comparison of absolute standardized differences in covariates, with an absolute standardized difference of <0.2 indicating good balance between the treatment groups (*98*).

The primary analysis was an intention-to-treat design, with follow-up beginning 1 day after indomethacin or celecoxib initiation and ending on the earliest occurrence of 30 days of follow-up reached or end of patient data. ORs for the primary outcome of all-cause inpatient hospitalization were estimated for the RSS-plus-PS–matched population as well as for the RSS-matched population. Our primary outcome definition required a record of inpatient hospital admission with a resulting inpatient stay; as a sensitivity, a broader outcome definition captured any hospital visit (defined with revenue and place of service codes).

Observation of mechanical ventilation outcomes in inpatient new users of typical antipsychotics (treatment arm) versus atypical antipsychotics (active comparator) using real-world data

We used an incident user, active comparator design (*95*, *96*) to assess the risk of mechanical ventilation among hospitalized COVID-19 patients treated with typical or atypical antipsychotics in an inpatient setting. See table S11 for a list of drugs included in each category. To permit assessment of day-level in-hospital confounders and outcomes, this analysis was restricted to hospitalized patients observable in hospital chargemaster data. Prevalent users of typical or atypical antipsychotics (any prescription fill or chargemaster-documented use in 60 days prior) and patients with evidence of mechanical ventilation in the 21 days before and including the date of treatment initiation were excluded from this analysis.

Using RSS, hospitalized patients treated with typical antipsychotics were matched at a 1:1 ratio to controls randomly selected among patients treated with atypical antipsychotics, with direct matching (1:1 fixed ratio) on calendar date of treatment (±7 days), age (±5 years), sex, Charlson comorbidity index (exact) (*97*), time since hospital admission, and disease severity as defined with a simplified version of the World Health Organization's ordinal scale for clinical improvement (*99*). This risk-set–sampled population was further matched on a PS estimated using logistic regression with 36 demographic and clinical risk factors, including covariates related to baseline medical history, admitting status, and disease severity at treatment (table S11). Balance between

typical and atypical treatment groups was evaluated by comparison of absolute standardized differences in covariates, with an absolute standardized difference of <0.2 indicating good balance between the treatment groups (*98*).

The primary analysis was an intention-to-treat design, with follow up beginning 1 day after the date of typical or atypical antipsychotic treatment initiation and ending on the earliest occurrence of 30 days of follow-up reached, discharge from hospital, or end of patient data. ORs for the primary outcome of inpatient mechanical ventilation were estimated for the RSS-plus-PS–matched population as well as for the RSS-matched population.

REFERENCES AND NOTES

1. J. Liu *et al*., A comparative overview of COVID-19, MERS and SARS: Review article. *Int. J. Surg.* **81**, 1–8 (2020). doi: 10.1016/j.ijsu.2020.07.032; pmid: 32730205
2. J. H. Beigel *et al*., Remdesivir for the treatment of Covid-19—Final report. *N. Engl. J. Med.* **383**, 1813–1826 (2020). doi: 10.1056/NEJMoa2007764
3. RECOVERY Collaborative Group, Dexamethasone in Hospitalized Patients with Covid-19 - Preliminary Report. *N. Engl. J. Med.* 10.1056/nejmoa2021436 (2020). doi: 10.1056/nejmoa2021436; pmid: 32678530
4. M. Becerra-Flores, T. Cardozo, SARS-CoV-2 viral spike G614 mutation exhibits higher case fatality rate. *Int. J. Clin. Pract.* **74**, e13525 (2020). doi: 10.1111/ijcp.13525; pmid: 32374903
5. D. E. Gordon *et al*., A SARS-CoV-2 protein interaction map reveals targets for drug repurposing. *Nature* **583**, 459–468 (2020). doi: 10.1038/s41586-020-2286-9; pmid: 32353859
6. G. Teo *et al*., SAINTexpress: Improvements and additional features in Significance Analysis of INTeractome software. *J. Proteomics* **100**, 37–43 (2014). doi: 10.1016/j.jprot.2013.10.023; pmid: 24513533
7. S. Jäger *et al*., Global landscape of HIV-human protein complexes. *Nature* **481**, 365–370 (2011). doi: 10.1038/nature10719; pmid: 22190034
8. J. C. Young, N. J. Hoogenraad, F. U. Hartl, Molecular chaperones Hsp90 and Hsp70 deliver preproteins to the mitochondrial import receptor Tom70. *Cell* **112**, 41–50 (2003). doi: 10.1016/S0092-8674(02)01250-3; pmid: 12526792
9. R. Lin, S. Paz, J. Hiscott, Tom70 imports antiviral immunity to the mitochondria. *Cell Res.* **20**, 971–973 (2010). doi: 10.1038/cr.2010.113; pmid: 20680033
10. B. Wei *et al*., Tom70 mediates Sendai virus-induced apoptosis on mitochondria. *J. Virol.* **89**, 3804–3818 (2015). doi: 10.1128/JVI.02959-14; pmid: 25609812
11. A. M. Edmonson, D. K. Mayfield, V. Vervoort, B. R. DuPont, G. Argyropoulos, Characterization of a human import component of the mitochondrial outer membrane, TOMM70A. *Cell Commun. Adhes.* **9**, 15–27 (2002). doi: 10.1080/15419060212186; pmid: 12200962
12. M. J. Baker, A. E. Frazier, J. M. Gulbis, M. T. Ryan, Mitochondrial protein-import machinery: Correlating structure with function. *Trends Cell Biol.* **17**, 456–464 (2007). doi: 10.1016/j.tcb.2007.07.010; pmid: 17825565
13. J. Brix, K. Dietmeier, N. Pfanner, Differential recognition of preproteins by the purified cytosolic domains of the mitochondrial import receptors Tom20, Tom22, and Tom70. *J. Biol. Chem.* **272**, 20730–20735 (1997). doi: 10.1074/jbc.272.33.20730; pmid: 9252394
14. J. Brix *et al*., The mitochondrial import receptor Tom70: Identification of a 25 kDa core domain with a specific binding site for preproteins. *J. Mol. Biol.* **303**, 479–488 (2000). doi: 10.1006/jmbi.2000.4120; pmid: 11054285
15. R. D. Mills *et al*., Domain organization of the monomeric form of the Tom70 mitochondrial import receptor. *J. Mol. Biol.* **388**, 1043–1058 (2009). doi: 10.1016/j.jmb.2009.03.070; pmid: 19358854
16. S. D. Weeks, S. De Graef, A. Munawar, X-ray Crystallographic Structure of Orf9b from SARS-CoV-2 (2020); https://doi.org/10.2210/pdb6z4u/pdb.
17. M. Bouhaddou *et al*., The Global Phosphorylation Landscape of SARS-CoV-2 Infection. *Cell* **182**, 685–712.e19 (2020). doi: 10.1016/j.cell.2020.06.034; pmid: 32645325
18. J. Li, X. Qian, J. Hu, B. Sha, Molecular chaperone Hsp70/Hsp90 prepares the mitochondrial outer membrane translocon receptor Tom71 for preprotein loading. *J. Biol. Chem.* **284**, 23852–23859 (2009). doi: 10.1074/jbc.M109.023986; pmid: 19581297
19. X.-Y. Liu, B. Wei, H.-X. Shi, Y.-F. Shan, C. Wang, Tom70 mediates activation of interferon regulatory factor 3 on mitochondria. *Cell Res.* **20**, 994–1011 (2010). doi: 10.1038/cr.2010.103; pmid: 20628368
20. Y. Liu *et al*., Elevated plasma levels of selective cytokines in COVID-19 patients reflect viral load and lung injury. *Natl. Sci. Rev.* **7**, 1003–1011 (2020). doi: 10.1093/nsr/nwaa037
21. C. Huang *et al*., Clinical features of patients infected with 2019 novel coronavirus in Wuhan, China. *Lancet* **395**, 497–506 (2020). doi: 10.1016/S0140-6736(20)30183-5; pmid: 31986264
22. C. Qin *et al*., Dysregulation of Immune Response in Patients With Coronavirus 2019 (COVID-19) in Wuhan, China. *Clin. Infect. Dis.* **71**, 762–768 (2020). doi: 10.1093/cid/ciaa248; pmid: 32161940
23. G. Chen *et al*., Clinical and immunological features of severe and moderate coronavirus disease 2019. *J. Clin. Invest.* **130**, 2620–2629 (2020). doi: 10.1172/JCI137244; pmid: 32217835
24. M. Zaretsky, R. Etzyoni, J. Kaye, L. Sklair-Tavron, A. Aharoni, Directed Evolution of a Soluble Human IL-17A Receptor for the Inhibition of Psoriasis Plaque Formation in a Mouse Model. *Chem. Biol.* **20**, 202–211 (2013). doi: 10.1016/j.chembiol.2012.11.012
25. M. Sohda *et al*., Identification of a soluble isoform of human IL-17RA generated by alternative splicing. *Cytokine* **64**, 642–645 (2013). doi: 10.1016/j.cyto.2013.09.012
26. J. Lokau, C. Garbers, Biological functions and therapeutic opportunities of soluble cytokine receptors. *Cytokine Growth Factor Rev.* **55**, 94–108 (2020). doi: 10.1016/j.cytogfr.2020.04.003
27. M. Sammel *et al.*, Differences in Shedding of the Interleukin-11 Receptor by the Proteases ADAM9, ADAM10, ADAM17, Meprin α, Meprin β and MT1-MMP. *Int. J. Mol. Sci.* **20**, 3677 (2019). doi: 10.3390/ijms20153677
28. B. B. Sun *et al*., Genomic atlas of the human plasma proteome. *Nature* **558**, 73–79 (2018). doi: 10.1038/s41586-018-0175-2; pmid: 29875488
29. Z. Zhu *et al*., Causal associations between risk factors and common diseases inferred from GWAS summary data. *Nat. Commun.* **9**, 224 (2018). doi: 10.1038/s41467-017-02317-2; pmid: 29335400
30. The COVID-19 Host Genetics Initiative, The COVID-19 Host Genetics Initiative, a global initiative to elucidate the role of host genetic factors in susceptibility and severity of the SARS-CoV-2 virus pandemic. *Eur. J. Hum. Genet.* **28**, 715–718 (2020). doi: 10.1038/s41431-020-0636-6; pmid: 32404885
31. B. E. Young, Effects of a major deletion in the SARS-CoV-2 genome on the severity of infection and the inflammatory response: An observational cohort study. *Lancet* **396**, 603–611 (2020). doi: 10.1016/S0140-6736(20)31757-8
32. C. Amici *et al*., Indomethacin has a potent antiviral activity against SARS coronavirus. *Antivir. Ther.* **11**, 1021–1030 (2006). pmid: 17302372
33. P. R. Rosenbaum, D. B. Rubin, The central role of the propensity score in observational studies for causal effects. *Biometrika* **70**, 41–55 (1983). doi: 10.1093/biomet/70.1.41
34. C. Abate, P. D. Mosier, F. Berardi, R. A. Glennon, A structure-affinity and comparative molecular field analysis of sigma-2 (σ2) receptor ligands. *Cent. Nerv. Syst. Agents Med. Chem.* **9**, 246–257 (2009). doi: 10.2174/1871524910909030246; pmid: 20021358
35. R. A. Glennon, Sigma receptor ligands and the use thereof, U.S. Patent 6,057,371 (2000); https://patentimages.storage.googleapis.com/dc/36/68/73f4ccdac4c973/US6057371.pdf.
36. R. R. Matsumoto, B. Pouw, Correlation between neuroleptic binding to σ_1 and σ_2 receptors and acute dystonic reactions. *Eur. J. Pharmacol.* **401**, 155–160 (2000). doi: 10.1016/S0014-2999(00)00430-1; pmid: 10924920
37. M. Dold, M. T. Samara, C. Li, M. Tardy, S. Leucht, Haloperidol versus first-generation antipsychotics for the treatment of schizophrenia and other psychotic disorders. *Cochrane Database Syst. Rev.* **1**, CD009831 (2015). doi: 10.1002/14651858.CD009831.pub2; pmid: 25592299
38. F. F. Moebius *et al*., Pharmacological analysis of sterol delta8-delta7 isomerase proteins with [3H]ifenprodil. *Mol. Pharmacol.* **54**, 591–598 (1998). doi: 10.1124/mol.54.3.591; pmid: 9730919
39. E. Gregori-Puigjané *et al*., Identifying mechanism-of-action targets for drugs and probes. *Proc. Natl. Acad. Sci. U.S.A.* **109**, 11178–11183 (2012). doi: 10.1073/pnas.1204524109; pmid: 22711801
40. Z. Hubler *et al*., Accumulation of 8,9-unsaturated sterols drives oligodendrocyte formation and remyelination. *Nature* **560**, 372–376 (2018). doi: 10.1038/s41586-018-0360-3; pmid: 30046109
41. F. F. Moebius, R. J. Reiter, M. Hanner, H. Glossmann, High affinity of sigma 1-binding sites for sterol isomerization inhibitors: Evidence for a pharmacological relationship with the yeast sterol C8-C7 isomerase. *Br. J. Pharmacol.* **121**, 1–6 (1997). doi: 10.1038/sj.bjp.0701079; pmid: 9146879
42. H.-W. Jiang *et al*., SARS-CoV-2 Orf9b suppresses type I interferon responses by targeting TOM70. *Cell. Mol. Immunol.* **17**, 998–1000 (2020). doi: 10.1038/s41423-020-0514-8; pmid: 32728199
43. J. J. Almagro Armenteros, C. K. Sønderby, S. K. Sønderby, H. Nielsen, O. Winther, DeepLoc: Prediction of protein subcellular localization using deep learning. *Bioinformatics* **33**, 3387–3395 (2017). doi: 10.1093/bioinformatics/btx431; pmid: 29036616
44. C. Chiva *et al*., QCloud: A cloud-based quality control system for mass spectrometry-based proteomics laboratories. *PLOS ONE* **13**, e0189209 (2018). doi: 10.1371/journal.pone.0189209; pmid: 29324744
45. J. Cox, M. Mann, MaxQuant enables high peptide identification rates, individualized p.p.b.-range mass accuracies and proteome-wide protein quantification. *Nat. Biotechnol.* **26**, 1367–1372 (2008). doi: 10.1038/nbt.1511; pmid: 19029910
46. M. Giurgiu *et al*., CORUM: The comprehensive resource of mammalian protein complexes-2019. *Nucleic Acids Res.* **47**, D559–D563 (2019). doi: 10.1093/nar/gky973; pmid: 30357367
47. E. L. Huttlin *et al*., The BioPlex Network: A Systematic Exploration of the Human Interactome. *Cell* **162**, 425–440 (2015). doi: 10.1016/j.cell.2015.06.043; pmid: 26186194
48. G. Yu, L.-G. Wang, Y. Han, Q.-Y. He, clusterProfiler: An R package for comparing biological themes among gene clusters. *OMICS* **16**, 284–287 (2012). doi: 10.1089/omi.2011.0118; pmid: 22455463
49. M. Remmert, A. Biegert, A. Hauser, J. Söding, HHblits: Lightning-fast iterative protein sequence searching by HMM-HMM alignment. *Nat. Methods* **9**, 173–175 (2011). doi: 10.1038/nmeth.1818; pmid: 22198341
50. J. Yang *et al*., Improved protein structure prediction using predicted interresidue orientations. *Proc. Natl. Acad. Sci. U.S.A.* **117**, 1496–1503 (2020). doi: 10.1073/pnas.1914677117; pmid: 31896580
51. Y. Zhai *et al*., Insights into SARS-CoV transcription and replication from the structure of the nsp7-nsp8 hexadecamer. *Nat. Struct. Mol. Biol.* **12**, 980–986 (2005). doi: 10.1038/nsmb999; pmid: 16228002
52. A. Waterhouse *et al*., SWISS-MODEL: Homology modelling of protein structures and complexes. *Nucleic Acids Res.* **46**, W296–W303 (2018). doi: 10.1093/nar/gky427; pmid: 29788355
53. J. Durairaj, M. Akdel, D. de Ridder, A. D. J. van Dijk, Geometricus Represents Protein Structures as Shape-mers Derived from Moment Invariants. bioRxiv 2020.09.07.285569 [Preprint]. 8 September 2020. .doi: 10.1101/2020.09.07.285569
54. M. Akdel, J. Durairaj, D. de Ridder, A. D. J. van Dijk, Caretta - A multiple protein structure alignment and feature extraction suite. *Comput. Struct. Biotechnol. J.* **18**, 981–992 (2020). doi: 10.1016/j.csbj.2020.03.011; pmid: 32368333
55. P. Shannon *et al*., Cytoscape: A software environment for integrated models of biomolecular interaction networks. *Genome Res.* **13**, 2498–2504 (2003). doi: 10.1101/gr.1239303; pmid: 14597658
56. R. T. Pillich, J. Chen, V. Rynkov, D. Welker, D. Pratt, NDEx: A Community Resource for Sharing and Publishing of Biological Networks. *Methods Mol. Biol.* **1558**, 271–301 (2017). doi: 10.1007/978-1-4939-6783-4_13; pmid: 28150243
57. D. K. W. Chu *et al*., Molecular Diagnosis of a Novel Coronavirus (2019-nCoV) Causing an Outbreak of Pneumonia. *Clin. Chem.* **66**, 549–555 (2020). doi: 10.1093/clinchem/hvaa029; pmid: 32031583
58. K. J. Livak, T. D. Schmittgen, Analysis of relative gene expression data using real-time quantitative PCR and the

2(-Delta Delta C(T)) Method. *Methods* **25**, 402–408 (2001). doi: 10.1006/meth.2001.1262; pmid: 11846609
59. R. Stoner, T. Maures, D. Conant, Methods and systems for guide RNA design and use, U.S. Patent 2019/0382797 A1 (2019); https://patentimages.storage.googleapis.com/95/c7/43/3d48387ce0f116/US20190382797A1.pdf.
60. T. Hsiau, D. Conant, N. Rossi, T. Maures, K. Waite, J. Yang, S. Joshi, R. Kelso, K. Holden, B. L. Enzmann, R. Stoner, Inference of CRISPR Edits from Sanger Trace Data. bioRxiv 251082 [Preprint]. 10 August 2018. .doi: 10.1101/251082
61. A. S. Jureka, J. A. Silvas, C. F. Basler, Propagation, Inactivation, and Safety Testing of SARS-CoV-2. *Viruses* **12**, 622 (2020). doi: 10.3390/v12060622; pmid: 32517266
62. A. C. Y. Fan, M. K. Bhangoo, J. C. Young, Hsp90 functions in the targeting and outer membrane translocation steps of Tom70-mediated mitochondrial import. *J. Biol. Chem.* **281**, 33313–33324 (2006). doi: 10.1074/jbc.M605250200; pmid: 16968702
63. S. Backes *et al*., Tom70 enhances mitochondrial preprotein import efficiency by binding to internal targeting sequences. *J. Cell Biol.* **217**, 1369–1382 (2018). doi: 10.1083/jcb.201708044; pmid: 29382700
64. J. J. Almagro Armenteros *et al*., Detecting sequence signals in targeting peptides using deep learning. *Life Sci. Alliance* **2**, e201900429 (2019). doi: 10.26508/lsa.201900429; pmid: 31570514
65. Y. Fukasawa *et al*., MitoFates: Improved prediction of mitochondrial targeting sequences and their cleavage sites. *Mol. Cell. Proteomics* **14**, 1113–1126 (2015). doi: 10.1074/mcp.M114.043083; pmid: 25670805
66. A. Drozdetskiy, C. Cole, J. Procter, G. J. Barton, JPred4: A protein secondary structure prediction server. *Nucleic Acids Res.* **43**, W389–W394 (2015). doi: 10.1093/nar/gkv332; pmid: 25883141
67. D. N. Mastronarde, Automated electron microscope tomography using robust prediction of specimen movements. *J. Struct. Biol.* **152**, 36–51 (2005). doi: 10.1016/j.jsb.2005.07.007; pmid: 16182563
68. S. Q. Zheng *et al*., MotionCor2: Anisotropic correction of beam-induced motion for improved cryo-electron microscopy. *Nat. Methods* **14**, 331–332 (2017). doi: 10.1038/nmeth.4193; pmid: 28250466
69. S. F. Altschul *et al*., Gapped BLAST and PSI-BLAST: A new generation of protein database search programs. *Nucleic Acids Res.* **25**, 3389–3402 (1997). doi: 10.1093/nar/25.17.3389; pmid: 9254694
70. P. Emsley, K. Cowtan, Coot: Model-building tools for molecular graphics. *Acta Cryst.* **D60**, 2126–2132 (2004). doi: 10.1107/S0907444904019158; pmid: 15572765
71. R. Y.-R. Wang *et al*., Automated structure refinement of macromolecular assemblies from cryo-EM maps using Rosetta. *eLife* **5**, e17219 (2016). doi: 10.7554/eLife.17219; pmid: 27669148
72. R. T. Kidmose *et al*., *Namdinator* - automatic molecular dynamics flexible fitting of structural models into cryo-EM and crystallography experimental maps. *IUCrJ* **6**, 526–531 (2019). doi: 10.1107/S2052252519007619; pmid: 31316797
73. T. I. Croll, ISOLDE: A physically realistic environment for model building into low-resolution electron-density maps. *Acta Cryst.* **D74**, 519–530 (2018). doi: 10.1107/S2059798318002425; pmid: 29872003
74. T. D. Goddard *et al*., UCSF ChimeraX: Meeting modern challenges in visualization and analysis. *Protein Sci.* **27**, 14–25 (2018). doi: 10.1002/pro.3235; pmid: 28710774
75. P. V. Afonine *et al*., New tools for the analysis and validation of cryo-EM maps and atomic models. *Acta Cryst.* **D74**, 814–840 (2018). doi: 10.1107/S2059798318009324; pmid: 30198894
76. E. Krissinel, K. Henrick, Inference of macromolecular assemblies from crystalline state. *J. Mol. Biol.* **372**, 774–797 (2007). doi: 10.1016/j.jmb.2007.05.022; pmid: 17681537
77. A. N. Honko, N. Storm, D. J. Bean, J. H. Vasquez, S. N. Downs, A. Griffiths, Rapid Quantification and Neutralization Assays for Novel Coronavirus SARS-CoV-2 Using Avicel RC-591 Semi-Solid Overlay. *Preprints* 2020050264 [Preprint]. 16 May 2020. www.preprints.org/manuscript/202005.0264/v1.
78. A. Šali, T. L. Blundell, Comparative protein modelling by satisfaction of spatial restraints. *J. Mol. Biol.* **234**, 779–815 (1993). doi: 10.1006/jmbi.1993.1626; pmid: 8254673
79. T. Yamada, J. Komoto, K. Watanabe, Y. Ohmiya, F. Takusagawa, Crystal structure and possible catalytic mechanism of microsomal prostaglandin E synthase type 2 (mPGES-2). *J. Mol. Biol.* **348**, 1163–1176 (2005). doi: 10.1016/j.jmb.2005.03.035; pmid: 15854652
80. W. Yin *et al*., Structural basis for inhibition of the RNA-dependent RNA polymerase from SARS-CoV-2 by remdesivir. *Science* **368**, 1499–1504 (2020). doi: 10.1126/science.abc1560; pmid: 32358203
81. D. Kozakov *et al*., The ClusPro web server for protein-protein docking. *Nat. Protoc.* **12**, 255–278 (2017). doi: 10.1038/nprot.2016.169; pmid: 28079879
82. B. G. Pierce *et al*., ZDOCK server: Interactive docking prediction of protein-protein complexes and symmetric multimers. *Bioinformatics* **30**, 1771–1773 (2014). doi: 10.1093/bioinformatics/btu097; pmid: 24532726
83. Y. Yan, H. Tao, J. He, S.-Y. Huang, The HDOCK server for integrated protein-protein docking. *Nat. Protoc.* **15**, 1829–1852 (2020). doi: 10.1038/s41596-020-0312-x; pmid: 32269383
84. A. Tovchigrechko, I. A. Vakser, GRAMM-X public web server for protein-protein docking. *Nucleic Acids Res.* **34**, W310–W314 (2006). doi: 10.1093/nar/gkl206; pmid: 16845016
85. M. Torchala, I. H. Moal, R. A. G. Chaleil, J. Fernandez-Recio, P. A. Bates, SwarmDock: A server for flexible protein-protein docking. *Bioinformatics* **29**, 807–809 (2013). doi: 10.1093/bioinformatics/btt038; pmid: 23343604
86. D. Schneidman-Duhovny, Y. Inbar, R. Nussinov, H. J. Wolfson, PatchDock and SymmDock: Servers for rigid and symmetric docking. *Nucleic Acids Res.* **33**, W363–W367 (2005). doi: 10.1093/nar/gki481; pmid: 15980490
87. G. Q. Dong, H. Fan, D. Schneidman-Duhovny, B. Webb, A. Sali, Optimized atomic statistical potentials: Assessment of protein interfaces and loops. *Bioinformatics* **29**, 3158–3166 (2013). doi: 10.1093/bioinformatics/btt560; pmid: 24078704
88. J. Armstrong, G. Hickey, M. Diekhans, A. Deran, Q. Fang, D. Xie, S. Feng, J. Stiller, D. Genereux, J. Johnson, V. D. Marinescu, D. Haussler, J. Alföldi, K. Lindblad-Toh, E. Karlsson, E. D. Jarvis, G. Zhang, B. Paten, Progressive alignment with Cactus: A multiple-genome aligner for the thousand-genome era. bioRxiv 730531 [Preprint]. 15 October 2019. https://doi.org/10.1101/730531.
89. B. Paten *et al*., Cactus: Algorithms for genome multiple sequence alignment. *Genome Res.* **21**, 1512–1528 (2011). doi: 10.1101/gr.123356.111; pmid: 21665927
90. M. D. Smith *et al*., Less is more: An adaptive branch-site random effects model for efficient detection of episodic diversifying selection. *Mol. Biol. Evol.* **32**, 1342–1353 (2015). doi: 10.1093/molbev/msv022; pmid: 25697341
91. S. L. K. Pond, S. D. W. Frost, S. V. Muse, HyPhy: Hypothesis testing using phylogenies. *Bioinformatics* **21**, 676–679 (2005). doi: 10.1093/bioinformatics/bti079; pmid: 15509596
92. K. S. Pollard, M. J. Hubisz, K. R. Rosenbloom, A. Siepel, Detection of nonneutral substitution rates on mammalian phylogenies. *Genome Res.* **20**, 110–121 (2010). doi: 10.1101/gr.097857.109; pmid: 19858363
93. M. J. Hubisz, K. S. Pollard, A. Siepel, PHAST and RPHAST: Phylogenetic analysis with space/time models. *Brief. Bioinform.* **12**, 41–51 (2011). doi: 10.1093/bib/bbq072; pmid: 21278375
94. R. Ramani, K. Krumholz, Y.-F. Huang, A. Siepel, PhastWeb: A web interface for evolutionary conservation scoring of multiple sequence alignments using phastCons and phyloP. *Bioinformatics* **35**, 2320–2322 (2019). doi: 10.1093/bioinformatics/bty966; pmid: 30481262
95. W. A. Ray, Evaluating medication effects outside of clinical trials: New-user designs. *Am. J. Epidemiol.* **158**, 915–920 (2003). doi: 10.1093/aje/kwg231; pmid: 14585769
96. S. Schneeweiss, A basic study design for expedited safety signal evaluation based on electronic healthcare data. *Pharmacoepidemiol. Drug Saf.* **19**, 858–868 (2010). doi: 10.1002/pds.1926; pmid: 20681003
97. H. Quan *et al*., Coding algorithms for defining comorbidities in ICD-9-CM and ICD-10 administrative data. *Med. Care* **43**, 1130–1139 (2005). doi: 10.1097/01.mlr.0000182534.19832.83; pmid: 16224307
98. P. C. Austin, Balance diagnostics for comparing the distribution of baseline covariates between treatment groups in propensity-score matched samples. *Stat. Med.* **28**, 3083–3107 (2009). doi: 10.1002/sim.3697; pmid: 19757444
99. World Health Organization (WHO), WHO R&D Blueprint, novel Coronavirus: COVID-19 Therapeutic Trial Synopsis (WHO, 2020); www.who.int/blueprint/priority-diseases/key-action/COVID-19_Treatment_Trial_Design_Master_Protocol_synopsis_Final_18022020.pdf.
100. Y. Perez-Riverol *et al*., The PRIDE database and related tools and resources in 2019: Improving support for quantification data. *Nucleic Acids Res.* **47**, D442–D450 (2019). doi: 10.1093/nar/gky1106; pmid: 30395289

ACKNOWLEDGMENTS

The authors acknowledge their partners and families for support in childcare and other matters during this time. The views, opinions, and findings contained in this study are those of the authors and do not represent the official views, policies, or endorsement of the Department of Defense or the U.S. Government. Imaging at the University of Sheffield was performed in the Wolfson Light Microscopy facility. A549 cells stably expressing ACE2 (A549-ACE2) were provided by O. Schwartz. We thank H. Malik for helpful discussions. We thank M. Akdel and J. Durairaj for input on analysis, R. Albrecht for support with the BSL3 facility and procedures at the ISMMS, and R. Cadagan for technical assistance. We thank the High Containment Core at Georgia State University for supporting the BSL3 facility and procedures. We thank B. L. Roth, A. Alon, and A. C. Kruse for helpful discussions on sigma receptor biology. We thank S. Deeks, P. J. Hunt, J. Gordan, C. Corbetta-Rastelli, and E. Lantos for insight on clinical applications for drug repurposing. **Funding:** This research was funded by grants from the National Institutes of Health (NIH) (P01AI063302, P50AI150476, R01AI120694, R01AI122747, R01AI143292, U19AI135972, and U19AI135990 to N.J.K.; P01AI120943 and R01AI143292 to C.F.B.; and U19 AI135990 to T.I.); by the National Institute of Allergy and Infectious Diseases (NIAID) R01AI128214 to O.S.R.; by the National Institute of Neurological Disorders and Stroke R01 NS089713, the NIH Office of the Director AI150476, and NIGMS R01 GM24485 to R.M.S.; by a Fast Grant for COVID-19 from the Emergent Ventures program at the Mercatus Center of George Mason University (N.J.K.) and a separate Fast Grant for COVID-19 (C.F.B.); by the Roddenberry Foundation Gladstone Institutes to K.S.P. and N.J.K.; from the Defense Advanced Research Projects Agency (HR0011-19-2-0020 to B.S., N.J.K., K.A.V., D.A.A., A.G.-S., and K.M.S.; HR0011-20-2-0040 to M.B.F.); NIGMS R35GM122481 (to B.S.); by CRIP (Center for Research for Influenza Pathogenesis), a NIAID supported Center of Excellence for Influenza Research and Surveillance (CEIRS, contract no. HHSN272201400008C) to A.G.-S.; by supplements to NIAID grant U19AI135972 and DoD grant W81XWH-20-1-0270 to A.G.-S.; by the Bill and Melinda Gates Foundation (INV-006099) and BARDA (ASPR-20-01495) to M.B.F.; by Howard Hughes Medical Institute to K.S.; by Damon Runyon Cancer Research Foundation DRG-2402-20 to C.P.; by Burroughs Wellcome Fund 1019894 to N.He.; by the Chan Zuckerberg Initiative to O.S.R. and T.Ko.; by Cytoscape: A modeling platform for biomolecular networks (NHGRI R01 HG009979) to T.I.; by the generous support of the JPB Foundation, the Open Philanthropy Project [research grant 2020-215611 (5384)] and by anonymous donors to A.G.-S.; a Laboratoire d'Excellence grant ANR-10-LABX-62-IBEID and the URGENCE COVID-19 Institut Pasteur fundraising campaign to M.V and N.Jo.; by grants from the BBSRC (BB/S009566/1 and BB/L002841/1) to A.A.P. and D.W. and by BBSRC White Rose DTP (BB/J014443/1) to A.S.S.-S.; by The Augusta University–Georgia State University Seed Grant program to C.F.B.; by the MRC grant MC PC 19026 to M.P.; by the MRC Grant MC_UU_12016/2 to D.A.; by the Medical Research Council (MC_UU_12016/2) to D.R.A.; by the DFG under Germany's Excellence Strategy (EXC-2189, project ID 390939984 to R.G.); and funding from F. Hoffmann-La Roche and Vir Biotechnology and gifts from The Ron Conway Family and Vir Biotechnology to the Quantitative Biosciences Institute Coronavirus Research Group (QCRG). J.H. was supported by the UCSF Medical Scientist Training Program (T32GM007618); P.F. was supported by the UCSF Medical Scientist Training Program (T32GM007618) and the NIH-NIAID (F30AI143401); M.B. was supported by the NCI at the NIH (F32CA239333); H.T.K. was supported by the NIH (K99GM138753); K.H. was supported by the National Science Foundation (1650113); B.T. was supported by the NIH (F32 CA239336); U.S.C. was supported by the National Institute of General Medical Sciences (F32GM137463). The QCRG Structural Biology Consortium has received support from: Quantitative Biosciences Institute, Defense Advance Research Projects Agency [HR0011-19-2-0020 to D.A.A. and K.A.V.; B.S., primary investigator (PI)], FastGrants COVID-19 grant (K.A.V., PI), Laboratory For Genomics Research (O.S.R., PI), and Laboratory For Genomics Research (R.M.S., PI). **Author contributions:** The following authors designed and conceptualized the study: A.A.P., A.G.-S., C.F.B., D.E.G., H.B., J.A.R., J.Ba., J.H., K.A.V., K.O., M.B., M.V., N.J.K., O.S.R., P.B., R.G., and R.M.K. The following authors

performed experiments or data acquisition: A.A.P., A.Du., A.G., A.J.H., A.L.L., A.R., A.R.W., A.S.J., A.S.S.-S., A.V.-G., B.T., C.J.H., C.A., C.Ba., C.F.B., C.J., C.K., C.R.S., D.B., D.E.G., D.K., D.L.S., D.M., D.M.W., D.R.A., D.S., E.M., E.P., E.H.P., E.R., E.W.T., F.Be., F.Br., G.J., G.K., H.F., H.L., I.B.-H., I.Du., J.A.R., J.A.S., J.Ba., J.C.-S., J.H., J.Lo., J.O., J.X., J.Z.G., K.A.B., K.C.K., K.H., K.M.W., L.M., M.A.K., M.B., M.B.F., M.Ch., M.C.M., M.D., M.El., M.Gu., M.Mod., M.M.K., M.McGra., M.McGre., M.U., M.V., N.G., N.Jo., P.B., P.D., P.F., R.Hü., R.Ha., R.J.K., R.M.K., R.R., R.To., S.G.W., S.P., S.Ra., S.U., S.Wei., S.Wes., T.Ke., T.M., T.V., T.W.O., V.V.R., Y.S., and Z.Z. The following authors conducted formal data analysis: A.A.P., A.Du., A.J.H., A.L.L., A.R.W., A.S., A.S.J., A.S.S.-S., A.V.-G., B.S., C.J.H., C.A., C.F.B., C.K., D.B., D.E.G., D.L.S., D.M., D.M.W., D.S., E.M., E.P., E.W.T., G.J., G.K., H.B., I.Du., J.A.R., J.A.S., J.Ba., J.H., J.Par., K.A.V., K.C.K., K.M.W., K.O., K.R.H., K.S.P., L.M., M.A.K., M.B., M.B.F., M.Ca., M.C.M., M.Ec., M.Gh., M.Gu., M.J.O., M.M.K., M.McGra., M.V., N.Jo., N.Ju., O.S.R., P.B., R.G., R.Hü., R.M.K., R.R., S.P., S.U., S.Wei., T.A.T., T.I., T.V., T.W.O., U.R., V.V.R., Y.Zho., Z.C., and Z.Z. The following authors supervised or managed research: A.A.P., A.F., A.G.-S., A.M., A.S., B.S., C.A., C.F.B., D.A.A., D.E.G., D.L.S., J.A.R., J.H., J.M.F., J.S.F., K.A.V., K.H., K.M.S., K.M.W., K.O., K.S.P., M.B., M.B.F., M.Ch., M.O., M.P., M.V., N.Jo., N.Ju., N.J.K., O.S.R., P.B., R.G., R.Hü., R.M.K., T.I., T.Ko., and Y.C. The following authors raised funds for these efforts: A.A.P., A.G.-S., B.S., C.F.B., D.A.A., D.E.G., D.R.A., J.M.F., K.M.S., K.O., K.S.P., M.P., M.V., N.Jo., N.J.K., O.S.R., P.B., R.G., and T.I. The following authors drafted the original manuscript: A.A.P., B.S., C.A., D.E.G., D.L.S., H.B., J.A.R., J.Ba., J.H., K.A.V., K.M.H., K.M.S., K.O., K.R.H., K.S.P., M.A.K., M.B., M.Ca., M.Ec., M.M.K., M.O., M.P., M.So., N.J.K., O.S.R., P.B., P.H., R.M.K., T.A.T., U.R., V.V.R., and Z.Z.C.N. The structural biology portion of this work was performed by the Quantitative Biosciences Institute Coronavirus Research Group Structural Biology Consortium. Listed below are the contributing members of the consortium, listed by teams in order of team relevance to the published work. The team leads are listed first (those responsible for organization and the experimental design utilized within each team), and the rest of team members are listed alphabetically. Bacterial expression team: A.D., M.G., E.W.T., J.C., L.D., S.F., M.J., H.T.K., V.L.L., Y.L., M.L., G.E.M., J.P., A.C.T., Z.Y., F.Z., and Y.Z. Protein purification team: M.M., T.W.O., S.P., C.M.A., C.M.C., B.F., M.G., K.K., J.P., J.K.P., K.S., and T.K.M.T. Cryo-EM grid freezing and collection team: C.M.A., A.F.B., G.E.M., C.P., A.N.R., M.S., J.R.B., M.G., F.L., K.E.L., A.M., F.M., J.P., T.H.P., Jr., S.P., A.M.S., P.V.T., F.W., and Z.Y. Cryo-EM data processing team: A.F.B., M.S.D., G.E.M., H.C.N., A.N.R., D.A., J.R.B., M.G.C., C.M.C., U.S.C., D.D., B.F., M.G., N.H., M.J., F.L., J.L., Y.L., J.P., T.H.P., Jr., S.P., S.S., R.T., D.T., E.T., K.Z., and F.Z. Mammalian cell expression team: C.B., M.G.C., D.D., C.N., A.M.S., J.Z., C.M.A., A.B., N.H., Y.L., P.N., C.P., M.S., S.S., K.S., R.T., T.K.M.T., and N.W. Crystallography team: N.H., H.T.K., U.S.-G., I.D.Y., J.B., I.D., and X.L. Infrastructure team: D.B., A.J., A.J., L.M., M.T., and E.T. Leadership team: O.S.R., K.A.V., D.A.A., Y.C., J.S.F., A.F., N.J., T.K., N.J.K., A.M., D.R.S., and R.M.S. All authors edited the manuscript. **Competing interests:** The Krogan Laboratory has received research support from Vir Biotechnology and F. Hoffmann-La Roche. T.I. is the cofounder of Data4Cure, Inc., with an equity interest, and he has a funded sponsored research agreement from Ideaya BioSciences, Inc., with an equity stake. The García-Sastre Laboratory has received research support from Pfizer, Senhwa Biosciences, and 7Hills Pharma; and A.G.-S. has consulting agreements for the following companies involving cash and/or stock: Vivaldi Biosciences, Contrafect, 7Hills Pharma, Avimex, Valneva, Accurius, and Esperovax. K.M.S. has consulting agreements for the following companies involving cash and/or stock compensation: Black Diamond Therapeutics, BridGene Biosciences, Denali Therapeutics, Dice Molecules, eFFECTOR Therapeutics, Erasca, Genentech/Roche, Janssen Pharmaceuticals, Kumquat Biosciences, Kura Oncology, Merck, Mitokinin, Petra Pharma, Qulab Inc. Revolution Medicines, Type6 Therapeutics, Venthera, and Wellspring Biosciences (Araxes Pharma). J.A.R. is an employee and shareholder of Aetion, Inc., a company that makes software for the analysis of real-world data. A.R.W. is an employee and shareholder of Aetion, Inc., a company that makes software for the analysis of real-world data. R.J.K. is an employee of HealthVerity, a company that links and deidentifies real-world data. J.S.F. is a founder of Keyhole Therapeutics and a shareholder of Relay Therapeutics and Keyhole Therapeutics. The Fraser laboratory has received sponsored research support from Relay Therapeutics. K.H., J.C.-S., J.O., and T.M. are employees and shareholders of Synthego Corporation. Aetion holds patents related to this work, including U.S. Patent no. 9,378,271; other patents are pending. **Data and materials availability:** Further information and requests for resources and reagents should be directed to and will be fulfilled by N.J.K. (nevan.krogan@ucsf.edu). The MS proteomics data have been deposited to the ProteomeXchange Consortium via the PRIDE partner repository with the dataset identifier PXD021588 (*100*). An interactive version of PPI data can be found at https://kroganlab.ucsf.edu/network-maps. Atomic coordinates and the cryo-EM map of the reported Tom70-ORF9b structure have been deposited in the Protein Data Bank under accession code 7KDT and in the Electron Microscopy Data Bank under accession code EMD-22829. Expression vectors used in this study are readily available from the authors for biomedical researchers and educators in the nonprofit sector. The Aetion Evidence Platform used for the clinical analysis is available under license from Aetion, New York, NY. To protect patient privacy, data used in real-world analyses are available for inspection by qualified researchers under confidentiality and third-party agreements with Aetion and/or HealthVerity. This work is licensed under a Creative Commons Attribution 4.0 International (CC BY 4.0) license, which permits unrestricted use, distribution, and reproduction in any medium, provided the original work is properly cited. To view a copy of this license, visit https://creativecommons.org/licenses/by/4.0/. This license does not apply to figures/photos/artwork or other content included in the article that is credited to a third party; obtain authorization from the rights holder before using such material.

SUPPLEMENTARY MATERIALS

science.sciencemag.org/content/370/6521/eabe9403/suppl/DC1
QCRG Structural Biology Consortium Author List
Zoonomia Consortium Author List
Figs. S1 to S25
Tables S1 to S15
Reference (*101*)
MDAR Reproducibility Checklist
Movie S1

View/request a protocol for this paper from *Bio-protocol*.

24 September 2020; accepted 12 October 2020
Published online 15 October 2020
10.1126/science.abe9403

RESEARCH ARTICLE SUMMARY

INNATE IMMUNITY

Enteroviral 3C protease activates the human NLRP1 inflammasome in airway epithelia

Kim S. Robinson, Daniel Eng Thiam Teo*, Kai Sen Tan*, Gee Ann Toh*, Hsiao Hui Ong*, Chrissie Kaishi Lim, Kenneth Lay, Bijin Veonice Au, Tian Sheng Lew, Justin Jang Hann Chu, Vincent Tak Kwong Chow, De Yun Wang, Franklin L. Zhong†, Bruno Reversade†

INTRODUCTION: The innate immune system uses a variety of sensor proteins to detect infections and injuries. The nucleotide-binding oligomerization domain, leucine-rich repeat, and pyrin domains-containing proteins (NLRPs) are a family of cytosolic sensors involved in the initiation of the host innate immune response. Upon activation, NLRPs form a multiprotein immune effector complex known as the inflammasome. Assembly of the inflammasome leads to caspase-1 activation, the secretion of proinflammatory cytokines such as interleukin-1β (IL-1β) and IL-18, and gasdermin D–dependent pyroptotic cell death. These processes orchestrate the downstream immune response to microbial infections and injuries. Genetic data support an important role for human NLRPs in antimicrobial defense. Dysregulated NLRP-driven inflammasome signaling also contributes to the pathogenesis of several autoimmune and autoinflammatory diseases.

RATIONALE: Understanding the molecular basis by which individual human NLRPs respond to specific stimuli is key to the study of innate immunity and inflammatory diseases. NLRP1 was one of the first human NLRPs to be described. Yet the pathogen-derived triggers for human NLRP1 have not been identified, and its mechanism of activation is much less understood than that of other NLRPs such as NLRP3. Although compelling evidence shows that rodent NLRP1 can be activated by specific bacterial toxins and protozoan infections, human NLRP1 is not triggered by these stimuli. Germline-activating NLRP1 mutations in humans cause a variety of inherited diseases characterized by sustained inflammation and hyperplasia in the skin and the airway. Thus, we hypothesized that some unknown molecule(s) from common skin or airway pathogens activate human NLRP1.

RESULTS: Here, we report that human NLRP1 senses and is activated by enteroviral infections. Enteroviruses cause a range of human diseases, including hand-foot-and-mouth disease, polio, and the common cold. In our model system, we show that NLRP1 is highly expressed in airway epithelia and is activated by the human rhinovirus (HRV), a type of enterovirus that causes the common cold. During infection, a HRV component known as 3C protease (HRV-3Cpro) cleaves NLRP1 specifically between amino acids Q130 and G131. This cleavage causes the autoinhibitory N-terminal fragment (amino acids 131 to 1212) to become recognized by the N-terminal glycine degron pathway and subsequently cleared by the proteasome. This sequence of events culminates in inflammasome activation mediated by the liberated NLRP1 C-terminal fragment (amino acids 1213 to 1474), resulting in caspase-1 activation, inflammatory cell death, and the secretion of inflammatory cytokines, such as IL-18, from infected airway epithelial cells. We also show that pharmacologic inhibition of the N-terminal glycine degron pathway by the NEDD8–cullin inhibitor MLN4924 effectively blocks the activation of NLRP1 inflammasome in HRV-infected primary human bronchial epithelial cells.

CONCLUSION: We establish that enteroviral 3Cpros, which have long been regarded as a key mediator of viral immune evasion, in fact act as a trigger for the NLRP1 inflammasome in primary human airway epithelial cells. These results provide a unified mechanism for proteolysis-mediated activation of NLRP1 in humans and rodents. Our results also reveal a role for the recently described N-terminal glycine degron pathway in human innate immunity. Thus, NLRP1 is a versatile sensor protein, which has evolved to respond to bacterial, viral, and protozoan infections in different species. As both HRV infection and inflammasome-dependent IL-1 cytokines are associated with acute exacerbations of asthma and chronic obstructive pulmonary disease, the NLRP1 inflammasome pathway holds potential as a therapeutic target in the treatment of inflammatory diseases involving the airway epithelia. ■

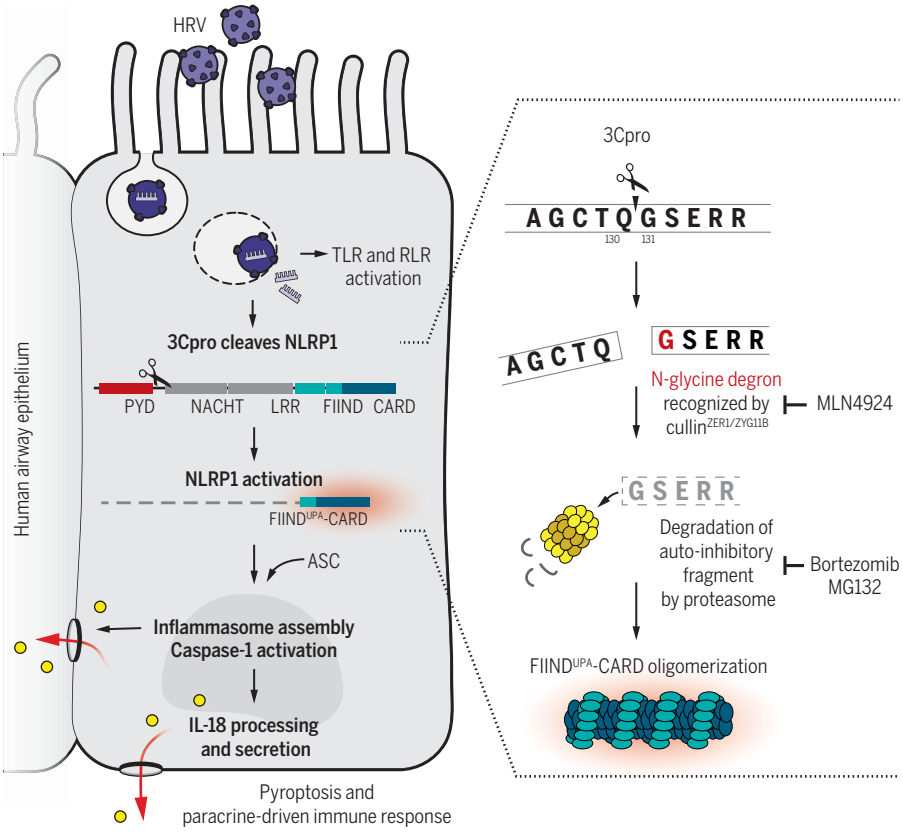

Proposed mechanism of NLRP1 activation by 3Cpro in HRV-infected human airway epithelium. TLR, Toll-like receptor; RLR, retinoic acid-inducible gene I–like receptors; Pyd, pyrin domain; LRR, leucine-rich repeat; FIIND, function to find domain; CARD, caspase recruitment domain; ASC, apoptosis-associated speck-like protein containing a CARD A, Ala; C, Cys; E, Glu; G, Gly; Q, Gln; R, Arg; S, Ser; T, Thr.

The list of author affiliations is available in the full article online.
*These authors contributed equally to this work.
†Corresponding author. Email: franklin.zhong@ntu.edu.sg (F.L.Z.); bruno@reversade.com (B.R.)
Cite this article as K. S. Robinson *et al.*, *Science* **370**, eaay2002 (2020). DOI: 10.1126/science.aay2002

READ THE FULL ARTICLE AT
https://doi.org/10.1126/science.aay2002

RESEARCH ARTICLE

INNATE IMMUNITY

Enteroviral 3C protease activates the human NLRP1 inflammasome in airway epithelia

Kim S. Robinson[1,2], Daniel Eng Thiam Teo[3]*, Kai Sen Tan[4]*, Gee Ann Toh[3]*, Hsiao Hui Ong[4]*, Chrissie Kaishi Lim[5], Kenneth Lay[2,6], Bijin Veonice Au[5], Tian Sheng Lew[7], Justin Jang Hann Chu[5,7], Vincent Tak Kwong Chow[7], De Yun Wang[4], Franklin L. Zhong[1,2,3,5]†, Bruno Reversade[2,5,6,8,9]†

Immune sensor proteins are critical to the function of the human innate immune system. The full repertoire of cognate triggers for human immune sensors is not fully understood. Here, we report that human NACHT, LRR, and PYD domains-containing protein 1 (NLRP1) is activated by 3C proteases (3Cpros) of enteroviruses, such as human rhinovirus (HRV). 3Cpros directly cleave human NLRP1 at a single site between Glu^{130} and Gly^{131}. This cleavage triggers N-glycine–mediated degradation of the autoinhibitory NLRP1 N-terminal fragment via the $cullin^{ZER1/ZYG11B}$ complex, which liberates the activating C-terminal fragment. Infection of primary human airway epithelial cells by live human HRV triggers NLRP1-dependent inflammasome activation and interleukin-18 secretion. Our findings establish 3Cpros as a pathogen-derived trigger for the human NLRP1 inflammasome and suggest that NLRP1 may contribute to inflammatory diseases of the airway.

The human innate immune system uses a multitude of sensor proteins to detect microbial infections and kick-start the immune response (*1*). Nod-like receptor (NLR) proteins are a family of innate immune sensors that can detect pathogen- and danger-associated molecular patterns (*1*–*3*). Upon activation, NLR proteins nucleate the assembly of inflammasome complexes, leading to pyroptotic cell death and secretion of processed inflammatory cytokines, such as interleukin-1β (IL-1β) and IL-18 (*4*). Among human NLR sensors, NLRP1 remains one of the few whose cognate trigger has not been identified. Human NLRP1 differs from rodent homologs in terms of domain organization, ligand specificity, and tissue distribution (*5*), and its exact role in human antimicrobial response is still unclear. However, NLRP1 does play an important role in inflammatory disorders. Germline-activating mutations in *NLRP1* cause a number of Mendelian syndromes characterized by multiple self-healing keratoacanthomas of the skin and hyperkeratosis in the laryngeal and corneal epithelia (*6*–*8*). Carriers of certain common *NLRP1* single-nucleotide polymorphisms experience increased risks for autoimmune diseases such as asthma and vitiligo (*9*, *10*).

Anthrax lethal factor (LF) is the most well-characterized trigger for murine NLRP1B (*11*–*15*). LF directly cleaves NLRP1B close to its N terminus (*13*–*15*). This cleavage causes N-degron–mediated degradation of the autoinhibitory N-terminal fragment, freeing the noncovalently bound $FIIND^{UPA}$-CARD fragment [FIIND, function to find domain; CARD, caspase recruitment domain; amino acids 1213 to 1474] to activate caspase-1 (*16*–*18*) (Fig. 1A). The consensus LF cleavage site is absent in human NLRP1. As a result, LF does not cleave or activate human NLRP1. Human NLRP1 also contains an N-terminal pyrin domain (PYD) not found in rodents (Fig. 1A). Despite these differences, both human NLRP1 and rodent homologs can be activated by chemical inhibitors of dipeptidases DPP8 and DPP9, although the underlying mechanisms remain to be fully elucidated (*19*–*21*). Rodent Nlrp1 can also be activated by *Toxoplasma gondii* infection in a process that does not appear to involve protease-mediated cleavage (*22*, *23*). Thus, multiple modes of activation exist for NLRP1 from different species. It remains unknown whether any naturally occurring pathogen-derived molecules can activate human NLRP1. In this study, we set out to identify the cognate pathogen-derived signal(s) that can activate human NLRP1 and assess the mechanisms by which they activate the NLRP1 inflammasome.

[1]Skin Research Institute of Singapore (SRIS), 8A Biomedical Grove, #06-06 Immunos, 138648, Singapore. [2]Institute of Medical Biology, Agency of Science, Technological and Research, 8A Biomedical Grove, #06-06 Immunos, 138648, Singapore. [3]Lee Kong Chian School of Medicine, Nanyang Technological University, 11 Mandalay Road, 308232, Singapore. [4]Department of Otolaryngology, Infectious Diseases Translational Research Programme, Yong Loo Lin School of Medicine, National University Health System, National University of Singapore, 10 Medical Drive, 117597, Singapore. [5]Institute of Molecular and Cell Biology, 61 Biopolis Drive, 138673, Singapore. [6]Genome Institute of Singapore, 60 Biopolis Street, 138672, Singapore. [7]Department of Microbiology and Immunology, Yong Loo Lin School of Medicine, National University Health System, National University of Singapore, 10 Medical Drive, 117597, Singapore. [8]Department of Paediatrics, Yong Loo Lin School of Medicine, National University Health System, National University of Singapore, 10 Medical Drive, 117597, Singapore. [9]The Medical Genetics Department, Koç University School of Medicine, 34010 Istanbul, Turkey.
*These authors contributed equally to this work.
†Corresponding author. Email: franklin.zhong@ntu.edu.sg (F.L.Z.); bruno@reversade.com (B.R.)

3Cpros activate human NLRP1 in vitro

From a survey of common human pathogens, we selected the human rhinovirus (HRV), which is the major causative agent for the common cold. HRV is a member of the Picornaviridae family of single-stranded RNA viruses, which cause a wide range of human diseases, including hand-foot-and-mouth disease, peri- and myocarditis, and poliomyelitis (*24*). HRV infection of primary human bronchial epithelial cells can induce caspase-1 activation and IL-1 secretion (*24*, *25*), although the upstream sensing mechanisms are unclear. All picornaviruses, including HRVs, encode two well-defined proteases called 2Apro and 3Cpro. These proteases are responsible for cleaving the viral genomic precursor proteins into individual components (*26*) and have also been shown to cleave host proteins to facilitate immune evasion (*27*–*30*).

To test whether HRV-3Cpro can activate human NLRP1, we expressed Myc-tagged HRV-3Cpro in a 293T reporter cell line that stably expressed ASC-GFP (ASC, apoptosis-associated speck-like protein containing a CARD domain; GFP, green fluorescent protein) and NLRP1-FLAG (called 293T-ASC-GFP-NLRP1-FLAG). As compared to vector-transfected cells, 3Cpros derived from two strains of HRV (HRV-14, serotype B, and HRV16, serotype A) and a closely related enterovirus (coxsackie B3) induced a significant increase in the percentage of cells aggregating ASC-GFP specks (Fig. 1B and fig. S1, A and B), similar to the dipeptidase inhibitor talabostat. By contrast, none of the other viral proteases tested were able to do so (Fig. 1B and fig. S1, A and B), despite similar or even higher levels of expression. The ability of HRV14-3Cpro to activate human NLRP1 was entirely dependent on its enzymatic activity, because mutating its catalytic cysteine residue (p.C146A; Cys^{146}→Ala) abrogated ASC-GFP speck formation (Fig. 1B and fig. S1B). In an orthogonal assay for NLRP1 activation, HRV14-3CPro and HRV16-3Cpro directly induced the formation of high-molecular-weight NLRP1 oligomers by native polyacrylamide gel electrophoresis (PAGE) at the expense of monomeric NLRP1 (fig. S1C). These findings establish enteroviral 3Cpros, such as those encoded by HRV, as robust activators for the reconstituted human NLRP1 inflammasome in vitro.

We and others have recently demonstrated that primary and immortalized human keratinocytes express components of the NLRP1 inflammasome complex endogenously and can undergo rapid pyroptosis in response to inflammasome agonists (*7*, *19*). This provides a robust cellular system to determine whether 3Cpros can activate the endogenous NLRP1 inflammasome. Immortalized human keratinocytes stably expressing GFP-tagged ASC and transfected with HRV14-3Cpro formed ASC-GFP

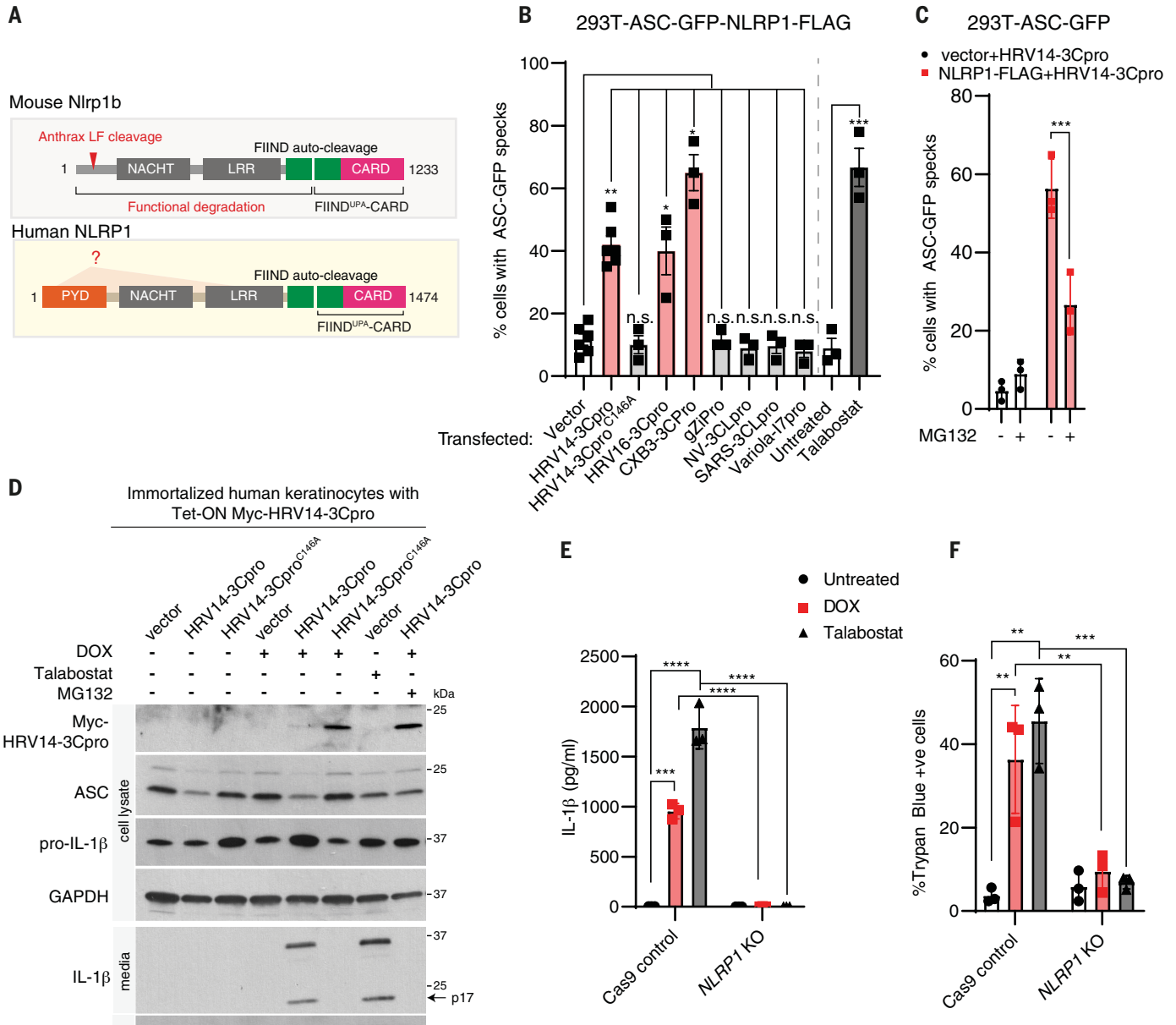

Fig. 1. Enteroviral 3Cpros activate the human NLRP1 inflammasome. (**A**) Domain structures of human NLRP1 and rodent NLRP1B. Murine NLRP1B is activated by anthrax LF toxin cleavage, followed by the proteasomal degradation of the autoinhibitory N-terminal fragment. LRR, leucine-rich repeat. (**B**) Percentage of 293T-ASC-GFP-NLRP1-FLAG cells with ASC-GFP specks after overexpression of Myc-tagged viral proteases. Cells were fixed 24 hours after transfection of the indicated proteases or empty vector control. Talabostat (2 μM, 24 hours) treatment was used as a positive control. The number of cells with ASC-GFP specks were visually scored with wide-field epifluorescence microscopy at 20× magnification. More than 100 cells were scored for ASC-GFP speck formation per condition. $*P < 0.05$, $**P < 0.01$, $***P < 0.001$ [two-way analysis of variance (ANOVA)]; n.s., not significant. Error bars represent SEM from three biological replicates. (**C**) The effect of MG132 on NLRP1-dependent ASC-GFP speck formation. 293T-ASC-GFP or 293T-ASC-GFP-NLRP1-FLAG cells were transfected with HRV14-3Cpro and treated with 2.5 μM MG132 6 hours after transfection. $***P < 0.001$ (two-way ANOVA). Error bars represent SEM from three biological replicates. (**D**) HRV14-3Cpro induces mature IL-1β secretion and ASC oligomerization in immortalized human keratinocytes. Tet-ON HRV-3Cpro or $3Cpro^{C146A}$ immortalized keratinocytes (N/TERT) were harvested 24 hours after 1 μg/ml doxycycline (DOX). Conditioned media was concentrated 10 times before SDS-PAGE. Endogenous ASC oligomers were extracted by 1% SDS after covalent cross-linking of the 1% NP40-insoluble pellets with 1 mM DSS in PBS. GAPDH, glyceraldehyde-3-phosphate dehydrogenase. (**E**) IL-1β ELISA of conditioned media from *NLRP1*$^{-/-}$ and Cas9 control Tet-ON HRV14-3Cpro N/TERT keratinocytes 24 hours after DOX induction. $***P < 0.001$; $****P < 0.0001$ (two-way ANOVA). $n = 3$ independent cell seedings and inductions. Error bars represent SEM. (**F**) Trypan blue exclusion assay of *NLRP1*$^{-/-}$ and Cas9 control Tet-ON HRV14-3Cpro N/TERT keratinocytes 24 hours after DOX induction. $**P < 0.01$; $***P < 0.001$ (two-way ANOVA), $n = 3$ independent cell seedings and inductions as in (E). Error bars represent SEM.

specks and underwent membrane permeabilization marked by propidium iodide (PI) staining (fig. S1D). Using a doxycycline-inducible expression system, we showed that only keratinocytes expressing active HRV14-3Cpro demonstrated cardinal features of pyroptosis, including the secretion of cleaved, mature IL-1β and the formation of detergent-insoluble ASC oligomers (Fig. 1D). This occurred despite the lower expression of wild-type 3Cpro compared to its inactive mutant (p.C146A) (Fig. 1D). The effect of 3Cpro requires continuous proteasome activity, as the proteasomal inhibitor MG132 significantly blocked HRV-3Cpro–induced ASC-GFP speck formation (Fig. 1C) in 293T-ASC-GFP-NLRP1 cells, as well as NLRP1 self-oligomerization (fig. S1C) and ASC oligomerization and IL-1β cleavage (Fig. 1D). Therefore, 3Cpro-induced human NLRP1 activation may also involve a functional degradation step that is analogous to LF-induced mouse NLRP1B activation.

HRV14-3Cpro–induced pyroptosis was entirely dependent on NLRP1, as its genetic ablation by CRISPR-Cas9 (*NLRP1*$^{-/-}$ Tet-ON HRV14-3Cpro) abrogated IL-1β secretion, ASC oligomerization (Fig. 1E and fig. S2A), and lytic cell death (Fig. 1F). In experiments with transiently transfected HRV14-3Cpro and HRV16-3Cpro, *NLRP1*, *ASC*, and *CASP1* deletion all had similar inhibitory effects (fig. S2, B to D). Therefore, HRV-3Cpro can act as a potent trigger of pyroptotic cell death in immortalized human keratinocytes by activating the endogenous NLRP1 inflammasome. Similar to reconstituted NLRP1 in 293T cells (Fig. 1C and fig. S1C), this effect required intact proteasome activity (fig. S1D). We also observed that a subset of 3Cpro-expressing keratinocytes underwent apoptotic cell death with annexin V staining but without PI inclusion (fig. S2E), in agreement with the reported proapoptotic roles of 3Cpros in other cell types (*31*, *32*).

3Cpros cleave human NLRP1 between p.Q130 and G131

Picornaviral 3Cpros, including HRV-3Cpro, are cysteine proteases with well-defined catalytic activity and substrate preferences (*26*, *33*). Just as anthrax LF cleaves rodent NLRP1B directly (*15*, *34*), we hypothesized that 3Cpros could activate human NLRP1 via direct cleavage. Overexpressed NLRP1 undergoes autocleavage within its FIIND and thus appears as two bands that differ by ~20 kDa when visualized with an N-terminal–specific antibody (*35*, *36*) (Fig. 2, A and B). In the presence of HRV14-3Cpro, two additional bands were visualized using the same antibody (Fig. 2B). By contrast, the C-terminal FIIND^{UPA}-CARD fragment remained intact, suggesting that the HRV14-3Cpro cleaved NLRP1 at a single site close to the N terminus and not within the FIIND^{UPA}-CARD fragment. To visualize the 3Cpro-specific cleavage more precisely, the same experiment was carried out using the NLRP1^{F1212A} mutant, which cannot undergo autocleavage within the FIIND and thus remained a single band by SDS–polyacrylamide gel electrophoresis (fig. S3A). With increasing amounts of HRV14-3Cpro, NLRP1^{F1212A} became cleaved into a single proteolytic product, which was ~20 kDa smaller than full-length NLRP1 (fig. S3A). In both experiments, the proteolytic banding patterns could be explained by a single cleavage site ~20 kDa from the NLRP1 N terminus. The same cleavage could be observed when NLRP1-expressing cell-free lysate was incubated with recombinant HRV14-3Cpro at 33°C (the preferred temperature for HRV infection) (fig. S3B). On the basis of these observations, the 3Cpro cleavage site was mapped to the linker region immediately after the PYD (Fig. 2A), a region that is not conserved in rodents. As 3Cpros require a glutamine residue at the P_1' substrate site (*33*), each of the 11 glutamine residues in this linker region was changed to alanine by site-directed mutagenesis. Of all the mutants tested, only the p.Q130A mutation abrogated NLRP1 cleavage by HRV14-3Cpro (Fig. 2C) and other 3CPros (fig. S3C). We next generated reporter 293T-ASC-GFP cells that stably expressed either wild-type NLRP1 or the uncleavable Q130A mutant (NLRP1^{Q130A}) (Fig. 2D). In contrast to wild-type NLRP1, NLRP1^{Q130A}-expressing cells no longer nucleated ASC-GFP specks in response to HRV14-3Cpro overexpression. However, their response to talabostat remained the same (Fig. 2E). Similar results were obtained using transfected NLRP1^{Q130A} and HRV16-3Cpro (fig. S3D).

To study the endogenous inflammasome response, we rescued human *NLRP1*$^{-/-}$ keratinocytes with either wild-type NLRP1 or the cleavage site mutant NLRP1^{Q130A}. Wild-type NLRP1, but not NLRP1^{Q130A}, restored HRV14-3Cpro–triggered IL-1β secretion, ASC oligomerization (Fig. 2F and fig. S4, A and B), and lytic cell death (Fig. 2G and fig. S2C). By contrast, both wild-type NLRP1 and NLRP1^{Q130A} enabled *NLRP1*$^{-/-}$ cells to respond to talabostat (Fig. 2, F and G, and fig. S4A). Thus, 3Cpro-triggered NLRP1 activation is a result of a discrete cleavage site between amino acids Q130 and G131, adjacent to the human-specific PYD. This site is not conserved in rodents, and as expected, HRV14-3Cpro did not induce pyroptotic cell death in murine RAW264.7 cells (fig. S4, C to E). This is consistent with the fact that HRV, like most pathogenic human enteroviruses, does not naturally infect rodents (*37*).

Degradation of the 3Cpro cleavage fragment (amino acids 131 to 1212) is required for NLRP1 activation

We next sought to further dissect how the cleavage of human NLRP1 by 3Cpros triggers proteasome-dependent inflammasome activation. Cleavage of human NLRP1 by HRV-3Cpro removes the entire PYD, where most disease-causing gain-of-function germline mutations occur (Fig. 1A) (*6*, *7*, *38*, *39*). It is conceivable that 3Cpro cleavage relieves an intrinsic autoinhibitory effect of the noncanonical NLRP1 PYD. Alternatively, the cleavage could trigger the destabilization of the entire N-terminal fragment (between the 3Cpro cleavage site and the FIIND autoproteolysis site, amino acids 131 to 1212). To distinguish between these two possibilities, we examined a truncation mutant of NLRP1 (amino acids 131 to 1474), which mimics the major product generated by HRV14-3Cpro cleavage except for the initiating methionine. Unexpectedly, this mutant did not cause increased ASC-GFP speck formation relative to wild-type NLRP1 in 293T-ASC-GFP cells, despite being fully sensitive to talabostat-mediated activation (Fig. 3A and fig. S5A). Thus, the removal of NLRP1 PYD appears to be insufficient by itself to account for HRV-3Cpro–triggered NLRP1 activation.

Recently, the mechanism by which anthrax LF activates NLRP1B has been reported (*16*, *17*, *40*). LF cleavage creates an N-terminal degron that is recognized by the type II N-degron receptors, such as UBR2, which degrade the inhibitory NLRP1B N-terminal fragment via the proteasome (Fig. 3B). We therefore hypothesized that an analogous pathway may account for the ability of HRV-3Cpro to activate human NLRP1. However, HRV-3Cpro cleavage of human NLRP1 generates an N-terminal glycine, which is not a canonical type II N-terminal degron recognized by related UBR proteins (*41*, *42*). A glycine-specific N-degron pathway has recently been described (*43*), which consists of receptors ZER1 and ZYG11B and their partner cullins CUL2 and CUL5 (called cullin$^{ZER1/ZYG11B}$). The cullin$^{ZER1/ZYG11B}$ machinery ubiquitinates substrate proteins with N-terminal glycine residues and causes their degradation via the proteasome. In contrast to the UBR system, the N-glycine degron pathway is not sensitive to type II free amino acids but can be inhibited by the NEDD8–cullin inhibitor MLN4924 (*43*) (Fig. 3B). In 293T-ASC-GFP-NLRP1 reporter cells, MLN4924 blocked HRV14-3Cpro–induced ASC-GFP speck formation (Fig. 3C) in a manner comparable to proteasomal inhibitors MG132 and bortezomib. MLN4924 similarly blocked HRV14-3Cpro NLRP1 self-oligomerization (Fig. 3D) in 293T-NLRP1-FLAG cells. Notably, MLN4924 stabilized the postcleavage NLRP1 fragment (corresponding to amino acids 131 to 1212, taking into account FIIND autoproteolysis) equivalently to MG132 and bortezomib (Fig. 3D). Type II N-degron inhibitor phenylalanine had no effect on either ASC-GFP speck formation or NLRP1 self-oligomerization (Fig. 3, C and D). Similarly, in keratinocytes, both MLN4924 and bortezomib completely blocked mature

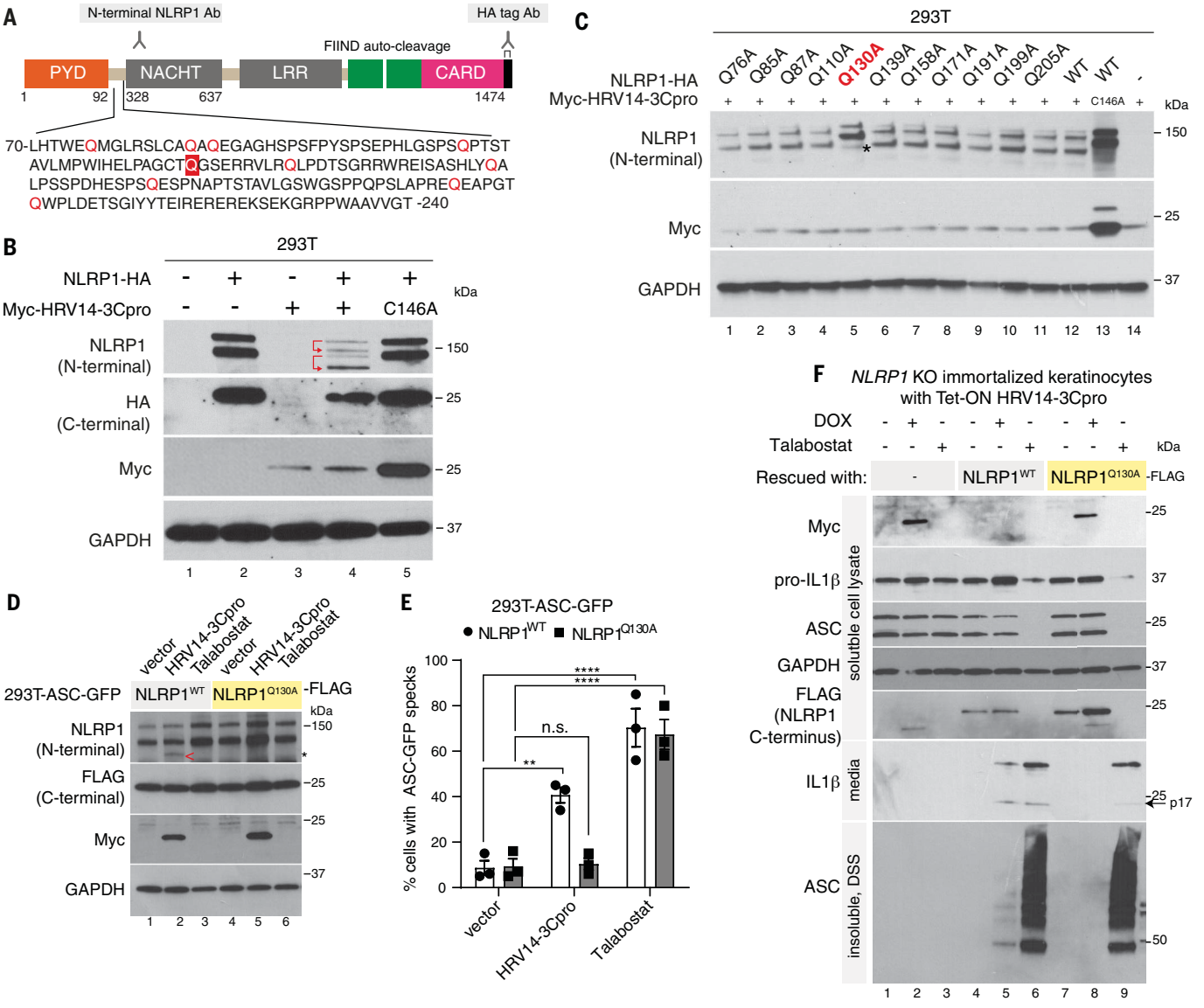

Fig. 2. 3CPros activate NLRP1 by direct cleavage at a single site between p.Glu130 and Gly131. (**A**) HRV14-3Cpro cleaves NLRP1 close to its N terminus. Schematic shows full-length NLRP1 and the antibodies used to detect the NLRP1 autoproteolytic fragments. The epitope of the N-terminal NLRP1 antibody is between NLRP1 amino acids 130 and 230. Single-letter abbreviations for the amino acid residues are as follows: A, Ala; C, Cys; D, Asp; E, Glu; F, Phe; G, Gly; H, His; I, Ile; K, Lys; L, Leu; M, Met; N, Asn; P, Pro; Q, Gln; R, Arg; S, Ser; T, Thr; V, Val; W, Trp; and Y, Tyr. (**B**) 293T cells were transfected with C-terminal HA-tagged NLRP1 and Myc-tagged HRV14-3Pro. Full-length NLRP1 and its cleavage products were visualized with the N-terminal fragment-specific NLRP1 antibody and an antibody against the C-terminal HA tag. Red arrows indicate the proposed proteolytic relationship between the observed NLRP1 fragments. Note that the presence of catalytically active 3Cpro decreased the expression of all transfected plasmids (see next panel). (**C**) To map the 3Cpro cleavage site, 293T cells were cotransfected with the indicated NLRP1 alanine mutants and HRV14-3Cpro. $3Cpro^{C146A}$ was used as a negative control. Total cell lysates were harvested 48 hours after transfection and analyzed by SDS-PAGE and immunoblotting. (**D**) Q130A abrogates HRV14-3Cpro cleavage. 293T-ASC-GFP-$NLRP1^{WT}$-FLAG and 293T-ASC-GFP-$NLRP1^{Q130A}$-FLAG cells were transfected with Myc-HRV14-3Cpro or treated with talabostat for 48 hours. Total cell lysates were analyzed by SDS-PAGE. The asterisk symbol indicates nonspecific NLRP1 degradation product. Red arrow, 3Cpro-dependent cleavage product (amino acids 131 to 1212). (**E**) Q130A abrogates 3CPro-dependent, but not talabostat-dependent, NLRP1 activation in 293T cells. Cells were transfected or treated with talabostat as in Fig. 1D and fixed 24 hours after transfection. The number of cells with ASC-GFP specks were visually scored with wide-field epifluorescence microscopy at 20× magnification. $^{**}P < 0.01$; $^{****}P < 0.0001$ (two-way ANOVA). $n = 3$ independent transfections per drug treatment. Error bars represent SEM. (**F**) Representative immunoblots demonstrate that wild-type NLRP1, but not $NLRP1^{Q130A}$, restores 3Cpro-dependent IL-1β secretion and ASC oligomerization. (**G**) Trypan blue exclusion assay demonstrates that wild-type NLRP1, but not $NLRP1^{Q130A}$, restores 3Cpro-triggered lytic cell death in *NLRP1*$^{-/-}$ human keratinocytes. $^{****}P < 0.0001$ (two-way ANOVA). $n = 3$ independent transfections per drug treatment. Error bars represent SEM.

IL-1β secretion and ASC oligomerization upon HRV14-3Cpro induction (Fig. 3E and fig. S5C) and stabilized the postcleavage NLRP1 fragment (fig. S5C). MLN4924 had a much smaller effect on talabostat-induced IL-1β secretion in keratinocytes (fig. S5B). Thus, the cullin$^{ZER1/ZYG11B}$ system does not appear to fully account for talabostat-mediated NLRP1 activation.

Given the known pleiotropic effects of MLN4924, we used CRISPR-Cas9 to delete *ZER1* and *ZYG11B* (called *ZZ*-dKO; dKO, double knockout) in 293T-ASC-GFP reporter cells

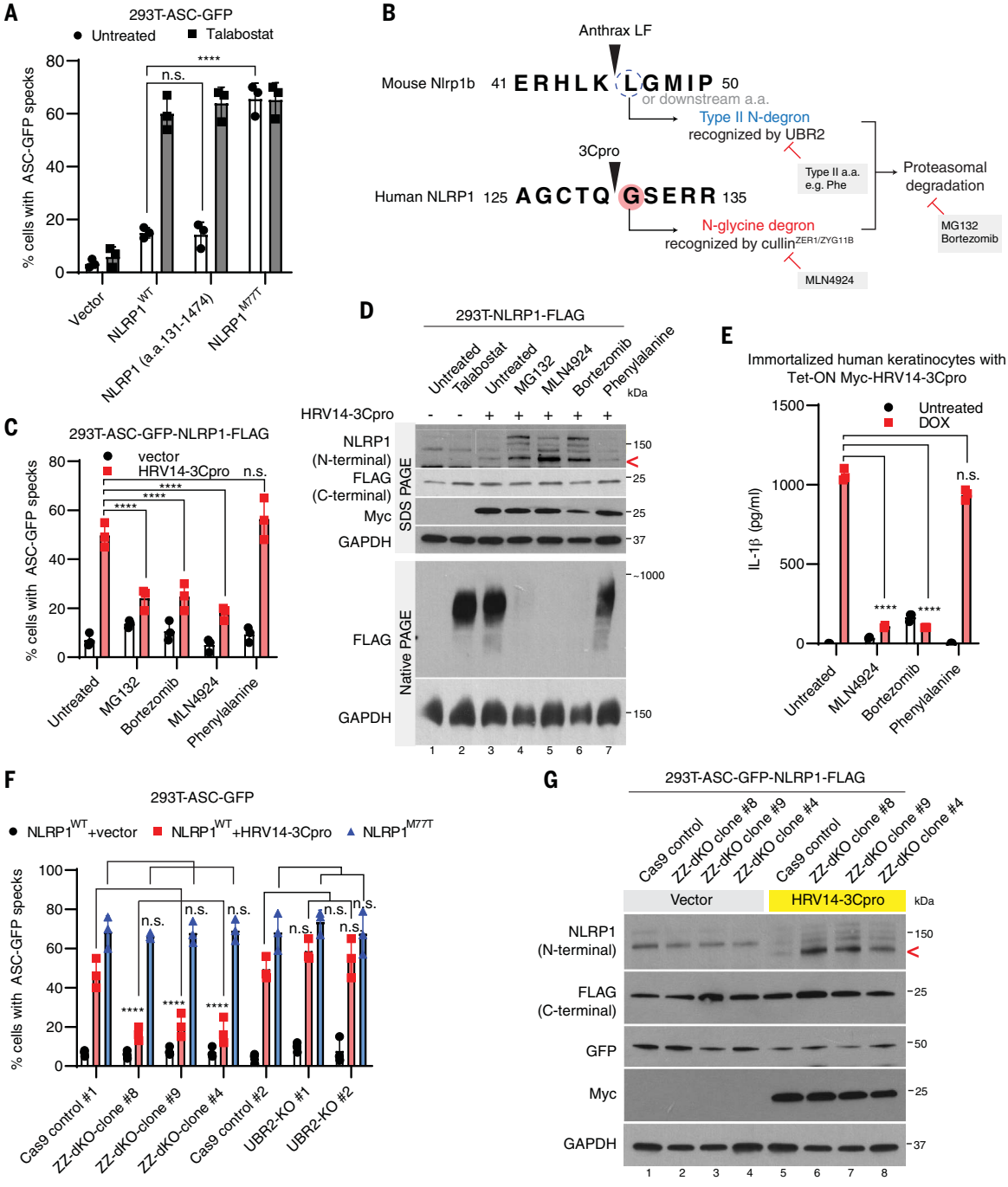

Fig. 3. 3Cpro-triggered NLRP1 activation requires the N-terminal glycine degron pathway. (**A**) Overexpressed NLRP1 (amino acids 131 to 1474) does not cause spontaneous ASC-GFP speck formation. 293T-ASC-GFP cells were transfected with wild-type NLRP1 or mutants and fixed 48 hours after transfection. ****$P < 0.0001$ (two-way ANOVA). n = 3 independent transfections per drug treatment. Error bars represent SEM. (**B**) Summary of the distinct pathways regulating postcleavage N-terminal fragment degradation in human NLRP1 and murine NLRP1B. The two types of N-degron pathway require distinct recognition receptors and demonstrate distinct sensitivities to small-molecule inhibitors. (**C**) MLN4924 and proteasomal inhibitors abrogate 3Cpro-induced ASC-GFP specks. 293T-ASC-GFP-NLRP1-FLAG cells were transfected with HRV14-3Cpro and treated with the indicated drugs for 24 hours: MLN4924 (1 μM), MG132 (2.5 μM), bortezomib (0.5 μM), or phenylalanine (1 mM). Wild-type NLRP1, but not NLRP1^{Q130A}, restores 3Cpro-dependent IL-1β secretion and ASC oligomerization. ****$P < 0.0001$ (one-way ANOVA). n = 3 independent transfections per drug treatment. Error bars represent SEM. (**D**) MLN4924 and bortezomib inhibit NLRP1 self-oligomerization and stabilize the 3Cpro cleavage fragment. 293T-NLRP1-FLAG cells were transfected with HRV14-3Cpro and treated with the indicated drugs 16 hours after transfection for another 24 hours. Lysates were analyzed by SDS-PAGE and immunoblot. The red arrowhead indicates the HRV14-3Cpro cleavage product (amino acids 131 to 1212). (**E**) IL-1β ELISA of conditioned media. ****$P < 0.0001$, one-way ANOVA. n = 3 independent doxycycline inductions per drug treatment. Error bars represent SEM. (**F**) Cullin$^{ZER1/ZYG11B}$, but not UBR2, is genetically required for 3Cpro-induced NLRP1 activation. The indicated CRISPR KO 293T-ASC-GFP cells were transfected with wild-type NLRP1 + HRV14-3Cpro (or vector) or with NLRP1^{M77T}. Cells were fixed 24 hours after transfection. ASC-GFP specks were scored using wide-field microscopy at 20×. ****$P < 0.0001$, one-way ANOVA. n = 3 transfections, >100 cells. Error bars represent SEM. (**G**) Cullin$^{ZER1/ZYG11B}$, but not UBR2, is responsible for the degradation of the 3Cpro cleavage product. CRISPR KO 293T-ASC-GFP cells stably expressing NLRP1-FLAG were transfected with HRV14-3Cpro. Cell lysates were harvested 48 hours after transfection. The red arrowhead indicates the 3Cpro cleavage product (amino acids 131 to 1212).

(data S1). The percentage of ASC-GFP specks in clonal *ZZ*-dKO 293T-ASC-GFP cells was significantly reduced after coexpression of wild-type NLRP1 and HRV14-3Cpro. By contrast, *UBR2*$^{-/-}$ cells were not significantly different from Cas9 control 293T-ASC-GFP cells (Fig. 3F and fig. S5E). As an additional control, we examined the patient-derived gain-of-function NLRP1 mutation, p.M77T, which by itself causes the destabilization of the N-terminal fragment (fig. S5A). Indeed, the percentage of ASC-GFP speck–forming cells induced by NLRP1^{M77T} did not differ among *ZZ*-dKO, *UBR2*$^{-/-}$, and control cells (Fig. 3F and fig. S5E). Therefore, cullin$^{ZER1/ZYG11B}$ is specifically required for HRV14-3Cpro–triggered human NLRP1 activation. The 3Cpro-cleaved NLRP1 fragment (amino acids 131 to 1212) was significantly stabilized in *ZZ*-dKO cells relative to control cells (Fig. 3G) but not in *UBR2*$^{-/-}$ cells (fig. S5D). Thus, the 3Cpro-cleaved NLRP1 N-terminal fragment is a substrate for the cullin$^{ZER1/ZYG11B}$-mediated N-terminal glycine degron pathway.

Live HRV infection activates the NLRP1 inflammasome in primary airway epithelial cells

We next tested the effect of live HRV infection in disease-relevant human epithelial cell types. In HeLa-Ohio cells overexpressing NLRP1–hemagglutinin tag (HA), robust HRV16 viral replication was achieved 16 hours after inoculation [multiplicity of infection (MOI) = 1], as evidenced by the accumulation of the viral capsid protein VP2 (fig. S6A, lanes 4, 5, 10, and 11). Viral replication was accompanied by the appearance of the ~120-kDa NLRP1 cleavage product in infected cells (fig. S6A). The small-molecule pan-HRV-3Cpro inhibitor rupintrivir completely abrogated NLRP1 cleavage (fig. S6A). Using HeLa-Ohio cells expressing ASC-GFP, we tested whether HRV16 infection could induce NLRP1 inflammasome complex assembly. Although HeLa-Ohio cells demonstrated less NLRP1 inflammasome activation than keratinocytes or HEK293T cells, HRV16 and talabostat caused significant ASC-GFP oligomerization (fig. S6B). These effects were only observed in HeLa-Ohio-ASC-GFP cells expressing wild-type NLRP1, not in cells expressing the cleavage-resistant NLRP1^{Q130A} mutant (fig. S6B). Thus, live HRV16 infection causes 3Cpro-dependent NLRP1 cleavage and activates the reconstituted human NLRP1 inflammasome.

HRV is one of the most common human viral pathogens responsible for respiratory tract infections. Human airway epithelial cells (AECs) are known to endogenously express multiple double-stranded RNA sensors such as TLR3, MDA5, and RIG-I, which all participate in antiviral defense. However, the repertoire of endogenous inflammasome components expressed in these cells has not been fully characterized. By examining published RNA sequencing (RNA-seq) datasets, we found that primary AECs (*44*–*48*) express a very restricted repertoire of NLR sensors (fig. S6C). Known inflammasome sensors such as *MEFV*, *NLRP3*, *NLRC5*, and *AIM2* were expressed at low levels or were undetectable (fig. S6E). We confirmed that *NLRP3* was not expressed in primary human bronchial epithelial cells [transcripts per million (TPM) < 1] (Fig. 4A and data S2). *NLRP3* was also undetectable in primary human nasal epithelium by RNA in situ staining (fig. S6D). The lack of NLRP3 inflammasome in primary normal human bronchial epithelial cells (NHBEs) was recently confirmed by an independent study (*49*). Although we cannot rule out that *NLRP3* mRNA may be transcriptionally induced under specific conditions, these results demonstrate that NLRP1, but not NLRP3, is the predominant inflammasome sensor constitutively expressed in human AECs. In addition to *NLRP1*, all AECs endogenously expressed *PYCARD* (*ASC*), *CASP1*, and the IL-1-family cytokines *IL1B* and *IL18* (Fig. 4A, data S2, and fig. S6C), suggesting that human AECs are capable of NLRP1-mediated inflammasome activation.

We next profiled the endogenous cytokine and chemokine response of NHBEs to live HRV16 infection (Fig. 4B). IL-18, whose secretion strictly depends on inflammasome activation, was the most highly induced cytokine in both HRV16-infected and talabostat-treated NHBEs (Fig. 4, C and D). IL-1β was also significantly secreted from HRV16-infected and talabostat-treated NHBEs, but its levels were lower and more variable than those of IL-18 (Fig. 4, E and F). This variability is likely due to the transcriptional regulation of *IL1B* mRNA. Similar results were obtained with primary nasal epithelial cells (fig. S6E). In agreement with the lack of endogenous *NLRP3* in NHBEs, neither IL-1β nor IL-18 secretion was affected by the NLRP3 inhibitor MCC950 after HRV16 infection or talabostat treatment. By contrast, the 3Cpro inhibitor rupintrivir completely abrogated HRV16-induced IL-1β and IL-18 secretion (Fig. 4, D and E). HRV16-infected NHBEs demonstrated cardinal features of inflammasome activation, including: (i) proteolytic processing of IL-18 and IL-1β into their p17 mature forms (Fig. 4F); (ii) endogenous ASC oligomerization (Fig. 4F); (iii) caspase-1 activation (fig. S7A); (iv) release of intact LDH activity (fig. S7B); and (v) characteristic membrane "ballooning" (fig. S7C). We then performed apical HRV16 infection of three-dimensional (3D) air-lifted human bronchial epithelium cultures and confirmed that this serotype induced the secretion of IL-18 (Fig. 5, A and B). Histologically, both HRV16 infection and talabostat treatment induced mucus cell metaplasia by Alcian blue and periodic acid–Schiff (AB-PAS) staining and gasdermin D (GSDMD) cleavage (Fig. 5C). Thus, HRV16 infection activates the NLRP1 but not NLRP3 inflammasome in primary NHBEs.

We next sought to further validate NLRP1 as the endogenous inflammasome sensor for HRV. CRISPR-Cas9–mediated deletion of *NLRP1*, *ASC*, or pro-caspase-1 in primary NHBEs completely eliminated IL-18 cleavage caused by HRV16 infection or talabostat treatment (Fig. 6A and fig. S7, D and E). Furthermore, HRV16-infected *NLRP1* knockout NHBEs were unable to cleave IL-18 into its mature p17 form (Fig. 6B) or assemble ASC into high-molecular-weight oligomers (Fig. 6B). This lack of inflammasome activation in KO cells was not caused by a general defect in viral biogenesis, as the maturation of capsid protein VP2, which itself is dependent on 3Cpro activity (*50*), was unaffected in *NLRP1*$^{-/-}$ or *ASC*$^{-/-}$ cells (Fig. 6B). These results provide further support that NLRP1 is the primary inflammasome sensor for HRV infection in human NHBEs. HRV-triggered inflammasome activation likely occurs in parallel with other immune sensing pathways, as *NLRP1*$^{-/-}$, *ASC*$^{-/-}$, and *CASP1*$^{-/-}$ NHBEs were still capable of undergoing cell death and producing other cytokines, such as IL-8 (fig. S7, F and G), upon HRV16 infection.

To confirm that HRV-induced NLRP1 activation requires the cleavage between residues Q130 and G131, we infected *NLRP1*$^{-/-}$ NHBEs rescued with either FLAG-tagged wild-type NLRP1 or NLRP1^{Q130A}. As observed previously with keratinocytes (Fig. 2, D to G), both wild-type NLRP1 and NLRP1^{Q130A} rescued talabostat-dependent IL-18 secretion in *NLRP1*$^{-/-}$ NHBEs (Fig. 6C and fig. S8B). However, only wild-type NLRP1, and not the uncleavable mutant Q130A, rescued HRV16-induced IL-18 secretion (Fig. 6C), despite similar levels of VP2 maturation. In addition, HRV16 induced strong degradation of the NLRP1 N-terminal fragment only in wild-type NLRP1 rescued NHBEs, but not NLRP1^{Q130A}-expressing cells (Fig. 6D). MLN4924 and bortezomib completely blocked HRV16-dependent IL-1β and IL-18 secretion in NHBEs (Fig. 6E and fig. S8A). MLN4924 pretreatment also stabilized the NLRP1 N-terminal cleavage fragments in HRV16-infected NHBEs expressing wild-type NLRP1 (Fig. 6G) without affecting the accumulation (Fig. 6F) of the activating C-terminal fragment of NLRP1 (Fig. 6G). Thus, both cullin$^{ZER1/ZYG11B}$ and the proteasome are necessary for HRV-triggered NLRP1 inflammasome activation in NHBEs.

Here, we report that enteroviral 3C proteases, such as HRV-3Cpro, activate the human inflammasome sensor NLRP1 via direct cleavage at a single site between amino acids Q130 and G131. This finding not only provides a unified mechanism for proteolysis-mediated activation of NLRP1 inflammasome in humans and rodents (*16*–*18*) but also reveals an unexpected role for the recently described N-terminal glycine degron pathway in human innate immunity.

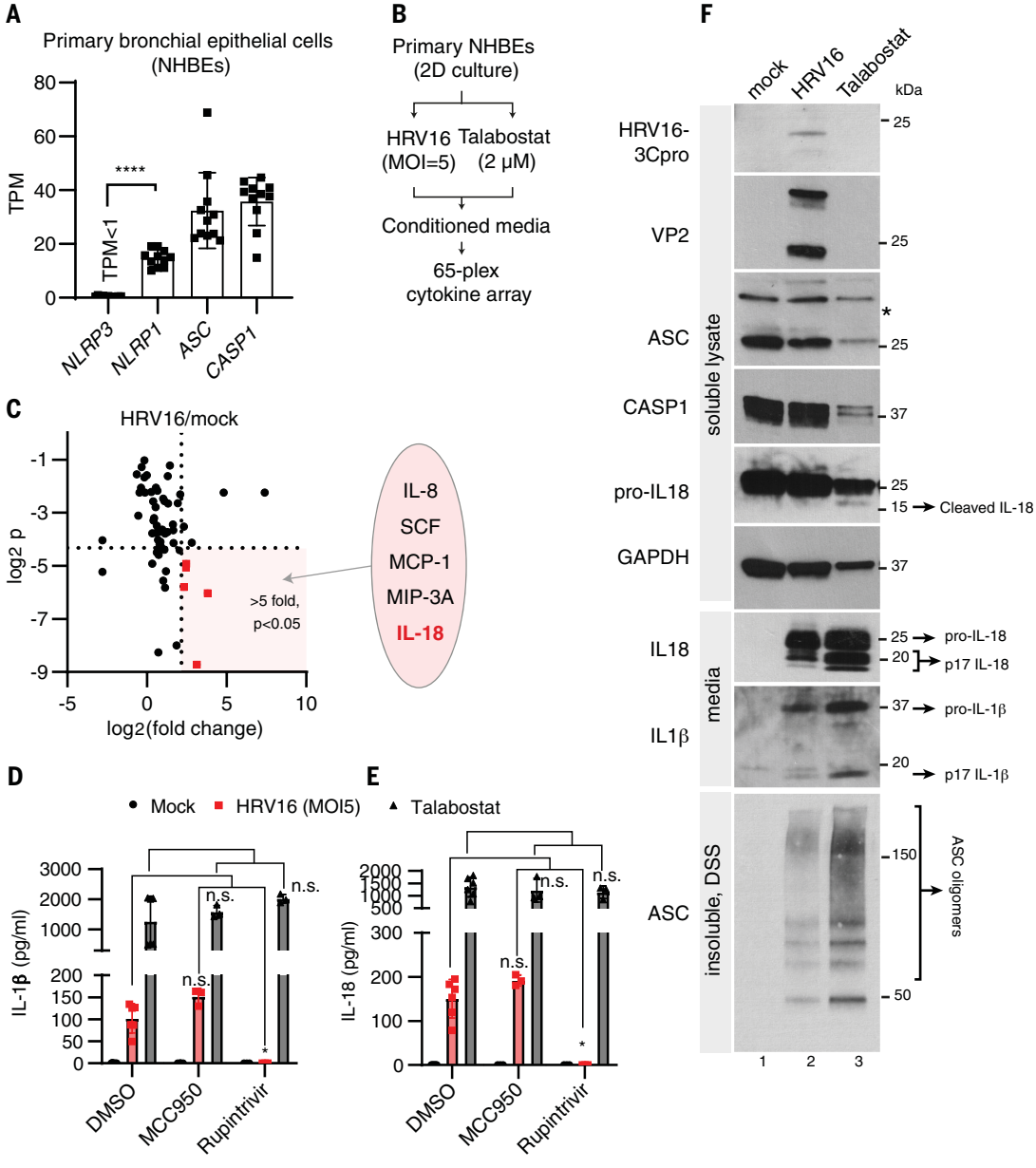

Fig. 4. HRV infection activates inflammasome-driven pyroptosis in NHBEs independently of NLRP3. (**A**) *NLRP1*, *NLRP3*, *PYCARD* (*ASC*), and *CASP1* mRNA expression (RNA-seq TPM) in NHBEs. $n = 11$, independent cultures of NHBEs. $^{****}P < 0.0001$, two-tailed Student's t test. Error bars represent SEM. (**B**) Overview of cytokine profiling of HRV16-infected and talabostat-treated NHBEs. (**C**) Cells were inoculated with HRV16 at MOI = 5 and cultured at 33°C for 48 hours. Luminex array was performed on conditioned media after removing cell debris. $n = 3$ independent infections and treatment. Cytokines and chemokines that were induced by at least fivefold, such as IL-18 ($P < 0.05$, Student's t test, lognormal values), are highlighted in red. (**D**) MCC950 did not affect HRV16-triggered IL-1β secretion in NHBEs. NHBEs were pretreated with MCC950 (5 μM) or rupintrivir (10 nM) before HRV16 inoculation or talabostat (2 μM) treatment. $^{*}P < 0.05$ (two-way ANOVA). $n = 3$ independent drug treatments. Error bars represent SEM. (**E**) MCC950 did not affect HRV16-triggered IL-18 secretion in NHBEs. NHBEs were pretreated with MCC950 (5 μM) or rupintrivir (10 nM) before HRV16 inoculation or talabostat (2 μM) treatment. $^{*}P < 0.05$ (two-way ANOVA). $n = 3$ independent drug treatments. Error bars represent SEM. (**F**) Representative immunoblot demonstrates the secretion of cleaved IL-1β and IL-18 and ASC oligomerization in HRV16-infected primary NHBEs. Cells were inoculated with HRV16 (MOI = 5) or treated with talabostat (2 μM) for 48 hours at 33°C.

Mechanistically, 3Cpro-cleavage leaves a glycine residue (p.G131) on the NLRP1 fragment, which is recognized by the cullin$^{ZER1/ZYG11B}$ N-glycine degron machinery and is subsequently degraded by the proteasome (Fig. 3B). This constitutes a key step in unleashing the NLRP1 FIIND^{UPA}-CARD fragment to fully assemble the inflammasome complex consisting of ASC and caspase-1. It is noteworthy that a single cleavage site mutation (Q130A) can completely block 3Cpros from activating the NLRP1 inflammasome without affecting talabostat-triggered NLRP1 activation. This suggests that NLRP1 can undergo multiple modes of activation.

The identification of enteroviral 3Cpros as a pathogen-derived trigger for human NLRP1 also sheds light on the evolutionary trajectory of NLRP1. The 3Cpro cleavage site arose in the common ancestor for simians and is absent in prosimians such as tarsiers and lemurs (fig. S9). It is conceivable that the more recently evolved, 3Cpro-responsive *NLRP1* allele has provided a selective survival advantage during the evolution of simian primates, including humans, presumably to sense and mount an appropriate immune response against certain simian-tropic enteroviral pathogens. Nevertheless, our work does not preclude the possibility that human NLRP1 can detect other pathogen- or danger-derived signals besides 3Cpros.

Our findings establish human NLRP1 as part of the repertoire of viral sensors in the airway epithelium and challenge the widely held notion that viral proteases largely serve to disable host immune sensing. As the inflammasome pathway does not require de novo protein synthesis, it is particularly well suited as a fail-safe, second-line defense. The inflammasome can commit the infected cells to pyroptosis and release IL-18 even after host transcription and translation have been shut off by viral virulence factors, thereby alerting other cell types

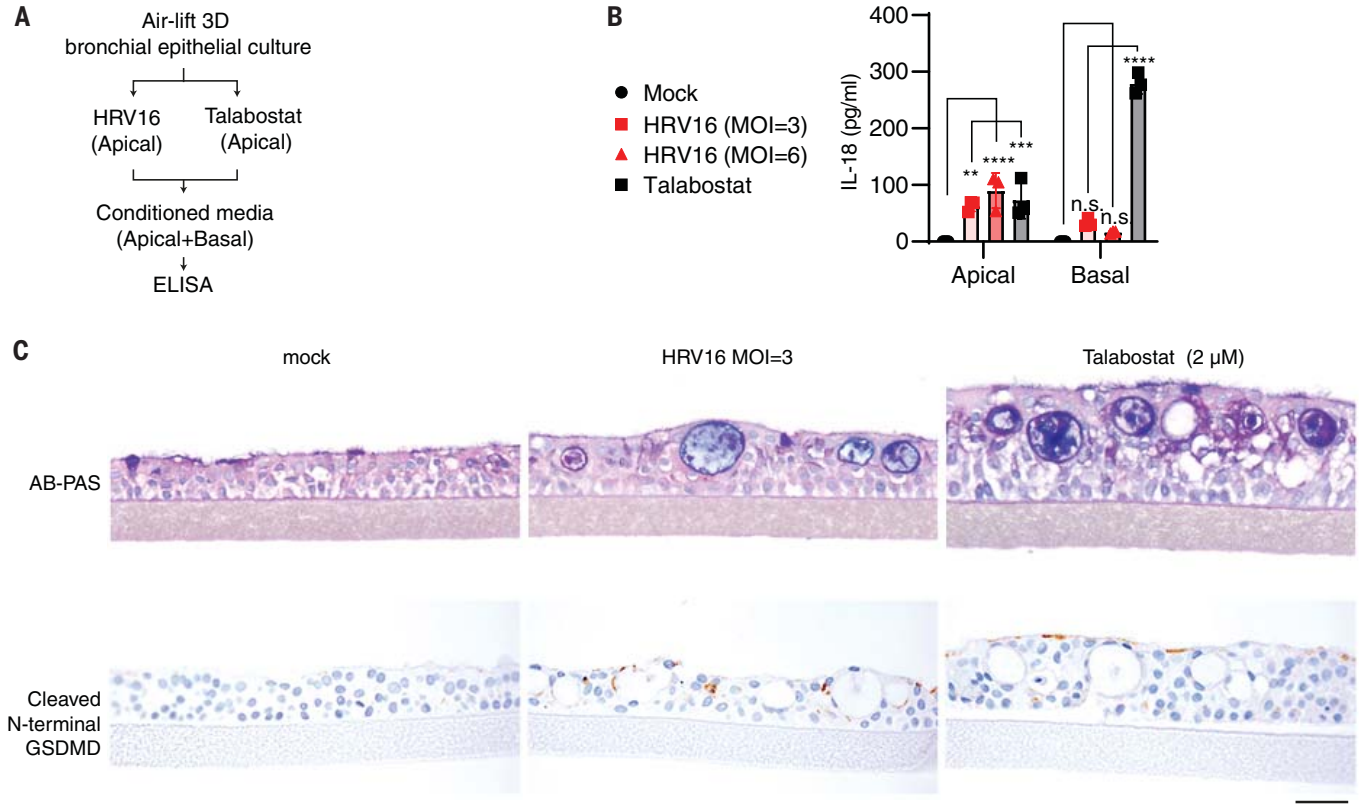

Fig. 5. HRV infection leads to inflammasome activation and IL-18 secretion in 3D bronchial epithelial cultures. (**A**) Overview of apical HRV infection in 3D human bronchial epithelial cultures. (**B**) IL-18 levels in apical or basal media 48 hours after infection or talabostat treatment. $^{**}P < 0.01$, $^{***}P < 0.001$, $^{****}P < 0.0001$ (two-way ANOVA). $n = 3$ independent infected or treated cultures. Error bars represent SEM. (**C**) Representative Alcian blue and periodic acid–Schiff (AB-PAS) staining (top) and immunohistochemical staining for cleaved (N-terminal) GSDMD (bottom) of HRV16-infected (MOI = 3) and talabostat (2 μM)–treated 3D human bronchial epithelial cultures. Staining performed on two sections from three independent 3D bronchial epithelial cultures. Scale bar, 50 μm.

via paracrine signaling. (*51*). In keeping with this notion, *NLRP1* knockout did not lead to an appreciable increase in infectious viruses 48 hours after inoculation (fig. S8C). We propose that the NLRP1 inflammasome plays an important role in antiviral immunity and inflammation in the human airway epithelium. Respiratory viral infections, including HRVs, are well-known risk factors for the exacerbation of asthma and chronic obstructive pulmonary disease (*52*). Therefore, the NLRP1 inflammasome pathway might serve as a potential therapeutic target to treat these diseases and their complications.

Materials and methods

Cell culture and chemicals

293Ts (ATCC #CRL-3216), HeLa-Ohio (ECACC General Cell Collection #84121901), and normal bronchial epithelial cells (NHBE, Lonza #CC-2541) were cultured according to the suppliers' protocols with modifications (*53*) Immortalized human keratinocytes (N/TERT-1, or N/TERT herein) were provided by H. Reinwald (MTA) (*54*). Primary nasal epithelial cells were obtained from nasal epithelial biopsies obtained from adult patients scheduled for rhinoplasty and obtained with informed consent at National University Hospital (NUH), Singapore. Fresh nasal epithelial tissues were used to derive nasal cells as previously described (*55*). All cell lines underwent routine Mycoplasma testing with Lonza MycoAlert (Lonza #LT07-118). The following drugs and chemicals were used as part of this study: MCC950 (MCE, #HY-12815), bortezomib, and MLN4924 (provided by D. Lane; p53, A*STAR, Singapore), rupintrivir (Sigma, #PZ0315), talabostat (MCE, #HY-13233), MG132 (MCE, #HY13259), A83-01 (MCE, #HY-10432A), Y-27632 (MCE, #HY-10583), isoprenaline (MCE, #HY-B0468).

Plasmid transfection and stable cell line generation using lentiviruses

293T-ASC-GFP, N/TERT-ASC-GFP, and N/TERT *NLRP1*-KO cells were described previously (*19*). All transient expression plasmids were cloned into the pCS2+ vector using standard restriction cloning using ClaI and XhoI flanking the open reading frames. P site–directed mutagenesis was carried out with QuickChangeXL II (Agilent #200522). Constitutive lentiviral expression was performed using pCDH vectors (SystemBio). Doxycycline-inducible Tet-ON lentiviral constructs were based on the pTRIPZ backbone (ThermoFisher Scientific).

Antibodies, staining reagents, and cytokine analysis

The following antibodies were used in this study: c-Myc (Santa Cruz Biotechnology, #sc-40), HA tag (Santa Cruz Biotechnology, #sc-805), GAPDH (Santa Cruz Biotechnology, #sc-47724), ASC (Adipogen, #AL-177), CASP1 (Santa Cruz Biotechnology, #sc-622), IL1B (R&D systems, #AF-201), FLAG (SigmaAldrich, #F3165), GFP (Abcam, #ab290), NLRP1 (R&D systems, #AF6788), IL18 (Abcam ab207324), cleaved GSDMD-NT (Asp^{275}) (Cell Signaling Technology, #36425), and HRV-VP2 (QED Bioscience, #18758). HRV16-3Cpro was detected by rabbit serum provided by A. Palmenberg and J. Gern (University of Wisconsin). All horseradish peroxidase (HRP)–conjugated secondary antibodies were purchased from Jackson Immunoresearch (goat anti-mouse IgG: 115-035-166; goat anti-rabbit IgG: 111-035-144; and donkey anti-goat IgG: 705-005-147). The protocol for blue native PAGE and disuccinimidyl suberate (DSS) cross-linking were performed as previously described (*7*). For AB-PAS staining and immunohistochemistry,

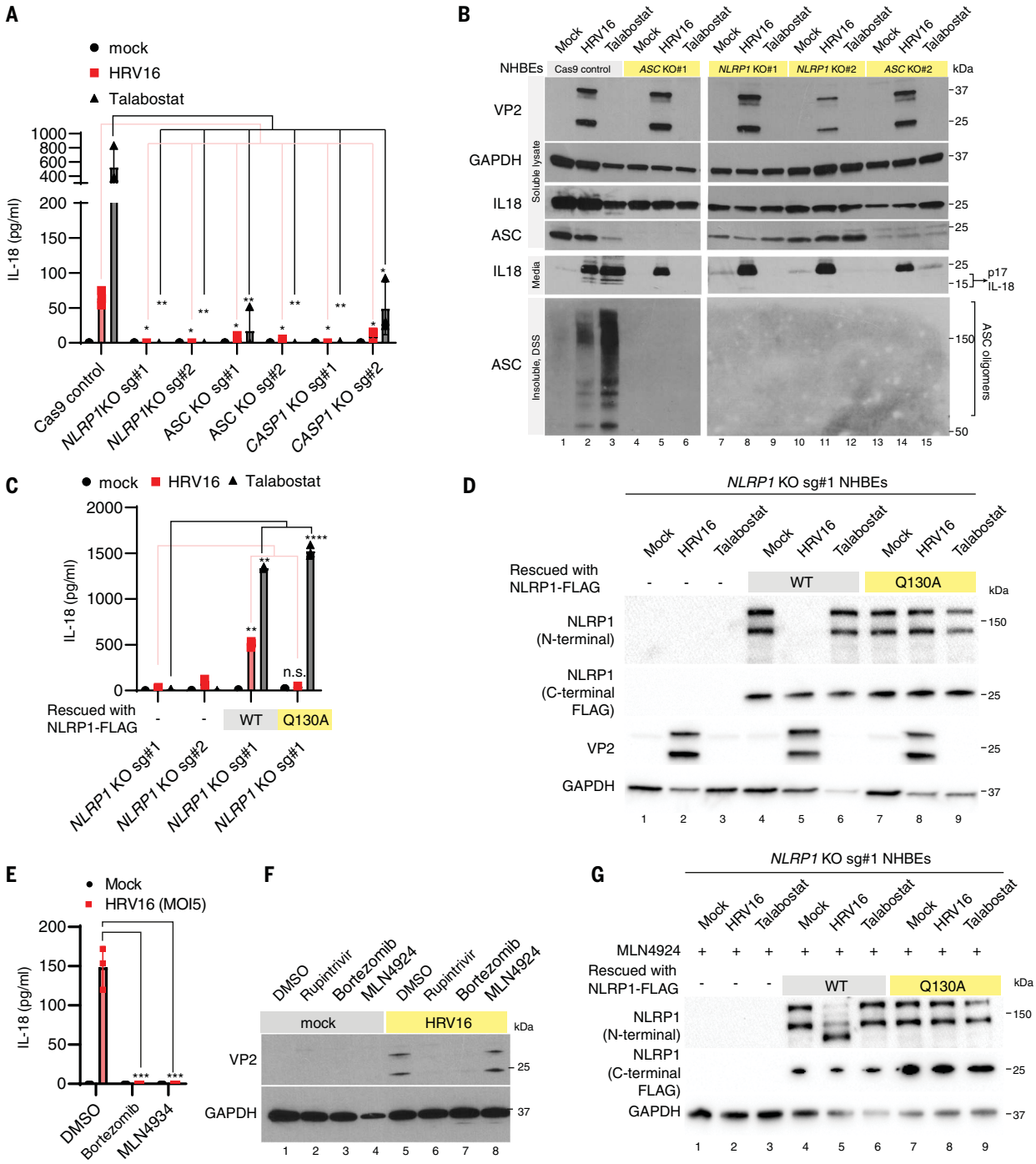

Fig. 6. NLRP1 cleavage and the N-glycine degron pathway are indispensable for HRV-dependent inflammasome activation in NHBEs. (**A**) Endogenous NLRP1, ASC, and caspase-1 are indispensable for HRV16-induced IL-18 secretion in NHBEs. Cas9-control, *NLRP1*$^{-/-}$, *ASC*$^{-/-}$, and *CASP1*$^{-/-}$ NHBEs were infected with HRV16 (MOI = 5). Conditioned media were harvested 48 hours after infection. *P < 0.05, **P < 0.001 (two-way ANOVA). n = 3 independent live viral infections per drug treatment. Error bars represent SEM. (**B**) *NLRP1* is genetically required for HRV16-induced IL-18 cleavage and ASC oligomerization. Cas9 control, *NLRP1*$^{-/-}$, and *ASC*$^{-/-}$ NHBEs were infected with HRV16, as before. Cleaved IL-18 are marked with arrows. (**C**) Mutating the NLRP1 cleavage site abrogates HRV16-triggered IL-18 secretion in NHBEs. *NLRP1*$^{-/-}$ NHBEs were rescued with lentiviral constructs expressing FLAG-tagged NLRP1^{WT} or NLRP1^{Q130A}, which carried silent mutations at the PAM site. The rescued cells were infected with HRV16 or treated with talabostat. Conditioned media was analyzed by IL-18 ELISA. **P < 0.01, ****P < 0.0001 (two-way ANOVA), n = 3 replicates from one of two independent infections. Error bars represent SEM. (**D**) HRV infection leads to NLRP1 cleavage and degradation of NLRP1 N-terminal fragments. *NLRP1*$^{-/-}$ or NLRP1^{WT}- or NLRP1^{Q130A}-rescued cells were infected with HRV16 or treated with talabostat. Cells were harvested 48 hours after infection. (**E**) MLN4924 and bortezomib block HRV16-induced IL-18 secretion. NHBEs were pretreated with MLN4924 (1 μM) or bortezomib (1 μM) before HRV16 infection or talabostat treatment. IL-18 levels were measured with ELISA. ***P < 0.001 (two-way ANOVA), n = 3 independent infections per treatment. Error bars represent SEM. (**F**) MLN4924 does not affect 3Cpro-dependent VP2 maturation in the course of HRV16 infection. Lysates from HRV16-infected NHBEs in Fig. 5F were analyzed by immunoblotting 48 hours after HRV1 inoculation. (**G**) MLN4924 stabilizes the 3Cpro cleavage fragment (amino acids 131 to 1212). NHBEs were pretreated with MLN4924 and infected with HRV as in (D).

5-μm formalin-fixed paraffin-embedded 3D bronchial epithelial sections were deparaffinized in xylenes and rehydrated through a series of alcohol before being hydrated in water. AB-PAS staining was then carried out using a staining kit (Abacm, ab245876) according to manufacturer's instructions. For immunohistochemistry staining to visualize cleaved GSDMD-N terminal fragment, a previously published protocol was used (*56*). For trypan blue staining, cells were incubated with trypan blue stain (ThermoFisher Scientific, #15250061), and the percentage of positively stained cells versus total cell count calculated. Three cell counts were performed per condition. For RNAscope, primary human nasal epithelium sections (normal) were obtained through the National University of Singapore (NUS/NUH, Singapore) with informed consent. Visualization of NLRP1 and NLRP3 RNA was performed according to manufacturer's instructions and recommendations (RNAscope 2.5 HD-Red, ACDbio).

Cytokine and chemokine measurements were carried out with human IL-1β enzyme-linked immunosorbent assay (ELISA) kit (BD, #557953), human IL-18 ELISA kit (MBL Bioscience, #7620), and Immune Monitoring 65-Plex Human ProcartaPlex Panel (ThermoFisher Scientific, EPX650-10065-901) according to the manufacturer's protocol. All primary antibodies were used at 250 ng/ml.

Immunoblotting

For whole cell lysates, cells were resuspended in tris-buffered saline 1% NP-40 with protease inhibitors (ThermoFisher Scientific, #78430). Protein concentration was determined using the Bradford assay (ThermoFisher Scientific, #23200) and 20 μg of protein loaded, unless stated otherwise. For analysis of IL-1β and IL-18 cleavage in the media by immunoblotting, samples were 10 times–concentrated using filtered centrifugation (Merck, Amicon Ultra, #UFC5003BIK). Protein samples were run using SDS-PAGE system (Bio-Rad), immunoblotted, and then visualized using x-ray film detector or ChemiDoc Imaging system (Bio-Rad).

Microscopy

Images of ASC-GFP specs were acquired in three random fields in 4′,6-diamidino-2-phenylindole (DAPI) (358 nm/461 nm) and GFP (469 nm/525 nm) channels using EVOS microscope (FL Auto M5000, ThermoFisher Scientific, #AMF5000) with a EVOS 20× Objective (achromat, LWD, phase-contrast, 0.40NA/6.92WD, ThermoFisher Scientific, #AMEP4934) and built-in camera (Sony IMX265 monochrome CMOS) according to manufacturer's protocol (EVOS M5000 Manual, ThermoFisher Scientific Publication Number MAN0017563). Counting of the number of ASC-GFP specks was performed using ImageJ Fiji "watershed" and "find maxima" built-in functions. Briefly, all DAPI images were subjected to thresholding to distinguish background from foreground to give a binary image. The watershed algorithm was used to separate touching objects, before segmented objects could be analyzed and counted to give a total nuclei count. The number of GFP-ASC specks was calculated by "find maxima" function and noise tolerance set accordingly to count the total number of specks per image. The number of specks was then calculated as a percentage of total nuclei in three representative fields of view. Brightfield images of stained sections were taken at 40× magnification using a widefield microscope (Zeiss AxioImager Z.2, Zeiss) with a 40× oil immersion objective (EC Plan Neofluar Antiflex, Zeiss). Images were acquired with the built-in camera (Axio Cam 506 mono 1.2 Mbps, Zeiss).

HRV16 virus propagation

HRV used in the study was HRV-A16 (strain 11757; ATCC VR-283, Manassas, VA, USA) and was propagated in HeLa cell line (HeLa Ohio, ECACC 84121901, Porton Down, Salisbury, Wiltshire, UK). HeLa cells were grown in Eagle's Minimum Essential Medium (EMEM) ATCC 30-2003, supplemented with 10% fetal bovine serum (FBS) (BioWest, Kansas City, MO, USA), 2% HEPES, and 1% Antibiotic-Antimycotic (Anti-Anti) (Gibco) and incubated at 37°C in a humidified incubator with 5% CO_2. To propagate HRV16, HeLa cells were first seeded to achieve 80 to 90% confluence in 24-well plates overnight. Cells were rinsed with 1X Dulbecco's phosphate-buffered saline (DPBS) and infected with HRV16 before addition of EMEM with 2% FBS, 2% HEPES, and 1% Anti-Anti. Infected HeLa cells were incubated at 33°C for 2 to 3 days. Viruses were harvested from the supernatants of infected HeLa cells when ~80% cytopathic effects (CPE) were observed. HRV stocks were centrifuged at 1500*g* for 10 min at 4°C to remove cellular debris and aliquoted into cryovials for storage at −80°C.

Inoculation of human rhinovirus

HRV was diluted using the respective cell culture medium and inoculated at MOI of 5.0 (NHBE) and 1.0 (HeLa), respectively. Infected cells were incubated at 33°C for 1 hour. Conditioned noninfected cell culture medium from viral propagation was added as an uninfected control. The HRV-infected and control cells were then incubated at 33°C for up to 48 hours post-infection (hpi). Cell culture supernatant and cell lysate were collected to perform relevant assays between 24 and 72 hpi.

Viral quantification using rhinovirus plaque assay

HeLa cells (at 85 to 95% confluence) in 24-well plates were incubated with 100 μl of serial dilutions from 10^{-1} to 10^{-6} of virus-containing conditioned media at 33°C for 1 hour. The plates were rocked every 15 min to ensure equal distribution of virus. The inoculum was removed and replaced with 1 ml of Avicel (FMC Biopolymer) overlay to each well and incubated at 33°C for 65 to 72 hours. The overlay components were optimized to obtain HRV plaques suitable for counting. Avicel powder was added into double-strength MEM to formulate 1.2% Avicel solution, with a final concentration comprising 3% FBS, 2% HEPES, 1.5% $NaHCO_3$, 3% $MgCl_2$, and 1% Anti-Anti. Avicel overlay was removed after the incubation period, and cells were fixed with 20% formalin in PBS for 1 hour. Formalin was removed, and cells were washed with PBS. The fixed cells were stained with 1% crystal violet for 15 min and washed. The plaque-forming units (PFU) were calculated as follows: number of plaques × dilution factor = number of PFU per 100 μl, which is then expressed as PFU per milliliter.

HRV16 infection of 3D reconstructed human bronchial epithelium

3D culture of bronchial epithelium was purchased from Mattek (AIR-1484 AIR-100 EpiAirway, 3D Respiratory Epithelial Human MicroTissues) and cultured using the Extended Culture protocol as advised by the supplier.

CRISPR-Cas9 knockout

CRISPR-Cas9 editing performed in 293T cells was performed according to the method reported by the Doyon group (*57*), except that single guide RNAs (sgRNAs) were cloned into pSpCas9(BB)-2A-Puro (PX459) V2.0 (Addgene 62988). Single clones of ouabain-resistant cells were selected for ZYG11B/ZER1 double knockout. Clones 1 to 6 were transfected with ZYG11B sg5 and 6. Clones 7 to 12 were transfected with ZYG11B sg7 and 8. All clones received three guides for ZER1, sg5, 6, 8. 293T UBR2 KOs were cultured as polyclonal pools after ouabain selection. N/TERT and NHBE KOs were performed using LentiCRISPR-V2 (Addgene 52961) and stable lentiviral transduction. The sgRNAs used are listed in Table 1. Knockout efficiency was tested with immunoblot or Sanger sequencing of the targeted genomic DNA locus 7 to 10 days after puromycin selection.

RNA-seq of NHBEs

Library preparation, quality control, and high-throughput sequencing were provided by Macrogen, Singapore. Total RNA isolated from NHBEs was processed using Library Kit TruSeq Stranded mRNA LT Sample Prep (Illumina) according the manufacturer's protocol specified in Library Protocol TruSeq Stranded mRNA Sample Preparation Guide, Part 15031047. Sequencing was carried out with NovaSeq 6000 with NovaSeq 6000 S4 Reagent Kit and Sequencing Protocol NovaSeq 6000 System User Guide Document 1000000019358 v02 (Illumina).

Table 1. CRISPR sgRNA sequences used to generate knockout 293Ts, immortalized keratinocytes, and NHBEs.

sgRNA used (gene and sgRNA number)	Sequence (5′ to 3′)
NLRP1#1	GATAGCCCGAGTGACATCGG
NLRP1#2	AGCCCGAGTGACATCGGTGG
CASP1#1	ACAGACAAGGGTGCTGAACA
CASP1#2	ATTGACTCCGTTATTCCGAA
CASP1#3	TGACTCCGTTATTCCGAAAG
ASC#2	GCTAACGTGCTGCGCGACAT
ASC#3	CATGTCGCGCAGCACGTTAG
UBR2#1	TGCATAACTTGAACTTTGAG
UBR2#2	TCCATGCACAAAACACAAGT
UBR2#3	ACTGTGGTGATACTGAAGCC
UBR2#4	TGATACTGAAGCCTGGAAAG
UBR2#5	TTGCATGCTGTTTAATGATG
ZER1#5	CAGGGACCCAATCAATCATG
ZER1#6	GGCAGGACGAGTCTATCCAG
ZER1#7	AGGCTGAAGAAGCTCTCGTG
ZER1#8	TGTAGGCTGGAATGTGCGTG
ZYG11B#5	AGCGCTCGTAAGGATCCTCG
ZYG11B#6	GCAGTGGCTTTGCAACCATG
ZYG11B#7	CTTGGTTAAGTTAAATACAC
ZYG11B#8	CAAGTTCCACTAACTTGTGG

Trimmed reads are mapped to reference genome with HISAT2. After the read mapping, Stringtie was used for transcript assembly. Expression profile was calculated for each sample and transcript/gene as read count and FPKM (fragment per kilobase of transcript per million mapped reads).

Analysis of published RNA-seq datasets

RNA-seq data for human AECs was extracted from the following published datasets: Nasal#1-GSE107898, Nasal#2-GSE55458, Bronchial#1-GSE107971, Bronchial#2-GSE107897, and Alveolar#1-GSE61220. In datasets where multiple treatment conditions were reported, only the basal/mock conditions were selected. RPM values Nasal#2-GSE55458 and Bronchial#1-GSE107971 were logged for heatmap generation. Color mapping was performed using the "Double gradient" method in Graphpad Prism 8.

Caspase-1 GLO and LDH release

Caspase-1 GLO (Promega, #G9951) and LDH release assay (Promega CytoTox96, #G1780) were both carried out according to protocols provided by the manufacturers.

Statistical analysis

Statistical analyses were performed using Prism 8 (GraphPad). The methods for analysis are included in the figure legends. Error bars show mean values with SEM.

REFERENCES AND NOTES

1. J. D. G. Jones, R. E. Vance, J. L. Dangl, Intracellular innate immune surveillance devices in plants and animals. *Science* **354**, aaf6395 (2016). doi: 10.1126/science.aaf6395; pmid: 27934708
2. M. H. Shaw, T. Reimer, Y.-G. Kim, G. Nuñez, NOD-like receptors (NLRs): Bona fide intracellular microbial sensors. *Curr. Opin. Immunol.* **20**, 377–382 (2008). doi: 10.1016/j.coi.2008.06.001; pmid: 18585455
3. T.-D. Kanneganti, M. Lamkanfi, G. Núñez, Intracellular NOD-like receptors in host defense and disease. *Immunity* **27**, 549–559 (2007). doi: 10.1016/j.immuni.2007.10.002; pmid: 17967410
4. E. Latz, The inflammasomes: Mechanisms of activation and function. *Curr. Opin. Immunol.* **22**, 28–33 (2010). doi: 10.1016/j.coi.2009.12.004; pmid: 20060699
5. J. Sand *et al*., Expression of inflammasome proteins and inflammasome activation occurs in human, but not in murine keratinocytes. *Cell Death Dis.* **9**, 24 (2018). doi: 10.1038/s41419-017-0009-4; pmid: 29348630
6. S. Grandemange *et al*., A new autoinflammatory and autoimmune syndrome associated with NLRP1 mutations: NAIAD (*NLRP1*-associated autoinflammation with arthritis and dyskeratosis). *Ann. Rheum. Dis.* **76**, 1191–1198 (2017). doi: 10.1136/annrheumdis-2016-210021; pmid: 27965258
7. F. L. Zhong *et al*., Germline NLRP1 mutations cause skin inflammatory and cancer susceptibility syndromes via inflammasome activation. *Cell* **167**, 187–202.e17 (2016). doi: 10.1016/j.cell.2016.09.001; pmid: 27662089
8. O. Mamaï *et al*., Multiple self-healing palmoplantar carcinoma: A familial predisposition to skin cancer with primary palmoplantar and conjunctival lesions. *J. Invest. Dermatol.* **135**, 304–308 (2015). doi: 10.1038/jid.2014.311; pmid: 25050600
9. J. Sui *et al*., NLRP1 gene polymorphism influences gene transcription and is a risk factor for rheumatoid arthritis in han chinese. *Arthritis Rheum.* **64**, 647–654 (2012). doi: 10.1002/art.33370; pmid: 21976003
10. C. B. Levandowski *et al*., NLRP1 haplotypes associated with vitiligo and autoimmunity increase interleukin-1β processing via the NLRP1 inflammasome. *Proc. Natl. Acad. Sci. U.S.A.* **110**, 2952–2956 (2013). doi: 10.1073/pnas.1222808110; pmid: 23382179
11. E. D. Boyden, W. F. Dietrich, *Nalp1b* controls mouse macrophage susceptibility to anthrax lethal toxin. *Nat. Genet.* **38**, 240–244 (2006). doi: 10.1038/ng1724; pmid: 16429160
12. Z. L. Newman *et al*., Susceptibility to anthrax lethal toxin-induced rat death is controlled by a single chromosome 10 locus that includes *rNlrp1*. *PLOS Pathog.* **6**, e1000906 (2010). doi: 10.1371/journal.ppat.1000906; pmid: 20502689
13. K. A. Hellmich *et al*., Anthrax lethal factor cleaves mouse Nlrp1b in both toxin-sensitive and toxin-resistant macrophages. *PLOS ONE* **7**, e49741 (2012). doi: 10.1371/journal.pone.0049741; pmid: 23152930
14. J. L. Levinsohn *et al*., Anthrax lethal factor cleavage of Nlrp1 is required for activation of the inflammasome. *PLOS Pathog.* **8**, e1002638 (2012). doi: 10.1371/journal.ppat.1002638; pmid: 22479187
15. J. Chavarría-Smith, R. E. Vance, Direct proteolytic cleavage of NLRP1B is necessary and sufficient for inflammasome activation by anthrax lethal factor. *PLOS Pathog.* **9**, e1003452 (2013). doi: 10.1371/journal.ppat.1003452; pmid: 23818853
16. A. J. Chui *et al*., N-terminal degradation activates the NLRP1B inflammasome. *Science* **364**, 82–85 (2019). doi: 10.1126/science.aau1208; pmid: 30872531
17. A. Sandstrom *et al*., Functional degradation: A mechanism of NLRP1 inflammasome activation by diverse pathogen enzymes. *Science* **364**, eaau1330 (2019). doi: 10.1126/science.aau1330; pmid: 30872533
18. H. Xu *et al*., The N-end rule ubiquitin ligase UBR2 mediates NLRP1B inflammasome activation by anthrax lethal toxin. *EMBO J.* **38**, e101996 (2019). doi: 10.15252/embj.2019101996; pmid: 31268597
19. F. L. Zhong *et al*., Human DPP9 represses NLRP1 inflammasome and protects against autoinflammatory diseases via both peptidase activity and FIIND domain binding. *J. Biol. Chem.* **293**, 18864–18878 (2018). doi: 10.1074/jbc.RA118.004350; pmid: 30291141
20. M. C. Okondo *et al*., Inhibition of Dpp8/9 Activates the Nlrp1b Inflammasome. *Cell Chem. Biol.* **25**, 262–267.e5 (2018). doi: 10.1016/j.chembiol.2017.12.013; pmid: 29396289
21. N. M. de Vasconcelos *et al*., DPP8/DPP9 inhibition elicits canonical Nlrp1b inflammasome hallmarks in murine macrophages. *Life Sci. Alliance* **2**, e201900313 (2019). doi: 10.26508/lsa.201900313; pmid: 30718379
22. K. M. Cirelli *et al*., Inflammasome sensor NLRP1 controls rat macrophage susceptibility to *Toxoplasma gondii*. *PLOS Pathog.* **10**, e1003927 (2014). doi: 10.1371/journal.ppat.1003927; pmid: 24626226
23. S. E. Ewald, J. Chavarria-Smith, J. C. Boothroyd, NLRP1 is an inflammasome sensor for *Toxoplasma gondii*. *Infect. Immun.* **82**, 460–468 (2014). doi: 10.1128/IAI.01170-13; pmid: 24218483
24. R. Zell, *Picornaviridae*—the ever-growing virus family. *Arch. Virol.* **163**, 299–317 (2018). doi: 10.1007/s00705-017-3614-8; pmid: 29058149
25. S. C. Piper *et al*., The role of interleukin-1 and interleukin-18 in pro-inflammatory and anti-viral responses to rhinovirus in primary bronchial epithelial cells. *PLOS ONE* **8**, e63365 (2013). doi: 10.1371/journal.pone.0063365; pmid: 23723976
26. A. C. Palmenberg, Proteolytic processing of picornaviral polyprotein. *Annu. Rev. Microbiol.* **44**, 603–623 (1990). doi: 10.1146/annurev.mi.44.100190.003131; pmid: 2252396
27. E. J. Walker *et al*., Rhinovirus 3C protease facilitates specific nucleoporin cleavage and mislocalisation of nuclear proteins in infected host cells. *PLOS ONE* **8**, e71316 (2013). doi: 10.1371/journal.pone.0071316; pmid: 23951130
28. S. N. Croft, E. J. Walker, R. Ghildyal, Human Rhinovirus 3C protease cleaves RIPK1, concurrent with caspase 8 activation. *Sci. Rep.* **8**, 1569 (2018). doi: 10.1038/s41598-018-19839-4; pmid: 29371673
29. S. de Breyne, J. M. Bonderoff, K. M. Chumakov, R. E. Lloyd, C. U. T. Hellen, Cleavage of eukaryotic initiation factor eIF5B by enterovirus 3C proteases. *Virology* **378**, 118–122 (2008). doi: 10.1016/j.virol.2008.05.019; pmid: 18572216
30. A. Mukherjee *et al*., The coxsackievirus B $3C^{pro}$ protease cleaves MAVS and TRIF to attenuate host type I interferon and apoptotic signaling. *PLOS Pathog.* **7**, e1001311 (2011). doi: 10.1371/journal.ppat.1001311; pmid: 21436888
31. E. J. Buenz, C. L. Howe, Picornaviruses and cell death. *Trends Microbiol.* **14**, 28–36 (2006). doi: 10.1016/j.tim.2005.11.003; pmid: 16337385
32. S. N. Croft, E. J. Walker, R. Ghildyal, Picornaviruses and apoptosis: Subversion of cell death. *mBio* **8**, e01009-17 (2017). doi: 10.1128/mBio.01009-17; pmid: 28928208
33. D. A. Matthews *et al*., Structure of human rhinovirus 3C protease reveals a trypsin-like polypeptide fold, RNA-binding site, and means for cleaving precursor polyprotein. *Cell* **77**, 761–771 (1994). doi: 10.1016/0092-8674(94)90059-0; pmid: 7515772

34. J. Chavarría-Smith, P. S. Mitchell, A. M. Ho, M. D. Daugherty, R. E. Vance, Functional and evolutionary analyses identify proteolysis as a general mechanism for NLRP1 inflammasome activation. *PLOS Pathog.* **12**, e1006052 (2016). doi: 10.1371/journal.ppat.1006052; pmid: 27926929
35. J. N. Finger *et al.*, Autolytic proteolysis within the function to find domain (FIIND) is required for NLRP1 inflammasome activity. *J. Biol. Chem.* **287**, 25030–25037 (2012). doi: 10.1074/jbc.M112.378323; pmid: 22665479
36. A. D'Osualdo *et al.*, CARD8 and NLRP1 undergo autoproteolytic processing through a ZU5-like domain. *PLOS ONE* **6**, e27396 (2011). doi: 10.1371/journal.pone.0027396; pmid: 22087307
37. R. B. Register, C. R. Uncapher, A. M. Naylor, D. W. Lineberger, R. J. Colonno, Human-murine chimeras of ICAM-1 identify amino acid residues critical for rhinovirus and antibody binding. *J. Virol.* **65**, 6589–6596 (1991). doi: 10.1128/JVI.65.12.6589-6596.1991; pmid: 1719231
38. S. B. Drutman *et al.*, Homozygous *NLRP1* gain-of-function mutation in siblings with a syndromic form of recurrent respiratory papillomatosis. *Proc. Natl. Acad. Sci. U.S.A.* **116**, 19055–19063 (2019). doi: 10.1073/pnas.1906184116; pmid: 31484767
39. T. Herlin *et al.*, Autoinflammatory disease with corneal and mucosal dyskeratosis caused by a novel NLRP1 variant. *Rheumatology* **59**, 2334–2339 (2020). doi: 10.1093/rheumatology/kez612; pmid: 31873740
40. H. Xu *et al.*, The N-end rule ubiquitin ligase UBR2 mediates NLRP1B inflammasome activation by anthrax lethal toxin. *EMBO J.* **38**, e101996 (2019). doi: 10.15252/embj.2019101996; pmid: 31268597
41. K. E. Wickliffe, S. H. Leppla, M. Moayeri, Killing of macrophages by anthrax lethal toxin: Involvement of the N-end rule pathway. *Cell. Microbiol.* **10**, 1352–1362 (2008). doi: 10.1111/j.1462-5822.2008.01131.x; pmid: 18266992
42. A. Varshavsky, N-degron and C-degron pathways of protein degradation. *Proc. Natl. Acad. Sci. U.S.A.* **116**, 358–366 (2019). doi: 10.1073/pnas.1816596116; pmid: 30622213
43. R. T. Timms *et al.*, A glycine-specific N-degron pathway mediates the quality control of protein *N*-myristoylation. *Science* **365**, eaaw4912 (2019). doi: 10.1126/science.aaw4912; pmid: 31273098
44. M. L. Landry, E. F. Foxman, Antiviral response in the nasopharynx identifies patients with respiratory virus infection. *J. Infect. Dis.* **217**, 897–905 (2018). doi: 10.1093/infdis/jix648; pmid: 29281100
45. V. T. Mihaylova *et al.*, Regional differences in airway epithelial cells reveal tradeoff between defense against oxidative stress and defense against rhinovirus. *Cell Rep.* **24**, 3000–3007.e3 (2018). doi: 10.1016/j.celrep.2018.08.033; pmid: 30208323
46. J. G. Clark, K.-H. Kim, R. S. Basom, S. A. Gharib, Plasticity of airway epithelial cell transcriptome in response to flagellin. *PLOS ONE* **10**, e0115486 (2015). doi: 10.1371/journal.pone.0115486; pmid: 25668187
47. U. Hedström *et al.*, Bronchial extracellular matrix from COPD patients induces altered gene expression in repopulated primary human bronchial epithelial cells. *Sci. Rep.* **8**, 3502 (2018). doi: 10.1038/s41598-018-21727-w; pmid: 29472603
48. B. Tian *et al.*, Analysis of the TGFβ-induced program in primary airway epithelial cells shows essential role of NF-κB/RelA signaling network in type II epithelial mesenchymal transition. *BMC Genomics* **16**, 529 (2015). doi: 10.1186/s12864-015-1707-x; pmid: 26187636
49. S. Lee *et al.*, Influenza restriction factor MxA functions as inflammasome sensor in the respiratory epithelium. *Sci. Immunol.* **4**, eaau4643 (2019). doi: 10.1126/sciimmunol.aau4643; pmid: 31653718
50. M. G. Cordingley, P. L. Callahan, V. V. Sardana, V. M. Garsky, R. J. Colonno, Substrate requirements of human rhinovirus 3C protease for peptide cleavage in vitro. *J. Biol. Chem.* **265**, 9062–9065 (1990). pmid: 2160953
51. L. Carrasco, A. E. Smith, Sodium ions and the shut-off of host cell protein synthesis by picornaviruses. *Nature* **264**, 807–809 (1976). doi: 10.1038/264807a0; pmid: 1012329
52. S. E. Jacobs, D. M. Lamson, K. St. George, T. J. Walsh, Human rhinoviruses. *Clin. Microbiol. Rev.* **26**, 135–162 (2013). doi: 10.1128/CMR.00077-12; pmid: 23297263
53. C. Zhang *et al.*, Long-term *in vitro* expansion of epithelial stem cells enabled by pharmacological inhibition of PAK1-ROCK-Myosin II and TGF-β signaling. *Cell Rep.* **25**, 598–610.e5 (2018). doi: 10.1016/j.celrep.2018.09.072; pmid: 30332641
54. M. A. Dickson *et al.*, Human keratinocytes that express hTERT and also bypass a $p16^{INK4a}$-enforced mechanism that limits life span become immortal yet retain normal growth and differentiation characteristics. *Mol. Cell. Biol.* **20**, 1436–1447 (2000). doi: 10.1128/MCB.20.4.1436-1447.2000; pmid: 10648628
55. Y. Yan *et al.*, Human nasal epithelial cells derived from multiple subjects exhibit differential responses to H3N2 influenza virus infection in vitro. *J. Allergy Clin. Immunol.* **138**, 276–281.e15 (2016). doi: 10.1016/j.jaci.2015.11.016; pmid: 26806046
56. K. Wang *et al.*, Structural mechanism for GSDMD targeting by autoprocessed caspases in pyroptosis. *Cell* **180**, 941–955.e20 (2020). doi: 10.1016/j.cell.2020.02.002; pmid: 32109412
57. D. Agudelo *et al.*, Marker-free coselection for CRISPR-driven genome editing in human cells. *Nat. Methods* **14**, 615–620 (2017). doi: 10.1038/nmeth.4265; pmid: 28417998

ACKNOWLEDGMENTS

We thank all members of the Reversade laboratory for support and helpful scientific discussion. We also acknowledge the generous support and advice from L. Dahai (NTU), W. Bin (NTU), R. Sobota (IMCB), and S. Masters (WEHI). **Funding:** This work was supported by the Agency for Science, Technology and Research (GODAFIT Strategic Positioning Fund, B.R.); National Medical Research Council, Singapore (NMRC/OFYIRG/0046/2017, F.L.Z.); Concern Foundation's Conquer Cancer Now Award (F.L.Z.); and National Research Foundation, Singapore (F.L.Z.). K.S.T. is a recipient of fellowship support from the EAACI Research Fellowship, 2019. B.R. is a fellow of the Branco Weiss Foundation and a recipient of the A*STAR Investigatorship, the Senior NRF Investigatorship, and EMBO Young Investigatorship. F.L.Z. is a Nanyang Assistant Professor and National Research Foundation Fellow. **Author contributions:** F.L.Z. initiated the project. K.S.R. designed and performed most of the experiments and analyzed the data with help from D.E.T.T., G.A.T., K.L., and K.S.T. K.S.R., K.S.T., H.H.O., and T.L.S. performed the viral infection experiments. B.V.A. performed Luminex assays. C.K.L., J.J.H.C., V.T.K.C., and D.Y.W. supervised virology experiments. F.L.Z. and B.R. jointly conceived of the study, supervised experiments, analyzed the data, and wrote the manuscript. **Competing interests:** B.R., F.L.Z., and K.S.R. are joint inventors of provisional patent application "Blocking human airway inflammation by pharmacological inhibition of components of the NLRP1 inflammasome and N-glycine degron pathway" (10202002526P, Singapore). **Data and materials availability:** Immortalized N/TERT keratinocytes are obtained under an MTA from Brigham and Women's Hospital. All other data are available in the manuscript and supplementary materials.

SUPPLEMENTARY MATERIALS

science.sciencemag.org/content/370/6521/eaay2002/suppl/DC1
Figs. S1 to S9
MDAR Reproducibility Checklist
Data S1 and S2

View/request a protocol for this paper from *Bio-protocol*.

20 June 2019; resubmitted 11 February 2020
Accepted 8 October 2020
Published online 22 October 2020
10.1126/science.aay2002

RESEARCH ARTICLE SUMMARY

EVOLUTION

Selection enhances protein evolvability by increasing mutational robustness and foldability

Jia Zheng, Ning Guo, Andreas Wagner*

INTRODUCTION: Natural selection plays a central role in adaptive evolution, but we still know little about its role in changing evolvability—the ability to bring forth new and adaptive phenotypes. Different kinds of selection may increase evolvability by different means. Weak purifying selection may enhance evolvability by promoting the accumulation of neutral or slightly deleterious mutations that can serve as stepping stones toward new phenotypes. By contrast, strong directional selection may enhance evolvability by favoring the accumulation of beneficial mutations that can enhance both fitness and evolvability, such as mutations that increase a protein's thermodynamic stability or its robustness to mutations.

RATIONALE: To find out how the strength of selection affects protein evolvability, we subjected populations of yellow fluorescent proteins to multiple rounds of directed evolution in *Escherichia coli*. To control the strength of selection with precision, we used high-throughput phenotypic screening via fluorescence-activated cell sorting. During a first phase of our experiment (phase I), we subjected our populations to either strong selection, weak selection, or no selection on the ancestral phenotype of yellow fluorescence. During the second phase (phase II), we evolved all populations under the same selection pressure toward the new phenotype of green fluorescence. We subsequently used high-throughput phenotypic screening to study how phenotypes evolved in all our populations. In every generation, we also studied genotypic evolution with single-molecule real-time sequencing. We then engineered key adaptive mutants and determined their phenotype and thermodynamic stability. In addition, we determined the robustness of their phenotype to DNA mutations. Furthermore, we quantified the foldability of these mutants by unfolding them and observing their refolding kinetics.

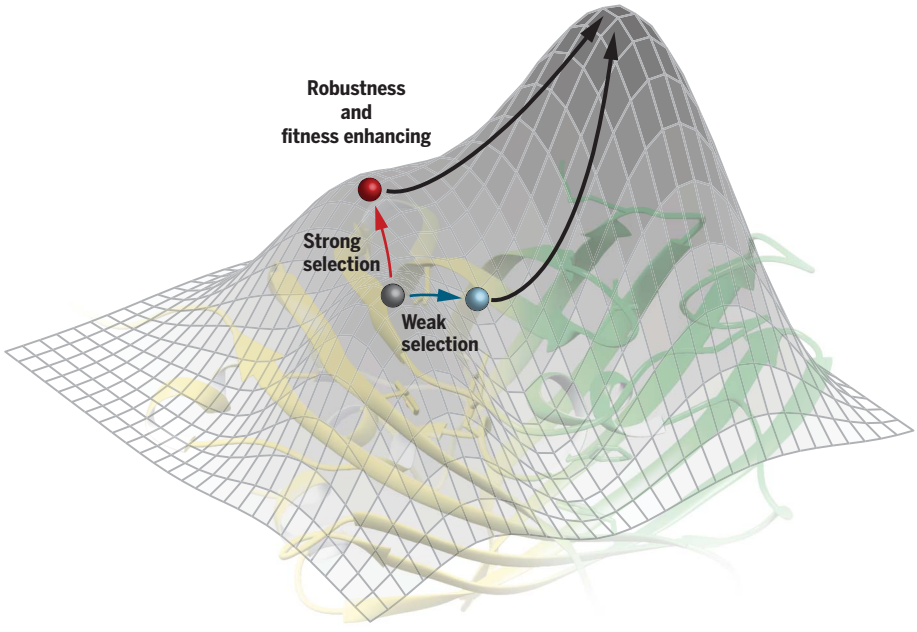

Selection can drive evolvability. Evolutionary theory holds that Darwinian evolution takes place on adaptive landscapes of fitness, which can be visualized as topological maps of high-fitness peaks and low-fitness valleys. This hypothetical landscape illustrates how mutations can increase evolvability by enhancing both fitness and mutational robustness. Favored by strong selection because they enhance fitness, such mutations move an evolving population into a region of low curvature and high robustness (red arrow), from which the population can bypass rather than traverse (blue arrow) an adaptive valley on its way to an adaptive peak.

RESULTS: We found that populations under strong selection for the ancestral yellow fluorescent phenotype during phase I subsequently evolved the new green fluorescent phenotype most rapidly during phase II. Compared to populations under weak or no selection, they reached higher green fluorescence during each generation of phase II and evolved a green emission peak more rapidly. Strong selection promoted both the elimination of deleterious mutations and the accumulation of foldability-improving mutations. As a result, proteins under strong selection evolved higher efficiency of protein folding (foldability) and, to an even greater extent, higher robustness to mutations than proteins under weak or no selection. Their robustness and foldability accelerated the selective sweeps of neofunctionalizing mutations that are necessary to evolve a new phenotype. By contrast, proteins under weak selection accrued more deleterious mutations that slowed down the fixation of neofunctionalizing mutations during the evolution of the new phenotype, even though neofunctionalizing mutations had initially risen to higher frequencies under weak selection.

CONCLUSION: Strong directional selection enhances the evolvability of a new phenotype to a greater extent than weak purifying selection. The responsible mutations enhance tolerance to mutations, improve protein foldability, and thus increase accessibility of a protein's native state. In doing so, they promote the formation of correctly folded states that can display new functions after incorporating neofunctionalizing mutations. Although "first order" selection of fitness-enhancing mutations can be in conflict with "second-order" selection of evolvability-enhancing mutations, our experiments demonstrate a class of mutations that avoid this conflict, because the mutations they reveal enhance both fitness and evolvability. In the context of an adaptive landscape (see figure), they do so by circumnavigating rather than traversing adaptive valleys, passing through flat regions of such a landscape, and thus allowing an evolving population to climb a new adaptive peak more rapidly. More generally, our experiments prove that natural selection itself can create the conditions under which Darwinian evolution can succeed. ■

The list of author affiliations is available in the full article online.
*Corresponding author. Email: andreas.wagner@ieu.uzh.ch
Cite this article as J. Zheng *et al.*, *Science* **370**, eabb5962 (2020). DOI: 10.1126/science.abb5962

READ THE FULL ARTICLE AT
https://doi.org/10.1126/science.abb5962

RESEARCH ARTICLE

EVOLUTION

Selection enhances protein evolvability by increasing mutational robustness and foldability

Jia Zheng[1,2], Ning Guo[3], Andreas Wagner[1,2,4]*

Natural selection can promote or hinder a population's evolvability—the ability to evolve new and adaptive phenotypes—but the underlying mechanisms are poorly understood. To examine how the strength of selection affects evolvability, we subjected populations of yellow fluorescent protein to directed evolution under different selection regimes and then evolved them toward the new phenotype of green fluorescence. Populations under strong selection for the yellow phenotype evolved the green phenotype most rapidly. They did so by accumulating mutations that increase both robustness to mutations and foldability. Under weak selection, neofunctionalizing mutations rose to higher frequency at first, but more frequent deleterious mutations undermined their eventual success. Our experiments show how selection can enhance evolvability by enhancing robustness and create the conditions necessary for evolutionary success.

Natural selection drives adaptation, but we still know little about its role in changing the evolvability of a trait or organism (*1*, *2*). On the one hand, strong selection for an ancestral phenotype may enhance evolvability for derived phenotypes, because it may favor mutations that enhance not just fitness but also evolvability. The available evidence is limited and indirect (*3*–*5*). For example, a cytochrome P450 BM3 variant engineered for greater stability and fitness buffers the destabilizing effect of mutations that are neofunctionalizing, i.e., that convey new protein activities (*5*, *6*).

On the other hand, strong selection may impair evolvability because it purges weakly deleterious mutations that can convey new functions (*7*). Evolutionary theory holds that selection helps populations find peaks in adaptive landscapes of fitness, which can be visualized as topological maps of peaks and valleys. Weakly deleterious "stepping-stone" mutations may help a population traverse the valleys that separate different fitness peaks. Such valleys, which are caused by epistatic interactions between different mutations, are abundant in the adaptive landscapes of evolving proteins (*8*–*11*). Weak selection that purges only the most detrimental mutations can aid such valley-crossing. Consistent with this view, when the enzyme β-lactamase TEM-1 is subject to "intense neutral drift" during experimental evolution—multiple rounds of mutation and selection to preserve its native phenotype of ampicillin resistance—the evolution of resistance to the newly introduced antibiotic cefotaxime is accelerated (*3*, *12*). More generally, experimental evolution shows that a population evolves a derived phenotype faster if it harbors genetic variation in the loci that affect the ancestral phenotype (*3*, *13*, *14*). Such standing genetic variation may even be adaptive if it has little effect on the ancestral phenotype (*15*). Therefore, conditionally neutral or weakly deleterious mutations can accelerate the adaptive evolution of a derived phenotype (*15*). Here we performed experiments aimed to find out whether strong or weak selection more effectively enhances evolvability.

[1]Department of Evolutionary Biology and Environmental Studies, University of Zurich, Zurich, Switzerland. [2]Swiss Institute of Bioinformatics, Quartier Sorge-Batiment Genopode, Lausanne, Switzerland. [3]Zwirnereistrasse 11, Wallisellen, Zurich, Switzerland. [4]The Santa Fe Institute, Santa Fe, NM, USA.
*Corresponding author. Email: andreas.wagner@ieu.uzh.ch

Results

Strong selection leads to greater evolvability than weak or no selection

We evolved yellow fluorescent protein [YFP, a variant of a jellyfish fluorescent protein (*16*)] in *Escherichia coli* from an ancestral phenotype (yellow fluorescence) to a derived phenotype (green fluorescence) (Fig. 1A). The protein was engineered to be well expressed in *E. coli* (*16*), but it is not native to *E. coli*, which minimizes interference with the native *E. coli* proteome. Studying evolvability in a single protein can help us analyze the causes of evolvability in molecular detail. In addition, the fluorescent phenotype permits us to control the strength of selection with precision, because fluorescence-activated cell sorting (FACS) can screen individual cells for their phenotype.

We subjected each of four replicate populations of *E. coli* expressing yellow fluorescent proteins to four rounds ("generations") of directed evolution. In phase I of our experiment (Fig. 1A), we selected for yellow fluorescence through either strong selection (populations S, the top ~20% of fluorescing cells survive) or weak selection (populations W, cells that fluoresce above background survive) (*17*). We also subjected four replicate populations of yellow fluorescent proteins to four rounds of directed evolution without any selection for fluorescence (populations N, subject only to neutral drift). After phase I evolution, we initialized phase II evolution by subjecting the same populations to another four rounds of directed evolution under selection for green fluorescence (Fig. 1A) (*17*). We used mutagenic polymerase chain reaction (PCR) to generate 0.84 amino acid–changing mutations per YFP molecule per generation (tables S1 to S3).

During phase I evolution, yellow fluorescence in the unselected populations N dropped rapidly and decreased to <5% of the ancestral YFP's intensity, indicating an accumulation of deleterious mutations (Fig. 1B). For populations under weak selection, W, the intensity of yellow fluorescence decreased after the first generation of evolution but remained constant in the next three generations (Fig. 1B). This suggests a mutation-selection balance between the production of new deleterious mutations and selection against such mutations. By contrast, yellow fluorescence in populations under strong selection, S, significantly increased by 92.5% after four generations of evolution (one-sided *t* test, $P < 0.001$; Fig. 1B), indicating a likely spread of beneficial mutations.

We genotyped ~500 to 1000 protein variants per population and generation (table S4), which revealed that our evolving populations harbored different amounts of genetic variation. Specifically, during phase I, populations W accumulated more amino acid–changing mutations and greater genetic diversity than populations S (figs. S1 and S2). Because greater genetic diversity may facilitate adaptive evolution, we hypothesized that populations W may have greater potential than populations S to evolve green fluorescence during phase II evolution. However, the opposite was the case. Populations S reached significantly higher green fluorescence than populations W during the first two generations of phase II evolution (one-sided Dunnett test with single-step adjustment, $P < 0.05$; Fig. 1C). In addition, populations S evolved a green (512 nm) emission peak more rapidly than populations W (fig. S3). Analogous differences exist between populations W and unselected populations N (Fig. 1C, and figs. S1 to S3). In sum, selection on an ancestral phenotype, and in particular strong selection, facilitates the evolution of a derived phenotype.

Strong selection on an ancestral phenotype leads to the most rapid fixation of neofunctionalizing mutations

To find out why strong selection causes greater evolvability than weak selection, we studied the dynamics of genetic polymorphisms in each replicate population during phase II (fig. S4).

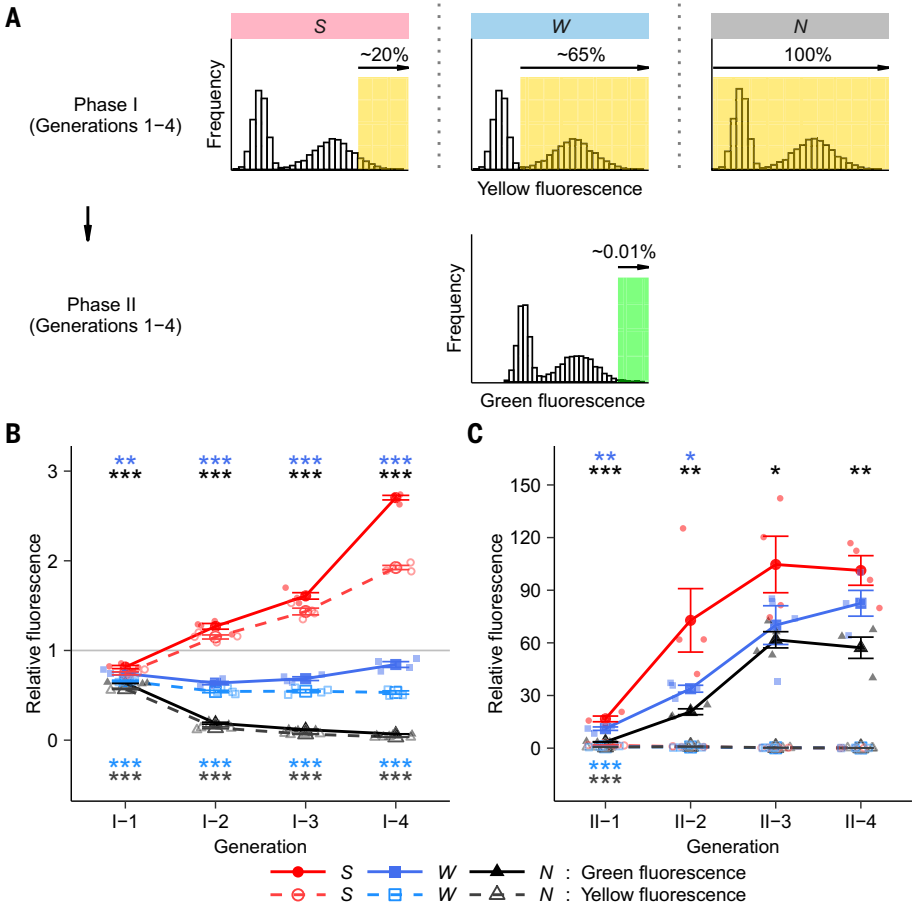

Fig. 1. Experimental evolution of yellow fluorescent protein. (**A**) We subjected four replicate *E. coli* populations for each experimental treatment to directed evolution under selection for yellow fluorescence (phase I, λ_{ex} = 488 nm and λ_{em} = 530 ± 15 nm). After four mutation-selection cycles, we continued directed evolution for four more cycles but under selection for green fluorescence (phase II, λ_{ex} = 405 nm and λ_{em} = 525 ± 25 nm) by selecting the top 0.01% of cells in each generation. The areas shaded in yellow or green indicate the proportion of a population allowed to survive to the next generation. (**B** and **C**) Fold-change of yellow (dashed lines) and green (solid lines) fluorescence intensity relative to ancestral YFP in each generation of phase I (B) and II (C). Error bars represent 1 SEM, from four replicate populations (single small symbols). *P < 0.05; **P < 0.01; ***P < 0.001 [one-sided Dunnett tests with single-step adjustment to compare S with W (blue) or N (black)].

Two mutations (G66S and Y204C) swept through each replicate S, W, and N population. Because of their ubiquity, we refer to these two mutations as universal mutations. In addition, another 20 mutations attained a frequency exceeding 30% in at least one replicate of populations S, W, and N. To determine whether all these (2 + 20) mutations are adaptive for green fluorescence, we engineered each of them into the ancestral YFP and measured their effects on green fluorescence. Only the two universal mutations G66S and Y204C caused green shifts of the emission peaks (Fig. 2A). Individually, these mutations caused a ~9-fold and ~2-fold increase in green fluorescence (fig. S5), and together they shifted the emission peak from yellow (530 nm) to green (512 nm; Fig. 2A). Thus, G66S and Y204C are the only neofunctionalizing mutations.

To further characterize the role of the remaining mutations, we engineered each of these mutations into the background of G66S+Y204C, referred to as genotype U for "universal," and measured the effect of these 20 genotypes on green fluorescence. Nine mutants significantly enhanced green fluorescence in the background of U (two-sided Dunnett test with single-step adjustment, P < 0.001; fig. S5), but none of these changed the emission spectrum (Fig. 2B). These mutations might increase the amount of soluble and functional fluorescent protein, which may help explain why green fluorescence also increased, albeit very modestly, during selection for yellow fluorescence in phase I (Fig. 1B).

Because only two mutations are responsible for the green shift in phase II, we suspected that the rapid spread of these two mutations resulted in faster adaptation of the strong selection (S) populations compared to the weak selection (W) and unselected (N) populations. Indeed, populations S displayed a higher frequency of the universal mutations G66S and Y204C, and of the universal genotype U, in at least last three of the four phase II generations (Fig. 2C).

Because the S, W, and N populations were subject to identical selection pressures during phase II, these faster sweeps likely originated in differences between populations at the end of phase I. We investigated if the reason was that the neofunctionalizing mutations had already attained a higher frequency in populations S at the end of phase I. However, this was not the case. Both universal mutations had lower frequency in populations S at the end of phase I evolution, and one of them (Y204C) had a significantly lower frequency in populations S than in populations W and N (one-sided Dunnett test with single-step adjustment, P < 0.001; fig. S6).

Strong selection leads to greater mutational robustness and higher foldability than weak selection

To resolve this apparent paradox—faster spreading of the neofunctionalizing mutations G66S and Y204C despite their lower initial frequency—it is relevant that our evolving sequences are likely to acquire one or more new mutations (with probability 0.53) in every generation (table S2). In addition, mutations that are different from the two neofunctionalizing mutations are expected to arise by chance alone 412-fold more often than these two mutations (table S2). This means that most variants containing neofunctionalizing mutations will also accumulate many other mutations, most of which are near-neutral or deleterious (*18*, *19*). Increased robustness to such slightly deleterious mutations would increase the fitness of genotypes carrying neofunctionalizing mutations and thus enable their spreading. We thus hypothesized that populations S had acquired genetic changes that cause greater robustness to deleterious mutations.

To validate this hypothesis, we mutagenized populations S, W, and N at the end of phase I and determined the residual fluorescence and the frequency of fluorescence-positive variants after mutagenesis. Populations S had indeed acquired greater mutational robustness, in both the ancestral yellow phenotype and the derived green phenotype. Specifically, populations S retained significantly higher yellow fluorescence intensity than populations W and N after mutagenesis (two-sided Dunnett test with single-step adjustment, P < 0.05 and 0.01 for comparing S with W and N; Fig. 3A). In addition, the postmutagenesis frequency of yellow-fluorescence–positive variants in S populations was 1.24-fold and

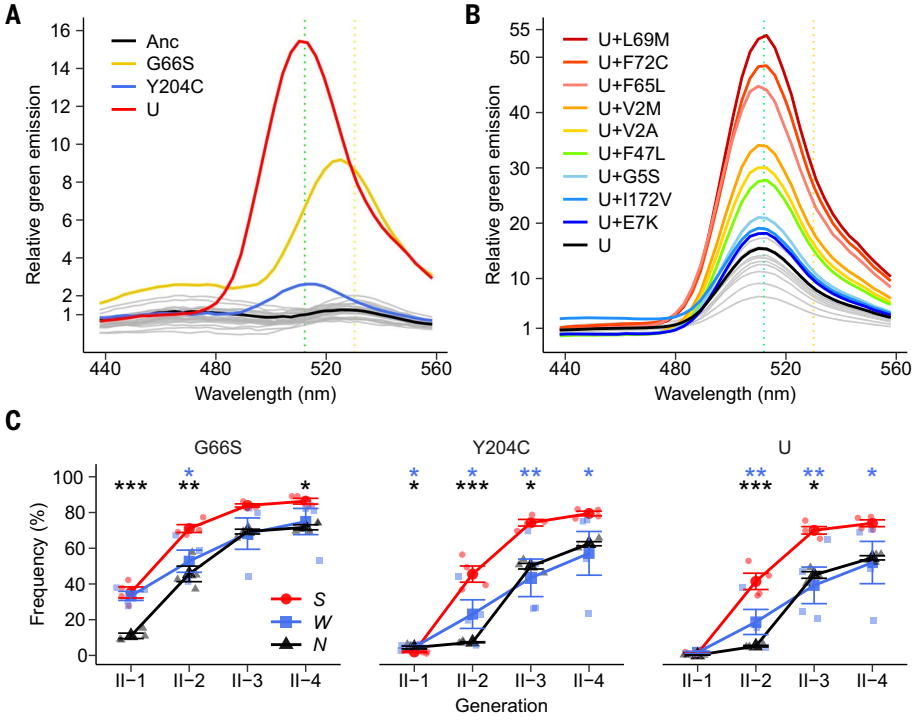

Fig. 2. Most rapid fixation of neofunctionalizing mutations after strong selection on the ancestral phenotype. (**A** and **B**) Emission spectra at the new excitation wavelength (405 nm) of mutants introduced into ancestral YFP (A) and U (B)**.** The vertical axes indicate the fold-change of green fluorescence intensity relative to ancestral YFP at a given emission wavelength (horizontal axes). Each curved line represents the emission spectrum of 1 of the 44 mutants (n = 3). Colored lines in (A) indicate those emission-shifted mutations, and colored lines in (B) indicate mutations that significantly improved green fluorescence in the genetic background U (two-sided Dunnett test with single-step adjustment, $P < 0.05$; fig. S5). Yellow and green vertical dashed lines indicate 530 nm (λ_{ex} = 485 nm) and 512 nm (λ_{ex} = 405 nm). (**C**) Frequencies of neofunctionalizing mutations G66S and Y204C or the double-mutant U during evolution. Error bars represent 1 SEM from four replicate populations. *$P < 0.05$; **$P < 0.01$; ***$P < 0.001$ [one-sided Dunnett tests with single-step adjustment to compare S with W (blue) or N (black)]. Abbreviations for the amino acid residues are as follows: A, Ala; C, Cys; E, Glu; F, Phe; G, Gly; I, Ile; K, Lys; L, Leu; M, Met; S, Ser; V, Val; and Y, Tyr.

13.0-fold higher than in W and N populations (Fig. 3B). Moreover, the postmutagenesis frequency of high-green variants, which have higher green fluorescence than the ancestral YFP, was 3.8-fold and 326.4-fold higher in S populations than in W and N populations, respectively (Fig. 3B).

Because most deleterious mutations reduce protein solubility by causing protein misfolding and instability (*20*, *21*), we suspected that populations S have evolved the ability to buffer such mutations by harboring protein variants with especially high foldability (folding efficiency) or stability (the free energy required to unfold a protein). Folding efficiency and stability can be jointly quantified by the concentrations of soluble protein in vivo (*22*). We thus measured and compared the amount of soluble fluorescent proteins in populations S, W, and N at the end of phase I (*17*). The amount of soluble proteins in populations S relative to that of ancestral YFP is 1.9-fold and 3.8-fold higher than that in populations W and N (Fig. 3C). By contrast, the fraction of insoluble protein in populations S is 2.8-fold and 2.5-fold lower than that in populations W and N (Fig. 3D and fig. S7), respectively.

We also analyzed the role of foldability more directly by quantifying the refolding yield of fluorescent proteins after unfolding (*17*). Indeed, a higher percentage of unfolded fluorescent proteins in populations S refolded than in populations W, N, and in ancestral YFP during 24 hours of refolding (Fig. 3E and fig. S8A). Also, fewer than 50% of unfolded proteins refolded correctly at 25°C within 24 hours (Fig. 3E), demonstrating that solubility is likely limited by correct protein folding. In addition, the foldability of populations S did not decrease after random mutagenesis, whereas it decreased in populations W and N (fig. S8B). This observation suggests that increased foldability also increases mutational robustness.

Foldability cannot be completely disentangled from protein stability, because many mutations affect both (*20*, *23*). Stability can be estimated by monitoring a protein's structural integrity over time, and we measured for all our populations the residual yellow fluorescence after 12 hours of incubation at 37°C, the temperature at which we had conducted our experiments. All populations retained more than 95% of yellow fluorescence (fig. S8, C and D). Populations S showed higher stability than populations W, N, and ancestral YFP only at higher, unphysiological temperatures above 65°C (fig. S8, E and F). In sum, our experiments suggest that the higher robustness of populations S is primarily caused by higher foldability.

Foldability-improving mutations result in greater mutational robustness and higher evolvability

We next aimed to identify the genetic changes that increased foldability and mutational robustness by examining our sequence data. We focused on the 2 neofunctionalizing and 20 non-neofunctionalizing mutations that reached a frequency exceeding 30% at the end of phase II in populations S, W, and N (fig. S4). The best candidates among them are four variants known to improve foldability (F47L, F65L, V164A, and I172V) (*23*–*25*). All of these mutations and a fifth one (K102E) reached a higher frequency at the end of phase I in S populations relative to both W and N populations (fig. S9).

When we unfolded these mutants and refolded them (*17*), all five mutants yielded more correctly refolded protein than ancestral YFP (Fig. 4A), and three of them also refolded more rapidly than ancestral YFP (table S5). In addition, the mutations cause increased protein solubility (figs. S10A and S11). Notably, four of them also increased foldability (figs. S10B and table S5), and two of them significantly increased solubility in the background U (one-sided Dunnett test with single-step adjustment, $P < 0.05$; figs. S10 C and S11), which folds with similarly low yield (~30%) as ancestral YFP (fig. S10D and table S5). The mutants also increased thermostability, albeit only at unphysiologically high temperatures (fig. S10, E to G, and table S6), indicating that they probably do not increase solubility by improving thermostability. In sum, all five key mutations improve foldability or protein solubility in the ancestral YFP background, and four of them do so in the green fluorescent protein background U.

To estimate the mutational robustness of specific mutants, we used PCR to introduce random mutations into ancestral YFP and into each of the 22 high-frequency YFP variants. We then calculated the percentage of fluorescence retained relative to fluorescence before mutagenesis. After random mutagenesis, four out of five foldability-improving mutants retained greater yellow fluorescence (by 13.3 to 25.2%) than ancestral YFP (Fig. 4B), which indicates that they increased robustness. In one of the mutants (K102E), the increase in robustness was marginally significant (two-sided Dunnett test with

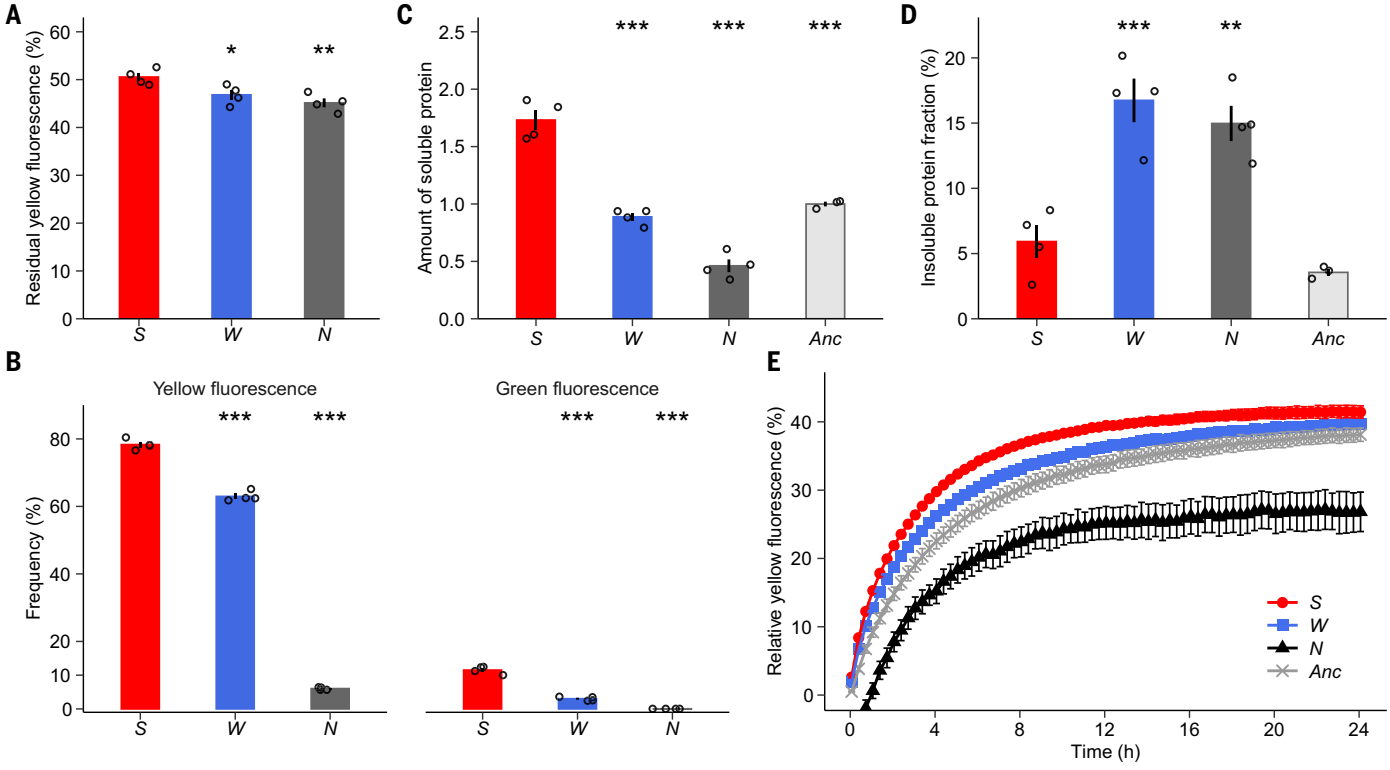

Fig. 3. Strong selection leads to greater mutational robustness and higher foldability than weak selection. (**A**) Yellow fluorescence retained by each population at the end of phase I after mutagenesis relative to its yellow fluorescence without mutagenesis. (**B**) Frequencies of cells fluorescing above background in yellow (left) (*17*) or above ancestral YFP (Anc) in green (right) (*17*) from each population at the end of phase I after mutagenesis. (**C** and **D**) Amount of soluble protein relative to ancestral YFP (C) and insoluble protein fraction (D) in each population at the end of phase I. (**E**) Recovery of yellow fluorescence over time (horizontal axis) during refolding of unfolded fluorescent proteins at 25°C (*17*). Error bars represent 1 SEM based on four replicate populations. *P < 0.05; **P < 0.01; ***P < 0.001 (two-sided Dunnett tests with single-step adjustment to compare S with W, N, or ancestral YFP).

single-step adjustment, P = 0.064; Fig. 4B). After random mutagenesis, none of the other 17 mutations significantly retained greater yellow fluorescence intensity than ancestral YFP (two-sided Dunnett test with single-step adjustment, P > 0.05; fig. S12). In addition, random mutations in all foldability-improving mutants created significantly more variants that remained yellow fluorescence–positive than ancestral YFP (two-sided Dunnett test with single-step adjustment, P < 0.05; Fig. 4C). Thus, foldability-improving mutations enhance the mutational robustness of the original yellow-fluorescence phenotype.

In addition, the five foldability-improving mutants also enhanced the robustness of the derived green fluorescence phenotype. First, after mutagenesis, they retained significantly higher green fluorescence intensity (15.2 to 35.3% higher) than randomly mutated ancestral YFP (two-sided Dunnett test with single-step adjustment, P < 0.05; Fig. 4B). Second, random mutations in the foldability-improving mutants created significantly more variants that remained green fluorescence–positive (14.6 to 37.5% more) than ancestral YFP (two-sided Dunnett test with single-step adjustment, P < 0.01; Fig. 4C). In addition, three foldability-improving mutations (F47L, F65L, and I172V) significantly improved green fluorescence (by more than 27.0%) when combined with the two neofunctionalizing mutations (two-sided Dunnett test with single-step adjustment, P < 0.001; fig. S5). These results suggest that the foldability-enhancing mutations can accelerate a selective sweep of neofunctionalizing mutants during phase II. In support of this observation, the foldability-improving mutations achieved higher frequency in S populations than in W and N populations during each generation of evolution (fig. S13). Moreover, populations S retained a greater percentage of cells with higher green fluorescence than the ancestor during phase II evolution (Fig. 5A).

The advantage of the foldability-enhancing mutations could be mainly caused by their effect on robustness or by their effect on increasing fluorescence. We distinguished these two possibilities by measuring the effect of each mutation on fluorescence with or without mutagenesis. For example, the mutant F47L alone caused a 1.067-fold increase in green fluorescence–positive cells relative to ancestral YFP. After random mutagenesis of the mutant F47L, the increase in green fluorescence–positive cells relative to the mutagenized ancestral YFP was 1.390-fold. Thus, mutational robustness was responsible for most [84.2% = 100 × (1.390 − 1.067)/(1.390 −1.0)] of the mutant's benefit for green fluorescence phenotype. This holds also for the other mutations, where we estimate that on average, >75% of the fluorescence benefit comes from increased robustness (Fig. 5B). Thus, foldability-improving mutations likely promoted the spreading of neofunctionalizing mutations by enhancing robustness. This is consistent with the observation that the foldability-improving mutations did not greatly increase specific green and yellow fluorescence on their own (table S7). In the genetic background U, three of these mutations (F47L, F65L, and I172V) also increased specific green fluorescence by more than 14% (table S7), and two of them (F47L and F65L) may have done so because of their spatial proximity to the chromophore (fig. S14). Such improvements in specific green fluorescence might additionally help promote the fixation of U.

Selection can eliminate deleterious mutations despite the presence of robustness-enhancing mutations

Although robustness-enhancing mutations augment the advantage of other beneficial mutations,

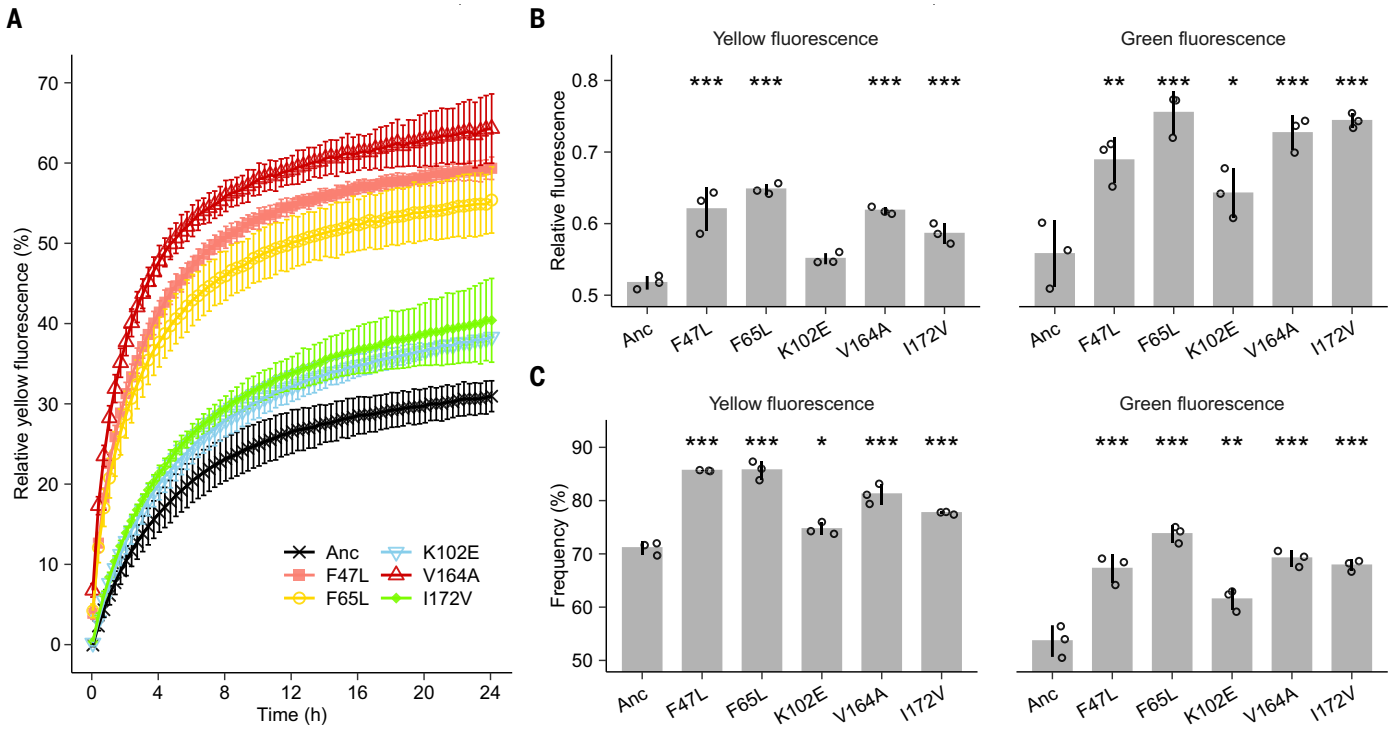

Fig. 4. Foldability-improving mutations enhance mutational robustness. (**A**) Recovery of yellow fluorescence during refolding of unfolded ancestral YFP and of the indicated variants at 25°C (*17*). (**B**) Fluorescence intensity retained relative to fluorescence without mutagenesis (*17*). (**C**) Frequencies of fluorescence-positive cells after random mutagenesis (*17*). Error bars represent 1 SD (n = 3). *P < 0.05; **P < 0.01; ***P < 0.001 [two-sided Dunnett tests with single-step adjustment to compare each variant with ancestral YFP in (B) and (C)].

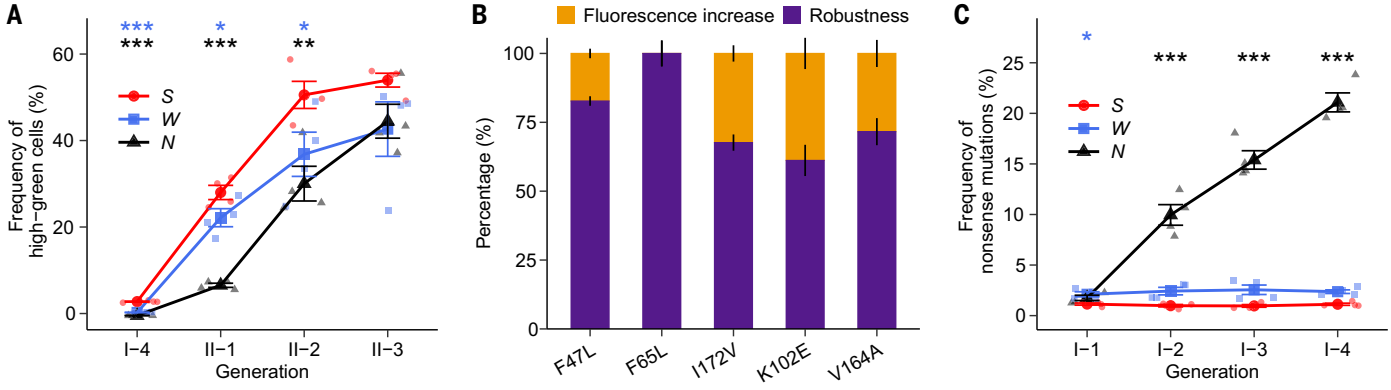

Fig. 5. Enhanced mutational robustness promotes sweeps of adaptive mutations. (**A**) Percentage of cells with higher green fluorescence than ancestral YFP in populations S, W, and N after mutagenesis during each generation of evolution (*17*). (**B**) Increased mutational robustness (purple) rather than fluorescence increase (orange) is the major contributor to the acceleration of green fluorescence evolution by foldability-increasing mutations. (**C**) Strong selection purges nonsense mutations most efficiently during phase I evolution. Error bars represent 1 SEM from four replicate populations [(A) and (C)] or 1 SD over three biological replicates (B). *P < 0.05; **P < 0.01; ***P < 0.001 [one-sided Dunnett tests with single-step adjustment to compare S with W (blue) or N (black)].

their interactions with deleterious mutations are more complex. If they completely mask the effects of a deleterious mutation, this mutation may be preserved. However, if the mutation remains somewhat deleterious even in the presence of robustness-enhancing mutations, it may still be eliminated by selection, and at a rate that depends on the strength of selection. To test whether selection in S populations was sufficiently strong to eliminate deleterious mutations, we first used nonsense mutations, which produce truncated protein isoforms (*26*). Indeed, the frequency of nonsense mutations remained 2.1-fold lower in S than in W populations and 18.7-fold lower than in N populations at the end of phase I (Fig. 5C).

To complement this analysis, we also used the FoldX algorithm to predict destabilizing mutations (*17*). Such destabilizing mutations too became depleted in S populations (figs. S15 to S17). Specifically, highly destabilizing mutations had a consistently lower frequency in S populations than in W and N populations throughout phase I evolution (figs. S15A to S17). At the end of phase I, this frequency was 2.4-fold and 9.7-fold lower in S populations than in W and N populations, respectively (figs. S15A). Also, the protein variants of populations S were on average more stable than

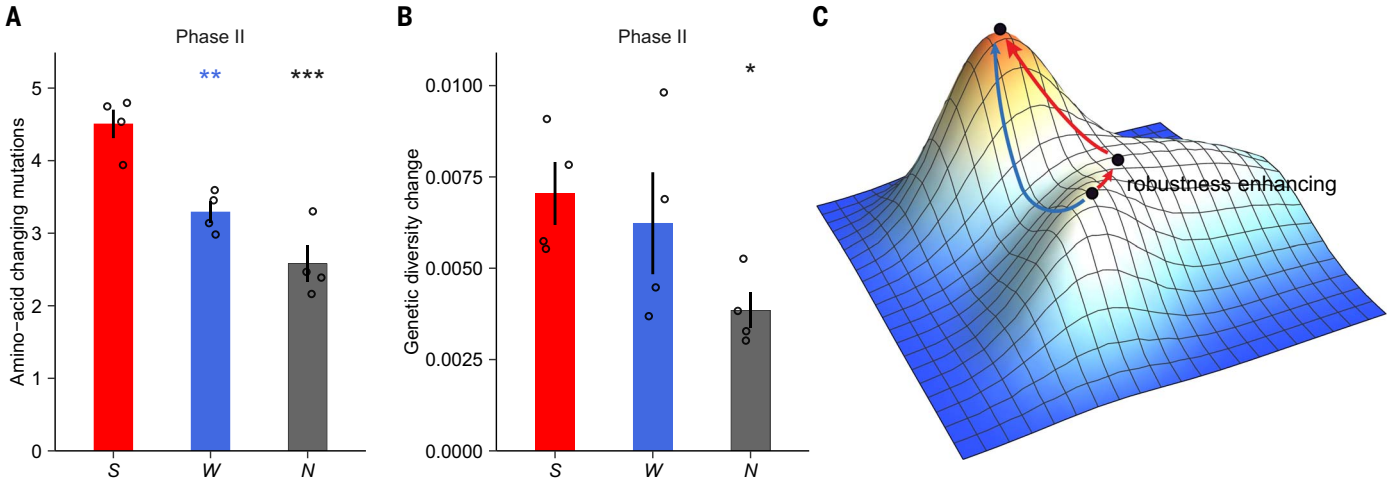

Fig. 6. Mutational robustness helps increase genetic diversity and evolvability. (**A**) Increase in the average number of amino acid–changing mutations per fluorescent protein molecule relative to the beginning of phase II for evolving populations S, W, and N. (**B**) Increase in genetic diversity relative to the beginning of phase II for evolving populations S, W, and N. The data show the increase in the number of amino acid–changing mutations (A) or in genetic diversity (B) in populations S, W, and N at the end of phase II, relative to the end of phase I. Error bars represent 1 SEM from four replicate populations. *P < 0.05; **P < 0.01; ***P < 0.001 [one-sided Dunnett tests with single-step adjustment to compare S with W (blue) or N (black)]. (**C**) Robustness-enhancing mutations can help evolving populations bypass fitness valleys in an adaptive landscape. Robustness-enhancing mutations (short red arrow) can help move a population to a region of an adaptive landscape with low curvature, from where an adaptive peak can be reached more easily (long red arrow) than without robustness-enhancing mutations (blue arrow). Strong selection can help increase the frequency of robustness-enhancing mutations, and more so if such mutations also enhance fitness.

those of populations W and N during phase I evolution (fig. S15B).

Because computational stability predictions may be inaccurate when a protein harbors multiple amino acid changes (*27*), we also experimentally measured the stability of fluorescent proteins expressed in our populations. In these experiments, proteins from S populations showed greater stability at 65° to 80° C than those from W and N populations (fig. S8E). This prevalence of more stable proteins in S populations also persisted after mutagenesis (fig. S8F). In sum, selection can purge strongly deleterious mutations even in the presence of robustness-enhancing mutations.

Robustness-enhancing mutations help increase genetic diversity in populations subject to selection

Though not completely preventing the purging of deleterious mutations, robustness-enhancing mutations can still increase genetic diversity within a population by helping a population tolerate some deleterious mutations. Specifically, we observed that in both S and W (but not N) populations, proteins that carried robustness-enhancing mutations also harbored a significantly greater number of other amino acid changes at the end of phase I (one-sided t tests, P < 0.05; fig. S18).

To further examine whether robustness-enhancing mutations help populations S tolerate deleterious mutations during phase II evolution, we focused on the 22 mutations that reached a frequency exceeding 30% at the evolutionary end point. Among these mutations, we identified four strongly deleterious mutations that significantly reduced the fluorescence of the universal green fluorescent genotype U by more than 20% (E18G, M79L, R110S, and N145S; two-sided Dunnett test with single-step adjustment, P < 0.001; fig. S5). Three of these deleterious mutations occurred in populations S, whereas only one of them occurred in any other population. Notably, more than 85% of the genetic variants that harbored one of these mutations also harbored at least one of the five foldability-improving mutations at the evolutionary end point (fig. S19). This suggests that robustness-enhancing mutations helped populations S tolerate strongly deleterious mutations. It is also consistent with the observation that populations S experienced greater increases in both the number of amino acid changes and genetic diversity than populations W and N during phase II evolution (Fig. 6, A and B).

Discussion

Neutral or weakly deleterious mutations can play an important role in adaptive evolution (*13*, *28*), because they can convey new functions. They also help populations respond rapidly to environmental changes (*3*, *7*, *12*, *13*) and traverse fitness valleys created by epistatic (nonadditive) mutational interactions (*29*). Weak purifying selection facilitates the accumulation of such mutations (*7*). If they were central to the evolution of a derived green fluorescence phenotype, our weak selection regime should have resulted in higher evolvability of this phenotype. However, we found that strong selection led to more rapid evolution of the green fluorescence phenotype (Fig. 1B).

To understand why, consider that many proteins are marginally foldable (*30*) and marginally stable (*31*). Also, most mutations accumulated during evolution will further reduce protein foldability and stability (*20*, *32*), especially under weak selection (*12*, *33*, *34*). To function well, most proteins must first fold correctly (high foldability) and maintain structural integrity after folding (high stability) (*35*), resulting in selection on the evolution of foldability and stability. As a result, strong selection not only can stop the erosion of foldability and stability by purging deleterious mutations, it also favors mutations that enhance both properties. This ability is especially important during the evolution of new phenotypes, because neofunctionalizing mutations usually destabilize proteins and reduce folding efficiency (*5*, *34*, *36*). In our experiments, strong selection favored mutations that increase foldability and, to an even greater extent, mutational robustness. In doing so, selection enhanced the penetrance of beneficial mutations (Fig. 5A) and accelerated selective sweeps (Fig. 2C). In addition, foldability-improving mutations may also promote the fixation of neofunctionalizing mutations by improving their specific protein activity during adaptive evolution (table S7). We anticipate that our observations apply to the evolution of most proteins in which foldability and stability are important.

Our experiments required high mutation rates so that we could observe adaptive evolution on a laboratory time scale. Comparable

mutation rates have been observed in viruses (*37*, *38*) and microbes, especially those that are challenged to evolve rapidly by environmental stressors (*39*–*42*). Such high mutation rates are also required for the evolution of robustness as a direct response to mutation pressure (*3*, *4*, *43*). However, because our evolvability-enhancing mutations increase both robustness and foldability (Fig. 6C), their direct fitness benefit (fig. S20) would help them accumulate also under much lower mutation rates. An important question is whether the advantage of strong selection for evolvability also persists at low mutation rates.

Our work highlights the important role of standing variation for evolvability (*13*, *14*, *20*, *44*–*46*). It shows that natural selection can play a crucial and active role in creating standing variation that is both beneficial and enhances evolvability—for example, by increasing robustness to deleterious mutations. This contrasts with some theoretical and experimental work, in which first-order selection for fitness conflicts with second-order selection for robustness (*47*, *48*). We predict that evolution can avoid this conflict when mutations with both fitness-enhancing and evolvability-enhancing roles exist.

Our work also suggests experimental designs that select for beneficial mutations without depleting genetic variation before selecting for a new phenotype. Such experiments could be further enhanced by starting with protein variants engineered for high robustness. Furthermore, our observations extend beyond bioengineering. We expect that the evolutionary rescue of populations after environmental challenges, like climate change, may be easier in cases when a population's evolutionary potential has been previously enhanced by strong selection. Most generally, our observations suggest that natural selection can create favorable conditions for Darwinian evolution.

Materials and methods summary

Plasmids and strains

We used the plasmid vector pBAD202/D-TOPO (K4202-01, Invitrogen) for cloning and expressing YFP alleles. This vector contains a kanamycin resistance marker and an arabinose-inducible *ara*BAD promoter. We used *E. coli* strain BW27783 (CGSC 12119) as a host to enable the homogeneous expression of the arabinose-inducible *ara*BAD promoter (*49*).

Creating mutant libraries

We used the same mutagenesis protocol during phase I and phase II of our experiments (*17*). Specifically, we performed mutagenic PCR (using the primers MutafpF and MutafpR, table S8) to randomly introduce mutations into the coding region of YFP, inserted the resulting mutant pool into the vector backbone by ligation, and then electroporated the ligation product into electrocompetent cells (*17*). After electroporation, we immediately added 1 ml of prewarmed SOC medium, incubated the recovering cell culture for 1.5 hours at 37°C with shaking at 220 rpm in a 50-ml tube, and used the recovered culture for further experiments.

To avoid the accumulation of mutations in the plasmid outside the YFP coding region, we inserted randomly mutated YFP genes into a fresh plasmid backbone in each generation. In addition, to avoid mutations that might accumulate in the *E. coli* genome, we transformed mutated YFP gene pools into fresh *E. coli* competent cells in each generation.

Directed evolution

We induced fluorescent protein expression in evolving populations at 37°C for 12 hours (with shaking at 220 rpm) by using 0.2% arabinose (*17*). We used an Aria III cell sorter (BD Biosciences) to sort cells at 4°C in the fluorescein isothiocyanate (FITC) channel (λ_{ex} = 488 nm, λ_{em} = 530 ± 15 nm; phase I evolution) or in the AmCyan channel (λ_{ex} = 405 nm, λ_{em} = 525 ± 25 nm; phase II evolution) according to the selection criteria described in Fig. 1. In phase I evolution, we collected ~10^6 selected cells in ~1 ml of cold phosphate-buffered saline (PBS) buffer at 4°C for each replicate population (*17*). In phase II evolution, we first selected ~5×10^4 cells with the top 1% of green fluorescence intensity, regrew the sorted cells, and repeated the sorting process by again selecting ~10^4 cells in the top 1% of green fluorescence intensity (*17*). In each round, we regrew sorted cells, and isolated plasmids from sorted cells and used them as templates for the next mutation-selection cycle and for single-molecule real-time (SMRT) sequencing (*17*). To prevent cell proliferation or death, we placed selected cells on ice before the subsequent steps.

Engineering YFP variants

We used whole-plasmid PCR to engineer single mutants and some double mutants by designing primers that carry the corresponding mutations (table S9) (*17*). We also used whole-plasmid PCR to engineer single mutations into the genetic backgrounds of G66S, Y204C, or U (G66T + Y204C) by using the mutants G66S, Y204C, or U as templates (*17*). We used Gibson Assembly Master Mix (E2611, NEB) to engineer the double-mutant U (G66T+Y204C) by using the primers G66Sf/Y204Cr and Y204Cr/G66Sf (table S9) (*17*).

Fluorescence assay using flow cytometry

We grew evolving populations or engineered variants in 200 μl or 2 ml of LB with 0.2% arabinose to induce the expression of YFP variants in evolving populations or engineered YFP variants (*17*). We added 40 μl of a culture to 160 μl of cold PBS buffer, transferred 20 μl of the resulting suspension to 180 μl of cold PBS buffer, and mixed the solution thoroughly. We used the resulting mixture to measure yellow fluorescence (λ_{ex} = 488 nm and λ_{em} = 530 ± 15 nm) and green fluorescence (λ_{ex} = 405 nm and λ_{em} = 525 ± 25 nm) using flow cytometry. We performed fluorescence assays at room temperature with a flow rate of ~3000 events/s by using a Fortessa cell analyzer (BD Biosciences). We performed at least three biological replicates for each replicate population or each variant and analyzed ~10^4 events per replicate. To prevent cell proliferation or death, we placed all samples on ice until we had finished all assays.

Flow cytometry data analysis

We performed flow cytometry data analysis by using FlowJo V10.4.2 (LLC). Briefly, we used forward scatter height (FSC-H) versus side scatter height (SSC-H) density plots to select a homogeneous cell population (p1 in fig. S21A), and used side scatter area (SSC-A) versus SSC-H density plots to exclude doublets (p2 in fig. S21B). We used the resulting filtered data p2 for determining the fluorescence intensity of evolving populations and for determining mutational robustness of evolving populations and those single mutants (Figs. 1, 3, 4, and 5 and fig. S12). We used FITC-height versus AmCyan-height density plots to select the dominant cell population (p3 in fig. S21C) and used the resulting filtered data p3 for determining the fluorescence intensity of each mutant (figs. S5 and S20).

Protein solubility determination and refolding kinetics measurements

We induced the expression of YFP variants in evolving populations or engineered mutants by growing cells in 2 ml of LB medium with 50 μg/ml of kanamycin and 0.2% arabinose in a 10-ml tube at 37°C and at 220 rpm for 12 hours (*17*). We used CelLytic B Cell Lysis Reagent (B7435-500ml, Sigma) to extract both soluble and insoluble proteins from the collected cells by following the manufacturer's protocol (*17*). We quantified the amount of both soluble and insoluble proteins in each sample by SDS–polyacrylamide gel electrophoresis (SDS-PAGE) (*17*).

To unfold proteins, we diluted 5 μl of crude lysate with 45 μl of 9 M urea (containing 10 mM dithiothreitol) and incubated the solution at 95°C for 5 min. To refold unfolded proteins, we diluted 10 μl of the unfolded samples with 180 μl of TNG buffer in a 96-well microplate and used an infinite F200 Pro (λ_{ex} = 485 nm, λ_{em}= 530 nm) or a Spark 10 M (λ_{ex} = 485 nm, λ_{em} = 530 nm and λ_{ex} = 405 nm, λ_{em} = 512 nm) microplate reader to measure fluorescence intensity at ~20-min intervals (*17*).

SMRT sequencing and sequence data analysis

We barcoded YFP variants of each replicate population by using PCR and ligation for SMRT

sequencing and used the Pacific Biosciences RS2 instrument (Pacific Biosciences) to perform sequencing (*17*). We used the SMRTAnalysis v2.3 package (*50*) to perform primary data analysis (*17*). We wrote Python scripts (Python 2.7.12) to identify point mutations and their combinations and to calculate genetic diversity in each replicate population from each generation of evolution (*17*).

Statistical analysis

Unless specified otherwise, we conducted pairwise comparisons by using a one-tailed t test and conducted multiple comparisons to a control by using a one-sided Dunnett test with single-step adjustment. We performed all statistical analysis using R version 3.4.1.

REFERENCES AND NOTES

1. M. Pigliucci, Is evolvability evolvable? *Nat. Rev. Genet.* **9**, 75–82 (2008). doi: 10.1038/nrg2278; pmid: 18059367
2. J. L. Payne, A. Wagner, The causes of evolvability and their evolution. *Nat. Rev. Genet.* **20**, 24–38 (2019). doi: 10.1038/s41576-018-0069-z; pmid: 30385867
3. S. Bershtein, K. Goldin, D. S. Tawfik, Intense neutral drifts yield robust and evolvable consensus proteins. *J. Mol. Biol.* **379**, 1029–1044 (2008). doi: 10.1016/j.jmb.2008.04.024; pmid: 18495157
4. J. D. Bloom *et al*., Evolution favors protein mutational robustness in sufficiently large populations. *BMC Biol.* **5**, 29 (2007). doi: 10.1186/1741-7007-5-29; pmid: 17640347
5. J. D. Bloom, S. T. Labthavikul, C. R. Otey, F. H. Arnold, Protein stability promotes evolvability. *Proc. Natl. Acad. Sci. U.S.A.* **103**, 5869–5874 (2006). doi: 10.1073/pnas.0510098103; pmid: 16581913
6. M. Soskine, D. S. Tawfik, Mutational effects and the evolution of new protein functions. *Nat. Rev. Genet.* **11**, 572–582 (2010). doi: 10.1038/nrg2808; pmid: 20634811
7. M. A. Stiffler, D. R. Hekstra, R. Ranganathan, Evolvability as a function of purifying selection in TEM-1 β-lactamase. *Cell* **160**, 882–892 (2015). doi: 10.1016/j.cell.2015.01.035; pmid: 25723163
8. C. Bank, S. Matuszewski, R. T. Hietpas, J. D. Jensen, On the (un)predictability of a large intragenic fitness landscape. *Proc. Natl. Acad. Sci. U.S.A.* **113**, 14085–14090 (2016). doi: 10.1073/pnas.1612676113; pmid: 27864516
9. T. N. Starr, L. K. Picton, J. W. Thornton, Alternative evolutionary histories in the sequence space of an ancient protein. *Nature* **549**, 409–413 (2017). doi: 10.1038/nature23902; pmid: 28902834
10. J. Domingo, P. Baeza-Centurion, B. Lehner, The Causes and Consequences of Genetic Interactions (Epistasis). *Annu. Rev. Genomics Hum. Genet.* **20**, 433–460 (2019). doi: 10.1146/annurev-genom-083118-014857; pmid: 31082279
11. D. M. Weinreich, N. F. Delaney, M. A. Depristo, D. L. Hartl, Darwinian evolution can follow only very few mutational paths to fitter proteins. *Science* **312**, 111–114 (2006). doi: 10.1126/science.1123539; pmid: 16601193
12. S. Bershtein, D. S. Tawfik, Ohno's model revisited: Measuring the frequency of potentially adaptive mutations under various mutational drifts. *Mol. Biol. Evol.* **25**, 2311–2318 (2008). doi: 10.1093/molbev/msn174; pmid: 18687656
13. E. J. Hayden, E. Ferrada, A. Wagner, Cryptic genetic variation promotes rapid evolutionary adaptation in an RNA enzyme. *Nature* **474**, 92–95 (2011). doi: 10.1038/nature10083; pmid: 21637259
14. J. Zheng, J. L. Payne, A. Wagner, Cryptic genetic variation accelerates evolution by opening access to diverse adaptive peaks. *Science* **365**, 347–353 (2019). doi: 10.1126/science.aax1837; pmid: 31346060
15. A. B. Paaby, M. V. Rockman, Cryptic genetic variation: Evolution's hidden substrate. *Nat. Rev. Genet.* **15**, 247–258 (2014). doi: 10.1038/nrg3688; pmid: 24614309
16. B. C. Stanton *et al*., Genomic mining of prokaryotic repressors for orthogonal logic gates. *Nat. Chem. Biol.* **10**, 99–105 (2014). doi: 10.1038/nchembio.1411; pmid: 24316737
17. See supplemental materials.
18. K. S. Sarkisyan *et al*., Local fitness landscape of the green fluorescent protein. *Nature* **533**, 397–401 (2016). doi: 10.1038/nature17995; pmid: 27193686
19. L. Rockah-Shmuel, Á. Tóth-Petróczy, D. S. Tawfik, Systematic Mapping of Protein Mutational Space by Prolonged Drift Reveals the Deleterious Effects of Seemingly Neutral Mutations. *PLOS Comput. Biol.* **11**, e1004421 (2015). doi: 10.1371/journal.pcbi.1004421; pmid: 26274323
20. N. Tokuriki, D. S. Tawfik, Chaperonin overexpression promotes genetic variation and enzyme evolution. *Nature* **459**, 668–673 (2009). doi: 10.1038/nature08009; pmid: 19494908
21. A. Bandyopadhyay *et al*., Chemical chaperones assist intracellular folding to buffer mutational variations. *Nat. Chem. Biol.* **8**, 238–245 (2012). doi: 10.1038/nchembio.768; pmid: 22246401
22. R. G. Smock, I. Yadid, O. Dym, J. Clarke, D. S. Tawfik, De Novo Evolutionary Emergence of a Symmetrical Protein Is Shaped by Folding Constraints. *Cell* **164**, 476–486 (2016). doi: 10.1016/j.cell.2015.12.024; pmid: 26806127
23. J.-D. Pédelacq, S. Cabantous, T. Tran, T. C. Terwilliger, G. S. Waldo, Engineering and characterization of a superfolder green fluorescent protein. *Nat. Biotechnol.* **24**, 79–88 (2006). doi: 10.1038/nbt1172; pmid: 16369541
24. T. H. Yoo, A. J. Link, D. A. Tirrell, Evolution of a fluorinated green fluorescent protein. *Proc. Natl. Acad. Sci. U.S.A.* **104**, 13887–13890 (2007). doi: 10.1073/pnas.0701904104; pmid: 17717085
25. A. Miyawaki, T. Nagai, H. Mizuno, Mechanisms of protein fluorophore formation and engineering. *Curr. Opin. Chem. Biol.* **7**, 557–562 (2003). doi: 10.1016/S1367-5931(03)00097-8; pmid: 14580558
26. A. A. Vakhrusheva, M. D. Kazanov, A. A. Mironov, G. A. Bazykin, Evolution of prokaryotic genes by shift of stop codons. *J. Mol. Evol.* **72**, 138–146 (2011). doi: 10.1007/s00239-010-9408-1; pmid: 21082168
27. J. Yang *et al*., Predicting the viability of beta-lactamase: How folding and binding free energies correlate with beta-lactamase fitness. *PLOS ONE* **15**, e0233509 (2020). doi: 10.1371/journal.pone.0233509; pmid: 32470971
28. E. Rigato, G. Fusco, Enhancing effect of phenotype mutational robustness on adaptation in *Escherichia coli*. *J. Exp. Zool. B Mol. Dev. Evol.* **326**, 31–37 (2016). doi: 10.1002/jez.b.22662; pmid: 26612084
29. B. Steinberg, M. Ostermeier, Environmental changes bridge evolutionary valleys. *Sci. Adv.* **2**, e1500921 (2016). doi: 10.1126/sciadv.1500921; pmid: 26844293
30. S. Govindarajan, R. A. Goldstein, The foldability landscape of model proteins. *Biopolymers* **42**, 427–438 (1997). doi: 10.1002/(SICI)1097-0282(19971005)42:4<427::AID-BIP6>3.0.CO;2-S; pmid: 9283292
31. D. M. Taverna, R. A. Goldstein, Why are proteins marginally stable? *Proteins* **46**, 105–109 (2002). doi: 10.1002/prot.10016; pmid: 11746707
32. R. Geller, S. Pechmann, A. Acevedo, R. Andino, J. Frydman, Hsp90 shapes protein and RNA evolution to balance trade-offs between protein stability and aggregation. *Nat. Commun.* **9**, 1781 (2018). doi: 10.1038/s41467-018-04203-x; pmid: 29725062
33. S. Bershtein, M. Segal, R. Bekerman, N. Tokuriki, D. S. Tawfik, Robustness-epistasis link shapes the fitness landscape of a randomly drifting protein. *Nature* **444**, 929–932 (2006). doi: 10.1038/nature05385; pmid: 17122770
34. N. Tokuriki, D. S. Tawfik, Stability effects of mutations and protein evolvability. *Curr. Opin. Struct. Biol.* **19**, 596–604 (2009). doi: 10.1016/j.sbi.2009.08.003; pmid: 19765975
35. J. M. Sanchez-Ruiz, Protein kinetic stability. *Biophys. Chem.* **148**, 1–15 (2010). doi: 10.1016/j.bpc.2010.02.004; pmid: 20199841
36. K. L. Petrie *et al*., Destabilizing mutations encode nongenetic variation that drives evolutionary innovation. *Science* **359**, 1542–1545 (2018). doi: 10.1126/science.aar1954; pmid: 29599247
37. A. S. Lauring, J. Frydman, R. Andino, The role of mutational robustness in RNA virus evolution. *Nat. Rev. Microbiol.* **11**, 327–336 (2013). doi: 10.1038/nrmicro3003; pmid: 23524517
38. S. Duffy, L. A. Shackelton, E. C. Holmes, Rates of evolutionary change in viruses: Patterns and determinants. *Nat. Rev. Genet.* **9**, 267–276 (2008). doi: 10.1038/nrg2323; pmid: 18319742
39. F. Taddei *et al*., Role of mutator alleles in adaptive evolution. *Nature* **387**, 700–702 (1997). doi: 10.1038/42696; pmid: 9192893
40. J. A. G. M. de Visser, C. W. Zeyl, P. J. Gerrish, J. L. Blanchard, R. E. Lenski, Diminishing returns from mutation supply rate in asexual populations. *Science* **283**, 404–406 (1999). doi: 10.1126/science.283.5400.404; pmid: 9888858
41. I. Bjedov *et al*., Stress-induced mutagenesis in bacteria. *Science* **300**, 1404–1409 (2003). doi: 10.1126/science.1082240; pmid: 12775833
42. R. C. MacLean, C. Torres-Barceló, R. Moxon, Evaluating evolutionary models of stress-induced mutagenesis in bacteria. *Nat. Rev. Genet.* **14**, 221–227 (2013). doi: 10.1038/nrg3415; pmid: 23400102
43. E. van Nimwegen, J. P. Crutchfield, M. Huynen, Neutral evolution of mutational robustness. *Proc. Natl. Acad. Sci. U.S.A.* **96**, 9716–9720 (1999). doi: 10.1073/pnas.96.17.9716; pmid: 10449760
44. R. D. Gupta, D. S. Tawfik, Directed enzyme evolution via small and effective neutral drift libraries. *Nat. Methods* **5**, 939–942 (2008). doi: 10.1038/nmeth.1262; pmid: 18931667
45. S. L. Rutherford, S. Lindquist, Hsp90 as a capacitor for morphological evolution. *Nature* **396**, 336–342 (1998). doi: 10.1038/24550; pmid: 9845070
46. N. Rohner *et al*., Cryptic variation in morphological evolution: HSP90 as a capacitor for loss of eyes in cavefish. *Science* **342**, 1372–1375 (2013). doi: 10.1126/science.1240276; pmid: 24337296
47. C. O. Wilke, J. L. Wang, C. Ofria, R. E. Lenski, C. Adami, Evolution of digital organisms at high mutation rates leads to survival of the flattest. *Nature* **412**, 331–333 (2001). doi: 10.1038/35085569; pmid: 11460163
48. M. S. Johnson, A. Martsul, S. Kryazhimskiy, M. M. Desai, Higher-fitness yeast genotypes are less robust to deleterious mutations. *Science* **366**, 490–493 (2019). doi: 10.1126/science.aay4199; pmid: 31649199
49. A. Khlebnikov, K. A. Datsenko, T. Skaug, B. L. Wanner, J. D. Keasling, Homogeneous expression of the P(BAD) promoter in Escherichia coli by constitutive expression of the low-affinity high-capacity AraE transporter. *Microbiology* **147**, 3241–3247 (2001). doi: 10.1099/00221287-147-12-3241; pmid: 11739756
50. PACBIO, Analytical solutions for PACBIO sequencing data. Pacific Biosciences DevNet; www.pacb.com/support/documentation//DevNet.
51. N. Guo, J. Zheng, Selection_strength_evolvability, Version 1.0, *Zenodo* (2020); https://doi.org/10.5281/zenodo.3819561.

ACKNOWLEDGMENTS

We acknowledge the experimental support of the flow cytometry facility and the functional genomics center at the University of Zurich. We thank H. E. L. Lischer, C. Bello, and G. Schweizer for help with SMRT sequencing data analysis or protein stability analysis. We thank Y. Schaerli, J. Duarte, M. Olombrada Sacristan, B. Ravi, P. Dasmeh, and K. Ramanadane for experimental assistance or comments on the manuscript. We thank B. Schuler and J. L. Payne for helpful discussions. **Funding:** This project has received funding from the European Research Council under grant agreement 739874 and from Swiss National Science Foundation grant 31003A_172887. **Author contributions:** J.Z. and A.W. designed the experiments. J.Z. performed the experiments. J.Z., N.G., and A.W. contributed to data analysis. J.Z. and A.W. wrote the paper. All authors read and edited the paper. **Competing interests:** The authors declare no competing interests. **Data and materials availability:** All data are available in the manuscript or supplementary materials. SMRT sequencing data are available at DDBJ, EMBL, and GenBank under accession numbers KEEO00000000 and KCZY00000000. Custom code used in this study is available at Zenodo under the accession number 3819561 (*51*).

SUPPLEMENTARY MATERIALS

science.sciencemag.org/content/370/6521/eabb5962/suppl/DC1
Materials and Methods
Figs. S1 to S21
Tables S1 to S12
References (*52*–*62*)
Database S1
MDAR Reproducibility Checklist

View/request a protocol for this paper from *Bio-protocol*.

9 March 2020; accepted 25 September 2020
10.1126/science.abb5962

RESEARCH ARTICLE SUMMARY

PLANT SCIENCE

Direct pathogen-induced assembly of an NLR immune receptor complex to form a holoenzyme

Shoucai Ma*, Dmitry Lapin*, Li Liu*, Yue Sun*, Wen Song*, Xiaoxiao Zhang, Elke Logemann, Dongli Yu, Jia Wang, Jan Jirschitzka, Zhifu Han, Paul Schulze-Lefert†, Jane E. Parker†, Jijie Chai†

INTRODUCTION: Discrimination of self from nonself is pivotal for cellular organisms, as it allows the perception of pathogenic invaders that might otherwise multiply unchecked and cause disease in the host. To recognize nonself and to repel intruders, multicellular organisms deploy complex immune systems, in which repertoires of dedicated immune receptors play a central role. Innate immunity is an evolutionarily ancient arm of immunity in plants and animals that relies on structurally related, germline-encoded receptors. One class of these immune receptors inside cells, called the NLR protein family, shares a nucleotide-binding domain and leucine-rich repeats (LRRs). Plant sensor NLRs are classified into two main groups that are defined by different N-terminal domains: a coiled-coil (CC) domain in CC-NLRs (CNLs) and a Toll–interleukin-1 receptor (TIR) domain in TIR-NLRs (TNLs). A deeper understanding of the principles that govern nonself recognition by NLRs and their activation of innate immune responses necessitates protein structure–based approaches and reconstitution of signaling-active receptor complexes.

RATIONALE: Host-adapted plant pathogens secrete numerous effectors into the host extracellular spaces or inside cells. These effectors promote virulence, often by interfering with defense responses. Plant NLRs typically detect strain-specific pathogen virulence factors (effectors) delivered into host cells. This triggers immune responses that curtail pathogen proliferation and often culminate in localized host cell death. During plant host-pathogen coevolution, positive selection of random mutations in effector genes that abrogate NLR recognition drives the diversification of NLR repertoires at the population level. A well-studied coevolved pathosystem involves *Arabidopsis thaliana* and the downy mildew pathogen *Hyaloperonospora arabidopsidis* (*Hpa*). The *A. thaliana* TNL receptor RPP1 confers strain-specific immunity through recognition of *Hpa* effector ATR1. Specific allelic variants of ATR1 in *Hpa* populations activate only certain RPP1 variants in particular *A. thaliana* accessions. Previous work detected a nicotinamide adenine dinucleotide (NAD^+)–consuming enzymatic activity mediated by the N-terminal TIR domains of TNLs. How the TIR-associated NAD^+ hydrolase (NADase) activity and downstream signaling is enabled by TNL effector recognition is unknown.

RESULTS: We coexpressed a naturally occurring *A. thaliana* RPP1 receptor variant with its matching *Hpa* effector ATR1 in insect cells. Protein purification revealed an oligomeric protein complex of ~600 kD consisting of RPP1 and ATR1, which we term the "RPP1 resistosome." Biochemical assays showed that the RPP1 resistosome displays much higher Mg^{2+}/Ca^{2+}-dependent NADase activity than RPP1 alone. Using cryo–electron microscopy, we resolved a structure of the oligomeric complex that contains four RPP1 and four ATR1 molecules and reveals a tetrameric assembly mediated entirely by RPP1 subdomains. In contrast to other adenosine triphosphate (ATP)–bound NLRs in their active forms, RPP1 in the resistosome is adenosine diphosphate–bound, probably because of the lack of a motif required for ATP binding. The structure also reveals direct binding of ATR1 to a C-terminal jelly roll/Ig-like domain (C-JID) and the LRRs of the RPP1 receptor. Protein sequences corresponding to contact regions between the receptor and the pathogen effector are polymorphic in naturally occurring RPP1 and ATR1 variants, explaining why only certain RPP1 variants can detect strain-specific ATR1 molecules. The sequence-diversified $RPP1^{C\text{-}JID}$ is shared by many other TNLs, but not CNLs, in diverse plant species and might serve a role in the detection of other pathogen effectors. Receptor tetramerization creates two potential NADase active sites, each formed by an asymmetric TIR homodimer. Structure-guided substitutions of residues at this homodimeric TIR interface abolished ATR1-induced cell death in planta, supporting an essential role of the TIR-TIR interface in RPP1 function. Our combined biochemical and in planta assays show that assembly of two asymmetric TIR homodimers by the tetrameric receptor complex is responsible for NAD^+ hydrolysis and RPP1-mediated immune signaling.

CONCLUSION: Our findings indicate that the RPP1 resistosome acts as a pathogen effector–inducible holoenzyme for NAD^+ hydrolysis. The tetrameric RPP1 oligomeric structure provides an example of direct pathogen effector recognition by a plant NLR receptor and uncovers the mechanism of strain-specific recognition leading to NLR conformational activation. Our work suggests a multilayered regulation of RPP1 tetramerization, including ATR1 binding, RPP1 oligomerization driven by interactions among nucleotide-binding domains, and $RPP1^{TIR}$ self-association. The analysis provides a structural insight to induced NAD^+ hydrolysis mediated by the RPP1 holoenzyme and a framework for TNL receptor signaling. As a holoenzyme, the RPP1 resistosome bears similarity to the animal apoptosome and inflammasome, which form holoenzymes after the recruitment of procaspases. ■

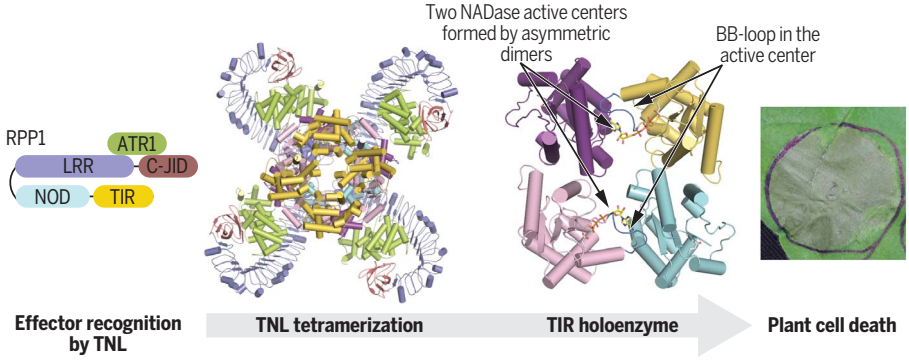

Pathogen activation of an NLR holoenzyme. Recognition of pathogen effector ATR1 via the C-JID and LRR domains of the plant TNL receptor RPP1 triggers the assembly of a tetrameric receptor complex with two asymmetric N-terminal TIR domain homodimers. This tetramer-induced TIR asymmetry creates, via two centrally located BB-loops, active sites for NAD^+ hydrolysis, which is essential for RPP1 signaling leading to host cell death.

The list of author affiliations is available in the full article online.
*These authors contributed equally to this work.
†Corresponding author. Email: chai@mpipz.mpg.de (J.C.); parker@mpipz.mpg.de (J.E.P.); schlef@mpipz.mpg.de (P.S.-L.)
Cite this article as S. Ma *et al.*, *Science* **370**, eabe3069 (2020). DOI: 10.1126/science.abe3069

READ THE FULL ARTICLE AT
https://doi.org/10.1126/science.abe3069

RESEARCH ARTICLE

PLANT SCIENCE

Direct pathogen-induced assembly of an NLR immune receptor complex to form a holoenzyme

Shoucai Ma[1]*, Dmitry Lapin[2]*, Li Liu[2]*, Yue Sun[1]*, Wen Song[3]*, Xiaoxiao Zhang[1], Elke Logemann[2], Dongli Yu[2,3], Jia Wang[1], Jan Jirschitzka[3], Zhifu Han[1], Paul Schulze-Lefert[2,4]†, Jane E. Parker[2,4]†, Jijie Chai[1,2,3,4]†

Direct or indirect recognition of pathogen-derived effectors by plant nucleotide-binding leucine-rich repeat (LRR) receptors (NLRs) initiates innate immune responses. The *Hyaloperonospora arabidopsidis* effector ATR1 activates the N-terminal Toll–interleukin-1 receptor (TIR) domain of *Arabidopsis* NLR RPP1. We report a cryo–electron microscopy structure of RPP1 bound by ATR1. The structure reveals a C-terminal jelly roll/Ig-like domain (C-JID) for specific ATR1 recognition. Biochemical and functional analyses show that ATR1 binds to the C-JID and the LRRs to induce an RPP1 tetrameric assembly required for nicotinamide adenine dinucleotide hydrolase (NADase) activity. RPP1 tetramerization creates two potential active sites, each formed by an asymmetric TIR homodimer. Our data define the mechanism of direct effector recognition by a plant NLR leading to formation of a signaling-active holoenzyme.

Intracellular nucleotide-binding leucine-rich repeat immune receptors (NLRs) have evolved independently in plants and animals to detect pathogen disturbance. Plant sensor NLRs are classified into two main groups that are defined by different N-terminal domains: a coiled-coil (CC) domain in CC-NLRs (CNLs) and a Toll–interleukin-1 receptor (TIR) domain in TIR-NLRs (TNLs). Direct or indirect recognition of pathogen effector proteins by plant NLRs triggers an immune response termed effector-triggered immunity (*1*–*6*), often characterized by rapid host cell death (a hypersensitive response) at sites of attempted infection. In addition to the C-terminal LRR domain, non-canonical integrated domains of plant NLRs play a critical role in conferring specific effector recognition (*7*). Although modes of effector recognition vary, ligand sensing is widely believed to induce oligomerization of NLRs for signaling. For example, a recent structural study of the CNL ZAR1 in *Arabidopsis* showed that the ZAR1 resistosome induced by bacterial effector AvrAC assumes a wheel-like structure similar to that of NLR inflammasomes in animals (*8*). A body of evidence suggests that the CC domains of CNLs and the TIR domains of TNLs mediate signaling upon NLR activation (*9*–*14*). A TIR domain signaling role is further supported by biochemical assays that detected NADase activity required for TNL-mediated immunity (*15*, *16*). Structural and functional studies with individual TIR domains revealed their capacity for self-association as homo- or heterodimers, which is important for immunity induction (*5*, *9*, *17*, *18*). How TIR domain signaling activity is enabled by TNL effector recognition in the context of full-length receptors is unknown.

Members of the *Arabidopsis* RPP1 (Recognition of *Peronospora parasitica* 1) TNL family specifically recognize cognate ATR1 (*Arabidopsis thaliana* Recognized 1) effector variants produced by the foliar oomycete pathogen *Hyaloperonospora arabidopsidis* (*Hpa*) (*19*, *20*). In host and pathogen populations, both *RPP1* from *Arabidopsis* accessions and *ATR1* from *Hpa* strains are highly polymorphic. Recognition of different ATR1 forms by RPP1 variants is *Hpa* race–specific, indicative of host-pathogen coevolution (*12*, *21*). Specific RPP1-ATR1 recognition in *Arabidopsis* leading to leaf macroscopic host cell death was recapitulated in tobacco transient gene expression assays. Coupled with biochemical data, these studies showed a requirement for the RPP1 C-terminal LRR domain in direct binding of recognized ATR1 forms (*20*, *22*).

Reconstitution and cryo-EM structure of the RPP1 resistosome

We coexpressed Strep-RPP1_WsB (residues 61 to 1221) with His-ATR1_Emoy2 (residues 52 to 311) as a matching TNL-effector pair (*12*, *21*) in insect cells. We used a tandem affinity purification procedure to isolate the complex. Gel filtration analysis showed that comigration of the RPP1 and ATR1 proteins corresponded to a molecular weight of ~600 kD (fig. S1), indicating that they form an oligomeric complex, which we term the "RPP1 resistosome." The complex obtained from gel filtration was used for structural analysis by cryo–electron microscopy (cryo-EM). After three-dimensional (3D) classification, a subset of 409,348 particles was used for image reconstruction, generating a map with a global resolution of 3.16 Å, as determined with a gold-standard Fourier shell correlation (Fig. 1A and fig. S2). Resolution of the core complex without inclusion of the LRR portion was 2.99 Å.

The cryo-EM structure of the RPP1 resistosome contains four RPP1 and four ATR1 molecules, which assemble into a tetrameric complex measuring 160 Å × 160 Å × 120 Å (Fig. 1B, fig. S3, A and B, and table S1). Tetramerization of the resistosome is mediated entirely by RPP1 subdomains. We discovered in the resistosome structure that RPP1 has a C-terminal domain in addition to the canonical TNL domains TIR, nucleotide-binding domain (NBD), helix domain 1 (HD1), winged helix domain (WHD), and LRRs (Fig. 1B and fig. S3, C to F). Structural searches of the Protein Data Bank (PDB) revealed that the C-terminal domain adopts a classical β–jelly roll and Ig-like fold (fig. S4A), which we designate C-JID (C-terminal jelly roll and Ig-like domain). The $RPP1^{C\text{-}JID}$ structure is similar to that of the TNL Roq1 (*23*) (fig. S4B). Whereas all canonical TNL-type domains of RPP1 are involved in resistosome assembly, $RPP1^{C\text{-}JID}$ mediates interaction with ATR1, assisted by the inner surface of $RPP1^{LRR}$ (Fig. 1B). The RPP1 resistosome is organized into a three-layered ring structure, with the top, middle, and bottom formed by the TIR domain, the NOD (nucleotide-binding oligomerization domain) module (i.e., NBD-HD1-WHD domains), and ATR1-bound LRR–C-JID, respectively (Fig. 1B). $RPP1^{NBD}$, $RPP1^{HD1}$, and $RPP1^{WHD}$ are positioned similarly to the corresponding domains of activated ZAR1, NLRC4, and Apaf-1 (fig. S4C), indicating that RPP1 adopts an active conformation in the resistosome.

$RPP1^{C\text{-}JID}$ is an essential structural determinant for ATR1-specific recognition

RPP1-bound ATR1 is nearly identical to a crystal structure of the ATR1 monomer alone (*24*) (fig. S4D). $RPP1^{LRR}$ and $RPP1^{C\text{-}JID}$ are comparatively less well defined than other RPP1 domains (fig. S2C). The cryo-EM density of $RPP1^{LRR}$ and $RPP1^{C\text{-}JID}$ was substantially improved by local refinement, sufficient for model building (figs. S2C and S3, G to I). ATR1 obliquely contacts $RPP1^{C\text{-}JID}$ and $RPP1^{LRR}$ via its N-terminal segment (residues 67 to 190) (Fig. 2A), consistent with an earlier report that residues 68 to 222 of ATR1 are sufficient

[1]Beijing Advanced Innovation Center for Structural Biology, Tsinghua-Peking Center for Life Sciences, Centre for Plant Biology, School of Life Sciences, Tsinghua University, 100084 Beijing, China. [2]Max Planck Institute for Plant Breeding Research, 50829 Cologne, Germany. [3]Institute of Biochemistry, University of Cologne, 50674 Cologne, Germany. [4]Cluster of Excellence in Plant Sciences (CEPLAS), 40225 Düsseldorf, Germany.
*These authors contributed equally to this work.
†Corresponding author. Email: chai@mpipz.mpg.de (J.C.); parker@mpipz.mpg.de (J.E.P.); schlef@mpipz.mpg.de (P.S.-L.)

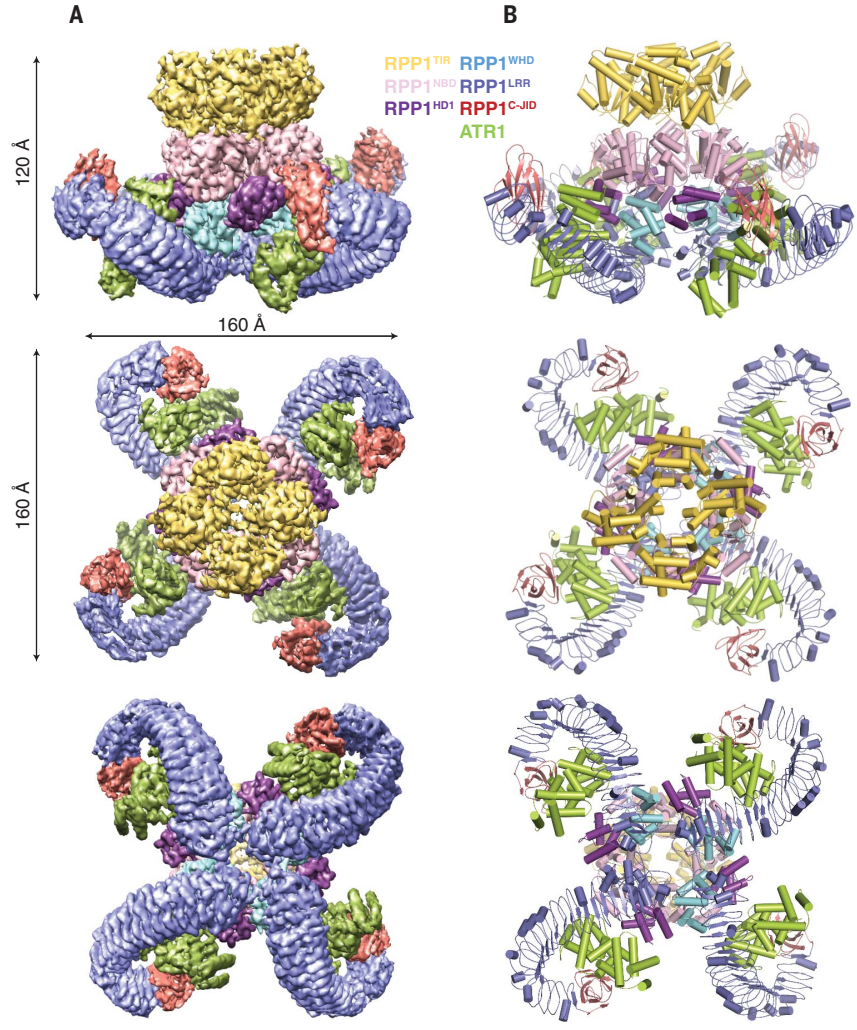

Fig. 1. Tetrameric assembly of the RPP1 resistosome. (**A**) Final 3D reconstruction of the RPP1 resistosome (oligomeric RPP1-ATR1 complex) in three orientations. (**B**) Final model of the RPP1 resistosome in three orientations. The reconstruction and model in each row are shown in the same orientation. Color codes for ATR1 and subdomains of RPP1 are indicated.

for RPP1 recognition (*24*). ATR1 interacts mainly with a flat exposed anti–β sheet surface of $RPP1^{C\text{-}JID}$ (interface 1), establishing hydrogen-bonding and hydrophobic interactions (Fig. 2B and fig. S5A). Contacts with nonconserved residues from the inner surface of the curved $RPP1^{LRR}$ further contribute to ATR1 interaction with RPP1 (interface 2) (Fig. 2C and figs. S5B and S6).

To verify the cryo-EM structure, we made substitutions of residues in ATR1 and RPP1 from interface 1 or 2, or both together. The various mutants were coexpressed in insect cells. Asp^{140} of ATR1_Emoy2 ($ATR1^{D140}$) that is conserved in RPP1_WsB-recognized ATR1_Maks9 and ATR1_Emco5, but not in nonrecognized ATR1_Cala2 and ATR1_Emwa1 (fig. S7), is located at the center of interface 1 (Fig. 2B). Substitution of this residue with a tyrosine present at the equivalent position of ATR1_Cala2 and ATR1_Emwa1 substantially reduced ATR1-Emoy2 binding to RPP1 in vitro (fig. S8A), indicating that interaction with $RPP1^{C\text{-}JID}$ is important for ATR1 recognition. This result also explains why the ATR1_Cala2 and ATR1_Emwa1 alleles are not recognized by RPP1_WsB (*12*, *21*). In further support of the cryo-EM structure, alanine substitutions of five residues from the loop region (E117A/L122A/D124A/T125A/Y126A) of ATR1 at interface 2 resulted in loss of interaction with RPP1 (fig. S8A). Substitutions of RPP1 residues at either of the two interfaces with amino acids at equivalent positions in other RPP1 variants (fig. S6) impaired interaction with ATR1_Emoy2 (fig. S8A).

We tested whether the above RPP1 and ATR1 substitutions affected ATR1-induced RPP1-dependent host cell death by using *Agrobacterium tumefaciens*–mediated transient gene expression to coexpress untagged RPP1 and hemagglutinin (HA)/StrepII (HS)–tagged ATR1 forms in leaves of *Nicotiana benthamiana*. Expectedly, coexpression of wild-type (WT) RPP1 with WT ATR1-HS resulted in cell death of infiltrated leaf zones (Fig. 2D). Epitope-tagged WT RPP1-HS also produced ATR1-dependent cell death in *N. benthamiana* and was detectable as a ~140-kD protein by immunoblotting (fig. S8, B and C). By contrast, cell death was strongly impaired with ATR1 proteins bearing substitutions that abolished or reduced interaction with RPP1 (Fig. 2, C and D, and fig. S8D). The loss of cell death induction by $ATR1^{E117A/L122A/D124A/T125A/Y126A}$ with multiple substitutions at interface 2 (Fig. 2, C and D) showed that in addition to $RPP1^{C\text{-}JID}$, $RPP1^{LRR}$ is important for ATR1 recognition, in agreement with previous data (*20*, *22*). Coexpression of RPP1 with $ATR1^{R177A/Y179A}$ that had no detectable interaction with RPP1 in vitro (fig. S8A) caused WT-like cell death (Fig. 2, C and D). The reason for the discrepancy remains unclear, but it is possible that a weak interaction between this ATR1 mutant and RPP1 was undetectable in vitro but was sufficient to support cell death. The RPP1 substitutions $RPP1^{S1123K/S1125Y/N1181R/S1183R}$ from interface 1 retained WT-like cell death activity when coexpressed with ATR1, but cell death was abolished with $RPP1^{Y869D/R895S/Y935E/R937M}$ substitutions from interface 2 (Fig. 2E). Collectively, our data indicate that $RPP1^{C\text{-}JID}$ and $RPP1^{LRR}$ are structural determinants for ATR1-specific binding and recognition of naturally occurring ATR1 variants. In support of this conclusion, a structure-guided RPP1 sequence alignment revealed that residues from these two domains, in particular those from $RPP1^{C\text{-}JID}$, are variable between different RPP1 proteins (fig. S6).

Assembly of the RPP1 resistosome is required for NADase activity

As observed in oligomerization of other NLR proteins (*8*, *25*–*27*), the RPP1 central NOD module (NBD-HD1-WHD domains) participates in tetramerization (Fig. 3A and fig. S9, A and B). In contrast to other NLRs, however, the loop region between β2 and α2 of $RPP1^{NBD}$ mediates RPP1 tetramerization by interacting with a groove between $RPP1^{NBD}$ and $RPP1^{WHD}$ of the adjacent protomer around the P-loop region (Fig. 3B and fig. S9C). Besides self-association (discussed below), the $RPP1^{TIR}$ stacks against $RPP1^{NBD}$ from an adjacent protomer (Fig. 3C and fig. S9, A, D, and E). Two adjacent $RPP1^{TIR}$s are positioned differently to engage in distinct interactions with $RPP1^{NBD}$ (Fig. 3A). A similar observation was reported for N-terminal CARD domains in the CED-4 apoptosome (*28*). In the RPP1 tetramer, the TIR loop region N-terminal to $RPP1^{NBD}$ (TIRa) is better defined than that of its neighboring TIR (TIRb). $RPP1^{TIRa}$ packs tightly against the top

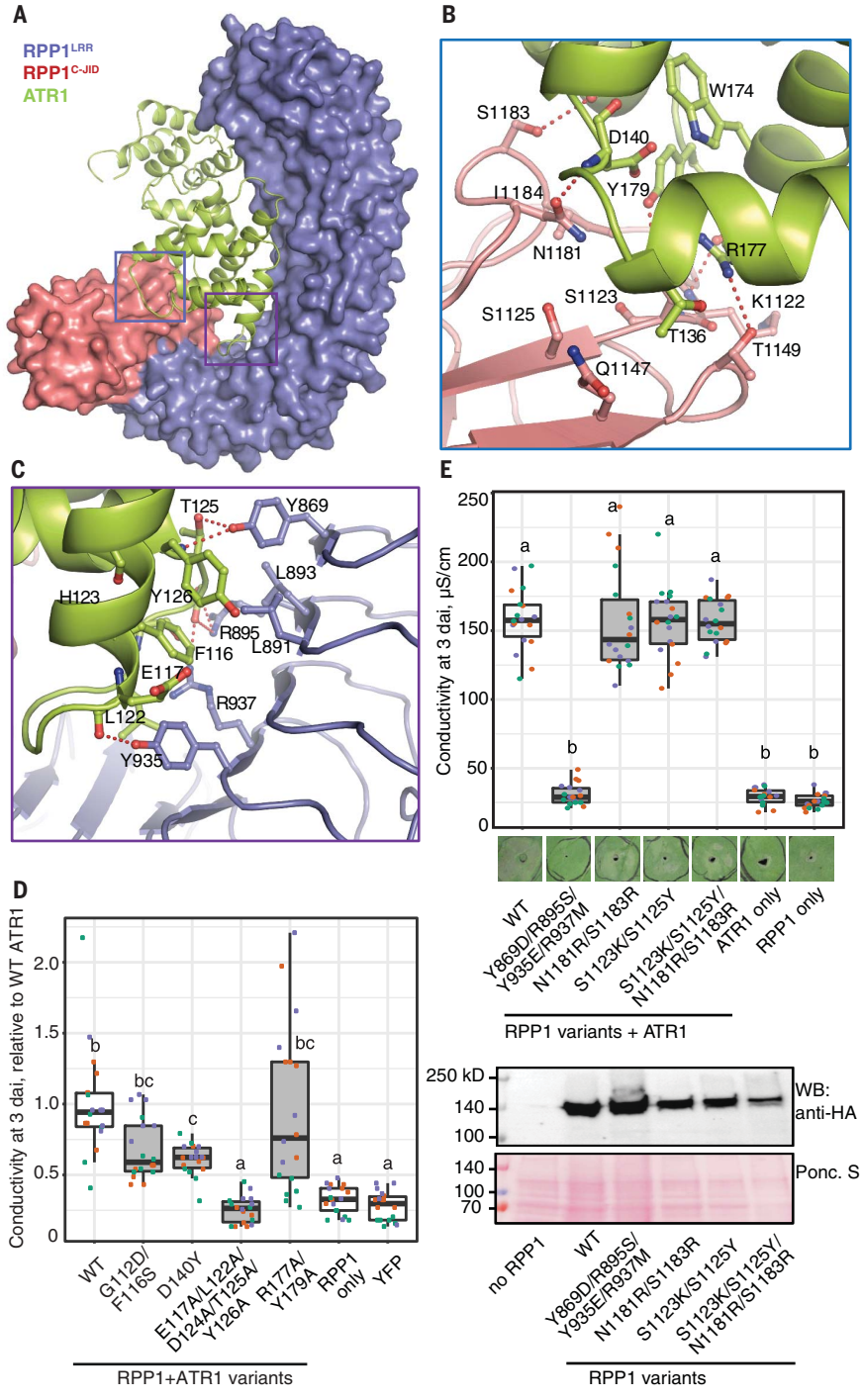

Fig. 2. Structural mechanism of ATR1 recognition by RPP1. (**A**) Structure of ATR1 (in cartoon) bound by the RPP1$^{LRR–C-JID}$ fragment (in surface) showing two interfaces with ATR1. (**B**) Detailed interactions between RPP1^{C-JID} and ATR1 at interface 1 [blue frame in (A)]. Red dashed lines indicate polar interactions. (**C**) Detailed interactions between RPP1^{LRR} and ATR1 at interface 2 [purple frame in (A)]. Red dashed lines indicate polar interactions. (**D**) Host cell death triggered by coexpression of untagged RPP1_WsB and HS-tagged ATR1_Emoy2 variants in leaves of *N. benthamiana*. WT, wild type. Cell death was quantified by a leaf disk ion leakage (conductivity) assay at 3 days after agro-infiltration (dai). Data are normalized to the mean value for samples with RPP1_WsB and WT ATR1_Emoy2 in each experiment. Results from three independent experiments are displayed on the plot (n = 18; Tukey's HSD test, α = 0.01; data points of the same color were recorded in one experiment; shared lowercase letters indicate no significant difference). (**E**) Top: Ion leakage assay of RPP1_WsB mutations at RPP1-ATR1 interfaces 1 and 2 on ATR1_Emoy-induced cell death in *N. benthamiana*. The assay was performed as described in (D) after agro-infiltration of C-terminally HA-StrepII–tagged RPP1_WsB (RPP1_WsB-HS) with ATR1_Emoy2-HS. Statistical analysis via Tukey's HSD test is based on data from three independent experiments (n = 18, α = 0.001; data points of the same color were recorded in one experiment; shared lowercase letters indicate no significant difference). Below are photographs of representative agro-infiltrated leaf zones at 4 dai. Bottom: Western blot analysis of total *N. benthamiana* leaf protein extracts at 2 dai probed with antibody to HA. Expression of RPP1_WsB-HS WT and mutant proteins produces a signal of the expected molecular weight (~140 kD). Ponceau S staining indicates equal loading of total leaf proteins on the blot.

of RPP1^{NBD} from an adjacent protomer via extensive interactions of C-terminal parts of helices αA and αE (Fig. 3C and fig. S5C). Less tight interactions are formed between TIRb and its adjacent RPP1^{NBD} (fig. S9D). As observed in the ZAR1 resistosome, interactions between two neighboring LRR domains (fig. S9, A and E) likely further stabilize the RPP1 tetrameric resistosome.

We next investigated whether formation of the RPP1 resistosome is required for NADase activity. A high-performance liquid chromatography (HPLC) assay with recombinant proteins purified from insect cells showed that the RPP1-ATR1 complex, but not RPP1 alone, hydrolyzed nicotinamide adenine dinucleotide (NAD^+) at 1.0 μM protein (Fig. 3D). Divalent ions were shown to be important for nucleoside hydrolase activities (*29*). We therefore tested whether Mg^{2+} or Ca^{2+} changed RPP1-ATR1 tetramer NAD^+ hydrolysis. Addition of 10 mM Mg^{2+} strongly promoted consumption of NAD^+ by RPP1 (Fig. 3D). The same concentration of Ca^{2+} had a weaker effect. By contrast, Mg^{2+} or Ca^{2+} did not increase the negligible NADase activity of RPP1 alone (Fig. 3D). These data show that assembly of the RPP1 tetramer is necessary for NAD^+ hydrolysis. Notably, the same concentration (1.0 μM) of RPP1^{TIR} (residues 60 to 254) purified from insect cells was much less efficient in NAD^+ hydrolysis (fig. S10A). At a higher concentration (70 μM), RPP1^{TIR} NADase activity

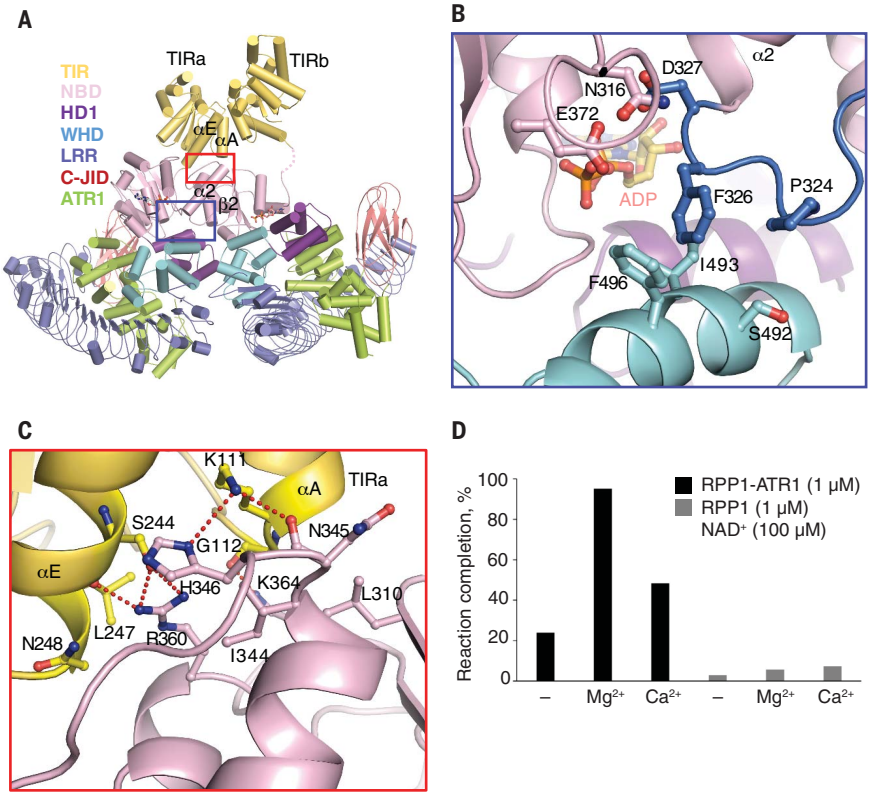

Fig. 3. The RPP1 resistosome, but not RPP1 alone, has Mg^{2+}/Ca^{2+}-dependent NADase activity. (**A**) A lateral RPP1 homodimer shown in cartoon. αA and αE are helices from the TIR domain (TIRa) in the left RPP1 protomer that interact with $RPP1^{NBD}$ of the right protomer. The dashed line in the right RPP1 indicates the flexible region C-terminal to the TIR domains. (**B**) Detailed interactions of the β2-α2 loop from the right protomer with $RPP1^{NBD}$ and $RPP1^{WHD}$ from the left protomer highlighted within the blue frame in (A). (**C**) Detailed interactions between $RPP1^{TIRa}$ and $RPP1^{NBD}$ highlighted within the red frame in (A). (**D**) NADase activity assay of the ATR1-RPP1 complex and RPP1 alone. The purified ATR1-RPP1 complex or RPP1 only was incubated with 100 μM NAD^+ in buffer with or without 10 mM Mg^{2+}/Ca^{2+}. After incubation at 25°C for 16 hours, reaction mixtures were centrifuged and immediately used for HPLC analysis. Reaction completion (%) of each sample was calculated as [1 − (concentration of unhydrolyzed NAD^+)/(concentration of NAD^+ before reaction)] × 100%.

was increased and promoted by Mg^{2+} and Ca^{2+} (fig. S10A), which suggests that high concentrations of TIR alone may drive it into oligomers with enzymatic activity (*5*). This notion is further supported by an earlier finding of $RPP1^{TIR}$ in vivo autoactivity that correlated with its self-association in solution (*30*). Also, induced TIR domain proximity led to cell death in planta (*31*). Collectively, our data indicate that ATR1-induced assembly of the RPP1 resistosome is required for RPP1 NADase activity and host cell death induction. Thus, the RPP1 resistosome can be viewed as a pathogen-inducible holoenzyme for NAD^+ hydrolysis.

Active sites are formed by asymmetric TIR homodimers

Whereas the four $RPP1^{NOD}$ modules in the RPP1 resistosome are approximately related with C_4 symmetry, the four TIR domains are related with C_2 symmetry because of the different positioning of two neighboring $RPP1^{TIR}$s (Fig. 4A). Thus, the tetrameric $RPP1^{TIR}$s contain two symmetric TIR homodimers that are nearly identical to those observed in the crystal structure of $RPP1^{TIR}$ (fig. S11, A and B) (*18*). Each of three tested substitutions of residues at this homodimeric "AE" interface (*9*, *17*, *18*) abolished ATR1-induced cell death in *N. benthamiana* (fig. S11C), supporting an essential role of the AE interface in RPP1 function. Functional relevance of the AE interface has been observed for TIR domains of other plant TNLs (*9*, *17*, *18*). In the RPP1 tetramer, opposite packing of the two symmetric TIR homodimers led to formation of two asymmetric head-to-tail $RPP1^{TIR}$ homodimers (Fig. 4A). The two $RPP1^{TIR}$s in an asymmetric homodimer have different conformations in the loop between αA and αB (equivalent to the BB-loop of other TIR domains, hereafter called the BB-loop) (Fig. 4B). The BB-loop is well defined in $RPP1^{TIRa}$ but is disordered in $RPP1^{TIRb}$ (fig. S12A). Asymmetric head-to-tail $RPP1^{TIR}$-$RPP1^{TIR}$ interaction is primarily mediated by the BB-loop of TIRa that contacts the opposite side of TIRb (Fig. 4, A and C, and fig. S12B).

From a sequence alignment (fig. S12C), the predicted catalytic $RPP1^{E158}$ is located at one end of the groove formed within an asymmetric $RPP1^{TIR}$ homodimer (fig. S13A), which suggests that this groove is important for RPP1-catalyzed NAD^+ hydrolysis and RPP1 function. To test this hypothesis, we mutated residues from the interface of the asymmetric $RPP1^{TIR}$ homodimer and evaluated the impact of these substitutions on the NADase activity of the RPP1 resistosome and ATR1-induced cell death in *N. benthamiana*. Substitutions RPP1 I121E, S124E, A222E, or G223A, which are predicted to disrupt the asymmetric $RPP1^{TIR}$ homodimers, all interacted with ATR1 (fig. S10B) but were strongly compromised in NAD^+ hydrolysis (Fig. 4D and fig. S13B). By contrast, an RPP1R123A exchange had less effect on NADase activity (Fig. 4D). In support of an essential role of NADase activity in RPP1 function, we also found that RPP1 I121E, A222E, E158A, or E158Q, but not RPP1 R123A, S124E, E122A/R123A/S124A/K125A/S126A, or G223A, displayed almost undetectable cell death activity (Fig. 4E). Taken together, these data show that the assembly of two TIRa-TIRb active sites in the RPP1 resistosome is responsible for NAD^+ hydrolysis and RPP1-mediated signaling.

A previous study showed that many single mutations in the TIR domain of the canonical *Arabidopsis* TNL RPS4 ($RPS4^{TIR}$) disrupted the cell death activity of $RPS4^{TIR}$ in tobacco (*13*). Mapping the equivalent residues onto the RPP1 resistosome revealed that most of them cluster around the asymmetric TIRa-TIRb groove (fig. S13C). We found that adenosine triphosphate (ATP), which was supplemented during protein purification, bound to this groove in the absence of NAD^+ (fig. S13A) and that the ATP binding groove is conserved among *Arabidopsis* TNLs (fig. S12C). The bound ATP likely acts as an analog of NAD^+ at the groove. Supporting this possibility, a structural comparison revealed that NAD^+ phosphate ($NADP^+$) bound to the TIR domain of plant TNL RUN1 (*9*, *17*, *18*) at a position similar to that of ATP in the RPP1 TIRa-TIRb groove (fig. S13D). These results provide additional evidence for the biological relevance of the asymmetric $RPP1^{TIR}$ homodimers in the resistosome.

ADP binds to the P-loop region of RPP1 in the resistosome

Previous studies demonstrated that structures of the NOD module from plant and animal NLRs are highly conserved in both inactive and active states (*32*). This is underscored here by the similar structures of $RPP1^{NOD}$ in the

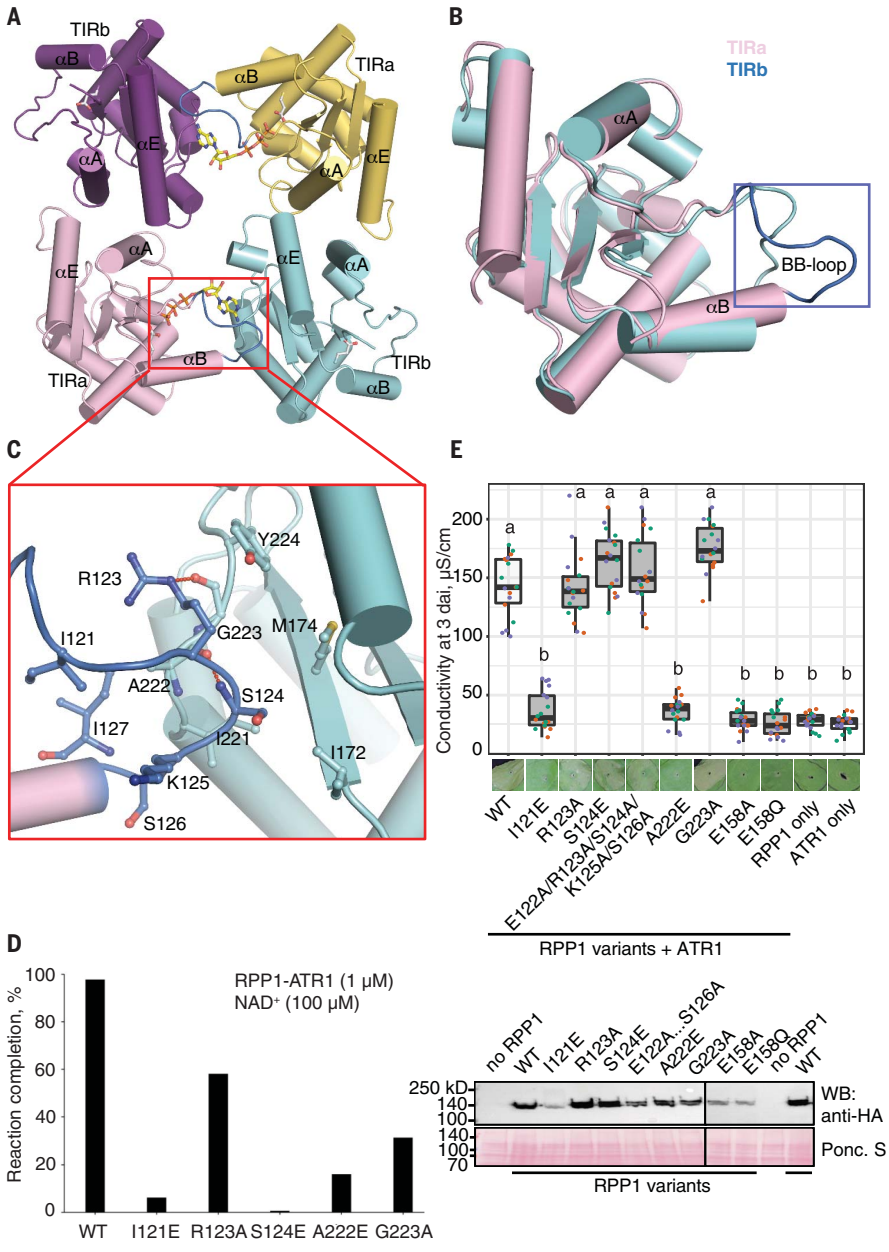

Fig. 4. Assembly of two active sites by two asymmetric RPP1^{TIR} dimers in the tetrameric RPP1 resistosome. (**A**) Tetrameric assembly of RPP1^{TIR}s in the resistosome. Some secondary structural elements are labeled. Two bound ATP molecules within the two asymmetric RPP1^{TIR} dimers (top and bottom dimer) are shown in stick. The loop region between αA and αB (BB-loop) from TIRa is framed in red and shown in blue. (**B**) Structural alignment of the two RPP1^{TIR} monomers from the asymmetric homodimer. The BB-loop from TIRa and TIRb is shown in blue and gray, respectively. The BB-loop is highlighted. (**C**) Detailed interactions of the BB-loop from TIRa with TIRb in the asymmetric dimer. (**D**) Mutagenesis analysis of the interactions shown in (C) using the NADase activity assay described in Fig. 3D. (**E**) Effects of mutations at sites mediating TIRa-TIRb interactions (AE interface) on RPP1_WsB-HS and ATR1_Emoy2-dependent cell death in *N. benthamiana* leaves. Host cell death was measured in a quantitative electrolyte leakage assay as described in Fig. 2, D and E. Top: Host cell death triggered by coexpression of RPP1_WsB-HS variants and ATR1_Emoy2-HS in leaves of *N. benthamiana*. Statistical analysis via Tukey's HSD test is based on data from three independent experiments (n = 18, α = 0.001; data points of the same color were recorded in one experiment; shared lowercase letters indicate no significant difference). RPP1 mutants E158A and E158Q were included as additional negative controls. Below are photographs of representative agro-infiltrated leaf zones at 4 dai. Bottom: Western blot analysis of total *N. benthamiana* leaf protein extracts at 2 dai probed with antibody to HA. Expression of RPP1_WsB-HS WT and mutant proteins produces a signal of the expected molecular weight (~140 kD). Ponceau S staining indicates equal loading of total leaf proteins in the tested samples.

RPP1 tetramer and ZAR1^{NOD} in the ZAR1 pentamer (fig. S4C). Furthermore, NLR activation involves conformational changes in the NBD relative to its C-terminal WHD, whereas no conformational change occurs in the WHD relative to its C-terminal portion, as demonstrated in activation of ZAR1, Apaf-1, and NLRC4 (*8*, *25*–*27*). A modeling study using the inactive ZAR1^{NOD} structure (*33*) as a template suggested that the LRR domain, in its pre-activation state, sequesters RPP1 from oligomerization, consistent with other NLR autoinhibition models (fig. S14). The modeled inactive RPP1 structure also suggested that ATR1 binding would sterically clash with RPP1^{NBD} (fig. S14B), inducing conformational changes in RPP1^{NBD} for activation. Positioning of inactive RPP1^{TIR} is difficult to predict because of the lack of a reliable template. However, overexpression of RPP1^{TIR}, but not RPP1$^{TIR\text{-}NBD}$, induced cell death in *N. benthamiana* (*12*, *30*). These data point to inhibition of RPP1^{TIR} by RPP1^{NOD}, presumably through interdomain interaction similar to that observed for the inactive ZAR1^{CC} (*33*). An inhibitory interaction between the TIR and NBD domains was also suggested for TNLs L6 and L7 from flax (*34*).

On the basis of current models (*5*, *32*), we expected an ATP molecule to be bound by the NBD of activated RPP1. Surprisingly, an adenosine diphosphate (ADP) molecule, which is unambiguously defined by the cryo-EM density, binds to the P-loop of RPP1 in the resistosome (Fig. 5A and fig. S5D). The ADP is recognized via RPP1 residues that are highly conserved in other NLR proteins (*33*, *35*–*37*). Recognition of the γ-phosphate group of deoxyadenosine triphosphate (dATP)/ATP in the ZAR1 resistosome (*8*) and Apaf-1 apoptosome (*27*) is mediated through an arginine residue in a "TT/SR" motif that is essential for their activation. The arginine is highly conserved in plant CNLs and animal NLRs (*38*) but is substituted with a differently charged or polar residue, creating "TTE/Q" in many known TNLs including RPP1 (fig. S15, A and B). In contrast to ZAR1 and Apaf-1, however, RPP1 tolerates such substitutions, which suggests that other interactions might compensate for loss of ATP-mediated stabilization of the RPP1 resistosome. Indeed, the β2-α2 loop contributes to RPP1 oligomerization by mediating NOD-NOD interactions (Fig. 3B and Fig. 5B). In further support of this hypothesis, the TNL Roq1 with the TT/SR motif has ATP bound in its activated form and the β2-α2 loop is not involved in formation of the Roq1 resistosome (*23*), similar to what was observed in the ZAR1 resistosome (Fig. 5, B and C). Besides Roq1, some other TNLs also carry the TT/SR motif (fig. S15A). Most of these TNLs have a shorter β2-α2 loop relative to those without the motif (fig. S15A), providing

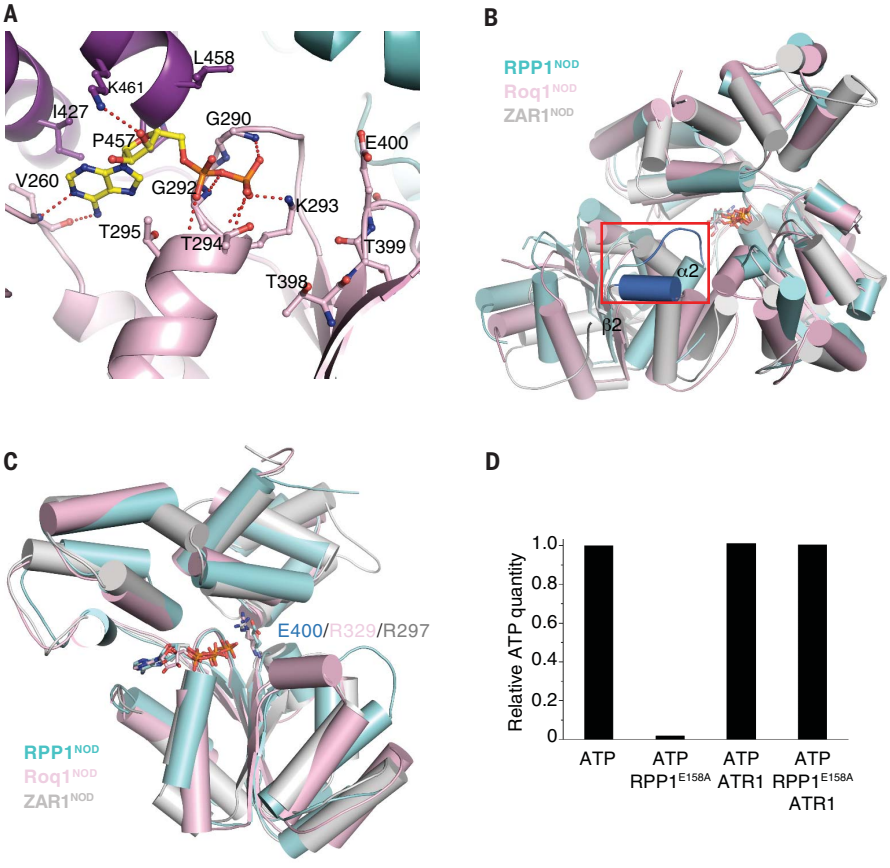

Fig. 5. Activation of RPP1 by ATR1. (**A**) ADP is bound between the NBD and HD1 domains in the cryo-EM structure of RPP1-ATR1. Red dashed lines represent polar interactions. A corresponding structure with EM density around the ADP-bound molecule is shown in fig. S5D. (**B**) Structural superposition of a lateral RPP1^{NOD} (cyan), Roq1^{NOD} (pink), and ZAR1^{NOD} (gray) homodimer. For clarity, only the NBD from the left NOD monomer is shown. The β2-α2 loop is shown in blue and framed in red. (**C**) Structural superposition of RPP1^{NOD} (cyan), Roq1^{NOD} (pink), and ZAR1^{NOD}. Arg^{329} and Arg^{297} from the TTR motif of Roq1 and ZAR1, respectively, and Glu^{400} from the equivalent position of RPP1 are indicated. The bound ADP in RPP1 and ATP in Roq1 and ZAR1 are shown in stick. (**D**) ATPase activity assay for RPP1^{E158A} and the RPP1^{E158A}-ATR1 complex with ATR1. The recombinant proteins were individually incubated with ATP (1.0 mM) in buffer containing 10 mM Mg^{2+}. After incubation at 25°C for 1 hour, samples were centrifuged and immediately used for HPLC analysis to measure ATP content. The vertical axis represents the ATP ratio after versus before the reaction.

additional evidence for the above hypothesis. Collectively, these results might explain why ADP is bound in the RPP1 tetramer, although exchange of ADP with ATP during RPP1 activation remains possible.

Bound ADP in the RPP1 resistosome might result from RPP1 intrinsic ATPase activity. To test this possibility, we used HPLC to measure the ATPase activity of the RPP1^{E158A} resistosome or nonactivated RPP1^{E158A} (to avoid potential interference from RPP1 NADase activity). In the presence of 10 mM Mg^{2+}, RPP1^{E158A} alone displayed ATPase activity that was more potent than that of Apaf-1 by a factor of ~3 to 4 (Fig. 5D and fig. S16) (*35*, *39*). In contrast, the ATR1-activated RPP1^{E158A} resistosome had much lower ATPase activity under the same conditions. Similar results were obtained with the Apaf-1 apoptosome (*39*). Hence, we propose that RPP1 ATPase activity also contributes to an ADP-bound resistosome.

Discussion

We reconstituted the RPP1 resistosome and solved its structure using cryo-EM at 3.16 Å. The structure reveals the mechanism of race-specific recognition of ATR1 by RPP1, leading to NLR conformational activation. We have presented evidence for the multilayered regulation of RPP1 tetramerization, including ATR1 binding (Fig. 2), RPP1^{NOD} oligomerization (fig. S9), and RPP1^{TIR} self-association (Fig. 4). RPP1 tetramerization results in the formation of two asymmetric RPP1^{TIR} homodimers, creating active sites for NAD^+ hydrolysis. Therefore, ATR1-induced receptor tetramerization links effector binding to the regulation of RPP1 NADase activity. Structural and biochemical characteristics of the activated RPP1 tetramer provide a template for understanding canonical plant TIR-type NLRs.

Besides the canonical TNL domains, the C-JID that could not be predicted by primary sequence was revealed in the cryo-EM structure of the RPP1 resistosome. Biochemical and functional data show that this novel structural domain is a major determinant for specific ATR1 recognition (Fig. 2). In contrast to integrated domains of plant NLRs that are sufficient for effector recognition (*7*), RPP1$^{C\text{-}JID}$ functions together with RPP1^{LRR} for specific recognition of ATR1. The sequence-diversified RPP1$^{C\text{-}JID}$ is predicted by a hidden Markov model (HMM) to be shared by many TNLs in dicotyledonous plant species (fig. S17, A to F). It comprises part of a C-terminal domain in *Arabidopsis* TNL receptor RPS4 that confers effector-triggered immunity as a heterodimer with TNL RRS1 (*17*, *40*). Mutations within the predicted RPS4$^{C\text{-}JID}$ (fig. S17E) disabled RRS1/RPS4 immunity (*40*, *41*), pointing to broader importance of the C-JID for TNL function. It is possible that the C-JID serves as a decoy that mimics common virulence targets of pathogen effectors (*7*). However, using HMM, we failed to detect the RPP1$^{C\text{-}JID}$ in CNLs and non-NLR plant proteins (fig. S17, B to D). We therefore speculate that the C-JID in different TNLs plays a more generic role, together with LRRs, in TNL-specific detection of unrelated pathogen effectors. Although direct RPP1 recognition of ATR1 leads to resistosome formation, many plant NLRs perceive their cognate effectors in an indirect manner typically involving other host proteins (*2*).

Assembly of NADase active sites is mediated principally by the TIR BB-loop, which undergoes a major conformational change after RPP1 tetramer formation (fig. S18A). The BB-loop of RRS1^{TIR} (four residues) is shorter than that of RPP1^{TIR} and other TNL TIR domains (>9 residues; fig. S18B). The RRS1^{TIR} BB-loop in the symmetric RRS1^{TIR} homodimer or the RPS4^{TIR}-RRS1^{TIR} heterodimer (*17*) cannot support an RPP1^{TIR}-like asymmetric homodimer (fig. S18B). Therefore, RRS1^{TIR} would sequester the symmetric RPS4^{TIR} homodimer from self-associating into asymmetric homodimers, potentially explaining RRS1^{TIR}-mediated in planta suppression of RPS4^{TIR}-triggered cell death (*17*). Structural alignment reveals that the asymmetric RPP1^{TIR} homodimer is similar to that of filaments formed by MAL^{TIR} in animals (fig. S18C) (*42*). However, there is no experimental evidence for a filament-forming activity of RPP1^{TIR} or other plant TIR domains. Notably, MAL^{TIR} can form cofilaments with TIR domains of other proteins such as human TLR4 and MyD88 (*42*). Many TIR-only genes are encoded in the genome of *Arabidopsis* (*43*), and TNLs have

been proposed to recruit TIR-only proteins for signaling (*44*, *45*). It will be interesting to determine whether the RPP1 resistosome can serve as a platform for interactions with TIR-only proteins or other oligomerized TNLs to amplify TNL-mediated immune signals.

Like the ZAR1 resistosome (*8*), the Apaf-1 apoptosome (*27*), and the NLRC4 inflammasome (*25*, *26*, *46*), the RPP1 tetramer forms a ring-like structure, despite the different oligomerization states of its components. The ZAR1 and RPP1 resistosomes contain, respectively, a stabilized funnel-shaped structure for plasma membrane targeting and a stabilized tetrameric $RPP1^{TIR}$ for NADase activity. This contrasts with relatively flexible apoptosome and inflammasome N-terminal CARD domains. Hence, the N-terminal domains of plant and animal NLRs likely engage different mechanisms for immune signaling. Nonetheless, a shared principle in signaling mediated by the ZAR1 resistosome and NLRC4 inflammasome was proposed (*8*). The ZAR1 resistosome and probably many other CNLs with an N-terminal "MADA" motif (*47*) might form a membrane-resident pore or channel to mediate immunity. This is conceptually analogous to signaling mediated by the NLRC4 inflammasome that activates the pore-forming protein GSDMD for immune responses through the protease caspase-1 (*48*). The RPP1 resistosome, as a holoenzyme, bears similarity to both the apoptosome and the inflammasome, which form holoenzymes after recruitment of procaspase-9 and procaspase-1, respectively. Building on current models of TNL-mediated immune signaling, the RPP1 resistosome NADase activity is responsible for activation of HeLo domain–containing signaling (helper) NLRs via the EDS1 family of lipase-like proteins (*49*–*51*). It was speculated that HeLo-NLRs function similarly to ZAR1 at host membranes (*8*, *11*, *47*). Thus, the RPP1 resistosome and NLRC4 inflammasome might represent comparable paradigms in innate immunity signaling.

Materials and methods

Protein expression and purification

Sequence alignment of RPP1_WsB with its alleles RPP1_WsA, RPP1_NdA, RPP1_EstA, and RPP1_ZdrA by Clustal Omega (*52*) indicated that the N-terminal 60 amino acids of RPP1_WsB are not conserved. Therefore, an N-terminally truncated form of WT RPP1_WsB (61-1221) was constructed for protein expression in insect cells. ATR1_Emoy2 with an N-terminal truncation of 51 residues used for crystallization in a previous study (*24*) was used for protein expression. ATR1_Emoy2 (residues 52 to 311) was sufficient for recognition by RPP1, as demonstrated (*24*). For purification of the RPP1-ATR1 complex, a codon-optimized RPP1_WsB (61-1221; GENEWIZ Inc.) construct was cloned into the pFastBac 1 vector (Invitrogen) with a C-terminal twin-StrepII tag. A codon-optimized ATR1_Emoy2 construct (52-311; GENEWIZ) was cloned into the pFastBac 1 vector with a C-terminal 10 × HIS tag. These constructs were coexpressed in Sf21 insect cells (Invitrogen) at 28°C. After recombinant baculovirus infection for 48 hours, infected cells were harvested and resuspended in buffer A (25 mM Tris-HCl, pH 8.0, 150 mM NaCl, 1 mM $MgCl_2$, and 0.3 mM ATP). After sonication and centrifugation, the RPP1-ATR1 complex was purified using Strep-Tactin resin (IBA Lifesciences) from the supernatant. Proteins bound to resin were eluted with buffer A supplemented with 2.5 mM D-desthiobiotin. The eluent from Strep-Tactin was loaded onto Ni-NTA resin (Novagen) and the resin was washed with buffer A containing 20 mM imidazole. Proteins bound to the Ni-NTA resin were eluted with buffer A plus 250 mM imidazole. The eluent was concentrated through a 30-kD MWCO Vivaspin 500 concentrator (GE Healthcare) to 100 μl and loaded onto a Superose 6 increase 5/150 column (GE Healthcare) with buffer E (10 mM Tris-HCl pH 8.0, 100 mM NaCl, and 1 mM DTT). Peak fractions were concentrated to 0.45 mg/ml for cryo-EM sample preparation. A similar procedure was used for purification of the $RPP1^{E158A}$ (61-1221)-ATR1 (52-311) complex.

Cryo-EM sample preparation and data collection

An aliquot of 3 μl of purified RPP1-ATR1 was applied to holey carbon grids (Quantifoil Au 1.2/1.3, 300 mesh) glow-discharged for 30 s at high level in Harrick Plasma after 2 min evacuation. Grids were then blotted on filter paper (Ted Pella Inc.) for 2.5 s at 8°C with 100% humidity and flash-frozen in liquid ethane using FEI Vitrobot Marked IV.

Two datasets of the WT RPP1-ATR1 complex were collected: one on a Titan Krios2 electron microscope operated at 300 kV, equipped with Gatan K3 Summit direct electron detector and a Gatan Quantum energy filter, the other on a Titan Krios3 electron microscope operated at 300 kV, equipped with a Cs-corrector, Gatan K3 Summit direct electron detector, and a Gatan Quantum energy filter. A total of 5701 and 3834 micrograph stacks were collected on Titan 2 and Titan 3, respectively. The micrograph stacks were automatically recorded using AutoEMation in superresolution mode (*53*), at a nominal magnification of 64,000× on Titan 2 and 81,000× on Titan 3. Defocus values varied from −1.0 μm to −2.0 μm for both datasets. Exposure rate of data collection on Titan 2 and Titan 3 was 23 and 24 electrons per pixel per second, respectively. The exposure time for both datasets was 2.56 s dose-fractionated into 32 subframes, leading to a total electron exposure of ~50 electrons per $Å^2$ for each stack.

Image processing and 3D reconstruction

The raw stacks of RPP1-ATR1 recorded in superresolution mode were motion-corrected by MotionCor2 and binned twofold, resulting in a physical pixel size of 1.0742 Å per pixel for Titan 2 motion-corrected micrographs and 1.0979 Å per pixel for Titan 3 motion-corrected micrographs (*54*). In the meantime, exposure rate for the summed micrographs was performed (*55*). Contrast transfer function (CTF) parameters were estimated by CTFFIND4 (*56*). Based on the CTF estimations, 5117 (Titan 2)/3123 (Titan 3) micrographs were manually picked, respectively, and were further processed in RELION3.1.

About 10,000 Laplacian-of-Gaussian auto-picked particles were subjected to 2D classification to generate initial templates for further auto-picking. For the dataset collected on Titan 2, 1,395,913 auto-picked particles were subjected to five rounds of 2D classification, which performed 25 iterations with regularization parameter $T = 2$ and number of classes = 100 to remove bad particles. Similar parameters were applied in three rounds of 2D classification of 1,125,203 auto-picked RPP1-ATR1 particles from Titan 3. After removal of bad particles, the remaining 661,434 particles on Titan 2 and 516,036 on Titan 3 for the RPP1-ATR1 complex were subjected to 3D classification with C_1 symmetry, using initial 3D reference models obtained by ab initio calculation from RELION3.1.

Particles (276,146 from Titan 2 and 133,202 from Titan 3 for RPP1-ATR1) from good 3D classes with clear overall structural features were selected for 3D refinement. At this stage, the 3D reconstructions clearly showed four RPP1 molecules in the complex. C_4 symmetry was therefore tested in the following 3D refinement. Resulting reconstructions showed that the global density, particularly that corresponding to the TIR part, became worse, indicating that lower or no symmetry exists in the RPP1-ATR1 complex. Subsequent 3D refinement with C_2 symmetry greatly improved the density quality and global resolution. After global 3D refinement with C_2 symmetry, CTF refinement, and postprocessing, the resolution of the RPP1-ATR1 reconstruction from the Titan 2 and Titan 3 datasets was 3.65 Å and 3.16 Å, respectively. Refined RPP1-ATR1 particles (409,348) from the two datasets were joined and subjected to a further round of 3D reconstruction, yielding a final cryo-EM map with 3.16 Å resolution.

A core region mask including the TIR, NBD, HD1, and WHD domains of RPP1 and ATR1 was generated by Chimera and then applied to 3D auto-refinement using C_2 symmetry and 409,348 particles from the final reconstruction with the merged datasets. In the end, the resolution of RPP1 core part reconstruction was 2.99 Å after postprocess.

The LRR and C-JID portions in the final EM map were more flexible relative to the other parts of the RPP1-ATR1 complex. To improve resolution of the local density, C_4 symmetry was first used to refine the joined particles, and the refined particles were expanded with C_4 symmetry for focused 3D classification. A local mask for LRR, C-JID, and ATR1 was generated using Chimera and then applied for focused 3D classification without alignment as described (*57*). After the focused 3D classification, a total of 222,015 particles were selected for C_1 focused 3D refinement, finally yielding a local reconstruction for LRR, C-JID, and ATR1 with 3.19 Å after postprocess.

2D classification, 3D classification, and 3D autorefinement were all performed with RELION3.1 (*58*–*60*). The resolutions were determined by gold-standard Fourier shell correlation (*61*). Local resolution distribution was evaluated using RELION (*62*).

Model building and refinement

The final RPP1-ATR1 EM map was generated by merging the global map and local LRR, C-JID, and ATR1 map, using combine_focused_map in PHENIX (*63*). For model building of the whole RPP1-ATR1 complex, the RPP1 TIR domain (PDB: 5TEB) (*18*) and ATR1 (PDB: 3RMR) were docked into the EM map in Chimera (*64*). The models of the NBD, HD1, and WHD domains of RPP1 were manually built in COOT based on the global EM map of RPP1-ATR1, and the LRR and C-JID domains in COOT using the local refined EM map (*65*). All the domains were then combined, generating a model containing four ATR1 molecules and four RPP1 molecules. The generated model was refined against the combined RPP1-ATR1 EM density using real-space refinement in PHENIX with secondary structure and geometry restraints (*63*). The final model after refinement was validated using MolProbity and EMRinger in the PHENIX package (*63*). Table S1 summarizes the model statistics.

In vitro NADase assays

Purified RPP1, RPP1-ATR1, mutant RPP1-ATR1, or $RPP1^{TIR}$ were used for NADase assays at the indicated concentrations. Proteins were individually incubated with 100 μM NAD^+ (final concentration) and 10 mM $MgSO_4$ or $CaCl_2$ in buffer containing 100 mM NaCl, 25 mM Tris-HCl pH 8.0. The total volume for each reaction was 100 μl. Reactions were performed in a thermoshaker at 25°C for 16 hours. After reaction, samples were centrifuged and immediately applied for HPLC analysis.

In vitro ATPase assays

Purified $RPP1^{E158A}$, $RPP1^{E158A}$-ATR1 complex, and ATR1 were used for ATPase assays with a protein concentration of 5 μM. Each protein was incubated with 100 μM ATP (final concentration) in buffer containing 10.0 mM $MgSO_4$, 100 mM NaCl, 25.0 mM Tris-HCl pH 8.0 at 25°C for the indicated times. The volume for reaction was 100 μl. After reaction, samples were centrifuged and immediately applied for HPLC analysis. 1.0 μM $RPP1^{E158A}$ was used to quantify its ATPase activity. Reactions were carried out as described above. Samples (50 μl) taken at different time points (1, 2, 3, 4, and 5 hours) were analyzed on an HPLC system to detect the formed ADP. By comparison with reference samples (ADP), the respective integrated ADP peak area was converted into concentration. The ATPase activity was calculated by five data points–based linear regression.

HPLC measurements

HPLC was performed on an Agilent 1260 bioinert HPLC system using a Synergi Fusion-RP 80 Å (4.6 × 150 mm, 4 μm) (Phenomenex) column. The samples were measured via an 8-min method. Samples (10 μl) were injected at 550 μl/min with ammonium formate (5 mM) in water and methanol used as mobile phases A and B, respectively. The elution profile was as follows: 0 to 3 min, 10 to 70% B; 3 to 6 min, 70% B; 6 to 6.1 min, 70 to 10% B; 6.1 to 8 min, 10% B. The autosampler temperature was maintained at 4°C and the column temperature at 25°C. UV signals were detected at 260 nm. Reference standards were used to determine respective retention times. The integrations of peak area were used to calculate relative concentrations.

Site-directed mutagenesis of RPP1_WsB and ATR1_Emoy2 for in planta analyses

For *N. benthamiana* transient expression analyses, the RPP1_WsB gene body (exons and introns) was PCR-amplified from the pENTR/D-TOPO pRPP1:gRPP1 construct provided by K. Krasileva (*12*, *19*) and cloned into pENTR/D-TOPO vector (Thermo Fisher Scientific, K240020). The ATR1_Emoy2 sequence starts with a codon corresponding to T19 in NCBI accession AAX51198 ATR1_Emoy2, thereby removing a signal peptide. Mutagenesis was performed using a QuikChange II site-directed mutagenesis kit (Agilent, 200523) or KOD-Plus-Mutagenesis kit (CosmoBio, SMK-101). Sequences of oligonucleotides are provided in table S2. Obtained pENTR/D-TOPO RPP1_WsB and pDONR207 ATR1_Emoy2 plasmids were LR-recombined (Thermo Fisher Scientific, 11791020) into pXCSG vectors (*66*) to allow expression of untagged $RPP1^{WsB}$, C-terminally tagged RPP1_WsB-3xHA-StrepII, and ATR1_Emoy2-3xHA-StrepII proteins under a 35S promoter. All constructs were verified by DNA sequencing. Generated binary constructs were transformed into *Agrobacterium tumefaciens* (*Rhizobium radiobacter*) GV3101 pMP90RK via electroporation.

Protein expression in N. benthamiana and Western blot analysis

RPP1_WsB-HS and ATR1_Emoy2-HS were expressed in *N. benthamiana* using agrobacteria-mediated transient expression assays in the presence of the P19 suppressor of RNAi silencing as in (*49*). The final OD_{600} for each strain was set to 0.2. To detect ATR1 variants, two 8-mm leaf discs per sample were harvested at 2 dai and boiled at 95°C in Laemmli buffer for 5 min. The ATR1-HS fusions were blotted onto nitrocellulose membranes and detected using primary α-HA antibodies (Sigma Aldrich, 11867423001 or H6908; Cell Signaling Technology, #3724) and secondary horseradish peroxidase (HRP)–conjugated antibodies (Santa Cruz, sc-2006; Sigma Aldrich, A5164) at dilution 1:5000 (3% milk powder in TBST). Detection was performed using enhanced chemiluminescence assays Clarity, Clarity Max Western ECL (Bio-Rad, #1705061 and #1705062). To detect RPP1_WsB-HS variants, infiltrated *N. benthamiana* leaves were collected at 2 dai, frozen in liquid nitrogen, and ground to a fine powder. Powder (~100 μl in a tube) was resuspended in 100 μl of urea-SDS sample buffer [50 mM Tris-HCl pH 6.8, 2% SDS, 8 M urea, 2% β-mercaptoethanol, 5% glycerol, protease inhibitor cocktail (Roche), and 0.004% Bromophenol Blue] and vortexed for 10 min at room temperature. No boiling step was included. After centrifugation at 16,000*g* for 10 min, 10 μl of the supernatant was loaded onto 8% SDS-PAGE and proteins were blotted onto a PVDF membrane. Immunoblot assay was performed using monoclonal rat anti-HA antibody (Sigma Aldrich, 11867423001) diluted 1:4000 and rabbit anti-rat antibody (Sigma Aldrich, A5164) diluted 1:5000 in 1× TBS, 0.1% Tween-20 with 3.5% w/v nonfat dry milk. RPP1_WsB-HS fusion proteins were detected using ECL SuperSignal West Femto Maximum Sensitivity Substrate and ECL Western Blotting substrate (Thermo Scientific) in a ratio of 2:1.

Cell death quantification in N. benthamiana

RPP1_WsB-HS and ATR1_Emoy2-HS WT and mutant protein combinations were transiently expressed in *N. benthamiana* as described above (*49*) and agrobacteria-infiltrated leaf zones used for cell death (ion leakage) assays at 3 dai as described (*49*). Statistical analysis was performed on conductivity data normalized to the mean level in samples containing WT RPP1_WsB and ATR1_Emoy2 samples via Tukey's HSD (honestly significant difference) test after checking normality of residuals distribution and homogeneity of variance using visual examination of the plots and Shapiro-Wilcoxon and Levene tests ($P > 0.05$). Images of agrobacteria-infiltrated leaf spots were taken at 4 to 5 dpi.

RPP1_WsB jelly roll/Ig-like (JID) sequence distribution across plants

Protein sequences of 32 representative plant species from green algae to *Arabidopsis thaliana* were obtained as in (*49*). Sequences similar to the jelly roll domain of RPP1_WsB (amino acids 1075 to 1195) were initially searched with BLASTP (-evalue 0.01). The jelly roll–like sequences were detected at this step only in *Brassicaceae* plants. The match sequences were extracted and aligned via the Muscle method. A hidden Markov model was built from the resulting alignment [hmmbuild in HMMER 3.1b2 (*67*), default settings]. This model (v1) identified 622 matches mainly in Brassicales but also in Fabales, Malpighiales, and Rosales (Reference Proteomes 2020_04, hmmsearch at EMBL-EBI–incE 0.01). To improve sensitivity of the search, a next version of the HMM model was prepared. For that, the v1 HMM was run against the 32 species protein database above (hmmsearch in HMMER 3.1b2,–incE 0.01) and not against public databases to avoid with redundancy and skewing toward *Brassicaceae* in public databases. The resulting matches were again extracted, aligned with Clustal Omega, and the obtained alignment served as an input for building the version 2 HMM, available as data S1. The v2 HMM run against Uniprot database (2019-10-03) at EMBL-EBI (hmmsearch -E1–domE 1–incE 0.001–incdomE 0.03–seqdb uniprotkb) identified 2711 hits, only in eudicots. The majority of found proteins have a typical TNL domain architecture, other hits have different arrangements/combinations of NBARC, LRR, TIR domains and occasionally other domains. Finally, to assess distribution of the RPP1_WsB-like JID across plants, the v2 HMM (data S1) was scanned against the above custom non-redundant database of protein sequences from 32 representative plant species (hmmsearch–incE 0.01).

REFERENCES AND NOTES

1. H. Burdett, B. Kobe, P. A. Anderson, Animal NLRs continue to inform plant NLR structure and function. *Arch. Biochem. Biophys.* **670**, 58–68 (2019). doi: 10.1016/j.abb.2019.05.001; pmid: 31071301
2. J. D. Jones, R. E. Vance, J. L. Dangl, Intracellular innate immune surveillance devices in plants and animals. *Science* **354**, aaf6395 (2016). doi: 10.1126/science.aaf6395; pmid: 27934708
3. S. Lolle, D. Stevens, G. Coaker, Plant NLR-triggered immunity: From receptor activation to downstream signaling. *Curr. Opin. Immunol.* **62**, 99–105 (2020). doi: 10.1016/j.coi.2019.12.007; pmid: 31958770
4. T. Maekawa, T. A. Kufer, P. Schulze-Lefert, NLR functions in plant and animal immune systems: So far and yet so close. *Nat. Immunol.* **12**, 817–826 (2011). doi: 10.1038/ni.2083; pmid: 21852785
5. S. Nimma, T. Ve, S. J. Williams, B. Kobe, Towards the structure of the TIR-domain signalosome. *Curr. Opin. Struct. Biol.* **43**, 122–130 (2017). doi: 10.1016/j.sbi.2016.12.014; pmid: 28092811
6. J. Wang, J. Chai, Molecular actions of NLR immune receptors in plants and animals. *Sci. China Life Sci.* **63**, 1–14 (2020). doi: 10.1007/s11427-019-1687-6; pmid: 32613490
7. E. Grund, D. Tremousaygue, L. Deslandes, Plant NLRs with Integrated Domains: Unity Makes Strength. *Plant Physiol.* **179**, 1227–1235 (2019). doi: 10.1104/pp.18.01134; pmid: 30530739
8. J. Wang *et al*., Reconstitution and structure of a plant NLR resistosome conferring immunity. *Science* **364**, eaav5870 (2019). doi: 10.1126/science.aav5870; pmid: 30948527
9. M. Bernoux *et al*., Structural and functional analysis of a plant resistance protein TIR domain reveals interfaces for self-association, signaling, and autoregulation. *Cell Host Microbe* **9**, 200–211 (2011). doi: 10.1016/j.chom.2011.02.009; pmid: 21402359
10. S. Cesari *et al*., Cytosolic activation of cell death and stem rust resistance by cereal MLA-family CC-NLR proteins. *Proc. Natl. Acad. Sci. U.S.A.* **113**, 10204–10209 (2016). doi: 10.1073/pnas.1605483113; pmid: 27555587
11. S. M. Collier, L. P. Hamel, P. Moffett, Cell death mediated by the N-terminal domains of a unique and highly conserved class of NB-LRR protein. *Mol. Plant Microbe Interact.* **24**, 918–931 (2011). doi: 10.1094/MPMI-03-11-0050; pmid: 21501087
12. K. V. Krasileva, D. Dahlbeck, B. J. Staskawicz, Activation of an Arabidopsis resistance protein is specified by the in planta association of its leucine-rich repeat domain with the cognate oomycete effector. *Plant Cell* **22**, 2444–2458 (2010). doi: 10.1105/tpc.110.075358; pmid: 20601497
13. M. R. Swiderski, D. Birker, J. D. Jones, The TIR domain of TIR-NB-LRR resistance proteins is a signaling domain involved in cell death induction. *Mol. Plant Microbe Interact.* **22**, 157–165 (2009). doi: 10.1094/MPMI-22-2-0157; pmid: 19132868
14. T. Maekawa *et al*., Coiled-coil domain-dependent homodimerization of intracellular barley immune receptors defines a minimal functional module for triggering cell death. *Cell Host Microbe* **9**, 187–199 (2011). doi: 10.1016/j.chom.2011.02.008; pmid: 21402358
15. L. Wan *et al*., TIR domains of plant immune receptors are NAD^+-cleaving enzymes that promote cell death. *Science* **365**, 799–803 (2019). doi: 10.1126/science.aax1771; pmid: 31439793
16. S. Horsefield *et al*., NAD^+ cleavage activity by animal and plant TIR domains in cell death pathways. *Science* **365**, 793–799 (2019). doi: 10.1126/science.aax1911; pmid: 31439792
17. S. J. Williams *et al*., Structural basis for assembly and function of a heterodimeric plant immune receptor. *Science* **344**, 299–303 (2014). doi: 10.1126/science.1247357; pmid: 24744375
18. X. Zhang *et al*., Multiple functional self-association interfaces in plant TIR domains. *Proc. Natl. Acad. Sci. U.S.A.* **114**, E2046–E2052 (2017). doi: 10.1073/pnas.1621248114; pmid: 28159890
19. M. A. Botella *et al*., Three genes of the Arabidopsis RPP1 complex resistance locus recognize distinct Peronospora parasitica avirulence determinants. *Plant Cell* **10**, 1847–1860 (1998). doi: 10.1105/tpc.10.11.1847; pmid: 9811793
20. A. D. Steinbrenner, S. Goritschnig, B. J. Staskawicz, Recognition and activation domains contribute to allele-specific responses of an Arabidopsis NLR receptor to an oomycete effector protein. *PLOS Pathog.* **11**, e1004665 (2015). doi: 10.1371/journal.ppat.1004665; pmid: 25671309
21. A. P. Rehmany *et al*., Differential recognition of highly divergent downy mildew avirulence gene alleles by RPP1 resistance genes from two Arabidopsis lines. *Plant Cell* **17**, 1839–1850 (2005). doi: 10.1105/tpc.105.031807; pmid: 15894715
22. S. Goritschnig, A. D. Steinbrenner, D. J. Grunwald, B. J. Staskawicz, Structurally distinct Arabidopsis thaliana NLR immune receptors recognize tandem WY domains of an oomycete effector. *New Phytol.* **210**, 984–996 (2016). doi: 10.1111/nph.13823; pmid: 26725254
23. R. Martin *et al*., Structure of the activated Roq1 resistosome directly recognizing the pathogen effector XopQ. bioRxiv 246413 [preprint]. 14 August 2020.
24. S. Chou *et al*., Hyaloperonospora arabidopsidis ATR1 effector is a repeat protein with distributed recognition surfaces. *Proc. Natl. Acad. Sci. U.S.A.* **108**, 13323–13328 (2011). doi: 10.1073/pnas.1109791108; pmid: 21788488
25. Z. Hu *et al*., Structural and biochemical basis for induced self-propagation of NLRC4. *Science* **350**, 399–404 (2015). doi: 10.1126/science.aac5489; pmid: 26449475
26. L. Zhang *et al*., Cryo-EM structure of the activated NAIP2-NLRC4 inflammasome reveals nucleated polymerization. *Science* **350**, 404–409 (2015). doi: 10.1126/science.aac5789; pmid: 26449474
27. M. Zhou *et al*., Atomic structure of the apoptosome: Mechanism of cytochrome c- and dATP-mediated activation of Apaf-1. *Genes Dev.* **29**, 2349–2361 (2015). doi: 10.1101/gad.272278.115; pmid: 26543158
28. S. Qi *et al*., Crystal structure of the Caenorhabditis elegans apoptosome reveals an octameric assembly of CED-4. *Cell* **141**, 446–457 (2010). doi: 10.1016/j.cell.2010.03.017; pmid: 20434985
29. T. Ogawa, Y. Ueda, K. Yoshimura, S. Shigeoka, Comprehensive analysis of cytosolic Nudix hydrolases in Arabidopsis thaliana. *J. Biol. Chem.* **280**, 25277–25283 (2005). doi: 10.1074/jbc.M503536200; pmid: 15878881
30. K. J. Schreiber, A. Bentham, S. J. Williams, B. Kobe, B. J. Staskawicz, Multiple Domain Associations within the Arabidopsis Immune Receptor RPP1 Regulate the Activation of Programmed Cell Death. *PLOS Pathog.* **12**, e1005769 (2016). doi: 10.1371/journal.ppat.1005769; pmid: 27427964
31. Z. Duxbury *et al*., Induced proximity of a TIR signaling domain on a plant-mammalian NLR chimera activates defense in plants. *Proc. Natl. Acad. Sci. U.S.A.* **117**, 18832–18839 (2020). doi: 10.1073/pnas.2001185117; pmid: 32709746
32. Y. Xiong, Z. Han, J. Chai, Resistosome and inflammasome: Platforms mediating innate immunity. *Curr. Opin. Plant Biol.* **56**, 47–55 (2020). doi: 10.1016/j.pbi.2020.03.010; pmid: 32554225
33. J. Wang *et al*., Ligand-triggered allosteric ADP release primes a plant NLR complex. *Science* **364**, eaav5868 (2019). doi: 10.1126/science.aav5868; pmid: 30948526
34. M. Bernoux *et al*., Comparative Analysis of the Flax Immune Receptors L6 and L7 Suggests an Equilibrium-Based Switch Activation Model. *Plant Cell* **28**, 146–159 (2016). doi: 10.1105/tpc.15.00303; pmid: 26744216
35. Z. Hu *et al*., Crystal structure of NLRC4 reveals its autoinhibition mechanism. *Science* **341**, 172–175 (2013). doi: 10.1126/science.1236381; pmid: 23765277
36. H. Sharif *et al*., Structural mechanism for NEK7-licensed activation of NLRP3 inflammasome. *Nature* **570**, 338–343 (2019). doi: 10.1038/s41586-019-1295-z; pmid: 31189953
37. J. F. C. Steele, R. K. Hughes, M. J. Banfield, Structural and biochemical studies of an NB-ARC domain from a plant NLR immune receptor. *PLOS ONE* **14**, e0221226 (2019). doi: 10.1371/journal.pone.0221226; pmid: 31461469
38. X. Yang, G. Lin, Z. Han, J. Chai, Structural Biology of NOD-Like Receptors. *Adv. Exp. Med. Biol.* **1172**, 119–141 (2019). doi: 10.1007/978-981-13-9367-9_6; pmid: 31628654
39. T. F. Reubold, S. Wohlgemuth, S. Eschenburg, A new model for the transition of APAF-1 from inactive monomer to caspase-activating apoptosome. *J. Biol. Chem.* **284**, 32717–32724 (2009). doi: 10.1074/jbc.M109.014027; pmid: 19801675
40. Y. Ma *et al*., Distinct modes of derepression of an *Arabidopsis* immune receptor complex by two different bacterial effectors. *Proc. Natl. Acad. Sci. U.S.A.* **115**, 10218–10227 (2018). doi: 10.1073/pnas.1811858115; pmid: 30254172
41. K. H. Sohn *et al*., The nuclear immune receptor RPS4 is required for RRS1SLH1-dependent constitutive defense activation in Arabidopsis thaliana. *PLOS Genet.* **10**, e1004655 (2014). doi: 10.1371/journal.pgen.1004655; pmid: 25340333
42. T. Ve *et al*., Structural basis of TIR-domain-assembly formation in MAL- and MyD88-dependent TLR4 signaling. *Nat. Struct. Mol. Biol.* **24**, 743–751 (2017). doi: 10.1038/nsmb.3444; pmid: 28759049
43. B. C. Meyers, M. Morgante, R. W. Michelmore, TIR-X and TIR-NBS proteins: Two new families related to disease resistance TIR-NBS-LRR proteins encoded in Arabidopsis and other plant genomes. *Plant J.* **32**, 77–92 (2002). doi: 10.1046/j.1365-313X.2002.01404.x; pmid: 12366802
44. R. S. Nandety *et al*., The role of TIR-NBS and TIR-X proteins in plant basal defense responses. *Plant Physiol.* **162**, 1459–1472 (2013). doi: 10.1104/pp.113.219162; pmid: 23735504
45. M. T. Nishimura *et al*., TIR-only protein RBA1 recognizes a pathogen effector to regulate cell death in *Arabidopsis*. *Proc. Natl. Acad. Sci. U.S.A.* **114**, E2053–E2062 (2017). doi: 10.1073/pnas.1620973114; pmid: 28137883
46. J. L. Tenthorey *et al*., The structural basis of flagellin detection by NAIP5: A strategy to limit pathogen immune evasion. *Science* **358**, 888–893 (2017). doi: 10.1126/science.aao1140; pmid: 29146805
47. H. Adachi *et al*., An N-terminal motif in NLR immune receptors is functionally conserved across distantly related plant species. *eLife* **8**, e49956 (2019). doi: 10.7554/eLife.49956; pmid: 31774397
48. L. Wang, H. Wu, Keeping the Death Protein in Check. *Immunity* **51**, 1–2 (2019). doi: 10.1016/j.immuni.2019.06.011; pmid: 31315028

49. D. Lapin *et al*., A Coevolved EDS1-SAG101-NRG1 Module Mediates Cell Death Signaling by TIR-Domain Immune Receptors. *Plant Cell* **31**, 2430–2455 (2019). doi: 10.1105/tpc.19.00118; pmid: 31311833
50. B. Castel *et al*., Diverse NLR immune receptors activate defence via the RPW8-NLR NRG1. *New Phytol.* **222**, 966–980 (2019). doi: 10.1111/nph.15659; pmid: 30582759
51. Z. Wu *et al*., Differential regulation of TNL-mediated immune signaling by redundant helper CNLs. *New Phytol.* **222**, 938–953 (2019). doi: 10.1111/nph.15665; pmid: 30585636
52. F. Sievers *et al*., Fast, scalable generation of high-quality protein multiple sequence alignments using Clustal Omega. *Mol. Syst. Biol.* **7**, 539 (2011). doi: 10.1038/msb.2011.75; pmid: 21988835
53. J. Lei, J. Frank, Automated acquisition of cryo-electron micrographs for single particle reconstruction on an FEI Tecnai electron microscope. *J. Struct. Biol.* **150**, 69–80 (2005). doi: 10.1016/j.jsb.2005.01.002; pmid: 15797731
54. S. Q. Zheng *et al*., MotionCor2: Anisotropic correction of beam-induced motion for improved cryo-electron microscopy. *Nat. Methods* **14**, 331–332 (2017). doi: 10.1038/nmeth.4193; pmid: 28250466
55. T. Grant, N. Grigorieff, Measuring the optimal exposure for single particle cryo-EM using a 2.6 Å reconstruction of rotavirus VP6. *eLife* **4**, e06980 (2015). doi: 10.7554/eLife.06980; pmid: 26023829
56. J. A. Mindell, N. Grigorieff, Accurate determination of local defocus and specimen tilt in electron microscopy. *J. Struct. Biol.* **142**, 334–347 (2003). doi: 10.1016/S1047-8477(03)00069-8; pmid: 12781660
57. X. C. Bai, E. Rajendra, G. Yang, Y. Shi, S. H. Scheres, Sampling the conformational space of the catalytic subunit of human γ-secretase. *eLife* **4**, e11182 (2015). doi: 10.7554/eLife.11182; pmid: 26623517
58. S. H. Scheres, RELION: Implementation of a Bayesian approach to cryo-EM structure determination. *J. Struct. Biol.* **180**, 519–530 (2012). doi: 10.1016/j.jsb.2012.09.006; pmid: 23000701
59. S. H. Scheres, A Bayesian view on cryo-EM structure determination. *J. Mol. Biol.* **415**, 406–418 (2012). doi: 10.1016/j.jmb.2011.11.010; pmid: 22100448
60. J. Zivanov, T. Nakane, S. H. W. Scheres, Estimation of high-order aberrations and anisotropic magnification from cryo-EM data sets in *RELION*-3.1. *IUCrJ* **7**, 253–267 (2020). doi: 10.1107/S2052252520000081; pmid: 32148853
61. P. B. Rosenthal, R. Henderson, Optimal determination of particle orientation, absolute hand, and contrast loss in single-particle electron cryomicroscopy. *J. Mol. Biol.* **333**, 721–745 (2003). doi: 10.1016/j.jmb.2003.07.013; pmid: 14568533
62. A. Kucukelbir, F. J. Sigworth, H. D. Tagare, Quantifying the local resolution of cryo-EM density maps. *Nat. Methods* **11**, 63–65 (2014). doi: 10.1038/nmeth.2727; pmid: 24213166
63. P. D. Adams *et al*., PHENIX: A comprehensive Python-based system for macromolecular structure solution. *Acta Crystallogr. D* **66**, 213–221 (2010). doi: 10.1107/S0907444909052925; pmid: 20124702
64. E. F. Pettersen *et al*., UCSF Chimera—A visualization system for exploratory research and analysis. *J. Comput. Chem.* **25**, 1605–1612 (2004). doi: 10.1002/jcc.20084; pmid: 15264254
65. P. Emsley, B. Lohkamp, W. G. Scott, K. Cowtan, Features and development of Coot. *Acta Crystallogr. D* **66**, 486–501 (2010). doi: 10.1107/S0907444910007493; pmid: 20383002
66. C. P. Witte, L. D. Noël, J. Gielbert, J. E. Parker, T. Romeis, Rapid one-step protein purification from plant material using the eight-amino acid StrepII epitope. *Plant Mol. Biol.* **55**, 135–147 (2004). doi: 10.1007/s11103-004-0501-y; pmid: 15604670
67. S. R. Eddy, Accelerated Profile HMM Searches. *PLOS Comput. Biol.* **7**, e1002195 (2011). doi: 10.1371/journal.pcbi.1002195; pmid: 22039361

ACKNOWLEDGMENTS

We thank J. Lei, X. Li, X. Fan, and N. Liu at Tsinghua University for data collection. We acknowledge the Tsinghua University Branch of the China National Center for Protein Sciences (Beijing) for providing the cryo-EM facility support and the computational facility support on the cluster of Bio-Computing Platform. **Funding:** Supported by the National Natural Science Foundation of China (31421001 to J.C. and 31971119 to Z.H.), the Alexander von Humboldt Foundation (a Humboldt professorship to J.C.), the Max-Planck-Gesellschaft (J.E.P. and P.S.-L., and a Max Planck fellowship to J.C.), Deutsche Forschungsgemeinschaft SFB-1403-414786233 (J.C., J.E.P., and P.S.-L.) and Germany's Excellence Strategy CEPLAS (EXC-2048/1, Project 390686111) (J.C., J.E.P., and P.S.-L.). **Author contributions:** Experimental design: J.C., J.E.P., P.S.-L., S.M., D.L.; recombinant protein expression assays, purification, structure determinations, modeling, and data analysis: S.M., X.Z., Y.S., W.S., J.W., and J.C.; biochemical assays: S.M., W.S., D.Y., J.J., Z.H.; plant expression and cell death assays: L.L., D.L., E.L.; HMM building: D.L.; data analysis: all authors; manuscript writing: J.C., J.E.P., P.S.-L. with contributions from other authors. **Competing interests:** The authors declare no competing interests. **Data and materials availability:** Plasmids for in planta expression of RPP1_WsB and ATR1_Emoy2 variants (table S2) are available from J.E.P. or P.S.-L. under a material agreement with Max Planck Institute for Plant Breeding Research. All data are available in the main text, supplementary materials, or the listed Protein Data Bank (PDB) files. For the RPP1 resistosome and RPP1LRR-C-JID-ATR1, the atomic coordinates have been deposited in the PDB with accession codes 7CRC and 7CRB, respectively. The EM maps have been deposited in the Electron Microscopy Database with accession codes EMD-30450 and EMD-30449, respectively.

SUPPLEMENTARY MATERIALS

science.sciencemag.org/content/370/6521/eabe3069/suppl/DC1
Figs. S1 to S18
Tables S1 and S2
Data S1
References (*68*–*71*)

13 August 2020; accepted 22 October 2020
10.1126/science.abe3069

RESEARCH ARTICLE SUMMARY

PLANT SCIENCE

Structure of the activated ROQ1 resistosome directly recognizing the pathogen effector XopQ

Raoul Martin*, Tiancong Qi*, Haibo Zhang, Furong Liu, Miles King, Claire Toth, Eva Nogales†, Brian J. Staskawicz†

INTRODUCTION: Plants and animals respond to pathogen invasion through intracellular nucleotide-binding leucine-rich repeat receptors (NLRs) that directly interact with pathogen proteins or indirectly detect pathogen-derived alterations in the host proteome. Upon recognition of pathogen invasion, NLRs trigger an immune response that resolves in a variety of ways depending on the type of NLR being activated. The overall architecture of NLRs is highly conserved, consisting of a C-terminal leucine-rich repeat (LRR) platform that determines substrate specificity and a central nucleotide-binding oligomerization domain. The N-terminal domain varies between NLRs and determines the mechanism used by the host to activate the immune response. Thus, NLRs in plants have been classified according to their N-terminal domain into Toll/interleukin 1 receptor (TIR) NLRs (TNLs), coiled-coil NLRs (CNLs), and RPW8-like coiled-coil NLRs (RNLs). Pathogen detection and oligomerization of the NLR activates these N-terminal domains by bringing them in close contact. In all three cases, association of the N-terminal domain leads to localized cell death and expression of disease resistance. The TIR domains of TNLs have been shown to have oligomerization-dependent NADase activity that is required for promoting cell death, but it is not understood how the interactions between TIR domains renders them catalytically active.

RATIONALE: The structure of the ROQ1 (recognition of XopQ 1)–XopQ (*Xanthomonas* outer protein Q) complex, an immune receptor bound to its pathogen substrate, was used as a model to study the mechanism of direct binding, oligomerization, and TIR domain activation of TNLs. ROQ1 has been shown to physically interact with the *Xanthomonas* effector XopQ, causing it to oligomerize and trigger a TIR-dependent hypersensitive cell death response. We coexpressed, extracted, and purified the assembled ROQ1-XopQ complex from ROQ1's native host, *Nicotiana benthamiana*, and solved its structure by cryo–electron microscopy to 3.8-Å resolution. The interactions described in our structure were further confirmed by in vivo mutational analysis.

RESULTS: Our structure reveals that ROQ1 forms a tetrameric resistosome upon recognizing XopQ. The LRR and a post-LRR domain named the C-terminal jelly-roll/Ig-like domain (C-JID), form a horseshoe-shaped scaffold that curls around the pathogen effector, thereby recognizing multiple regions of the substrate. Binding of the ROQ1 LRR to XopQ occurs through surface-exposed residues that make up the scaffold of the domain, as well as an elongated loop between two LRRs that forms a small amphipathic α-helix at the site of interaction. The mode of substrate recognition by the C-JID is reminiscent of that used by immunoglobulins to bind their antigen. Similar to the complementary-determining regions of antibodies, interconnecting loops emerging from the C-JID β-sandwich structure make substrate-specific contacts with XopQ. In particular, an extended loop of the C-JID dives into the active-site cleft of XopQ and interacts with conserved residues required for nucleoside binding, suggesting that ROQ1 not only recognizes its substrate but also inhibits its ligand-binding function.

The nucleotide-binding domain (NBD), helical domain 1 (HD1) and the winged-helix domain (WHD), termed NB-ARC because of their presence in Apaf-1, R proteins, and CED-4 (ARC), are responsible for ROQ1 oligomerization in an ATP-bound state. Individual protomers intercalate in a similar fashion as found in other NLR structures, promoting association between the N-terminal TIR domains. The TIR domains bind to each other through two distinct interfaces (called AE and BE), causing them to form a dimer of dimers. BE-interface contacts cause a conformational rearrangement in a loop, called the BB-loop, at the periphery of the TIR domain active site that exposes the putative catalytic glutamate that is suggested to cleave NAD^+. These results provide a rationale for the previously determined oligomerization dependence of TIR domain NADase activity.

CONCLUSION: We propose a step-by-step mechanism for ROQ1 immune signaling based on our structure of the activated complex and on previous biochemical studies. The LRR and C-JID of ROQ1 recognize the pathogen effector through direct contacts with its surface and active-site residues. Detection of the substrate releases autoinhibitory contacts between the NB-ARC domain and the LRR, allowing the NB-ARC domain to transition to an ATP-bound, oligomerization-prone state. Complex assembly brings the TIR domains in close contact, leading to opening of the NADase active site in an interface-dependent manner. Cleavage of NAD^+ by the TIR domain results in the release of adenosine diphosphate ribose, a signaling molecule that triggers cytosolic Ca^{2+} influx, a widely used chemical cue in response to various biotic and abiotic stresses, leading to downstream activation of localized cell death and disease resistance. ■

The list of author affiliations is available in the full article online.
*These authors contributed equally to this work.
†Corresponding author. Email: enogales@lbl.gov (E.N.); stask@berkeley.edu (B.J.S.)
Cite this article as: R. Martin *et al.*, *Science* **370**, eabd9993 (2020). DOI: 10.1126/science.abd9993

READ THE FULL ARTICLE AT
https://doi.org/10.1126/science.abd9993

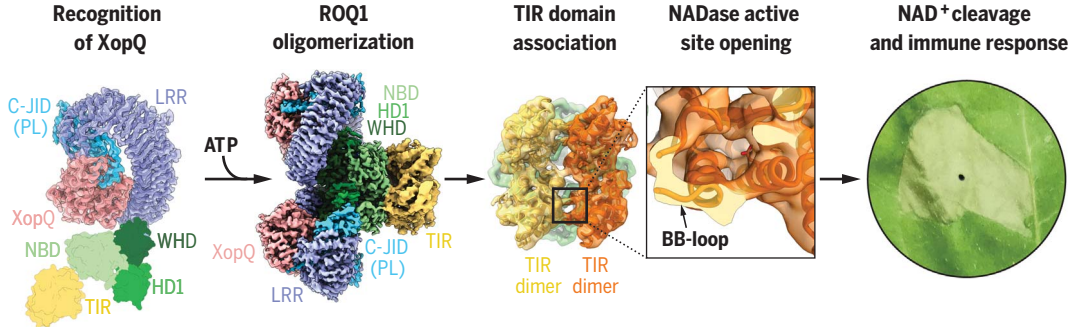

Proposed mechanism of ROQ1 activation. The LRR and C-JID of ROQ1 recognize the pathogen effector XopQ. ROQ1 oligomerizes through the NB-ARC domain (NBD, HD1, WHD) in an ATP-bound state. TIR domain association causes a conformational rearrangement of the BB-loop and opens the NADase active site. Catalytic activity of the TIR domains further signals the immune response, resulting in cell death.

RESEARCH ARTICLE

PLANT SCIENCE

Structure of the activated ROQ1 resistosome directly recognizing the pathogen effector XopQ

Raoul Martin[1,2]*, Tiancong Qi[3,4]*, Haibo Zhang[3], Furong Liu[5], Miles King[5], Claire Toth[6], Eva Nogales[2,6,7,8]†, Brian J. Staskawicz[4,5]†

Plants and animals detect pathogen infection using intracellular nucleotide-binding leucine-rich repeat receptors (NLRs) that directly or indirectly recognize pathogen effectors and activate an immune response. How effector sensing triggers NLR activation remains poorly understood. Here we describe the 3.8-angstrom-resolution cryo–electron microscopy structure of the activated ROQ1 (recognition of XopQ 1), an NLR native to *Nicotiana benthamiana* with a Toll-like interleukin-1 receptor (TIR) domain bound to the *Xanthomonas euvesicatoria* effector XopQ (*Xanthomonas* outer protein Q). ROQ1 directly binds to both the predicted active site and surface residues of XopQ while forming a tetrameric resistosome that brings together the TIR domains for downstream immune signaling. Our results suggest a mechanism for the direct recognition of effectors by NLRs leading to the oligomerization-dependent activation of a plant resistosome and signaling by the TIR domain.

Plants have a sophisticated and finely tuned innate immune system that recognizes invading phytopathogens to protect from infection and disease. Pathogen recognition is facilitated by both membrane-anchored pattern recognition receptors and intracellular innate immune receptors (*1*). The latter include the nucleotide-binding leucine-rich repeat receptors (NLRs) (*2*). Although some NLR immune receptors directly bind pathogen effector proteins, others, such as ZAR1, monitor effector-mediated alterations of host targets to activate effector-triggered immunity (ETI) (*3*–*5*). ETI activation is often accompanied by localized cell death referred to as the hypersensitive response (HR). Animals also use NLR proteins as intracellular immune receptors to recognize potential pathogens, and the NLR domain architecture is highly conserved, with each region playing a specific role in its mechanism of action (*6*). Plant NLRs generally consist of three domains: an N-terminal region that is either a coiled-coil (CC) domain or a Toll-like interleukin-1 receptor (TIR) domain, a central nucleotide-binding (NB) domain conserved in APAF-1, other R-proteins, and CED-4 (NB-ARC), and the C-terminal leucine-rich repeat (LRR) domain (*2*). Plant NLRs are divided into TIR-NLRs (TNLs), CC-NLRs (CNLs), and RPW8-like CC (CC_R)-NLRs (RNLs) based on their N-terminal domains, with experimental evidence consistently suggesting that oligomerization of the N-terminal domains is required for signal transduction and expression of disease resistance (*3*).

Although the activation mechanism of a plant CNL resistosome has been elucidated (*7*, *8*), the mechanism of TNL activation remains elusive. There is still no structural evidence for TNL resistosome formation. TIR domains of both plant and animal NLRs were reported to have a nicotinamide adenine dinucleotide (NAD^+) nucleosidase activity that requires TIR domain oligomerization to trigger hypersensitive cell death (*9*, *10*). Whether the NADase activity of the TIR domain is fully responsible for ETI activation and why NAD^+ cleaving only happens in the presence of TIR self-association require further investigation.

To further our understanding of the molecular events that control the direct recognition of pathogen effectors and activation of TNL immune receptors, we transiently coexpressed *Xanthomonas euvesicatoria* type III effector XopQ (*Xanthomonas* outer protein Q) and its TNL receptor ROQ1 (recognition of XopQ 1) in *Nicotiana benthamiana eds1-1* mutant leaves, copurified them by sequential affinity chromatography, and solved a 3.8-Å cryo–electron microscopy (cryo-EM) structure of the assembled protein complex. XopQ is highly conserved across various *Xanthomonas* species and has been shown to have nucleoside hydrolase activity, to physically interact with 14-3-3 proteins of the plant host, and to suppress ETI (*11*). Nevertheless, the precise mechanism of XopQ that promotes pathogen virulence remains unclear. Recognition of XopQ by ROQ1 has been shown to trigger downstream ETI signal transduction, leading to a hypersensitive cell death response and resistance to pathogen invasion (*11*, *12*). Our structural data reveal that ROQ1 directly binds XopQ to activate a tetrameric resistosome. We identified a series of necessary contacts for XopQ recognition by ROQ1 and describe the structure of a post-LRR (PL) domain that is essential in effector binding. We also describe the overall oligomeric state of ROQ1 and the interfaces formed by the NB-ARC domain in an open conformation. Finally, we provide an explanation for the requirements of oligomerization in TIR activation, which involves opening of the NADase active site in an interface-dependent manner. Together, our results provide the structural basis for direct effector recognition, oligomerization, and activation of TNLs that reveals how these immune receptors detect pathogens and signal an immune response.

Overall structure of the ROQ1 resistosome

XopQ recognition by ROQ1 triggers a rapid cell death response in wild-type *N. benthamiana* leaves, making it difficult to obtain sufficient protein for expression and purification (*11*). All plant TNLs require the downstream EDS1 protein to achieve cell death and express disease resistance (*13*). To obtain live tissue for protein purification, we transiently coexpressed ROQ1 and XopQ by *Agrobacterium*-mediated transformation in CRISPR-induced *eds1-1* mutants of *N. benthamiana* known to prevent ROQ1-induced cell death (*12*). Cryo-EM imaging and analysis of the affinity-purified complex yielded a reconstruction at 3.8-Å overall resolution with C4 symmetry imposed (figs. S1 and S2) and showed that the ROQ1 protomers assemble into a tetrameric, four-leaf clover structure with XopQ present in a 1:1 ratio (Fig. 1). Further image processing was required to allow building of atomic models (fig. S3). We found that the nucleotide-binding domain (NBD), helical domain 1 (HD1), and winged helix domain (WHD) provide the necessary contacts for ROQ1 oligomerization and bring together the four TIR domains. The LRR features the characteristic horseshoe shape and wraps around the XopQ effector protein, recognizing its surface residues. The cryo-EM map also reveals a PL domain at the C-terminal end of the LRR connected by a short 10-residue linker (Figs. 1A and 2). To improve the density of ROQ1 bound to XopQ, we applied symmetry expansion and focused refinement around the LRR-PL-XopQ region (figs. S1 and S3). The improved reconstruction showed that the XopQ effector is in its open conformation, exposing the cleft of the predicted nucleoside hydrolase

[1]Biophysics Graduate Group, University of California, Berkeley, CA 94720, USA. [2]QB3, University of California, Berkeley, CA 94720, USA. [3]Center for Plant Biology, School of Life Sciences, Tsinghua University, Beijing 100084, China. [4]Department of Plant and Microbial Biology, University of California, Berkeley, CA 94720 USA. [5]Innovative Genomics Institute, University of California, Berkeley, CA 94720 USA. [6]Department of Molecular and Cellular Biology, University of California, Berkeley, CA 94720, USA. [7]Howard Hughes Medical Institute, University of California, Berkeley, CA 94720, USA. [8]Molecular Biophysics and Integrated Bioimaging Division, Lawrence Berkeley National Laboratory, University of California, Berkeley, CA 94720, USA.
*These authors contributed equally to this work.
†Corresponding author. Email: enogales@lbl.gov (E.N.); stask@berkeley.edu (B.J.S.)

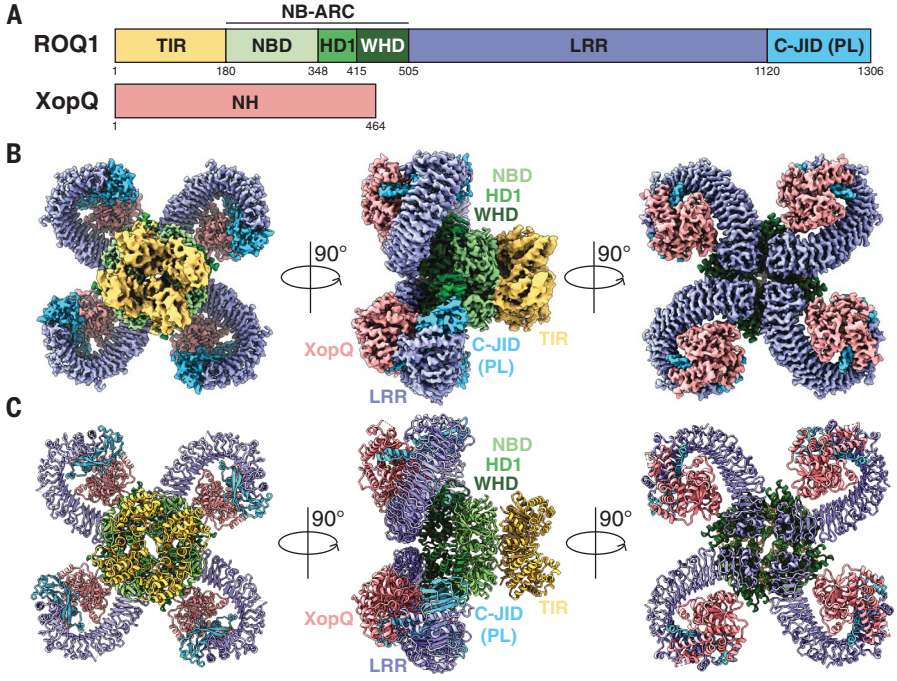

Fig. 1. Overall structure of the ROQ1-XopQ complex. (**A**) Schematic representations of ROQ1 and XopQ with color-coded domain architecture: TIR, yellow; NB-ARC NDB, HD1, and WHD, light green, green, and dark green, respectively; LRR, violet; C-JID (or PL domain), light blue; and XopQ, salmon. (**B** and **C**) Composite density map of the ROQ1-XopQ complex from three cryo-EM reconstructions (B) and corresponding atomic model (C) shown in three orthogonal views. Colors are according to the nomenclature in (A).

active site (Fig. 2E). XopQ's specific substrate remains unidentified, but previous studies have shown that XopQ binds adenosine diphosphate ribose (ADPR), an important immune signaling molecule in plants, consistent with its immunosuppressive function (*14*).

Recognition of XopQ by ROQ1

The 24 LRRs of ROQ1 form a 150-Å-long scaffold that bends around XopQ, displaying key contact residues along its surface (Fig. 2). We found that the LRR of ROQ1 interacts with the effector in two different ways. First, in the region where XopQ is in close contact with the LRR scaffold, several side chains exposed on the surface of the LRR directly interact with the substrate (Fig. 2A). A similar mechanism is used by the LRRs of the CNL ZAR1 to recognize RKS1 and TLR3 to recognize double-stranded RNA (*8*, *15*). Most of these residues have large aromatic side chains that recognize hydrophobic patches and grooves on the surface of XopQ. Second, in regions where the LRR scaffold is too far away to interact with the effector directly, we found an elongated linker between two LRRs (LRRs 23 and 24) that reaches over to bind XopQ (Fig. 2C). A small amphipathic α-helix is formed at the site of contact, with hydrophobic side chains recognizing conserved residues at the outer edge of XopQ's active site cleft ($Y311^{XopQ}$, $H433^{XopQ}$) (Fig. 2C). The extended linker then loops back toward the scaffold and forms the next repeat in the LRR. Mutating the residues that form the hydrophobic face of the α-helix ($L1075^{ROQ1}$, $W1079^{ROQ1}$, $I1078^{ROQ1}$) to alanines resulted in loss of the HR phenotype, suggesting that these interactions are critical for XopQ recognition (fig. S4).

A 10-residue linker (amino acids 1120 to 1129) connects the C-terminal end of the LRR to the PL domain, which also interacts with XopQ (Fig. 2, B and D). This domain folds into a β-sandwich, with nine antiparallel β-strands arranged into two β-sheets (fig. S5). The last LRR forms hydrogen bonds with one of the β-strands, thereby rigidifying the conformation between the two domains. Because PLs serving in pathogen detection have been found in other TNLs but remain poorly characterized, we sought to further investigate the possible structural homology of the ROQ1 PL domain with published structures (*16*). Analysis using the CATH database (*17*) revealed proteins with immunoglobulin-like and jelly-roll folds as the closest structural homologs (fig. S5A). Furthermore, the PL domain of RPP1, another TNL, shares a similar structure to the PL domain in ROQ1 (*18*) despite having low sequence identity (14.29%) (fig. S5). The core of this domain in RPP1 also folds into a β-sandwich structure that forms hydrogen bonds with the last β-strand of the LRR (*18*). Both share the same β-strand topology, with the exception of a ninth C-terminal β-strand present in Roq1 (fig. S5B). The major structural differences in the ROQ1 and RPP1 PL domain are found in the loops that interconnect the β-strands and serve to recognize their respective substrates. Domains fused to the C terminus of LRRs are found in many other NLRs (*3*, *16*) and are likely to differ in structure and function. Therefore, to address the specific type of PL domain used by ROQ1 and RPP1, we refer to it as the C-terminal jelly-roll/Ig-like domain (C-JID).

The mode of recognition used by the C-JID to detect the foreign protein is reminiscent of the way immunoglobulins bind to their antigen (fig. S6). Loops emerging from the β-sandwich structure target sites in XopQ to form substrate-specific contacts with the pathogen protein in a manner that resembles the complementarity-determining regions found in antibodies. The loop between β-strands 7 and 8 of the ROQ1 C-JID simultaneously recognizes a hydrophobic pocket through the insertion of an isoleucine ($I1277^{ROQ1}$) and an area of negative potential targeted by $R1280^{ROQ1}$ (Fig. 2B). Disrupting these interactions with a ROQ1 double mutant (R1280D and I1277A) prevented HR in tobacco leaves, suggesting that these interactions are essential for XopQ detection by ROQ1 (fig. S4).

The greatest number of contacts between the C-JID and XopQ are made by a 33-residue loop (amino acids 1163 to 1196) that dives into the active-site cleft of the effector and positions side chains in close contact with conserved sites required for ADPR binding (Fig. 2, D and E) (*14*). We refer to this loop as the NR loop for its ability to bind residues in XopQ responsible for nucleoside recognition. Two α-helical segments of the loop bring together large hydrophobic side chains that interface with the interior lid region of XopQ (Fig. 2, D and E). The conserved XopQ residues targeted in this region ($W361^{XopQ}$, $F366^{XopQ}$, $L345^{XopQ}$) serve to recognize the base moiety of ADPR (*14*). Active-site residues that would otherwise stabilize the α-phosphate of the ligand ($Y311^{XopQ}$ and $Y398^{XopQ}$) are recognized by ROQ1 $V1171^{ROQ1}$, $H1178^{ROQ1}$, and $H1179^{ROQ1}$ (*14*). Additionally, $H1179^{ROQ1}$ interacts with $D120^{XopQ}$, which is involved in the recognition of one of the sugar moieties in ADPR (*14*). In summary, the conserved residues in XopQ involved in recognizing the base, α-phosphate, and ribose moieties in ADPR are targeted by the ROQ1's NR loop. Mutating the NR loop to a short flexible linker (-SGGGSGGS-) resulted in the loss of HR, suggesting that the ROQ1 mutant could no longer recognize XopQ (fig. S4). Comparison of our structure of XopQ, which is in an open state, with the closed, ADPR-bound state (PDB: 4P5F) shows that the NR loop overlaps with ADPR and thus would prevent the ligand from entering the active-site cleft or interacting with XopQ (Fig. 2E). The presence of the NR loop

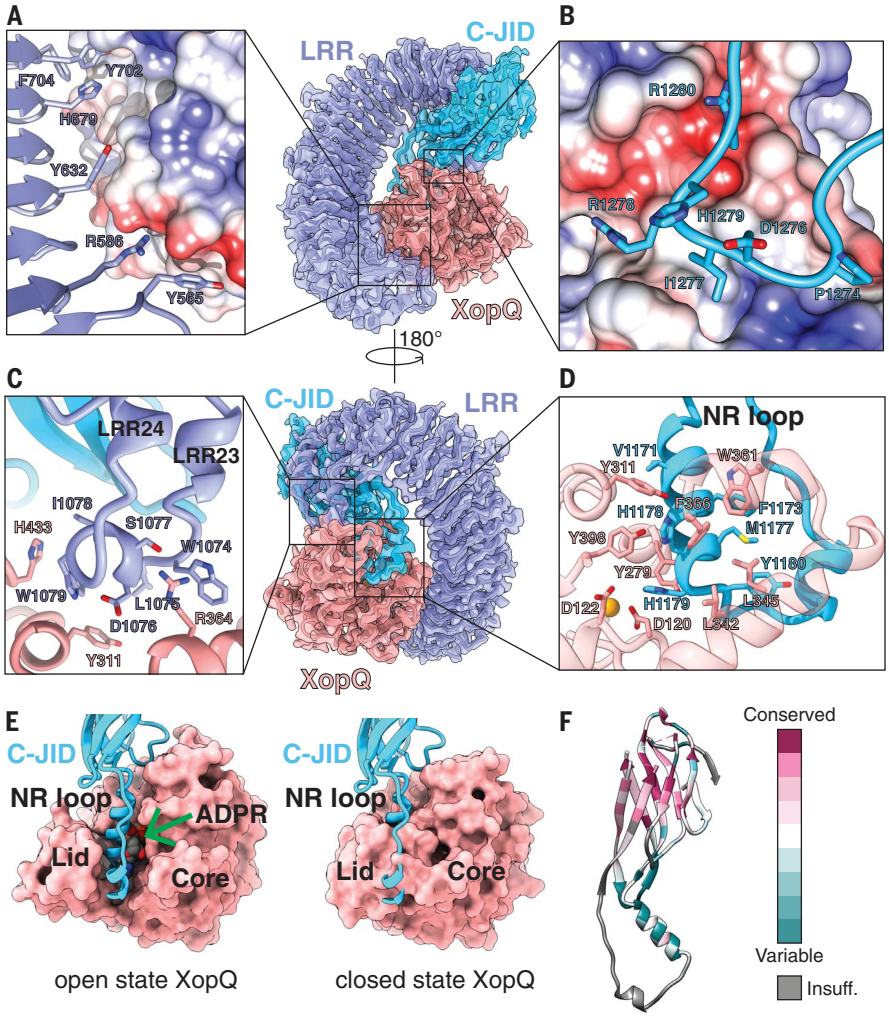

Fig. 2. Structure of the ROQ1 LRR and C-JID (PL domain) binding to XopQ. (**A**) Surface contacts between the N-terminal region of the LRR, shown with a violet ribbon, and XopQ, represented by its Coulombic surface potential. (**B**) Surface contacts made by the loop between β-strands 7 and 8 of the C-JID domain (light blue) and XopQ. (**C**) The elongated LRR between repeats 23 and 24 (violet) interacting with XopQ (salmon). (**D**) Interactions between the NR loop (light blue) and active-site residues of XopQ required for ADPR binding. Catalytic Ca^{2+} is shown in gold. (**E**) Left: Structure of XopQ in the open conformation built from our cryo-EM density, with the NR loop inserted into the active-site cleft. The position of ADPR (green arrow) from the close state of XopQ (PDB: 4P5F) is modeled to show its overlapping position with the NR loop. Right: ADPR-bound, closed state of XopQ. The NR loop is modeled to demonstrate the clashes that would occur upon XopQ closure. (**F**) Residue conservation of the C-JID. Regions where too few sequences aligned to calculate a reliable conservation score are colored in gray (labeled "Insuff.").

may also block XopQ from transitioning to the closed state because the NR loop would clash with the lid region capping the active site. These observations led us to hypothesize that ROQ1 not only recognizes the pathogen effector but may also inhibit its mechanism of ligand binding (*19*).

The C-JID of ROQ1 has a conserved β-sandwich core that may be found in the NLRs of other members of the nightshade family (Fig. 2F). We ran a BLAST search using the sequence of the C-JID (amino acids 1129 to 1306) and found multiple hits corresponding to resistance genes in other species of tobacco, as well as in various species of potatoes, peppers, and morning glories. The more conserved residues are within the strands of the β-sandwich, whereas the loop residues pointing toward XopQ are more variable (Fig. 2F). The NR loop is only found in three other tobacco species, with minor sequence differences (V1171→I, Y1195→F). This pattern of conservation suggests that the variable loops emerging from the C-JID core of related NLRs could serve to recognize different pathogen effectors using a mechanism similar to that used by ROQ1. Such a strategy would be akin to that of sequence variations in the complementarity-determining regions of antibodies that enable them to recognize a diversity of epitopes.

Previous studies suggested that it was difficult to identify mutations in XopQ that could evade ROQ1 recognition (*20*). This is consistent with our results demonstrating that the LRR and C-JID of ROQ1 make multiple contacts with XopQ, suggesting that this gene may be durable in the field and difficult for the pathogen to evade. In the future, these contacts could be modified to build synthetic receptors targeting various pathogen effectors, resulting in new recognitional specificities.

Oligomerization of ROQ1

NLRs are generally thought to exist in an inhibited state mediated by either intra- or intermolecular contacts that prevent oligomerization between protomers and activation of the immune response (*6*, *21*). Structural studies of inactive NLRs suggested that these inhibitory contacts hold the nucleotide-binding region (NBD, HD1, WHD) in a closed state (*7*, *22*, *23*). Upon activation, these interactions must be disrupted to transition to the oligomerization-prone state, where the WHD is moved away from the nucleotide-binding site, thereby displacing the ADP-specific MHD motif on the WHD and allowing adenosine triphosphate (ATP) or deoxyadenosine triphosphate (dATP) binding (NLRs have been shown to bind both ATP and dATP in their active state; in this study, we used ATP) (*8*, *24*–*27*). We expect ROQ1 to be similarly regulated by autoinhibitory contacts with the LRR based on evidence demonstrating that a truncated version of ROQ1 missing the LRR and C-JID regions spontaneously triggers an immune response in the absence of effectors (*12*). We sought to determine whether the C-JID could play a role in autoinhibition. Removing the C-JID of ROQ1 (ΔPL) resulted in loss of HR in planta, suggesting that the LRR, not the C-JID, is involved in making the intramolecular contacts that obstruct a conformational switch to the active state (fig. S4).

Four ROQ1 protomers oligomerize through the NB-ARC domains upon substrate recognition (*12*). Our density map reveals the molecular contacts between the three subdomains of the NB-ARC (NBD, HD1, and WHD) in the context of the resistosome, as well as the presence of ATP at the nucleotide-binding pocket, consistent with an activated state of ROQ1 (Fig. 3). The ATP molecule is stabilized at the interface between the NBD and HD1, with the NBD recognizing the β-phosphate through the canonical P loop (K224 and T225). The two aspartates (D300 and D301) in the Walker B motif are in close proximity to a Mg^{2+} ion that is further coordinated by the β- and γ-phosphate of ATP as well as T225 of the P-loop (Fig. 3A) (*28*). Further recognition of the ligand is provided by R329 of the TTR motif (amino

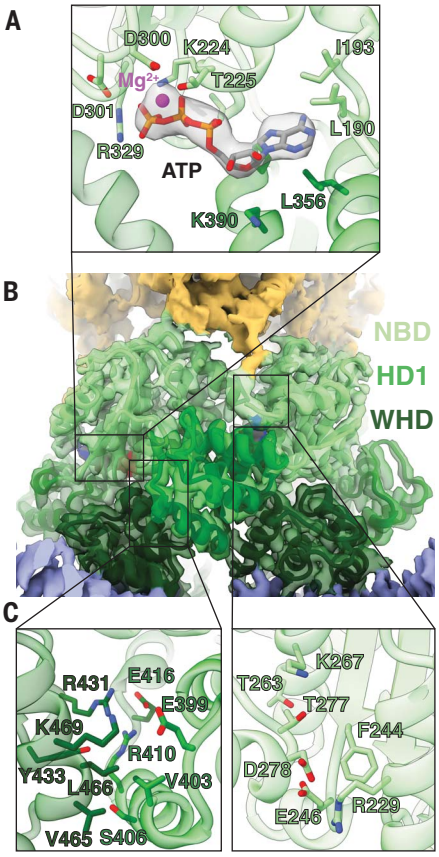

Fig. 3. Oligomerization interfaces between NB-ARC domains. (**A**) ATP modeled in the cryo-EM density (4.8σ) near an oligomerization interface, showing the side chains of residues involved in ATP and Mg^{2+} (magenta) binding. (**B**) Interface between two NB-ARC domains of neighboring protomers. (**C**) Left: Contacts between the WHD and HD1. Right: Contacts between neighboring NBDs. Colors are according to the nomenclature in Fig. 1.

acids 327 to 329) that interacts with the ATP γ-phosphate and by residues forming a pocket around the base moiety (L190, I193, L356). The role of R329 in sensing the ATP molecule is highlighted by a loss of HR phenotype when it is mutated to an alanine (fig. S4).

In agreement with published NLR structures in the active state (*8*, *24*–*27*), the WHD of activated ROQ1 is rotated away from the nucleotide-binding site, thereby displacing the MHD motif and exposing the oligomerization interface (Fig. 3, B and C). This arrangement allows the NBD-HD1 surface of a protomer to intercalate with the NBD-WHD surface of its neighbor. The major interactions involve an HD1-WHD interface and an NBD-NBD interface (Fig. 3C). HD1 binds to the neighboring WHD using a mixture of polar and hydrophobic contacts. Residues in the fourth α-helix of HD1 (amino acids 401 to 413) play an important role in forming the ROQ1 tetramer (Fig. 3C, left). Single point mutations changing the character of these residues (E399R, V403D, and R410A) resulted in loss of HR, suggesting that ROQ1 oligomerization was disrupted (fig. S4). Similar results were observed when mutating a charged residue that brings together NBD domains (R229D) (fig. S4). In other structures of multimeric NLRs (*8*, *24*–*27*), the contacts between the NBDs also involve their N-terminal linker. The equivalent linker in ROQ1 is poorly resolved in our cryo-EM map compared with the surrounding NBD, for which we observed well-defined side-chain densities, indicating that the linker region in ROQ1 is flexible in the tetrameric state. Furthermore, the same linker in other NLRs provides contacts that are in part responsible for properly positioning the NBDs relative to each other. In fact, in NLRs that form larger-order oligomers, the linker forms an α-helix, whereas in smaller complexes such as the pentameric ZAR1, the N-terminal linker forms a slim structured loop without any secondary structure, allowing for the NBD to pack more tightly (fig. S7). Similarly, the poorly defined structure in the ROQ1 linker could explain the tight packing between NBDs that results in tetramerization instead of higher oligomeric states.

Mechanisms have been proposed for the oligomerization of NLRs with differing reliance on nucleotide binding (*21*). In the case of ZAR1, indirect substrate recognition mediated by the guard protein RKS1 causes a conformational change in the NBD and triggers ADP release, but the individual ZAR1 protomers are still unable to oligomerize independently of ATP (*7*, *8*). By contrast, the direct recognition of flagellin by the NLR NAIP5 induces a large conformational transition to the active state (*26*, *29*) and has been shown to activate even when the ATP-binding P-loop motif was mutated (*30*). The structure of the ROQ1 NB-ARC domain closely resembles that of ZAR1 (fig. S8) and shares a 22.2% sequence similarity. Previous studies have also shown that mutation in the P-loop of ROQ1 prevented oligomerization (*12*), suggesting that ATP binding is required for assembly. On the basis of these observations, we expect ROQ1 to follow a similar oligomerization mechanism to ZAR1, in which substrate recognition by the LRR and C-JID of ROQ1 induces a conformational change in the NBD that releases ADP. ATP binding would then be required to transition to the oligomerization-prone state.

TIR domain oligomerization and activation

Tetramerization of the NB-ARC domains brings the TIR domains into close proximity (Fig. 4). The individual TIR domains interact with each other upon resistosome assembly, allowing them to become active NADases and trigger HR (*31*). The mechanism for how this association renders TIRs catalytically active remains poorly understood. Many structural studies on TNL have relied on truncated TIR-containing proteins that are missing the subunits driving oligomerization (*10*, *32*–*36*). Here, we describe a mechanism for TIR association and activation in context of the fully assembled ROQ1 TNL.

Our initial fourfold symmetric reconstruction of ROQ1-XopQ could not clearly resolve the density corresponding to the TIR domains. Further analysis (see the materials and methods) revealed that the four TIR domains do not assemble in a fourfold symmetric fashion, but rather form a twofold symmetric dimer of dimers. The change in symmetry at the TIR domains highlights the importance for flexibility in the linker that connects them to the NBDs, as discussed previously. After adjusting the symmetry for this region and performing focused refinement, the TIR domains reached an overall resolution of 4.6 Å, allowing us to visualize secondary structure elements and trace the polypeptide backbone (figs. S1 and S3). The TIR domains are arranged forming two types of interfaces. First, TIR domains engage in a head-to-head, symmetric interaction involving alpha helices the αA and αE_2 of each protomer [nomenclature of TIR structural motifs as in (*37*), shown as interaction between the same color protomers; Fig, 4, A and B]. This interface, previously called the AE interface, is also found in many crystal structures of isolated plant TIR domains, including RPP1, RUN1, and SNC1 (fig. S9) (*10*, *32*). Consistent with published studies on these plant TNLs, mutating residues in the αA helix of ROQ1 (H30A) disrupts HR and highlights the functional importance of these contacts (fig. S4).

In our structure of ROQ1-XopQ, TIR domains engaged in an AE-AE interaction then further dimerize head-to-tail, forming what is described as the BE interface (*38*) (shown as interactions between the different colored protomers; Fig. 4, A and C). In the BE interaction, the so-called BB-loop (residues between βB and αB) of one TIR domain plugs beneath the loop between αD_3 and αE_1 of the adjacent one (Fig. 4C). Previous mutational analyses already demonstrated a functionally important role for the BB-loop in TIR domains (*10*, *39*). We further mutated residues in the αD_3-αE_1 loop (I151A and G153A) that are in close contact with the BB-loop and found that they independently resulted in loss of the HR phenotype (fig. S4).

Association between plant TIR domains at the DE surface (formed in part by the αD_3-αE_1 loop) has previously been observed in crystallographic studies, but their conformations are different from the ones defined by our cryo-EM analysis. For example, the TIR domains of RPP1, SNC1, and L6 face each other head-to-head at their DE surfaces with different rotational angles relative to each other

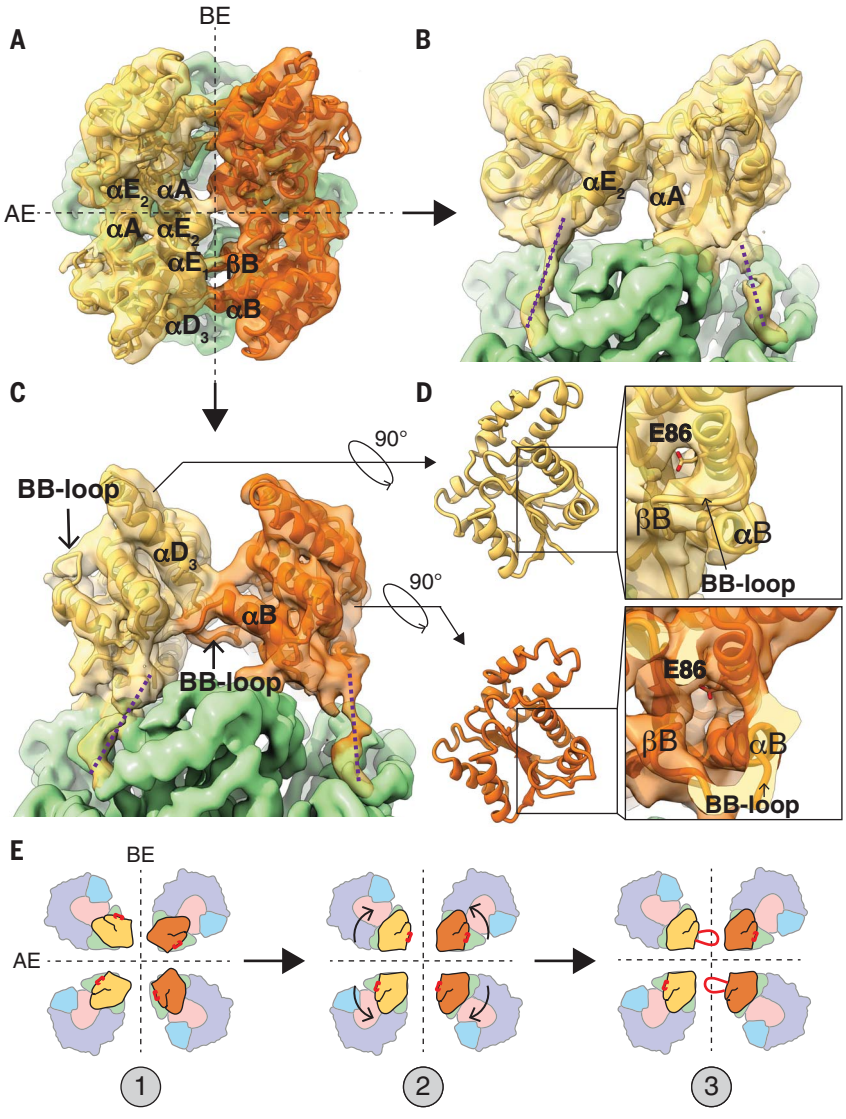

Fig. 4. TIR domain interfaces and conformational rearrangement of the BB-loop. (**A**) Top view of ROQ1 displaying the four TIR domains organized as a dimer of dimers (each symmetric dimer shown in distinct yellow and orange). The two interfaces are marked with black dotted lines; the AE interface is formed between TIR domains shown in the same color. (**B**) Orthogonal view from (A) of the AE interface. (**C**) Orthogonal view from (A) of the BE interface marking the BB-loop positioned under the αD_3 to αE_1 helices. The proposed paths of the protein chain linking the TIR domain to the NBD are shown with purple dotted lines. (**D**) Top: NADase active site of a TIR domain for which the BB-loop is not interfacing with the DE surface. Bottom: Conformational rearrangement in the BB-loop bound to the DE surface. The side chain of the putative catalytic glutamate (E86) is shown in stick representation. (**E**) Hypothetical mechanism of TIR oligomerization with the position of the BB-loop in red. (1) Individual TIR domains are brought in close proximity. (2) TIR domains recognize each other at the AE and BE interface. (3) Assembly causes the conformational rearrangement in the BB-loop that opens the NADase active site. A Gaussian filter was applied to the map in (A) to (D) (width 1.5 Å) to reduce noise.

instead of interacting in a head-to-tail fashion (*32*), perhaps because the TIR domains were visualized in isolation and the NB-ARC domain responsible for driving oligomerization was truncated. These studies highlighted the importance of the DE surface in plant TIR domain oligomerization, but the proper interactions remained unclear because of the variability in conformation between structures. The BE interaction is found in more distant phyla. The crystal structures of TIR domains from the human SARM1 (*10*) and MAL (*40*) proteins, as well as TRR-2 (unpublished, PDB: 4W8G and 4W8H) from *Hydra magnipapillata* share a similar BB-loop conformation to that found in the activated ROQ1 tetramer, in which it fits under the αD_3-αE_1 loop (fig. S10). This structural relationship suggests shared mechanistic features for TIR domain assembly and activation between animals and plants. In fact, the human SARM1 TIR domains simultaneously form AE and BE interfaces in the crystal lattice (figs. S9 and S10) (*10*).

Our structure now demonstrates that the BB-loop takes on two different conformations within the activated ROQ1 tetramer and undergoes a conformational switch as TIR domains interact at a BE interface. In the protomer in which the BB-loop is unbound (the one that is contributing to the BE contacts through its DE surface), it is seen in an upward position along the rim of the NADase active site (Fig. 4C). This conformation is the same as that found in the TIR crystal structures lacking BE contacts (*32*). In the other protomer, the BB-loop interfacing with the adjacent DE surface has been repositioned by a downward motion of ~12 Å (Fig. 4D, bottom). A highly conserved glycine residue ($G52^{ROQ1}$) in the BB-loop likely provides the flexibility required to undergo this conformational switch (fig. S11). Mutating this glycine to a proline resulted in loss of HR (fig. S4). Similarly, mutating the equivalent glycine in SARM1 (G601P) was shown to hinder flexibility and prevent a transition to the engaged state, resulting in a defective BE interface with the loop stuck in the upward position and a severe decrease in NADase activity (fig. S11) (*10*).

Repositioning of the BB-loop induced by the BE interface opens the NADase active site (Fig. 4D). Large, positively charged side chains (of $K50^{ROQ1}$, $R51^{ROQ1}$, and $K53^{ROQ1}$) that would otherwise crowd the entrance of the active site are moved down with the BB-loop. The structure of a SARM1 mutant (G601P), in which the BB-loop is trapped in the unengaged state, reveals a lysine inserted inside the active-site cleft; this indicates that these side chains may act to prevent substrate binding (*10*). Furthermore, NADase activity increased when equivalent BB-loop arginines were mutated to alanines in the plant RUN1 TIR domain (*10*). Together, these studies suggest that these large, positively charged side chains serve to inhibit NADase function and must be displaced for TIR activation.

Freeing the active site exposes conserved residues that have been proposed to recognize NAD^+ based on biochemical and structural studies using chemical analogs (*9*, *10*). The nicotinamide moiety of the substrate is supposed to fit in the active-site cleft of the TIR domain, bringing the covalently linked ribose in close proximity to the catalytic glutamate. Mutating the putative catalytic glutamate in ROQ1 ($E86^{ROQ1}$) to an alanine abrogates HR (fig. S4), suggesting loss of NADase activity. No NAD^+ was observed in our structure, which could have been cleaved by the activated TIR

domain, yet we still observed a small density positioned above the TIR domain active site at the BE interface (fig. S12). An ATP molecule was modeled at this position in Ma *et al.* (*18*). The corresponding density in our map is weak compared with that of neighboring residues (W82), with only part of an ATP molecule fitting in the density even at low contour levels (fig. S12). Therefore, it was left unmodeled. Further investigation will be required to determine the position of NAD^+ within the ROQ1 TIR domain active site. Mechanistic details of NAD^+ cleavage and product formation remain unresolved and have been found to vary among TIR domains (*31*). The steps in this enzymatic reaction involve breaking the glycosidic bond that connects nicotinamide to ADPR and, in some cases, a structural rearrangement in ADPR that leads to the formation of cyclic-ADPR or variant-cyclic-ADPR (*9*, *41*). ADPR and cyclic-ADPR have been shown to modulate the Ca^{2+} level in plant cells, which is a widely used chemical signal for responding to various biotic and abiotic stresses (*42*).

In the case of the fully assembled ROQ1 TNL, it is clear that the AE and BE interfaces are essential in TIR signaling. Both interfaces align the TIR domains in a conformation inducive to NADase active-site opening (Fig. 4E). Whether this mechanism of TIR association can be applied to other TNL remains to be determined. Similar to ROQ1, the TIR domains of the activated RPP1 tetramer form a dimer of dimers through AE- and BE-interface contacts, causing a rearrangement in the BB-loop (*18*). Nevertheless, there are likely to be alternative ways for TIR domains to assemble based on the number of protomers required to build the active complex, heterocomplex formation with other NLRs, and interface requirements for activation.

Summary

Our structure of the ROQ1-XopQ complex, together with previous biochemical studies, led us to propose a mechanism for TNL immune signaling: (i) both the LRR and C-JID recognize the pathogen effector, at which point the NR loop inserts itself into the active-site cleft of XopQ and targets conserved residues required for nucleoside-binding; (ii) the NB-ARC domain is released by the LRR and undergoes a conformational switch to the ATP-bound oligomerization state; (iii) ROQ1 protomers associate into a four-leaf-clover structure and the TIR domains are brought in close contact; (iv) the TIR domains bind to each other, forming distinct AE and BE interfaces and causing a conformational rearrangement in the BB-loop of two of the subunits; and (v) the NADase active site is exposed, allowing for the cleavage of NAD^+. Future work will be required to identify the exact molecular species produced by the TIR domains and how they are used by the immune system of the host to trigger a response to pathogen invasion.

Methods summary

ROQ1-3Flag and StrepII-XopQ were transformed into *Agrobacterium* GV3101 and coexpressed in *N. benthamiana eds1-1* mutant leaves through transient agroinfiltration. Leave tissue was harvested 30 hours after infiltration and ground with a mortar and pestle. The powdered leaf material was then resuspended in a buffer supplemented with protease inhibitors and further lysed by sonication. Two rounds of centrifugation were required to separate cell debris from the soluble fraction of the lysate. Purification of the assembled Roq1-XopQ complex was performed by sequential affinity chromatography. First, we selected for ROQ1-3Flag by Flag-immunoprecipitation. Strep-tactin resin was then used to capture the StrepII-XopQ containing complex. Individual steps can be visualized on a SDS–polyacrylamide gel electrophoresis gel in fig. S13.

The purified Roq1-XopQ complex was deposited on a freshly plasma cleaned holey carbon grid (QUANTIFOIL R2/2) coated with a thin layer of carbon. The original buffer used in the purification of the sample was removed and replaced with a similar buffer containing 3% trehalose instead of NP-40 and glycerol. The grid was mounted onto a Thermo Fisher Scientific Mk. IV Vitrobot, blotted, and plunged-frozen in liquid ethane.

Data were collected using a Titan Krios cryo–electron microscope operating at 300 kV and equipped with a K3 direct electron detector camera mounted behind a BioQuantum energy filter. A total of 11,134 dose-fractionated movies were acquired in superresolution counting mode, with an electron exposure of 50 $e^-/Å^2$ and defocus values ranging from –0.9 to –2.5 µm.

All processing steps were done in Relion 3.1 (*43*). CTF fits were calculated in Gctf (*44*). Particles were selected from the motion corrected micrographs (*45*) using an unbiased Laplacian-of-Gaussian autopicker and were subjected to an initial round of 3D classification. One more round of refinement followed by alignment-free 3D classification resulted in a class of 15,263 particles with a broad distribution of projection directions that converged to 3.8-Å resolution [Fourier shell correlation (FSC) = 0.143]. Symmetry expansion and focused refinement were required to resolve the LRR-PL-XopQ and TIR domain regions at a resolution of 3.8 and 4.6 Å, respectively. A detailed procedure is described in figs. S2 and S3.

Individual models were built for each of the three cryo-EM reconstructions. An initial model for the NB-ARC domain, TIR domain, and XopQ were generated using structures of homologous proteins in the PDB (6J5T, 5KU7, and 4KL0, respectively). The LRR and PL domain of ROQ1 were built manually in COOT (*46*). Models were refined and validated in Phenix (*47*). A final model versus map FSC was calculated using MTRIAGE (*48*). Model validation statistics can be found in table S1.

For HR phenotype observation, ROQ1-3Flag mutants and StrepII-XopQ were transiently coexpressed in *N. tabacum roq1-1* mutant leaves through *Agrobacterium*-mediated transformation. HR phenotypes were observed and imaged 2 days after infiltration. To test for protein expression, ROQ1-3Flag mutants and StrepII-XopQ were coexpressed and extracted from *N. benthamiana eds1-1* mutant leaves and detected by Western blotting.

Conservation scores for residues in the ROQ1 C-JID were calculated in Consurf (*49*) from a multiple sequence alignment provided in the supplementary materials (sequence alignment file S1).

REFERENCES AND NOTES

1. J. L. Dangl, D. M. Horvath, B. J. Staskawicz, Pivoting the plant immune system from dissection to deployment. *Science* **341**, 746–751 (2013). doi: 10.1126/science.1236011; pmid: 23950531
2. J. Wang, J. Chai, Structural insights into the plant immune receptors PRRs and NLRs. *Plant Physiol.* **182**, 1566–1581 (2020). doi: 10.1104/pp.19.01252; pmid: 32047048
3. J. Tamborski, K. V. Krasileva, Evolution of plant NLRs: From natural history to precise modifications. *Annu. Rev. Plant Biol.* **71**, 355–378 (2020). doi: 10.1146/annurev-arplant-081519-035901; pmid: 32092278
4. J. M. Feehan, B. Castel, A. R. Bentham, J. D. G. Jones, Plant NLRs get by with a little help from their friends. *Curr. Opin. Plant Biol.* **56**, 99–108 (2020). doi: 10.1016/j.pbi.2020.04.006; pmid: 32554226
5. L. M. Jubic, S. Saile, O. J. Furzer, F. El Kasmi, J. L. Dangl, Help wanted: Helper NLRs and plant immune responses. *Curr. Opin. Plant Biol.* **50**, 82–94 (2019). doi: 10.1016/j.pbi.2019.03.013; pmid: 31063902
6. J. D. G. Jones, R. E. Vance, J. L. Dangl, Intracellular innate immune surveillance devices in plants and animals. *Science* **354**, aaf6395 (2016). doi: 10.1126/science.aaf6395; pmid: 27934708
7. J. Wang *et al.*, Ligand-triggered allosteric ADP release primes a plant NLR complex. *Science* **364**, eaav5868 (2019). doi: 10.1126/science.aav5868; pmid: 30948526
8. J. Wang *et al.*, Reconstitution and structure of a plant NLR resistosome conferring immunity. *Science* **364**, eaav5870 (2019). doi: 10.1126/science.aav5870; pmid: 30948527
9. L. Wan *et al.*, TIR domains of plant immune receptors are NAD^+-cleaving enzymes that promote cell death. *Science* **365**, 799–803 (2019). doi: 10.1126/science.aax1771; pmid: 31439793
10. S. Horsefield *et al.*, NAD^+ cleavage activity by animal and plant TIR domains in cell death pathways. *Science* **365**, 793–799 (2019). doi: 10.1126/science.aax1911; pmid: 31439792
11. A. Schultink, T. Qi, A. Lee, A. D. Steinbrenner, B. Staskawicz, Roq1 mediates recognition of the Xanthomonas and Pseudomonas effector proteins XopQ and HopQ1. *Plant J.* **92**, 787–795 (2017). doi: 10.1111/tpj.13715; pmid: 28891100
12. T. Qi *et al.*, NRG1 functions downstream of EDS1 to regulate TIR-NLR-mediated plant immunity in *Nicotiana benthamiana*. *Proc. Natl. Acad. Sci. U.S.A.* **115**, E10979–E10987 (2018). doi: 10.1073/pnas.1814856115; pmid: 30373842
13. D. Lapin, D. D. Bhandari, J. E. Parker, Origins and immunity networking functions of EDS1 family proteins. *Annu. Rev. Phytopathol.* **58**, 253–276 (2020). doi: 10.1146/annurev-phyto-010820-012840; pmid: 32396762
14. S. Yu, I. Hwang, S. Rhee, The crystal structure of type III effector protein XopQ from Xanthomonas oryzae complexed with adenosine diphosphate ribose. *Proteins* **82**, 2910–2914 (2014). doi: 10.1002/prot.24656; pmid: 25079351
15. L. Liu *et al.*, Structural basis of toll-like receptor 3 signaling with double-stranded RNA. *Science* **320**, 379–381 (2008). doi: 10.1126/science.1155406; pmid: 18420935

16. C. Van Ghelder, D. Esmenjaud, TNL genes in peach: Insights into the post-LRR domain. *BMC Genomics* **17**, 317 (2016). doi: 10.1186/s12864-016-2635-0; pmid: 27129402
17. I. Sillitoe *et al*., CATH: Expanding the horizons of structure-based functional annotations for genome sequences. *Nucleic Acids Res.* **47** (D1), D280–D284 (2019). doi: 10.1093/nar/gky1097; pmid: 30398663
18. S. Ma *et al*., Direct pathogen-induced assembly of an NLR immune receptor complex to form a holoenzyme. *Science* 10.1126/science.abe3069 (2020). doi: 10.1126/science.abe3069
19. W. Li, Y.-H. Chiang, G. Coaker, The HopQ1 effector's nucleoside hydrolase-like domain is required for bacterial virulence in arabidopsis and tomato, but not host recognition in tobacco. *PLOS ONE* **8**, e59684 (2013). doi: 10.1371/journal.pone.0059684; pmid: 23555744
20. N. Adlung, U. Bonas, Dissecting virulence function from recognition: Cell death suppression in Nicotiana benthamiana by XopQ/HopQ1-family effectors relies on EDS1-dependent immunity. *Plant J.* **91**, 430–442 (2017). doi: 10.1111/tpj.13578; pmid: 28423458
21. Y. Xiong, Z. Han, J. Chai, Resistosome and inflammasome: Platforms mediating innate immunity. *Curr. Opin. Plant Biol.* **56**, 47–55 (2020). doi: 10.1016/j.pbi.2020.03.010; pmid: 32554225
22. J. F. C. Steele, R. K. Hughes, M. J. Banfield, Structural and biochemical studies of an NB-ARC domain from a plant NLR immune receptor. *PLOS ONE* **14**, e0221226 (2019). doi: 10.1371/journal.pone.0221226; pmid: 31461469
23. Z. Hu *et al*., Crystal structure of NLRC4 reveals its autoinhibition mechanism. *Science* **341**, 172–175 (2013). doi: 10.1126/science.1236381; pmid: 23765277
24. Y. Pang *et al*., Structure of the apoptosome: Mechanistic insights into activation of an initiator caspase from Drosophila. *Genes Dev.* **29**, 277–287 (2015). doi: 10.1101/gad.255877.114; pmid: 25644603
25. S. Qi *et al*., Crystal structure of the *Caenorhabditis elegans* apoptosome reveals an octameric assembly of CED-4. *Cell* **141**, 446–457 (2010). doi: 10.1016/j.cell.2010.03.017; pmid: 20434985
26. J. L. Tenthorey *et al*., The structural basis of flagellin detection by NAIP5: A strategy to limit pathogen immune evasion. *Science* **358**, 888–893 (2017). doi: 10.1126/science.aao1140; pmid: 29146805
27. L. Zhang *et al*., Cryo-EM structure of the activated NAIP2-NLRC4 inflammasome reveals nucleated polymerization. *Science* **350**, 404–409 (2015). doi: 10.1126/science.aac5789; pmid: 26449474
28. V. Bonardi, K. Cherkis, M. T. Nishimura, J. L. Dangl, A new eye on NLR proteins: Focused on clarity or diffused by complexity? *Curr. Opin. Immunol.* **24**, 41–50 (2012). doi: 10.1016/j.coi.2011.12.006; pmid: 22305607
29. X. Yang *et al*., Structural basis for specific flagellin recognition by the NLR protein NAIP5. *Cell Res.* **28**, 35–47 (2018). doi: 10.1038/cr.2017.148; pmid: 29182158
30. E. F. Halff *et al*., Formation and structure of a NAIP5-NLRC4 inflammasome induced by direct interactions with conserved N- and C-terminal regions of flagellin. *J. Biol. Chem.* **287**, 38460–38472 (2012). doi: 10.1074/jbc.M112.393512; pmid: 23012363
31. A. M. Bayless, M. T. Nishimura, Enzymatic functions for Toll/interleukin-1 receptor domain proteins in the plant immune system. *Front. Genet.* **11**, 539 (2020). doi: 10.3389/fgene.2020.00539; pmid: 32582284
32. X. Zhang *et al*., Multiple functional self-association interfaces in plant TIR domains. *Proc. Natl. Acad. Sci. U.S.A.* **114**, E2046–E2052 (2017). doi: 10.1073/pnas.1621248114; pmid: 28159890
33. S. J. Williams *et al*., Structural basis for assembly and function of a heterodimeric plant immune receptor. *Science* **344**, 299–303 (2014). doi: 10.1126/science.1247357; pmid: 24744375
34. K.-G. Hyun, Y. Lee, J. Yoon, H. Yi, J.-J. Song, Crystal structure of Arabidopsis thaliana SNC1 TIR domain. *Biochem. Biophys. Res. Commun.* **481**, 146–152 (2016). doi: 10.1016/j.bbrc.2016.11.004; pmid: 27818198
35. M. Bernoux *et al*., Structural and functional analysis of a plant resistance protein TIR domain reveals interfaces for self-association, signaling, and autoregulation. *Cell Host Microbe* **9**, 200–211 (2011). doi: 10.1016/j.chom.2011.02.009; pmid: 21402359
36. S. J. Williams *et al*., Structure and function of the TIR domain from the grape NLR protein RPV1. *Front. Plant Sci.* **7**, 1850 (2016). pmid: 28008335
37. Y. Xu *et al*., Structural basis for signal transduction by the Toll/interleukin-1 receptor domains. *Nature* **408**, 111–115 (2000). doi: 10.1038/35040600; pmid: 11081518
38. S. Nimma, T. Ve, S. J. Williams, B. Kobe, Towards the structure of the TIR-domain signalosome. *Curr. Opin. Struct. Biol.* **43**, 122–130 (2017). doi: 10.1016/j.sbi.2016.12.014; pmid: 28092811
39. L. Vyncke *et al*., Reconstructing the TIR side of the myddosome: A paradigm for TIR-TIR interactions. *Structure* **24**, 437–447 (2016). doi: 10.1016/j.str.2015.12.018; pmid: 26876098
40. T. Ve *et al*., Structural basis of TIR-domain-assembly formation in MAL- and MyD88-dependent TLR4 signaling. *Nat. Struct. Mol. Biol.* **24**, 743–751 (2017). doi: 10.1038/nsmb.3444; pmid: 28759049
41. K. Essuman *et al*., TIR domain proteins are an ancient family of NAD^+-consuming enzymes. *Curr. Biol.* **28**, 421–430.e4 (2018). doi: 10.1016/j.cub.2017.12.024; pmid: 29395922
42. Y. Wu *et al*., Abscisic acid signaling through cyclic ADP-ribose in plants. *Science* **278**, 2126–2130 (1997). doi: 10.1126/science.278.5346.2126; pmid: 9405349
43. S. H. W. Scheres, RELION: Implementation of a Bayesian approach to cryo-EM structure determination. *J. Struct. Biol.* **180**, 519–530 (2012). doi: 10.1016/j.jsb.2012.09.006; pmid: 23000701
44. K. Zhang, Gctf: Real-time CTF determination and correction. *J. Struct. Biol.* **193**, 1–12 (2016). doi: 10.1016/j.jsb.2015.11.003; pmid: 26592709
45. S. Q. Zheng *et al*., MotionCor2: Anisotropic correction of beam-induced motion for improved cryo-electron microscopy. *Nat. Methods* **14**, 331–332 (2017). doi: 10.1038/nmeth.4193; pmid: 28250466
46. P. Emsley, K. Cowtan, Coot: Model-building tools for molecular graphics. *Acta Crystallogr. D Biol. Crystallogr.* **60**, 2126–2132 (2004). doi: 10.1107/S0907444904019158; pmid: 15572765
47. P. D. Adams *et al*., PHENIX: Building new software for automated crystallographic structure determination. *Acta Crystallogr. D Biol. Crystallogr.* **58**, 1948–1954 (2002). doi: 10.1107/S0907444902016657; pmid: 12393927
48. P. V. Afonine *et al*., New tools for the analysis and validation of cryo-EM maps and atomic models. *Acta Crystallogr. D Struct. Biol.* **74**, 814–840 (2018). doi: 10.1107/S2059798318009324; pmid: 30198894
49. H. Ashkenazy *et al*., ConSurf 2016: An improved methodology to estimate and visualize evolutionary conservation in macromolecules. *Nucleic Acids Res.* **44** (W1), W344–W350 (2016). doi: 10.1093/nar/gkw408; pmid: 27166375

ACKNOWLEDGMENTS

We dedicate this work to the memory of André Martin (1929–2020). We thank P. Grob and D. Toso for electron microscopy support; A. Chintangal and P. Tobias for computational support; N. Haloupek and P. Grob for advice with cryo-EM grid preparation of NLR samples; B. Greber for advice with data processing and with model building and refinement; K. Krasileva, D. Prigozhin, and K. Verster for useful discussion on PL domain conservation and LRR-effector interactions; and B. Kobe for useful discussion on TIR domains. Data were collected at the BACEM facility, Berkeley QB3. Molecular graphics and analyses were performed with UCSF Chimera and UCSF ChimeraX. **Funding:** This work was supported by the Founders Fund from the Innovative Genomics Institute of the University of California–Berkeley (to B.J.S.) and by funds from the Tsinghua-Peking Center for Life Sciences (to T.Q.). T.Q. was supported by a Tang Distinguished Scholarship from the University of California–Berkeley. E.N. is a Howard Hughes Medical Institute Investigator. **Author contributions:** E.N. and B.J.S. supervised the work. T.Q. constructed ROQ1 and XopQ vectors and expressed the ROQ1-XopQ protein complex in *N. benthamiana*. R.M. and T.Q. established purification protocols and purified the ROQ1-XopQ complex. R.M. prepared cryo-EM grids, collected and processed cryo-EM data, and performed model building, refinement, and interpretation. C.T. assisted in purification and grid making. R.M., T.Q., H.Z., and F.L. constructed ROQ1 mutants. T.Q. and H.Z. detected protein expression and HR phenotypes. M.K. assisted in ROQ1 and XopQ protein expression in *N. benthamiana*. R.M. wrote the initial draft of the manuscript. All authors contributed to the final version of the paper. **Competing interests:** B.J.S. is the scientific cofounder and serves on the board of directors of Mendel Biotechnology and is on the scientific advisory boards of Verinomics and the Sainsbury Laboratory. R.M. and B.J.S. are inventors on a patent application held by the University of California that covers the ability to engineer new plant immune receptors. **Data and materials availability:** Materials are available from B.J.S. CryoEM density maps and fitted models have been deposited in the Electron Microscopy Data Bank (EMDB) and the Protein Data Bank (PDB). The maps for initial reconstruction of the ROQ1-XopQ complex, focused refinement around the LRR-C-JID-XopQ region, and TIR domains have been deposited with the EMDB accession codes 22381, 22380, and 22383, respectively. The refined coordinate models have been deposited with PDB accession codes 7JLV, 7JLU, and 7JLX, respectively. All other data are available either in the main paper or the supplementary materials.

SUPPLEMENTARY MATERIALS

science.sciencemag.org/content/370/6521/eabd9993/suppl/DC1
Materials and Methods
Figs. S1 to S13
Table S1
References (*50*–*58*)
Movie S1
Sequence Alignment File S1
MDAR Reproducibility Checklist

View/request a protocol for this paper from *Bio-protocol*.

31 July 2020; accepted 19 October 2020
10.1126/science.abd9993

RESEARCH ARTICLE

DEVELOPMENTAL BIOLOGY

The N-glycome regulates the endothelial-to-hematopoietic transition

Dionna M. Kasper[1,2,3], Jared Hintzen[1,2,3], Yinyu Wu[1,2,3], Joey J. Ghersi[1,2,3], Hanna K. Mandl[1,2,3], Kevin E. Salinas[1,2,3], William Armero[1,2,3], Zhiheng He[1,2,3], Ying Sheng[4], Yixuan Xie[4], Daniel W. Heindel[5], Eon Joo Park[3,6], William C. Sessa[3,6], Lara K. Mahal[5,7], Carlito Lebrilla[4], Karen K. Hirschi[1,2,3,8]*, Stefania Nicoli[1,2,3,6]*

Definitive hematopoietic stem and progenitor cells (HSPCs) arise from the transdifferentiation of hemogenic endothelial cells (hemECs). The mechanisms of this endothelial-to-hematopoietic transition (EHT) are poorly understood. We show that microRNA-223 (miR-223)–mediated regulation of N-glycan biosynthesis in endothelial cells (ECs) regulates EHT. miR-223 is enriched in hemECs and in oligopotent nascent HSPCs. miR-223 restricts the EHT of lymphoid-myeloid lineages by suppressing the mannosyltransferase *alg2* and sialyltransferase *st3gal2*, two enzymes involved in protein N-glycosylation. ECs that lack miR-223 showed a decrease of high mannose versus sialylated sugars on N-glycoproteins such as the metalloprotease Adam10. EC-specific expression of an N-glycan Adam10 mutant or of the N-glycoenzymes phenocopied miR-223 mutant defects. Thus, the N-glycome is an intrinsic regulator of EHT, serving as a key determinant of the hematopoietic fate.

In vertebrates, definitive hematopoietic stem and progenitor cells (HSPCs) are specified during embryogenesis by the transdifferentiation of endothelial cells (ECs) within the aorta-gonad-mesonephros (AGM) region of the dorsal aorta (*1*–*3*). This endothelial-to-hematopoietic transition (EHT) occurs in hemogenic ECs (hemECs), a subset of ECs that coexpress vascular and hematopoietic genes. The precise interplay between multiple signaling cascades (*1*, *2*, *4*) enables the progressive loss of endothelial and concomitant increase of hematopoietic gene expression, with hemECs giving rise to nascent HSPCs (*2*, *3*). HSPCs then delaminate from the vascular wall and enter the circulation to colonize secondary hematopoietic organs, where they generate all blood cells throughout life (*5*–*7*). The EC and/or hemEC determinants that regulate EHT and thus HSPC production is not completely understood.

[1]Yale Cardiovascular Research Center, Department of Internal Medicine, Section of Cardiology, Yale University School of Medicine, New Haven, CT 06511, USA. [2]Department of Genetics, Yale University School of Medicine, New Haven, CT 06510, USA. [3]Vascular Biology and Therapeutics Program, Yale University School of Medicine, New Haven, CT 06520, USA. [4]Department of Chemistry, University of California, Davis, CA 95616, USA. [5]Biomedical Chemistry Institute, Department of Chemistry, New York University, New York, NY 10003, USA. [6]Department of Pharmacology, Yale University School of Medicine, New Haven, CT 06510, USA. [7]Department of Chemistry, University of Alberta, Edmonton, AB T6G 2G2, Canada. [8]Developmental Genomics Center, Cell Biology Department, University of Virginia School of Medicine, Charlottesville, VA 22908, USA.
*Corresponding author. Email: stefania.nicoli@yale.edu (S.N.); kkh4yy@virginia.edu (K.K.H.)

miR-223 is expressed in ECs undergoing EHT

Genetic deletion of microRNA-223 (miR-223$^{\Delta/\Delta}$) results in excess nascent HSPCs in the zebrafish AGM (*8*). However, the mechanisms underlying miR-223 function in EHT are unknown (*8*–*11*). To examine miR-223 expression during EHT, we generated a zebrafish transgenic reporter in which miR-223–expressing ECs are labeled with both green fluorescent protein (GFP) and mCherry (miR-223:GFP$^+$ kdrl:mCH$^+$) (Fig. 1A, fig. S1A, and materials and methods). Endogenous miR-223 expression was enriched in miR-223:GFP$^+$ kdrl:mCH$^+$ cells versus miR-223:GFP$^-$ kdrl:mCH$^-$ cells (fig. S1B). Moreover, reexpression of miR-223 from its promoter in miR-223:Gal4$^+$ cells rescued the *cmyb*$^+$ HSPC overexpansion in miR-223$^{\Delta/\Delta}$ (fig. S1C). Thus, miR-223:GFP$^+$ cells report the endogenous expression and function of miR-223.

miR-223:GFP$^+$ kdrl:mCH$^+$ cells were dispersed in a salt-and-pepper pattern, mostly within the AGM (Fig. 1A and fig. S1, D and E). The AGM population of miR-223:GFP$^+$ kdrl:mCH$^+$ cells increased from the onset to the peak of EHT, at 24 to 32 hours after fertilization (fig. S1E). They manifested a heterogeneous pattern of flat to bulging morphologies and underwent delamination from the AGM (Fig. 1A; fig. S1, F and G; and movie S1). miR-223:GFP$^+$ kdrl:mCH$^+$ cells showed elevated expression of endothelial (*kdrl*) and EHT markers, including *gata2b* and *runx1* in hemECs (*12*) and *cmyb* in nascent HSPCs (*5*) (fig. S1H). Accordingly, nascent HSPCs showed elevated expression of endogenous mature miR-223 (fig. S1I), suggesting that miR-223 is expressed in ECs undergoing EHT.

To further discern the distinct molecular subtypes among miR-223–expressing ECs, we performed single-cell RNA-sequencing (scRNA-seq) (fig. S2A and materials and methods). Kdrl:mCH$^+$ ECs formed a vascular tree composed of branches that corresponded to embryonic specification trajectories, identified through the expression of known markers (fig. S2, A and B, and data file S1). We observed the arterial trajectory from which cells coexpress a continuum of early and late EHT markers in hemECs and in nascent HSPCs (Fig. 1B, fig. S2B, and data file S1). This branch split into two trajectories that included nascent HSPCs expressing early primed markers for the lymphoid-myeloid lineages or lymphoid-erythroid lineages (Fig. 1C, fig. S2B, and data file S1). Gene ontology classifications of branch-defining genes confirmed that as ECs progressed through the EHT trajectories, they lost vascular development terms while gaining hematopoietic, protein biosynthesis, and N-glycosylation terms (*13*). Cell migration and cell cycle transcripts were mostly acquired within primed nascent HSPCs, when they likely begin to delaminate and/or amplify (fig. S2C and data file S2) (*1*, *2*). Thus, our data suggest that oligopotent nascent HSPCs are produced during EHT in the AGM.

Additionally, we found that ECs that express *miR-223:gfp* transcripts comprised ~73 to 100% of hemEC-nascent HSPC and lymphoid-myeloid–primed HSPC branches and only ~17% of the lymphoid-erythroid–primed HSPC branch (Fig. 1D and fig. S2, D and E). *miR-223:gfp*$^+$ ECs had enriched expression of EHT, lymphoid-myeloid–, and lymphoid-erythroid– primed HSPC lineage markers in the relevant trajectories (fig. S2F and data file S1). Together, these analyses suggest that miR-223 is enriched in hemECs and nascent HSPCs during the EHT of oligopotent lymphoid-myeloid–primed HSPCs (Fig. 1E).

miR-223 limits hemEC and lymphoid-myeloid–HSPC production

To test miR-223 function in EHT, we phenotyped miR-223 mutants. Zebrafish miR-223$^{\Delta/\Delta}$ compared with wild-type embryos displayed an increase in gata2b:GFP$^+$ or runx1:GFP$^+$ hemECs in the AGM (Fig. 2A and fig. S3, A and B). As observed previously, cmyb:GFP$^+$ kdrl:mCH$^+$ nascent HSPCs were increased at 32 and 36 hours after fertilization in miR-223$^{\Delta/\Delta}$ (Fig. 2B) (*8*). Similarly in mice, miR-223 was abundantly expressed in ECs and hemECs from the embryonic day 10.5 (E10.5) AGM. Moreover, global removal of miR-223 (*9*) displayed elevated hemECs in the E10.5 AGM and HSPCs at secondary hematopoietic sites (fig. S3, C to F). These results suggest that miR-223 is a conserved inhibitor of hemEC and HSPC production.

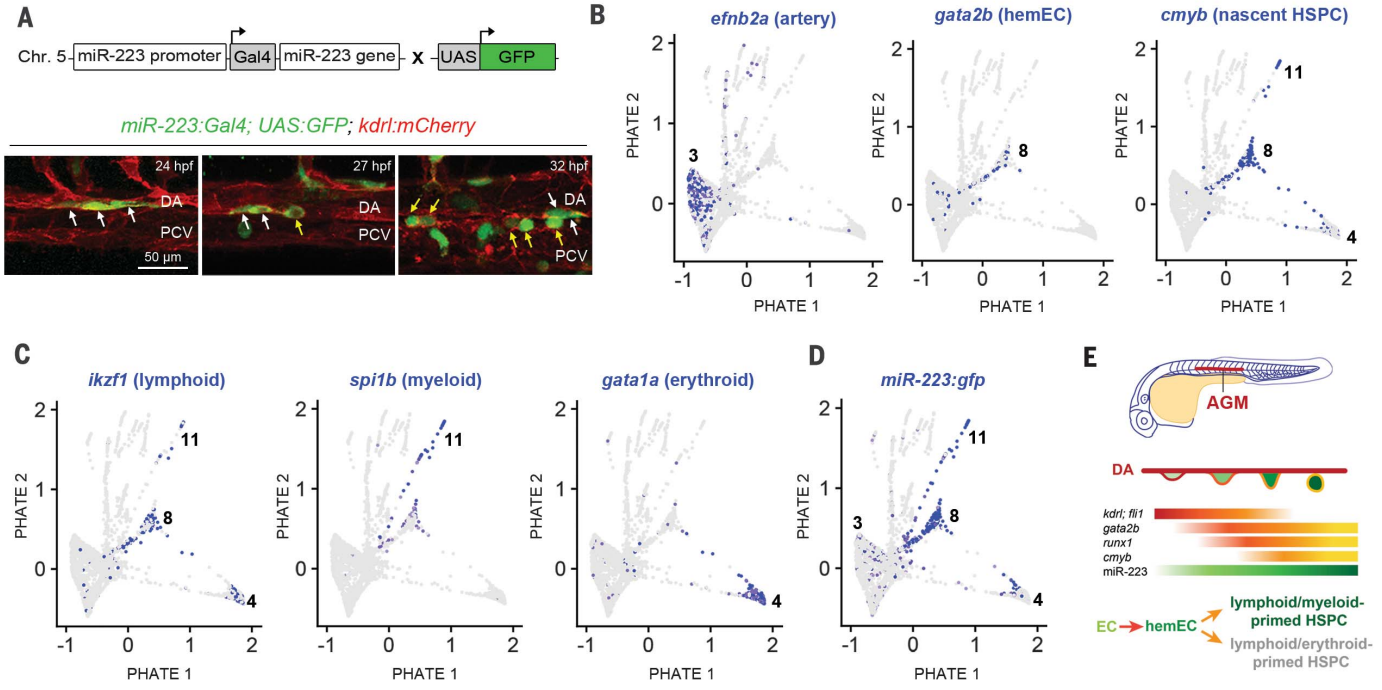

Fig. 1. miR-223 is expressed in hemECs undergoing EHT. (**A**) (Top) Schematic of miR-223:GFP reporter. (Bottom) Lateral Z-projections of the zebrafish AGM. White and yellow arrows point to flat and budding miR-223:GFP$^+$ kdrl:mCH$^+$ cells, respectively. (**B** to **D**) Plots of wild-type kdrl:mCH$^+$ trunk ECs 27 hours after fertilization showing expression of (B) EHT, (C) blood lineage, and (D) *miR-223:gfp* genes (n = 6227 cells). Arterial (branch 3) and EHT (branches 8, 11, and 4) trajectories are indicated. (**E**) During EHT, a flattened EC (red outline) gains hemogenic potential (orange outline) and buds as a oligopotent nascent HSPC (yellow outline) from the DA wall. Gradients for endothelial and EHT markers are colored on the basis of their expression in the indicated cell types. The green gradient and text represent miR-223 expression. DA, dorsal aorta; hpf, hours post fertilization; PCV, posterior cardinal vein

Next, we determined whether nascent HSPCs in miR-223$^{\Delta/\Delta}$ zebrafish have altered behaviors. First, miR-223$^{\Delta/\Delta}$ versus control nascent HSPCs had increased proliferative capacity (fig. S4A). Second, delamination times from the AGM were significantly longer (2.3 ± 0.9 hours) for miR-223$^{\Delta/\Delta}$ as compared with wild-type nascent HSPCs (fig. S4B and movies S2 and S3). Although slowed, *cmyb*$^+$ HSPCs eventually delaminated and were still expanded in secondary hematopoietic organs of miR-223$^{\Delta/\Delta}$ embryos—namely, in the caudal hematopoietic tissue (CHT) at 2.5 days after fertilization (*8*), as well as in the thymus and kidney marrow at 6 days after fertilization (fig. S4C). Thus, the excess HSPCs in miR-223$^{\Delta/\Delta}$ exhibit aberrant proliferation and delamination.

Last, we examined how miR-223 loss affects blood lineage differentiation of the supernumerary HSPCs. Consistent with the relatively high expression of *miR-223:gfp* in lymphoid-myeloid–primed HSPCs in the AGM (Fig. 1D and fig. S2E), lymphoid and myeloid progenitors and differentiated cells were significantly expanded in secondary hematopoietic organs, whereas the erythroid lineage was unchanged (Fig. 2C and fig. S4D). Reexpression of wild-type miR-223 in miR-223$^{\Delta/\Delta}$ ECs normalized *cmyb*$^+$ HSPCs in the AGM and the lymphoid and myeloid blood cell lineages to control levels (Fig. 2, C and D, and fig. S4E). These data suggest that miR-223 functions in ECs to restrict the EHT of lymphoid-myeloid–primed HSPCs.

miR-223 regulates N-glycosylation enzymes during EHT

miRNAs typically bind miRNA-responsive elements (MREs) within 3′ untranslated regions (3′UTRs) to fine-tune mRNA levels through decay and/or translational repression (*14*). Therefore, to identify miR-223 targets involved in EHT, we focused on transcripts that were upregulated in miR-223$^{\Delta/\Delta}$ ECs and harbored a miR-223 MRE (*8*). We found that four out of the top eight candidate genes encode enzymes that regulate N-glycosylation (fig. S5, A to C, and data file S3).

N-glycosylation begins in the endoplasmic reticulum (ER), where a preassembled glycan core is attached onto specific asparagines (N) of nascent polypeptides. The glycan is progressively modified by glycosidases and glycosyltransferases as the protein traffics from the ER to the Golgi (fig. S5C) (*15*). The rate of glycan flux and/or the expression level of N-glycan biosynthesis enzymes (N-glycoenzymes) produce a diverse N-glycan repertoire, which determines protein activity and fundamental cell behaviors in reprogramming and oncogenesis (*16*, *17*). However, N-glycosylation has not yet been implicated in EHT.

We investigated three canonical N-glycoenzymes that were derepressed in miR-223$^{\Delta/\Delta}$ ECs: *alg2*, an ER-resident mannosyltransferase that incorporates mannose moieties in the N-glycan core; *lman2lb*, a mannose-binding lectin that promotes N-glycoprotein transport from the ER to the Golgi; and *st3gal2*, a Golgi-resident sialyltransferase that terminally modifies N-glycoproteins with sialic acid sugars (fig. S5C and data file S3).

To determine whether miR-223 negatively regulates these N-glycoenzyme transcripts through their 3′UTRs, we constructed sensors consisting of mCherry fused to a 3′UTR fragment of *alg2*, *lman2lb*, or *st3gal2* that contains the putative miR-223 MRE (fig. S5D). The *alg2* and *st3gal2* 3′UTR sensors showed significant mCherry repression in the AGM of miR-223$^{\Delta/\Delta}$ versus control embryos. By contrast, the *lman2lb* 3′UTR sensor was similar between wild-type and mutant embryos (fig. S5D). These data suggest that miR-223 represses *alg2* and *st3gal2* transcripts through their 3′UTR in AGM ECs.

We next investigated how *alg2* or *st3gal2* repression contributes to miR-223–mediated regulation of EHT and HSPC production. We found that similar to miR-223, *alg2* and *st3gal2* were

expressed in ECs and increased in nascent HSPCs at 27 hours after fertilization (fig. S6A). Morpholino-induced down-regulation of *alg2* or *st3gal2* expression reduced nascent HSPCs in the AGM, without otherwise affecting development (fig. S6, B to E). Moreover, partial down-regulation of *alg2* or *st3gal2*, which had no effect on wild-type embryos, rescued HSPC expansion in miR-223$^{\Delta/\Delta}$ embryos (fig. S6F). Congruently, *alg2* and *st3gal2* gain of function in ECs increased nascent HSPCs (fig. S7A). Likewise, mutation of the miR-223 MRE in the *alg2* or *st3gal2* 3′UTR (fig. S7, B to D) also recapitulated miR-223$^{\Delta/\Delta}$ phenotypes: hemECs and HSPCs were expanded in the AGM, as were HSPCs and differentiated lymphoid-myeloid lineage cells within the secondary hematopoietic tissues (Fig. 3, A and B, and fig. S7, E and F). Together, these data suggest that miR-223 posttranscriptionally represses *alg2* or *st3gal2* to regulate EHT and HSPC differentiation.

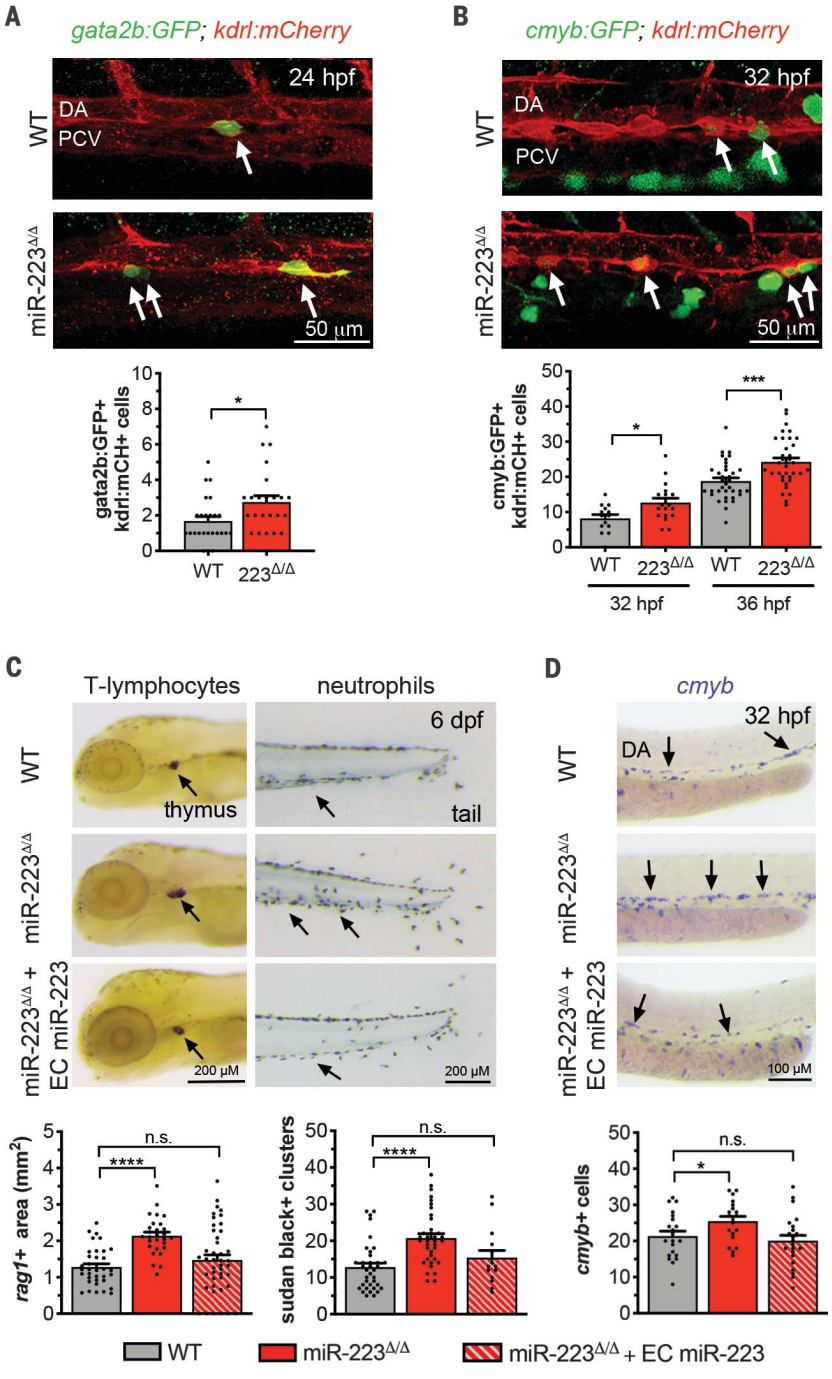

Fig. 2. miR-223 is an endothelial inhibitor of EHT and lymphoid-myeloid–oligopotent HSPC production. (**A** and **B**) (Top) Z-projections or (bottom) mean ± SEM numberof gata2b:GFP$^+$ kdrl:mCH$^+$ hemECs [*n* = 24 or 25 embryos, (A)] or cmyb:GFP$^+$ kdrl:mCH$^+$ nascent HSPCs [*n* = 13 to 18, 32 hours after fertilization; *n*= 34 to 36, 36 hours after fertilization (*8*), (B)]. (**C** and **D**) (Top) Representative images or (bottom) mean ± SEM area of (C) T-lymphocyte marker *rag1* expression (*n* = 18 to 35 embryos) and Sudan black$^+$ neutrophil clusters (*n* = 36 or 37 embryos) and (D) *cmyb* expression (*n* = 18 to 21 embryos). The EC miR-223 rescuing construct is described in fig. S4E. DA, dorsal aorta; dpf, days post fertilization; hpf, hours post fertilization; PCV, posterior cardinal vein. Significance is represented as not significant (n.s.) $P > 0.05$, *$P \le 0.05$, **$P \le 0.01$, ***$P \le 0.01$, ****$P \le 0.0001$, unpaired, two-tailed Mann-Whitney *U* test.

The N-glycome controls EHT protein function

To test whether an altered N-glycome in ECs might lead to aberrant EHT in miR-223$^{\Delta/\Delta}$, we first profiled changes in specific glycan subtypes between wild-type and miR-223$^{\Delta/\Delta}$ ECs (Fig. 4A and fig. S8A). We found that high mannose (~71%) and sialylated complex/hybrid (C/H) (~18%) were the predominant glycans on proteins from wild-type ECs. By contrast, sialylated C/H (~97%) and sialofucosylated C/H (~3%) glycans were on proteins from ECs lacking miR-223, which was concomitant with a remarkable loss of high mannose type N-glycans (Fig. 4, B and C, and data file S4). Whole embryos overexpressing *alg2* or *st3gal2* in ECs or treated with the sialic acid precursor N-acetylmannosamine possessed both HSPC expansion and increased sialylated glycan subtypes at the expense of high mannose modifications, similar to those of miR-223$^{\Delta/\Delta}$ embryos (Fig. 4D; figs. S7A and S8, B to D; and data file S4). Thus, our analysis supports that the balance between high mannose versus sialic acid–containing N-glycan subtypes in ECs is regulated through miR-223–mediated repression of *alg2* or *st3gal2* N-glycoenzymes.

We next identified the N-glycoproteins that were altered in miR-223$^{\Delta/\Delta}$ compared with wild-type embryos (fig. S8E). The N-glycoproteins with reduced high mannose and/or increased sialylated C/H and sialofucosylated C/H modifications in miR-223$^{\Delta/\Delta}$ have known biological functions relevant to EHT and HSPC production, and their transcripts were expressed in ECs during EHT (Fig. 5A, fig. S8F, and data file S4). Of high interest was the metalloprotease Adam10a, which is critical for the proteolytic release of several cell surface proteins such as Notch, Vegfr2, tumor necrosis factor–α (TNF-α), and other EHT growth factor signaling molecules (*18*, *19*). We found that the number of nascent HSPCs were significantly decreased in the AGM of *adam10a* guide RNA (gRNA)/Cas9–injected embryos, which is consistent with Adam10-mediated regulation of several EHT factors (Fig. 5, B and C, and fig. S8G). Down-regulation of *adam10a* in miR-223$^{\Delta/\Delta}$ decreased nascent

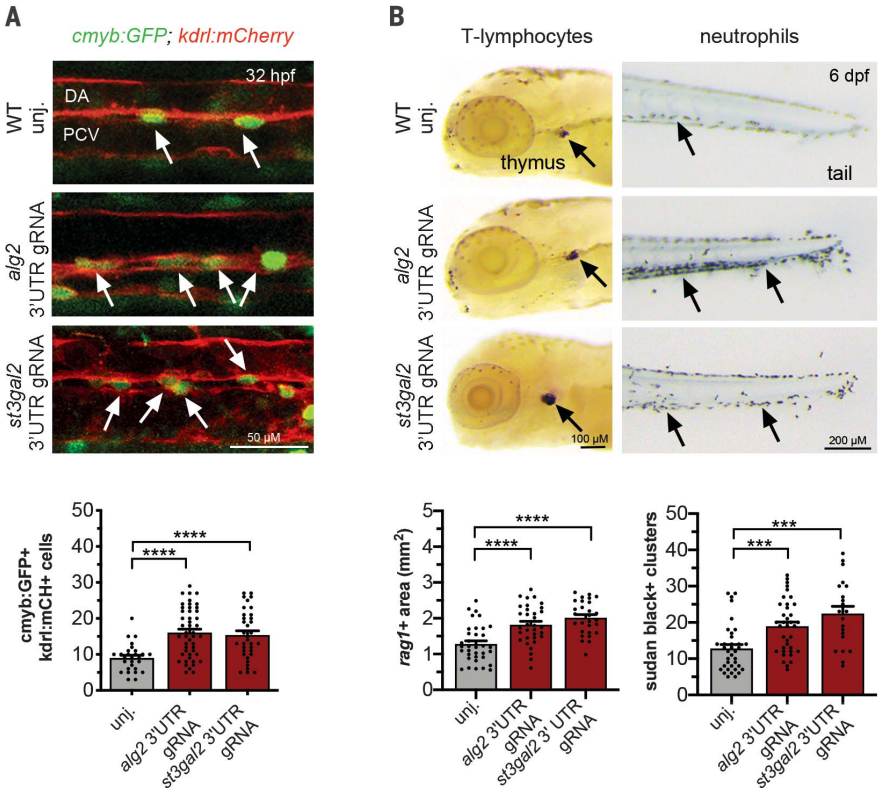

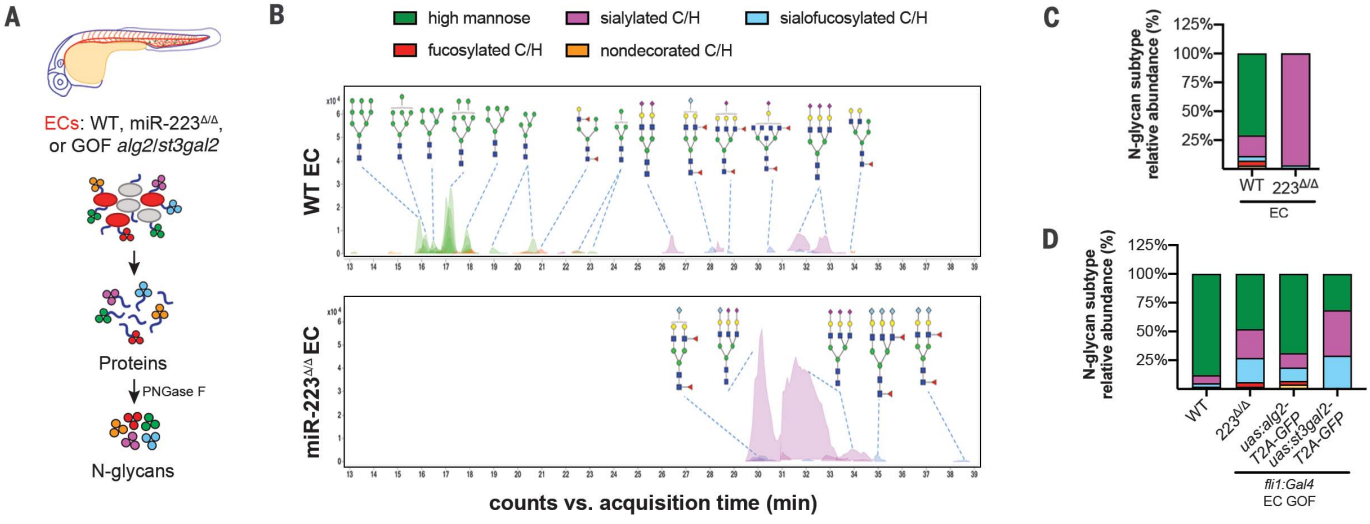

Fig. 3. miR-223 limits EHT and lymphoid-myeloid–oligopotent HSPC production through repression of *alg2* and *st3gal2*. (**A**) (Top) Arrows indicate cmyb:GFP^{+} kdrl:mCh^{+} nascent HSPCs in the zebrafish AGM. (Bottom) Mean ± SEM of cmyb:GFP^{+} kdrl:mCH^{+} cells (n = 28 to 48 embryos). (**B**) (Top) Images or (bottom) mean ± SEM area of T-lymphocyte marker *rag1* expression (n = 28 to 35) embryos and Sudan black^{+} neutrophil clusters (n = 21 or 37 embryos). Abbreviations and significance calculations are as in Fig. 2.

Fig. 4. miR-223 regulates the endothelial glycome. (**A**) Extraction procedure to assess endothelial N-glycan profiles 27 hours after fertilization. Extracted N-glycans were analyzed by means of mass spectrometry (MS). (**B**) MS chromatograms for ECs showing relative abundance of N-glycan subtypes. A subset of the identified N-glycan structures are shown (monosaccharide legend is provided in fig. S8A). (**C** and **D**) Relative abundance of N-glycan subtypes in (C) ECs 27 hours after fertilization or (D) whole embryos. N-glycan subtypes are colored as in (B). EC GOF, endothelial cell gain of function.

HPSC numbers to wild-type levels, suggesting that Adam10a function was enhanced upon miR-223 loss (Fig. 5, B and C). We then overexpressed in ECs the wild-type *adam10a* or a N279 mutant version that prevents the high mannose attachment at this site (fig. S8, H and I) (*20*). We found that wild-type *adam10a*—and, even further, the *adam10a* N279mut—exhibited an expansion of nascent HSPCs in the zebrafish AGM (Fig. 5, B and C). These data suggest that decreased high mannose terminal modification of Adam10a promotes its function and contributes to the EHT phenotype of miR-223$^{\Delta/\Delta}$ embryos.

Discussion

Our study reveals a role for the N-glycan biosynthesis pathway in restricting the production of hemECs, HSPCs, and distinct blood lineages. We discovered an intrinsic mechanism that negatively regulates the transdifferentiation of ECs into oligopotent HSPCs on

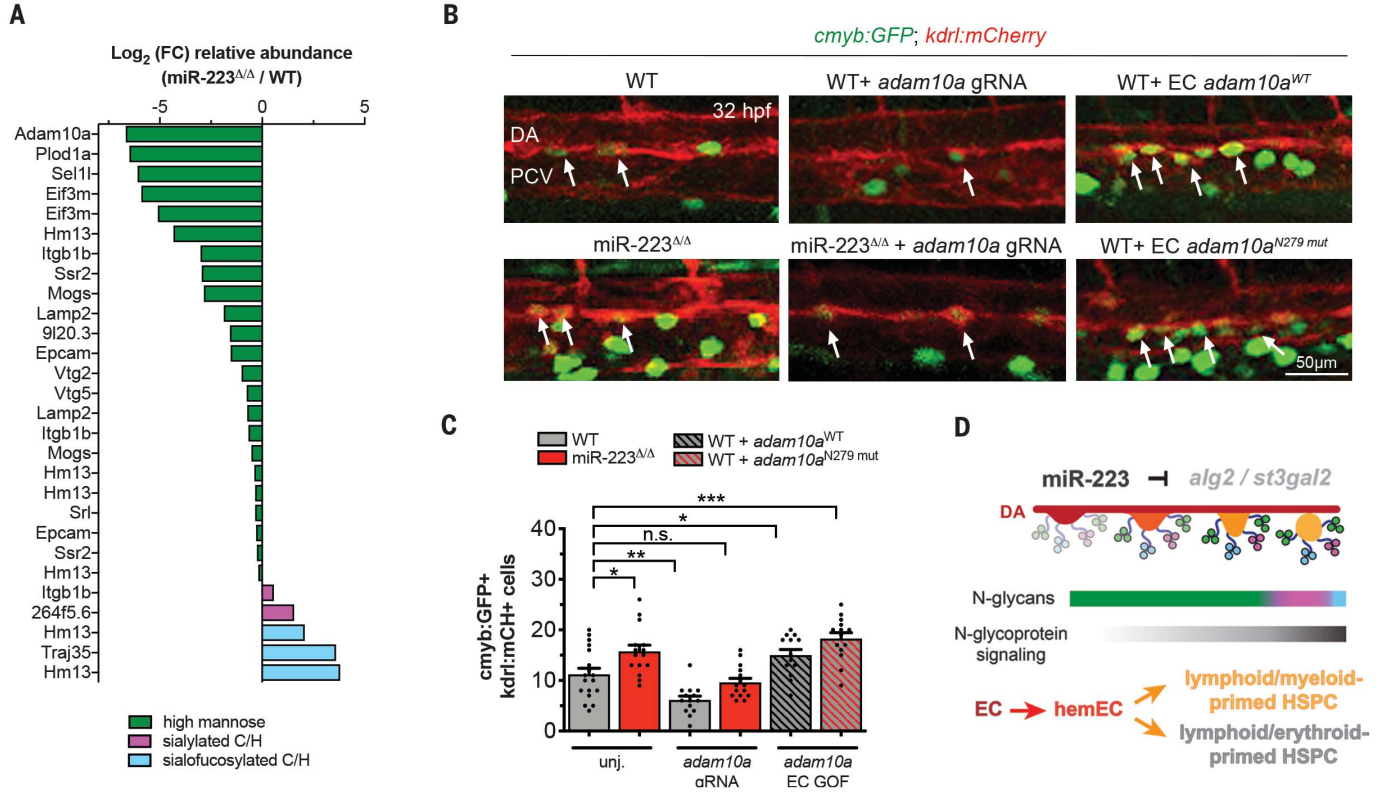

Fig. 5. A distinct N-glycan repertoire regulates protein function to limit EHT. (**A**) Log_2 (fold change) of N-glycan relative abundance for miR-223–regulated N-glycopeptides (n = 3 replicates). (**B**) White arrows indicate nascent HSPCs in the zebrafish AGM of embryos injected with a gRNA that diminishes *adam10a* or with EC gain of function (GOF) *adam10a* constructs. (**C**) Mean ± SEM number of cmyb:GFP$^+$ kdrl:mCH$^+$ HSPCs (n = 13 to 18 embryos). Abbreviations and significance calculations are as in Fig. 2. (**D**) miR-223–dependent regulation of the N-glycome restricts EHT and lymphoid-myeloid HSPC production. In ECs, miR-223 represses *alg2* and *st3gal2* N-glycoenzymes, leading to high mannose-modified (green gradient) versus sialylated-modified (pink and blue gradients) proteins, which restricts (opacity) their signaling (black gradient). EHT cell types and N-glycan subtypes are colored according to Fig. 1E and Fig. 4B, respectively.

the basis of a "sugar code" comprising specific cell-surface glycans, high mannose, and sialylated C/H subtypes. This regulation is mediated through miR-223–dependent repression of N-glycan biosynthesis genes, which controls the glycan repertoire to ensure normal HSPC production and differentiation (Fig. 5D and fig. S8J).

Loss of miR-223–mediated regulation of N-glycoenzymes causes a switch in N-glycans and enhances the function of N-glycoproteins. For example, Adam10a EC-autonomous activity is required for EHT but causes excessive HSPC production when lacking high mannose, probably through enhanced regulation of Notch, TNF-α, and/or other Adam10-dependent signaling pathways.

Furthermore, because EHT is a heterogeneous continuum of cell states (*13*), particular hemECs and nascent HSPCs could require miR-223 regulation of N-glycoprotein–dependent signaling to restrict EHT and balance blood production (Fig. 5D and fig. S8J). Congruently, N-glycoproteins throughout the EHT process could influence the differentiation of oligopotent HSPCs. Our findings lay the foundation for mechanistic studies of how protein N-glycosylation balances the diverse array of hematopoietic regulators during EHT.

The discovery that EHT is regulated by a specific glycan profile provides avenues to explore for the regulation of in vivo and ex vivo blood stem cell production (*21*). The wide variety of known glycan metabolism modifiers and inhibitors could be used to glyco-engineer hemECs, optimizing the production of glycoforms that facilitate somatic cell reprogramming to HSPCs (*22*). Thus, our findings could inform pharmacological strategies to produce HSPCs for therapeutic interventions.

REFERENCES AND NOTES

1. W. K. Clements, D. Traver, *Nat. Rev. Immunol.* **13**, 336–348 (2013).
2. E. Gritz, K. K. Hirschi, *Cell. Mol. Life Sci.* **73**, 1547–1567 (2016).
3. M. Jagannathan-Bogdan, L. I. Zon, *Development* **140**, 2463–2467 (2013).
4. D. M. Kasper, S. Nicoli, *Curr. Stem Cell Rep.* **4**, 22–32 (2018).
5. J. Y. Bertrand *et al.*, *Nature* **464**, 108–111 (2010).
6. J. C. Boisset *et al.*, *Nature* **464**, 116–120 (2010).
7. K. Kissa, P. Herbomel, *Nature* **464**, 112–115 (2010).
8. D. M. Kasper *et al.*, *Dev. Cell* **40**, 552–565.e5 (2017).
9. J. B. Johnnidis *et al.*, *Nature* **451**, 1125–1129 (2008).
10. M. C. Trissal, R. A. DeMoya, A. P. Schmidt, D. C. Link, *PLOS ONE* **10**, e0119304 (2015).
11. W. Zhou *et al.*, *Cell Rep.* **22**, 1810–1823 (2018).
12. E. Butko *et al.*, *Development* **142**, 1050–1061 (2015).
13. C. S. Baron *et al.*, *Nat. Commun.* **9**, 2517 (2018).
14. D. P. Bartel, *Cell* **173**, 20–51 (2018).
15. K. W. Moremen, M. Tiemeyer, A. V. Nairn, *Nat. Rev. Mol. Cell Biol.* **13**, 448–462 (2012).
16. P. M. Lanctot, F. H. Gage, A. P. Varki, *Curr. Opin. Chem. Biol.* **11**, 373–380 (2007).
17. S. S. Pinho, C. A. Reis, *Nat. Rev. Cancer* **15**, 540–555 (2015).
18. G. van Tetering *et al.*, *J. Biol. Chem.* **284**, 31018–31027 (2009).
19. A. Hikita *et al.*, *Biochem. Cell Biol.* **87**, 581–593 (2009).
20. C. Escrevente *et al.*, *Biochim. Biophys. Acta* **1780**, 905–913 (2008).
21. J. R. Perlin, A. L. Robertson, L. I. Zon, *J. Exp. Med.* **214**, 2817–2827 (2017).
22. K. R. Boheler, R. L. Gundry, *Stem Cells Transl. Med.* **6**, 131–138 (2017).

ACKNOWLEDGMENTS

We thank M. Cavanaugh for fish husbandry and care and S. Mehta and the Yale Center for Genome Analysis for scRNA-seq bioinformatic analysis. We also thank A. Andersen (Life Science Editors), V. Greco, D. DiMaio, L. C. Boraas, and S. (Lily) Chen for critical reading of the manuscript. We apologize to those whose original work could not be cited because of space limitations. **Funding:** This work was supported by grants from the NIH (F32HL132475, U54DK106857, and 1K99HL141687 to D.K.; R01HL130246 and R56DK118728 to S.N.; R01HL146056 and R01HL128064 to K.K.H; R01DK118728 to S.N. and K.K.H.; and R01GM049077 to C.L.) and the AHA (19PRE34380749 to Y.W. and 19TPA34890046 to S.N.). **Author contributions:** D.M.K., J.H., and S.N. designed and conducted experiments, analyzed data, and wrote the manuscript. J.G., H.K.M., K.E.S., and W.A. carried out zebrafish experiments and analyzed data. K.K.H., Y.W., and Z.H. designed and performed mouse phenotypic experiments and analyses. C.L., Y.S., and Y. X. conducted glycomic and glycoproteomic analyses. L.K.M., D.W.H., W.C.S., and E.J.P.

contributed N-glycome–related expertise and preliminary data. All authors edited the paper. **Competing interests:** The authors declare no competing interests. **Data and materials availability:** Bulk and single-cell RNA-seq data are submitted to the Gene Expression Omnibus (www.ncbi.nlm.nih.gov/geo/): GSE81341 and GSE135246. Raw Quant-seq reads are in the Sequence Read Archive (www.ncbi.nlm.nih.gov/sra): SRP099466.

SUPPLEMENTARY MATERIALS

science.sciencemag.org/content/370/6521/1186/suppl/DC1
Materials and Methods
Figs. S1 to S8
References (*23*–*28*)
Movies S1 to S3
Data Files S1 to S4

View/request a protocol for this paper from *Bio-protocol*.

21 August 2019; resubmitted 20 May 2020
Accepted 27 October 2020
10.1126/science.aaz2121

NEUROSCIENCE

Shape perception via a high-channel-count neuroprosthesis in monkey visual cortex

Xing Chen[1]*, Feng Wang[1], Eduardo Fernandez[2], Pieter R. Roelfsema[1,3,4]*

Blindness affects 40 million people across the world. A neuroprosthesis could one day restore functional vision in the blind. We implanted a 1024-channel prosthesis in areas V1 and V4 of the visual cortex of monkeys and used electrical stimulation to elicit percepts of dots of light (called phosphenes) on hundreds of electrodes, the locations of which matched the receptive fields of the stimulated neurons. Activity in area V4 predicted phosphene percepts that were elicited in V1. We simultaneously stimulated multiple electrodes to impose visible patterns composed of a number of phosphenes. The monkeys immediately recognized them as simple shapes, motions, or letters. These results demonstrate the potential of electrical stimulation to restore functional, life-enhancing vision in the blind.

Electrical stimulation of the visual cortex has long been proposed as an approach to restore vision in blind people, bypassing severe retinal degeneration or damage to the eye or the optic nerve. Experiments in humans (*1*–*10*) and animals (*11*–*20*) have shown that electrical stimulation of visual cortex can reliably evoke the perception of a dot of light, known as a phosphene. The phosphenes elicited in the primary visual cortex are typically perceived as white or gray dots, although they are occasionally colored (*2*–*4*, *8*), and range in size from a pinpoint to about 2 cm in diameter at arm's length. Subjects perceive phosphenes at the location of the receptive field of the stimulated neurons (*9*, *10*, *17*, *20*). Notably, phosphenes induced in blind but previously sighted subjects are comparable to those in normally sighted subjects, even after decades without sight (*2*, *4*, *8*).

A typical visual prosthesis system would consist of a camera that the user wears on a pair of glasses and a portable processor that transforms camera footage into instructions for electrical stimulation of the visual cortex (*21*). We hypothesized that simultaneous stimulation of multiple electrodes would create recognizable shapes in the user's perception. The generation of artificial percepts would require a substantial number of functional electrodes in the visual cortex, covering a sufficiently large fraction of the visual field. Most previous studies have focused on the properties of individual phosphenes and the electrical stimulation parameters that reliably evoke them. One recent study (*22*) demonstrated shape perception by sequentially stimulating a number of electrodes positioned on the surface of the visual cortex, to trace out a shape. However, sequential stimulation limits the amount of information that can be transferred per unit of time, and the generation of shapes via simultaneous electrical stimulation of multiple electrodes in the visual cortex remains to be demonstrated (*23*, *24*).

[1]Department of Vision & Cognition, Netherlands Institute for Neuroscience, Meibergdreef 47, 1105 BA Amsterdam, Netherlands. [2]Bioengineering Institute and CIBER-BBN, Miguel Hernández University of Elche, Elche, Spain. [3]Department of Integrative Neurophysiology, VU University, De Boelelaan 1085, 1081 HV Amsterdam, Netherlands. [4]Department of Psychiatry, Academic Medical Centre, Postbus 22660, 1100 DD Amsterdam, Netherlands.
*Corresponding author. Email: x.chen@nin.knaw.nl (X.C.); p.roelfsema@nin.knaw.nl (P.R.R.)

An implant with 1024 electrodes in the visual cortex

Most [although not all (*3*, *8*)] previous studies in humans used electrodes that were positioned on the surface of the brain and required delivery of currents in the milliampere range, limiting the number of electrodes that could safely be stimulated at the same time. Surface electrodes activate several millimeters of cortex and produce large phosphenes, and this results in low spatial resolution. Furthermore, previous studies have observed interference between the percepts elicited by simultaneous stimulation on nearby electrodes (*2*, *3*, *11*, *22*). By contrast, microstimulation by intracortical electrodes requires currents that are two orders of magnitude lower (*3*, *8*, *15*, *16*, *19*), activates neurons located within a few hundred micrometers of the electrode tip, and potentially yields higher-resolution phosphene percepts (*25*) (supplementary text).

To investigate the generation of artificial visual percepts using a large number of intracortical electrodes, we created a 1024-channel implant consisting of a titanium pedestal connected to 16 Utah arrays (*26*), each with eight rows and columns of 1.5-mm-long shanks (fig. S1A). We tested the system in two macaque monkeys, L and A. In both monkeys, 14 arrays were tiled across the left primary visual cortex (area V1) (Fig. 1, A and B). Two arrays were placed in V4 (fig. S2), allowing us to monitor the effects of V1 stimulation on neuronal activity in a higher cortical area.

We presented moving bars (*27*) and obtained multiunit receptive fields (RFs) on 820 of 896 and 616 of 896 V1 electrodes and on 120 of 128 and 92 of 128 V4 electrodes in monkeys L and A, respectively (movies S1 and S2). In accordance with known retinotopy (*28*), the RFs covered the foveal and parafoveal regions of the lower right visual field, with V1 RF eccentricities of ≤9° and ≤5° (Fig. 1, C and D) and V4 RF eccentricities of ≤5° and ≤15° in monkeys L and A, respectively (fig. S2).

Saccade-to-phosphene task

We used a saccade-to-phosphene task (Fig. 2A and movie S3) to investigate phosphene locations and determine current thresholds for phosphene perception (N = 184 electrodes in monkey L, and N = 164 in monkey A). The monkeys had previously been trained to make eye movements to visually presented dots on a computer monitor, and we replaced the visual stimuli by electrical microstimulation on individual V1 electrodes. Figure 2B shows the probability of saccade execution as a function of current amplitude during stimulation of an example V1 electrode in monkey L. The current threshold, C_{50}, defined as the level at which the monkey reported the phosphene 50% of the time, was 12.6 μA. Across electrodes, the median threshold in monkey L was 23 μA [interquartile range (IQR), 6 to 40 μA] and in monkey A it was 50 μA (IQR, 43 to 58 μA) (Fig. 2C).

We recorded neuronal activity in V4 during V1 microstimulation (Fig. 2D) and removed the electrical artifacts caused by stimulation from the V4 signal (*28*). Figure 2E shows the mean response across 17 V4 electrodes, during the same session as that in Fig. 2B. The V4 activity increased as a function of V1 current amplitude, with a particularly steep relationship around the C_{50} of the electrode (Fig. 2F). We calculated the neurometric threshold, R_{50}, as the current amplitude at which V4 activity reached 50% of its maximum. The R_{50} was 12.4 μA, similar to the C_{50} of 12.6 μA. Across the currents tested on this V1 electrode, the correlation between the V4 activity level and hit rate was significant [correlation coefficient (r) = 0.94, $p < 0.001$ (Pearson's correlation)].

It would be advantageous if V4 activity could be used more generally to estimate V1 current thresholds, because prospective prosthesis users might experience fatigue during the determination of thresholds on hundreds of electrodes based on visibility reports. The R_{50} could be measured while the user is engaged in an unrelated activity. We observed a high correlation between the R_{50} and C_{50} in both animals [monkey L: r = 0.98, N = 169, $p < 0.001$, 104 unique V1 electrodes for which stimulation artifacts were removed successfully; monkey A: r = 0.96, N = 64, $p < 0.001$, 44 V1

electrodes (Pearson's correlation)] (Fig. 2G). To further test how well V4 activity relates to phosphene visibility, we divided the V1 electrodes into three equally large groups based on the C_{50} and determined the average V4 response as a function of V1 current amplitude within each group (Fig. 2H). The shape of V4 response as a function of current amplitude resembled the psychometric function within each group, confirming that V4 activity can be used to estimate V1 current thresholds.

Although we used a large target window (see methods), the monkeys' eye movements were generally directed toward the RFs of the stimulated neurons (*14*) (compare Fig. 1, E and F to C and D; movie S3). To quantify this relationship, we computed the correlation between the polar angle of the mean saccadic end point and that of the RF (Fig. 2, I and J), which was significant in both monkeys (monkey L: $r = 0.77$, $p < 0.001$, $N = 184$; monkey A: $r = 0.67$, $p < 0.001$, $N = 164$). The correlation between the eccentricity of the saccade end point and that of the RF was also significant [monkey L: $r = 0.90$, $p < 0.001$; monkey A, $r = 0.72$, $p < 0.001$ (Pearson's correlation)], although there was a consistent undershoot of the saccade relative to the RF [saccade amplitude as a fraction of RF eccentricity in monkey L: 0.77 ± 0.18 (mean ± SD), $N = 184$; monkey A: 0.71 ± 0.21, $N = 164$], which was more pronounced for weaker stimulation currents (fig. S3). These findings confirm that phosphenes are perceived at the RF of the stimulated neurons (*9*, *10*, *12*, *14*, *17*, *20*). The next experiments addressed whether multielectrode stimulation elicits interpretable artificial percepts.

Generation of composite visual percepts

First, we tested whether the monkeys could report the spatial alignment of two phosphenes (vertical or horizontal) by requiring them to saccade to a target above or below the fixation spot, respectively (Fig. 3A and movie S4). Before array implantation, the animals were trained extensively on a visual version of the task, in which they reported the relative position of two small dots on a screen. In every session of the microstimulation task, we selected unfamiliar pairs of electrodes for simultaneous stimulation, such that the RFs of the stimulated neurons were vertically or horizontally aligned.

Figure 3B shows the results for an example session, with mean accuracies of 91 and 88% for the vertical and horizontal conditions, respectively. Performance was above chance level from the start of the session even though the electrode set was novel, which suggests that the monkey generalized its understanding from the visual to the phosphene version of the task. The average accuracy across sessions with novel electrode pairs was significantly above chance [monkey L: 70 ± 13%, $N = 19$ electrode sets, $t_{18} = 6.6$, $p < 0.001$; monkey A: 64 ± 18%, $N = 11$, $t_{10} = 2.6$, $p = 0.026$ (one-sample t test)] (Fig. 3C). We also ran a visual version of the task in which we presented dots on the screen at the RF locations. Monkey L reached an accuracy of 83 ± 10% ($t_{18} = 15$, $p < 0.001$), and monkey A 79 ± 15% ($t_{10} = 6.2$, $p < 0.001$). These visually presented dot configurations were not always novel, that is, the monkeys had seen some of these dot pairs in previous sessions.

We rewarded the monkeys after correct saccades; hence, they might have learned to associate arbitrary phosphene percepts with specific targets by trial and error. We therefore computed the mean accuracy across electrode sets during the first 30 trials of the microstimulation task (Fig. 3D). The animals' accuracies remained relatively stable across time. For both monkeys, we determined the critical trial, c, for which the accuracy was higher than chance ($p < 0.05$, binomial test) when trials 1 through c were included, across electrode sets (*28*). In monkey L, c was the first trial [responses were correct on 17 of 19 electrode sets; $p < 0.001$ (binomial test)], and in monkey A, c was the fourth trial (30 of 44 electrode sets and trials; $p = 0.011$). Furthermore, no significant improvement in performance occurred between trials 1 to 10 and trials 21 to 30 [monkey L: $t_{18} = 0.0$, $p = 1.0$; monkey A: $t_{10} = 0.17$, $p = 0.87$ (paired t test)]. We conclude that the monkeys generalized from their experience on the visual task to judge whether novel phosphene pairs were horizontally or vertically aligned.

Direction-of-motion task

The monkeys had also been trained to report the apparent motion direction of a sequence of visually presented dots. We investigated whether the monkeys could interpret the direction of successively generated phosphenes (Fig. 3E and movie S5). We selected three electrodes with a vertical or horizontal offset and stimulated them sequentially such that their RFs formed a sequence, going from top to bottom or bottom

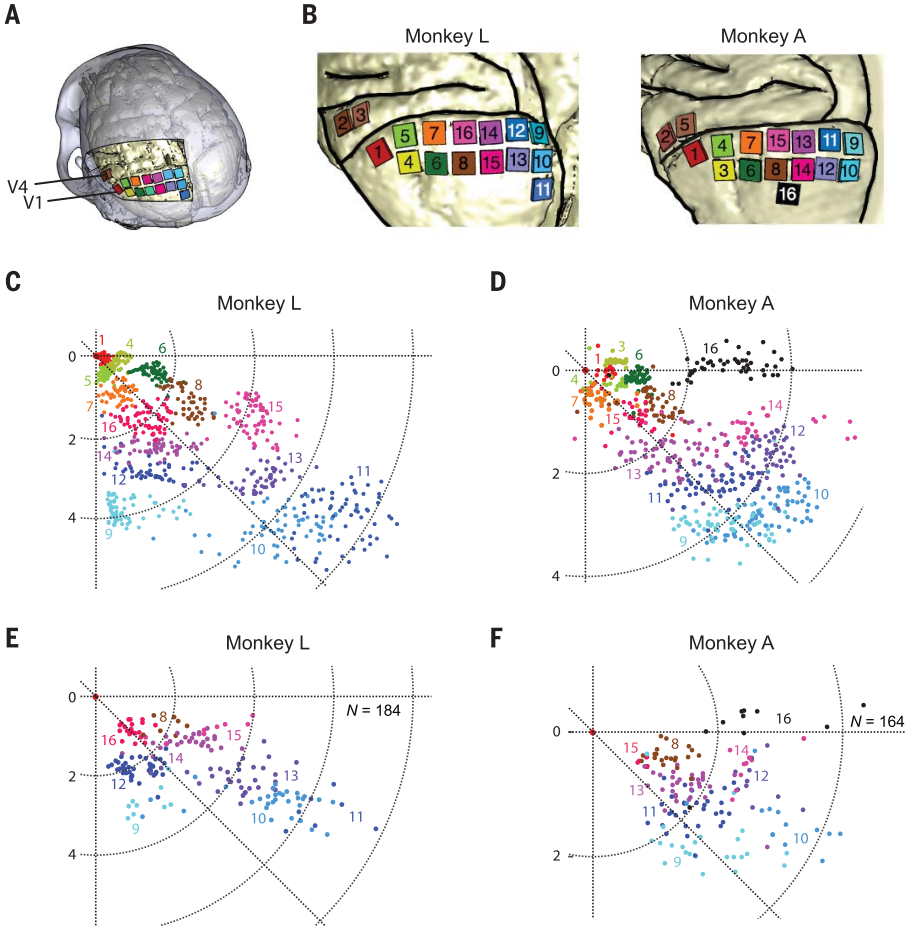

Fig. 1. Location of electrodes and receptive fields. (**A**) Locations of arrays in areas V1 and V4 of the visual cortex in the left hemisphere of monkey L. (**B**) Higher-magnification view of array locations. Array numbers correspond to the order of attachment between the arrays and the pedestal. (**C** and **D**) RF centers. Colors correspond to those of the arrays in (A) and (B). (**E** and **F**) Average saccadic end points. Colors correspond to those of the arrays in (A) and (B).

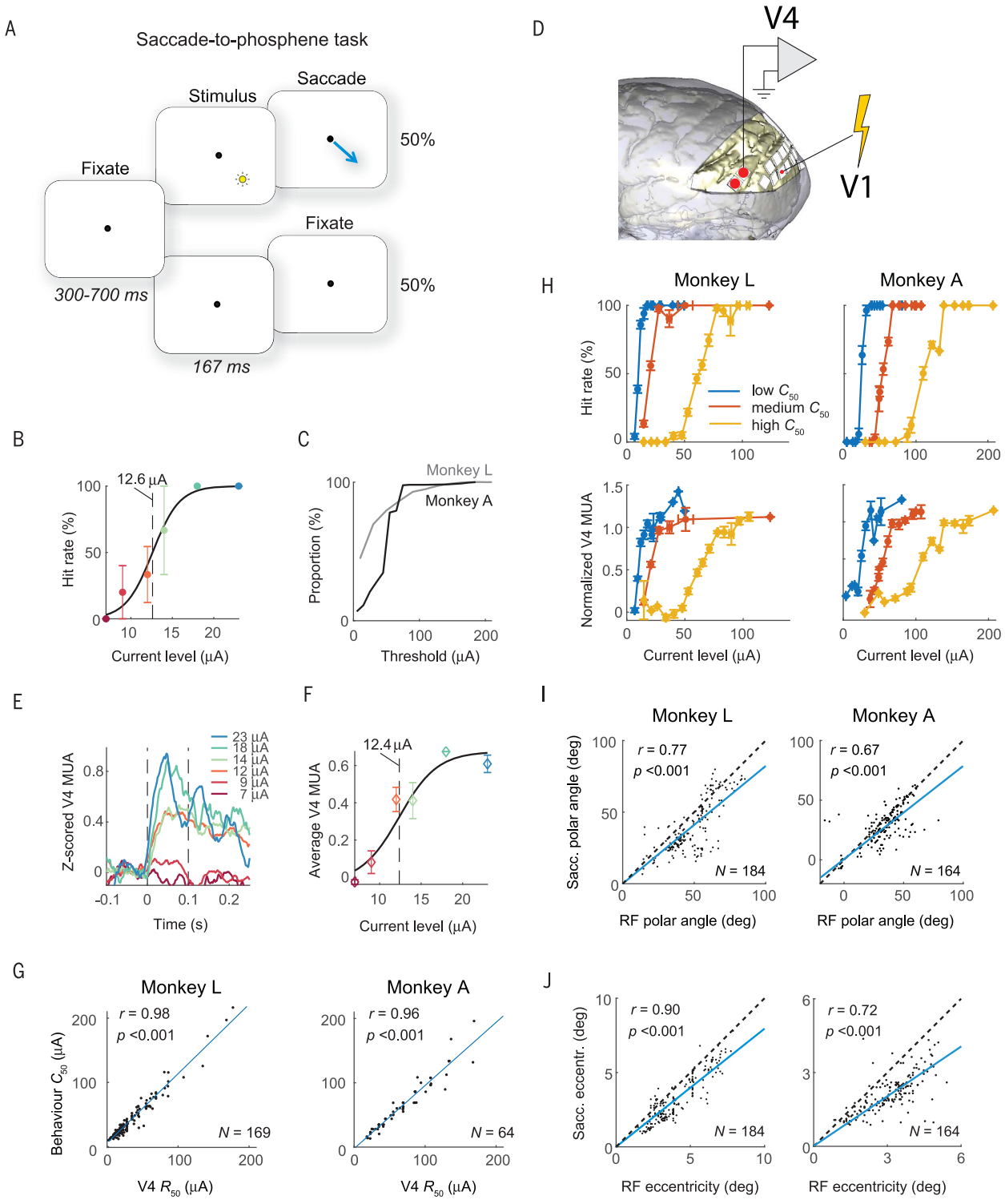

Fig. 2. Saccade-to-phosphene task. (**A**) Illustration of the task. The yellow circle represents a phosphene; the arrow represents an eye movement to the artificially induced perception. (**B**) Probability of eliciting a saccade, as a function of current amplitude, during stimulation on an example V1 electrode in monkey L. The dashed line indicates the current threshold; error bars represent SEM. (**C**) Cumulative distribution of current thresholds. (**D**) Schematic showing recording from V4 during V1 microstimulation. (**E**) Time course of activity (relative to stimulation onset), averaged across V4 channels during V1 microstimulation [same session as in (B)]. The dashed lines indicate the time window during which V4 activity was measured. (**F**) V4 activity as a function of stimulation current [same session as in (B) and (E)]. The dashed line indicates the current threshold; error bars represent SEM. (**G**) Correlation between current thresholds derived from neurometric (R_{50}) and psychometric functions (C_{50}). (**H**) Mean performance (top) and mean V4 response (bottom) as a function of current amplitude for V1 electrodes with low (blue), intermediate (red), and high thresholds (yellow; tertiles). Vertical error bars represent SEM of performance levels (upper) or V4 responses (lower); horizontal error bars represent SEM of current levels. (**I** and **J**) Comparison of polar angle (I) and eccentricity (J) between RFs and saccadic end points. The blue line shows a linear regression, which was constrained to pass through the origin.

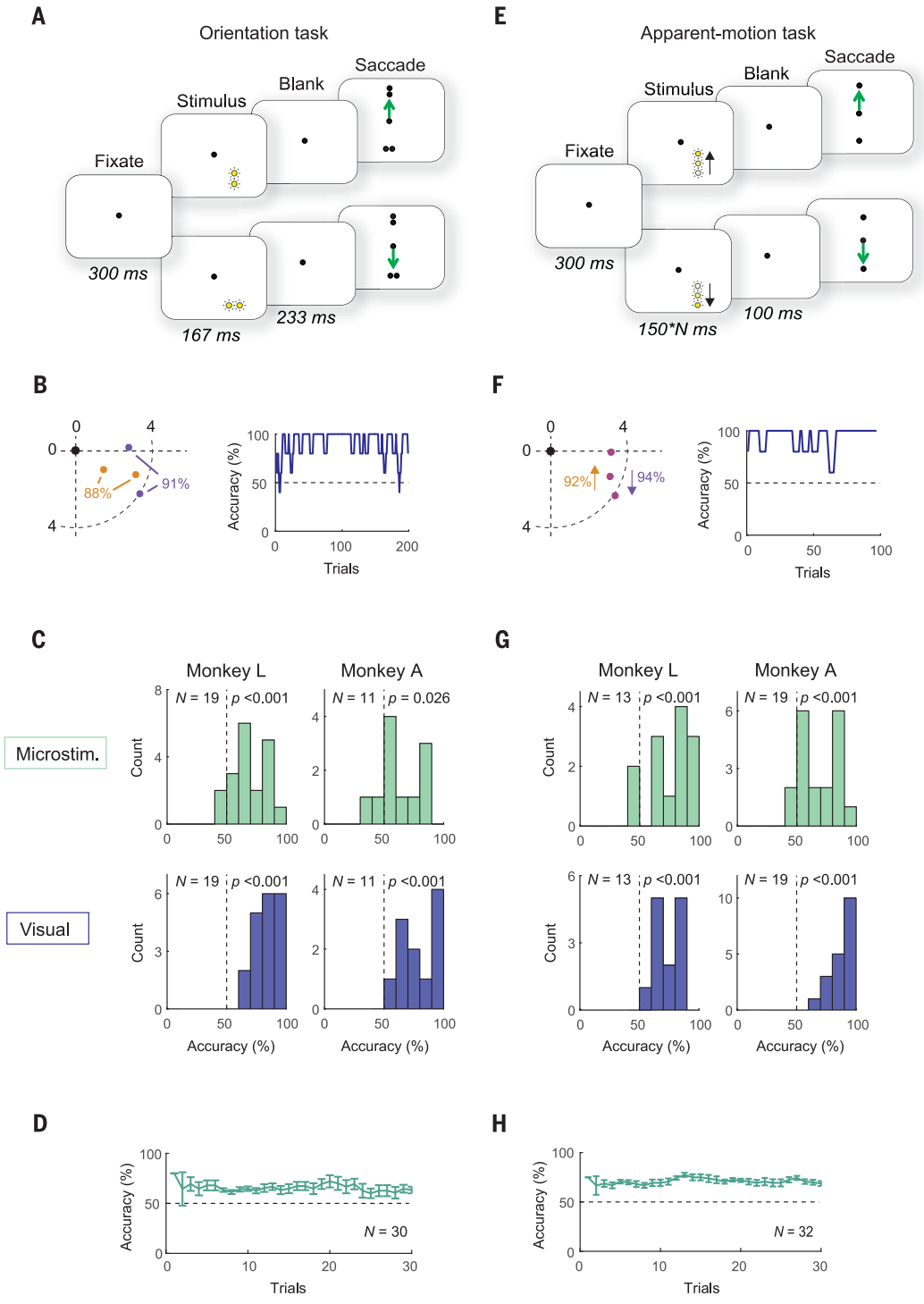

Fig. 3. Two-phosphene orientation and direction of motion task. (**A**) Two-phosphene orientation discrimination task. The monkey reported with an eye movement whether two phosphenes (or visually presented dots) were oriented horizontally or vertically. (**B**) (Left) RF centers for an example set of four electrodes in monkey A. Black circle, fixation point; orange dots, horizontal condition; purple dots, vertical condition. (Right) Accuracy (averaged across five trials) for this example set. (**C**) Distribution of accuracies across electrode sets during microstimulation (green) and visual (blue) versions of the task. (**D**) Mean accuracy across electrode sets and monkeys, as a function of trial number, on the microstimulation version of the task (averages and SEM across five trials). (**E**) Direction-of-motion task. (**F**) (Left) RF centers for an example set of three electrodes, stimulated in sequence (indicated by arrows). (Right) Accuracy for this example set. (**G** and **H**) Similar to (C) and (D), for the direction-of-motion task.

to top for "vertical" sets of electrodes and left to right or right to left for "horizontal" sets of electrodes. Figure 3F illustrates an example session in monkey A, in which the RFs had a vertical offset and the monkey reached high accuracy from the first trial onward. Across all electrode sets of the microstimulation task (Fig. 3G), the average accuracies of monkeys L and A were 76 ± 17% [$N = 13$, $t_{12} = 5.5$, $p < 0.001$ (t test)] and 69 ± 16% ($N = 19$, $t_{18} = 5.2$, $p < 0.001$), respectively. The monkeys' accuracies for novel electrode combinations were higher than chance from the first trials onward. The critical trial c was trial 1 in monkey L (correct on the first trial in 11 of 13 sessions; $p = 0.011$) and trial 4 in monkey A (trials 1 to 4, 48 of 76 correct; $p = 0.014$) (Fig. 3H), indicating that they were able to generalize their understanding of apparent motion from the visual to the phosphene task. No significant improvement in performance occurred between trials 1 to 10 and trials 21 to 30 [monkey L: $t_{12} = 1.35$, $p = 0.2$; monkey A: $t_{18} = -1.85$, $p = 0.08$ (paired t test)]. The accuracies of monkeys L and A in the task with a sequence of visually presented dots were 74 ± 11% ($t_{12} = 8.2$, $p < 0.001$) and 89 ± 11% ($t_{18} = 15.6$, $p < 0.001$), respectively, although these dot combinations were not always novel.

Letter task

Next, we examined the possibility of creating more complex shape percepts. We delivered

stimulation on 8, 10, or 15 electrodes in V1 simultaneously, selecting the electrode sets such that the RFs collectively formed the shape of one of two letters. The number of stimulated electrodes was always the same between the two conditions in a given session. Before electrode implantation, the monkeys had learned to report the identity of 16 visually presented letters on a screen by making an eye movement to a target. The training program also included letters presented as sparse dot patterns, designed to simulate phosphene vision (fig. S4) (*29*). After array implantation, the training continued, and we initially alternated visual and microstimulation blocks. Thereafter, sessions consisted solely of visual or microstimulation trials. During visual trials, one of two letters was presented as a dot pattern on the screen. During microstimulation trials, we delivered simultaneous electrical stimulation to a novel set of electrodes for 167 ms (50 pulses at 300 Hz) (Fig. 4A and movie S6).

Figure 4B shows the accuracy of monkey A for an example set of electrodes on the microstimulation version of the task. In one condition, the RFs of the stimulated electrodes formed the letter T (orange dots) and in the other condition they formed the letter L (purple dots). In this example session, accuracy was 0.89 and 0.96 for the T and L conditions, respectively, and it was relatively high from the first trial onward. Across all electrode sets (Fig. 4C), the average accuracy of monkey L was 81 ± 18% [$N = 9$, $t_8 = 5.4$, $p < 0.001$ (t test)] and the accuracy of monkey A was 71 ± 18% ($N = 10$, $t_9 = 3.6$, $p = 0.006$) on the microstimulation version of the task. Accuracy on the visual version of the task was 88 ± 5% for monkey L ($t_8 = 23.1$, $p < 0.001$) and 93 ± 4% for monkey A ($t_9 = 36.7$, $p < 0.001$), although some of these dot displays were not novel.

To control for the possibility that the monkeys learned to map arbitrary percepts onto saccade targets, we examined the accuracy time course (Fig. 4D). The critical trial c (accuracy above chance level, binomial test) was trial 3 in monkey L (20 of 27 correct, $p = 0.0096$), and trial 7 in monkey A (43 of 70 correct, $p = 0.036$). No significant improvement in performance occurred between trials 1 to 10 and trials 21 to 30 [monkey L: $t_8 = -0.7$, $p = 0.5$; monkey A: $t_9 = 0.7$, $p = 0.5$ (paired t test)].

As a further control, we examined how long it took the monkeys to associate arbitrary microstimulation patterns with eye movements. We selected novel, nonoverlapping combinations of electrodes, such that their RFs did not form any recognizable letter ($N = 10$ electrode sets in both monkeys). The mean accuracy of monkeys L and A during the first 100 trials was close to chance level (48.2 and 46.9%; $p > 0.2$ in both monkeys) (gray data points in Fig. 4D) and lower than during the first 100 trials of the microstimulation task with familiar letters (monkey L, $t_{17} = 5.7$, $p < 0.001$; monkey A, $t_{18} = 2.4$, $p = 0.03$). We also ran a visual version of the control task, in which the monkeys saw two novel visual dot stimuli. The mean accuracies of monkeys L and A were 50.5 and 49.9%, respectively ($p > 0.9$), indicating that they also failed to rapidly learn to map unfamiliar dot stimuli onto saccade targets (Fig. 4D and fig. S5).

These results indicate that the monkeys' abilities to perform the letter task were not due to rapid learning of new associations between stimuli and eye movement targets. Rather, the phosphene percepts must have borne a close resemblance to the visually presented letters, allowing the monkeys to benefit from their extensive prior experience.

Discussion

We demonstrated that the simultaneous stimulation of multiple electrodes in V1 gives rise to the perception of shape and that successive stimulation gives rise to the perception of motion, providing proof of concept for the use of electrical microstimulation to create a form of artificial vision in the blind. Previous studies suggested that the successful generation of phosphene percepts can be read out in higher visual cortical areas (*30*, *31*). Here, we demonstrated how V4 activity can be used to determine phosphene thresholds in V1, circumventing a time-consuming calibration process in which the prosthesis user has to report whether currents are above or below the perceptual threshold on hundreds of electrodes.

These results capitalized on several developments. First, we implanted a large number of electrodes with foveal and parafoveal coverage of one quadrant of the visual field. Simulations of phosphene vision estimated that whereas letter recognition is possible with a few hundred electrodes, fluent reading and object recognition in crowded scenes may require thousands of electrodes (*32*, *33*). By implanting more than 1000 electrodes across a large area of V1, we could generate numerous phosphenes across a contiguous region of the visual field (Fig. 1) and elicit recognizable shapes (Figs. 3 and 4).

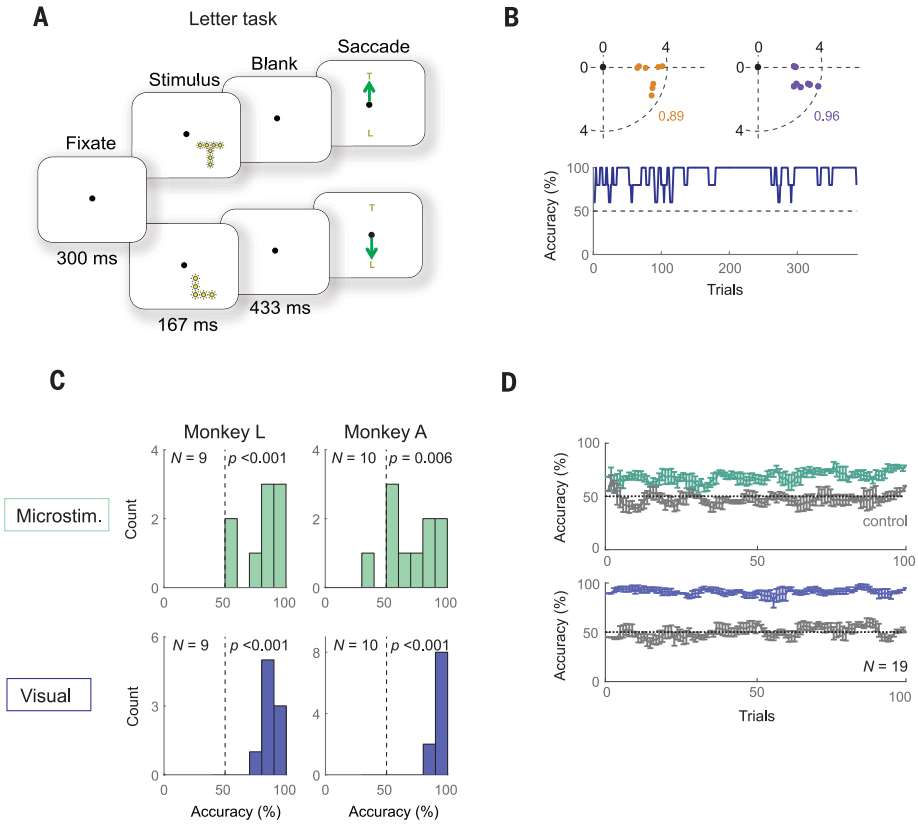

Fig. 4. Letter recognition task. (**A**) Illustration of the task. The monkey reported letter identity with an eye movement. (**B**) (Top) RF centers of eight stimulated V1 electrodes whose RF centers formed a T or an L (orange and purple circles). (Bottom) Accuracy (smoothed across five trials) for this example set. (**C**) Accuracy for sessions on microstimulation (green) and visual (blue) versions of the task. (**D**) Mean accuracy across electrode sets and monkeys, as a function of trial number (average and SEM across five trials) in the microstimulation (green) and visual (blue) versions of the task. In a control task with novel electrical stimulation and visually presented dot patterns, the accuracy was close to chance (gray).

Secondly, we used intracortical electrodes, which have advantages over the subdural electrodes used in previous human studies (*2*, *10*, *34*). Subdural electrodes require currents in the milliampere range and activate populations of neurons across millimeters of cortex (*9*, *10*), which limits their resolution. Furthermore, the stimulation of adjacent subdural electrodes may cause interference, generating a single, large phosphene instead of several small ones. Using depth electrodes, we elicited phosphenes with median stimulation currents of 23 to 50 μA, which activate small populations of neurons located within a few hundred micrometers of the electrode tip (*25*). Hence, intracortical electrodes induce smaller and more precise phosphene percepts (*3*, *8*), but a systematic comparison of phosphenes produced by subdural and intracortical stimulation has yet to be performed (supplementary text) (*24*).

Third, before implantation the monkeys underwent intensive training on visual versions of the tasks, in which they saw shapes composed of small dots, designed to simulate phosphene percepts (*29*). As a result, the monkeys were immediately able to correctly interpret shape and motion stimuli composed of multiple phosphenes. Nevertheless, the monkeys made mistakes and even performed close to chance for several electrode sets. The accuracy in the tasks with visually presented dot patterns was also not perfect, indicating that the monkeys did not always recognize them, although this may have been caused by occasional drops in motivation (e.g., at the end of a recording session). We expected the accuracy for the tasks with electrical stimulation to be worse, because it is not possible to control the appearance of individual phosphenes. Humans report that phosphenes induced by stimulation of early visual cortical areas vary in color, brightness, shape, and perceived distance (*3*, *6*, *8*, *35*). Furthermore, simultaneous stimulation on two electrodes that are a few hundred micrometers apart can yield fused phosphenes (*3*). Such variability and potential interactions may make electrically induced percepts more difficult to interpret than visually presented ones.

A number of technical hurdles still have to be overcome before a visual cortical prosthesis is available for humans. The mean surface area of human primary visual cortex is 25 to 30 cm^2 per hemisphere, and future implants should cover a large enough region of the visual field with a sufficient density of phosphenes to generate interpretable percepts (*36*, *37*). Furthermore, it will be necessary to create wireless technology with high channel counts and to develop long-lasting, biocompatible electrodes that minimize the risk of gliosis, tissue trauma, and encapsulation (*38*). Much progress is being made in the development of brain-computer interfaces for sensory restoration and motor prostheses (*39*–*41*). Combined with the present demonstration of artificial vision, these developments place a light at the end of the tunnel for those without sight.

REFERENCES AND NOTES

1. W. H. Dobelle, M. G. Mladejovsky, J. P. Girvin, *Science* **183**, 440–444 (1974).
2. J. Button, T. Putnam, *J. Iowa Med. Soc.* **52**, 17 (1962).
3. G. S. Brindley, W. S. Lewin, *J. Physiol.* **196**, 479–493 (1968).
4. M. Bak *et al*., *Med. Biol. Eng. Comput.* **28**, 257–259 (1990).
5. W. H. Dobelle, M. G. Mladejovsky, J. R. Evans, T. S. Roberts, J. P. Girvin, *Nature* **259**, 111–112 (1976).
6. J. R. Evans, J. Gordon, I. Abramov, M. G. Mladejovsky, W. H. Dobelle, *Sens. Processes* **3**, 82–94 (1979).
7. D. N. Rushton, G. S. Brindley, in *Physiological Aspects of Clinical Neurology*, F. C. Rose, Ed. (Blackwell Scientific Publications, ed. 1, 1977), pp. 123–153.
8. E. M. Schmidt *et al*., *Brain* **119**, 507–522 (1996).
9. J. Winawer, J. Parvizi, *Neuron* **92**, 1213–1219 (2016).
10. W. H. Bosking *et al*., *J. Neurosci.* **37**, 7188–7197 (2017).
11. J. R. Bartlett *et al*., *J. Neurophysiol.* **94**, 3430–3442 (2005).
12. D. C. Bradley *et al*., *J. Neurophysiol.* **93**, 1659–1670 (2005).
13. E. A. DeYoe, J. D. Lewine, R. W. Doty, *J. Neurophysiol.* **94**, 3443–3450 (2005).
14. T. S. Davis *et al*., *J. Neural Eng.* **9**, 065003 (2012).
15. B. Dagnino, M. A. Gariel-Mathis, P. R. Roelfsema, *J. Neurophysiol.* **113**, 730–739 (2015).
16. D. K. Murphey, J. H. R. Maunsell, *Curr. Biol.* **17**, 862–867 (2007).
17. E. J. Tehovnik, W. M. Slocum, P. H. Schiller, *Eur. J. Neurosci.* **17**, 870–878 (2003).
18. E. J. Tehovnik, W. M. Slocum, *Eur. J. Neurosci.* **29**, 1477–1489 (2009).
19. K. Torab *et al*., *J. Neural Eng.* **8**, 035001 (2011).
20. P. Troyk *et al*., *Artif. Organs* **27**, 1005–1015 (2003).
21. P. M. Lewis, J. V. Rosenfeld, *Brain Res.* **1630**, 208–224 (2016).
22. M. S. Beauchamp *et al*., *Cell* **181**, 774–783.e5 (2020).
23. W. H. Bosking, M. S. Beauchamp, D. Yoshor, *Annu. Rev. Vis. Sci.* **3**, 141–166 (2017).
24. A. N. Foroushani, C. C. Pack, M. Sawan, *J. Neural Eng.* **15**, 021005 (2018).
25. M. H. Histed, V. Bonin, R. C. Reid, *Neuron* **63**, 508–522 (2009).
26. P. J. Rousche, R. A. Normann, *J. Neurosci. Methods* **82**, 1–15 (1998).
27. Materials and methods are available as supplementary materials.
28. R. B. Tootell, E. Switkes, M. S. Silverman, S. L. Hamilton, *J. Neurosci.* **8**, 1531–1568 (1988).
29. N. J. Killian, M. Vurro, S. B. Keith, M. J. Kyada, J. S. Pezaris, *Sci. Rep.* **6**, 36329 (2016).
30. M. S. Beauchamp, P. Sun, S. H. Baum, A. S. Tolias, D. Yoshor, *Nat. Neurosci.* **15**, 957–959 (2012).
31. B. van Vugt *et al*., *Science* **360**, 537–542 (2018).
32. B. Bourkiza, M. Vurro, A. Jeffries, J. S. Pezaris, *PLOS ONE* **8**, e73592 (2013).
33. J.-H. Jung, D. Aloni, Y. Yitzhaky, E. Peli, *Vision Res.* **111**, 182–196 (2015).
34. W. H. Dobelle, M. G. Mladejovsky, *J. Physiol.* **243**, 553–576 (1974).
35. P. H. Schiller, W. M. Slocum, M. C. Kwak, G. L. Kendall, E. J. Tehovnik, *Proc. Natl. Acad. Sci. U.S.A.* **108**, 17809–17814 (2011).
36. L. E. Hallum, G. Dagnelie, G. J. Suaning, N. H. Lovell, *J. Neural Eng.* **4**, S58–S71 (2007).
37. S. C. Chen, G. J. Suaning, J. W. Morley, N. H. Lovell, *Vision Res.* **49**, 2329–2343 (2009).
38. L. Luan *et al*., *Sci. Adv.* **3**, e1601966 (2017).
39. P. R. Roelfsema, D. Denys, P. C. Klink, *Trends Cogn. Sci.* **22**, 598–610 (2018).
40. S. N. Flesher *et al*., *Sci. Transl. Med.* **8**, 361ra141 (2016).
41. L. R. Hochberg *et al*., *Nature* **485**, 372 (2012).
42. X. Chen, F. Wang, E. Fernandez, P. Roelfsema, Data repository for "Shape perception via a high-channel-count neuroprosthesis in monkey visual cortex," Version 1, Mendeley Data (2020); https://doi.org/10.17632/gx39r48w3b.1.

ACKNOWLEDGMENTS

We thank K. Brandsma, A. Ditewig, and L. Beekman for biotechnical support; M. Self and R. Schuurman for assistance during surgeries; and B. Li, R. van Wezel, J.-A. Sahel, S. Picaud, R. Goebel, M. Self, and G. Dagnelie for feedback on the manuscript. We thank F. Solzbacher, M. Gerhardt, R. Franklin, N. Halper, S. Hou, K. Torab, and others at Blackrock Microsystems for assistance. **Funding:** The work was supported by NWO (STW-Perspectief P15-42 "NESTOR"), the European Union FP7 (ERC 339490 "Cortic_al_gorithms"), the Human Brain Project (agreements 720270 and 785907, "Human Brain Project SGA1 and SGA2"), and the Friends Foundation of the Netherlands Institute for Neuroscience. **Author contributions:** X.C. and P.R.R. designed the study with input from E.F.; X.C. ran the experiments and collected the data; X.C. and F.W. analyzed the data; X.C., P.R.R., and F.W. wrote the manuscript with advice from E.F.; and P.R.R. supervised the project. **Competing interests:** P.R.R. and X.C. are cofounders and shareholders of a neurotechnology start-up, Phosphoenix (Netherlands). P.R.R. and X.C. registered a patent related to this work, WO2020043790 (A1). **Data and materials availability:** The data and the computer code used to analyze the data are available for download from Mendeley Data (*42*).

SUPPLEMENTARY MATERIALS

science.sciencemag.org/content/370/6521/1191/suppl/DC1
Materials and Methods
Supplementary Text
Figs. S1 to S6
References (*43*–*56*)
MDAR Reproducibility Checklist
Movies S1 to S6

View/request a protocol for this paper from *Bio-protocol*.

14 July 2020; accepted 19 October 2020
10.1126/science.abd7435

REPORT

PLANT SCIENCE

The exploitative segregation of plant roots

Ciro Cabal[1]*, Ricardo Martínez-García[2,1], Aurora de Castro Aguilar[3], Fernando Valladares[3,4], Stephen W. Pacala[1]

Plant roots determine carbon uptake, survivorship, and agricultural yield and represent a large proportion of the world's vegetation carbon pool. Study of belowground competition, unlike aboveground shoot competition, is hampered by our inability to observe roots. We developed a consumer-resource model based in game theory that predicts the root density spatial distribution of individual plants and tested the model predictions in a greenhouse experiment. Plants in the experiment reacted to neighbors as predicted by the model's evolutionary stable equilibrium, by both overinvesting in nearby roots and reducing their root foraging range. We thereby provide a theoretical foundation for belowground allocation of carbon by vegetation that reconciles seemingly contradictory experimental results such as root segregation and the tragedy of the commons in plant roots.

A root system's ability to obtain soil resources essential for growth and survival determines a plant's yield and is highly influenced by competition with other plants' roots (*1*). However, we have few observations of intact root systems in soil and lack a comprehensive theory for root system responses to their environment (*2*). Agricultural technologists need to understand the mechanisms by which plants compete belowground to design and breed ideal cultivars (*3*). Understanding the response of these cultivars to different plant densities is crucial to optimize crop resource-use efficiency and maximize food production (*4*). Additionally, plant roots represent a large carbon pool that stores approximately a third of the world's phytomass (*5*), and understanding how roots respond to belowground competition is critical to predict vegetation carbon uptake and to design strategies to mitigate climate change (*6*). Here, we develop a game-theoretic model that predicts how one plant's roots will respond to roots of nearby plants. We also present a dataset describing spatial distributions of root density for individual plants, and how these respond to competition, confirming model predictions.

Plants can sense soil resources (*7*) and the presence of nonself (*8*) and nonkin roots (*9*) and respond phenotypically to these stimuli (*10*). However, published data have been contradictory about the direction of the belowground plastic responses to the presence of competitors and unclear about the mechanisms. Studies of changes in vertical or horizontal root foraging ranges often conclude that neighboring plants tend to minimize the overlap between their root systems (root segregation) (*11*). A second group of studies examines the effect of competition on the total carbon allocated to roots (*12*). Among these, some report a decrease in plants' allocation of carbon to roots (*13*, *14*), presumably in accordance with root segregation; others report an increase (*15*–*17*); and still others find no significant effect (*18*, *19*). Neither of these approaches is complete. The former considers only the foraging range but neglects the distribution of root density within that range,

[1]Department of Ecology and Evolutionary Biology, Princeton University, Princeton, NJ 08544, USA. [2]ICTP-South American Institute for Fundamental Research–Instituto de Física Teórica da UNESP, Rua Dr. Bento Teobaldo Ferraz 271, 01140-070 Sao Paulo SP, Brazil. [3]Department of Biogeography and Global Change, National Museum of Natural Sciences MNCN, CSIC, Madrid 28006, Spain. [4]Department of Biology, Geology, Physics and Inorganic Chemistry, Rey Juan Carlos University, Móstoles 28933, Spain.
*Corresponding author. Email: ccabal@princeton.edu

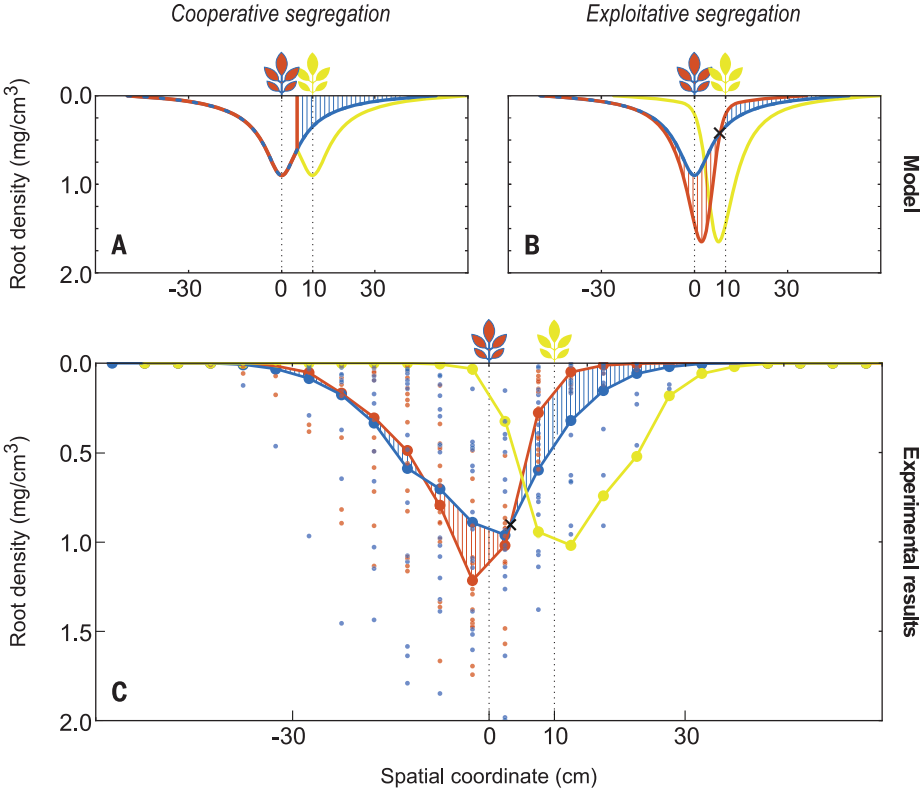

Fig. 1. Spatial distribution across one horizontal dimension of root density in solitary plants and pairs of interacting individuals separated by a distance *d* = 10 cm. The *y* axis measures root density, not depth. (**A** to **C**) Results from the mathematical model solved under (A) Pareto conditions and (B) an ESS equilibrium, and (C) empirical results. Orange lines (and circles) correspond to a focal plant that is interacting with a neighbor (yellow), and blue lines (and circles) correspond to solitary plant, both centered at the zero spatial coordinate. Areas shaded with vertical bars indicate the differences between the root systems of the solitary and the focal interacting plants at each distance from their insertion to the substrate, orange bars indicate local root overproduction, and blue bars indicate local root underproliferation of the focal interacting plant. The black cross indicates the position of the shifting point (*S*). In (c), small circles represent the data, large circles represent the mean root density at a given spatial coordinate, and lines represent linear interpolations between the means. See materials and methods (supplementary material) for details.

and the latter ignores the spatial distribution of roots. Few have considered both features of root systems together [but see (*20*)].

Theoretical studies have added to the confusion in the literature. Some modeling studies rely on simple optimization, in which roots are assumed to equalize average nutrient uptake per unit rooting effort across space (*21*). Others incorporate game theory (*22*) and predict that plants will engage in a belowground tragedy of the commons (*23*–*25*) sensu Hardin (*26*) and should thus overallocate to roots in the presence of a neighbor. Game-theoretical approaches, like the empirical ones, have generally not looked simultaneously at total allocation and spatial distribution [but see (*27*)].

We developed a spatially explicit game-theoretical framework describing plant competition for a soil resource (supplementary materials). Our model explicitly incorporates soil resource dynamics and a distance-dependent foraging cost. The fitness cost of accessing a soil patch at a distance from the stem accounts for the cost of proliferating and maintaining absorbing roots inside the patch and transporting roots from the patch to the stem. Game-theoretic equilibrium solutions can be obtained either by assuming that plants adopt the strategy that produces the highest possible fitness for the collective (cooperative equilibrium) or by maximizing their competitive ability [evolutionary stable strategy (ESS)] (*28*). Cooperative fitness maximization implies that plants should collectively maximize resource uptake per unit of root cost (a fitness surrogate). To do so, they would need either to directly recognize nonself roots and their cost to the neighbor or to have been artificially selected to deploy roots that maximize collective production given a fixed spatial pattern of individuals. This strategy represents a potential target for crop optimization. In the ESS, each individual plant maximizes its own uptake per unit cost. This is the plant strategy that presumably evolves by natural selection.

To analyze the phenotypical response of plants to competition, we compared root spatial distributions predicted by a model of a solitary plant (bell-shaped root distribution centered at the insertion to the substrate) and a plant facing a neighbor. When plants in competition were assumed to follow a cooperative strategy (Fig. 1A), root behavior showed cooperative segregation; that is, each plant withdrew from any location where it sensed nonself roots having lower exploitation costs. However, when plants were assumed to embrace an ESS, the model predicted exploitative segregation; that is, the range of the root system was shortened on the side facing a neighbor, but plants locally overproliferated roots close to their own insertion point (Fig. 1B; see supplementary materials for representations in three dimensional soil). The shifting point S defines the distance from the plant-shoot insertion to the substrate at which the strategy shifts from root overproliferation to underproliferation. Both the over- and underproliferation predicted by the ESS simply optimize a plants' resource economy when in competition and do not require direct sensing of nonself roots.

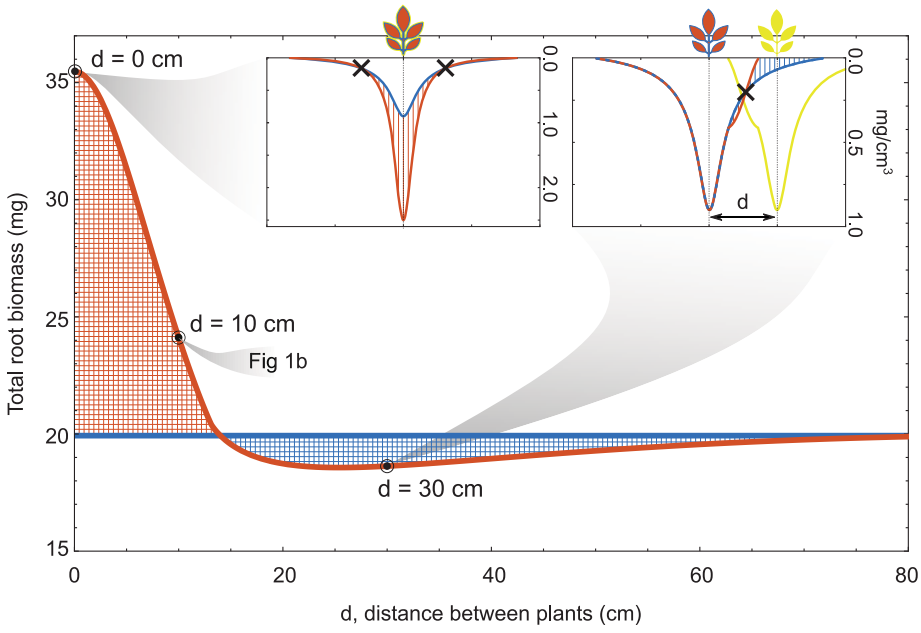

Fig. 2. ESS model prediction of a plant's total root biomass (integral of the spatial distribution of root density). The blue line indicates a solitary plant andthe orange line indicates a focal interacting plant, at increasing distance from an interacting neighbor (*d*, centimeters). The orange-hatched area indicates an increase and blue-hatched area a decrease in total plant root biomass as a response to the presence of the neighbor at each distance. (Insets) The root density distribution in space of plants at d = 0 cm (maximum total biomass increase) and at d = 30 cm (total biomass decreases). Insets' color codes, abscissa axis values, and model parameterization are the same as in Fig. 1. See materials and methods (supplementary material) for details.

For a solitary plant, the benefit of proliferating roots in a given location decelerates as local root density increases, because, even within a single plant's root network, individual root branches compete with one another for the same resource. As roots proliferate, the solitary plant gains more total resource but also steals more resource from itself. When a neighbor is present, two opposing forces are at work: (i) Some of the stolen resource comes from the neighbor, promoting overproliferation. (ii) Increased proliferation of a neighbor's roots depletes soil resource, promoting underproliferation. The cost of growing a unit of absorbing root surface increases with distance from the plant because the root surface must be connected to the stem by a xylem conduit. When the local cost of roots is low, force (i) dominates and plants should overproliferate roots. However, in locations far from a focal plant but close to its neighbor, force (ii) dominates, leading to local underproliferation by the focal plant.

Exploitative segregation can explain seemingly contradictory results reported in the literature. When two competing plants are very close to each other, plants should respond to competition by increasing biomass allocation to roots (Fig. 2) and should exhibit a root tragedy of the commons. However, as plants are set farther apart, local underproliferation in distant areas compensates for local overproliferation near the plant, resulting in a slight decrease in total root allocation. Also, as in the literature, such plants should exhibit range segregation by decreasing the total spatial spread of their root systems.

We tested these predictions in a greenhouse experiment using a traditional cultivar variety of pepper plant (*Capsicum annuum* L. var. luesia, Solanaceae) (supplementary materials). Plants were grown in gutters alone or paired with a competitor located at 10-cm distance. Root systems of competing individuals were stained in situ with different colors, and the spatial distribution of root density of each plant was mapped in the horizontal axis of the gutter. We thereby obtained data integrating spatial information and plant allocation strategy.

We did not observe a root tragedy of the commons at that given plant-plant distance, as there were no significant differences in total root biomass (t = −0.9422, P = 0.3573), shoot: root ratio (U = 116, P = 0.9025), or reproductive

yield (t = −0.6177, P = 0.5417) between solitary and competing plants. We detected evidence for root segregation, as we found significant differences (t = −5.3362, P < 0.0001) between the observed root overlap in interacting plants (20 cm of overlap) and the expected overlap between solitary-like distributed root systems (40 cm). Plants exhibited an exploitative segregation response to competitors (Fig. 1c) as predicted by the ESS equilibrium of our model. Each plant overproliferated roots near to its own stem and underproliferated roots closer to its neighbor's stem than to its own. Both of these effects are statistically significant: overproliferation of roots with increasing competitor root density (F = 11.6013, P < 0.001) and negative interaction between length and competitor root density (F = 58.2655, P < 0.001). This negative interaction indicates that plants responded to competitor root density by shifting from local overproliferation at low transporting lengths to underproliferation as the transporting length between the plant shoot and the soil patch increased.

We thus demonstrated experimentally the predictions of our ESS model: Plants do both locally overproliferate roots near their stem and reduce their foraging range when it overlaps with a neighboring root system. By integrating root allocation and spatial information, the exploitative segregation theory reconciles hypotheses that have been largely considered contradictory: root segregation and the tragedy of the commons.

REFERENCES AND NOTES

1. J. F. Cahill Jr., G. G. McNickle, *Annu. Rev. Ecol. Evol. Syst.* **42**, 289–311 (2011).
2. J. Klimešová, J. Martínková, G. Ottaviani, *Funct. Ecol.* **32**, 2115–2126 (2018).
3. L. Song *et al*., *J. Agron. Crop Sci.* **196**, 323–335 (2010).
4. M. D. Hernández *et al*., *Field Crops Res.* **254**, 107844 (2020).
5. D. Robinson, *Proc. Biol. Sci.* **274**, 2753–2759 (2007).
6. J. Xia, W. Yuan, Y. P. Wang, Q. Zhang, *Sci. Rep.* **7**, 3341 (2017).
7. G. E. D. Oldroyd, O. Leyser, *Science* **368**, eaba0196 (2020).
8. A. Novoplansky, *Semin. Cell Dev. Biol.* **92**, 126–133 (2019).
9. S. Fang *et al*., *Proc. Natl. Acad. Sci. U.S.A.* **110**, 2670–2675 (2013).
10. J. F. Cahill Jr *et al*., *Science* **328**, 1657 (2010).
11. H. J. Schenk, R. M. Callaway, B. E. Mahall, *Adv. Ecol. Res.* **28**, 145–180 (1999).
12. B. J. Enquist, K. J. Niklas, *Science* **295**, 1517–1520 (2002).
13. B. E. Mahall, R. M. Callaway, *Proc. Natl. Acad. Sci. U.S.A.* **88**, 874–876 (1991).
14. B. J. W. Chen *et al*., *Funct. Ecol.* **29**, 1383–1391 (2015).
15. G. G. Maina, J. S. Brown, M. Gersani, *Plant Ecol.* **160**, 235–247 (2002).
16. E. E. O'Brien, M. Gersani, J. S. Brown, *New Phytol.* **168**, 401–412 (2005).
17. O. Falik, H. de Kroon, A. Novoplansky, *Plant Signal. Behav.* **1**, 116–121 (2006).
18. L. Hess, H. De Kroon, *J. Ecol.* **95**, 241–251 (2007).
19. M. Semchenko, M. J. Hutchings, E. A. John, *J. Ecol.* **95**, 252–260 (2007).
20. M. K. Ljubotina, J. F. Cahill Jr., *Proc. Biol. Sci.* **286**, 20190955 (2019).
21. G. G. McNickle, J. S. Brown, *J. Ecol.* **102**, 963–971 (2014).
22. G. G. McNickle, R. Dybzinski, *Ecol. Lett.* **16**, 545–555 (2013).
23. M. Gersani, J. Brown, E. E. O'Brien, G. M. Maina, Z. Abramsky, *J. Ecol.* **89**, 660–669 (2001).
24. E. Zea-Cabrera, Y. Iwasa, S. Levin, I. Rodríguez-Iturbe, *Water Resour. Res.* **42**, 1–12 (2006).
25. C. E. Farrior, R. Dybzinski, S. A. Levin, S. W. Pacala, *Am. Nat.* **181**, 314–330 (2013).
26. D. J. Rankin, K. Bargum, H. Kokko, *Trends Ecol. Evol.* **22**, 643–651 (2007).
27. C. E. Farrior, *Proc. Biol. Sci.* **286**, 20191129 (2019).
28. J. E. Cohen, *Proc. Natl. Acad. Sci. U.S.A.* **95**, 9724–9731 (1998).

ACKNOWLEDGMENTS

We thank D. Quiroga, A Mas, and E. Garzo for their technical support, F.G.T. for their statistics advice, and three anonymous reviewers for their insightful comments on the initial version of our manuscript. **Funding:** This work was supported by the Princeton University May Fellowship in the department of Ecology and Evolutionary Biology; the Gordon and Betty Moore Foundation (grant GBMF2550.06); Instituto Serrapilheira (grant Serra-1911-31200); FAPESP (grants ICTP-SAIFR 2016/01343-7 and Programa Jovens Pesquisadores em Centros Emergentes 2019/24433-0, 2019/05523-8); the Simons Foundation; the Spanish Ministry for Science, Innovation and Universities (COMEDIAS grant CGL2017-83170-R); and the Princeton Environmental Institute Carbon Mitigation Initiative. **Author contributions:** Conceptualization, C.C. and S.W.P.; Methodology, C.C., R.M.-G., A.C., and F.V.; Formal analysis, C.C., R.M.-G., and A.C.; Investigation, C.C. and A.C.; Writing – Original draft, C.C.; Writing – Review and editing, C.C., R.M.-G., A.C., F.V., and S.W.P.; Funding acquisition, R.M.-G., F.V., and S.W.P.; Supervision, F.V. and S.W.P. **Competing interests:** The authors declare no competing interests. **Data and materials availability:** All data and code are available as supplementary materials. Materials are also available by contacting C.C.

SUPPLEMENTARY MATERIALS

science.sciencemag.org/content/370/6521/1197/suppl/DC1
Materials and Methods
Figs. S1 to S16
Tables S1 to S5
References (*29*–*41*)
Data and Code S1
MDAR Reproducibility Checklist

View/request a protocol for this paper from *Bio-protocol*.

3 April 2020; accepted 14 October 2020
10.1126/science.aba9877

PHYSICS

Directly visualizing the momentum-forbidden dark excitons and their dynamics in atomically thin semiconductors

Julien Madéo[1]*, Michael K. L. Man[1]*, Chakradhar Sahoo[1,2], Marshall Campbell[3], Vivek Pareek[1], E. Laine Wong[1]†, Abdullah Al-Mahboob[1], Nicholas S. Chan[1], Arka Karmakar[1], Bala Murali Krishna Mariserla[1,4], Xiaoqin Li[3], Tony F. Heinz[5,6], Ting Cao[5,7], Keshav M. Dani[1]‡

Resolving momentum degrees of freedom of excitons, which are electron-hole pairs bound by the Coulomb attraction in a photoexcited semiconductor, has remained an elusive goal for decades. In atomically thin semiconductors, such a capability could probe the momentum-forbidden dark excitons, which critically affect proposed opto-electronic technologies but are not directly accessible using optical techniques. Here, we probed the momentum state of excitons in a tungsten diselenide monolayer by photoemitting their constituent electrons and resolving them in time, momentum, and energy. We obtained a direct visual of the momentum-forbidden dark excitons and studied their properties, including their near degeneracy with bright excitons and their formation pathways in the energy-momentum landscape. These dark excitons dominated the excited-state distribution, a surprising finding that highlights their importance in atomically thin semiconductors.

The discovery of two-dimensional (2D) semiconductors launched exciting opportunities in exploring excited-state physics and opto-electronic technologies (*1*–*3*), driven in part by the existence of robust, few-particle excitonic states. As a prototypical 2D semiconductor in the transition metal dichalcogenide (TMD) family, WSe_2 monolayers exhibit a band structure that hosts two degenerate valence band maxima but eight nearly degenerate conduction band minima in the hexagonal Brillouin zone (BZ) (*4*, *5*). At the K and K′ valleys, the conduction and valence band energies are both at local extrema, giving rise to two direct bandgap transitions and the bright excitons (denoted as K-K excitons) (Fig. 1, A and B). These excitons, also called direct excitons in the traditional semiconductor literature, are behind the strong light absorption and photoluminescence in the WSe_2 monolayer (*6*, *7*) and have been extensively investigated in various optical spectroscopy experiments.

Few experiments, however, have been capable of probing the indirect or momentum-forbidden dark excitons in monolayer TMDs, which consist of an electron and a hole residing at different valleys (*8*). Such dark excitons may interact with bright excitons, serve as the preferred carriers of information and energy, or form collective states such as exciton liquids and condensates (*9*, *10*). Therefore, determining the properties and controlling the population of the dark excitons, as well as their interactions with the bright excitons, is the key to a complete understanding of the underlying physics and developing future technologies. Because of the six other conduction band minima at the Q valleys (also denoted as Λ or Σ in the literature) in WSe_2 monolayers, dark excitons may form with an electron in the Q valley and a hole in the K (or K′) valley (Fig. 1A) (*5*, *11*). Compared with other TMDs, a near degeneracy between the Q- and K-valley states of WSe_2 has been predicted (*12*), furthering the possibility that these dark excitons play an important role in the optical properties (*13*). The crystal momentum mismatch between the electrons and holes makes them inaccessible in first-order optical processes such as absorption and photoluminescence (*14*, *15*).

Momentum-resolved studies of excitons have been a long-standing goal (*16*–*23*). Such studies would provide the resolution to directly access the recently sought-after dark excitons in monolayer TMDs (*14*, *24*). In general, angle-resolved photoemission spectroscopy (ARPES)–based techniques have been one of the most successful in providing momentum information (*25*). For example, ARPES techniques have successfully probed free carriers in bulk TMDs (*26*–*28*) and specially prepared monolayers (*30*–*32*). However, observing strongly bound, few-particle excitonic states is not straightforward even conceptually, as discussed in a number of recent theoretical studies (*19*–*23*). Experimentally, serious challenges include the need for high-energy extreme ultraviolet (XUV) photons to access states at the BZ vertices (XUV-ARPES), spatial resolution to study the typical high-quality micrometer-scale TMD samples (μ-ARPES) (*8*), and time resolution through a pump-probe configuration (TR-ARPES) to access the dynamics of the short-lived excitonic states after photoexcitation (*33*–*36*). Here, we successfully overcame these experimental challenges in a single platform to perform TR-XUV-μ-ARPES, providing a direct visualization of dark excitons in a WSe_2 monolayer. We report on dark exciton formation pathways under different photoexcitation conditions, the nature of their spectral degeneracy relative to bright excitons, and the dominant role they play in the quasi-equilibrium distribution at long time delays. Our experiments represent a milestone in studies of photoexcited states by providing a global view over the entire BZ, along with exclusive insights inaccessible otherwise.

We studied an exfoliated WSe_2 monolayer placed on an hBN buffer layer supported by an Si substrate (Fig. 1C). The sample was probed at a temperature of 90 K under ultrahigh vacuum conditions (details about sample preparation and characterization are provided in the supplementary materials). Our experiments are enabled by a custom-built platform that combines an ultrafast, tabletop XUV source with a spatially resolving photoemission electron microscope (PEEM) (Fig. 1D and supplementary text, section 2). First, we performed an XUV-μ-ARPES measurement to obtain the band structure of the nonphotoexcited WSe_2 monolayer (Fig. 2A). For this, we used ultrafast XUV probe pulses (21.7 eV) to photoemit electrons from the sample. Using the high-resolution spatial imaging capabilities of our PEEM apparatus, we isolated photoelectrons emitted from only the monolayer region of the sample (see the supplementary text, section 3). The reciprocal images of these photoelectrons were then dispersed in energy in a time-of-flight detector, thereby resolving the angle (i.e., momentum) and energy (with an energy resolution of 0.03 eV) of each photoelectron (*37*, *38*) (Fig. 1D and supplementary text, sections 2 to 4). The measured band structure showed the spin-split valence band extrema at the K,K′ valleys and had excellent agreement with GW calculations (Fig. 2A and materials and methods). The energy differences between the K- and Q-valley conduction bands were sensitive to the lattice parameters and functional used in the calculation (see the materials and methods).

Next, to measure the excitonic states of the TMD monolayer, we excited the sample with an ultrafast pump pulse tunable over the

[1]Femtosecond Spectroscopy Unit, Okinawa Institute of Science and Technology, Okinawa, Japan 904-0495. [2]School of Physics, University of Hyderabad, Gachibowli, Hyderabad-500046, Telangana, India. [3]Physics Department, Center for Complex Quantum System, The University of Texas at Austin, Austin, TX 78712, USA. [4]Department of Physics, Indian Institute of Technology, Jodhpur, Rajasthan, India 342037. [5]Department of Applied Physics, Stanford University, Stanford, CA 94305, USA. [6]SLAC National Accelerator Laboratory, Menlo Park, CA 94720, USA. [7]Department of Materials Sciences and Engineering, University of Washington, Seattle, WA 98195, USA.
*These authors contributed equally to this work.
†Present address: Center for Nano Science & Technology, Italian Institute of Technology, 20133 Milan, Italy.
‡Corresponding author. Email: KMDani@oist.jp

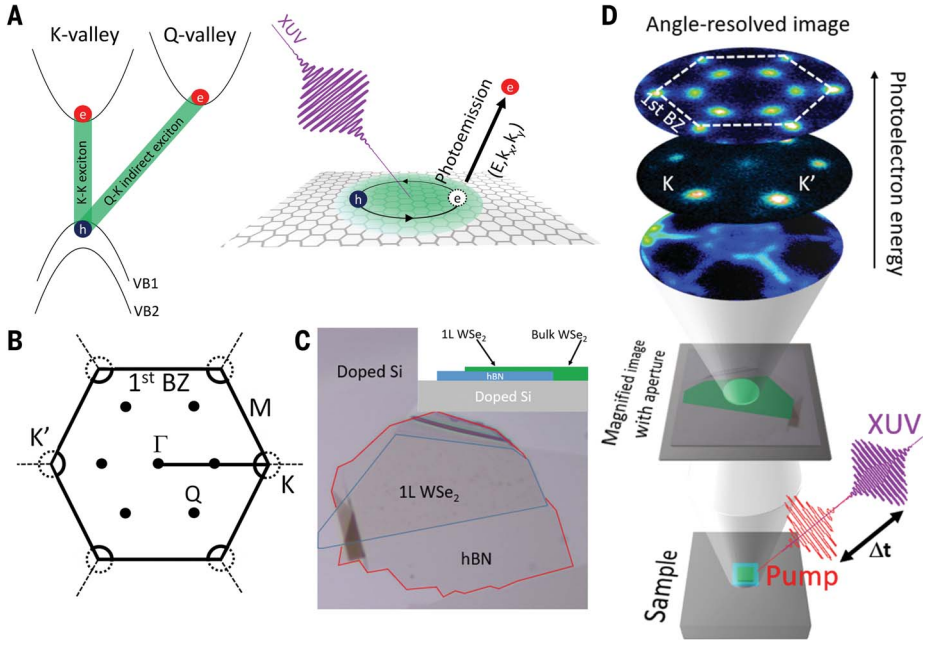

Fig. 1. Time-resolved-XUV-μ-ARPES of excitons in a WSe_2 monolayer. (**A**) Left: Diagram showing the configuration for K-K direct excitons and Q-K indirect excitons with holes located in the K valleys and electrons in K and Q valleys, respectively. Right: Representation of the exciton photoemission process. XUV photons photoemit electrons, leaving holes from the bound electron-hole pairs. (**B**) Schematic of the k-space structure of monolayer WSe_2 showing the first BZ composed of six Q valleys and two K valleys (each K valley is shared between three BZs, so only one-third of each falls within the first BZ). (**C**) Optical image of the sample composed of a monolayer WSe_2 (blue outline) on hBN (red outline) on an *n*-doped Si substrate. Inset is a side view of the sample. (**D**) Schematic of the experimental setup.

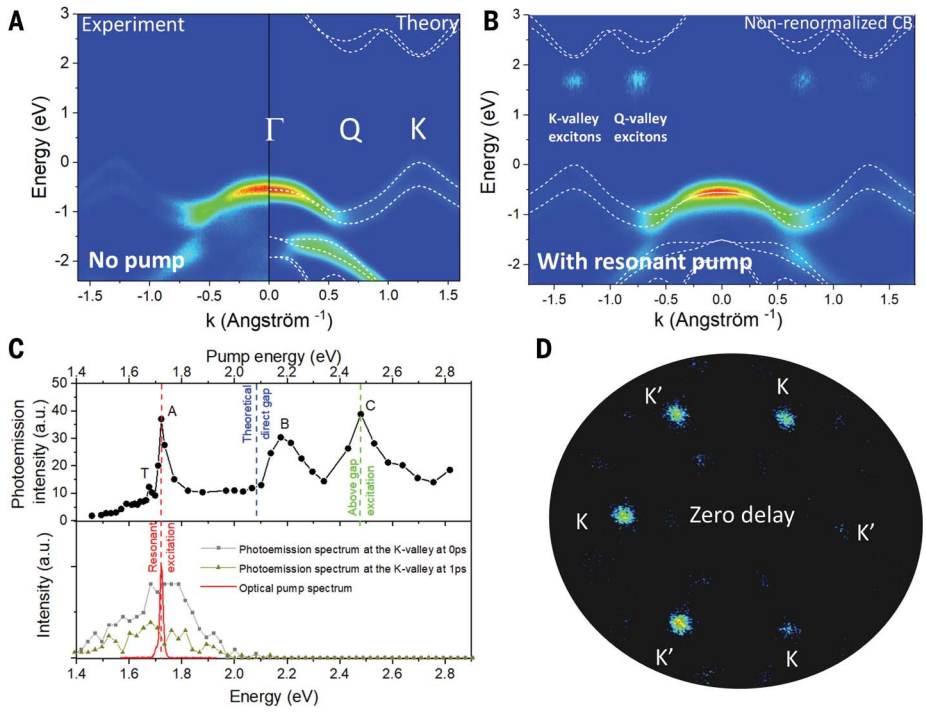

Fig. 2. Excitonic resonances. (**A**) Experimental and theoretical XUV-μ-ARPES results from the WSe_2 monolayer without optical excitation. The dispersion of the occupied quasiparticle bands (false color scale of electron emission intensity) is shown, together with the calculated band structure plotted along Γ-Q-K-M (dashed white lines). (**B**) Experimental band structure with a 1.72-eV photoexcitation resonant with the A exciton at a 0.5-ps delay showing below conduction band direct and indirect excitonic states. The experimental data were compared with nonrenormalized conduction bands with exciton-induced bandgap renormalization effects estimated to be <100 meV (*20*). (**C**) Top: Photoemission intensity integrated from 1 to 3 eV above the valence band maximum (VBM) versus optical pump energy. Seen clearly is the spectrum dominated by resonance at 1.73, 2.17, and 2.48 eV, corresponding to the A, B, and C excitons described in the literature, respectively. The observed resonance at low energy is attributed to the trion peak (*8*). Bottom: Spectrum of the resonant optical pump (red) and photoemission energy spectrum integrated within a ±0.015 $Å^{-1}$ k-space range at the center of the K valley at zero time delay (gray) and also at later time delays (green). (**D**) Corresponding momentum-resolved photoemission intensity integrated from 1 to 3 eV above the VBM showing the exciton signals in the K valley for a resonant excitation with the A exciton at zero time delay. The observed asymmetry in the intensity distribution is largely caused by the matrix element effect determined by the polarization and incidence angle of the photoemission probe.

visible and near-infrared range of the spectrum. Then, the ultrafast XUV probe pulse discussed above was introduced at a variable time delay to measure the time-, angle-, and energy-resolved photoelectron spectrum from the WSe_2 monolayer (TR-XUV-μ-ARPES). Recent theoretical studies have predicted photoemission signals from excitons exhibiting an energy-momentum distribution centered in the corresponding conduction band valley but binding energy below the conduction band minimum. In our measurements, after resonant photoexcitation of the A exciton, a substantial photoemission signal at positive time delay was seen below the bandgap centered at the K (K′), located at ±1.26 $Å^{-1}$, and Q valleys, located at ±0.75 $Å^{-1}$ (Fig. 2B) (*21*). To ensure that the detected signals corresponded to excitonic states, we measured the photoemission excitation spectrum (Fig. 2C, top panel), i.e., the integrated photoemission

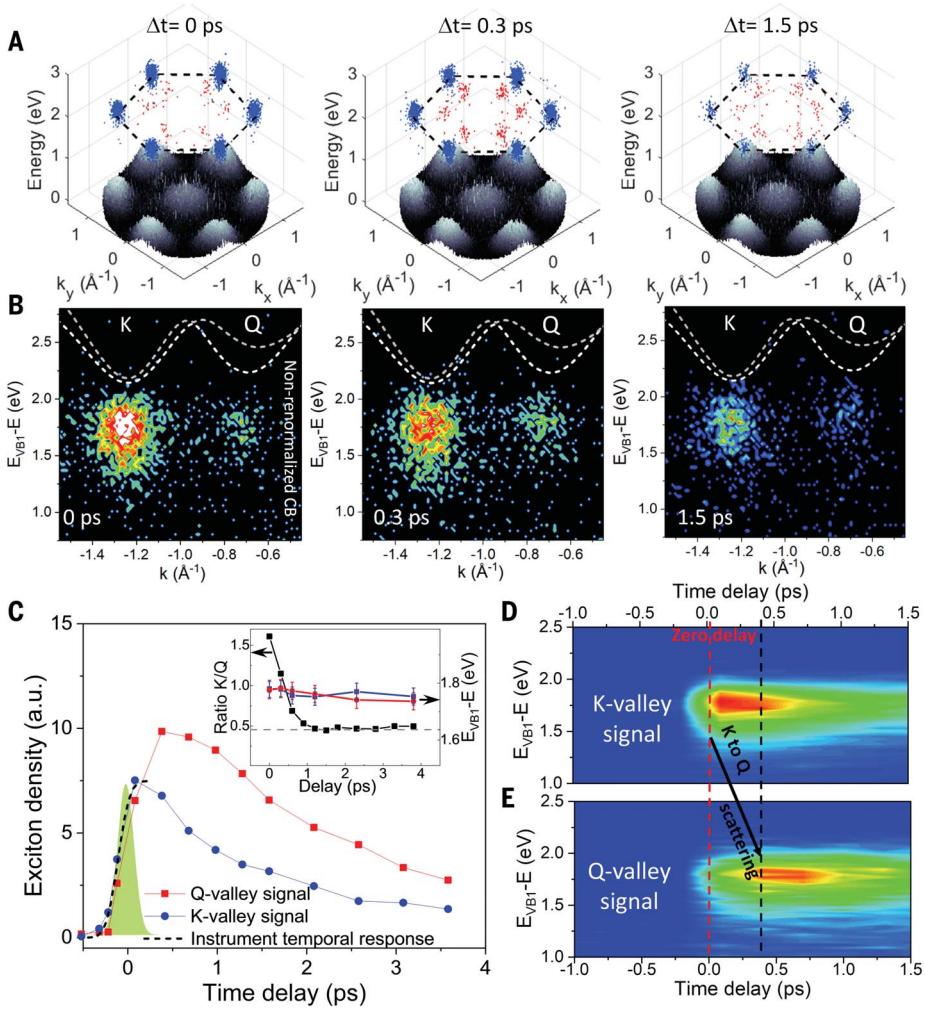

Fig. 3. Exciton dynamics after resonant excitation. (**A**) TR-ARPES data for delay times of 0, 0.3, and 1.5 ps for the full 2D BZ (in-plane) and emission energy (vertical). The top of the valence bands is displayed in grayscale; emission from the K-valley (Q-valley) excitons is plotted in blue (red) dots (see the supplementary materials). The black dashed line defines the boundary of the first BZ. (**B**) TR-ARPES data for delay times of 0, 0.3, and 1.5 ps along the line connecting the K and Q valleys. The dotted lines show the calculated (spin-split) conduction bands. (**C**) Exciton density versus time delay at Q valleys (red) and K valleys (blue). The exciton density was determined by the ARPES signal integrated over the two K valleys or six Q valleys of the first BZ and an energy range from 1 to 2.5 eV, with a correction factor for the respective photoemission matrix elements. The dotted black line shows the instrument response function, i.e., the convolution of the pump and probe pulse. The corresponding Gaussian pulse is plotted in green. Inset is the ratio of the K/Q population (black) obtained by dividing the data in Fig. 3C showing dominant K-valley exciton population initially but a ratio approaching ~0.5 at longer time delays. The blue and red curves correspond to the center energy of a Gaussian fit of the distributions of the K- and Q-valley signals, respectively. (**D**) Time-resolved spectrum of the K-valley signal integrated over the first BZ. (**E**) Time-resolved spectrum of the Q-valley signal integrated over the first BZ. K-valley excitons are populated directly upon photoexcitation. We observed a clear delay in the rise of the Q-valley population caused by K to Q scattering.

intensity (from 1 to 2.5 eV above VB1 in the first BZ), versus the optical excitation energy (varied from 1.58 to 2.85 eV). In the photoemission excitation spectrum, we clearly observed the distinctive A-, B-, and C-exciton resonances as previously reported in optical absorption (*6*). This energy dependence confirms the dominance of excitons under the experimental conditions used in this work, namely photoexcitation density, sample structure, and photoemission probe. Then, we tuned our pump pulse to 1.72 eV to match the A-exciton resonance as shown in the bottom panel of Fig. 2C. This choice of pump wavelength ensured that we were predominantly and resonantly exciting excitons. Finally, looking at the energy- and momentum-resolved photoemission signal under these pump conditions, we clearly saw a signal in the K valley and also at exactly the energy of the A exciton. This confirms that the photoemission signal at ~1.73 eV, located at ±1.26 Å^{-1} along the K-Γ cut (i.e., in the K-valley), corresponds to excitons in the K valley, in agreement with previous theoretical calculations (*39*) and optical experiments (*40*). By extension, given the expected near degeneracy, we attribute the signal at 1.73 eV and ±0.75 Å^{-1} momentum along the K-Γ cut to excitons in the Q valley. We assigned these two signals in part to the bright K-K and momentum-forbidden dark Q-K excitons, respectively (see the supplementary text, section 7). Given the large inhomogeneous broadening (~250 meV) in the photoemission spectrum of our sample (see the supplementary text, section 5), we expect that the K-valley signal also constitutes other excitonic states that are nearly resonant with the bright K-K exciton, such as the spin-dark K-K exciton, the indirect K-K′ exciton, as well as trions and biexcitons. Similar considerations also apply for the Q-valley signal. In the following, we will refer to the ensemble of excitonic states that constitutes the K- and Q-valley signals as K- and Q-valley excitons. We note that the calculated single-particle band structure in this work does not include renormalization effects caused by the exciton density, but we estimate this renormalization to be <100 meV (*20*). We also observed the K- and Q-valley excitons with electrons at the K,K′ and Q valleys and the presence of holes that could be seen by the depletion of electrons in the K,K′ valley by taking the difference between the band structures without and after photoexcitation (fig. S14A). The photoemission spectrum taken at different time delays (fig. S14B) after photoexcitation then allowed us to follow the formation dynamics of these dark indirect excitons and learn other aspects of their nature. To eliminate rigid energy shifts or offsets of the entire band structure caused by surface photovoltage effect or other similar phenomena, we set the peak of the upper spin-split valence band as the zero-energy reference for every time delay (see the supplementary text, section 8). We also used an optical excitation spot much larger than the sample to eliminate any lateral contribution to surface photovoltage caused by local variations of intensity (*41*).

To study the formation dynamics, we next resonantly excited the optically allowed K-K exciton as seen in Fig. 2C. We used linearly

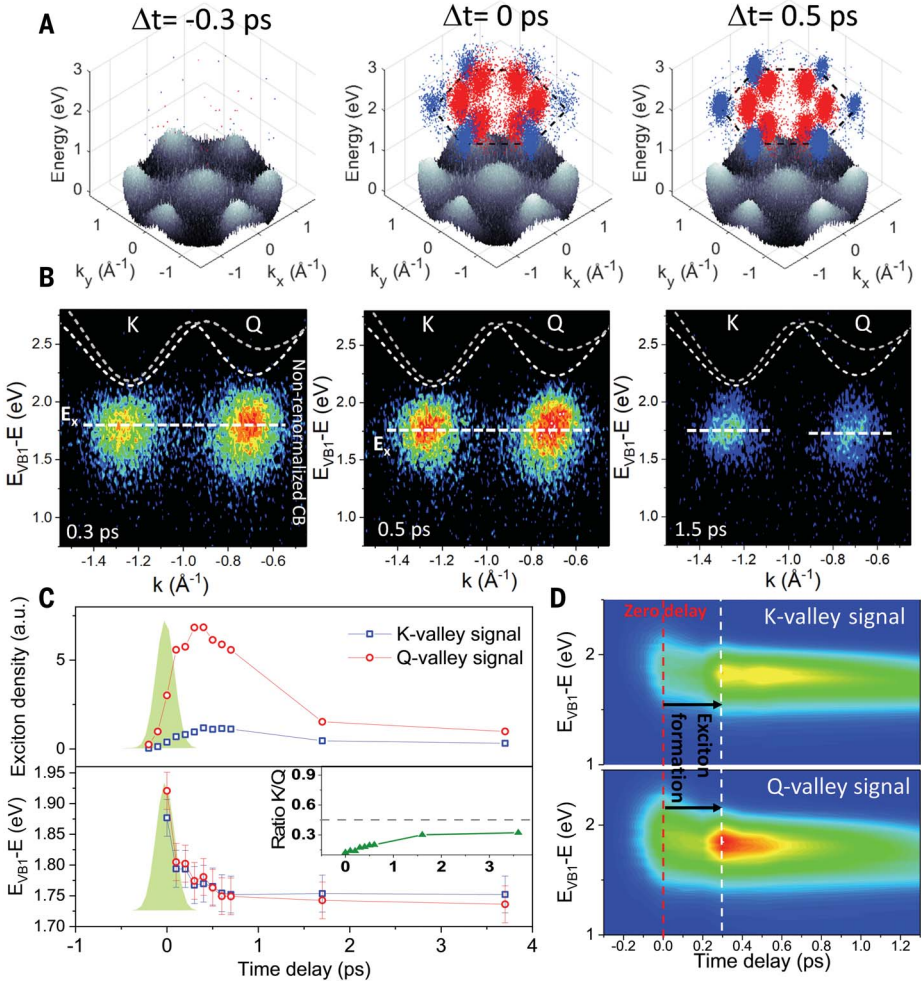

Fig. 4. Exciton formation and dynamics after above-gap excitation. (**A**) 3D plots of the experimental data at 0.3-, 0.5-, and 1.5-ps time delays. The top of the valence bands is displayed in grayscale. The K-valley (Q-valley) excitons are plotted in blue (red) dots. The black dashed line defines the boundary of the first BZ. (**B**) ARPES data at the K and Q valleys for 0.3-, 0.5-, and 1.5-ps time delays. Dotted line is the theoretical calculation of the conduction bands. (**C**) Top: K-valley (blue) and Q-valley (red) exciton density over the first BZ from 1 to 2 eV. Bottom: Center energy of the photoexcited population obtained from fits with Gaussian function at the center of the K and Q valley. Inset is the ratio of the total populations between the K and Q valleys extracted from the top panel. (**D**) Time-resolved spectra at the K valley (top) and the Q valley (bottom) showing the formation and relaxation of excitons.

polarized pump pulses at 1.72 eV with a fluence chosen to produce an estimated exciton density of 2.4 × 10^{12}/cm^2 (see the materials and methods and supplementary text, section 16). At zero-time delay, we observed only the K-valley excitons (Fig. 3, A and B). As expected for resonant excitation, the formation of K-valley excitons was rapid, as seen in Fig. 3C. The energy of the K-valley exciton (1.73 ± 0.03 eV) was consistent with the energy of the pump excitation, within experimental uncertainty, and did not change for longer delay times (Fig. 3C). At later times, we saw a clear buildup of the dark Q-valley exciton population at energies nearly degenerate (within our 0.03-eV energy resolution) with the K-valley excitons (Fig. 3D). Through the momentum sensitivity of the measurement, we directly observed the formation of the dark Q-valley excitons through scattering from the K-valley excitons on an ~400-fs time scale (see the supplementary text, section 13). Theoretical studies and indirect optical measurements have reported on phonon-assisted intervalley scattering of excitons (*23*, *42*–*44*) that are fundamentally different from the electron-phonon interactions seen in bulk TMDs (*28*). Our measurements directly accessed this exciton-phonon scattering and are consistent with the reported time scales of few hundred femtoseconds. Given the presence of resident carriers from unintentional doping, exciton-plasmon scattering could also play a role. Future experiments varying the doping concentration would allow one to tease out this contribution. The Q and K signals also showed similar recovery times, which is consistent with previous studies showing that the dark Q-K exciton acts as a long-lived reservoir for the K-K exciton (*45*). The extracted decay times were 1.7 and 2.5 ps for K- and Q-valley excitons, respectively (see the supplementary text, section 14), reflecting an average decay time corresponding to all the different excitonic states probed. Future experiments using samples with narrower linewidths in the ARPES signal could allow one to distinguish between the different excitonic states and the corresponding dynamics between them. Also of importance is the evolution to a quasi-equilibrium distribution of excitons. We initially created a larger K-valley population by resonant excitation with the A exciton, but within a picosecond, the Q-valley exciton population dominated, with the K-valley/Q-valley ratio tending toward ~0.5 (Fig. 3C, inset). We note that in calculating the ratio, we included the population in the entire first BZ comprising six Q valleys and two K valleys, as well as a normalization factor arising from the different photoemission matrix elements (between band states and photoelectron states) at the K and Q valleys (see the supplementary text, section 10). Assuming this limiting ratio reflects equilibrium at the lattice temperature of 90 K and assuming a density of state factor on the order of 1 (for details, see the supplementary materials), one can obtain a tighter bound of <0.015 eV on the energy difference of the two exciton species. A video of the exciton dynamics measured over the full BZ after resonant photoexcitation is provided in the supplementary materials (movie S1).

Finally, we turned our attention to the dynamics after above-gap excitation. We used a 2.48-eV linearly polarized pump pulse to excite carriers well above bandgap, producing an estimated carrier density of 1.6 × 10^{12}/cm^2 (see the materials and methods and supplementary text, section 16). Unexpectedly, the

exciton relaxation pathways, particularly for the dark Q-valley excitons, were substantially different from those observed for resonant excitation. Figure 4A shows snapshots of the full ARPES data at different time delays at the K and Q valleys (movie S2). Immediately after excitation (zero delay), we observed a broad distribution in the K and Q valleys centered at an energy of ~1.90 eV (fig. S11) that could involve contributions from both free carriers and excited excitonic states. Future experiments with improved time and energy resolution are needed to explore these very early dynamics (see the supplementary text, section 11). Beyond this regime, we observed full relaxation into the K- or Q-valley excitons within 500 fs (Fig. 4B). Previously, optical and mid-infrared spectroscopic measurements had reported the subpicosecond formation of exciton dynamics (*46*, *47*) but lacked separate access to the dynamics of the different types of excitonic states, such as the dark Q-valley excitons. The relaxation process can also be described by plotting the average energy of the photoemission signal versus time (Fig. 4C), giving an energy relaxation time of 500 fs. Beyond 500 fs, the peak energy of the distribution at the Q and K valleys remained constant at ~1.73 eV, matching the exciton energies under resonant conditions (Figs. 3C, inset, and 4C). A marked departure from the resonant excitation case is that Q-valley excitons appeared coincident with the K-valley excitons (rather than at a finite delay after scattering of the K-valley excitons as for the resonant excitation). We also observed that the dark Q-valley exciton density dominated the direct K-valley density at all time delays (Fig. 4C, and see inset), in contrast to the resonant excitation case. However, at long time delays, under both resonant and above-gap excitation, the system evolved to a similar quasi–steady state, with a nearly identical K-valley/Q-valley exciton population ratio and nearly degenerate exciton energies with respect to the valence band maximum. The exciton-binding energy is given by the difference between the conduction band minimum and the energy of the constituent electron photoemitted from the center of the valley at long time delays, where quasi-equilibrium is reached (*44*). Accordingly, we estimated binding energies as ~390 and ~480 meV (with respect to the conduction band minima) for the K-valley and Q-valley excitons, respectively, with a combined uncertainty of ~150 meV caused by theoretical errors, bandgap renormalization effects, and experimental uncertainty. Although the former can be compared to results of various optical spectroscopy measurements (*3*), the binding energy and momentum-space distributions of the dark exciton in monolayer TMDs are not easily accessible to other experiments (*23*).

Our measurements using TR-XUV-μ-ARPES to access strongly bound, few-particle excitonic states in 2D semiconductors and their dynamics open new possibilities. Such direct access to dark excitons or other valley- and spin-polarized excitons will enable their utility in quantum information (*48*) and valleytronic and spintronic schemes and in creating new many-body excitonic states (*9*, *10*). Energy- and momentum-resolved photoemission studies of excitons could directly image excitonic wavefunctions in momentum space. On the basis of the energy-momentum dispersion relationship, one could measure important physical properties, such as the kinetic energy and temperature of photoexcited excitons (*20*–*23*). Future measurements could access few-particle excitations, such as trions, biexcitons, and interlayer excitons in TMD heterostructures, which may be expected to have their own specific photoemission signatures. Also, the use of circularly polarized excitation would provide direct access to the nature of K to K′ exciton scattering, critical information in the context of valleytronics. Finally, we expect our measurements to extend to other condensed-matter systems in providing a complete picture of the transformation of their electronic structure along energy and momentum axes after optical illumination.

REFERENCES AND NOTES

1. P. Ajayan, P. Kim, K. Banerjee, *Phys. Today* **69**, 38–44 (2016).
2. Q. H. Wang, K. Kalantar-Zadeh, A. Kis, J. N. Coleman, M. S. Strano, *Nat. Nanotechnol.* **7**, 699–712 (2012).
3. G. Wang *et al*., *Rev. Mod. Phys.* **90**, 021001 (2018).
4. G.-B. Liu, D. Xiao, Y. Yao, X. Xu, W. Yao, *Chem. Soc. Rev.* **44**, 2643–2663 (2015).
5. P. V. Nguyen *et al*., *Nature* **572**, 220–223 (2019).
6. Y. Li *et al*., *Phys. Rev. B Condens. Matter Mater. Phys.* **90**, 205422 (2014).
7. K. F. Mak, C. Lee, J. Hone, J. Shan, T. F. Heinz, *Phys. Rev. Lett.* **105**, 136805 (2010).
8. M. Cattelan, N. A. Fox, *Nanomaterials (Basel)* **8**, 284 (2018).
9. J. M. Blatt, K. W. Böer, W. Brandt, *Phys. Rev.* **126**, 1691–1692 (1962).
10. L. V. Keldysh, P. N. Lebedev, *Contemp. Phys.* **27**, 395–428 (1986).
11. M. Selig *et al*., *Nat. Commun.* **7**, 13279 (2016).
12. A. Kormányos *et al*., *2D Mater.* **2**, 022001 (2015).
13. J. Lindlau *et al*., *Nat. Commun.* **9**, 2586 (2018).
14. E. Malic *et al*., *Phys. Rev. Mater.* **2**, 014002 (2018).
15. Y. Uchiyama *et al*., *npj 2D Mater. Appl.* **3**, 26 (2019).
16. G. Dresselhaus, *J. Phys. Chem. Solids* **1**, 14–22 (1956).
17. J. Shah, *Ultrafast Spectroscopy of Semiconductors and Semiconductor Nanostructures* (Springer, 1999)
18. H. Wang, J. Shah, T. C. Damen, L. N. Pfeiffer, *Phys. Rev. Lett.* **74**, 3065–3068 (1995).
19. E. Perfetto, D. Sangalli, A. Marini, G. Stefanucci, *Phys. Rev. B* **94**, 245303 (2016).
20. A. Steinhoff *et al*., *Nat. Commun.* **8**, 1166 (2017).
21. A. Rustagi, A. F. Kemper, *Phys. Rev. B* **97**, 235310 (2018).
22. A. Rustagi, A. F. Kemper, *Phys. Rev. B* **99**, 125303 (2019).
23. D. Christiansen, M. Selig, E. Malic, R. Ernstorfer, A. Knorr, *Phys. Rev. B* **100**, 205401 (2019).
24. C. Poellmann *et al*., *Nat. Mater.* **14**, 889–893 (2015).
25. A. Damascelli, *Phys. Scr.* **2004**, T109 (2004).
26. P. Hein *et al*., *Phys. Rev. B* **94**, 205406 (2016).
27. R.-Y. Liu *et al*., *Sci. Rep.* **7**, 15981 (2017).
28. R. Wallauer, J. Reimann, N. Armbrust, J. Güdde, U. Höfer, *Appl. Phys. Lett.* **109**, 162102 (2016).
29. R. Bertoni *et al*., *Phys. Rev. Lett.* **117**, 277201 (2016).
30. A. Grubišić Čabo *et al*., *Nano Lett.* **15**, 5883–5887 (2015).
31. S. Ulstrup *et al*., *Phys. Rev. B* **95**, 041405 (2017).
32. F. Liu, M. E. Ziffer, K. R. Hansen, J. Wang, X. Zhu, *Phys. Rev. Lett.* **122**, 246803 (2019).
33. J. H. Buss *et al*., *Rev. Sci. Instrum.* **90**, 023105 (2019).
34. M. Puppin *et al*., *Rev. Sci. Instrum.* **90**, 023104 (2019).
35. A. K. Mills *et al*., Cavity-enhanced high harmonic generation for XUV time-resolved ARPES. arXiv:1902.05997 [physics.optics] (15 February 2019).
36. E. J. Sie, T. Rohwer, C. Lee, N. Gedik, *Nat. Commun.* **10**, 3535 (2019).
37. A. Oelsner *et al*., *J. Electron Spectrosc. Relat. Phenom.* **178-179**, 317–330 (2010).
38. K. Medjanik *et al*., *Nat. Mater.* **16**, 615–621 (2017).
39. X.-X. Zhang *et al*., *Nat. Nanotechnol.* **12**, 883–888 (2017).
40. A. Arora *et al*., *Nanoscale* **7**, 10421–10429 (2015).
41. E. L. Wong *et al*., *Sci. Adv.* **4**, eaat9722 (2018).
42. S. Brem, M. Selig, G. Berghaeuser, E. Malic, *Sci. Rep.* **8**, 8238 (2018).
43. M. Selig *et al*., *2D Mater.* **5**, 035017 (2018).
44. C. Ruppert, A. Chernikov, H. M. Hill, A. F. Rigosi, T. F. Heinz, *Nano Lett.* **17**, 644–651 (2017).
45. X.-X. Zhang, Y. You, S. Y. F. Zhao, T. F. Heinz, *Phys. Rev. Lett.* **115**, 257403 (2015).
46. P. Steinleitner *et al*., *Nano Lett.* **17**, 1455–1460 (2017).
47. F. Ceballos, Q. Cui, M. Z. Bellus, H. Zhao, *Nanoscale* **8**, 11681–11688 (2016).
48. K.-D. Park, T. Jiang, G. Clark, X. Xu, M. B. Raschke, *Nat. Nanotechnol.* **13**, 59–64 (2018).

ACKNOWLEDGMENTS

We thank the OIST engineering support section for their support. T.C. and K.M.D. thank F. H. da Jordana for discussions. J.M., M.K.L.M., and K.M.D. thank D. Bacon for experimental support. **Funding:** This work was supported by JSPS KAKENHI grant no. JP17K04995 and by the Femtosecond Spectroscopy Unit, Okinawa Institute of Science and Technology Graduate University. Theoretical analysis and first-principle calculations were partially supported by the National Science Foundation (NSF) through the University of Washington Materials Research Science and Engineering Center DMR-1719797. Analysis at SLAC was supported by the AMOS program, Chemical Sciences, Geosciences, and Biosciences Division, Basic Energy Sciences, U.S. Department of Energy under contract no. DE-AC02-76-SF00515. T.C. acknowledges support from the Micron Foundation and a GLAM postdoctoral fellowship at Stanford. Computational resources were provided by Hyak at the University of Washington and the Extreme Science and Engineering Discovery Environment (XSEDE), which is supported by the NSF under grant no. ACI-1053575. The work of M.C. and X.L. at University of Texas at Austin was partially supported by the NSF through the Center for Dynamics and Control of Materials (NSF MRSEC under cooperative agreement no. DMR-1720595) and the facility supported by the center. **Author contributions:** J.M., M.K.L.M., and K.M.D. designed the experimental setup. J.M., M.K.L.M., and C.S. built the experimental setup. J.M., M.K.L.M., C.S., E.L.W., and A.A.M. performed the experiments. J.M., M.K.L.M., A.A.M., and N.S.C. analyzed the data. J.M., C.S., E.L.W., and B.M.K.M. designed and built the XUV source. V.P. and A.K. characterized the sample. M.C. and X.L. prepared the sample. T.F.H. and T.C. provided theoretical support. T.C. performed first-principle theoretical calculations. K.M.D. supervised the project. All authors contributed to discussions and manuscript preparation. **Competing interests:** J.M., M.K.L.M., and K.M.D. are inventors on a patent application related to this work filed by the Okinawa Institute of Science and Technology School Corporation (US 2020/0333559 A1 published on October 22, 2020). The authors declare no other competing interests. **Data and materials availability:** All data are available in the manuscript or supplementary materials.

SUPPLEMENTARY MATERIALS

science.sciencemag.org/content/370/6521/1199/suppl/DC1
Materials and Methods
Figs. S1 to S14
References (*49*–*60*)
Movies S1 and S2

20 April 2020; accepted 29 September 2020
10.1126/science.aba1029

SPECTROSCOPY

Super-resolution lightwave tomography of electronic bands in quantum materials

M. Borsch[1]*, C. P. Schmid[2]*, L. Weigl[2], S. Schlauderer[2], N. Hofmann[2], C. Lange[2]†, J. T. Steiner[3], S. W. Koch[3], R. Huber[2]‡, M. Kira[1]‡

Searching for quantum functionalities requires access to the electronic structure, constituting the foundation of exquisite spin-valley–electronic, topological, and many-body effects. All-optical band-structure reconstruction could directly connect electronic structure with the coveted quantum phenomena if strong lightwaves transported localized electrons within preselected bands. Here, we demonstrate that harmonic sideband (HSB) generation in monolayer tungsten diselenide creates distinct electronic interference combs in momentum space. Locating these momentum combs in spectroscopy enables super-resolution tomography of key band-structure details in situ. We experimentally tuned the optical-driver frequency by a full octave and show that the predicted super-resolution manifests in a critical intensity and frequency dependence of HSBs. Our concept offers a practical, all-optical, fully three-dimensional tomography of electronic structure even in microscopically small quantum materials, band by band.

Band-structure engineering (*1*–*3*) strives to design the dependence of energies and geometric phases (*4*) of electronic states of solids on the wave vector, $\mathbf{k}$. These attributes ultimately control emergent quantum phenomena, ranging from excitons (Coulomb-bound electron-hole pairs) (*5*, *6*) to many-body complexes (*7*) and quantum phase transitions (*8*). Monolayers of transition-metal dichalcogenides, such as tungsten diselenide (WSe_2), host a bounty of such quantum effects (*1*, *6*, *8*, *9*). Angle-resolved photoelectron spectroscopy has championed electronic band-structure mapping (*10*–*13*) in samples of sufficient size, measured at ultrahigh vacuum conditions. All-optical techniques, such as harmonic sideband (HSB) (*14*–*17*) and high-harmonic generation (HHG) (*18*–*27*), promise in situ probing of even microscopically small and/or atomically thin solids in ambient. Yet, HHG mapping encounters challenges: Atomically strong lightwaves inherently spread electrons broadly throughout the Brillouin zone (BZ) (*20*) and induce electronic interferences (*21*) as well as transport among multiple bands.

Such contributions become disentangled in HSB generation, in which an optical field selects electronic bands by resonantly exciting coherences between a specific valence-conduction band pair, creating an electron-hole (*e*-*h*) excitation (Fig. 1A, top red lines). If tuned in resonance with the 1*s* A exciton of monolayer WSe_2, the pulse selectively prepares an excitonic wave packet defined by the microscopic interband polarization $P_{\mathbf{k}}$ (Fig. 1A, color map at time $t = 0$) close to the K point where the energy difference $E^{\mathrm{eh}}_{\mathbf{k}}$ (Fig. 1A, bottom red line) between the two bands is minimal. Unlike in HHG, $P_{\mathbf{k}}$ is strongly localized and oscillates with the frequency ν_{1s} corresponding to the 1*s*-exciton energy, $h\nu_{1s}$ (where h is Planck's constant). A strong multi-terahertz field at a frequency $\nu_{\mathrm{THz}} \ll E^{\mathrm{eh}}_{\mathbf{k}}/h$ then creates HSBs by transporting $P_{\mathbf{k}}$ from the K point to $\mathbf{k}$ (Fig. 1A, color map at $t > 0$). The resulting increase, $E^{\mathrm{eh}}_{\mathbf{k}} - E^{\mathrm{eh}}_{\mathbf{k}=K}$, in the energy of $P_{\mathbf{k}}$ is emitted as HSB radiation, connecting the HSB spectrum with the band structure. Considerable spreading of $P_{\mathbf{k}}$—although much weaker than in HHG—and many-body contributions to the emission energy may complicate a direct inference of $E^{\mathrm{eh}}_{\mathbf{k}}$ from HSB spectra. Nevertheless, the HSB emission can be elegantly linked with $E^{\mathrm{eh}}_{\mathbf{k}}$ because the polarization wave packet $P_{\mathbf{k}}$ starts from the K point and is almost sinusoidally translated by the multiterahertz field (*28*).

The connection of the HSB spectrum with this well-synchronized motion and $E^{\mathrm{eh}}_{\mathbf{k}}$ becomes apparent when $P_{\mathbf{k}}(t) \equiv P^{\mathrm{rot}}_{\mathbf{k}}(t)e^{-2\pi i\nu_{\mathrm{opt}}t}$ is analyzed in a frame rotating with the optical excitation frequency ν_{opt}. The nth HSB is generated if $P^{\mathrm{rot}}_{\mathbf{k}}(t)$ oscillates with the frequency $\nu_n = n\,\nu_{\mathrm{THz}}$, which occurs only if $P^{\mathrm{rot}}_{\mathbf{k}}(t)$ has been translated to a $\mathbf{k}$ value where the HSB-photon energy, $E^{\mathrm{HSB}}_n \equiv h\nu_{\mathrm{opt}} + h\nu_n$, matches the energy of $P_{\mathbf{k}}$—that is, $E^{\mathrm{HSB}}_n = E^{\mathrm{eh}}_{\mathbf{k}}$. As illustrated in Fig. 1B for the 5th HSB, the oscillating polarization, $P^{\mathrm{rot}}_{\mathbf{k}}(t)$ crosses a given $\mathbf{k}$ value twice during a single multiterahertz cycle. In a simplified picture, the multiterahertz field purely translates $P^{\mathrm{rot}}_{\mathbf{k}}(t) = P^{\mathrm{rot}}_{\mathbf{k}(t)}$ with $\mathbf{k}(t) = \mathbf{k} - 2\pi|e|/h\int_{-\infty}^{t}\mathrm{d}t'\,\mathbf{E}_{\mathrm{THz}}(t')$ so that these two crossings (sparks) can be viewed as separate polarization bursts, adding up as a coherent superposition to the total spectral component

$$P^{\mathrm{rot}}_{\mathbf{k}}(\nu_5) = \int \mathrm{d}t\, P^{\mathrm{rot}}_{\mathbf{k}}(t)e^{+2\pi i\nu_5 t} \qquad (1)$$

The phase evolution between these bursts is defined by the spectrum-projecting kernel, $e^{+2\pi i\nu_5 t}$, which oscillates five times faster than

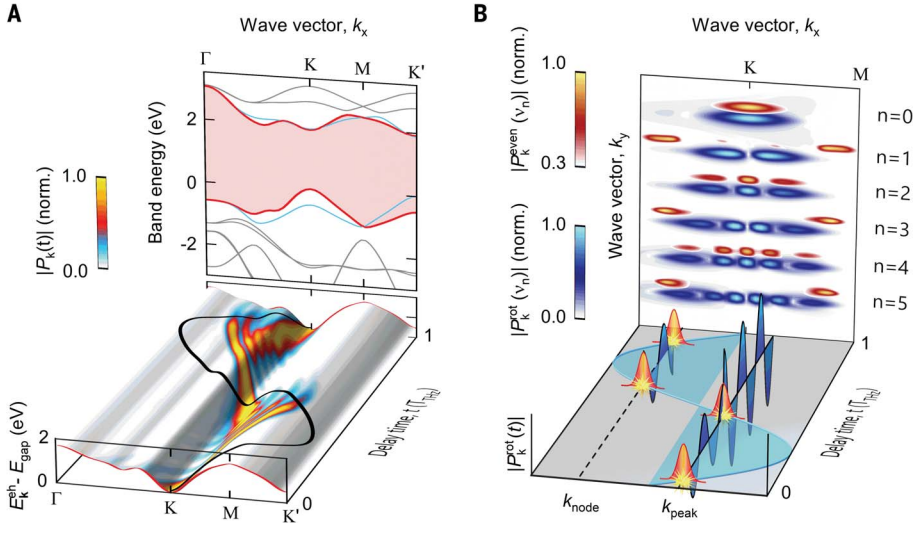

Fig. 1. Harmonic sideband generation and crystal momentum combs. (**A**) Band structure (top) of monolayer WSe_2 and typical exciton wave-packet dynamics (bottom) (color map $|P_k(t)|$ of many-body computation) in HSB. The red lines indicate the *e*-*h* bands, and the thick black line indicates the driving multiterahertz field (cycle duration, $T_{\mathrm{THz}} = \nu^{-1}_{\mathrm{THz}}$), projected onto the $E^{\mathrm{eh}}_{\mathbf{k}}$ surface (gray). (**B**) Schematics of a $|P^{\mathrm{rot}}_{\mathbf{k}}(t)|$ (Gaussians) on a sinusoidal path (transparent area) crossing a given $\mathbf{k}$ point twice during a multiterahertz cycle. These crossings (sparks) yield HSB-emission contributions interfering as waves (blue shaded areas). The screen compares $\mathbf{k}$ combs (blue-white color maps) with their even parts (red-yellow color maps) for 0th to 5th HSBs on the basis of full many-body computations.

[1]Department of Electrical Engineering and Computer Science, University of Michigan, Ann Arbor, MI, USA. [2]Department of Physics, University of Regensburg, Regensburg, Germany. [3]Department of Physics, University of Marburg, Marburg, Germany.
*These authors contributed equally to this work.
†Present address: Fakultät Physik, Technische Universität Dortmund, Otto-Hahn-Straße 4, 44227 Dortmund, Germany.
‡Corresponding author. Email: mackkira@umich.edu (M.K.); rupert.huber@ur.de (R.H.)

the $\mathbf{k}(t)$ trajectory (Fig. 1B, light blue area). Hence, there are, respectively, six or five $\mathbf{k}$ values where the first and second bursts are in (Fig. 1B, solid line) or out of phase (Fig. 1B, dashed line), leading to interference maxima or minima. Generally, $P_{\mathbf{k}}^{\mathrm{rot}}(\nu_n)$ exhibits a $\mathbf{k}$-space interference pattern with $(n + 1)$ maxima (screen), which we call a $\mathbf{k}$ comb in analogy to frequency combs (*29*, *30*) created by multiple time-domain pulses. Because $\mathbf{k}$ combs are the projections of $P_{\mathbf{k}}^{\mathrm{rot}}(t)$ (having the energy $E_{\mathbf{k}}^{\mathrm{eh}}$) onto a given $h\nu_n$, their amplitude decreases with increasing HSB-to-band energy difference.

In reality, $P_{\mathbf{k}}^{\mathrm{rot}}(t)$ cannot be reduced to a simple $\mathbf{k}(t)$ translation because many-body interactions distort the path, dephase the polarization, and renormalize the emission energies. We performed full quantum-kinetic computations with a state-of-the-art dynamic cluster-expansion approach (supplementary materials) (*5*) to systematically predict the HSB properties on the basis of fundamental electronic band structure, geometric phase effects, and the strong light-matter as well as the many-body Coulomb interactions. Although many-body and interference effects spread $P_{\mathbf{k}}$ and create new oscillating features (Fig. 1A, blue regions), the $(n + 1)$–peak structure of $\mathbf{k}$ combs remains robust (Fig. 1B, blue color maps). At the K point, all $\mathbf{k}$ combs of odd order exhibit a node, whereas those of even order feature a peak, implying a dominantly odd and even symmetry, respectively. This symmetry can be broken only by transporting $P_{\mathbf{k}}^{\mathrm{rot}}(t)$ to inversion asymmetric regions of the bands where $E_{\mathbf{k}}^{\mathrm{eh}} \neq E_{-\mathbf{k}}^{\mathrm{eh}}$.

Because $P_{\mathbf{k}}$ defines the coherent transition amplitude for *e-h* recombination (*5*) associated with the dipole moment $d_{\mathbf{k}}$, its symmetry affects the total HSB intensity

$$I_{\mathrm{HSB}}(\nu) \propto \left| (\nu_{\mathrm{opt}} + \nu) \sum_{\mathbf{k}\in \mathrm{BZ}} d\mathbf{k}\, P_{\mathbf{k}}^{\mathrm{rot}}(\nu) \right|^2 \quad (2)$$

where the $\mathbf{k}$ sum includes the entire BZ. For symmetric systems ($E_{\mathbf{k}}^{\mathrm{eh}} = E_{-\mathbf{k}}^{\mathrm{eh}}$ and $d_{\mathbf{k}} = d_{-\mathbf{k}}$), odd-order sidebands vanish because the odd-order $\mathbf{k}$ combs eliminate the total sum in $I_{\mathrm{HSB}}(\nu)$. Monolayer WSe_2 has inversion symmetric bands close to the K point, with asymmetric features ($E_{\mathbf{k}}^{\mathrm{eh}} \neq E_{-\mathbf{k}}^{\mathrm{eh}}$) emerging toward the M point. Only the even part of each comb, $P_{\mathbf{k}}^{\mathrm{even}}(\nu_n) \equiv \frac{1}{2}[P_{\mathbf{k}}^{\mathrm{rot}}(\nu_n) + P_{-\mathbf{k}}^{\mathrm{rot}}(\nu_n)]$, contributes to $I_{\mathrm{HSB}}(\nu_n)$, assuming that $d_{\mathbf{k}}$ is symmetric. $P_{\mathbf{k}}^{\mathrm{even}}(\nu_n)$ (Fig. 1B, red color map) for n = 0, 2, and 4 closely follows the respective $\mathbf{k}$ comb (Fig. 1B, blue color map). In stark contrast, odd orders produce a $P_{\mathbf{k}}^{\mathrm{even}}(\nu_n)$ that vanishes over the inversion-symmetric region of the bands and peaks sharply at the onset of the band asymmetry. Thus, odd-order sidebands solely originate from the outermost comb line. Although the $P_{\mathbf{k}}^{\mathrm{even}}(\nu_n)$ of the even HSBs are not localized, their $\mathbf{k}$ combs have a sharp leading edge whose energy and momentum overlap with the band structure determines the strength of the respective HSB emission. In any case, the position of the outermost comb line locates the origin of HSB at

$$k(n) = \frac{|e|E_{\mathrm{THz}}}{h\nu_{\mathrm{THz}}} C_n(E_{\mathrm{THz}}, \nu_{\mathrm{THz}}) \quad (3)$$

which can be interpreted as the maximum excursion of a classical trajectory times a many-body quantum correction C_n. The latter typically assumes a value between 0.5 and 1.5. The super-resolution follows as the width of the outermost comb line locates the nth HSB emission to an $(n + 1)$ times narrower $\mathbf{k}$ range than the excursion scale of the wave packets (supplementary materials), which improves the $\mathbf{k}$ resolution linearly with n. The vectorial position of the $\mathbf{k}$ comb is assigned by $k(n)$ times the direction of the multiterahertz field.

To show that super-resolution prominently manifests in experimental HSB spectra, we resonantly excited the 1*s* A exciton resonance in monolayer WSe_2 with an optical pulse (duration, 100 fs) centered at the photon energy of $h\nu_{\mathrm{opt}}$ = 1.665 eV. A linearly polarized multiterahertz transient centered at ν_{THz} = 42 THz accelerates $P_{\mathbf{k}}$ (supplementary materials) along the Γ-K direction. We controlled $k(n)$ by tuning the peak electric field $E_{\mathrm{THz}}^{\mathrm{peak}}$ from 7 to 19 MV cm^{-1} (in vacuum). The shape of the HSB spectra (Fig. 2A) changes strongly as function of $E_{\mathrm{THz}}^{\mathrm{peak}}$ and covers the entire visible spectrum. The third-order sideband emerges only for the highest fields, whereas the 5th order sets in steeply at $E_{\mathrm{THz}}^{\mathrm{peak}} = 7$ MV cm^{-1}, reaches its maximum at 13 MV cm^{-1}, and decreases for yet stronger fields (Fig. 2C). The 4th order exhibits a nonmonotonic scaling, too (supplementary materials), albeit not as steep as that of the 5th.

To connect this characteristic scaling behavior with the $\mathbf{k}$ combs, we compared the experiment with our full many-body computations. All HSB spectra (Fig. 2B) and the intensity scaling agree quantitatively, as shown for the 5th-order sideband in Fig. 2C. This allows us to faithfully assign a specific crystal momentum $k(5)$ (Fig. 2C, bottom scale) to each $E_{\mathrm{THz}}^{\mathrm{peak}}$ value (Fig. 2C, top scale) using Eq. 3. The computed $|P_{\mathbf{k}}^{\mathrm{even}}(\nu_5)|^2$ combs (Fig. 2D, color map) and $k(5)$ (Fig. 2D, blue lines) are shown in Fig. 2D as a function of $E_{\mathrm{THz}}^{\mathrm{peak}}$. In Fig. 2E, the corresponding dispersion relation $E_{\mathbf{k}}^{\mathrm{eh}}$ (dark area) is superimposed with $E_{-\mathbf{k}}^{\mathrm{eh}}$ (dotted line) to easily identify the band asymmetry ($E_{\mathbf{k}}^{\mathrm{eh}} \neq E_{-\mathbf{k}}^{\mathrm{eh}}$). The onset of the 5th HSB intensity (Fig. 2C) occurs precisely when $k(5)$ passes the band asymmetry (Fig. 2, C to E, arrow), verifying the super-resolution connection of odd-order HSB intensity and the position of the outermost comb line. Shifting the $\mathbf{k}$ comb further by larger $E_{\mathrm{THz}}^{\mathrm{peak}}$ inevitably increases the central energy of the polarization compared with that of the 5th HSB (Fig. 2E, blue line), reducing the energetic overlap, and thus decreases the 5th HSB intensity. Such a sharp $E_{\mathrm{THz}}^{\mathrm{peak}}$-dependent maximum in HSB intensity signifies a distinctive super-resolution signature for HSB spectroscopy. We verified similar but slightly less stringent super-resolution for even HSBs (supplementary materials).

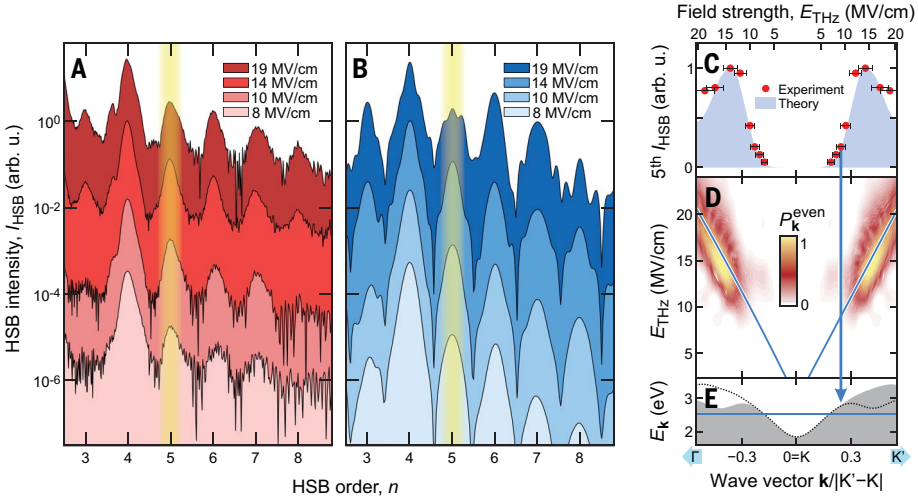

Fig. 2. Super-resolution band-structure tomography with a field-strength scan. (**A**) Measured versus (**B**) computed HSB intensity spectra for different E_{THz} (shifted for visibility) at fixed ν_{THz} = 42 THz. The 5th HSB intensity, I_{HSB}, includes the spectral range of the yellow transparent regions. (**C**) E_{THz} dependence (top axis) of measured (circles and error bars) and computed (shaded area) 5th I_{HSB}. The corresponding $k(5)$ is assigned in the bottom axis by using Eq. 3. (**D**) The computed E_{THz} dependence of the symmetric part of $|P_{\mathbf{k}}^{\mathrm{even}}(\nu_5)|$ and the comb position (blue line). (**E**) Electron-hole dispersion (gray area) in units of the K-to-K′ valley separation $|K' - K|$ and $E_{-\mathbf{k}}^{\mathrm{eh}}$ (dotted line) are connected with the HSB and $\mathbf{k}$ comb through the blue arrow.

To tomographically scan the $k(n)$–dependent crossing of the $\mathbf{k}$ comb with $E^{\mathrm{eh}}_{\mathbf{k}}$, we have developed a setup to quantitatively compare HSB spectra while varying ν_{THz} over a full optical octave, from 27 to 54 THz. The field strength is fixed at $E^{\mathrm{peak}}_{\mathrm{THz}} = 14\ \mathrm{MV\ cm^{-1}}$ to ensure efficient sideband generation (Fig. 3A) while suppressing parasitic interband excitations by the multiterahertz field. The 5th HSB is essentially absent for ν_{THz} = 27 THz, sets on sharply for larger THz frequencies (Fig. 3C), and peaks at around 40 THz. The computed spectra (Fig. 3B) and their scaling behavior as function of ν_{THz} (Fig. 3B) reproduce all these signatures very well. The ν_{THz} dependence of $|P^{\mathrm{even}}_{\mathbf{k}}(\nu_5)|^2$ (Fig. 3D, color map) confirms that the HSB peak coincides with the $\mathbf{k}$-comb peak (Fig. 3D, blue arrow) for ν_{THz} = 42 THz, where the single comb line (Fig. 3D, blue line) both overlaps with the asymmetric region ($E^{\mathrm{eh}}_{\mathbf{k}} \neq E^{\mathrm{eh}}_{-\mathbf{k}}$) (Fig. 3D, solid versus dashed lines) and has an energy close to the polarization ($E^{\mathrm{eh}}_{\mathbf{k}}$). For other ν_{THz} values, the HSB intensity becomes weaker because the $\mathbf{k}$ comb either does not reach the asymmetric range (high ν_{THz}) or differs substantially from the band energy (low ν_{THz}), creating a narrow ν_{THz}-dependent peak in the 5th HSB.

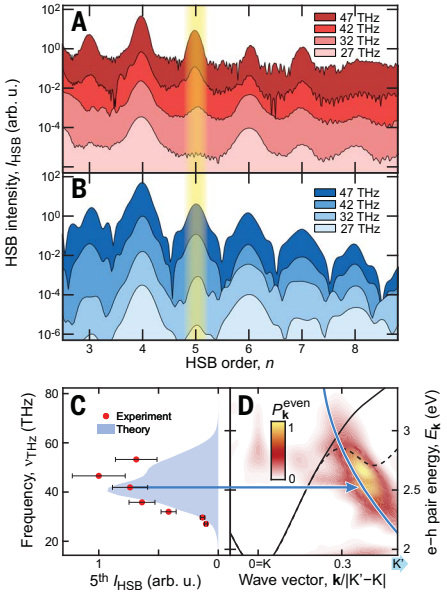

Fig. 3. Super-resolution band-structure tomography with a frequency scan. (**A**) Measured versus (**B**) computed HSB intensity spectra for different multiterahertz frequencies ν_{THz} (shifted for visibility), at fixed E_{THz} = 14 MV/cm. The yellow regions indicate the spectral range of the 5th I_{HSB}. (**C**) Measured (circles and error bars) and computed (shaded) 5th-order I_{HSB} as function of ν_{THz} (scale left) and the corresponding HSB energy (scale right). (**D**) The 5th HSB $\mathbf{k}$-comb position (blue line), $k(5)$ from Eq. 3 in units of the K-to-K′ valley separation $|K' - K|$, and symmetric part of $|P^{\mathrm{even}}_{\mathbf{k}}(\nu_5)|^2$ (color map) as function of ν_{THz} (left) and band energy (right) are compared with the electron-hole energy (solid line) and $E^{\mathrm{eh}}_{-\mathbf{k}}$ (dashed line). The blue arrow assigns the peak HSB-emission conditions.

These combined experimental and theoretical results herald super-resolution lightwave tomography: Because the $\mathbf{k}$ combs localize the HSB emission to a single ($\mathbf{k}$, energy)–point whose connection to the experimental parameters (E_{THz}, ν_{THz}) is known, scanning (E_{THz}, ν_{THz}) tomographically maps $E^{\mathrm{eh}}_{\mathbf{k}}$. Shown in Fig. 4 is the computed HSB intensity, $I_{\mathrm{HSB}}(\nu_n)$, resulting from a comprehensive (E_{THz}, ν_{THz}) scan, each point assigned to a single $[k(n), E^{\mathrm{HSB}}_n]$ pair by means of Eq. 3, for n = 3, 4, 5, 6 (Fig. 4, A to D) together with the $E^{\mathrm{eh}}_{\mathbf{k}}$ (solid lines) and $E^{\mathrm{eh}}_{-\mathbf{k}}$ (dashed lines) bands. The edges of $I_{\mathrm{HSB}}(\nu_n)$ track the entire band structure in remarkable detail, confirming that the overlap of the $\mathbf{k}$ combs with the band structure defines the strength of the HSB emission. As a stress test for our tomography, we measured the same $I_{\mathrm{HSB}}(\nu_n)$ with one-dimensional E_{THz} and ν_{THz} scans across few band-structure features and calibrated the experiment-theory intensities with a single factor that does not affect the assessed (E_{THz}, ν_{THz}) dependence. The experimental HSB scans (Fig. 4, A to D, within black bars) and the computations match nearly perfectly.

Also, the microscopic dipole, $d_{\mathbf{k}}$, affects the HSB intensity Eq. 3, which may distort the tomography by overemphasizing momentum regimes with large $d_{\mathbf{k}}$. However, super-resolution of a $\mathbf{k}$ comb locates the odd-order HSBs to a single pair ($\mathbf{k}$, energy), whereas $d_{\mathbf{k}}$ changes slowly over the $\mathbf{k}$ comb. Consequently, taking ratios of two HSB intensities, such as $R_{5\mathrm{th/3rd}} \equiv I_{\mathrm{HSB}}(\nu_5)/I_{\mathrm{HSB}}(\nu_3)$, eliminates distortions by $d_{\mathbf{k}}$. In Fig. 4E, blue color maps show the first positive peak of gradient $\frac{\partial}{\partial k} R_{5\mathrm{th/3rd}}$, and red color maps show the first negative peak of gradient $\frac{\partial}{\partial \mathrm{energy}} R_{5\mathrm{th/3rd}}$, starting from the K point (2 eV) to locate $E^{\mathrm{eh}}_{\mathbf{k}}$ (Fig. 4E, solid line). The resulting $R_{5\mathrm{th/3rd}}$ gradients track the band dispersion close to the band asymmetry, as expected for the odd $\mathbf{k}$ combs (HSBs), more accurately than the raw HSB intensities (Fig. 4, A and C). Nevertheless, $d_{\mathbf{k}}$ can be measured most sensitively through the rich details of HSB spectra (supplementary materials). The same analysis is repeated for the ratio of 6th and 4th HSBs in Fig. 4F for $\frac{\partial}{\partial \mathbf{k}} R_{6\mathrm{th/4th}}$ (blue color maps), $\frac{\partial}{\partial \mathrm{energy}} R_{6\mathrm{th/4th}}$ (red color maps), and $E^{\mathrm{eh}}_{\mathbf{k}}$ (black line). The peaks of these gradients track the band dispersion, although less sharply than for the odd HSBs because the latter benefits from super-resolution, as discussed above. The gradient approach also allows us to unfold the left- and right-hand side of the bands with respect to the K point. We have furthermore verified that using C_n = 1.3 in Eq. 3 yields only minor tomographic aberrations, making purely experimental super-resolution tomography possible, whereas fixing these aberrations yields a nontrivial value of C_n and thus experimental access to intriguing many-body effects in quantum materials (supplementary materials).

We introduce a powerful all-optical band-structure tomography by merging three complementary advantages of the harmonic sideband generation: An optical field selects a pair of

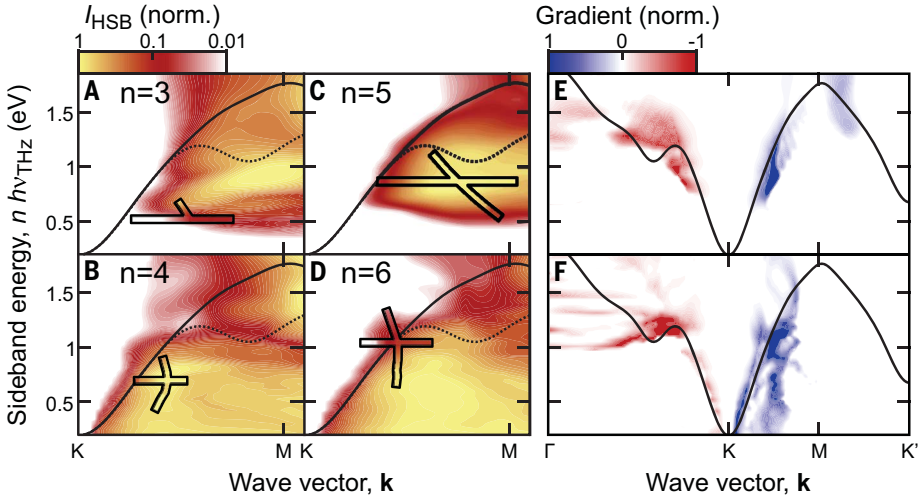

Fig. 4. Super-resolution lightwave tomography. (**A** to **D**) Color maps show the computed (A) 3rd, (B) 4th, (C) 5th, and (D) 6th HSB intensity constructed from a comprehensive (E_{THz}, ν_{THz}) scan and compared with one-dimensional experimental (E_{THz} and ν_{THz}) scans (black boxes). Each (E_{THz}, ν_{THz}) is connected with the wave vector by using Eq. 3 and the nth HSB energy $h(\nu_{\mathrm{opt}} + n\nu_{\mathrm{THz}})$. Also, the electron-hole dispersion (black line) and $E^{\mathrm{eh}}_{-\mathbf{k}}$ (dotted line) are shown. (**E** and **F**) Computed gradients of 5th:3rd (E) and 6th:4th (F) HSB taken in $\mathbf{k}$ (blue color map) and energy (red color map) directions, compared with the $E^{\mathrm{eh}}_{\mathbf{k}}$ (black line); only the first encountered gradient peaks are shown.

valence and conduction bands at a time, a strong multiterahertz field introduces crystal-momentum combs (**k** combs) that localize the origin of the emission to a small region within these bands, and the resulting excitations directly involve the quasiparticles relevant for quantum effects. The **k** combs are demonstrated to deliver a super-resolution lightwave tomography of quantum materials by using one- and two-dimensional multiterahertz frequency–field strength scans. Our approach can be straightforwardly generalized for a fully three-dimensional band tomography by adding the direction of the multiterahertz field as the third scanned variable. Also, geometric phase effects can be characterized by measuring the polarization of the sideband emission with respect to optical excitation. The introduced methodology seems optimally suited for high-precision characterization and control of quantum materials such as two-dimensional monolayer heterostructures, even on microscopic scales.

REFERENCES AND NOTES

1. A. K. Geim, I. V. Grigorieva, *Nature* **499**, 419–425 (2013).
2. M. Schwarze *et al*., *Science* **352**, 1446–1449 (2016).
3. M. S. Rudner, N. H. Lindner, *Nat. Rev. Phys.* **2**, 229–244 (2020).
4. E. Cohen *et al*., *Nat. Rev. Phys.* **1**, 437–449 (2019).
5. M. Kira, S. W. Koch, *Semiconductor Quantum Optics* (Cambridge Univ. Press, 2011).
6. H. Yu, X. Cui, X. Xu, W. Yao, *Natl. Sci. Rev.* **2**, 57–70 (2015).
7. A. E. Almand-Hunter *et al*., *Nature* **506**, 471–475 (2014).
8. Y. Cao *et al*., *Nature* **556**, 43–50 (2018).
9. K. F. Mak, C. Lee, J. Hone, J. Shan, T. F. Heinz, *Phys. Rev. Lett.* **105**, 136805 (2010).
10. T. Ohta, A. Bostwick, T. Seyller, K. Horn, E. Rotenberg, *Science* **313**, 951–954 (2006).
11. Y. L. Chen *et al*., *Science* **325**, 178–181 (2009).
12. J. Reimann *et al*., *Nature* **562**, 396–400 (2018).
13. B. Lv, T. Qian, H. Ding, *Nat. Rev. Phys.* **1**, 609–626 (2019).
14. B. Zaks, R. B. Liu, M. S. Sherwin, *Nature* **483**, 580–583 (2012).
15. F. Langer *et al*., *Nature* **533**, 225–229 (2016).
16. H. B. Banks *et al*., *Phys. Rev. X* **7**, 041042 (2017).
17. F. Langer *et al*., *Nature* **557**, 76–80 (2018).
18. A. H. Chin, O. G. Calderón, J. Kono, *Phys. Rev. Lett.* **86**, 3292–3295 (2001).
19. S. Ghimire *et al*., *Nat. Phys.* **7**, 138–141 (2011).
20. O. Schubert *et al*., *Nat. Photonics* **8**, 119–123 (2014).
21. M. Hohenleutner *et al*., *Nature* **523**, 572–575 (2015).
22. G. Vampa *et al*., *Phys. Rev. Lett.* **115**, 193603 (2015).
23. M. Sivis *et al*., *Science* **357**, 303–306 (2017).
24. N. Tancogne-Dejean, O. D. Mücke, F. X. Kärtner, A. Rubio, *Phys. Rev. Lett.* **118**, 087403 (2017).
25. T. Higuchi, C. Heide, K. Ullmann, H. B. Weber, P. Hommelhoff, *Nature* **550**, 224–228 (2017).
26. N. Yoshikawa, T. Tamaya, K. Tanaka, *Science* **356**, 736–738 (2017).
27. A. J. Uzan *et al*., *Nat. Photonics* **14**, 183–187 (2020).
28. F. Bloch, *Z. Phys.* **52**, 555–600 (1929).
29. J. L. Hall, *Rev. Mod. Phys.* **78**, 1279–1295 (2006).
30. N. Picqué, T. W. Hänsch, *Nat. Photonics* **13**, 146–157 (2019).
31. M. Borsch, Data for figures: Super-resolution lightwave tomography of electronic bands in quantum materials. Zenodo (2020).

ACKNOWLEDGMENTS

We thank F. Langer for technical support and scientific discussions. **Funding:** The Michigan portion of this collaboration is supported by the Army Research Office (ARO) through award W911NF1810299 and College of Engineering Blue Sky Research Program, the Regensburg effort by the Deutsche Forschungsgemeinschaft (DFG; German Research Foundation)–Project-ID, 314695032–SFB 1277 (Subproject A05) and project HU1598/8, and the Marburg part by DFG, Project-ID 223848855-SFB 1083. **Author contributions:** M.B., C.P.S., L.W., S.S., N.H., C.L., J.T.S., S.W.K., R.H., and M.K. conceived the study. M.B., J.T.S., S.W.K., and M.K. developed and performed the many-body computations and analyzed the data. C.P.S., L.W., S.S., N.H., C.L., and R.H. carried out the experiment and analyzed the data. All authors discussed the results and contributed to the writing of the manuscript. **Competing interests:** None declared. **Data and materials availability:** All data presented in the figures are accessible online (*31*). All other data needed to evaluate the conclusions in the paper are present in the paper or the supplementary materials.

SUPPLEMENTARY MATERIALS

science.sciencemag.org/content/370/6521/1204/suppl/DC1
Materials and Methods
Supplementary Text
Figs. S1 to S7
References (*32*–*43*)

7 August 2020; accepted 28 October 2020
10.1126/science.abe2112

CORONAVIRUS

De novo design of potent and resilient hACE2 decoys to neutralize SARS-CoV-2

Thomas W. Linsky[1]*, Renan Vergara[1]*, Nuria Codina[1]*, Jorgen W. Nelson[1]*, Matthew J. Walker[1], Wen Su[2], Christopher O. Barnes[3], Tien-Ying Hsiang[4], Katharina Esser-Nobis[4], Kevin Yu[1], Z. Beau Reneer[5], Yixuan J. Hou[4], Tanu Priya[1], Masaya Mitsumoto[1], Avery Pong[1], Uland Y. Lau[1], Marsha L. Mason[1], Jerry Chen[1], Alex Chen[1], Tania Berrocal[1], Hong Peng[1], Nicole S. Clairmont[1], Javier Castellanos[1], Yu-Ru Lin[1], Anna Josephson-Day[1], Ralph S. Baric[6], Deborah H. Fuller[7], Carl D. Walkey[1], Ted M. Ross[5,8], Ryan Swanson[1], Pamela J. Bjorkman[3], Michael Gale Jr.[4], Luis M. Blancas-Mejia[1], Hui-Ling Yen[2], Daniel-Adriano Silva[1]†

We developed a de novo protein design strategy to swiftly engineer decoys for neutralizing pathogens that exploit extracellular host proteins to infect the cell. Our pipeline allowed the design, validation, and optimization of de novo human angiotensin-converting enzyme 2 (hACE2) decoys to neutralize severe acute respiratory syndrome coronavirus 2 (SARS-CoV-2). The best monovalent decoy, CTC-445.2, bound with low nanomolar affinity and high specificity to the receptor-binding domain (RBD) of the spike protein. Cryo–electron microscopy (cryo-EM) showed that the design is accurate and can simultaneously bind to all three RBDs of a single spike protein. Because the decoy replicates the spike protein target interface in hACE2, it is intrinsically resilient to viral mutational escape. A bivalent decoy, CTC-445.2d, showed ~10-fold improvement in binding. CTC-445.2d potently neutralized SARS-CoV-2 infection of cells in vitro, and a single intranasal prophylactic dose of decoy protected Syrian hamsters from a subsequent lethal SARS-CoV-2 challenge.

Since its emergence as a global pandemic in December of 2019, severe acute respiratory syndrome coronavirus 2 (SARS-CoV-2) has caused millions of COVID-19 cases. The need for effective strategies to prevent and treat the disease remains urgent (*1*). There are multiple ongoing efforts to develop prophylactics and therapeutics using various approaches (*2*) such as vaccination (*3*), traditional protein engineering (*1*, *4*, *5*), de novo protein design (*6*), and small-molecule drug discovery (*7*). A challenge is that the high mutational rate of positive sense single-strand RNA (+ssRNA) viruses (*8*–*10*) can often lead to viral escape (*11*), which could compromise the efficacy of many SARS-CoV-2 therapeutics under development. Several mutations have already occurred in the S protein of SARS-CoV-2 in the infected population (*12*, *13*). Deep-sequencing studies of the receptor-binding domain (RBD) have shown that simple mutations can enable the virus to escape known netralizing antibodies or to increase its binding affinity for human angiotensin-converting enzyme 2 (hACE2) (*14*, *15*), the membrane protein that the virus exploits to gain entry into the cell. There is thus a pressing need to develop new therapeutics that can be more resistant to SARS-CoV-2 mutational escape.

Traditional approaches to combatting viruses (e.g., vaccination and monoclonal antibodies) rely on molecules interacting with the pathogens in a way that is fundamentally different from how the pathogen engages with its cellular targets (*16*, *17*). Viruses can be selected to evade neutralization, undergoing protein mutations that prevent recognition by the neutralizing molecules (e.g., antibodies) while preserving viral fitness. To address these challenges, we have developed a computational protein design strategy that enables the rapid and accurate design of hyperstable de novo protein "decoys" that replicate the protein receptor interface to which a virus binds to infect a cell. The decoys can achieve a similar or even higher affinity than the original protein receptor by stabilizing the binding interface. Therefore, at an optimal concentration, the decoys can outcompete viral interaction with the cell.

SARS-CoV-2 invades host cells in a two-step process (*18*–*20*). The S protein RBD attaches to the cell by binding to hACE2, a membrane-associated protein, triggering protease-mediated fusion with the cell membrane (*21*). The process is similar to the beta-coronaviruses HCoV-NL63 and SARS-CoV-1, which also target hACE2 for cellular entry (*22*). In principle, inhibiting the viral interaction with hACE2 should prevent infection. We applied our design strategy to engineer, validate, and optimize de novo hACE2 decoys to neutralize SARS-CoV-2 infection (Fig. 1J and fig. S1). The design of the decoys started by identifying the structural motifs that form the hACE2 binding interface with the SARS-CoV-2 RBD. We based our effort on three publicly available structures of hACE2 in complex with the RDB of the S protein for SARS-CoV-1 (PDB: 6CS2) and SARS-CoV-2 (PDBs: 6VW1 and 6M17) (*23*–*25*). Four discontiguous binding elements were identified (Fig. 1A) and the three largest interacting motifs were selected to build the de novo decoys: two long alpha helices (H1 and H2) and a short beta hairpin (EE3) (Fig. 1A and fig. S2). To generate molecules that are biologically inert for humans, our computational design strategy avoided incorporating elements of hACE2 that are known (or predicted) to be biologically active, such as the catalytic site. Inspired by recent developments in the design of de novo structural elements (*26*–*29*), we built new disembodied de novo secondary structure elements tailored to support the target structural elements in a way that is both compatible with globular folding and would stabilize the binding interface (Fig. 1B and materials and methods). Then, in a strategy similar to the design of Neoleukin-2/15 (Neo-2/15) (*26*, *30*), a combinatorial design approach based on Rosetta's "protein_mimic_designer" was used to generate multiple fully connected protein topologies containing all of the desired structural and binding elements (*26*). The design of the protein decoys was constrained to fully preserve (intact up to each amino acid's conformation) the target binding interface (Fig. 1, A and B, and fig. S2) so that the de novo proteins would be resilient to viral mutational escape. Rosetta (*31*) was then used to generate amino acid sequences predicted to fold into the target structures, and the designs were evaluated with an automatic filtering pipeline based on nine computational parameters, including predictions of smooth folding funnels into a stable native state (Fig. 1, C and D) (*32*).

Approximately 35,000 computational ACE2 decoys were generated, and the top-ranking 196 designs (see the materials and methods) were selected for experimental testing for binding to SARS-CoV-2 RBD using yeast display (Fig. 1E). With no further optimization, the design CTC-445 showed strong (nanomolar) and specific binding for SARS-CoV-2 RBD (Fig. 1E, fig. S3, and materials and methods). CTC-445 is a 160–amino acid protein comprising 18 of the natural amino acids; it does not contain cysteine or tryptophan residues. It exhibited ~10-fold weaker binding affinity for SARS-CoV-2 than did hACE2 [disassociation constant (K_D) ~ 357 nM, K_D ~ 31 nM, respectively; table S1] and, as a result, CTC-445 was a weak competitor of SARS-CoV-2 RBD binding to hACE2 [median inhibitory concentration ($IC_{50\ @\ hACE2[0.4nM]}$) = 1.7 μM; Fig. 1I). We determined that low potency of CTC-445 was due to a certain degree

[1]Neoleukin Therapeutics Inc., Seattle, WA, USA. [2]School of Public Health, Li Ka Shing Faculty of Medicine, University of Hong Kong, Hong Kong Special Administrative Region, China. [3]Division of Biology and Biological Engineering, California Institute of Technology, Pasadena, CA, USA. [4]Center for Innate Immunity and Immune Disease, Department of Immunology, University of Washington, Seattle, WA, USA. [5]Center for Vaccines and Immunology, University of Georgia, Athens, GA, USA. [6]Department of Epidemiology, University of North Carolina at Chapel Hill, Chapel Hill, NC, USA. [7]Department of Microbiology, University of Washington, Seattle, WA, USA. [8]Department of Infectious Diseases, University of Georgia, Athens, GA, USA.
*These authors contributed equally to this work.
†Corresponding author. Email: dadriano@neoleukin.com

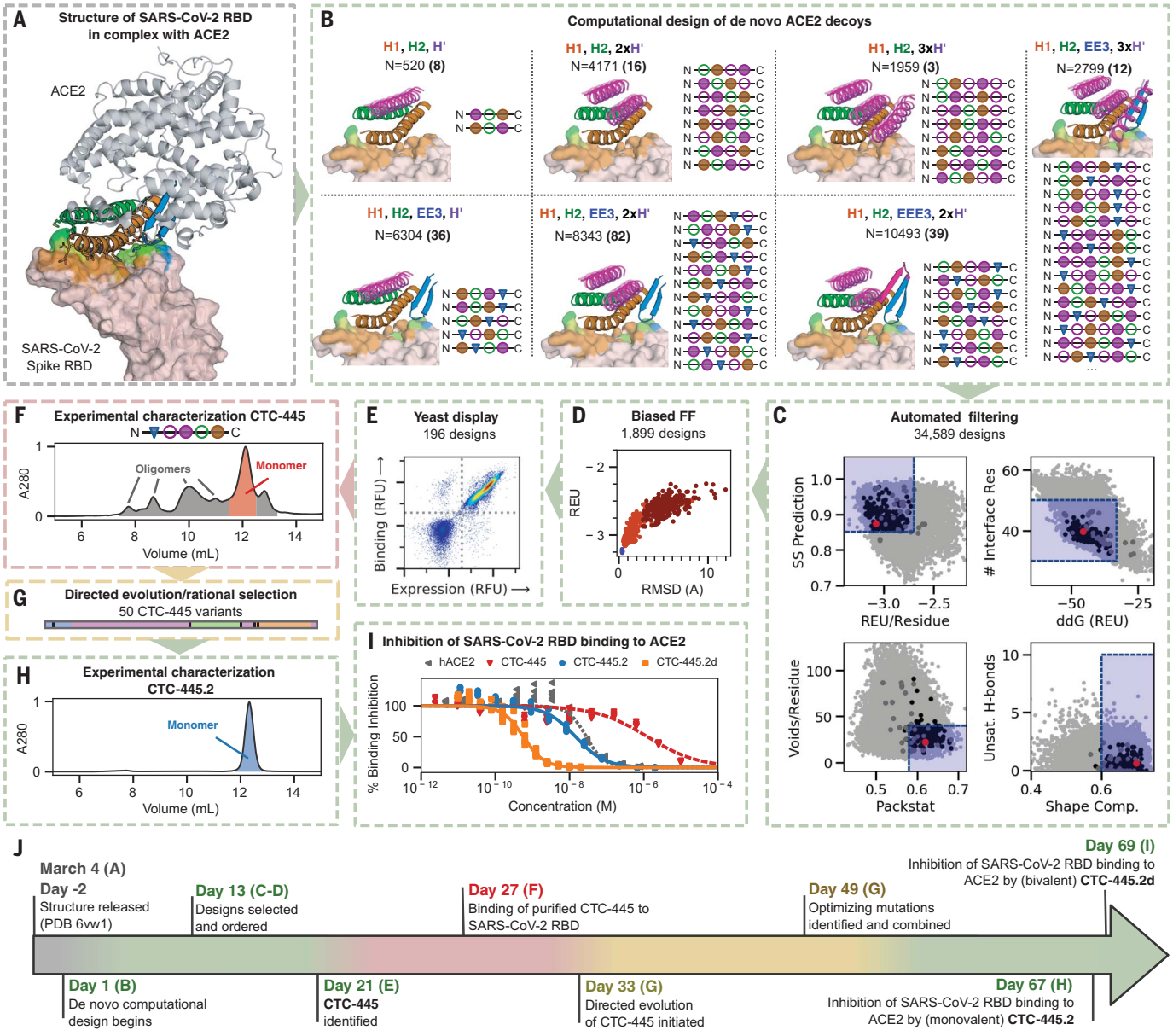

Fig. 1. Design and characterization of de novo ACE2 decoys. (**A**) ACE2 (gray) and its binding motifs (H1 19-52, orange; H2 55-84, green; EE3 346-360, blue) in complex with SARS-CoV-2 RBD (pink). Three starting structures were simultaneously used as targets (see main text); 6VW1 is shown. (**B**) De novo secondary structure elements (magenta) were computationally generated to stabilize H1, H2, and EE3. Seven combinations of secondary structure elements were considered. Circles are α-helices, triangles are β-sheets, filled circles are helices oriented forward, and empty circles are helices oriented backward. We used Rosetta to generate fully connected backbones (using the "protein_mimic_designer" algorithm) and amino acid sequences predicted to fold into the target structure. In all cases, the binding interface of ACE2 with the SARS-CoV-2 RBD was preserved intact (see the materials and methods). (**C**) Automatic computational filtering based on eight metrics selected the best candidates. The RMSD of the binding motifs to ACE2 was also used as a quality check. The dots indicate the mean computational score for each design scored against the three target RBD structures. Designs selected for experimental testing are shown in black. Our best design, CTC-445, is shown in red. The blue boxes indicate the filtering thresholds (see the materials and methods). (**D**) Designs that passed filtering were subjected to biased forward folding simulations (see the materials and methods), here shown for CTC-445, including the unsalted biased simulation (brown), the native-salted simulation (orange), and relaxation (blue). (**E**) The top 196 designs were selected for yeast display screening using a combination of Rosetta score per residue, the ddG Rosetta filter, and the folding simulations (see the materials and methods). The designs were individually assessed for specific binding to SARS-CoV-2 spike RBD (Fc fusion, 200 nM). The plot for CTC-445 is shown. (**F**) CTC-445 was recombinantly expressed and purified by affinity chromatography (see the materials and methods). Analytical size exclusion chromatography (SEC) for CTC-445 revealed the presence of oligomeric species. (**G** and **H**) CTC-445 was optimized by directed evolution and rational combination of the observed favorable mutations (G), leading to CTC-445.2 (SEC), which is mainly monomeric in solution (H) and ~1000× more potent to compete with ACE2 than its parent [see (G)]. We further optimized the potency of our molecule by generating a bivalent version named CTC-445.2d. (**I**) Potency of designs to outcompete binding of SARS-CoV-2 RBD to ACE2, as measured by competition enzyme-linked immunosorbent assay (ELISA) using a constant concentration of 0.4 nM ACE2. (**J**) Timeline of the de novo protein design and optimization pipeline. Timewise, green indicates phases that we believe were performed optimally, red indicates those that can potentially be avoided in future efforts, and yellow indicates phases that can potentially be expedited by using more advanced and/or automated methods for gene synthesis, cloning, and high-throughput screening.

of instability of its folded state [free energy difference between folded and intermediate states (ΔG_{NI}) ~−2.7 kcal mol^{-1}, melting transition temperature (T_m) ~75.3°C; Figs. 1F and 2B and fig. S5]. A single round of directed evolution to improve stability and binding affinity, and subsequently the rational combination of the five most frequent observed mutations (none of them in the binding interface), led to the protein decoy CTC-445.2 (Fig. 1G, figs. S6 and S7, table S2, and materials and methods). CTC-445.2 is predominantly monomeric (Fig. 1H and fig. S8), thermodynamically hyperstable (ΔG_{NI} ~−5.0 kcal mol^{-1}, T_m ~93°C; Fig. 2B and fig. S5), exhibits low nanomolar affinity for the RBD of SARS-CoV-2 (K_D ~21.0 nM; table S1), has improved cross-reactivity to SARS-CoV-1 (K_D ~7.1 μM; Fig. 2C and table S1), and can efficiently compete hACE2 binding to the SARS-CoV-2 RBD ($IC_{50\ @\ hACE2[0.4nM]}$ ~10.4 nM; Fig. 1I). The amino acid sequence of CTC-445.2 has little identity with hACE2, in terms of either linear or structurally aligned sequence (ClustalW ~22%, MICAN ~ 4%, respectively; fig. S9). Serial duplication (i.e., increase in avidity) of CTC-445.2 led to higher-potency molecules with favorable biochemical properties. For example, CTC-445.2d (Fig. 2A), a bivalent version of CTC-445.2, had an ~10-fold improvement in binding affinity for both SARS-CoV-2 RBD (K_D ~3.5 nM; table S1) and SARS-CoV-1 RBD (K_D ~587 nM; Fig. 2C and table S1), and a similar increase in its ability to compete with hACE2 binding to SARS-CoV-2 RBD ($IC_{50\ @\ hACE2[0.4nM]}$ ~700 pM; Fig. 1I). A trivalent version of CTC-445.2 resulted in even higher (picomolar) binding affinity and a matching hACE2 competition potency (K_D ~270 pM, $IC_{50\ @\ hACE2[0.4nM]}$ ~10 pM; fig. S10 and table S1). In a cross-reactivity binding assay containing >21,000 human proteins, we confirmed that CTC-445.2d bound to the SARS-CoV-2 RBD with high selectivity (fig. S11 and materials and methods).

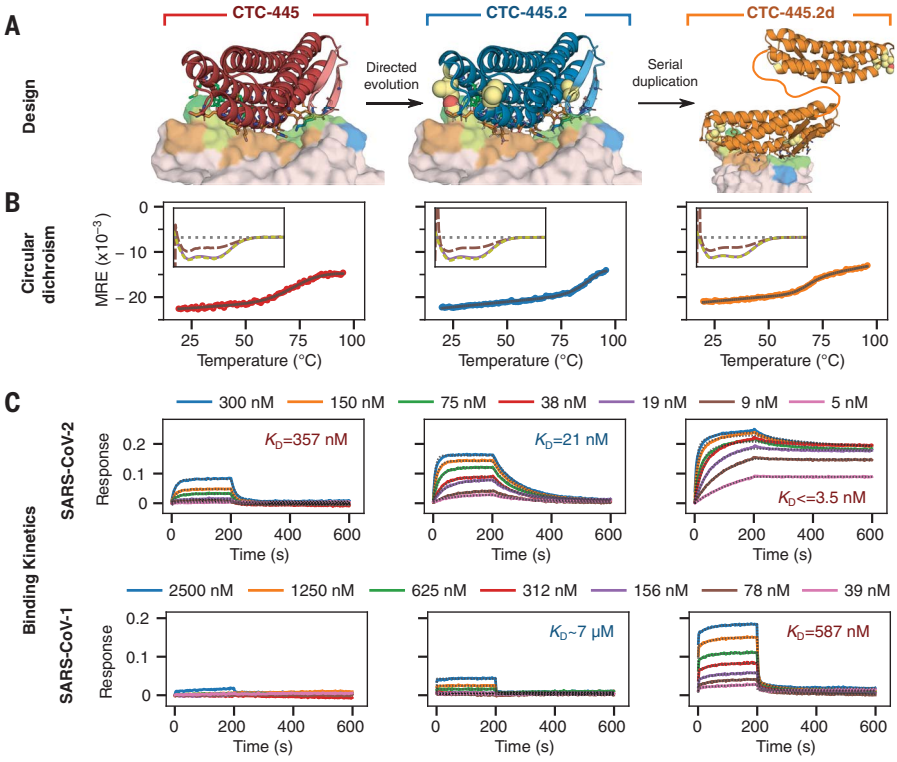

Fig. 2. Stability and binding of the de novo protein decoys CTC-445, CTC-445.2, and CTC-445.2d. (**A**) Design models of CTC-445, CTC-445.2, and CTC-445.2d. CTC-445.2 contains five mutations that were guided by directed evolution experiments. CTC-445.2d is a bivalent variant composed of two CTC-445.2 subunits linked by a 16-mer flexible GS linker (sequence -GGGSGGSGSGGSGGGS-). (**B**) Circular dichroism of recombinantly expressed CTC-445 (red), CTC-445.2 (blue), and CTC-445.2d (orange). Thermally induced melting of the decoys was followed by its circular dichroism signal at 208 nm (heating rate, 2°C/min). The inset shows far ultraviolet (UV) wavelength spectra at 20°C (purple), after heating to ~95°C (brown), and after cooling the heated sample to 20°C (green dashed). Complete ellipticity spectra recovery (full reversibility) upon cooling was observed in all cases. Calculated T_m values for CTC-445, CTC-445.2, and CTC-445.2d are 75.3 ± 0.2°C, ≈93°C, and 71.7.± 0.2°C, respectively. (**C**) Binding was assessed using biolayer interferometry (OCTET) binding assays of CTC-445, CTC-445.2, and CTC-445.2d against immobilized SARS-CoV-2 RBD (top) or SARS-CoV-1 RBD (bottom) (see table S1). The model fitting is shown with dotted black lines.

Single-particle cryo-EM structures of CTC-445.2 in complex with the SARS-CoV-2 S trimer showed that the de novo decoy is capable of simultaneous binding to all three RBDs of the SARS-CoV-2 trimeric S protein, both in the "up" and "partially down" RBD conformations (Fig. 3, A to D, and fig. S12). To accurately model the CTC-445.2-RBD interactions, we used focused classification and local refinement on the subset of particles that showed CTC-445.2 bound to a partially down RBD, which yielded a 4.1-Å map with improved CTC-RBD features relative to CTC-RBD regions on the up RBDs (Fig. 3, A to D, and figs. S12 and S13). The computationally derived model of CTC-445.2 closely matched the cryo-EM–determined structure [Cα root mean square deviation (RMSD) = 1.1 Å], with minor differences observed in the N-terminal EE3 and H2 helix (Fig. 3, E to H). As designed, the binding interface of the SARS-CoV-2 RBD with CTC-445.2 closely mirrored the target hACE2 interface. We used site saturation mutagenesis (SSM; see the materials and methods) (*33*, *34*) to explore the effect of single–amino acid substitutions in CTC-445.2 on its binding to the SARS-CoV-2 RBD (Fig. 3, I and J). The experiment showed that mutations in the core of the design are disallowed, and mutations in surface or exposed residues are generally tolerated (Fig. 3, I and J). The SSM experiment also revealed that there is room to further improve the affinity of the protein by introducing mutations in the binding interface (Fig. 3I), although doing so would break the hACE2 structural mirroring of the de novo decoy.

We also performed an SSM experiment for the SARS-CoV-2 RBD binding interface to compare the effect of single–amino acid substitution on binding to hACE2 or CTC-445.2. As predicted, the effects of ~1700 SARS-CoV-2 RBD mutations showed a strong correlation between binding to hACE2 and CTC-445.2 (R^2 = 0.84, Pearson's r = 0.92; Fig. 4 and fig. S14), highlighting the decoy's intrinsic resiliency to mutational escape. At low target concentrations (100 pM), CTC-445.2 had a large binding advantage over ACE2 for many of the RBD mutations (fig. S14), likely a result of both its higher stability and smaller size. Although CTC-445.2 was resilient to viral mutations in the RBD-binding interface, we observed some decoy-binding–weakening mutations that had a lesser effect on hACE2 binding. Therefore, viral mutational escape might still be possible if multiple (decoy-binding–weakening) RBD mutations are combined.

The high and specific binding affinity of the optimized de novo protein decoys translated into effective and specific in vitro neutralization of SARS-CoV-2 viral infection (Fig. 5). In vitro, the presence of the de novo decoys had no impact on mammalian cell viability (Fig. 5A and fig. S15) or the enzymatic activity of hACE2 (fig. S16). Both of the decoys were able to fully

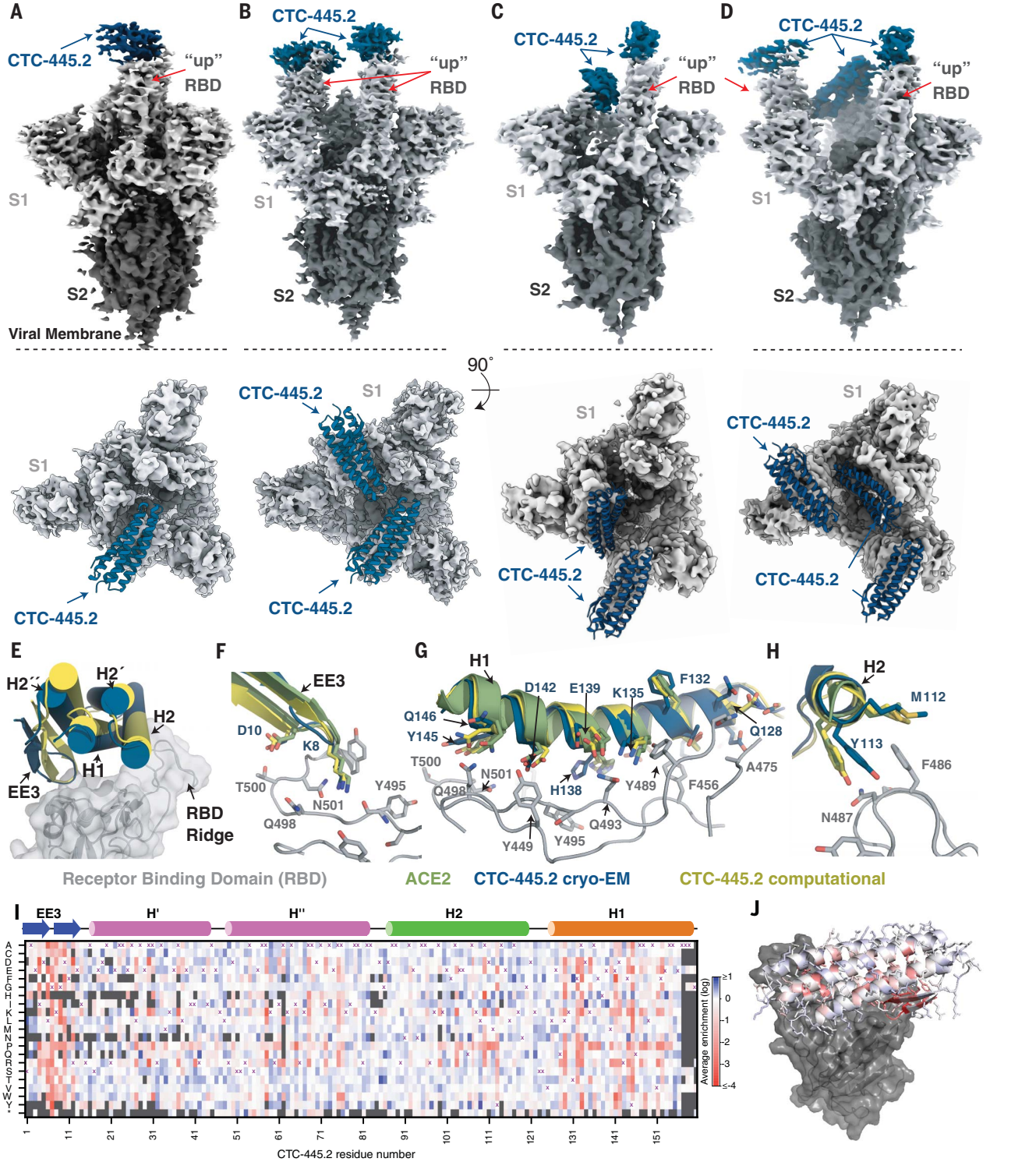

Fig. 3. Cryo-EM structure of the CTC-445.2–S complex. (**A** to **D**) Cryo-EM reconstructions of CTC-445.2 (blue) bound to soluble spike trimers (gray). 3D classification revealed four distinct classes: one CTC-445.2 bound to an "up" RBD (A), two CTC-445.2 bound to two "up" RBDs (B), two CTC-445.2 bound to one "up" and one "down" RBD (C), and three CTC-445.2 bound to two "up" and one "down" RBD (D). (**E**) Overlay of CTC-445.2-RBD computationally modeled (yellow) and experimentally determined using cryo-EM (blue). The Cα RMSD between the design model and the refined experimental structure is 1.1 Å. (**F** to **H**) Comparison of cryo-EM CTC-445.2 (blue), computationally modeled CTC-445.2 (yellow), and hACE2 (green) at the interface of the RBD (gray). (**I**) Deep mutational scanning heatmap showing the average effect on the enrichment for single site mutants of CTC-445.2 when assayed by yeast display for binding to the SARS-CoV-2 RBD (binding assayed at RBD concentrations of 100, 50, 25, 12.5, 6.25, 3.125, and 1.5625 pM; see the materials and methods). (**J**) Design model of CTC-445.2 colored by average enrichment at each residue position [from the data in (I)] bound to SARS-CoV-2 RBD (gray). As expected, mutations in the core of the design or to positions involved in binding to the RBD are generally disallowed. The deep mutational scanning revealed that there is still room to further improve the binding affinity of CTC-445.2, including mutations in the binding interface that in principle could afford higher potency and selectivity at the cost of compromising the decoy's mutational escape resiliency (see Fig. 4).

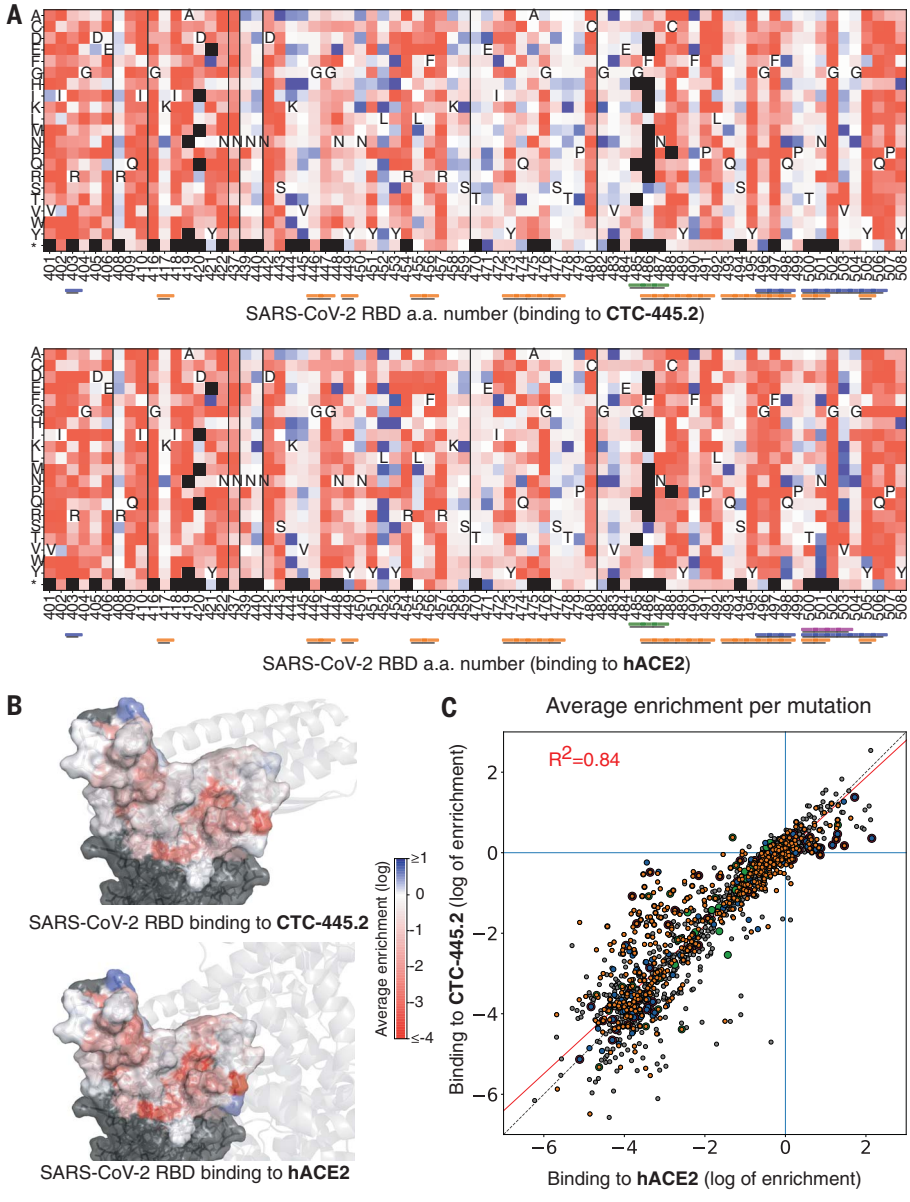

Fig. 4. Resilience of CTC-445.2 to SARS-CoV-2 RBD mutational escape. (**A**) Deep mutational scanning (DMS) of the SARS-CoV-2 RBD interface was performed to assess the effect on binding (by yeast display) to CTC-445.2 (top) or hACE2 (bottom) at eight different concentrations (656, 218, 72, 24, 8, 2, 0.3, and 0.1 nM; fig. S16 and materials and methods). The heatmaps indicate the effect on binding for each possible single amino acid mutation in the hACE2-binding interface of the RBD (see the materials and methods). The results are the average over all the concentrations tested. A black square represents lack of expression in the naive (unselected) library. The color bars at the bottom indicate the secondary structure element with which a given RBD residue interacts: H1, orange; H2, green; EE3, blue; and H4, magenta. Approximately 1700 single mutations were targeted by the experiment. (**B**) The SARS-CoV-2 RBD surface is colored according to the per-residue-averaged enrichments for binding to CTC-445.2 (top) or hACE2 (bottom). For reference, the structure of CTC-445.2 or ACE2 (respectively) is shown in semitransparent gray cartoons. (**C**) The 2D scatter plots compare the enrichment values [as in (A)] for the DMS of the RBD binding to CTC-445.2 (*y*-axis) versus hACE2 (*x*-axis). There is a high correlation between the effect of RBD mutations in the binding of both molecules, demonstrating the mutational resilience of the de novo decoy (Pearson's r = 0.92).

neutralize viral infection in in vitro systems of cell infection. Briefly, in a vesicular stomatitis virus (VSV) pseudovirus system expressing the SARS-CoV-2 S protein, the decoys specifically protected human embryonic kidney (HEK) 293T cells overexpressing hACE2 from infection (fig. S15). The decoys also were able to fully neutralize infection by SARS-CoV-2 (SARS-CoV-2 nanoLuc; see the materials and methods) in the lung epithelial cell line Calu-3 expressing both ACE2 and the transmembrane protease serine 2 (TMPRSS2) (*35*, *36*) [median effective concentration < 5 nM at a multiplicity of infection (MOI) of 1.0; Fig. 5A]. In an in vitro time-of-addition assay using the Vero E6 cell line, CTC-445.2 and CTC-445.2d were most effective at neutralizing SARS-CoV-2 infection when continuously present in the cell media throughout the full course of infection (as opposed to only before or after infection; Fig. 5A and figs. S16 to S18), confirming that their mechanism of viral inhibition is extracellular neutralization of the virus.

To determine the potential of our molecules to be used as respiratory-delivered therapeutics, we intranasally administered a single dose of CTC-445.2d to Balb/c mice (100 μg dose of CTC-445.2d in a 30-μL droplet) and observed the presence of the fully functional decoy for >24 hours in the lungs and respiratory tract of mice (Fig. 5B and fig. S19). A 14-day course of daily CTC-445.2d intranasal administration in mice (100 μg of CTC-445.2d in a 30-μL droplet) was well tolerated, causing no adverse effects (Fig. 5B). In a Syrian hamster model for SARS-CoV-2 infection, a single prophylactic intranasal dose of CTC-445.2d (560 μg of CTC-445.2d in a 100-μL droplet) administered 12 hours before the viral challenge afforded 100% survival from a lethal SARS-CoV-2 challenge (5×10^5 plaque-forming units of SARS-CoV-2; Fig. 5C). Specifically, by day 7, all control animals that received the viral challenge but not CTC-445.2d (n = 7) exhibited severe distress and required euthanasia. By contrast, hamsters that received a single dose of CTC-445.2d 12 hours before challenge all survived (n = 8), with modest weight loss and few or no clinical signs of distress (Fig. 5C and table S5).

Our de novo protein design approach to generate decoys is orthogonal to traditional therapeutics and has the potential to better overcome mutational viral evasion. Natural proteins repurposed often present substantial challenges for development as therapeutics; these include low stability, which can complicate manufacturing, transport, and storage;

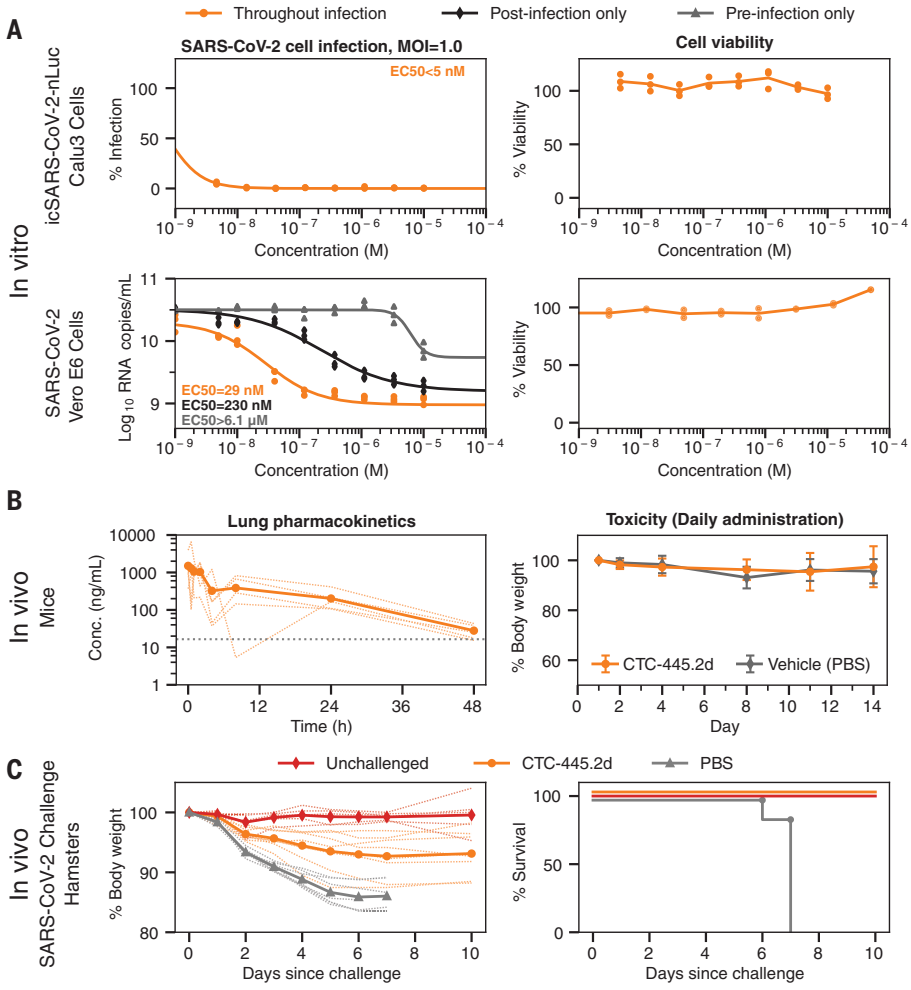

Fig. 5. In vitro virus neutralization by CTC-445.2d. (**A**) Top left: In vitro neutralization of NanoLuc SARS-CoV-2 by CTC-445.2d in Calu-3 cells after 72 hours of incubation at a MOI of 1.0. Top right: A cell viability assay (48 hours) confirmed that the decoys are not cytotoxic to Calu-3. Bottom left: In vitro neutralization of live BetaCoV/Hong Kong/VM20001061/2020 SARS-CoV-2 virus in Vero E6 cells at a MOI of 1.0. The cells were incubated with CTC-445.2d throughout infection and the colors indicate the following: orange, before infection, during infection, and after infection; black, after infection only; and gray, before infection only. SARS-CoV-2 RNA copy numbers were determined by quantitative real-time reverse transcription polymerase chain reaction. All assays were performed in triplicate unless otherwise noted, and all data points are shown. Bottom right: Cell viability in Vero E6 cells was independently performed (CCK8 assay) and it was confirmed that the de novo decoys are not cytotoxic. (**B**) In vivo mouse pharmacokinetics and tolerability of intranasally administered CTC-445.2d. Left: Plot showing the concentration of fully functional CTC-445.2d (i.e., capable of binding to the SARS-CoV-2 RBD; see the materials and methods) found in homogenized lungs of Balb/c mice after a single 100 μg dose, measured at various times after dosing (n = 5 mice). Right: Body weight of mice after repeat daily intranasal doses of CTC-445.2d (100 μg; n = 18 at day 0) compared with control [phosphate-buffered saline (PBS)–treated] mice (n = 5). At each time point, three CTC-445.2d–treated mice were sacrificed for lung examination. Weight data shown are for the remaining mice (n = 18, 15, 12, 9, 6, and 3 at days 1, 2, 4, 8, 11, and 14, respectively). No significant weight loss or lung abnormalities were observed. Error bars indicate the standard deviation. (**C**) In vivo Syrian hamster SARS-CoV-2 challenge. Left: Body weight measurements through day 10 for unchallenged hamsters (n = 5, red) compared with SARS-CoV-2–challenged hamsters treated either with a single dose of CTC-445.2d (day 0 at −12 hours; n = 8, orange) or PBS (day −1, day 0 at −12 hours, day 1, and day 2; n = 7, gray). Right: Survival plot. Hamsters were euthanized when they displayed clinical signs of distress according to protocol clinical scoring criteria (see the materials and methods). At the end of the experiment, all hamsters treated with the de novo decoy CTC-445.2d survived, exhibiting moderate weight loss, whereas hamsters treated with vehicle did not survive past day 7 because of severe weight loss and other complications from the viral infection (see table S5).

residual (and undesirable) biological activity; and the risk of eliciting an autoimmune response (*37*–*46*). By contrast, the de novo protein decoys are amenable for large-scale manufacturing in traditional bacterial systems, and their thermodynamic hyperstability can enable simplified transport and storage. Other recent protein-engineering efforts have generated neutralizing proteins characterized by extremely high binding affinities for SARS-CoV-2, with K_Ds ranging from low nanomolar to femtomolar [e.g., mAb 2B04 (*47*); LCB1 (*6*); and the nanobody Nb6 (*48*)]. Nevertheless, the de novo decoy's resilience to viral escape is a distinctive feature of our design strategy (Fig. 4 and figs. S14 and S20). A possible shortcoming is that a decoy's requirement to replicate a natural binding interface can intrinsically limit the maximum binding affinity attainable. However, we have demonstrated that the binding affinity (and potency) of the de novo decoys can be increased both by further sequence optimization (e.g., CTC-445.3d; fig. S21) or through avidity, allowing our trivalent decoy CTC-445.2t to reach the picomolar affinity range (Fig. 3I and fig. S10). It is possible that avid versions of CTC-445.2 coupled with more refined linkers (rigid and with proper spacing for binding simultaneously to multiple RBD subunits) might lead to larger increases in binding potency.

We demonstrate rapid design of a therapeutic lead; further speed improvements to our pipeline are theoretically attainable, for example by using high-throughput experiments to rapidly select and optimize the designs (Fig. 1G).

REFERENCES AND NOTES

1. D. E. Gordon *et al.*, *Nature* **583**, 459–468 (2020).
2. C. Liu *et al.*, *ACS Cent. Sci.* **6**, 315–331 (2020).
3. W.-H. Chen, U. Strych, P. J. Hotez, M. E. Bottazzi, *Curr. Trop. Med. Rep.* **7**, 1–4 (2020).
4. K. K. Chan *et al.*, *Science* **369**, 1261–1265 (2020).
5. J. D. Walter *et al.*, bioRxiv 045419 [Preprint]. 16 May 2020. https://doi.org/10.1101/2020.04.16.045419.
6. L. Cao *et al.*, *Science* **370**, 426–431 (2020).
7. L. Zhang *et al.*, *Science* **368**, 409–412 (2020).
8. E. C. Smith, M. R. Denison, *PLOS Pathog.* **9**, e1003760 (2013).
9. S. Duffy, *PLOS Biol.* **16**, e3000003 (2018).
10. Z. Zhao *et al.*, *BMC Evol. Biol.* **4**, 21 (2004).
11. M. B. Doud, S. E. Hensley, J. D. Bloom, *PLOS Pathog.* **13**, e1006271 (2017).
12. T. Phan, *Infect. Genet. Evol.* **81**, 104260 (2020).
13. J. Hu *et al.*, bioRxiv 161323 [Preprint]. 6 July 2020. https://doi.org/10.1101/2020.06.20.161323.
14. A. Baum *et al.*, *Science* **369**, 1014–1018 (2020).
15. T. N. Starr *et al.*, *Cell* **182**, P1295–P1310.E20 (2020).
16. J. ter Meulen *et al.*, *PLOS Med.* **3**, e237 (2006).
17. L. Enjuanes, S. Zuñiga, C. Castano-Rodriguez, J. Gutierrez-Alvarez, J. Canton, I. Sola, in *Advances in Virus Research*, J. Ziebuhr, Ed. (Elsevier, 2016), vol. 96, pp. 245–286.
18. S. Belouzard, V. C. Chu, G. R. Whittaker, *Proc. Natl. Acad. Sci. U.S.A.* **106**, 5871–5876 (2009).
19. J. Shang *et al.*, *Proc. Natl. Acad. Sci. U.S.A.* **117**, 11727–11734 (2020).

20. J. K. Millet, G. R. Whittaker, *Proc. Natl. Acad. Sci. U.S.A.* **111**, 15214–15219 (2014).
21. X. Ou *et al*., *Nat. Commun.* **11**, 1620 (2020).
22. Z. Song *et al*., *Viruses* **11**, 59 (2019).
23. R. Yan *et al*., *Science* **367**, 1444–1448 (2020).
24. Q. Wang *et al*., *Cell* **181**, 894–904.e9 (2020).
25. J. Lan *et al*., *Nature* **581**, 215–220 (2020).
26. D.-A. Silva *et al*., *Nature* **565**, 186–191 (2019).
27. F. Sesterhenn *et al*., *Science* **368**, eaay5051 (2020).
28. J. Zhou, A. E. Panaitiu, G. Grigoryan, *Proc. Natl. Acad. Sci. U.S.A.* **117**, 1059–1068 (2020).
29. D.-A. Silva, B. E. Correia, E. Procko, in *Computational Design of Ligand Binding Proteins*, B. L. Stoddard, Ed. (Humana, 2016), vol. 1414, pp. 285–304.
30. A. Quijano-Rubio, U. Y. Ulge, C. D. Walkey, D.-A. Silva, *Curr. Opin. Chem. Biol.* **56**, 119–128 (2020).
31. A. Leaver-Fay *et al*., *Methods Enzymol.* **487**, 545–574 (2011).
32. E. Marcos, D.-A. Silva, *WIREs Comput Mol Sci* **8**, e1374 (2018).
33. A. Chevalier *et al*., *Nature* **550**, 74–79 (2017).
34. T. A. Whitehead *et al*., *Nat. Biotechnol.* **30**, 543–548 (2012).
35. M. Hoffmann *et al*., *Cell* **181**, 271–280.e8 (2020).
36. W. Sungnak *et al*., *Nat. Med.* **26**, 681–687 (2020).
37. M. P. Baker, H. M. Reynolds, B. Lumicisi, C. J. Bryson, *Self Nonself* **1**, 314–322 (2010).
38. N. Casadevall *et al*., *N. Engl. J. Med.* **346**, 469–475 (2002).
39. M. G. Tovey, C. Lallemand, *Ther. Adv. Drug Saf.* **2**, 113–128 (2011).
40. J. Li *et al*., *Blood* **98**, 3241–3248 (2001).
41. M. P. Ettinger *et al*., *JAMA* **289**, 1826–1832 (2003).
42. M. Findeisen *et al*., *Nature* **574**, 63–68 (2019).
43. G. Gao *et al*., *Blood* **103**, 3300–3302 (2004).
44. H. Schellekens, N. Casadevall, *J. Neurol.* **251** (suppl. 2), 114–119 (2004).
45. I. Mukovozov, T. Sabljic, G. Hortelano, F. A. Ofosu, *Thromb. Haemost.* **99**, 874–882 (2008).
46. M. Sauerborn, V. Brinks, W. Jiskoot, H. Schellekens, *Trends Pharmacol. Sci.* **31**, 53–59 (2010).
47. W. B. Alsoussi *et al*., *J. Immunol.* **205**, 915–922 (2020).
48. M. Schoof *et al*., bioRxiv 238469 [Preprint]. 17 August 2020. https://doi.org/10.1101/2020.08.08.238469.

ACKNOWLEDGMENTS

We thank M. Dougan, L. Aberman, U. Ulge, J. Rathbun, and J. Drachman for useful discussions and comments on this manuscript; Neoleukin Therapeutics, Inc. ("Neoleukin") for supporting this work; S. Chen and A. Malyutin (Caltech) for maintaining electron microscopes; and J. Vielmetter and the Protein Expression Center in the Beckman Institute at Caltech for expression assistance. All of the computational resources for the de novo protein design were provided by Neoleukin's high-performance "Neo" computational cluster. **Funding:** This work was supported by NIH grants AI145296 and AI127463 and a Department of Defense grant subcontract to M.G.; NIH grant P50 8 P50 AI150464-13 and the Caltech Merkin Institute for Translational Research to P.J.B.; the Hanna Gray Fellowship Program from the Howard Hughes Medical Institute and the Post-doctoral Enrichment Program from the Burroughs Wellcome Fund to C.O.B; NIH NIAID grant HHSN272201400006C to H.-L.Y.; and NIH grant R01 AI089728 to R.S.B. Electron microscopy was performed at the Caltech Beckman Institute Resource Center for Transmission Electron Microscopy. This project was also supported by the North Carolina Policy Collaboratory at the University of North Carolina at Chapel Hill with funding from the North Carolina Coronavirus Relief Fund established and appropriated by the North Carolina General Assembly. T.M.R. is supported by the Georgia Research Alliance as an Eminent Scholar. "Neoleukin" is a trademark of Neoleukin Therapeutics, Inc. The views and opinions expressed in this article are those of the authors and do not necessarily reflect the position of Neoleukin. **Author contributions:** T.W.L. designed and coordinated the research, developed computational design methods, designed de novo protein decoys of ACE2, characterized designs, and wrote the manuscript. R.V. designed de novo proteins, performed molecular biology, characterized and optimized the designs, and wrote the manuscript. N.C. designed de novo proteins, characterized and optimized the designs, and wrote the manuscript. J.W.N. designed de novo proteins, characterized and optimized the designs, performed molecular biology, performed SSM experiments, and wrote the manuscript. M.J.W. designed de novo proteins, performed molecular biology, characterized and optimized the designs, and wrote the manuscript. W.S. performed neutralization assays with the live SARS-CoV-2 virus in Vero E6 cells and edited the manuscript. C.O.B. performed cryo-EM data collection and structure solutions and analyzed the structure together with P.J.B. T.-Y.H. performed cell-neutralization assays with the live SARS-CoV-2 NanoLuc virus in Calu-3 cells. K.E.-N. performed cell-neutralization assays with the live SARS-CoV-2 NanoLuc virus in Calu-3 cells. Y.J.H. developed the nLUC reporter virus. K.Y. designed and performed ACE2 competition assays and developed methods to quantify the de novo designs in tissue lysates. T.P. designed, purified, and characterized de novo proteins. M.M. designed de novo proteins. A.P. designed de novo proteins and performed binding characterizations. U.Y.L. designed de novo proteins. M.L.M. performed pharmacokinetic studies in mice, coordinated the research for cross-reactivity binding assay, and edited the manuscript. J.C. performed pharmacokinetic studies in mice. Z.B.R. and T.M.R. performed the SARS-CoV-2 viral protection studies in hamsters. A.C. performed the ACE2 enzymatic assay and cytotoxicity assays with VeroE6. T.B. purified and characterized de novo proteins. H.P. performed mass spectrometry. N.S.C. performed molecular biology. J.Ca. developed and implemented computational tools for collaborative de novo protein design. Y.-R.L. designed de novo proteins. A.J.-D. coordinated project operations and wrote the manuscript. R.S.B. coordinated the development of the nLUC reporter virus and edited the manuscript. C.D.W. coordinated the research for ACE2 competition assays and methods to quantify the de novo designs and edited the manuscript. R.S. coordinated the research for in vitro neutralization testing, in vivo viral challenge modeling, and in vivo pharmacokinetics of the de novo proteins and edited the manuscript. D.H.F. designed the in vivo experiments. M.G. coordinated and directed the research for in vitro NanoLuc SARS-CoV-2 neutralization and edited the manuscript. L.M.B.-M. designed de novo proteins, coordinated the purification and characterization of the de novo proteins, and edited the manuscript. H.-L.Y. coordinated the research for in vitro SARS-CoV-2 neutralization and edited the manuscript. D.-A.S. generated the original idea to design the de novo decoys to neutralize SARS-CoV-2, designed the research, developed computational design selection strategies, wrote the manuscript, and directed the effort. **Competing interests:** T.W.L., N.C., J.W.N., and D.-A.S. are inventors on provisional patent applications for the de novo decoys described in this work. D.-A.S. and C.D.W. are cofounders of Neoleukin Therapeutics. Neoleukin authors own options and/or stock in the company. **Data and materials availability:** PyRosetta code used to generate initial perturbations for mobile secondary structure elements is available in the supplemental materials, appendix A. The cryo-EM maps generated from cryo-EM studies of the CTC-445.2-S 6P complex (states 1 to 4) have been deposited at the Electron Microscopy Databank (EMDB 786 http://www.emdataresource.org/) under the following accession codes: EMD-22913 (state 1), EMD-22914 (state 2), EMD-22915 (state 3), and EMD-22916 (state 4). The atomic coordinates for the CTC-445.2-S 6P complex (state 4) have been deposited at the PDB (http://www.rcsb.org/) under the accession code 7KL9. Neoleukin materials may be made available to academic noncommercial researchers through a material transfer agreement upon request. This work is licensed under a Creative Commons Attribution 4.0 International (CC BY 4.0) license, which permits unrestricted use, distribution, and reproduction in any medium, provided the original work is properly cited. To view a copy of this license, visit https://creativecommons.org/licenses/by/4.0/. This license does not apply to figures/photos/artwork or other content included in the article that is credited to a third party; obtain authorization from the rights holder before using such material.

SUPPLEMENTARY MATERIALS

science.sciencemag.org/content/370/6521/1208/suppl/DC1
Materials and Methods
Figs. S1 to S21
Tables S1 to S5
Appendix A: Python/PyRosetta code to generate multiple initial perturbations for mobile secondary structure elements
References (*49*–*61*)
MDAR Reproducibility Checklist

31 July 2020; accepted 29 October 2020
Published online 5 November 2020
10.1126/science.abe0075

BIOMECHANICS

Mechanisms of collision recovery in flying beetles and flapping-wing robots

Hoang Vu Phan[1,2]* and Hoon Cheol Park[1,2]*

At rest, beetles fold and tuck their hindwings under the elytra. For flight, the hindwings are deployed through a series of unfolding configurations that are passively driven by flapping forces. The folds lock into place as the wing fully unfolds and thereafter operates as a flat membrane to generate the aerodynamic forces. We show that in the rhinoceros beetle (*Allomyrina dichotoma*), these origami-like folds serve a crucial shock-absorbing function during in-flight wing collisions. When the wing collides with an object, it collapses along the folds and springs back in place within a single stroke. Collisions are thus dampened, helping the beetle to promptly recover the flight. We implemented this mechanism on a beetle-inspired wing on a flapping-wing robot, thereby enabling it to fly safely after collisions.

Most flying insects live in cluttered forest environments that are covered by dense vegetation, tree branches, and bushes. Although insects are capable of obstacle avoidance using their sensory systems (*1*, *2*) in such complex conditions, obstacle collisions of the wings of insects are more likely and may affect their flight performance or even cause wing damage (*3*). Because of their vulnerable wings, insects use biomechanical strategies to protect them (*4*, *5*). When at rest, the wings of most insects are able to fold along the body to reduce the risk of damage (*6*). In particular, beetles (Coleoptera) use a pair of hardened forewings (elytra) to protect their flexible hindwings and body. Most beetles are capable of performing many modes of locomotion, such as flying, crawling, and even burrowing their way underground. Such abilities are supported by a hard exoskeleton covering the body and the ability of foldable hindwings. To generate lift, the hindwings are often larger and longer than the body and elytra and must be therefore folded so they can be tucked under the hard protective elytra. Much progress has been made in addressing questions on the structures and operations of the folding mechanism, when the beetles are at rest (*7*–*11*). Most birds and bats are capable of partial wing-folding during the upstroke and full wing extension during the downstroke to create efficient flight (*12*, *13*). In particular, pigeons were found to use a wing-folded posture when traversing confined spaces (*14*). By contrast, beetles rarely use the folding mechanism during their normal flight locomotion, because beetles (and most insects) cannot actively flex their wings, as compared with birds and bats.

To explore the use of folding mechanism during beetle flight, we performed experiments and analyses of free-flying rhinoceros beetles [*Allomyrina dichotoma* (fig. S1)] under collision impact on the hindwing, mimicking the challenges that they face when flying in cluttered habitats. We first investigated how this beetle unfolds its hindwings for flight. Typically, two unfolding patterns of the hindwing are observed in most beetles: (i) unfolding completely before flapping [examples: earwigs *Forficula auricularia* (*10*) and ladybird beetles *Coccinella septempunctata* (*11*)] and (ii) flapping before unfolding [examples: sun beetles *Pachnoda marginata* (*9*) and stag beetles *Dorcus titanus platymelus* (*15*)]. In the first pattern, the unfolding is driven by stored elastic energy in the wing (*7*, *10*). Beetles with the second unfolding pattern actively use their

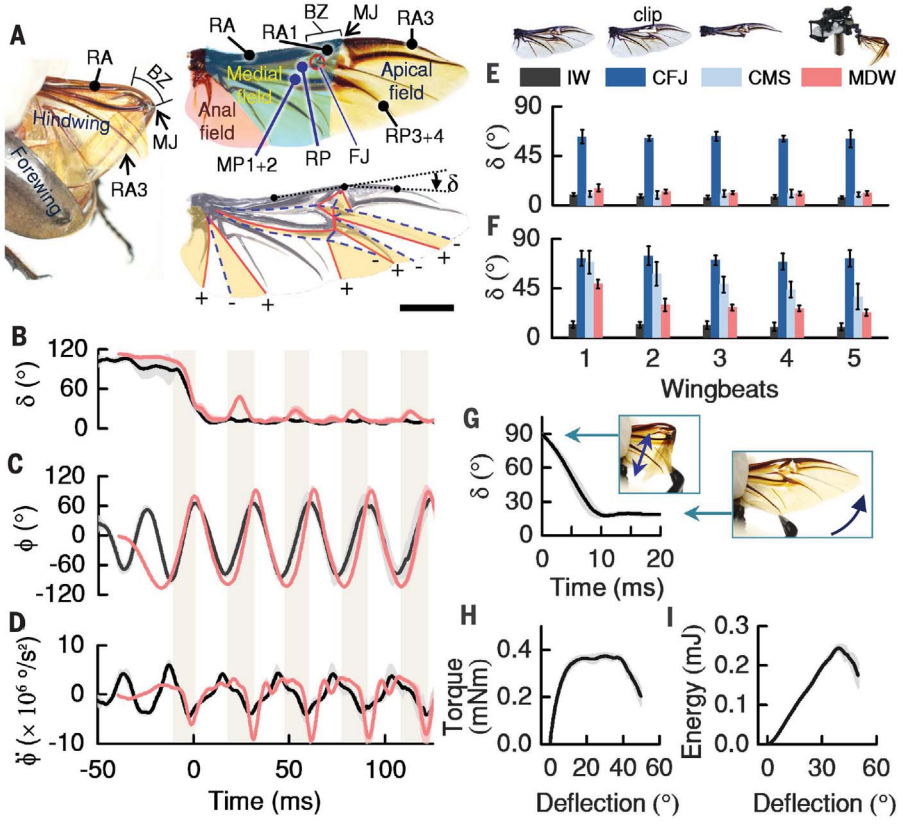

Fig. 1. Beetles flap their hindwings using wing inertial effect to unfold. (**A**) Detail of the hindwing and folding patterns. RA, radius anterior; BZ, bending zone; MJ, marginal joint; MP, media posterior; FJ, flexible joint; RP, radius posterior; +, convex fold; -, concave fold. The orange-shaded areas denote the reverse-folding area. Scale bar, 1 cm. (**B** to **D**) Time history of the data during the hindwing unfolding process driven by the beetle (black) and a flapping mechanism (red): (B) fold angle (δ); (C) stroke angle (ϕ); (D) stroke acceleration ($\ddot{\phi}$). Lines, shaded areas, and shaded columns denote the average, ±SD, and the upstroke motion, respectively. (**E** and **F**) Fold angles in the first five wing beats in various unfolding tests of intact wing (IW), clipped flexible joint (CFJ), clipped membrane surface (CMS), and motor-driven wing (MDW) during (E) downstroke and (F) upstroke motions. Error bars represent ±SD. (**G**) The apical field is unable to be locked in its folded configuration and unfolds quickly to outspread shape. (**H**) Torque-deflection relationship of the RA3 (wing tip) while folding creases are tightened. (**I**) Stored energy with respect to the deflection angle enabling the self-unfolding of the wing tip.

thoracic muscles (*6*, *9*) or hydraulic mechanism (*15*) to unfold. The rhinoceros beetle uses the second pattern by first opening its elytra to promote the hindwings at the wing base while retaining the same folded configuration at the marginal joint (MJ; Fig. 1A). The wing starts to flap and unfolds completely within two wing beats (movie S1). The unfolding process occurs often during the upstroke and reaches fully extended configuration at the dorsal stroke reversal, at which the wing angular acceleration reaches its peak (Fig. 1, B to D). Thus, we hypothesized that the unfolding is aided by flapping forces, i.e., inertial and aerodynamic forces during fast flapping speed (fig. S2), rather than from active thoracic muscular control.

To address the hypothesis, we cut off the hindwing of the beetle at the wing base and immediately attached it to a flapping mechanism (fig. S3). By actuating the hindwing at a similar frequency to that operated by the beetle (38 Hz), we observe that the hindwing is successfully unfolded at the MJ to deploy the apical field, even though the radius anterior 3 (RA3) was not fully retained in the outstretched configuration during the upstroke (Fig. 1, B to F, and movie S1). To keep the apical field in the outstretched shape, the flexible joint (FJ) connecting the radius posterior (RP) and RA1 is a necessary component (Fig. 1, E and F; fig. S4; and movie S2). The flapping forces trigger the folding-hand-fan–like movement of the media posterior 1 and 2 (MP1+2), RP, and RA1 to tighten the FJ and the diamond-shaped creases at the MJ (figs. S5 and S6). As a result, the RA3 can be unfolded to fully deploy the apical field. Without the membrane, the hindwing requires more flaps to unfold (fig. S4 and movie S2), suggesting that aerodynamic forces also play a role in the unfolding.

By tightening the FJ and folding creases in the median field, we found that the wing tip is unable to lock in the fold configuration and springs back to an outstretched shape (Fig. 1G and movie S3). In the outspread wing, the measured torque-deflection response of the MJ shows that the torque increases and remains maximum (locking torque) as the deflection angle increases (Fig. 1H). Subsequently, the torque declines at high deflection angles (>40°). During folding, energy is stored, enabling the self-unfolding of the wing tip (Fig. 1I). These observations suggest that the foldability allows wings to act as shock absorbers during in-flight collisions. They also explain how the wing maintains its outspread shape during flapping motions. After flight, the hindwings can be folded and tucked under the elytra. The fold can be triggered by the abdominal movement to push the RP3+4 for its transverse fold, resulting in a locked configuration of the creases (movie S4) (*7*, *11*).

We conducted experiments in which beetles flew past and often collided with fixed vertical posts made of carbon tubes (fig. S7). We observed two kinds of collisions: mid-wing collision (from the wing base to the MJ) and wing-tip collision (from the MJ to the wing tip). Because the collisions occur randomly during free flights, we counted the collision patterns and flight behaviors after collision (table S1 and fig. S8). In each collision pattern, we classified three groups of behaviors: stable flight, tumble, and perching. Among a total 127 flight trials of 8 individuals (14.9 ± 6.6 trials per individual,

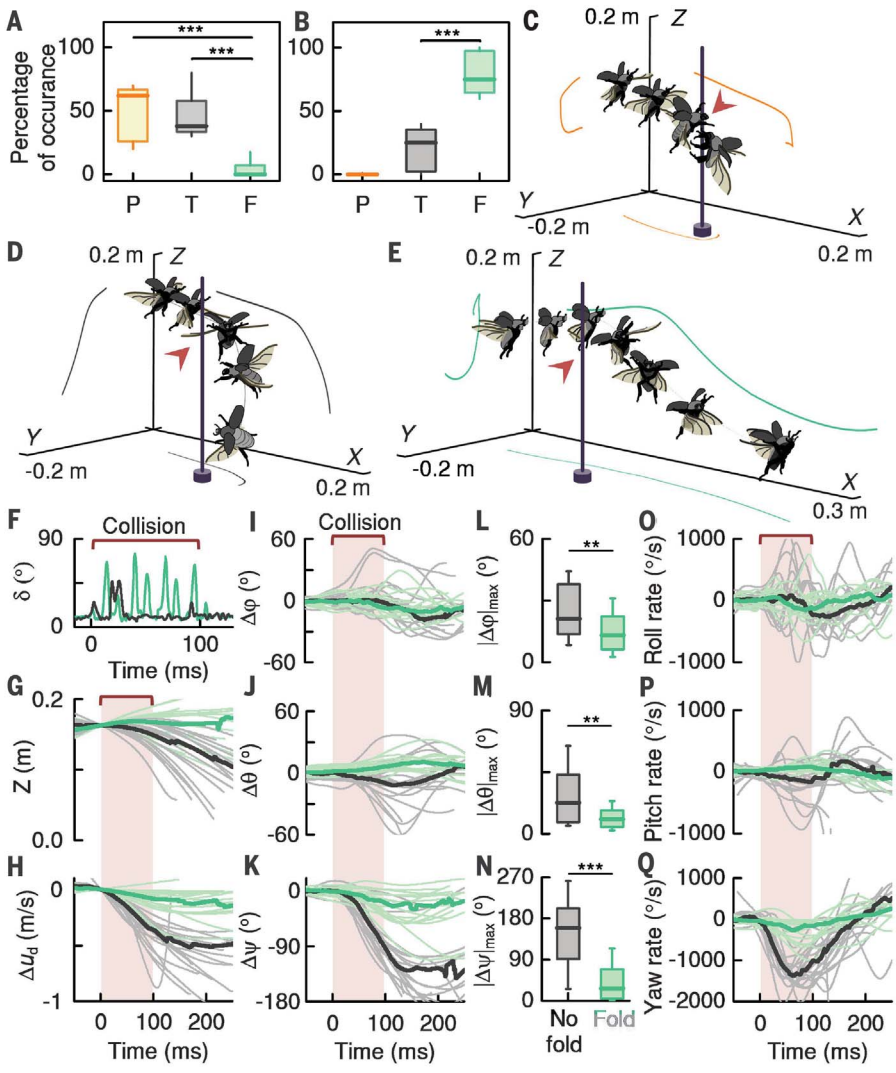

Fig. 2. Beetles survive in-flight wing collision by collapsible wings. (**A** and **B**) Flight behavior after wing collisions: (A) mid-wing collision and (B) wing-tip collision (median, interquartiles, and range). P, perching; T, tumble; F, stable flight. ***$P < 0.001$ (two-sample, two-tailed t test). (**C** to **E**) Sequential sketches of representative colliding flights with different behaviors after collision: (C) perching, (D) tumble, and (E) stable flight. (**F**) Fold angles of the collided wings in (D) (black) and (E) (green). (**G** to **Q**) Flight trajectories, body attitudes, and body rates of the beetles during collision flights with presence (green) and absence (black) of the folding function. (G) Flight trajectories (Z) and (H) changes in downward velocity (Δu_d). (I to K) Time course of the body attitude angles: (I) roll ($\Delta\varphi$), (J) pitch ($\Delta\theta$), and (K) yaw ($\Delta\psi$). These angles were biased from initial state and adjusted corresponding to the right wing collisions. (L to N) Maximum deviation between the attitude angles before and after the collision: (L) roll ($|\Delta\varphi|_{max}$), (M) pitch ($|\Delta\theta|_{max}$), and (N) yaw ($|\Delta\psi|_{max}$). **$P < 0.01$, ***$P < 0.001$. (O to Q) Time course of the body angular rates. Thin lines indicate individual flight trials and thick lines represent median values. The time instant when the wing first hits the post is set at 0 ms.

[1]Department of Smart Vehicle Engineering, Konkuk University, Seoul 05029, South Korea. [2]Artificial Muscle Research Center, Konkuk University, Seoul 05029, South Korea.
*Corresponding author. Email: vu113@konkuk.ac.kr (H.V.P.); hcpark@konkuk.ac.kr (H.C.P.)

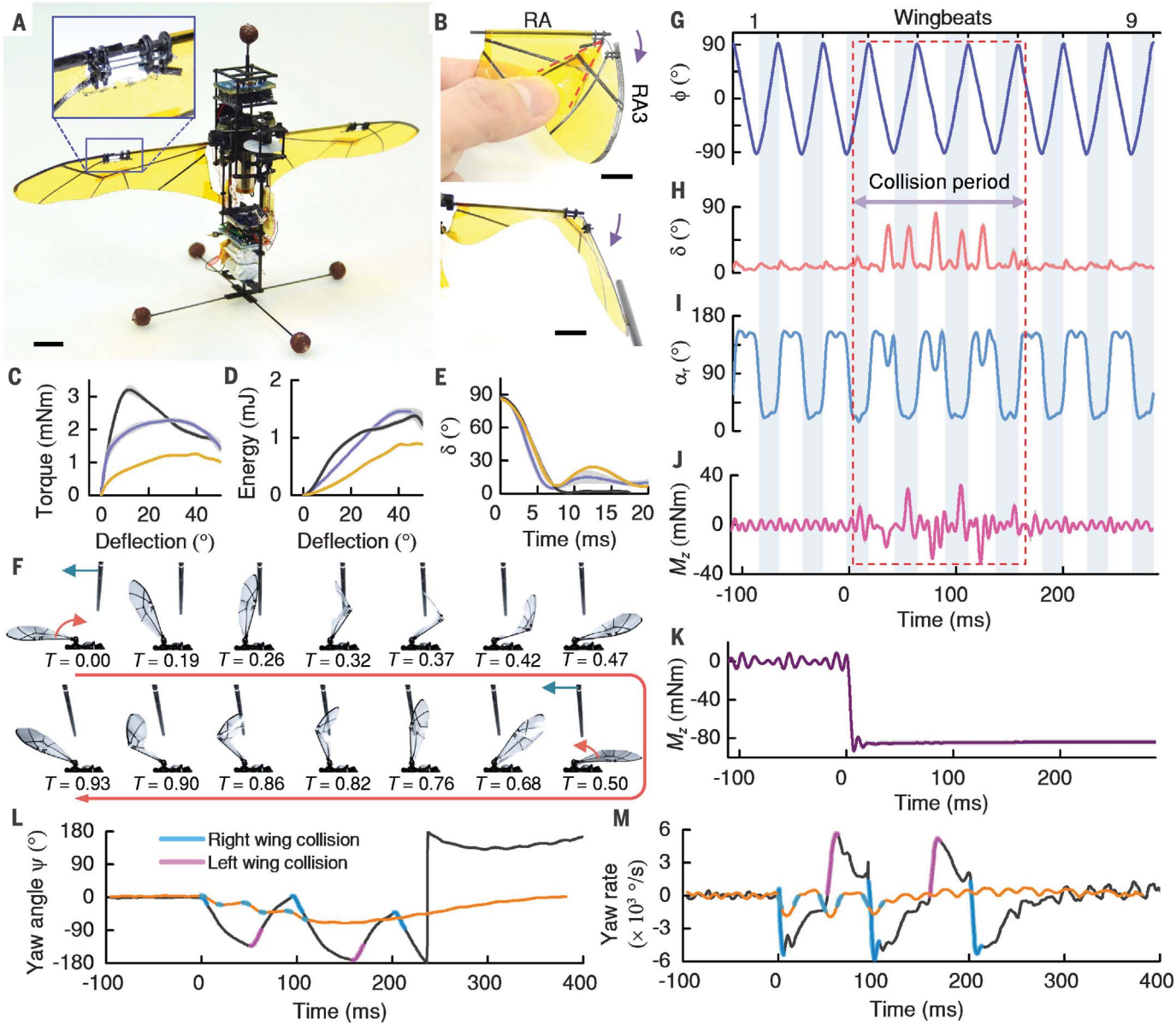

Fig. 3. A mechanical wing can be passively folded and speedily unfolded adapting the beetle's hindwing. (**A**) Implementation of the folding wings on the 17.8-g tailless flapping-wing robot. (**B**) Folding wing in fold configurations: longitudinal fold (top) and transverse fold (bottom). Scale bar, 1 cm. (**C**) Torque required to fold the wing tip at the BJ in longitudinal (dark blue) and transverse (black) folds. Yellow color denotes the longitudinal fold behavior without the reinforced linkage (RV3 in fig. S17). (**D**) Stored energy during folding. (**E**) Self-unfolding response of the wing tip. Line and shaded area denote the average ± SD. (**F**) Image sequence of the colliding flapping motion in one flapping cycle. (**G** to **J**) Time course of the data in the colliding flapping motion: (G) stroke angle (ϕ); (H) fold angle (δ); (I) wing rotational angle (α_r) at 75% wingspan; (J) yaw torque (M_z) produced during wing-tip collision. Red-dashed frame denotes the collision period. Shaded column denotes the upstroke motion. (**K**) Yaw torque production in wing collision without folding mechanism. (**L**) Heading angle and (**M**) rate of the 17.8-g robot in wing-tip collision trials with (orange) and without (black) folding mechanism.

mean ± SD), 58 were "mid-wing collision" and 69 were "wing-tip collision" (Fig. 2). The beetles approached the posts at a mean flight speed of 0.59 ± 0.12 m/s per flight trial (fig. S9). In "mid-wing collision," the beetles used their outspread legs to catch the obstacle for perching (movie S5), followed by "tumble" events (movie S6), and only a few "stable flight" events occurred. During flight, the legs were outspread with their lengths covering most of the RA length (fig. S10). Thus, if the obstacle approached the RA, the beetles were able to use either front legs or middle legs with hooks at the tip to catch the obstacle. By contrast, in "wing-tip collision," the beetles were mostly able to recover stable flight (movie S7). A few "wing-tip collision" cases caused the beetles to tumble, but none of the beetles used their legs to perch. Most of the "stable flight" events were assisted by the folding mechanism, which is passively folded in longitudinal pattern at the MJ because of the collision (Fig. 2F). Before flapping, the folding plane was parallel to the body and approximately normal to the stroke plane (fig. S10). However, during flapping, the RA twisted near the wing base to rotate the plane of folding at the stroke reversals, enabling the folding plane to approach the stroke plane. The change of folding plane allows the MJ (and the wing) to

avoid critical collision damage caused by out-of-plane deformation.

To investigate the role of the folding mechanism on the flight of the beetle, we classified the collisions into two events, "collision without folding" found in both mid-wing and wing-tip collisions and "collision with folding" in wing-tip collision, and analyzed the flight paths and body attitude angles [DLTdv digitizing tool (*16*); Fig. 2, G to Q, and fig. S11]. In the "collision without folding" events, the wing hit the post 4.75 ± 1.45 times per flight trial (fig. S9). The post disrupted the flapping wing motion (mostly during downstroke), causing substantial changes in the flight path and body attitude. As a result, the beetle lost altitude and often tumbled. However, in the "collision with folding" events with 5.47 ± 3.12 collisions per trial, the flight paths and body kinematics were less perturbed than those in the "collision without folding" events. When the wing tip hit the obstacle, it collapsed along the folds. After passing the obstacle, the wing tip returned to its outstretched configuration in less than 4 ms within the stroke (12.5 ms at 40 Hz) owing to the tightened creases, and hence, the collision occurred during both downstroke and upstroke motions. Thus, the folding mechanism absorbed the reaction force of the obstacle affecting the hindwing without disrupting flapping motion.

We analyzed the wing kinematics of the left and right hindwings in a representative "collision with folding" flight trial (Fig. 2E and figs. S12 to S15). We found that collisions altered the deviation and reduced the stroke amplitude and frequency in the collided wing, causing asymmetric force generation of the two wings and changes in the body attitude. To stabilize, the beetle immediately increased the stroke amplitude of the right-collided wing while reducing that of the left wing. Using a quasi-steady blade element model (*17*) (see supplementary materials), we showed that alterations in the stroke amplitudes produced unequal vertical forces in the two wings, which predominantly contribute to roll-torque generation (figs. S12 to S15 and table S2). However, this alteration caused reduction of the lift force, resulting in loss of flight altitude. Other components were not considerably affected by the alteration. Although the cycle-average yaw torque or flapping yaw counter-torque (*18*) is negligible, we observed yaw angle change in the recovery phase. This yaw motion could be generated from the coupling result of the roll torque and forward motion (*19*). Thus, the beetle can actively alter stroke amplitudes of the two wings, creating compensating torques to recover flight stability. In the "collision without folding" events, despite increasing the stroke amplitude in the collided wing after collision, the beetles could not significantly recover the flight, because of high-collision impacts (fig. S16).

These results show that the rhinoceros beetle leverages folding mechanism to mitigate the impact of wing-tip collision on its flight performance. This mechanism is appealing for application in small flying robots, in particular, bioinspired flapping-wing robots (*20*, *21*). Many insect-inspired flying robots have been developed (*22*–*26*), with the aim of use in confined space and hazardous environments. To mitigate the risk of in-flight collisions, approaches using folding frames (*27*) or protective systems (*28*, *29*) have been considered in rotary-wing drones. However, these concepts are not applicable on flapping-wing robots, as they are either unable to support flight recovery or heavy and cumbersome.

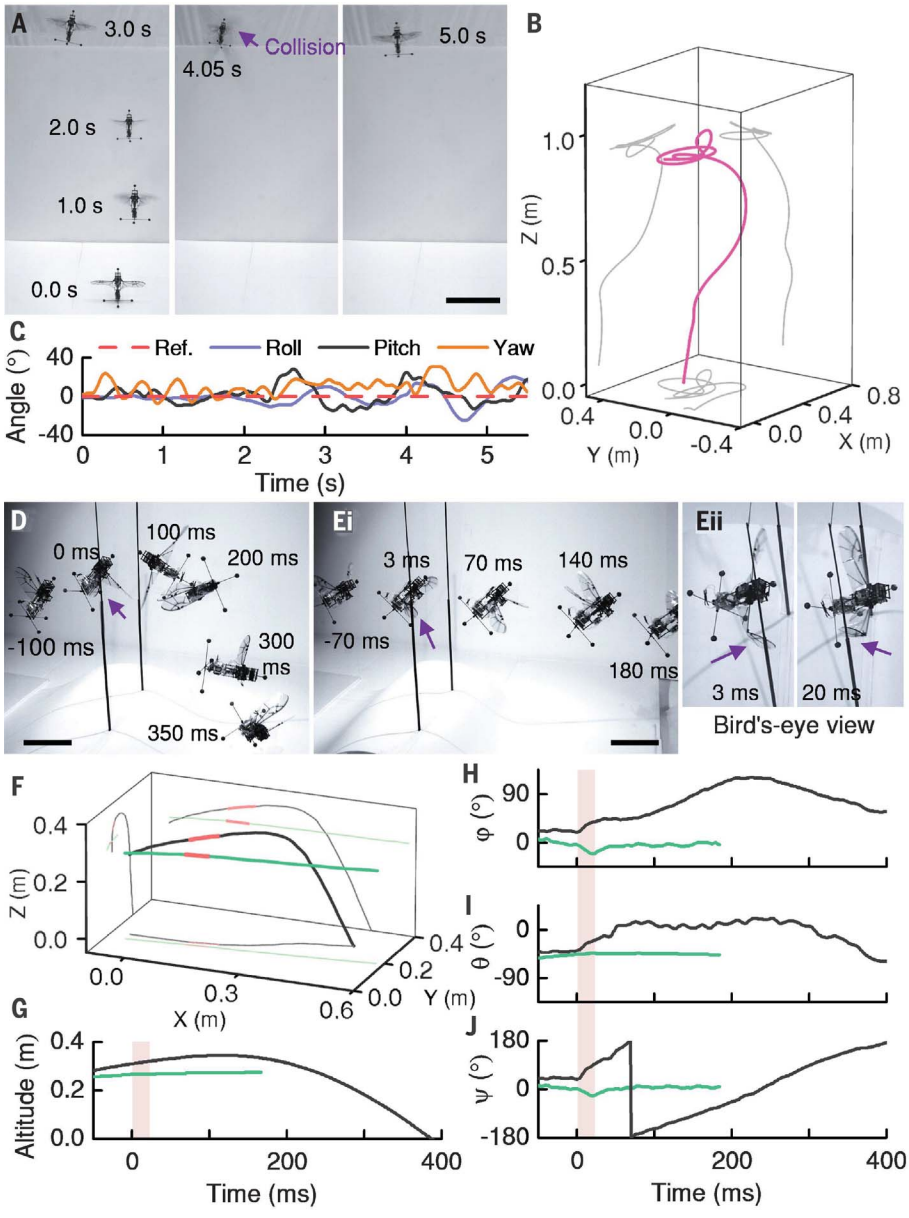

Fig. 4. A beetle-inspired, hover-capable, flapping-wing robot can fly with foldable wings after sustaining wing-tip collision. (**A** to **C**) Free hovering flight performance of the robot: (A) composite images in time sequences of takeoff and hovering flight (scale bar, 20 cm); (B) three-dimensional flight trajectory; (C) attitude angles. Ref., reference. (**D** to **J**) Remotely piloted flight demonstrations with wing collision. (D and E) Composite side-view images of the robot in time sequences of wing-collision flights without (D), and with (Ei) wing-folding function (scale bar, 10 cm). (Eii) Bird's-eye view snapshot images of the robot in (Ei) during upstroke (3 ms) and downstroke (20 ms) wing-tip collisions. (F) Corresponding flight trajectory, (G) altitude versus time, and body attitude angles [(H) roll, (I) pitch, and (J) yaw] of the robot with the presence (green) and absence (black) of the folding mechanism. The wing starts to hit the obstacle at time t = 0 ms.

Adapting the beetle's hindwing, we built a passively foldable wing on a 17.8-g beetle-inspired flying robot (Fig. 3A and tables S3 and S4) (*30*). The wing could be passively folded and rapidly unfolded (within 7 ms) at the bending joint (BJ) located at the mid-span of the leading edge, which mimics the MJ of the beetle's hindwing (Fig. 3, B to E; figs. S17 and S18; and movie S8). It can perform two folding modes at the BJ, i.e., longitudinal fold and transverse fold, owing to the vein arrangement. The longitudinal fold is triggered by the BJ made of 0.2-mm super-elastic nickel–titanium alloy and the hand-fan–like fold of the reinforced vein (RV3 in fig. S17), which prevents undesired folds during flapping motion (see supplementary materials, figs. S19 and S20, and movie S9). In this folding mode, the shape of the torque-deflection curve (Fig. 3C, dark blue) is similar to that of the beetle's hindwing. Meanwhile, the transverse fold is formed by the buckling of the BJ. Energy stored during folding enables the rapid unfolding of the wing tip (Fig. 3, D and E). This folding mechanism thus allows the wing tip to collapse and cross the obstacle, before quickly returning to an outstretched shape within a single flapping stroke (Fig. 3, F to J, and movie S10). To investigate the wing performance, we measured yaw torque and response due to collision in the presence and absence of the folding mechanism. The results showed that the folding mechanism substantially reduces the collision impacts (up to two-thirds of the yaw torque and yaw rate) and thus minimizes change in the heading direction (Fig. 3, J to M, and fig. S21).

The flying robot integrated with the foldable wings could generate enough vertical force to freely take off and hover with onboard electronics and power source (Fig. 4, A to C; figs. S22 and S23; table S5; and movie S11). To demonstrate the use of the folding mechanism during flight, we conducted experiments on wing-collision flight of the robot with vertical posts (Fig. 4, D to J; figs. S24 to S26; and movies S12 to S14). The tests show that the folding mechanism enables the robot to maintain stable flight after wing-tip collision. In the absence of the folding mechanism, the robot tumbles. This confirms the usefulness of a passive-folding wing in mitigating in-flight wing-collision impacts. The tests also demonstrate the capability of the robot in flying through a narrow gap that is smaller than its wingspan, which is impossible for conventional flying robots without a folding function.

In summary, we demonstrated that the rhinoceros beetle uses different biomechanical strategies to survive in-flight collision by passive-folding mechanism or by legs, depending on collision points. Inspired by the beetle's hindwing, we showed how the passively foldable wing can be implemented in a hover-capable flapping-wing robot to recover the flight after collision. The foldable wing thus presents an effective approach to deal with the wing collisions, helping to increase the mission durations of the robot. However, adding the folding mechanism comes at a cost of reduced power efficiency, as it requires more inertial power to accelerate the wing. Any undesired deflection of the BJ during flapping motion also affects the aerodynamics and flight stability. Despite the trade-offs, the above findings and results bring us closer to biological locomotion strategies existing in nature for potential applications in flying robots, which can perform multiple locomotion modes as a current trend of bio-inspired robotic technology (*23*).

REFERENCES AND NOTES

1. J. R. Serres, F. Ruffier, *Arthropod Struct. Dev.* **46**, 703–717 (2017).
2. E. Baird, M. Dacke, *Proc. Biol. Sci.* **283**, 20152988 (2016).
3. D. J. Foster, R. V. Cartar, *J. Exp. Biol.* **214**, 1896–1901 (2011).
4. J. H. Dirks, D. Taylor, *PLOS ONE* **7**, e43411 (2012).
5. A. M. Mountcastle, S. A. Combes, *J. Exp. Biol.* **217**, 1108–1115 (2014).
6. F. Hass, *Arthropod Syst. Phylogeny* **64**, 149–158 (2006).
7. F. Haas, S. Gorb, R. Blickhan, *Proc. Biol. Sci.* **267**, 1375–1381 (2000).
8. F. Haas, R. J. Wootton, *Proc. Biol. Sci.* **263**, 1651–1658 (1996).
9. F. Haas, R. G. Beutel, *Zoology* **104**, 123–141 (2001).
10. F. Haas, S. Gorb, R. J. Wootton, *Arthropod Struct. Dev.* **29**, 137–146 (2000).
11. K. Saito, S. Nomura, S. Yamamoto, R. Niiyama, Y. Okabe, *Proc. Natl. Acad. Sci. U.S.A.* **114**, 5624–5628 (2017).
12. D. Lentink *et al*., *Nature* **446**, 1082–1085 (2007).
13. D. K. Riskin, A. Bergou, K. S. Breuer, S. M. Swartz, *Proc. Biol. Sci.* **279**, 2945–2950 (2012).
14. C. D. Williams, A. A. Biewener, *Proc. Natl. Acad. Sci. U.S.A.* **112**, 3392–3396 (2015).
15. J. Sun, M. Ling, W. Wu, B. Bhushan, J. Tong, *Int. J. Mol. Sci.* **15**, 6009–6018 (2014).
16. T. L. Hedrick, *Bioinspir. Biomim.* **3**, 034001 (2008).
17. Q. T. Truong *et al*., *Bioinspir. Biomim.* **6**, 036008 (2011).
18. T. L. Hedrick, B. Cheng, X. Deng, *Science* **324**, 252–255 (2009).
19. M. Karásek, F. T. Muijres, C. De Wagter, B. D. W. Remes, G. C. H. E. de Croon, *Science* **361**, 1089–1094 (2018).
20. A. K. Stowers, D. Lentink, *Bioinspir. Biomim.* **10**, 025001 (2015).
21. A. M. Mountcastle, E. F. Helbling, R. J. Wood, *J. R. Soc. Interface* **16**, 20180618 (2019).
22. M. T. Keennon, K. Klingebiel, H. Won, A. Andriukov, Development of the Nano Hummingbird: A Tailless Flapping Wing Micro Air Vehicle, paper presented at the 50th AIAA Aerospace Sciences Meeting, Nashville, TN, 9 to 12 January 2012.
23. H. V. Phan, H. C. Park, *Prog. Aerosp. Sci.* **111**, 100573 (2019).
24. Q. V. Nguyen, W. L. Chan, *Bioinspir. Biomim.* **14**, 016015 (2018).
25. Y. Chen *et al*., *Nature* **575**, 324–329 (2019).
26. Z. Tu, F. Fei, X. Deng, *IEEE Robot. Autom. Lett.* **5**, 4194–4201 (2020).
27. S. Mintchev, J. Shintake, D. Floreano, *Sci. Robot.* **3**, eaau0275 (2018).
28. P. Sareh, P. Chermprayong, M. Emmanuelli, H. Nadeem, M. Kovac, *Sci. Robot.* **3**, eaah5228 (2018).
29. A. Briod, P. Kornatowski, J. C. Zufferey, D. Floreano, *J. Field Robot.* **31**, 496–509 (2014).
30. H. V. Phan, S. Aurecianus, T. K. L. Au, T. Kang, H. C. Park, *IEEE Robot. Autom. Lett.* **5**, 5059–5066 (2020).
31. H. V. Phan, H. C. Park, Online data: Mechanisms of collision recovery in flying beetles and flapping-wing robots, Figshare (2020); https://dx.doi.org/10.6084/m9.figshare.13056188.

ACKNOWLEDGMENTS

We thank S. P. Sane for helpful comments, revisions, and suggestions on the manuscript; Q. T. Truong for his early work on the force estimation model; S. Aurecianus and T. Kang for comments on the robot flight stability program; K. J. Yoon for lending us the high-speed cameras; and N. S. Goo for allowing us to use the heating chamber. **Funding:** H.V.P. was partially supported by the 2020 KU Brain Pool Program of Konkuk University. H.C.P was partially supported by the National Research Foundation of Korea (NRF) grant funded by the Korea government (MSIT) (NRF-2018R1A4A1024191). **Author contributions:** H.V.P. proposed and designed the research, performed all experiments and simulations, designed and built the robot, analyzed and interpreted the data, and wrote the manuscript. H.C.P. contributed advice on mechanical wing design and supervised the research. Both authors contributed to editing the manuscript and gave final approval for publication. **Competing interests:** Some of this work was used to support the patent application (KR 10-2020-0088666) submitted by Konkuk University. The authors declare no other competing interests. **Data and materials availability:** All data needed to evaluate the conclusions in the paper are present in the paper or the supplementary materials, as well as online at figshare (*31*).

SUPPLEMENTARY MATERIALS

science.sciencemag.org/content/370/6521/1214/suppl/DC1
Materials and Methods
Supplementary Text
Figs. S1 to S26
Tables S1 to S5
References (*32*–*44*)
Movies S1 to S14

View/request a protocol for this paper from *Bio-protocol*.

23 July 2020; accepted 28 October 2020
10.1126/science.abd3285

TROPICAL FOREST

Long-term collapse in fruit availability threatens Central African forest megafauna

Emma R. Bush[1,2]*†, Robin C. Whytock[1,3]*†, Laila Bahaa-el-din[4], Stéphanie Bourgeois[3], Nils Bunnefeld[1], Anabelle W. Cardoso[5,6], Jean Thoussaint Dikangadissi[3], Pacôme Dimbonda[3], Edmond Dimoto[3], Josué Edzang Ndong[3], Kathryn J. Jeffery[1], David Lehmann[3], Loïc Makaga[3], Brice Momboua[3], Ludovic R. W. Momont[7], Caroline E. G. Tutin[1], Lee J. T. White[1,8,9], Alden Whittaker[10], Katharine Abernethy[1,9]

Afrotropical forests host much of the world's remaining megafauna, although these animals are confined to areas where direct human influences are low. We used a rare long-term dataset of tree reproduction and a photographic database of forest elephants to assess food availability and body condition of an emblematic megafauna species at Lopé National Park, Gabon. Our analysis reveals an 81% decline in fruiting over a 32-year period (1986–2018) and an 11% decline in body condition of fruit-dependent forest elephants from 2008 to 2018. Fruit famine in one of the last strongholds for African forest elephants should raise concern about the ability of this species and other fruit-dependent megafauna to persist in the long term, with potential consequences for broader ecosystem and biosphere functioning.

The largest plants and animals on the planet are disproportionately important for the metabolism and functioning of our ecosystems (*1*). However, they are also more susceptible to extinction (*2*), and "global downsizing" through loss of megafauna and megaflora is likely to have negative consequences for the biosphere (*1*). The African tropics are home to much of the world's remaining wild megafauna, but even here they are mainly confined to areas where direct human influences are low (*3*, *4*). Securing the future of these megafauna populations will depend on our ability to protect against human threats, such as habitat loss and hunting for international trade (*5*, *6*), as well as to maintain the health and productivity of the habitats that support these species. The creeping influence of the Anthropocene means that rapid climate and atmospheric changes will be felt even where direct human pressures are low, with potential for far-reaching impacts on habitats and species (*7*). Detecting, quantifying, and understanding changes to the health and functioning of the remaining safe havens for threatened megafauna should be a key conservation priority during this time of rapid change. In this study, we used a rare long-term dataset of plant reproduction and a photographic database of forest elephants to assess food availability and body condition of an emblematic species of megafauna within a Central African rainforest.

Fruit is a keystone resource for many of the African megafauna (*8*–*10*). Fruit production is highly dependent on climatic cues, and there is abundant evidence that climate change has already caused shifts in the timing of plant reproduction in temperate regions (*11*–*13*). Data on reproduction of tropical plants are generally scarce or have not been recorded for long enough to track such changes (*14*). However, tropical plants will be affected by climate change, and changes in tropical tree reproduction have been detected at several sites for which long-term data are available (*15*–*17*). The mechanistic causes of these changes are not universal and are mostly unknown. The critical minimum temperature hypothesis describes how, in some Afrotropical plant species, flowering is not triggered until temperatures drop below a certain threshold (*18*). For these species, we would expect reproduction to be cued less often as temperatures rise.

Lopé National Park, Gabon, is a nationally designated protected area and a UNESCO (United Nations Educational, Scientific and Cultural Organization) World Heritage site and is a relative safe haven for Central African megafauna, such as great apes and forest elephants (*3*, *4*, *19*). It also hosts the longest continuous study of tropical tree phenology in Africa (*20*). From 1986 to the present, researchers at the site have monitored tree species that are important to the diet of gorillas, chimpanzees, and elephants. Once a month, focal tree crowns are observed from the ground (via binoculars), and the proportions of each canopy that are covered with flowers, fruit, and leaves are recorded (*21*). We used these data to quantify changes in the probability of encountering flowers, unripe fruit, and ripe fruit for 73 species over a 32-year period (1986–2018; n = 260,431 monthly crown observations, n = 2007 focal tree crowns; tables S1 and S2), while accounting for individual and species-level variation by using generalized linear mixed models (GLMMs) with a binomial error structure (*22*). We replicated this analysis for a subset of species (n = 14 species) that bear fruit previously identified as especially important in the diet of forest elephants during a 30-month dung study and an 8-year observational study of elephant diet at the site (*9*). We also calculated a ripe fruit availability score for each year as a proportion of maximum theoretical fruit availability (equivalent to all trees of all species bearing 100% canopy cover of ripe fruit for 12 months of the year) by selecting species that had been monitored continuously throughout the study period (n = 40 species) and, separately, a subset of these species that are especially important components of the elephant diet (n = 7 species).

We found that trees at Lopé are reproducing less often and that the probability of encountering flowers and fruit has declined significantly over time (GLMM; tables S3 and S4 and fig. S1). The average rate of encountering ripe fruit for all species (n = 73) dropped from 1 in every 10 trees in any given month in 1987 to fewer than 1 in 50 by 2018, a substantial 80.9% decline (Fig. 1A and table S4). Although there was some variation between species, all species declined except one (*Dacryodes buettneri*; table S5 and fig. S2). Encounters of ripe fruit important for elephants (n = 14) declined at an even faster rate (−87.8%), from one in five trees in 1987 to fewer than 1 in 40 in 2018 (Fig. 1A). A general reduction in fruit availability for species monitored throughout the time period demonstrates that larger fruiting events have not compensated for the diminished frequency of fruit encounters (Fig. 1B). Availability of fruit important for elephants dropped steeply between 2000 and 2003, and the yields of the best years for fruit production after 2004 were lower than those of the poor-production years before 2000 (Fig. 1B). Although the long dry season (June to September) has always been a time of fruit scarcity (*10*), historical seasonality in fruit availability has disappeared in recent years, owing to a major reduction in ripe fruit observed from October to March, which was previously the season of abundance (Fig. 1C).

Our results showing declines in the probability of encountering flowers and unripe fruit (fig. S1) indicate that suppressed production of ripe fruit is not primarily a pollination or fruit maturation issue. Nor is it likely to be due to any negative consequences of tree senescence, because we removed trees that died or were diseased prior to analysis and found no evidence that tree size (as a proxy for tree age) influenced reproduction over time (fig. S3).

[1]Faculty of Natural Sciences, University of Stirling, Stirling, UK. [2]Royal Botanic Garden Edinburgh, Edinburgh, UK. [3]Agence Nationale des Parcs Nationaux (ANPN), Libreville, Gabon. [4]School of Life Sciences, University of KwaZulu-Natal, Durban, South Africa. [5]Department of Ecology and Evolutionary Biology, Osborne Memorial Laboratories, Yale University, New Haven, CT, USA. [6]Environmental Change Institute, School of Geography and the Environment, Oxford University, Oxford, UK. [7]Independent researcher, Saint-Maur-des-Fossés, France. [8]Ministère des Eaux, des Forêts, de la Mer, de l'Environnement Chargé du Plan Climat, des Objectifs de Development Durable et du Plan d'Affectation des Terres, Boulevard Triomphale, Libreville, Gabon. [9]Institut de Recherche en Ecologie Tropicale, CENAREST, Libreville, Gabon. [10]Independent researcher, Denver, CO, USA.
***Corresponding author. Email: emma.bush.ecology@gmail.com (E.R.B.); robbie.whytock1@stir.ac.uk (R.C.W.)**
†These authors contributed equally to this work.

Instead we consider it likely that climate changes experienced at the site have contributed to this shift in reproduction. Global warming has caused minimum daily temperature to increase, on average, by 0.25°C per decade at Lopé (*23*), which may be a key factor in reduced reproduction for some tree species that rely on a critical minimum temperature to trigger flowering (*18*). Rainfall has simultaneously decreased at the site by 75 mm per decade (*23*); thus, all tree species might be suffering because of water stress (*24*).

Given the decline in fruit since 1986, it is likely that fruit-dependent wildlife—such as forest elephants, great apes, monkeys, and many bird species—has been affected. Long-term population data are not available for these species at Lopé. Other measures of population health, such as body condition, can be used to gauge population responses to environmental change over relatively short periods. Forest elephants, the largest frugivores in the ecosystem (*9*), have been consistently photographed by researchers and visitors to the site since the late 1990s, resulting in a large photographic database (>80,000 photos). We used this database to evaluate annual and seasonal trends in the external body condition of forest elephants between 1997 and 2018, hypothesizing that elephant body condition has declined along with reduced food availability. Elephant body condition in photos was scored systematically by means of a custom-built web application and user interface (*22*). Scorers (n = 6 individuals) did not have access to the time and date of photographs, nor to the research question and hypothesis. Scoring effort (number of photos viewed per scorer) varied, but we found high agreement among scorers who used a standardized test database (mean intraclass correlation coefficient of 0.89, n = 200 photos). A total of 2823 photos met the strict image-quality criteria for scoring, and we used linear mixed effects models (LMMs) to quantify changes in elephant body condition (accounting for elephant age) over the full 21-year period, as well as separately for the first 11 years (1997 to 2007) and last 11 years (2008 to 2018) of data.

We detected long-term declines in forest elephant body condition at Lopé (LMM). For the period between 1997 and 2018, mean body condition of the population declined by 5.0% for all age classes. However, uncertainty was high, ranging from a small improvement in body condition to a large decline [LMM; 95% confidence interval (CI) = +0.9 to −11.2%; table S6]. The change was most pronounced in the second half of the time period (2008–2018) when body condition declined, on average, by 11.1% (LMM; 95% CI = −4.3 to −15.6%; Fig. 2A and table S6). Body condition varied seasonally in the first half of the time period (1997–2007), appearing to track fruit availability (dipping in June and peaking after the long dry season) without any obvious lag at the monthly resolution of this analysis (Fig. 1B). The sharp drop in body condition in November during 1997–2007 was inconsistent with fruit availability, but closer inspection of the data indicated that this finding was highly influenced by one very thin individual (body condition score = 2), recorded in November 1999, out of only three photos available for this calendar month during this period (table S7). In the 2008–2018 period, the peak in body condition after the long dry season had disappeared (Fig. 2B and table S6). However, the sparse data for 1997–2007 and high uncertainty in the CIs for seasonality in body

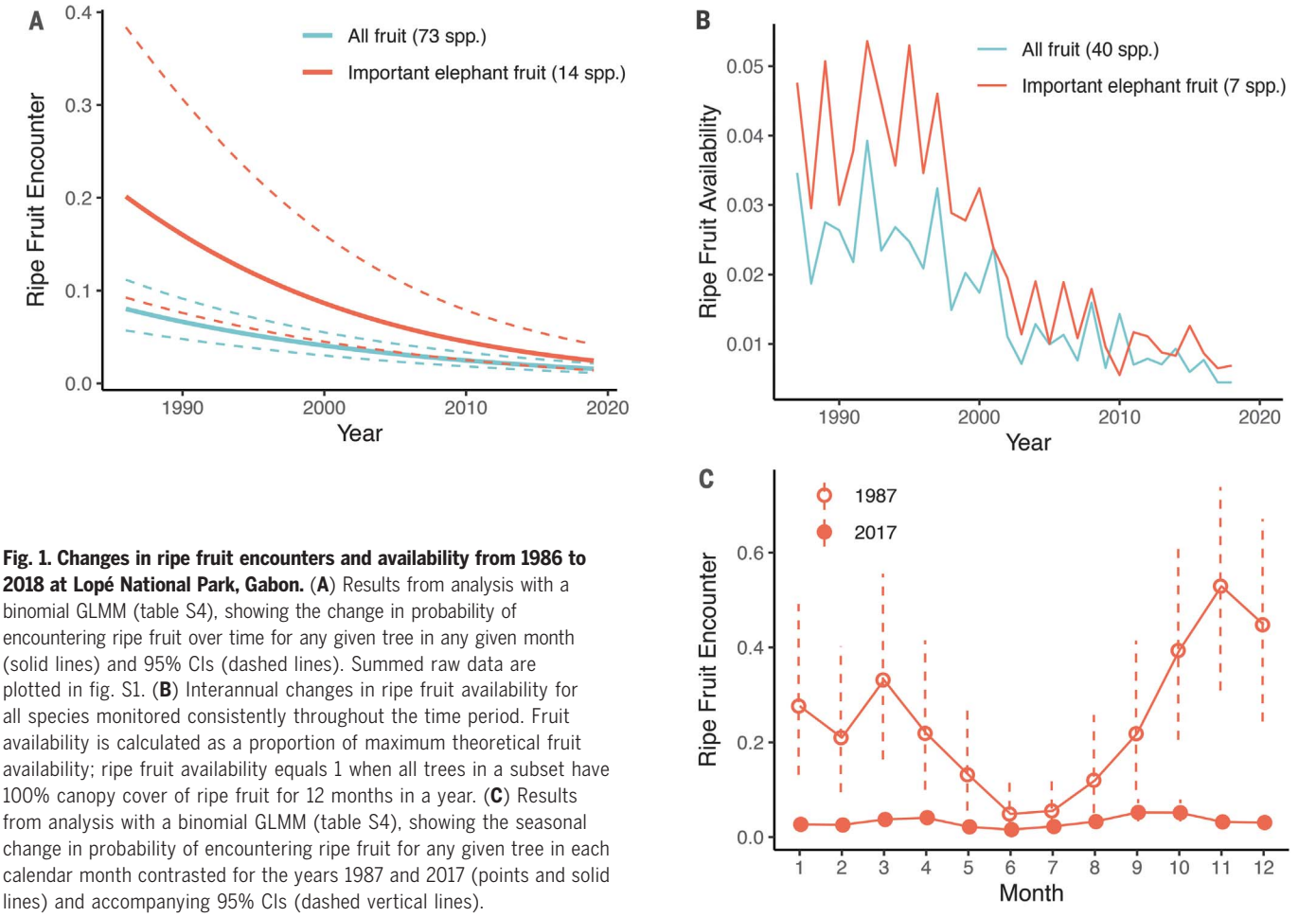

Fig. 1. Changes in ripe fruit encounters and availability from 1986 to 2018 at Lopé National Park, Gabon. (**A**) Results from analysis with a binomial GLMM (table S4), showing the change in probability of encountering ripe fruit over time for any given tree in any given month (solid lines) and 95% CIs (dashed lines). Summed raw data are plotted in fig. S1. (**B**) Interannual changes in ripe fruit availability for all species monitored consistently throughout the time period. Fruit availability is calculated as a proportion of maximum theoretical fruit availability; ripe fruit availability equals 1 when all trees in a subset have 100% canopy cover of ripe fruit for 12 months in a year. (**C**) Results from analysis with a binomial GLMM (table S4), showing the seasonal change in probability of encountering ripe fruit for any given tree in each calendar month contrasted for the years 1987 and 2017 (points and solid lines) and accompanying 95% CIs (dashed vertical lines).

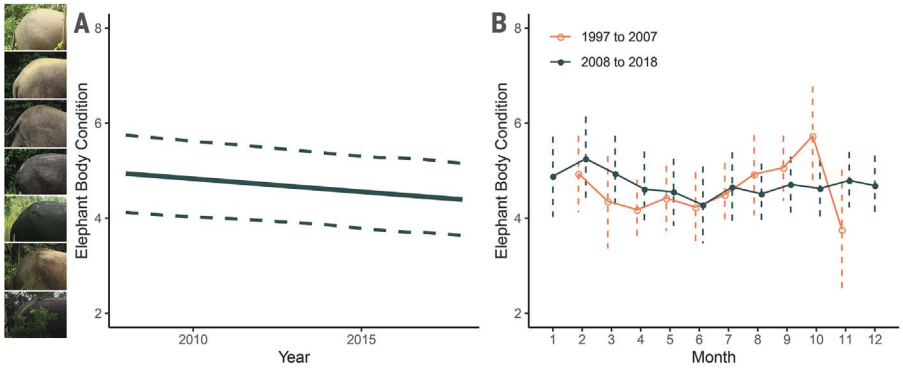

Fig. 2. Long-term and seasonal changes in elephant body condition from 1997 to 2018 at Lopé National Park, Gabon. (**A**) Change in elephant body condition from 2008 to 2018. Mean change (solid line) and 95% CIs (dashed lines) are from analysis with a LMM (table S6). Example images of different elephant body condition scores are shown at left; see fig. S4 for enlarged images. (**B**) Mean monthly elephant body condition and 95% CIs from analysis with LMMs (table S6) for the periods from 1997 to 2007 (no data for January and December) and from 2008 to 2018.

condition mean that comparisons between the early and late time periods should be made with caution (tables S6 and S7).

It is not known whether the changes observed in body condition in this study have affected forest elephant population health or dynamics in the study area. However, studies of African savanna elephants show that environmental stressors can have substantial long-term consequences for both individual fitness and population dynamics, with reproductive females and calves particularly affected (*25*). Reduced food availability could also act in synergy with other factors (such as disease) to magnify negative physiological consequences (table S8). Although the biological mechanisms and consequences of declining body condition are unclear at this point, the effects on forest elephant populations across the region are unlikely to be benign, particularly when coupled with illegal hunting, habitat loss, and habitat degradation (*3*).

These declines in both plant reproduction and elephant body condition are indicative of system-wide change and are expected to have disproportionate impacts on the functioning and metabolism of the ecosystem. A reduction or displacement of historic populations of large frugivores in this region, along with diminished availability of seeds, could lead to collapse of seed dispersal (*8*), landscape-level shifts in habitat structure (*26*), reduction of carbon stocks (*27*), and potential for increased competition with humans for food (*28*). However, long-lived plant and animal species are able to buffer environmental change to a certain extent (*1*), and the broad diet of forest elephants (*9*) means that alternative food sources could offer some relief. Nonetheless, environmental stress can have lifelong negative impacts on elephant survival and fitness (*25*), and the impacts of these changes should be closely monitored.

The long-term plant and animal datasets presented here are rare for the tropics, and it is possible that such changes may be occurring elsewhere, undocumented. These data serve as a reminder that even where direct human pressures are low, plant and animal communities may not be protected from the creeping influences of the Anthropocene. Coordinated international efforts to relieve direct human pressures and to halt and reverse climate change will be critical to saving the remaining megafauna and megaflora of the African tropics and preserving their specialized roles in the functioning of our biosphere.

REFERENCES AND NOTES

1. B. J. Enquist, A. J. Abraham, M. B. J. Harfoot, Y. Malhi, C. E. Doughty, *Nat. Commun.* **11**, 699 (2020).
2. R. Dirzo *et al.*, *Science* **345**, 401–406 (2014).
3. F. Maisels *et al.*, *PLOS ONE* **8**, e59469 (2013).
4. S. Strindberg *et al.*, *Sci. Adv.* **4**, eaar2964 (2018).
5. W. J. Ripple *et al.*, *R. Soc. Open Sci.* **3**, 160498 (2016).
6. A. Benítez-López *et al.*, *Science* **356**, 180–183 (2017).
7. J. Barlow *et al.*, *Nature* **559**, 517–526 (2018).
8. A. Campos-Arceiz, S. Blake, *Acta Oecol.* **37**, 542–553 (2011).
9. L. J. T. White, thesis, University of Edinburgh (1992).
10. C. E. G. Tutin, L. J. T. White, in *Dynamics of Tropical Communities: 37th Symposium of the British Ecological Society*, D. M. Newbery, H. H. T. Prins, N. Brown, Eds. (Blackwell Science, 1998), pp. 309–338.
11. G. R. Walther *et al.*, *Nature* **416**, 389–395 (2002).
12. C. Parmesan, G. Yohe, *Nature* **421**, 37–42 (2003).
13. C. Rosenzweig *et al.*, in *Climate Change 2007: Impacts, Adaptation and Vulnerability. Contribution of Working Group II to the Fourth Assessment Report of the Intergovernmental Panel on Climate Change*, M. L. Parry, O. F. Canziani, J. P. Palutikof, P. J. van der Linden, C. E. Hanson, Eds. (Cambridge Univ. Press, 2007), pp. 79–131.
14. K. Abernethy, E. R. Bush, P. M. Forget, I. Mendoza, L. P. C. Morellato, *Biotropica* **50**, 477–482 (2018).
15. C. A. Chapman, K. Valenta, T. R. Bonnell, K. A. Brown, L. J. Chapman, *Biotropica* **50**, 384–395 (2018).
16. S. Pau, D. K. Okamoto, O. Calderón, S. J. Wright, *Global Change Biol.* **24**, 2105–2116 (2018).
17. L. Polansky, C. Boesch, *Biotropica* **45**, 434–440 (2013).
18. C. E. G. Tutin, M. Fernandez, *J. Trop. Ecol.* **9**, 241–248 (1993).
19. P. D. Walsh *et al.*, *Nature* **422**, 611–614 (2003).
20. G. S. Adamescu *et al.*, *Biotropica* **50**, 418–430 (2018).
21. E. R. Bush *et al.*, *Biotropica* **50**, 455–464 (2018).
22. See supplementary materials.
23. E. R. Bush *et al.*, *PeerJ* **8**, e8732 (2020).
24. T. J. Brodribb, J. Powers, H. Cochard, B. Choat, *Science* **368**, 261–266 (2020).
25. P. C. Lee, L. F. Bussière, C. E. Webber, J. H. Poole, C. J. Moss, *Biol. Lett.* **9**, 20130011 (2013).
26. A. W. Cardoso *et al.*, *Ecosystems* **23**, 602–616 (2020).
27. F. Berzaghi *et al.*, *Nat. Geosci.* **12**, 725–729 (2019).
28. S. Ngama *et al.*, *PLOS ONE* **14**, e0213971 (2019).
29. R. C. Whytock, rcwhytock/Bush_Whytock_etal_2020: R code for Bush and Whytock et al. 2020, Version V2.0, Zenodo (2020); http://doi.org/10.5281/zenodo.4022665.

ACKNOWLEDGMENTS

We acknowledge A. Deasey, A. Dibambou, S. Obiang, N. Orbell, A. White, I. White, W. White, S. Schuttler, and F. Maisels for their contributions to data collection and F. Maisels, D. Dent, L. Bussiere, and three anonymous reviewers for their comments, which improved the final manuscript. **Funding:** During analysis and writing, E.R.B. was funded by a University of Stirling Impact studentship and the Gabonese National Park Agency (Total Climate Change award), K.A. was funded by University of Stirling, R.C.W. was funded by the EU 11th FED ECOFAC6 program in Gabon, and N.B. was funded by the European Research Council under the European Union's H2020/ERC grant 679651 (ConFooBio). During their respective data collections, L.J.T.W., K.J.J., L.R.W.M., and A.W. were funded by the Wildlife Conservation Society; L.J.T.W., R.C.W., K.J.J., E.D., J.T.D., P.D., B.M., L.M., and D.L. were funded by the Gabon National Parks Agency; and K.A., D.L., and K.J.J. were funded by the University of Stirling. Additionally, E.D., J.T.D., C.E.G.T., K.A., and K.J.J. were funded by CIRMF; L.B. was funded by Panthera; and A.W.C. was funded by the University of Oxford's Hertford College Mortimer-May scholarship. **Author contributions:** Conceptualization of the phenology and elephant monitoring research: L.J.T.W. and C.E.G.T.; Conceptualization of this analysis: E.R.B., R.C.W., L.J.T.W., and K.A.; Data curation: E.R.B., R.C.W., K.J.J., D.L., J.E.N., L.R.W.M., K.A., C.E.G.T., and L.M.; Formal analysis: E.R.B., R.C.W., and N.B.; Funding acquisition: L.J.T.W., K.A., C.E.G.T., and K.J.J.; Investigation: E.R.B., R.C.W., L.B., S.B., A.W.C., J.T.D., P.D., E.D., J.E.N., K.J.J., D.L., L.R.W.M., B.M., L.M., C.E.G.T., L.J.T.W., A.W., and K.A.; Methodology: E.R.B., R.C.W., N.B., C.E.G.T., L.J.T.W., K.A., and S.B.; Project administration: E.R.B., R.C.W., K.J.J., K.A., and L.J.T.W.; Resources: R.C.W., L.B., A.W.C., L.R.W.M., and A.W.; Software: E.R.B. and R.C.W.; Visualization: E.R.B. and R.C.W.; Writing – original draft: E.R.B., R.C.W., and K.A.; Writing – review and editing: E.R.B., R.C.W., L.B., S.B., N.B., A.W.C., J.T.D., P.D., E.D., J.E.N., K.J.J., D.L., L.M., B.M., L.R.W.M., C.E.G.T., L.J.T.W., A.W., and K.A. **Competing interests:** L.J.T.W. is Minister of Water, Forests, Seas, Environment and Climate Change for the Gabonese Republic. The Agence Nationale des Parcs Nationaux (ANPN) is an agency of the Gabonese government. **Data and materials availability:** All data are available from the University of Stirling's online data repository (http://hdl.handle.net/11667/159). All code is available at Zenodo (*29*).

SUPPLEMENTARY MATERIALS

science.sciencemag.org/content/370/6521/1219/suppl/DC1
Materials and Methods
Figs. S1 to S7
Tables S1 to S14
References (*30*–*54*)

21 May 2020; accepted 10 September 2020
Published online 24 September 2020
10.1126/science.abc7791

PHOTOS: ANABELLE W. CARDOSO AND LAILA BAHAA-EL-DIN

QUANTUM GASES

Universal sound diffusion in a strongly interacting Fermi gas

Parth B. Patel[1,2,3], Zhenjie Yan[1,2,3], Biswaroop Mukherjee[1,2,3], Richard J. Fletcher[1,2,3], Julian Struck[1,2,3,4], Martin W. Zwierlein[1,2,3]*

Transport of strongly interacting fermions is crucial for the properties of modern materials, nuclear fission, the merging of neutron stars, and the expansion of the early Universe. Here, we observe a universal quantum limit of diffusivity in a homogeneous, strongly interacting atomic Fermi gas by studying sound propagation and its attenuation through the coupled transport of momentum and heat. In the normal state, the sound diffusivity *D* monotonically decreases upon lowering the temperature, in contrast to the diverging behavior of weakly interacting Fermi liquids. Below the superfluid transition temperature, *D* attains a universal value set by the ratio of Planck's constant and the particle mass. Our findings inform theories of fermion transport, with relevance for hydrodynamic flow of electrons, neutrons, and quarks.

Transport in fermionic quantum matter lies at the heart of phenomena as varied as superconductivity in cuprates (*1*) and bilayer graphene (*2*), inspirals of neutron star binaries (*3*), and perfect fluidity of the early universe (*4*). For hydrodynamic flow, transport is governed by diffusion, which facilitates the decay of spatial variations in globally conserved quantities—such as momentum, energy, charge, or spin—at a rate set by the corresponding diffusivity. A ubiquitous example is the attenuation of sound in fluids, where the modulation in current density and temperature causes diffusion of momentum and heat, leading to attenuation of sound at a rate set by the sound diffusivity *D*. The magnitude and temperature dependence of sound diffusivity reveal many of the characteristic features of the underlying substance.

Kinetic theory yields an estimate of $D \simeq vl$, where v is the average velocity of the particles and l is their mean free path, which can vary over many orders of magnitude across substances. However, for strongly interacting quantum liquids and gases, a certain universality of diffusion coefficients may be expected. Here, the mean free path becomes on the order of the interparticle spacing, and the velocity takes on the Heisenberg-limited value $v \sim \hbar/ml$, where $\hbar$ is the reduced Planck's constant and m is the particle mass. This leads to a limiting value of $D \sim \hbar/m$, with a numerical prefactor of order unity determined by the specific microscopic interactions. Such Heisenberg-limited values were observed for the spin diffusivity in a unitary Fermi gas (*5*–*7*), as well as the momentum diffusivity (the shear viscosity) in both the quark-gluon plasma of the early Universe and the unitary Fermi gas (*4*). Notably, the quantum liquids of bosonic ^{4}He and fermionic ^{3}He display similar sound diffusivities of $D \sim \hbar/m$ around 4 K (*8*, *9*). However, upon lowering the temperature into the deeply degenerate regime, these two quantum liquids display markedly different behaviors in the damping of sound. Down to about 1 K, the sound attenuation in ^{4}He does not vary strongly with temperature, decreasing only by a factor of two across the superfluid transition, with a minimum of $D \simeq 0.5\hbar/m$ (*8*, *10*). By contrast, ^{3}He features a diverging diffusivity ($\propto 1/T^2$), characteristic of a Fermi liquid, growing to $\sim 50{,}000\hbar/m$ around 2 mK, followed by a steep drop at the superfluid transition and settling to a value of $\sim 5000\hbar/m$ (*9*). A priori, it is unclear whether the temperature dependence of sound attenuation in a strongly interacting, fermionic gas—of atoms, electrons, or neutrons—should resemble that of a quantum liquid, and if so, whether it corresponds more closely to the strongly interacting, but bosonic, liquid ^{4}He or to the fermionic, but weakly interacting, liquid ^{3}He.

Ultracold atomic Fermi gases at unitarity are a prototypical strongly interacting quantum fluid for transport experiments (*11*–*15*). Featuring a mean free path as short as one interparticle spacing, these systems display the most robust form of fermionic superfluidity and near-perfect hydrodynamic flow even in the normal state (*16*–*18*). The presence of scale invariance leads to universality in physics properties (*13*–*15*, *19*–*21*), including transport (*5*, *22*–*24*). The universality directly connects this system to a host of other strongly interacting Fermi systems across all energy and length scales from nuclear matter to neutron stars. For the unitary Fermi gas, scale invariance implies that sound diffusivity must remain the same upon changing all length scales by the same factor. The diffusivity is thus $\hbar/m$ times a universal function of T/T_F, where the temperature T is normalized by the Fermi temperature T_F that only depends on the particle density n (*25*). At nondegenerate temperatures $T \gg T_F$, we expect a unitary Boltzmann gas, where the thermal wavelength $\lambda = \sqrt{2\pi\hbar^2/(mk_BT)}$ (k_B, Boltzmann constant) sets both the mean free path and the typical velocity of excitations, $l \sim 1/(n\lambda^2)$ and $v \sim \hbar/(m\lambda)$, implying $D \sim (\hbar/m)(T/T_F)^{3/2}$. In the quantum critical regime of the unitary gas (*26*, *27*), at $T \sim T_F$, the interaction and thermal energies are comparable and even the nature of the equilibrium state is a subject of debate (*28*, *29*). At low temperatures $T \ll T_F$, it remains unknown whether the sound diffusivity diverges as $1/T^2$ (*30*), as in the Fermi liquid ^{3}He (*31*, *32*), and whether any sudden drop in the sound diffusion occurs upon entering the superfluid regime. Calculation of such transport parameters is very difficult; for example, predictions for the shear viscosity vary from zero (*33*), as suggested by experiments on expanding inhomogeneous gases (*22*, *24*), to infinity if phonon damping dominates (*23*, *34*–*36*).

Transport experiments on Fermi gases have thus far used harmonic traps (*15*) or terminal configurations (*37*, *38*) and have been used to probe collective oscillations (*39*–*41*), spin transport (*5*, *7*, *42*), viscosity (*22*), conductivity (*37*), and Josephson oscillations (*38*). However, obtaining transport coefficients of homogeneous matter from inhomogeneous samples in atom traps requires sophisticated analysis and assumptions on the spatial flow profile (*5*, *22*, *43*). With the recent advent of optical box traps (*44*–*47*), it is now possible to directly probe the transport properties of homogeneous quantum gases (*47*–*50*). The gas is then in the same state throughout, and transport properties are identical across the system.

Measurements of transport properties involve the response of a system to an external drive. In linear response, an applied potential change δV couples to perturbations in the fluid density $\delta n = -\chi\delta V$ by the density response function χ. Sound corresponds to a resonant response, that is, a pole in χ at a frequency $\omega = ck$, set by the speed of sound c and wave number k, in the vicinity of which $\chi(\omega, k) \sim 1/(\omega^2 - c^2k^2 + i\Gamma\omega)$ (*51*, *52*). Here, i is the unit imaginary number and Γ is the damping rate of sound, given by $\Gamma = Dk^2$ (*53*) for hydrodynamic systems. Measurements of χ and Γ thus directly provide the sound diffusivity. Experiments involving liquid helium have used a number of techniques to measure χ, from free decay of resonant modes in a cylindrical resonator (*8*, *9*) to Brillouin scattering off of sound waves (*54*).

In our homogeneous quantum gas, the constant background density enables an ideal realization of a density response measurement

[1]Department of Physics, Massachusetts Institute of Technology, Cambridge, MA 02139, USA. [2]MIT-Harvard Center for Ultracold Atoms, Cambridge, MA 02139, USA. [3]Research Laboratory of Electronics, Massachusetts Institute of Technology, Cambridge, MA 02139, USA. [4]Département de Physique, Ecole Normale Supérieure/PSL Research University, CNRS, 24 rue Lhomond, 75005 Paris, France.
*Corresponding author. Email: zwierlei@mit.edu

(Fig. 1A). We use an equal two-state mixture of ^{6}Li atoms with resonant interstate interactions, confined to a cylindrical optical box potential composed of three repulsive laser beams: a hollow cylindrical beam providing the radial confinement (radius 60 μm) and two sheets of light serving as endcaps (length $L \sim 100$ μm) (*45*). The number $N \sim 10^6$ of atoms per spin state yields a Fermi energy of $E_F = \hbar^2 k_F^2/(2m) \sim h \times 10\text{kHz}$. To inject sound waves, we sinusoidally modulate the intensity of one endcap beam, which drives the gas at a well-defined frequency ω, and a wide range of spatial wave numbers, Fourier limited by the width ~4 μm of the endcap potential's edge (*55*). At the given driving frequency, the resonant sound response of the gas is dominated by a specific wave number $k = \omega/c$, resulting in a traveling wave of sound. An in situ absorption image is taken after an evolution time sufficiently short such that no reflections occur, and the resonant wave number k is directly measured (Fig. 1B, ii to iv). By repeating this protocol for different drive frequencies, we obtain the dispersion relation $\omega(k)$ for wave numbers $k < 0.14k_F$ (Fig. 1C). It is linear within our measurement error, corresponding to a constant speed of sound $c = \omega/k$ as a function of wave number. We note that at wavelengths approaching the interparticle spacing, and thus at momenta $\hbar k$ approaching the Fermi momentum ($k \sim k_F$), deviations from linear sound dispersion are expected for the unitary Fermi gas (*56*).

The precise measurement of the speed of sound allows a sensitive test of scale invariance of the unitary Fermi gas. In general, the speed of isentropic sound propagation c is directly tied to the equation of state by the hydrodynamic relation $mc^2 = (\partial P/\partial n)|_S = (V^2/N)(\partial^2 E/\partial V^2)|_S$. Here, E is the energy, S is the entropy, V is the volume, and $P = -(\partial E/\partial V)|_S$ is the pressure of the gas. A notable property of all nonrelativistic scale invariant systems in three dimensions is that their total energy scales as $E \propto V^{-2/3}$; this follows from the scaling behavior $E \rightarrow E/\lambda^2$ under dilation of space by a factor λ. This directly yields $mc^2 = (10/9)E/N$, independent of temperature or the phase of matter. In Fig. 1D, we show the measured speed of sound as a function of the energy per particle E/N, obtained from an isoenergetic expansion of the gas from the box into a harmonic trap (*57*). For both superfluid and normal samples (blue and red, respectively), the scale invariant prediction (solid black line) captures the data well with no free parameters. This demonstrates the universality of the speed of sound and scale invariance in the unitary Fermi gas in the explored window of temperature.

The attenuation of sound is already apparent in the spatial decay of the traveling waves shown in Fig. 1. For a precision measurement of the sound diffusivity, we now turn to the steady-state response of the system to a continuous drive, which directly reveals the density response function χ. The intensity of one of the endcaps is modulated for a sufficiently long time such that the density evolution has reached a steady state. After an integer number of driving cycles, the spatial Fourier transform of the density yields the out-of-phase response of the system, or $\text{Im}[\chi(\omega, k)]$ (*55*). This quantity also gives the average power absorbed by the system for a drive at frequency ω and spatial frequency k, and thus directly reveals the poles of χ as resonances. The measurements are summarized in Fig. 2. Each row of pixels in Fig. 2B shows the fractional density modulation at a particular drive frequency after integration along the radial axis. This "sonogram" reveals discrete normal modes, the first five of which are shown in Fig. 2A. The spatial Fourier transform, giving the out-of-phase response function, is shown in Fig. 2C. For each normal mode in the box, it features a peak at $\omega = ck$. The sound attenuation rate can be seen to increase with k, revealed in both a broadened frequency response as well as a reduced peak height.

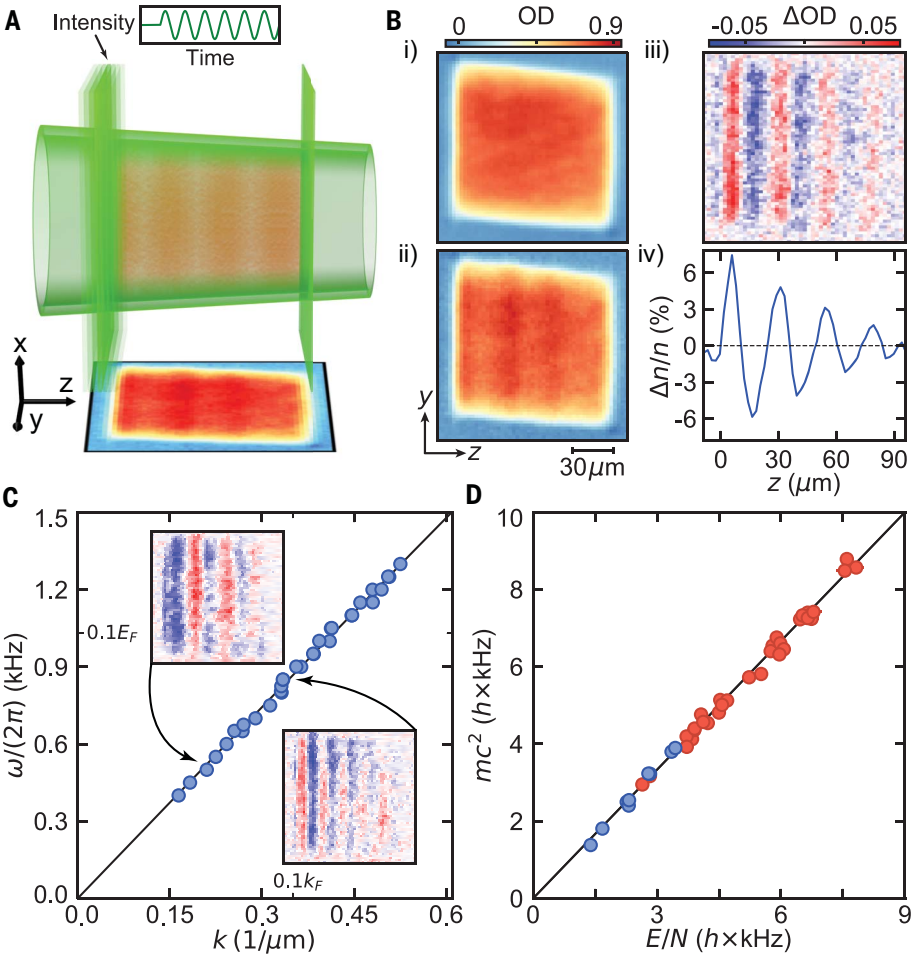

Fig. 1. Sound waves in a homogeneous unitary Fermi gas. (**A**) Fermionic ^{6}Li atoms are trapped in a three-dimensional cylindrical box made from green laser beams. Sound is excited by modulating the intensity of one of the laser walls. (**B**) The resulting density wave is observed via an in situ absorption image, shown as optical density (OD) for both an unperturbed (i) and modulated (ii) sample. Here, the modulation frequency is $2\pi \times 600$ Hz. Taking their difference (iii) and integrating along the homogeneous radial trap axis reveals (iv) a perturbation in the fractional density difference $\Delta n/n$, propagating along the axial direction z and exhibiting a well-defined wave number k corresponding to the applied modulation frequency ω. (**C**) Dispersion of sound $\omega(k)$. The fitted slope (black line) provides the speed of sound. The insets display sound waves observed at $\omega = 2\pi \times 600$ Hz and $\omega = 2\pi \times 850$ Hz. Errors in the measured k are smaller than the point size. (**D**) Measurement of the universal relation between the measured speed of sound and the energy-per-particle E/N (see text). The black solid line shows the predicted linear dependence for any nonrelativistic scale invariant system in three dimensions; $mc^2 = \frac{10}{9}E/N$. Data are shown for both the normal (red) and the superfluid (blue) phase.

The density response $\mathrm{Im}[\chi(\omega, k_j)]$ at the wave number $k_j = j\pi/L$ of the j^{th} normal mode of the box is shown in Fig. 3A, along with Lorentzian fits (solid lines). The full-width at half-maximum yields the damping rate of sound Γ, which is shown as a function of k in Fig. 3B, for gases both above (red and green) and below (blue) the superfluid transition. At temperatures above the superfluid transition temperature $T_C = 0.17T_F$ (*20*), we observe $\Gamma(k)$ to increase quadratically with k for all explored wave numbers ($k \lesssim 0.3\ mc/\hbar$). This establishes diffusive damping of sound in the normal regime, as expected in the collisionally hydrodynamic regime (*16*, *58*).

Below the superfluid transition temperature, $T < T_C$, we observe a crossover from quadratic scaling of $\Gamma(k)$ at wave numbers $k \lesssim 0.2mc/\hbar$ to linear behavior, indicating a departure from purely hydrodynamic transport at high wave numbers. This is expected when the modulation frequency becomes comparable to the damping rate of thermal phonons Γ_{ph} (*36*, *59*). Collisionless or Landau damping of sound is caused by nonlinearities resulting from the kinetic energy density carried by sound and the density dependence of the speed of sound. Fermi's golden rule yields a rate $\Gamma_{\mathrm{ph}} \propto k$ (*36*, *51*) proportional to the energy $\hbar ck$ carried by a phonon. Including a nonzero damping rate of phonons Γ_{ph} yields a crossover from hydrodynamic to collisionless damping as the sound frequency ck exceeds Γ_{ph} (*59*). The relation $\Gamma = Dk^2 f(ck/\Gamma_{\mathrm{ph}})$ with $f(x) = \tan^{-1}(x)/x$ (*59*) shows a good agreement with the data (solid line). The scale of the fitted relaxation rate $\Gamma_{\mathrm{ph}} = 0.27(8)k_B T/\hbar$ is on the order of the gas temperature, hinting toward quantum critical damping (*27*). We note that the observation of quadratic scaling of Γ with k at low wave numbers implies that sound is primarily attenuated in the bulk, and that edge effects are negligible (*53*, *60*).

As the main result of this work, we present in Fig. 4 the sound diffusivity D of the unitary Fermi gas. This is obtained as $D = \Gamma/k^2$ using the $j = 2$ normal mode, for which ck/Γ_{ph} is always less than 0.25, ensuring that it is well described by a hydrodynamic framework. The measured values are shown in units of $\hbar/m$ and, at low temperatures, exhibit a numerical prefactor ~1. This demonstrates universal sound diffusion, with no dependence on microscopic parameters of the gas.

Generally, the sound diffusivity contains contributions from both the bulk and shear viscosity, ζ and η, respectively (which damp momentum gradients), and the thermal conductivity κ (which damps temperature gradients) (*53*). However, for a scale-invariant fluid, the bulk viscosity vanishes (*61*) and $D = D_\eta + D_\kappa$ only, with $D_\eta = 4\eta/(3mn)$ and $D_\kappa = 4\kappa T/(15P)$ (*55*). We note that our measurements of D therefore constrain the relationship between the viscosity and thermal conductivity, which is usually quantified by the Prandtl number $\mathrm{Pr} = c_P\eta/\kappa$ (*53*), where c_P is the specific heat at constant pressure (*55*).

The solid black line in Fig. 4 shows a prediction $D = 6.46\ (\hbar/m)(T/T_F)^{3/2}$, which uses the high-temperature results for viscosity (*23*, *62*) and thermal conductivity (*23*, *25*), along with the ideal gas equation of state. This simple model captures the high-temperature behavior well without any free parameters. However, it is expected to underestimate D when $T/T_F \lesssim 1$ because it neglects the suppression of scattering arising from Pauli blocking.

As the temperature is reduced, D smoothly drops to a value $\sim\hbar/m$, consistent with Heisenberg-limited diffusivity. Notably, at intermediate temperatures, we observe neither the $D \sim 1/T^2$ scaling typical of a Fermi liquid nor any sudden change at the superfluid transition. This is further demonstrated by the inset of Fig. 4, where we show a magnified plot of D (blue points) in the vicinity of the superfluid transition (vertical red line) (*20*). Also shown is the pair condensate fraction (red points) obtained from the measured pair center-of-mass momentum distribution (*63*), which

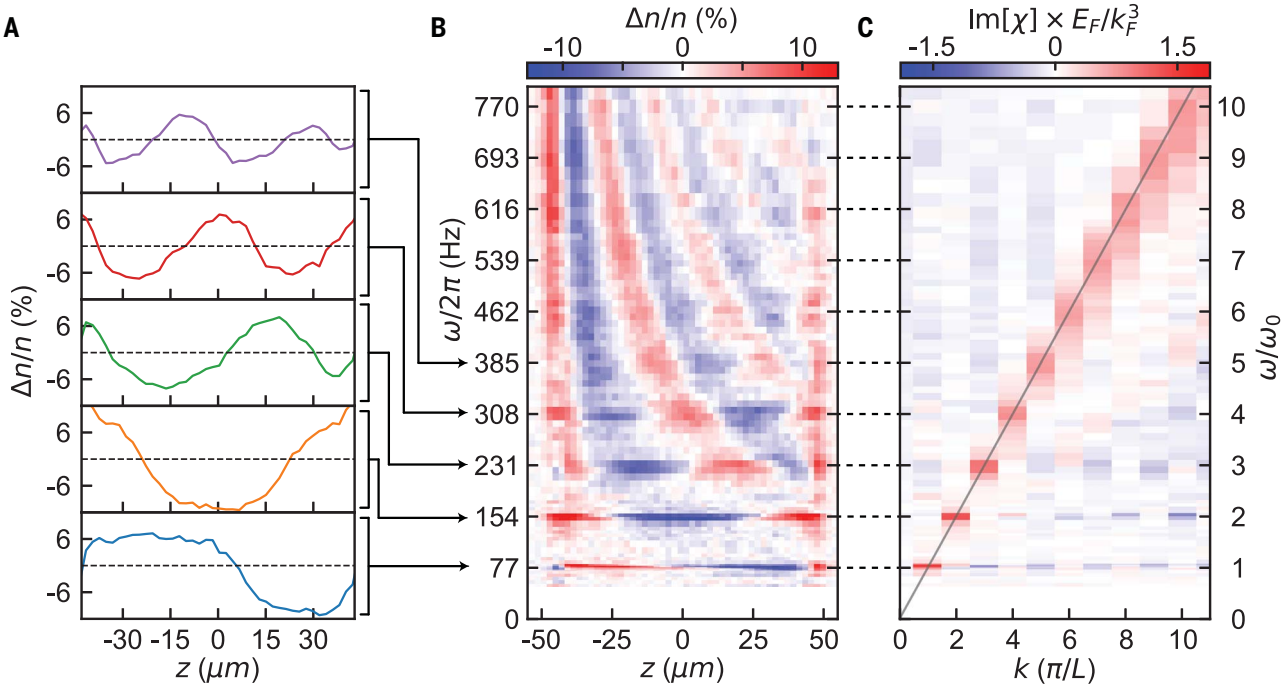

Fig. 2. Normal modes of the cylindrical box trap. (**A** and **B**) The steady-state density response of the gas is obtained by modulating the container walls at frequency ω for 30 cycles of the drive. Standing waves of sound corresponding to the normal modes in the box are observed at frequencies $\omega_j = j\pi c/L \approx 2\pi j \times 77\mathrm{Hz}$ (where $j \in \mathbb{Z}$), the first five of which are shown in (A). The full sonogram is shown in (B). Here, each row of pixels corresponds to a particular realization of the experiment at a given frequency. (**C**) The spatial Fourier transform directly yields the density response function $\mathrm{Im}[\chi(k, \omega)]$. It reveals well-defined resonance peaks exhibiting both the linear dispersion of sound and increasing widths in frequency at higher wave numbers, corresponding to increased rates of sound attenuation.

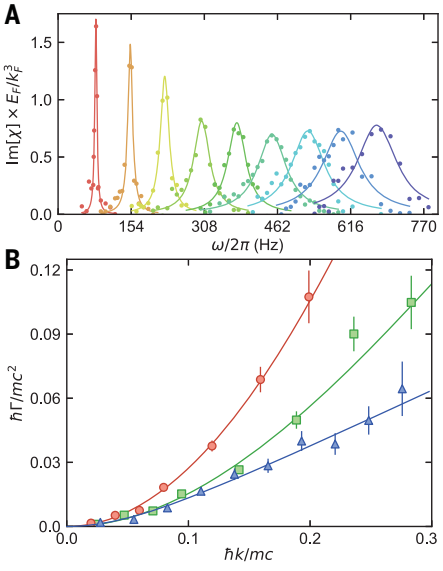

Fig. 3. Spectral response of sound and its attenuation rate. (**A**) The imaginary part of the density response function at each normal mode wave number k_j displays a well-defined peak in frequency, whose full-width at half-maximum yields the mode damping rate Γ. This is obtained from a Lorentzian fit, shown by solid lines. (**B**) Damping rate $\Gamma(k)$ for gas temperatures $T/T_F = 0.36(5)$ (red circles), $T/T_F = 0.21(3)$ (green squares), and $T/T_F = 0.13(2)$ (blue triangles). For all temperatures, $\Gamma(k)$ displays a quadratic scaling at low momenta characteristic of diffusive damping. For our coldest samples, as k increases, we observe a deviation from this behavior, revealed by a crossover to linear scaling. At all temperatures and wave numbers, our data are well captured by the model of (*59*) (solid lines), which accounts for the finite relaxation rate of the fluid. Error bars represent 1σ statistical uncertainty.

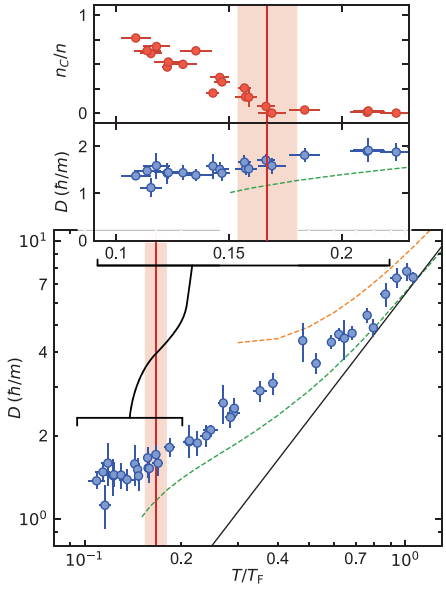

Fig. 4. Temperature dependence of the sound diffusivity. For temperatures comparable to the Fermi temperature, the sound diffusivity (D, normalized by $\hbar/m$; blue circles) approaches the expected high-temperature scaling of $T^{3/2}$ (solid black line). As the temperature is lowered, D decreases monotonically and attains a quantum-limited value close to $\hbar/m$. Below the superfluid transition [vertical red line, from (*20*)], D is observed to be almost independent of temperature and condensate fraction (n_C/n, red circles in inset). From the transition temperature ($n_C/n = 0$) to the coldest temperatures ($n_C/n \sim 0.8$), the changes in D are within the standard error of the measurements. Theoretical predictions for D are as follows: The dashed orange line is from the sound attenuation length calculated in the framework of kinetic theory (*25*), and the dashed green line is from a calculation of shear viscosity (*23*), assuming a Prandtl number of 2/3. Bars denote statistical error arising from the uncertainty in Γ. Additionally, the dominant systematic uncertainty in D is an error of 13% arising from the nonzero width of the endcaps. The red shaded regions represent the uncertainty in the superfluid transition temperature (*20*).

serves as both an indicator of superfluidity and a robust thermometer in the superfluid phase (*15*). Despite the definitive onset of pair condensation, we observe no measurable sharp feature in the diffusivity, which remains approximately constant as the temperature is reduced. Our nonvanishing diffusivity therefore contrasts previous measurements of a vanishing viscosity in the low-temperature limit (*24*).

This behavior can qualitatively be understood as follows. In the superfluid phase, viscosity arises entirely from the normal component, giving a diffusivity $D \sim (n_n/n)lv$ where $l = 1/(n_n\sigma)$ is the mean free path of a typical excitation with scattering cross section σ, velocity v, and density n_n (*30*, *64*). The dependence on the (strongly temperature-dependent) n_n therefore cancels, giving $D \sim v/(\sigma n)$. At the temperatures studied here, the normal component is dominated by broken pairs (*15*), whose velocity and cross section are only weakly temperature-dependent. Broken pairs are primarily formed at the Fermi surface, which is broadened by the pairing gap Δ. This results in a typical velocity $v \sim \hbar k_F/m$ and cross section $\sigma \sim k_F^{-2}(\Delta/E_F)^2$, where the $(\Delta/E_F)^2$ accounts for the restriction of phase space available for scattering arising from Pauli blocking. In the unitary Fermi gas, $\Delta \sim 0.4E_F$ (*41*, *65*), giving a diffusivity $D \sim \hbar/m$, consistent with our observations. By contrast, the pairing gap in ^{3}He is $\Delta \sim 10^{-3}E_F$, leading to a much larger value of $D \sim 5000\hbar/m$ (*60*, *66*).

We have measured the sound diffusivity of the unitary Fermi gas. The diffusivity approaches a Heisenberg-limited value of $\hbar/m$ at low temperatures, similar to the strongly interacting, bosonic quantum fluid ^{4}He. In contrast to Fermi liquid behavior seen in weakly interacting fermionic systems, the diffusivity monotonically increases with increasing temperatures and eventually follows the high-temperature behavior $D \sim \hbar/m(T/T_F)^{3/2}$. The measured sound diffusivity constrains the shear viscosity and thermal conductivity of the unitary Fermi gas. In particular, combined with the calculated shear viscosity in (*23*), we find a Prandtl number strictly lower than unity for all explored temperatures (*55*). This excludes the existence of a relativistic conformal gravity dual of the unitary Fermi gas (*67*), because this would require $\mathrm{Pr} = 1$. Thanks to the scale invariance of the unitary Fermi gas, the results obtained here apply broadly to other strongly interacting forms of fermionic matter, from hydrodynamic electron flow to nuclei and neutron matter.

REFERENCES AND NOTES

1. P. A. Lee, N. Nagaosa, X.-G. Wen, *Rev. Mod. Phys.* **78**, 17–85 (2006).
2. Y. Cao *et al.*, *Nature* **556**, 43–50 (2018).
3. M. G. Alford, L. Bovard, M. Hanauske, L. Rezzolla, K. Schwenzer, *Phys. Rev. Lett.* **120**, 041101 (2018).
4. A. Adams, L. D. Carr, T. Schäfer, P. Steinberg, J. E. Thomas, *New J. Phys.* **14**, 115009 (2012).
5. A. Sommer, M. Ku, G. Roati, M. W. Zwierlein, *Nature* **472**, 201–204 (2011).
6. A. B. Bardon *et al.*, *Science* **344**, 722–724 (2014).
7. C. Luciuk *et al.*, *Phys. Rev. Lett.* **118**, 130405 (2017).
8. K. H. Bennemann, J. B. Ketterson, *The Physics of Liquid and Solid Helium* (Wiley, 1976).
9. D. Vollhardt, P. Wölfle, *The Superfluid Phases of Helium 3* (Dover Publications, Inc., 2013).
10. V. S. L'vov, L. Skrbek, K. R. Sreenivasan, *Phys. Fluids* **26**, 041703 (2014).
11. W. Ketterle, M. W. Zwierlein, in *Ultra-cold Fermi Gases*, vol. 164 of *Proceedings of the International School of Physics "Enrico Fermi"*, M. Inguscio, W. Ketterle, C. Salomon, Eds. (IOS Press, 2007), pp. 95–287.
12. I. Bloch, J. Dalibard, W. Zwerger, *Rev. Mod. Phys.* **80**, 885–964 (2008).
13. S. Giorgini, L. P. Pitaevskii, S. Stringari, *Rev. Mod. Phys.* **80**, 1215–1274 (2008).
14. W. Zwerger, Ed., *The BCS-BEC Crossover and the Unitary Fermi Gas* (Springer, 2012).
15. M. W. Zwierlein, *Novel Superfluids* (Oxford Univ. Press, 2014), pp. 269–422.
16. K. M. O'Hara, S. L. Hemmer, M. E. Gehm, S. R. Granade, J. E. Thomas, *Science* **298**, 2179–2182 (2002).
17. A. Altmeyer *et al.*, *Phys. Rev. Lett.* **98**, 040401 (2007).
18. M. K. Tey *et al.*, *Phys. Rev. Lett.* **110**, 055303 (2013).
19. T.-L. Ho, *Phys. Rev. Lett.* **92**, 090402 (2004).
20. M. J. H. Ku, A. T. Sommer, L. W. Cheuk, M. W. Zwierlein, *Science* **335**, 563–567 (2012).
21. M. Randeria, E. Taylor, *Annu. Rev. Condens. Matter Phys.* **5**, 209–232 (2014).
22. C. Cao *et al.*, *Science* **331**, 58–61 (2011).
23. T. Enss, R. Haussmann, W. Zwerger, *Ann. Phys.* **326**, 770–796 (2011).
24. J. A. Joseph, E. Elliott, J. E. Thomas, *Phys. Rev. Lett.* **115**, 020401 (2015).
25. M. Braby, J. Chao, T. Schäfer, *Phys. Rev. A* **82**, 033619 (2010).
26. P. Nikolić, S. Sachdev, *Phys. Rev. A* **75**, 033608 (2007).
27. T. Enss, *Phys. Rev. A* **86**, 013616 (2012).
28. S. Nascimbène *et al.*, *Phys. Rev. Lett.* **106**, 215303 (2011).
29. I. Z. Rothstein, P. Shrivastava, *Phys. Rev. B* **99**, 035101 (2019).

30. H. Smith, H. H. Jensen, *Transport Phenomena* (Clarendon, 1989).
31. M. A. Black, H. E. Hall, K. Thompson, *J. Phys. C Solid State Phys.* **4**, 129–142 (1971).
32. C. N. Archie, T. A. Alvesalo, J. D. Reppy, R. C. Richardson, *J. Low Temp. Phys.* **42**, 295–332 (1981).
33. H. Guo, D. Wulin, C.-C. Chien, K. Levin, *New J. Phys.* **13**, 075011 (2011).
34. G. Rupak, T. Schäfer, *Phys. Rev. A* **76**, 053607 (2007).
35. M. Mannarelli, C. Manuel, L. Tolos, *Ann. Phys.* **336**, 12–35 (2013).
36. H. Kurkjian, Y. Castin, A. Sinatra, *Ann. Phys.* **529**, 1600352 (2017).
37. S. Krinner, T. Esslinger, J.-P. Brantut, *J. Phys. Condens. Matter* **29**, 343003 (2017).
38. G. Valtolina *et al*., *Science* **350**, 1505–1508 (2015).
39. M. Bartenstein *et al*.,*Phys. Rev. Lett.* **92**, 203201 (2004).
40. J. Kinast, S. L. Hemmer, M. E. Gehm, A. Turlapov, J. E. Thomas, *Phys. Rev. Lett.* **92**, 150402 (2004).
41. S. Hoinka *et al*., *Nat. Phys.* **13**, 943–946 (2017).
42. M. Koschorreck, D. Pertot, E. Vogt, M. Köhl, *Nat. Phys.* **9**, 405–409 (2013).
43. M. Bluhm, J. Hou, T. Schäfer, *Phys. Rev. Lett.* **119**, 065302 (2017).
44. A. L. Gaunt, T. F. Schmidutz, I. Gotlibovych, R. P. Smith, Z. Hadzibabic, *Phys. Rev. Lett.* **110**, 200406 (2013).
45. B. Mukherjee *et al*., *Phys. Rev. Lett.* **118**, 123401 (2017).
46. K. Hueck *et al*., *Phys. Rev. Lett.* **120**, 060402 (2018).
47. L. Baird, X. Wang, S. Roof, J. E. Thomas, *Phys. Rev. Lett.* **123**, 160402 (2019).
48. N. Navon, A. L. Gaunt, R. P. Smith, Z. Hadzibabic, *Nature* **539**, 72–75 (2016).
49. J. L. Ville *et al*., *Phys. Rev. Lett.* **121**, 145301 (2018).
50. S. J. Garratt *et al*., *Phys. Rev. A (Coll. Park)* **99**, 021601 (2019).
51. P. C. Hohenberg, P. C. Martin, *Ann. Phys.* **34**, 291–359 (1965).
52. P. C. Hohenberg, *J. Low Temp. Phys.* **11**, 745–750 (1973).
53. L. D. Landau, E. M. Lifshitz, *Fluid Mechanics* (Elsevier, 1959).
54. J. A. Tarvin, F. Vidal, T. J. Greytak, *Phys. Rev. B* **15**, 4193–4210 (1977).
55. See supplementary materials.
56. H. Kurkjian, Y. Castin, A. Sinatra, *Phys. Rev. A* **93**, 013623 (2016).
57. Z. Yan *et al*., *Phys. Rev. Lett.* **122**, 093401 (2019).
58. M. J. Wright *et al*., *Phys. Rev. Lett.* **99**, 150403 (2007).
59. C. J. Pethick, D. Ter Haar, *Physica* **32**, 1905–1920 (1966).
60. G. Eska *et al*., *Phys. Rev. Lett.* **44**, 1337–1340 (1980).
61. D. T. Son, *Phys. Rev. Lett.* **98**, 020604 (2007).
62. G. M. Bruun, H. Smith, *Phys. Rev. A* **72**, 043605 (2005).
63. B. Mukherjee *et al*., *Phys. Rev. Lett.* **122**, 203402 (2019).
64. C. J. Pethick, H. Smith, P. Bhattacharyya, *Phys. Rev. B* **15**, 3384–3400 (1977).
65. A. Schirotzek, Y. I. Shin, C. H. Schunck, W. Ketterle, *Phys. Rev. Lett.* **101**, 140403 (2008).
66. Y. A. Ono, J. Hara, K. Nagai, *J. Low Temp. Phys.* **48**, 167–188 (1982).
67. M. Rangamani, S. F. Ross, D. Son, E. G. Thompson, *J. High Energy Phys.* **2009**, 075 (2009).
68. P. B. Patel *et al*., Replication data for: Universal sound diffusion in a strongly interacting Fermi gas. Harvard Dataverse (2020); https://doi.org/10.7910/DVN/UVM2KN.

ACKNOWLEDGMENTS

We thank Y. Castin, T. Enss, T. Schäfer, C. J. Vale, and W. Zwerger for helpful discussions. **Funding:** This work was supported by the National Science Foundation (Center for Ultracold Atoms award nos. PHY-1734011 and PHY- 1506019), U.S. Air Force Office of Scientific Research (FA9550-16-1-0324 and MURI Quantum Phases of Matter FA9550-14-1-0035), U.S. Office of Naval Research (N00014-17-1-2257), and the David and Lucile Packard Foundation. J.S. was supported by LabEX ENS-ICFP: ANR-10-LABX-0010/ANR-10-IDEX-0001-02 PSL*. **Author contributions:** P.B.P., Z.Y., and J.S. performed the experimental measurements and data analysis. All authors contributed to the interpretation of the data and the preparation of the manuscript. **Competing interests:** The authors declare no competing interests. **Data and materials availability:** All data shown in this work can be found at Harvard Dataverse (*68*).

SUPPLEMENTARY MATERIALS

science.sciencemag.org/content/370/6521/1222/suppl/DC1
Materials and Methods
Supplementary Text
Figs. S1 and S2
References (*69*–*73*)

20 September 2019; accepted 24 October 2020
10.1126/science.aaz5756

CORONAVIRUS

Robust neutralizing antibodies to SARS-CoV-2 infection persist for months

Ania Wajnberg[1]*, Fatima Amanat[2,3], Adolfo Firpo[4], Deena R. Altman[5], Mark J. Bailey[1], Mayce Mansour[1], Meagan McMahon[2], Philip Meade[2,3], Damodara Rao Mendu[4], Kimberly Muellers[1], Daniel Stadlbauer[2], Kimberly Stone[1], Shirin Strohmeier[2], Viviana Simon[2], Judith Aberg[5], David L. Reich[6], Florian Krammer[2]*, Carlos Cordon-Cardo[4]*

Severe acute respiratory syndrome coronavirus 2 (SARS-CoV-2) has caused a global pandemic with millions infected and more than 1 million fatalities. Questions regarding the robustness, functionality, and longevity of the antibody response to the virus remain unanswered. Here, on the basis of a dataset of 30,082 individuals screened at Mount Sinai Health System in New York City, we report that the vast majority of infected individuals with mild-to-moderate COVID-19 experience robust immunoglobulin G antibody responses against the viral spike protein. We also show that titers are relatively stable for at least a period of about 5 months and that anti-spike binding titers significantly correlate with neutralization of authentic SARS-CoV-2. Our data suggest that more than 90% of seroconverters make detectable neutralizing antibody responses. These titers remain relatively stable for several months after infection.

Severe acute respiratory syndrome coronavirus 2 (SARS-CoV-2) has infected millions of individuals globally and, as of October 2020, has led to the death of >1 million individuals. Although the antibody responses in severe COVID-19 cases have been relatively well characterized (*1*, *2*), assessing the response in mild and asymptomatic cases is of great importance because they constitute most infections. It will be critical to understand the robustness of the antibody response in these mild cases, including its longevity and functionality, so as to inform serosurveys and to determine levels and duration of antibody titers that may be protective against reinfection (*3*).

Antibodies to SARS-CoV-2 can target many of its encoded proteins, including structural and nonstructural antigens. Thus far, two structural proteins have been used as target antigens for serological assays. One is the abundant nucleoprotein (NP), which is found inside the virus or inside infected cells. However, because of the biological function of NP and because it is shielded from antibodies by viral or cellular membranes, it is unlikely that NP antibodies can directly neutralize SARS-CoV-2. The second structural protein often used as a target for characterizing the immune response to SARS-CoV-2 is the spike protein. The spike is a large trimeric glycoprotein that contains the receptor binding domain, which the virus uses to dock to its cellular receptor, angiotensin-converting enzyme 2, and for fusion of viral and cellular membranes (*4*, *5*). It is known from other coronaviruses—and it holds true for SARS-CoV-2—that the spike is the main, and potentially the only, target for neutralizing antibodies (*6*). Therefore, the assay used in this study to characterize the antibody response to SARS-CoV-2 is based on the trimerized, stabilized ectodomain of the spike protein (*7*). An enzyme-linked immunosorbent assay (ELISA) initially developed in early 2020 has been extensively used in research (*7*–*10*). This so-called Mount Sinai ELISA has high sensitivity (92.5%) and specificity (100%), as determined with an initial validation panel of samples (table S1). Furthermore, it has a positive predictive value (PPV) of 100%, with a negative predictive value (NPV) of 99.6%.

In March 2020, the Mount Sinai Health System began screening individuals for antibodies to SARS-CoV-2 to recruit volunteers as donors for convalescent plasma therapy (*11*). Screened patients had either polymerase chain reaction (PCR)–confirmed SARS-CoV-2 infections or suspected disease, which is defined as being told by a physician that symptoms may be related to SARS-CoV-2 or exposure to someone with confirmed SARS-CoV-2 infection. Most of the symptomatic patients who were screened experienced mild-to-moderate disease, with <5% requiring emergency department evaluation or hospitalization. Mount Sinai also offered the antibody test to all employees in its health system on a voluntary basis. By 6 October 2020, Mount Sinai had screened 72,401 individuals, with a total of 30,082 individuals testing positive (defined as detectable antibodies to the spike protein at a titer of 1:80 or higher) and 42,319 testing negative. The clinical laboratory ELISA set up results in discrete titers of either 1:80, 1:160, 1:320, 1:960, or ≥1:2880. Titers of 1:80 and 1:160 were categorized as low titers, 1:320 as moderate, and 1:960 and ≥1:2880 as high titers. For plasma therapy, titers of 1:320 or higher were initially deemed eligible. Of the 30,082 positive samples, 690 (2.29%) had a titer of 1:80; 1453 (4.83%), 1:160; 6765 (22.49%), 1:320; 9564 (31.79%), 1:960; and 11,610 (38.60%), ≥1:2880 (Fig. 1). Thus, we conclude that the vast majority of positive individuals have moderate-to-high titers of anti-spike antibodies. Of course, the argument could be made that we could be missing a number of individuals who had been infected with SARS-CoV-2 and did not produce antibodies, given that many individuals included in our dataset had never been tested by a nucleic acid amplification test for the virus. An earlier analysis performed with a smaller subset of 568 PCR-confirmed individuals using the same ELISA showed that >99% developed an anti-spike antibody response (*8*). In a later dataset of 2347 patients who self-reported positive PCR, 95% had positive antibody titers, which indicates that we did not miss large numbers of patients and confirms our prior sensitivity findings. Thus, the rate of individuals who do not seroconvert after SARS-CoV-2 infection is low, although such individuals may exist, and the majority of responders mount titers of 1:320 or higher.

Determining the neutralizing effects of SARS-CoV-2 spike antibodies is critical to understanding possible protective effects of the immune response. Therefore, we performed a well-established quantitative microneutralization assay (*12*) based on authentic SARS-CoV-2 with 120 samples of known ELISA titers ranging from negative to ≥1:2880. Neutralization titers significantly correlated (Spearman ρ = 0.87, $P < 0.0001$) with spike-binding titers (Fig. 2A). Although there was some variability, sera with 1:320, 1:960, and ≥1:2880 ELISA titers had geometric mean 50% inhibitory dilutions (ID_{50}) of about 1:30, 1:75, and 1:550, respectively. If any and all neutralizing activity above background is considered, then ~50% of sera in the 1:80 to 1:160 titer range, 90% in the 1:320 range, and all sera in the 1:960 to ≥1:2880 range had neutralizing activity (Fig. 2B). Only one of the negative samples showed activity slightly above background, which was potentially an ELISA false negative.

Another important question is longevity of the antibody response to the spike. To assess the medium-range stability of serum antibody titers against the spike protein, we recalled 121 plasma donors at a variety of titer levels who had initially been screened at around day 30

[1]Department of General Internal Medicine, Icahn School of Medicine at Mount Sinai, New York, NY 10029, USA. [2]Department of Microbiology, Icahn School of Medicine at Mount Sinai, New York, NY 10029, USA. [3]Graduate School of Biomedical Sciences, Icahn School of Medicine at Mount Sinai, New York, NY 10029, USA. [4]Clinical Microbiology Laboratory, Department of Pathology, Icahn School of Medicine at Mount Sinai, New York, NY 10029, USA. [5]Division of Infectious Diseases, Department of Medicine, Icahn School of Medicine at Mount Sinai, New York, NY 10029, USA. [6]Department of Anesthesiology, Perioperative and Pain Medicine, Icahn School of Medicine at Mount Sinai, New York, NY 10029, USA.
*Corresponding author. Email: ania.wajnberg@mountsinai.org (A.W.); florian.krammer@mssm.edu (F.K.); carlos.cordon-cardo@mssm.edu (C.C.-C.)

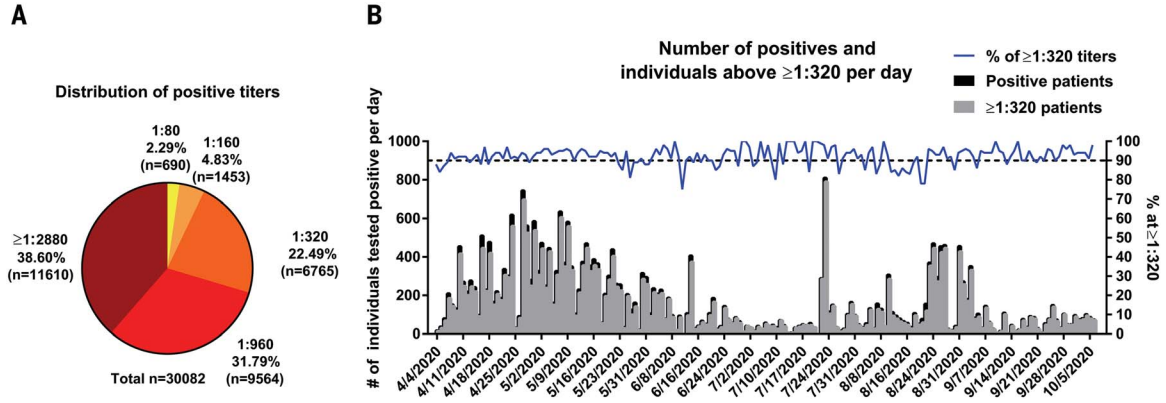

Fig. 1. SARS-CoV-2 spike antibody titers in 30,082 individuals. (**A**) The percentage of individuals with antibody titers of 1:80 (low), 1:160 (low), 1:320 (moderate), 1:960 (high), and ≥1:2880 (high). (**B**) Absolute numbers of individuals testing positive and percent of individuals with titers of 1:320 over time. Testing of each sample was performed once in a Clinical Laboratory Improvement Amendments (CLIA)–certified laboratory using an assay that received emergency use authorization (EUA) from the U.S. Food and Drug Administration (FDA).

Fig. 2. Neutralizing activity of serum samples in relation to ELISA titers. (**A**) A correlation analysis between ELISA titers on the *x* axis and neutralization titers in a microneutralization assay on the *y* axis. The Spearman ρ was determined. Red bars indicate the geometric mean. (**B**) The proportion of sera that exert any neutralizing activity in each of the ELISA titer categories. Testing was performed once, using an FDA EUA ELISA in a CLIA laboratory, or twice, following a standardized neutralization protocol.

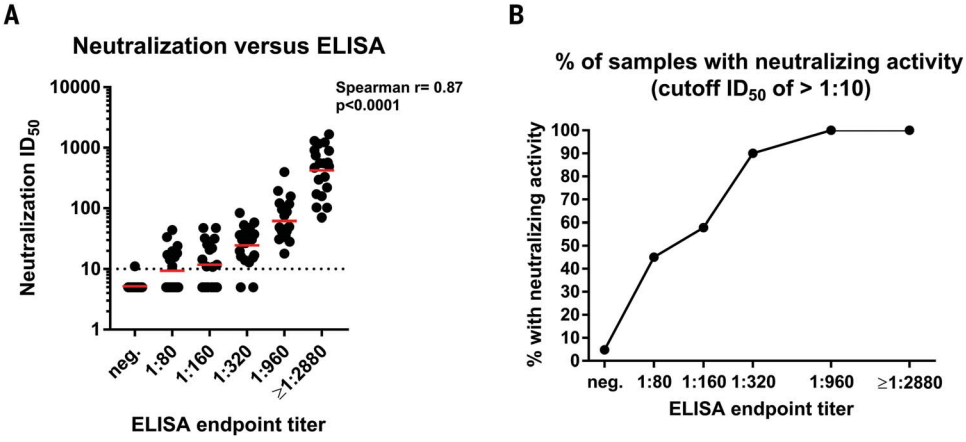

after symptom onset for two additional time points. The mean interval between the initial titer measurement and the second was 52 days (range: 33 to 67 days). This set the second time point at a mean of 82 days after symptom onset (range: 52 to 104 days) and the third time point at 148 days after symptom onset (range: 113 to 186 days). In comparing overall titers, we observed a slight drop from a geometric mean titer (GMT) of 764 to a GMT of 690 from the first to the second time point and another drop to a GMT of 404 for the last time point (Fig. 3A). In the higher titer range of ≥1:2880 and 1:960, we also observed a slow decline in titer over time (Fig. 3, B and C). Unexpectedly, but in agreement with earlier observations that seroconversion in mild COVID-19 cases might take a longer time to mount (*8*), we saw an increase in individuals who had an initial titer of 1:320, 1:160, or 1:80 (Fig. 3, D to F) from day 30 to day 82. Titers in these groups declined to about day 30 levels on day 148. Notably, one individual in the initial 1:80 group dropped from a 1:80 titer to being negative at the day 82 time point, and two others lost reactivity at the day 148 time point, indicating that very low initial titers might drop to undetectable levels over time. Neutralizing antibody titers followed titers measured by ELISA (Fig. 3G), and a good correlation between neutralization and ELISA titers was still observed on day 148 (Fig. 3H). The initial serum antibody titer was likely produced by plasmablasts, and plasmablast-derived antibodies peak 2 to 3 weeks after symptom onset. Given an immunoglobulin G half-life of ~21 days, the sustained antibody titers observed here over time are likely produced by long-lived plasma cells in the bone marrow. Note that our observations contrast with a recent report that found waning titers at 8 weeks after virus infection (*13*). Especially in asymptomatic cases, antibody responses disappeared after 8 weeks in 40% of individuals in that study. However, the antibodies measured in that paper targeted the NP plus a single linear spike epitope. The same paper also reported relatively stable (slightly declining) neutralizing antibody titers, which shows much higher concordance with our present findings. Thus, the stability of the antibody response over time may also depend on the target antigen.

Correlates of protection have been established for many different viral infections. These correlates are usually based on a specific level of antibody acquired through vaccination or natural infection that substantially reduces the risk of (re)infection. One example is the hemagglutination inhibition titer for the influenza virus, where a 1:40 titer reduces the risk of getting infected by 50% (*14*). Similar titers have been established for the measles virus (an ID_{50} titer of 1:120), hepatitis A virus, hepatitis B virus, and many others (*15*). These titers have facilitated vaccine development considerably. For some viruses and vaccines, the kinetics of the antibody response is also known, allowing for an accurate prediction of how long protection will last (*16*).

It is still unclear whether infection with SARS-CoV-2 in humans protects from reinfection and, if it does, for how long. We know from work with common human coronaviruses that neutralizing antibodies are induced and that these antibodies can last for years and provide protection from reinfection or, in the event of reinfection, attenuate disease (*17*). Furthermore, we now know from nonhuman

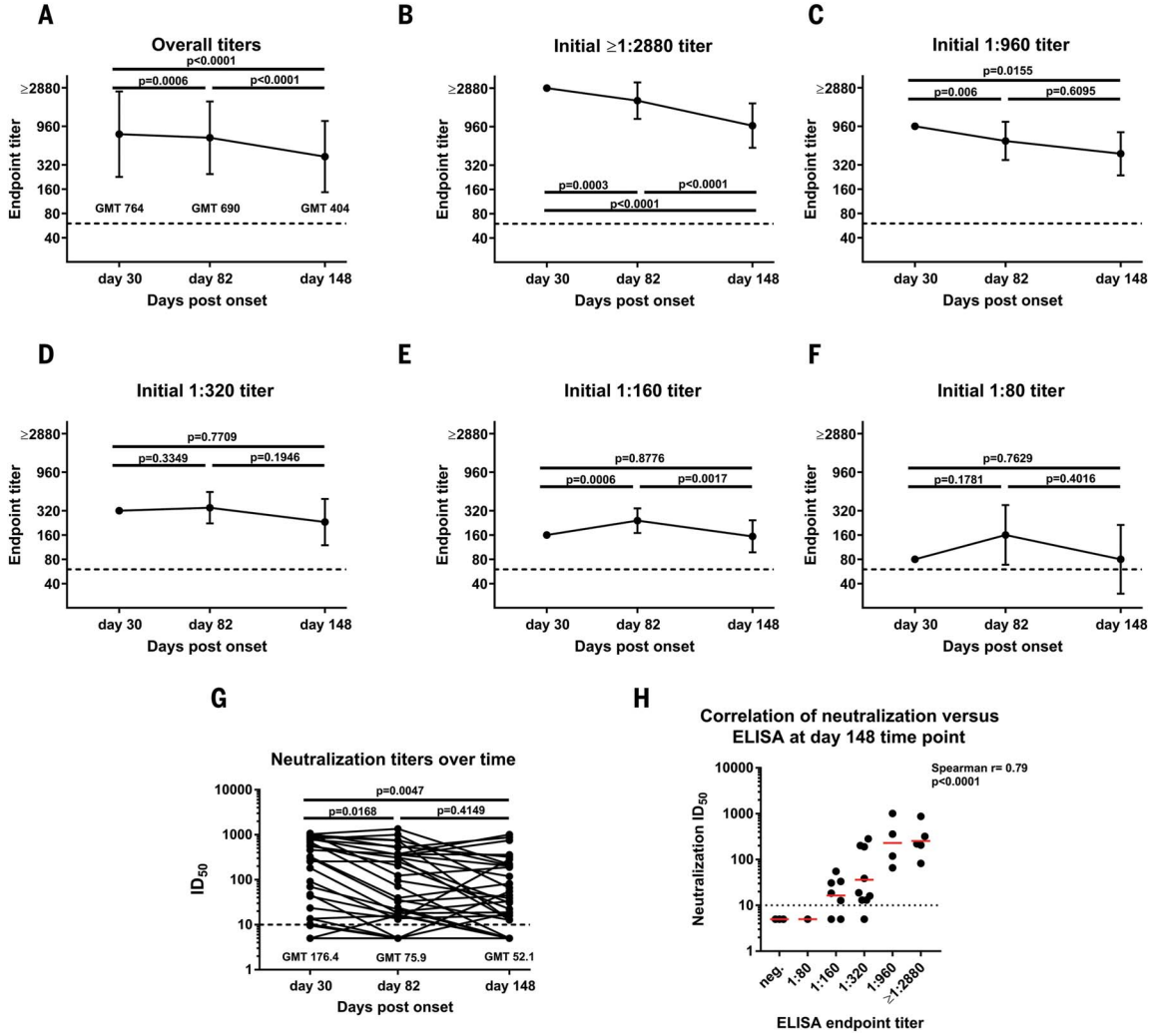

Fig. 3. Antibody titer stability over time. (**A**) Titers of 121 volunteers whose blood was initially drawn ~30 days after COVID-19 symptom onset and who were then recalled for additional blood draws at ~82 days and 148 days after symptom onset. (**B** to **F**) The same data as in (A), but stratified by the initial (day 30) titer. Titers are graphed as geometric mean titers (GMT) with geometric standard error. (**G**) Neutralization titers of 36 individuals over time. A paired one-way analysis of variance corrected for multiple comparison was used to determine statistical significance. (**H**) A correlation analysis between ELISA titers on the *x* axis and neutralization titers in a microneutralization assay on the *y* axis at day 148. Red bars indicate the geometric mean. The Spearman ρ was determined. Testing was performed once, using an FDA EUA ELISA in a CLIA-certified laboratory, or twice, following a standardized neutralization protocol.

primate models that infection with SARS-CoV-2 does protect from reinfection for at least some time (*18*, *19*). We also know that transferring serum of convalescent animals or neutralizing monoclonal antibodies to naïve animals can be protective and reduces virus replication significantly (*20*, *21*). Finally, vaccine-induced neutralizing antibody titers have been established as a correlate of protection in non-human primates (*22*). Notably, these vaccine-induced titers were relatively low and in the lower range of the titers observed in this study. Our data reveal that individuals who have recovered from mild COVID-19 experience relatively robust antibody responses to the spike protein, which correlate significantly with neutralization of authentic SARS-CoV-2 virus. Furthermore, the vast majority of individuals with antibody titers of 1:320 or higher show neutralizing activity in their serum. We also find stable antibody titers over a period of at least 3 months and only modest declines at the 5-month time point, which is consistent with data for the human coronaviruses SARS-CoV-1 and Middle East respiratory syndrome–related coronavirus (MERS-CoV) (*17*). We plan to follow this cohort over longer intervals of time. Although we cannot provide conclusive evidence that these antibody responses protect from reinfection, we believe it is very likely that they will decrease the odds ratio of reinfection and may attenuate disease in the case of breakthrough infection. We believe that it is imperative to swiftly perform studies to investigate and establish a correlate of protection from SARS-CoV-2 infection. A correlate of protection, combined with a better understanding of antibody kinetics to the spike protein, would inform policy regarding the COVID-19 pandemic and would be beneficial to vaccine development efforts.

REFERENCES AND NOTES

1. L. Liu *et al.*, *Emerg. Microbes Infect.* **9**, 1664–1670 (2020).
2. Q. X. Long *et al.*, *Nat. Med.* **26**, 845–848 (2020).
3. F. Krammer, V. Simon, *Science* **368**, 1060–1061 (2020).
4. D. Wrapp *et al.*, *Science* **367**, 1260–1263 (2020).
5. M. Letko, A. Marzi, V. Munster, *Nat. Microbiol.* **5**, 562–569 (2020).
6. F. Amanat, F. Krammer, *Immunity* **52**, 583–589 (2020).
7. F. Amanat *et al.*, *Nat. Med.* **26**, 1033–1036 (2020).
8. A. Wajnberg *et al.*, *Lancet* **1**, e283–e289 (2020).
9. D. Stadlbauer *et al.*, medRxiv 2020.06.2028.20142190 [Preprint]. 29 June 2020. https://doi.org/10.1101/2020.06.28.20142190.
10. D. Stadlbauer *et al.*, *Curr. Protoc. Microbiol.* **57**, e100 (2020).
11. S. T. H. Liu *et al.*, *Nat. Med.* 10.1038/s41591-020-1088-9 (2020).
12. F. Amanat *et al.*, *Curr. Protoc. Microbiol.* **58**, e108 (2020).
13. Q. X. Long *et al.*, *Nat. Med.* **26**, 1200–1204 (2020).

14. F. Krammer, J. P. Weir, O. Engelhardt, J. M. Katz, R. J. Cox, *Influenza Other Respir. Viruses* **14**, 237–243 (2020).
15. S. A. Plotkin, *Clin. Vaccine Immunol.* **17**, 1055–1065 (2010).
16. K. Van Herck, P. Van Damme, *J. Med. Virol.* **63**, 1–7 (2001).
17. A. T. Huang *et al.*, *Nat. Commun.* **11**, 4704 (2020).
18. W. Deng *et al.*, *Science* **369**, 818–823 (2020).
19. A. Chandrashekar *et al.*, *Science* **369**, 812–817 (2020).
20. R. Shi *et al.*, *Nature* **584**, 120–124 (2020).
21. M. Imai *et al.*, *Proc. Natl. Acad. Sci. U.S.A.* **117**, 16587–16595 (2020).
22. J. Yu *et al.*, *Science* **369**, 806–811 (2020).

ACKNOWLEDGMENTS

We are grateful for the continuous expert guidance provided by the ISMMS Program for the Protection of Human Subjects (PPHS). We also thank R. A. Albrecht for oversight of the conventional Biosafety Level 3 biocontainment facility, the medical students involved in the plasma convalescence program, and D. Adhimoolam for invaluable help with data curation. Furthermore, we thank E. Lium and team at Mount Sinai Innovation Partners for continuous support and V. Sarić and team at Mount Sinai's Development Office for fundraising and for taking many little things off our shoulders during this difficult time. Finally, we thank P. Palese and the Department of Microbiology and D. Charney and the Icahn School of Medicine at Mount Sinai's Dean's Office for strong institutional support of our work. **Funding:** This work was partially supported by NIAID Centers of Excellence for Influenza Research and Surveillance (CEIRS) contract HHSN272201400008C (F.K.) and by Collaborative Influenza Vaccine Innovation Centers (CIVIC) contract 75N93019C00051 (F.K.). Support was also provided by the JPB Foundation, the Open Philanthropy Project (#2020-215611), and other philanthropic donations. This effort was deliberated with Leidos Biomedical Research Inc./NCI over the last several months and is now going to be supported by the Serological Sciences Network (SeroNet). This project will be funded in whole or in part with federal funds from the National Cancer Institute, National Institutes of Health, under contract 75N91019D00024, task order 75N91020F00003, as well as U54 CA260560. The content of this publication does not necessarily reflect the views or policies of the Department of Health and Human Services, nor does mention of trade names, commercial products, or organizations imply endorsement by the U.S. government. **Author contributions:** A.W., D.R.A., M.J.B., M.Ma., K.M., K.S., and J.A. performed clinical activities. A.W., J.A., D.L.R., F.K., and C.C.-C. designed the study. A.W. and F.K. analyzed the data. A.F., M.Mc., P.M., D.R.M., D.S., and S.S. performed experiments. A.W., C.C.-C., and F.K. wrote the manuscript. All authors edited and approved the manuscript. **Competing interests:** Mount Sinai has licensed serological assays to commercial entities and has filed for patent protection for serological assays. J.A. reports grants for multicenter clinical trials: Atea (COVID), Frontier Technology (HIV), Gilead Sciences (COVID and HIV), Janssen (COVID and HIV), Merck (HIV), Pfizer (COVID), Regeneron (COVID), and Viiv (HIV). J.A. has received personal fees for serving on the HIV scientific advisory boards of Gilead, Janssen, Merck, Theratechnology, and Viiv. **Data and materials availability:** All data are available in the manuscript or the supplementary materials. This work is licensed under a Creative Commons Attribution 4.0 International (CC BY 4.0) license, which permits unrestricted use, distribution, and reproduction in any medium, provided the original work is properly cited. To view a copy of this license, visit https://creativecommons.org/licenses/by/4.0/. This license does not apply to figures/photos/artwork or other content included in the article that is credited to a third party; obtain authorization from the rights holder before using such material.

SUPPLEMENTARY MATERIALS

science.sciencemag.org/content/370/6521/1227/suppl/DC1
Materials and Methods
Table S1
References
MDAR Reproducibility Checklist

View/request a protocol for this paper from *Bio-protocol*.

10 July 2020; accepted 26 October 2020
Published online 28 October 2020
10.1126/science.abd7728

DEEP BIOSPHERE

Temperature limits to deep subseafloor life in the Nankai Trough subduction zone

Verena B. Heuer[1]*, Fumio Inagaki[2,3]*†, Yuki Morono[3]*, Yusuke Kubo[4]‡, Arthur J. Spivack[5], Bernhard Viehweger[1], Tina Treude[6], Felix Beulig[7]§, Florence Schubotz[1], Satoshi Tonai[8], Stephen A. Bowden[9], Margaret Cramm[10]¶, Susann Henkel[11], Takehiro Hirose[3], Kira Homola[5], Tatsuhiko Hoshino[3], Akira Ijiri[3], Hiroyuki Imachi[12], Nana Kamiya[13]#, Masanori Kaneko[14], Lorenzo Lagostina[15]**, Hayley Manners[16], Harry-Luke McClelland[17]††, Kyle Metcalfe[18], Natsumi Okutsu[19]†, Donald Pan[20]‡‡, Maija J. Raudsepp[21]§§, Justine Sauvage[5]¶¶, Man-Yin Tsang[22], David T. Wang[23]##, Emily Whitaker[24], Yuzuru Yamamoto[25]***, Kiho Yang[26]†††, Lena Maeda[4]†, Rishi R. Adhikari[1], Clemens Glombitza[27], Yohei Hamada[3], Jens Kallmeyer[28], Jenny Wendt[1], Lars Wörmer[1], Yasuhiro Yamada[2]†, Masataka Kinoshita[29], Kai-Uwe Hinrichs[1]‡‡‡

Microorganisms in marine subsurface sediments substantially contribute to global biomass. Sediments warmer than 40°C account for roughly half the marine sediment volume, but the processes mediated by microbial populations in these hard-to-access environments are poorly understood. We investigated microbial life in up to 1.2-kilometer-deep and up to 120°C hot sediments in the Nankai Trough subduction zone. Above 45°C, concentrations of vegetative cells drop two orders of magnitude and endospores become more than 6000 times more abundant than vegetative cells. Methane is biologically produced and oxidized until sediments reach 80° to 85°C. In 100° to 120°C sediments, isotopic evidence and increased cell concentrations demonstrate the activity of acetate-degrading hyperthermophiles. Above 45°C, populated zones alternate with zones up to 192 meters thick where microbes were undetectable.

Scientific ocean drilling has demonstrated the ubiquity of microbial life in deep subseafloor environments down to 2.5 km below seafloor (*1*–*3*). Because sediment temperature increases with burial depth, more than 50% of the global marine sediment volume is situated above 40°C (*4*). So far, the vast majority of subseafloor-life studies have targeted environments with in situ temperatures <30°C; the habitability of hotter sediments is largely unexplored. Microbes with growth temperatures up to 122°C have been isolated at hydrothermal vents (*5*), where the metabolism of these hyperthermophiles is fueled by high fluxes of oxidants and reductants (*6*). However, in deeply buried sediments, energy is limited, and with increasing depth and temperature, the slow-growing microbial communities struggle to meet the cellular maintenance energy requirement (*3*, *7*, *8*). Even in organic matter–rich petroleum reservoirs, microbial activity appears to cease at temperatures of ~80°C (*9*, *10*).

Aiming to fill the vast knowledge gaps regarding the response of microbial life to increasing temperature, we investigated up to 1.2-km-deep and up to 120°C hot sediments in the Nankai Trough off Cape Muroto, Japan (fig. S1). In this area, an up to 16-million-year-old, ~600-m-thick succession of hemipelagic mudstones and tuffs has been rapidly buried by an equally thick layer of trench deposits over the past ~0.4 million years (My) [(*11*); fig. S2]. Sediments concurrently heated by about 50°C and the onset of subduction formed a décollement separating the accreting and underthrusted domains (*11*, *12*). First indications for the presence of microbial life in ~800-m-deep, ~80° to 90°C warm sediments at a nearby drill site date back two decades (*11*, *12*). However, insufficient sensitivity in cell detection at that time compromised the habitability assessment of this environment (*11*, *12*). We designed Expedition 370 of the International Ocean Discovery Program (IODP) to achieve maximal sensitivity in life detection together with accurate determination of in situ temperatures, and established Site C0023 (32°22.0018′N, 134°57.9844′E, 4776-m water depth; fig. S1) in the vicinity of the previous drill site [(*13*); see supplementary materials]. Rigorous precautions during sampling and improvements in cell enumeration techniques increased the sensitivity in cell detection by five orders of magnitude compared with the previous study (*12*). For the quantification of cells that can be stained by a fluorescent dye (hereafter termed vegetative cells), the procedural blank was 4.2 ± 4.0 cells cm^{-3} of sediment (N = 20), thereby yielding a minimum quantification limit (MQL) of 16 cells cm^{-3}. Temperature measurements in the borehole constrained a steady-state temperature profile with a gradient of 110°C km^{-1} and a temperature of 120° ± 3°C in the deepest core retrieved from the basement at 1177 m below seafloor (mbsf) (figs. S3 and S4). The combination of authigenic minerals and thermally altered biomarkers reveals a history of episodic, short-term ingression of ~140° to 220°C hot hydrothermal fluids along permeable strata in the underthrust domain [(*14*); fig. S2].

At Site C0023, the depth profile of cell concentrations deviates notably from the global

[1]Center for Marine Environmental Sciences (MARUM), University of Bremen, Bremen, Germany. [2]Research and Development Center for Ocean Drilling Science, Japan Agency for Marine-Earth Science and Technology (JAMSTEC), Yokohama, Japan. [3]Kochi Institute for Core Sample Research, JAMSTEC, Kochi, Japan. [4]Center for Deep Earth Exploration (CDEX), JAMSTEC, Yokohama, Japan. [5]Graduate School of Oceanography, University of Rhode Island, Narragansett, RI, USA. [6]Department of Earth, Planetary, and Space Sciences, Department of Atmospheric and Oceanic Sciences, University of California, Los Angeles (UCLA), Los Angeles, CA, USA. [7]Center for Geomicrobiology, Department of Bioscience, Aarhus University, Aarhus, Denmark. [8]Faculty of Science and Technology, Kochi University, Kochi, Japan. [9]Department of Geology and Petroleum Geology, School of Geosciences, University of Aberdeen, Aberdeen, UK. [10]Department of Biological Sciences, University of Calgary, Calgary, AB, Canada. [11]Alfred Wegener Institute, Helmholtz Centre for Polar and Marine Research, Bremerhaven, Germany. [12]Institute for Extra-cutting-edge Science and Technology Avantgarde Research, JAMSTEC, Yokosuka, Japan. [13]Graduate School of Integrated Basic Sciences, Nihon University, Tokyo, Japan. [14]Geomicrobiology Research Group, National Institute of Advanced Industrial Science and Technology (AIST), Tsukuba, Japan. [15]Department of Environmental Systems Science, ETH Zürich, Zürich, Switzerland. [16]School of Geography, Earth and Environmental Sciences, Faculty of Science and Engineering, Plymouth University, Plymouth, UK. [17]Department of Earth and Planetary Sciences, Washington University in St. Louis, St. Louis, MO, USA. [18]Division of Geological and Planetary Sciences, California Institute of Technology, Pasadena, CA, USA. [19]Atmosphere and Ocean Research Institute, University of Tokyo, Tokyo, Japan. [20]Department of Subsurface Geobiological Analysis and Research, JAMSTEC, Yokosuka, Japan. [21]School of Earth Sciences, University of Queensland, St. Lucia, QLD, Australia. [22]Department of Earth Sciences, University of Toronto, Toronto, ON, Canada. [23]Department of Earth, Atmospheric and Planetary Sciences, Massachusetts Institute of Technology, Cambridge, MA, USA. [24]Department of Oceanography, Texas A&M University, College Station, TX, USA. [25]Department of Mathematical Science and Advanced Technology, JAMSTEC, Yokosuka, Japan. [26]Department of Earth System Sciences, Yonsei University, Seoul, Republic of Korea. [27]Institute of Biogeochemistry and Pollutant Dynamics, ETH Zürich, Zürich, Switzerland. [28]GFZ German Research Centre for Geosciences, Potsdam, Germany. [29]Earthquake Research Institute, University of Tokyo, Tokyo, Japan.

*These authors contributed equally to this work. †Present address: Institute for Marine-Earth Exploration & Engineering (MarE3), JAMSTEC, Yokohama, Japan. ‡Present address: Kochi Institute for Core Sample Research, JAMSTEC, Kochi, Japan. §Present address: Department of Ecological Microbiology, University of Bayreuth, Bayreuth, Germany. ¶Present address: Queen Mary University of London, School of Geography, London, UK. #Present address: Graduate School of Engineering, Kyoto University, Kyoto, Japan. **Present address: Robert Koch-Institut, Berlin, Germany. ††Present address: School of Earth Sciences, University of Melbourne, Melbourne, VIC, Australia. ‡‡Present address: Department of Ecology & Environmental Studies, The Water School, Florida Gulf Coast University, Fort Myers, FL, USA. §§Present address: Department of Earth and Atmospheric Sciences, The University of Alberta, Edmonton, AB, Canada. ¶¶Present address: Department of Marine Sciences, University of Gothenburg, Gothenburg, Sweden. ##Present address: ExxonMobil, 22777 Springwoods Village Parkway, Spring, TX, USA. ***Present address: Graduate School of Geoscience, Kobe University, Kobe, Japan. †††Present address: Department of Oceanography, Pusan National University, Busan, Republic of Korea.

‡‡‡Corresponding author. Email: khinrichs@uni-bremen.de

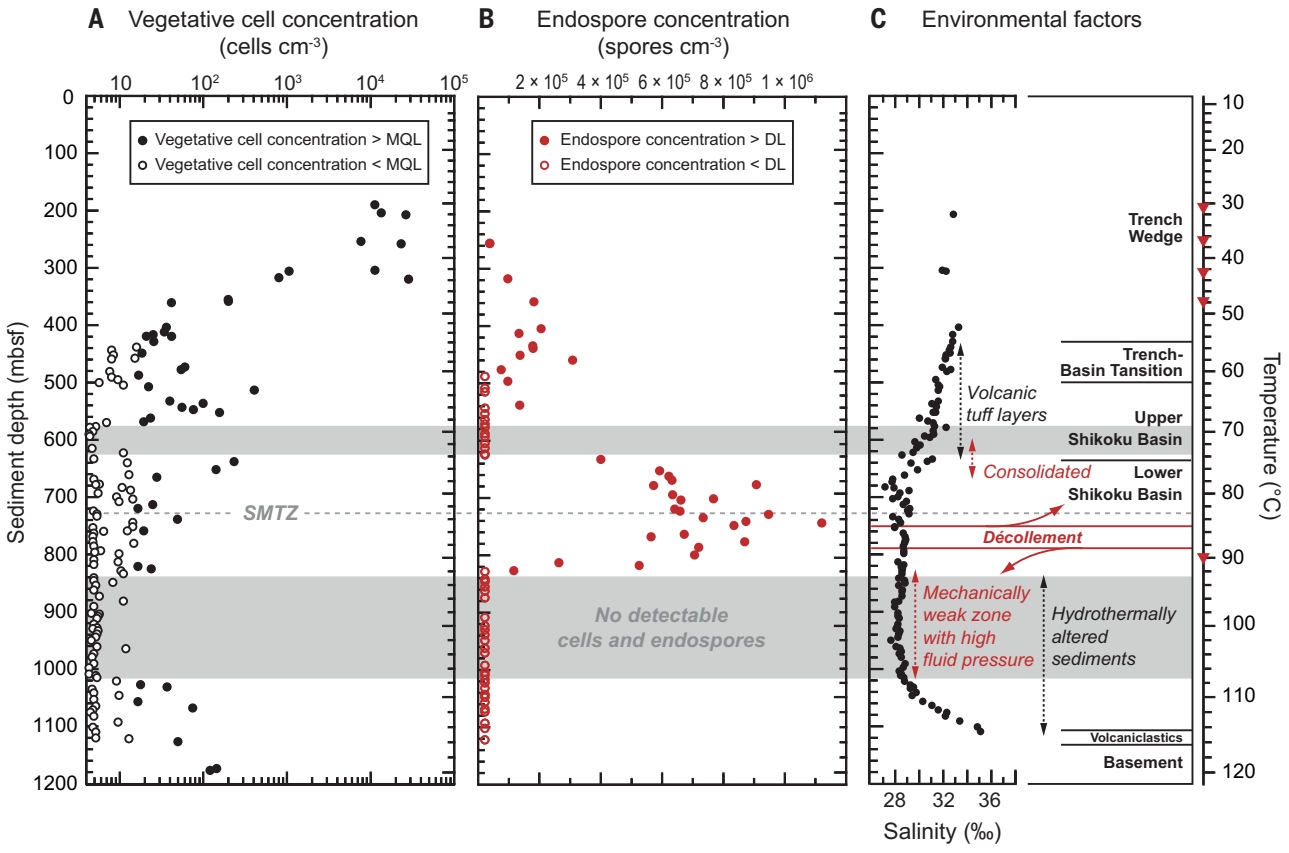

Fig. 1. Depth profiles of vegetative cells and endospores in relation to environmental factors at IODP Site C0023. (**A**) Concentrations of vegetative cells determined by counting of microbial cells fluorescently stained with SYBR Green I. (**B**) Concentrations of bacterial endospores derived from analysis of the diagnostic biomarker DPA; analytical sensitivity corresponds to a detection limit (DL) of 2.2×10^4 endospores cm^{-3}. (**C**) A schematic summary of temperature, tectonic units, and salinity showing the geochemical influence of basalt alteration in the basement; red symbols on the temperature axis designate the depth horizons where in situ temperature measurements were made. Gray shading indicates zones where concentrations of both vegetative cells and endospores were undetectable in all samples; the gray dashed line indicates the location of the SMTZ (compare Fig. 2).

trend of gradually decreasing cell concentrations observed in similarly deep but substantially colder (<30°C) sediments (*1*, *2*). At ~300 to 400 mbsf, concentrations of vegetative cells drop abruptly by two orders of magnitude and approach the MQL as temperature rises from 40° to 50°C (Fig. 1A). Concurrently, concentrations of endospores—that is, dormant, resistant structures affiliated with the bacterial phylum Firmicutes (fig. S5), which are widely found in marine sediments and soils (*15*, *16*)—increase to 2×10^5 cm^{-3} (Fig. 1B). Nevertheless, a small microbial population persists at >50°C in the form of both vegetative cells and endospores (Fig. 1). Down to the 120°C hot basement, sediments harboring microbial communities with up to 400 vegetative cells cm^{-3} are interspersed with intervals of up to 192-m thickness, in which no cells were detected (Fig. 1A and fig. S6). We rule out the possibility that the detection of cells resulted from contamination because cell concentration is neither related to the abundance of fractures in sediment cores nor related to the concentration of the perfluorocarbon-based contamination tracer supplied during the drilling operation (fig. S7); such relationships would be expected if contaminant cells were introduced by drilling fluids. Consistent with the extremely low concentrations of vegetative cells and the difficulty of extracting DNA from endospores (*17*), DNA yields were insufficient for producing reliable DNA-based community data for samples buried more deeply than 320 mbsf (*13*). In samples shallower than 320 mbsf, the community resembled those found in shallow subsurface sediments (*13*).

In contrast to the scattered distribution of vegetative cells in sediments >50°C, endospores show a clear zonation (Fig. 1B), as quantified by measurement of the diagnostic biomarker dipicolinic acid (DPA) (*18*). We rule out that substantial levels of DPA could have accumulated after the decay of endospores, given the propensity of 2-carboxylated pyridines to decarboxylate upon moderate short-term heating (*19*). Endospore concentrations rise prominently in a ~200-m interval of 75° to 90°C hot sediments, with a maximum of 1.2×10^6 endospores cm^{-3} at 85°C. The average endospore-to-vegetative cell ratio exceeds 6000 in sediments below 350 mbsf (table S1) and is thus two to three orders of magnitude higher than that in cold subseafloor sediments (*18*). Plausible scenarios for the accumulation of endospores in sediments that are nearly barren of vegetative cells relate to the thermal history of the site since the onset of trench conditions ~0.4 My ago (*12*, *14*) and involve the transitory growth of a thermophilic population of endospore formers [compare (*16*)] after temperature rose to ~50°C and its subsequent sporulation (fig. S8). Interestingly, in two expanded horizons, at 570 to 633 mbsf and 829 to 1021 mbsf, neither vegetative cells nor endospores were detected (Fig. 1 and fig. S6).

Pore-water profiles of microbial substrates and products provide evidence for microbial activity down to the ~16-My-old oceanic crust (Fig. 2). High concentrations of methane with a mean carbon isotopic composition ($\delta^{13}C$-CH_4)

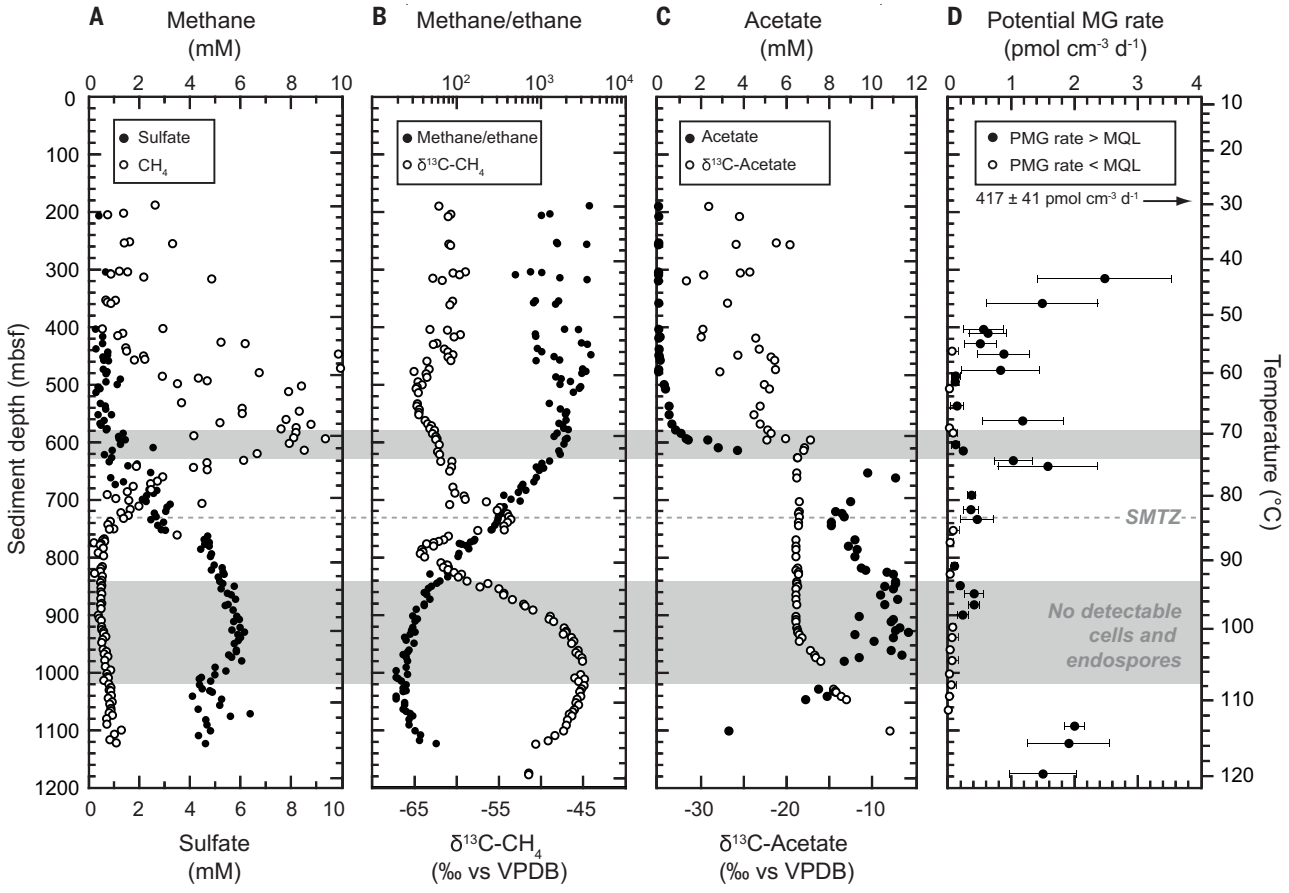

Fig. 2. Geochemical signals of microbial metabolism at Site C0023. (**A** to **D**) (A) Dissolved methane (*13*) and sulfate (*13*), (B) methane/ethane ratios (*13*) and δ^{13}C-CH_4, (C) dissolved acetate and δ^{13}C-acetate, and (D) potential rates of methanogenesis (MG) based on conversion of ^{14}C-CO_2 to ^{14}C-CH_4; note that the value at 180 mbsf is off-scale. Potential MG (PMG) rates were determined at 40°C for ≤360 mbsf, 60°C for 405 to 585 mbsf, 80°C for 604 to 775 mbsf, and 95°C for ≥816 mbsf. The MQL was 0.094 pmol CH_4 cm^{-3} day^{-1}. Gray shading, SMTZ, and the temperature axis are as in Fig. 1. VPDB in (B) and (D) is the Vienna Pee Dee Belemnite standard. In (D), error bars represent the standard deviation of three replicates.

of −61.3 ± 3.0 per mil (‰) (Fig. 2, A and B) indicate biogenic methanogenesis at least down to the 80° to 85°C hot sulfate methane transition zone (SMTZ) at ~730 mbsf. The positive excursion in δ^{13}C-CH_4 in the SMTZ (Fig. 2B) points to a biogenic methane sink and is consistent with previous observations from cultivation-based approaches that demonstrated the activity of thermophilic anaerobic methane-oxidizing communities at these temperatures (*20*, *21*). Below the SMTZ, methane is only present in micromolar concentrations, with rising δ^{13}C-CH_4 values and decreasing methane/ethane ratios indicating a relative increase of thermogenic hydrocarbons (Fig. 2B). Notably, a reversal of this trend at >1000 mbsf hints at a biogenic methane source above 100°C.

Diffusive profiles of pore-water constituents do not allow the distinction between current and recent in situ biogeochemical processes, whereas radiotracer experiments specifically target on-going microbial activity, albeit with some unavoidable deviation from in situ conditions. At Site C0023, radiotracer experiments reveal present-day methanogenic activity in 65% of the investigated samples (Fig. 2D). Potential rates of methanogenesis via CO_2 reduction in sediments below 300 mbsf are generally below 4 pmol cm^{-3} day^{-1} and thus within the range of previous observations made in the deep subseafloor (*22*). Their depth distribution is consistent with cellular concentrations (Fig. 1) and activities deduced from the pore-water profiles of methane (Fig. 2, A and B). Rates are highest in the methanic zone, decrease distinctly to <0.6 pmol cm^{-3} day^{-1} below the SMTZ, and drop to undetectable levels in 63% of the samples taken from the deep expanded horizon with no detectable cells and endospores (Fig. 2D). Notably, potential methanogenesis rates rise again to values observed in the methanic zone in the three deepest samples (Fig. 2D), thus confirming the existence of active methanogenic communities in 110° to 120°C hot sediments and pillow basalts above the basement.

Acetate is a key microbial substrate, and its generation from sedimentary organic matter upon heating has been suggested to fuel microbial life in deeply buried sediments (*23*). Throughout the sediment column of Site C0023, reactions degrading acetate via sulfate reduction and methanogenesis are exergonic, with Gibbs free energy yields becoming increasingly negative with depth (fig. S9). The concentrations of acetate and its carbon isotopic compositions (δ^{13}C-acetate) (Fig. 2C) indicate distinct changes in acetate utilization with temperature and depth. In the up-to-60°C hot upper 600 mbsf, low concentrations of acetate around 26 ± 22 μM (N = 19) are consistent with a steady state governed by tightly coupled microbial production and consumption, as observed in other sedimentary environments. The fluctuation of δ^{13}C-acetate around its average of −25.5 ± 3.4‰ implies ongoing metabolic activity (*24*). In sharp contrast, acetate utilization is minimal at 60° to 100°C. At 60° to 75°C, acetate concentrations rise steeply with the simultaneous decline of methane concentrations and accumulation of endospores, suggesting that microbial

consumption is no longer balancing the release of acetate from sedimentary organic matter. Nevertheless, a local minimum in acetate concentration at the SMTZ (Fig. 2C) is consistent with some microbial utilization at this geochemical interface. Below the SMTZ, acetate concentrations level at 9.2 ± 2.4 mM with an invariable δ^{13}C-acetate around −18.8 ± 0.5‰. The combination of high concentration and low isotopic variability implies an acetate pool without substantial turnover within the endospore-dominated zone as well as in the underlying 200-m-thick zone, where neither cells nor endospores were detected.

At >1030 mbsf, however, acetate concentrations decline and δ^{13}C-acetate monotonically increases with depth, reaching a maximum of −7.9‰ in the deepest pore-water sample recovered from 1101 mbsf. This trend is consistent with active hyperthermophiles degrading preferentially ^{13}C-depleted acetate, leaving the residual acetate isotopically enriched. Without continued consumption, diffusion would homogenize δ^{13}C-acetate variations, as observed in the overlying sediments. The drawdown of the acetate pool requires isotopic fractionation factors of −7.7 to −15.4‰ (fig. S10), which are consistent with those observed in lab cultures (*25*). The size of the sink would have to be on the order of 5×10^{-12} mol cm^{-3} year^{-1}. Given cellular concentrations of 10 to 100 cm^{-3} in sediments corresponding to this acetate sink, the required cellular metabolic rates are two to three orders of magnitude lower than those observed in lab cultures of the hyperthermophilic archaea *Pyrococcus furiosus* (*26*) and *Archaeoglobus fulgidus* (*27*) but two to three orders higher than in situ rates in deep sediments with temperatures <30°C (*28*). Thus, acetate profiles are consistent with the existence of a small acetate-utilizing microbial community at >100°C and suggest that the microbes at this high temperature require more energy and therefore turn over substrates faster than at lower temperature (*8*). Syntrophic acetate oxidation coupled to consumption of the resulting CO_2 and electrons by methanogens is a known acetate sink in deep sediments (*29*) and is considered to be particularly important at increased temperatures (*30*). This process is exergonic under in situ conditions (fig. S9) and could account for the increased methanogenesis rates (Fig. 2D) and the isotopic signature of methane (Fig. 2B) in the deepest portion of the borehole.

Our findings reveal the impact of increasing temperature with depth on microbial life. This is exemplified in the massive collapse of the population of vegetative cells in <0.4-My-old sediments at 300 to 400 mbsf. In this interval, temperatures of 40° to 50°C are within the upper growth range of mesophiles. The coincident accumulation of endospores as a result of a putative sporulation of mesophilic endospore-forming Firmicutes (Fig. 1) supports the conclusion that the abundance of microbial populations is primarily controlled by temperature-dependent physiological factors down to 600 mbsf. In the deeper portion of Site C0023, geological processes may exert additional control. A sharp decline in biogenic methanogenesis and acetate utilization at 70° to 75°C coincides with the upper growth range of thermophiles, but notably, this depth interval concurrently spans the lithological boundary between Upper and Lower Shikoku Basin (compare Fig. 1). At this boundary, tuffs (indurated volcanic ash) cease to be present. Tuff alteration forms smectite, and microbial reduction of Fe(III) in smectite serves as an energy-yielding process and has indeed been found to promote smectite-to-illite conversion at 500 to 600 mbsf at Site C0023 (*31*). Thus, a modulation of some types of microbial activity by microbe-mineral interactions is conceivable. Peak endospore concentrations at 85°C coincide with both the SMTZ and the plate boundary décollement. In this zone, brief periods of frictional heating during differential plate motion (*32*) likely cause additional challenges for microorganisms, but endospores and high acetate concentrations may provide a seed bank and energy, respectively, for an ecosystem recovery from episodic perturbations.

In the upper 200 m of the underthrust domain, at ~90° to 100°C, an expanded zone without detectable cells and with no geochemical signs of microbial activity traverses the sparsely populated sediments (Figs. 1 and 2). In this zone, undercompacted and mechanically weak sediments are overpressurized and affected by ~145° to 220°C hot fluids for short durations (*14*, *33*). The transient heating events may have locally sterilized sediment (*14*), but microbial cells, acetate consumption, and methanogenic activity prevail again in >100°C sediments, where mechanical strength and salinity increase toward the sediment-basement interface (Figs. 1 and 2 and fig. S2). Hydraulic communication between basalts and overlying sediment is evidenced by shared styles of epigenetic mineralization in the form of calcite veins and ferruginous metal oxides. Mass transfer between basal sediment and a basalt-hosted aquifer would increase the habitability of the basal sediment by reducing formation fluid pressure and by replenishing otherwise depleted substrates such as reduced iron and sulfate (*34*).

Our study reveals the dependence of microbial abundance and activity to critical temperatures around 40° to 50°C and 70°C; it moreover shows that life in the deep subseafloor is not constrained by an upper temperature limit below 120°C. Our findings highlight the interplay of geological processes, temperature, and microbial life in the deep, hot sediments of the Nankai Trough and suggest a critical influence of subduction-related geological processes on habitability.

REFERENCES AND NOTES

1. J. Kallmeyer, R. Pockalny, R. R. Adhikari, D. C. Smith, S. D'Hondt, *Proc. Natl. Acad. Sci. U.S.A.* **109**, 16213–16216 (2012).
2. R. J. Parkes *et al.*, *Mar. Geol.* **352**, 409–425 (2014).
3. F. Inagaki *et al.*, *Science* **349**, 420–424 (2015).
4. D. E. LaRowe, E. Burwicz, S. Arndt, A. W. Dale, J. P. Amend, *Geology* **45**, 275–278 (2017).
5. K. Takai *et al.*, *Proc. Natl. Acad. Sci. U.S.A.* **105**, 10949–10954 (2008).
6. J. P. Amend, E. L. Shock, *FEMS Microbiol. Rev.* **25**, 175–243 (2001).
7. M. A. Lever *et al.*, *FEMS Microbiol. Rev.* **39**, 688–728 (2015).
8. M. H. Møller *et al.*, *Front. Microbiol.* **9**, 967 (2018).
9. A. Wilhelms *et al.*, *Nature* **411**, 1034–1037 (2001).
10. I. M. Head, D. M. Jones, S. R. Larter, *Nature* **426**, 344–352 (2003).
11. G. F. Moore, A. Taira, A. Klaus, Expedition 190 Scientists, in *Proceedings of the Ocean Drilling Program, Initial Reports* (Ocean Drilling Program, College Station, TX, 2001), vol. 190.
12. B. Horsfield *et al.*, *Earth Planet. Sci. Lett.* **246**, 55–69 (2006).
13. V. B. Heuer, F. Inagaki, Y. Morono, Y. Kubo, L. Maeda, Expedition 370 Scientists, "Temperature limit of the deep biosphere off Muroto" in *Proceedings of the International Ocean Discovery Program* (International Ocean Discovery Program, College Station, TX, 2017), vol. 370.
14. M.-Y. Tsang *et al.*, *Mar. Pet. Geol.* **112**, 104080 (2020).
15. T. Aüllo, A. Ranchou-Peyruse, B. Ollivier, M. Magot, *Front. Microbiol.* **4**, 362 (2013).
16. C. Hubert *et al.*, *Science* **325**, 1541–1544 (2009).
17. S. Filippidou *et al.*, *Comput. Struct. Biotechnol. J.* **13**, 299–306 (2015).
18. L. Wörmer *et al.*, *Sci. Adv.* **5**, eaav1024 (2019).
19. A. R. Katritzky, A. R. Lapucha, M. Siskin, *Energy Fuels* **4**, 506–510 (1990).
20. J. Kallmeyer, A. Boetius, *Appl. Environ. Microbiol.* **70**, 1231–1233 (2004).
21. T. Holler *et al.*, *ISME J.* **5**, 1946–1956 (2011).
22. R. J. Parkes, B. A. Cragg, P. Wellsbury, *Hydrogeol. J.* **8**, 11–28 (2000).
23. P. Wellsbury *et al.*, *Nature* **388**, 573–576 (1997).
24. V. B. Heuer, J. W. Pohlman, M. E. Torres, M. Elvert, K.-U. Hinrichs, *Geochim. Cosmochim. Acta* **73**, 3323–3336 (2009).
25. D. Goevert, R. Conrad, *FEMS Microbiol. Ecol.* **71**, 218–225 (2010).
26. S. H. Brown, R. M. Kelly, *Appl. Environ. Microbiol.* **55**, 2086–2088 (1989).
27. D. E. Canfield, K. S. Habicht, B. Thamdrup, *Science* **288**, 658–661 (2000).
28. G. Z. Wang, A. J. Spivack, S. Rutherford, U. Manor, S. D'Hondt, *Geochim. Cosmochim. Acta* **72**, 3479–3488 (2008).
29. F. Beulig, H. Røy, C. Glombitza, B. B. Jørgensen, *Proc. Natl. Acad. Sci. U.S.A.* **115**, 367–372 (2018).
30. J. Dolfing, S. R. Larter, I. M. Head, *ISME J.* **2**, 442–452 (2008).
31. J. Kim *et al.*, *Geology* **47**, 535–539 (2019).
32. P. M. Fulton *et al.*, *Science* **342**, 1214–1217 (2013).
33. Y. Hamada *et al.*, *Prog. Earth Planet. Sci.* **5**, 70 (2018).
34. M. E. Torres *et al.*, *Geobiology* **13**, 562–580 (2015).
35. V. B. Heuer *et al.*, Dataset: Microbial abundance and activity at IODP Site C0023, Nankai Trough subduction zone. PANGAEA (2020); https://doi.org/10.1594/PANGAEA.923088.

ACKNOWLEDGMENTS

This research used samples and data provided by the International Ocean Discovery Program (IODP). The authors thank IODP and the Ministry of Education, Culture, Sports, Science, and Technology of Japan (MEXT) for providing an opportunity to explore the deep biosphere during Expedition 370. The expedition comprised simultaneous offshore and onshore work, conducted on the drilling vessel *DV Chikyu* and in the Kochi Core Center (KCC), respectively. We thank all operational and technical staff members on *Chikyu* and at KCC. In particular, we thank K. Akiyama, K. Aoike, N. Eguchi, M. Kyo, Y. Namba, and T. Sugihara for their knowledgeable support during project design; T. Saruhashi, I. Sawada, and T. Ikawa for successful drilling operations; and the Marine Works Japan, Co. for their technical support. We also thank K. Hagino and N. Tomioka at KCC for their contributions to sediment-age determination and electron microscopic

observations, respectively. This is a contribution to the Deep Carbon Observatory (DCO) and the Earth 4D: Subsurface Science and Exploration, CIFAR. **Funding:** This work was supported in part by the Japan Society for the Promotion of Science (JSPS) Strategic Fund for Strengthening Leading-Edge Research and Development (to JAMSTEC and F.I.); the JSPS Funding Program for Next Generation World-Leading Researchers (GR102 to F.I.); JSPS Grants-in-Aid for Scientific Research JP26251041, JP19H05503, and JP20K20429 (to F.I. and T.Ho.) and JP19H00730 (to Y.M., A.I., and T.Ho.); the Deutsche Forschungsgemeinschaft through projects 387745511 (to V.B.H.), 408178672 (to F.S.), 408249062 (to J.K.), 279667358, Hi 616-14-1 (to K.-U.H.), and through the Cluster of Excellence "The Ocean Floor – Earth's Uncharted Interface" (project 390741603), the IODP U.S. Science Support Program (National Science Foundation prime award OCE-1450528 to T.T.), and the Natural Environment Research Council awards NE/P015182/1 and NE/R003408/1 (to S.A.B. and H.M., respectively). Additional support enabling this project was provided by the DCO. **Author contributions:** K.-U.H., F.I., V.B.H., and Y.M. designed the research; V.B.H., F.I., and Y.M. lead IODP Expedition 370 as co-chief scientists; Y.K. and L.M. coordinated research operations during IODP Expedition 370; V.B.H., F.I., Y.M., A.J.S., B.V., T.T., F.B., F.S., S.T., S.A.B., M.C., S.H., T.Hi., K.H., T.Ho., A.I., H.I., N.K., M.Ka., L.L., H.M., H.-L.M., K.M., N.O., D.P., M.J.R., J.S., M.-Y.T., D.T.W., E.W., Y.Yamam., K.Y., R.R.A., C.G., Y.H., J.K., J.W., and L.W. performed research; Y.Yamad. and M.Ki. provided crucial methods; V.B.H., F.I., Y.M., A.J.S., B.V., T.T., F.B., F.S., S.T., L.W., and K.-U.H. analyzed data; and V.B.H. and K.-U.H. wrote the paper with input from all authors. **Competing interests:** None. **Data availability:** All shipboard data are documented and are openly accessible in the IODP Expedition 370 Proceedings (*13*), with references to the respective tables and figures given in the supplementary materials. All shore-based data are accessible in the PANGAEA database (*35*).

SUPPLEMENTARY MATERIALS

science.sciencemag.org/content/370/6521/1230/suppl/DC1
Materials and Methods
Supplementary Text
Figs. S1 to S10
Tables S1 and S2
References (*36*–*83*)
MDAR Reproducibility Checklist

View/request a protocol for this paper from *Bio-protocol*.

15 July 2020; accepted 13 October 2020
10.1126/science.abd7934

Real-Time PCR Systems

Bio-Rad Laboratories now offers the CFX Opus 96 and CFX Opus 384 Real-Time PCR Systems along with BR.io, a cloud-based instrument connectivity, data-management, and analysis platform. These systems represent the next generation of the company's CFX Real-Time PCR Systems, which are used in research and genomic testing as well as pathogen detection and infectious disease testing. A patent-pending block design delivers tight thermal uniformity for improved well-to-well consistency during real-time PCR experiments. A redesigned touchscreen interface and flexible connectivity options provide an intuitive, efficient experience for real-time PCR users. Bio-Rad's entire line of CFX systems have been instrumental in the company's global response to the COVID-19 pandemic.

Bio-Rad Laboratories
For info: 800-424-6723
bio-rad.com

Extracellular Vesicles RNA Purification System

EVeryRNA is a column-based, phenol-free way to purify the full range of RNAs hidden within extracellular vesicles (EVs)—even very small RNAs. EVeryRNA streamlines your workflows and is complete in less than 30 min. The EVeryRNA EV RNA Purification System captures RNAs with a wide distribution of lengths, including small RNAs, concentrated into a 10-µL final volume per reaction. It comes as a stand-alone product or bundled with ExoQuick, ExoQuick-TC, or SmartSEC Single. We also offer the EVeryRNA cDNA Synthesis & Pre-Amplification Kit, which is optimized to work with the EVeryRNA EV RNA Purification System.

System Biosciences
For info: 888-266-5066
systembio.com

High-Throughput Viral RNA extraction

The NucleoSpin 96 Virus kit from MACHEREY-NAGEL is designed for the extraction of viral nucleic acids—RNA and DNA viruses—from cell-free, biological fluids, such as saliva, urine, serum, or plasma, and from sample homogenates (particle-free supernatants), for example, from swabs, tissue, or stool. It uses a purification process based on binding nucleic acids to a silica membrane column in a high-throughput, 96-well format. The NucleoSpin 96 silica membrane extraction plates can be processed in about 60 min using vacuum or positive pressure in an automated laboratory setup, such as the Resolvex A200 positive-pressure workstation from Tecan.

MACHEREY-NAGEL
For info: 888-321-6224
www.mn-net.com

NGS Panel for Constitutional Cytogenetics

Oxford Gene Technology has launched a transformative NGS panel for constitutional cytogenetics research. The CytoSure Constitutional NGS Panel contains the most up-to-date, hand-curated content for intellectual disability and developmental delay research. Delivering accurate, reliable detection of copy number variations, single-nucleotide variations, insertion/deletions (indels), and loss of heterozygosity—including in mosaic samples—the panel combines the benefits of NGS and microarrays in one cost-effective assay. Data produced from the panel is of the highest quality and shows excellent concordance with arrays. The intuitive, user-friendly software means there is no need for large bioinformatics teams to work alongside labs for data analysis.

Oxford Gene Technology
For info: +44-(0)-1865-856800
www.ogt.com/cytosure-ngs

Electrophoresis System

miniPCR bio announces the launch of the GELATO, an integrated DNA analysis system. GELATO combines gel electrophoresis with transillumination technology, allowing for simultaneous nucleic acid separation and visualization in a single, compact system. Despite a small footprint, GELATO's range of casting options allows users to process up to 50 nucleic acid samples at a time. Its variable-voltage, built-in power supply allows for fast separation of DNA, and its integrated blue-light transilluminator makes it safe for use in all settings. GELATO features a cell-phone compatible documentation hood and a built-in cutting tray for direct gel excision. While it offers the flexibility and features that professional laboratory users expect, its user-friendly interface makes the system fit for the novice as well.

miniPCR bio
For info: 781-990-8727
www.minipcr.com

Whole-Genome Amplification Kits

ResolveDNA kits form the core of whole-genome sequencing workflows, enabling single-nucleotide variant and copy number variant analysis in application areas such as cancer genomics, cardiology, neurology, immunology, toxicology, and preimplantation genetic testing. The kits contain all the enzymes and reagents needed for versatile, scalable whole-genome amplification from single cells or ultralow DNA inputs. BioSkryb offers an end-to-end workflow solution, including TrailBlazer, a cloud-based bioinformatics platform that allows users to explore single-cell human genomic datasets generated with ResolveDNA products. TrailBlazer access is included with the purchase of a kit or the use of BioSkryb custom services.

BioSkryb
For info: 919-370-0841
bioskryb.com

Electronically submit your new product description or product literature information! Go to www.sciencemag.org/about/new-products-section for more information.

Newly offered instrumentation, apparatus, and laboratory materials of interest to researchers in all disciplines in academic, industrial, and governmental organizations are featured in this space. Emphasis is given to purpose, chief characteristics, and availability of products and materials. Endorsement by *Science* or AAAS of any products or materials mentioned is not implied. Additional information may be obtained from the manufacturer or supplier.

Founded in 1979, Tianjin University of Technology is located in the Southwest of Tianjin with a modern and ecological campus. Over the past 40 years, Tianjin University of Technology has developed into a multidisciplinary university highlighting engineering while promoting coordinated development of engineering, science, management, literature and art. In recent years, its comprehensive educational strength has been enhanced significantly, demonstrating the huge potential for further development. Chemistry, material science and engineering of the university have entered the top 1% of ESI ranking; the university ranks top 100 in the Nature Index among universities in China, which is the highest rank in the universities of Tianjin. Our university has been listed in the High-level Universities in Tianjin. Among the 25 young universities with the fastest rise in the Global Nature Index between 2015 and 2018, our university ranks 14th globally and 8th domestically.

Sticking to the philosophy of " talents are the first resource, and the more talents, the stronger TUT", we have made great efforts to implement the strategy of furthering its development with talents and introduced a high-level research team including well-known professors and young talents. To serve such an aim, Tianjin University of Technology has launched "The Mingli Scholars' Project ". We extend our sincere welcome to talents from home and abroad to join us and to work together towards our future in the new era.

Contact information

Ms.Zhang Mr. Zhu
Tel: +86-22-60215166
E-mail: lgzp@tjut.edu.cn

Greetings from Tianjin University of Technology!
Founded in the era of China's Reform and Opening up, Tianjin University of technology has undertaken the important mission of serving for the regional development of Tianjin. We are striving for the goal of building the first-class university in China with TUT characteristics. We know deeply that talents are the most important resources to promote the development of our university. We welcome excellent talents from different fields to join us and work together to create our future in the new era.

Best Wishes,
Yang Qingxin
President of Tianjin University of Technology
National candidate for "New Century Talents Project", Special Allowance Expert of the State Council, and Chairman of China Electrotechnical Society

ADVERTISEMENT

Jiangxi University of Traditional Chinese Medicine Invites Global Talent

Jiangxi University of Traditional Chinese Medicine was established in 1959, co-constructed by National Administration of Traditional Chinese Medicine and the People's Government of Jiangxi Province, as a national doctoral degree conferring institution. The school is located in Nanchang, the provincial capital of Jiangxi Province. At present, Jiangxi University of Traditional Chinese Medicine has 15 secondary colleges (schools), 3 directly affiliated hospitals, and 9 non-directly affiliated hospitals. The school offers 1 provincial first-level discipline, 2 national characteristic disciplines, 1 national comprehensive reform pilot discipline, 3 national first-level bachelor's degree disciplines. And there are 3 national scientific research platforms, 46 provincial and ministerial scientific research platforms including the Key Laboratory of the Ministry of Education, 1 academician workstation, 2 post-doctoral mobile stations, 1 workstation, and 4 provincial collaborative innovation centers.

In recent years, JXUTCM has achieved leapfrog development, and has become a higher school with distinctive characteristics of Chinese medicine education as the main body, with coordinated development of multiple disciplines, and an institution with combination of production, education and research.

For more information about us please visit: www.jxutcm.edu.cn

RESEARCH AREAS

Pharmacy, pharmacology, medicinal chemistry, biology, biomedical engineering, medicine, computer science and technology, information and communication engineering, psychology, food science and engineering, management and other disciplines related to the school development.

QUALIFICATION

I. Distinguished Talents with reputation among the world, such as the Academician of Chinese Academy of Sciences, Academician of Chinese Academy of Engineering.

II. Leading Talents with national-wide influence, winners of national talent projects such as National Prominent Education, and National Funds for Distinguished Youth.

III. Academic leaders with high influence in their research areas

A.Experts with high academic influence in various provinces (or municipalities directly under the Central Government), such as Distinguished professors of various provinces (or municipalities directly under the Central Government).

B. Senior professional and technical faculty working in the world's top 300 universities or with research discipline ranking in the top 100 (the internationally accepted ranking standards).

IV. Excellent docs

Talents with a doctoral degree in the world's top 300 universities or disciplines ranked in the world's top 100 (the internationally accepted ranking standards).

V. Post-doc faculty

Doctoral talents, having get the authorized doctoral degree for no more than 2 years.

SALARY & BENEFITS

Class I. Salary negotiable

Class II.

1. Annual salary: 1-1.3 million RMB
2.House purchase subsidies and resettlement expenses: 2-4 million RMB
3.Research start-up fund: 3-10 million RMB.

Class III.

1. Annual salary: 200 thousand -300 thousand RMB
2.House purchase subsidies and resettlement expenses: 350 thousand-1.1 million RMB
3.Research start-up fund: 100 thousand-800 thousand RMB.

Class IV.

1. Enjoy salary and welfare benefits according to the policy stipulated by the government
2.Research start-up fund and platform construction fees: 100 thousand RMB
3.House purchase subsidies and resettlement expenses: 300 thousand-500 thousand RMB

Class V(Post-doc faculty)

1.Annual salary: 250 thousand RMB
2.Enjoys other benefits and rewards of the school during the employment (2 years)
3. Those who are willing to stay in school to work will sign a stay agreement with the school, and enjoy housing subsidies and settlement expenses of 650 thousand RMB, and a research start-up fund of 100 thousand RMB.

APPLICATION

Applicants should send application materials (including but not limited to resume, application form, relevant qualification certification materials, scientific research results certification materials, etc.) to jzrsc2008@163.com.

Contact: Mr. Wu
Tel: 0791-87119112
E-mail: jzrsc2008@163.com
Jiangxi University of Traditional Chinese Medicine: **www.jxutcm.edu.cn**
Jiangxi University of Traditional Chinese Medicine Talent Office:
http://rsc.jxutcm.edu.cn

Forge ahead through a hundred years, now NCU portrays a new blueprint

High level Talent Introduction Plan of Nanchang University

It is located in the tourist resort - Jiangxi, surrounded by mountains and lakes, where the state leaders praised that "Crossing these blue hills adds nothing to one's years, the landscape here is beyond compare.";

It is located in Nanchang, a famous national historical and cultural city. Wang Bo, one of the Four Great Poets of Early Tang Dynasty, called it "God-blessed land rich in culture and for nurturing talented people";

It is a well-known institution of higher learning in China, established in 1921, after years of ups and downs and historical changes, it is about to celebrate its centenary;

It is a university co-constructed by the Ministry of Education and Jiangxi province, a key national "211 Project" university, and one the first batch of universities listed in National"Double First-Class"Initiative.

That is Nanchang University (NCU) , who always devoted to the motto "Seek strength from truth, foster virtue through education".

The history of NCU dates from Jiangxi Public Medical College and National Chungcheng University, which were founded in 1921 and 1940 respectively. In 1993, Jiangxi University merged with Jiangxi Industrial University into Nanchang University. In 2005, NCU and Jiangxi Medical College merged to form the new NCU, unveiling it a new page of reform and development.

The year of 2021 marks its 100th anniversary. Now NCU provides an excellent platform for aspiring young people to realize their ambitions!

Firstly listed in the "Double First-Class" Initiative, with strong developing momentum

The subjects of Chemistry, Clinical Medicine, Agricultural Science (mainly food science and engineering), Engineering, Materials Science, Pharmacology and Toxicology, Biology and Biochemistry have entered top 1% of the ESI world rankings, of which Agricultural Science (mainly food science and engineering) ranks the top 1.3‰, the Clinical medicine ranks the top 2.85‰ , and the Chemistry ranks the top 3.64‰. In the 4th round of national subject evaluation, the subject of Food Science and Engineering ranks in the 3rd place in China.

Full Construction in Subjects, with remarkable innovative achievements

NCU now has 96 undergraduate majors with 12 subjects categories, 3 national key (cultivation) disciplines, 15 first-level subjects with doctor's degree authorization, 47 first-level subjects with master's degree authorization, 1 professional doctoral degree category and 28 master's professional degree category and 11 postdoctoral scientific research stations. NCU also has 5 directly affiliated hospitals and a total of 9 national key clinical disciplines.

TALENT INTRODUCTION POLICY

1.Generous Rewards for High-level Talent

Distinguished Talent

What we offer: Pre-tax annual salary of 1.8-2 million yuan, house purchase subsidies and resettlement expenses no less than 5 million yuan, scientific research subsidies negotiable for each one person, flexible working environment, academic team and scientific research assistants.

Academic Leaders

What we offer: Pre-tax annual salary of 800 thousand-1.2 million yuan, house purchase subsidies and resettlement expenses no less than 1.8 million yuan, scientific research subsidies negotiable for each one person, flexible working environment, academic team and scientific research assistants.

Group leaders

What we offer: Pre-tax annual salary of 500-800 thousand yuan, house purchase subsidies and resettlement expenses 1-1.8 million yuan, scientific research subsidies negotiable for each one person.

Outstanding Scholars

What we offer: Pre-tax annual salary of 300-500 thousand yuan; house purchase subsidies and resettlement expenses 500 thousand-1 million yuan; scientific research subsidies negotiable for each one person.

FACULTIES WITH MULTIPLE SUBJECTS

Faculty of Humanities

Subjects: Chinese Language and Literature, Foreign Language and Literature, Journalism and Communication

Faculty of Social Science

Subjects: Law, Applied Economics, Theoretical Economics, Sociology, Politics, Management Science and Engineering, Tourism Management, Exhibition Economy and Management, Hotel Management, Marxist Theory

Faculty of Science and Engineering (Division I)

Subjects: Luminescent Materials and Devices, Ferroelectric Materials and Chemistry, Space Science and Technology, Energy Materials and Devices, Ultra-high Temperature Materials and Equipment, Information Materials and Devices, Rare Earth Materials, Basic Mathematics, Computational Mathematics, Condensed Matter Physics, Plasma Physics, Optics, Synthesis and Catalysis, Intelligent Manufacturing Engineering, Mechanical Engineering, Material Shaping and Control, Information and Communication Engineering, Computer Science and Technology, Electrical Engineering, Intelligent Technology and Big Data, Software Engineering, Cyber Security, etc.

Faculty of Science and Engineering (Division II)

Subjects: Food Science and Engineering, Biology, Botany, Ecology, Aquaculture, Environmental Science and Engineering, Chemical Engineering and Technology, Process Equipment and Control Engineering, Resource Cycle Science and Engineering, Mechanics

Faculty of Medicine

Subjects: Basic Medicine, Clinical Medicine, Pharmacy, Nursing, Public Health and Preventive Medicine, etc.

APPLICATION

1. Applicants may log on to the recruitment system of Nanchang University Personnel Office http://zpjob.acabridge.cn/school/526 (Acabridge) to select the position and apply;
2. Those who pass the school primary selection, will be contacted to fill in the application form, and provide materials such as representative academic achievements, recommendation letters and in the end communicate with the school.

CONTACT

Contact: Mr. Yang, Mr. Chen
Tel: +86-791-83969074
Email: rscrsk@ncu.edu.cn
Address: No. 999 Xuefu Avenue, Honggutan New District, Nanchang, Jiangxi Province

ScienceCareers online @sciencecareers.org

U.S. FOOD & DRUG ADMINISTRATION

STAFF FELLOW
CELL THERAPY REVIEW SCIENTIST

OFFICE OF TISSUES AND ADVANCED THERAPIES (OTAT)
CENTER FOR BIOLOGICS EVALUATION
AND RESEARCH (CBER)
FOOD AND DRUG ADMINISTRATION (FDA)
DEPARTMENT OF HEALTH AND HUMAN SERVICES (HHS)

The FDA's Center for Biologics Evaluation and Research (CBER), Office of Tissues and Advanced Therapies' (OTAT), Division of Cellular and Gene Therapies (DCGT), Cell Therapies Branch (CTB) is recruiting **full-time review scientists**. DCGT is strongly committed to bringing FDA and other scientists, patient advocates, and the public together in partnership to develop new therapies for the 21st Century, while protecting human subjects and ensuring product safety. The candidate will be a part of a cutting-edge and fast-paced scientific and regulatory environment.

Responsibilities: As the selected candidate, you will have the opportunity to:

- Perform scientific review, interpretation, and documentation of product manufacturing data to evaluate the safety and quality of cell therapy products (e.g., stem cells, cancer vaccines, cellular immunotherapies, engineered tissue, medical devices) in regulatory submissions to FDA.
- Contribute to guidance and policy development activities relevant to cell therapy.

Basic Qualifications: Ph.D. or equivalent advanced degree with a strong research background in cell therapy, cell and stem cell biology, microbiology, cellular immunology, cancer biology, regenerative medicine, and/or biomedical engineering. Occupational series which may be considered include **General Natural Resources Management and Biological Sciences (0401), Microbiology (0403), and Biomedical Engineering (0858)**. Please refer to the link for each occupational series for more information regarding specific education requirements.

Additional Qualifications: Candidates are expected to be proficient in applying relevant scientific knowledge and research experience to support multi-disciplinary scientific and review of regulatory submissions. In addition, the candidate must have strong collaborative skills, excellent written and oral communication skills, and evidence of leadership potential.

Salary: Salary is commensurate with education/experience.

Location: FDA White Oak Campus in Silver Spring, MD

Conditions of Employment: This position will be filled through the Service Fellowship program. The appointment provides up to (4) years with opportunities for renewal. **Applications will ONLY be accepted from U.S. citizens and/or permanent residents (green card)**. For more information about the FDA's Staff Fellowship program, please visit the FDA's Jobs Page at **www.fda.gov/jobs**.

How to Apply: Submit a statement of interest, resume or curriculum vitae (CV) detailing relevant experience, transcripts, names/contact information for three references, proof of U.S. citizenship or lawful permanent residency status, and other supporting documentations to Melanie Eacho at **melanie.eacho@fda.hhs.gov**. Applications will be accepted through **January 10, 2021**.
Please reference **Job Code: OTAT-21-02-SCI**.

Department of health and human services is an equal opportunity employer smoke free environment

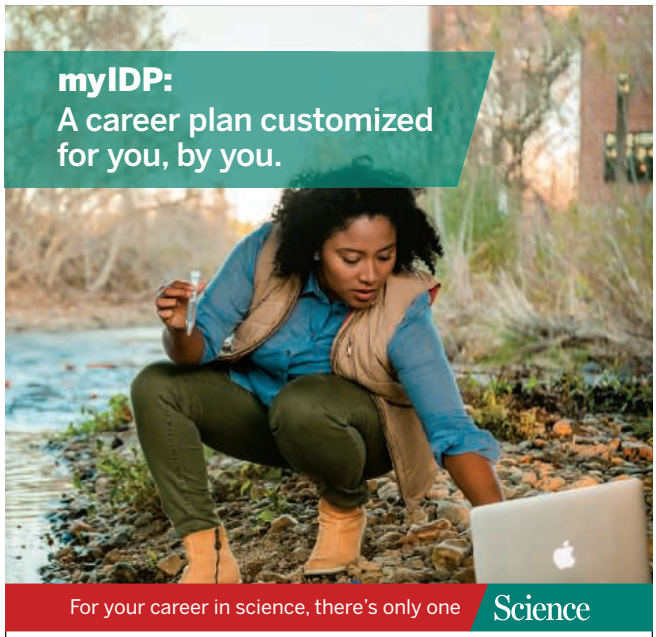

Features in myIDP include:

- Exercises to help you examine your skills, interests, and values.
- A list of 20 scientific career paths with a prediction of which ones best fit your skills and interests.
- A tool for setting strategic goals for the coming year, with optional reminders to keep you on track.
- Articles and resources to guide you through the process.
- Options to save materials online and print them for further review and discussion.
- Ability to select which portion of your IDP you wish to share with advisors, mentors, or others.
- A certificate of completion for users that finish myIDP.

myIDP

Visit the website and start planning today!
myIDP.sciencecareers.org

Science Careers AAAS In partnership with:

UCSF University of California San Francisco
UIC
BURROUGHS WELLCOME FUND
UMASS University of Massachusetts Medical School
FASEB Federation of American Societies for Experimental Biology

UNIVERSITÉ DE GENÈVE

The Faculty of Medicine of the University of Geneva
is seeking to fill a position of:

FULL OR ASSOCIATE PROFESSOR
IN THE FIELD OF BACTERIOLOGY

CHARGE: This full-time position will involve teaching in bacteriology at the bachelor, master and postgraduate level, as well as supervising Masters' and doctoral theses. The incumbent will undertake fundamental research in this area (with a preferred emphasis on antibiotic resistance mechanisms) at the highest national and international levels and secure external funding. He/She will be an active member of the vibrant research community of the Department of Microbiology and Molecular Medicine and contribute to its strong academic renown. The incumbent will also take up administrative and organizational duties within that Department as well as the Faculty of Medicine.

He/She is also expected to show the capacity to carry out a transversal mission through strong collaboration with partner services.

REQUIREMENTS:
PhD, MD-PhD or equivalent is required.
Full postgraduate training in bacteriology is an advantage.
Previous teaching and independent research experience.
Publications in leading international journals.

STARTING DATE: October 1st 2021, or according to agreement.

Mandatory online registration before **January 24th 2021** at: **http://www.unige.ch/academ**

Additional information may be obtained from:
Viviane.burghardt@unige.ch

Women are encouraged to apply

TEXAS A&M UNIVERSITY
Biology

The Department of Biology at Texas A&M University (TAMU) invites applications for tenure-track **assistant** or tenured **associate professor** positions in biological timing (3 positions) and prokaryotic/eukaryotic microbiology (1 position).

All candidates are required to have a Ph.D. in biology or related field, and we desire candidates who display uniqueness, creativity, and excellence in the pursuit of innovative research. Expectations for the successful candidates are to develop an externally funded research program and to teach undergraduate and graduate courses.

This search represents the beginning of a multi-year strategic hiring effort to move several cutting-edge research areas within the biological sciences at Texas A&M University to preeminence. This is an exciting opportunity for new hires to be a part of developing interdisciplinary teams to tackle important problems in biology. Please see **www.bio.tamu.edu** for more information about our department.

For full consideration, applicants should submit a letter of intent, curriculum vitae, a statement of research and teaching interests, a statement addressing past and/or potential contributions to diversity and inclusion through teaching, professional activity, and/or service, and three letters of recommendation by **December 15, 2020**. Application materials must be submitted online at **http://apply.interfolio.com/81015**.

If you have questions about this search, please direct e-mails to Dr. Deborah Bell-Pedersen, Chair of the Search Committee, at **facultysearch@bio.tamu.edu**.

Bryan-College Station, home to Texas A&M University, is a vibrant, dynamic, and rapidly growing community that offers cultural diversity, arts and entertainment, job opportunities, and overall quality of life. Located in the heart of the Houston-Dallas-Austin triangle, the region offers the modern amenities of a big city with a warm, small-town charm, and the community's low cost of living is advantageous to the student and general populations, making it an ideal place to live.

Texas A&M University is committed to enriching the learning and working environment for all visitors, students, faculty, and staff by promoting a culture that embraces inclusion, diversity, equity, and accountability. Diverse perspectives, talents, and identities are vital to accomplishing our mission and living our core values.

Equal Opportunity/AffirmativeAction/Veterans/Disability
Employer committed to diversity.

ScienceCareers online @sciencecareers.org

By **Bec Roldan**

Coming out

My hands shook as I sat down to write the email. "I wanted to let y'all know that I use they/them/theirs pronouns," I typed. "I know that gender-neutral/non-binary pronouns are not a common staple in our language, but I ask that you please do your best to respect them." Proclaiming my identity—one I had still not quite figured out yet—to a group of co-workers made me feel incredibly vulnerable. But I knew that if I wanted to survive graduate school, I needed to be open with my labmates, no matter how scared I was. After a few anxious moments, I clicked "send."

During the months leading up to graduate school, I had been exploring the idea of using gender-neutral pronouns. I didn't know whether they'd suit me; I just knew the words "she" and "woman" didn't feel quite right when they were used to describe me.

I had come out as queer during my last year of college, thanks in large part to support from the tight-knit queer community I'd discovered there. Starting graduate school at a new institution, I wouldn't have that support system. I feared I'd be navigating my journey to discover myself completely on my own.

Those fears evaporated when I learned that roughly one-quarter of my Ph.D. cohort identified as LGBTQ. We gravitated toward one another, and I decided to come out as nonbinary to some of them. From then on, whenever our small group got together, my friends would say "they" when speaking about me. The more I heard that word roll off their tongues, the more I felt at home in my own body.

"I'm constantly learning how to exist in this world as my true self."

As time wore on, it became increasingly difficult to show up to work and exist as a gender that no longer felt like my own. Hiding what I knew to be true about myself was exhausting and painful. So, at the start of my second semester, I decided I needed to come out to my adviser and labmates.

A flurry of questions ran through my mind: "What should I tell them? How long will it take colleagues to get used to my pronouns? Will some people choose to actively misgender me?" For advice, I turned to my friend Isaac, who is a year ahead of me in my program and is nonbinary. We met up for a coffee and they told me their own story of coming out to their lab. It was a relief to hear that their experience had been largely positive, and they put me at ease about my own decision.

I set up a time to meet with my adviser the following day. When I stepped into his office, he could tell how nervous I was, and he was concerned. I told him not to worry. As soon as I informed him about my identity, he was supportive, asking what he could do to help me come out to others in the lab. For the first time in months, my fears eased.

I sent the email to my labmates the next morning, not knowing what to expect. That day was surprisingly quiet. But the 6 months that have passed since then haven't always been easy. The word "she" has slipped out in conversations more times than I can count, and every time, it feels like a knife is being stabbed into my stomach. Whether malicious or accidental, the impact is always the same: I feel as though the act of misgendering erases the person I have worked so long and hard to become. After one particularly tough week, I cried in the bathroom and left work early.

But I've also been heartened to see how many people have stepped up to support me. My adviser and closest friends in the lab quickly caught on to my pronouns, and they soon took the responsibility to correct others when they misgender me. They've listened to me patiently as I've explained how transphobia makes it hard for me to show up to work. And my adviser invited Isaac to speak to our lab group about gender identity and inclusivity, so I didn't have to carry the burden of education and advocacy all by myself.

I'm still navigating my path forward. But I will never regret my decision to come out. I'm constantly learning how to exist in this world as my true self, and I know I'm not on this journey alone. Many friends and colleagues—both cisgender and transgender, queer and straight—are standing by me every step of the way. That means the world to me. ■

Bec Roldan is a Ph.D. student at the University of Michigan, Ann Arbor.

ILLUSTRATION: ROBERT NEUBECKER

Published by AAAS